UNIVERSIDADE D
COIMBRA

João Paulo Martins Brito

Desenvolvimento e Implementação de Potenciais Plásticos de base Numérica para Materiais Metálicos Anisotrópicos Porosos

Tese no âmbito do Doutoramento em Engenharia Mecânica no ramo de Sistemas Avançados de Produção orientada pela Professora Doutora Marta Cristina Cardoso de Oliveira e pelo Professor Doutor José Luís de Carvalho Martins Alves e apresentada ao Departamento de Engenharia Mecânica da Faculdade de Ciências e Tecnologia da Universidade de Coimbra

Dezembro de 2023

UNIVERSIDADE D
COIMBRA

NUMERICAL-BASED PLASTIC POTENTIALS FOR ANISOTROPIC POROUS METALLIC MATERIALS: DEVELOPMENT AND IMPLEMENTATION

by

JOÃO PAULO MARTINS BRITO

Dissertation submitted to the Department of Mechanical Engineering of the University of Coimbra in partial fulfilment of the requirements for the

DOCTORAL DEGREE IN MECHANICAL ENGINEERING

Scientific advisers:	Prof. Marta Cristina Cardoso de Oliveira
	Prof. José Luís de Carvalho Martins Alves
Chair of Committee:	Prof. José Domingos Moreira da Costa
Committee Members:	Prof. Fernando Jorge Ventura Antunes
	Prof. Francisco Manuel Andrade Pires
	Prof. Gabriela Tamara Vincze
	Prof. Maria Beatriz Cipriano de Jesus Silva

December 2023

This research was carried out under the doctoral grant ref SFRH/BD/144347/2019 of the Portuguese Foundation for Science and Technology (FCT, I. P.), founded by the Portuguese state budget through the Ministry for Science, Technology and Higher Education (MCTES) and cofounded by the European Social Fund (ESF) through the PORTUGAL2020 programme, namely the Human Capital Operational Programme (PO CH).

Aos meus pais.

Acknowledgements

This work was only possible thanks to a number of people who, in one way or the other, assisted and encouraged its realisation, to whom I must express my gratitude. The reader will excuse my decision to express the following acknowledgements in my mother tongue, which I find more personal.

Antes de mais, quero expressar o meu sincero agradecimento aos meus orientadores científicos.

À Professa Marta Oliveira pelo desafio que lançou e pela oportunidade de realizar o programa doutoral sob a sua orientação. Pelo constante acompanhamento, zelo, apoio e entusiasmo. Por proporcionar as melhores condições para a realização deste trabalho. Pela sempre pronta disponibilidade e paciência. Pelos comentários, rigor científico, espírito crítico e revisão minuciosa. Pela confiança que depositou em mim. O meu muito obrigado.

Ao Professor José Luís Alves, pelas dezenas de reuniões virtuais nas quais proporcionou um precioso auxílio. Os seus comentários e sugestões em relação ao trabalho em geral e sobre os aspetos algorítmicos, em particular, foram cruciais para a concretização desta dissertação. Pela sua disponibilidade, orientação e encorajamento, o meu muito obrigado.

Foi um privilégio trabalhar com os meus orientadores.

Gostaria ainda de agradecer:

Ao Centro de Engenharia Mecânica, Materiais e Processos (CEMMPRE), na pessoa do seu presidente, Professor Albano Cavaleiro, pelos meios disponibilizados que garantiram todas as condições para que o plano de trabalhos fosse realizado com sucesso e pelo apoio financeiro concedido para a participação em conferências.

Aos meus colegas da Universidade de Coimbra e aos restantes membros do centro de investigação, pela camaradagem, boa disposição e pelas inúmeras discussões científicas e não-científicas.

À Fundação para a Ciência e Tecnologia (FCT, IP) pelo apoio financeiro concedido através da Bolsa de Doutoramento SFRH/BD/144347/2019.

À minha família, em especial à Beatriz, pelo apoio incondicional e encorajamento não só neste trabalho, mas durante todo o meu percurso académico. Sem eles, esta jornada seria muito mais difícil.

Abstract

Modelling the plastic deformation and the onset of fracture of structural and functional ductile metallic materials is a long-standing problem in the field of solid mechanics. Given the intimate relationship between the porosity degree and the occurrence of failure in a ductile material, the framework of porous media offers a powerful and natural approach for modelling damage phenomena. Traditionally, the development of plastic potentials for porous solids based on homogenization theories is aimed at obtaining a final expression in analytical form. This is in line with the well-known micromechanical-inspired criterion of Gurson (1977). However, due to the complexity of the upscaling analysis, obtaining closed-form expressions often entails the adoption of several simplification hypotheses, or may even be impossible. This is particularly true when dealing with complex plasticity criteria for the matrix (i.e. the dense phase of the porous aggregate). Opportunely, the ever-increasing computational power-cost ratio has been empowering the adoption of a numerical approach to this problem, which, by its very nature, bypass the above limitations, while allowing the numerical simulation of large-scale engineering problems to be carried out in a reasonable computational time.

The aim of this dissertation is to develop and implement numerical-based plastic potentials for ductile porous materials whose matrix behaviour is governed by advanced orthotropic criteria which account both for tension-compression asymmetry and an arbitrary number of linear transformations. The analysis follows the kinematical Hill-Mandel homogenization scheme and considers porous solids containing randomly distributed spherical voids. The matrix behaviour is described by the Plunkett *et al.* (2008) orthotropic yield criterion, and two types of trial velocity fields are adopted: those of Rice and Tracey (1969); and the so-called Eshelby-type fields, based on the exterior point solution of the well-known Eshelby (1959) inclusion problem for the particular case of a spherical inclusion. The microscale strain-rate potential is a key ingredient of the upscaling analysis. The exact dual of non-quadratic stress potential of Plunkett *et al.* (2008) is therefore derived.

The novelty of this contribution is that the macroscopic potentials are no longer evaluated analytically, but by numerical integration of the relevant local fields entering the homogenization scheme. Hence, an efficient cubature method for the volume averaging operations over the spherical domain is developed. The proposed method is grounded on the split of the volume integrals into surface integrals over the spherical surfaces and one-dimensional integrals over the radial direction. The former are evaluated based on the theory of spherical *t*-designs and the latter are determined using a tailor-made adaptative integration scheme based on cubic splines. It is shown that the computational cost of evaluating

the proposed macroscopic strain-rate potentials, with a tolerance compatible with that usually used in nonlinear computational continuum mechanics, is not prohibitively expensive.

Finite element-based limit analyses on spherical unit cells are performed in order to assess the accuracy of the developed criteria. The results show that the proposed numerical-based potentials are in very good agreement with the finite element results and that their predictive performance is far superior to that of analytical criteria in the literature.

The numerical-based criteria proposed in this work are formulated with the aim of being easily incorporated into actual engineering simulations. In order to demonstrate this process, these are implemented in a large-strain constitutive framework grounded on an hyperelastic-based elastic-plastic multiplicative split formulation coupled with a strain-rate potential flow rule for describing the plastic dissipation. The efficiency and performance of the developed constitutive framework is assessed by means of two application examples with industrial relevance.

Undoubtedly, analytical solutions are preferable, both from a conceptual and computational point of view. However, if these are obtained at the cost of an oversimplification of the underlying problem, then their relevance is questionable. This work demonstrates that existing analytical porous criteria are incapable of representing important porosity-induced micro-macro plasticity couplings observed in unit cell micromechanical studies. The key conclusion is that these limitations are not attributable to the quality of the employed velocity fields, but to the simplification hypotheses, whether or not upper-bound preserving, employed in the respective analytical analyses which, ultimately, erase the intrinsic modelling capability of the homogenization. This clearly emphasizes the value of pursuing a numerical-based homogenization approach, since the predicted micro-macro plasticity couplings are as accurate as permitted by the scale transition operation.

Keywords: Plastic potentials, Porous solids, Plastic anisotropy, Tension-compression asymmetry, Ductile damage

Resumo

A modelação da deformação plástica e da fratura de materiais dúcteis metálicos é um problema de longa data no domínio da mecânica dos sólidos. Dada a relação íntima entre o teor de porosidade e a ocorrência de rutura num material dúctil, a teoria dos meios porosos constitui uma abordagem poderosa e natural para modelar fenómenos de dano. Tradicionalmente, o desenvolvimento de potenciais plásticos para sólidos porosos com base em teorias de homogeneização é efetuado de modo a obter uma expressão final analítica. Esta abordagem está em consonância com a conhecida teoria de Gurson (1977). No entanto, devido à complexidade da análise de homogeneização, a obtenção de expressões analíticas implica frequentemente a adoção de várias hipóteses de simplificação, ou pode mesmo ser impossível. Isto é especialmente evidente quando são considerados critérios de plasticidade complexos para a descrever o comportamento da matriz. Oportunamente, o aumento constante da relação potência/custo computacional permite atualmente a adoção de uma abordagem numérica para este problema, que, pela sua própria natureza, contorna as limitações acima referidas permitindo, no entanto, que a simulação numérica de problemas de engenharia seja realizada num tempo computacional razoável.

O objetivo desta dissertação é desenvolver e implementar potenciais plásticos de base numérica para materiais porosos dúcteis cujo comportamento da matriz é regido por critérios ortotrópicos avançados, que têm em conta a assimetria tensão-compressão e um número arbitrário de transformações lineares. A análise segue o método de homogeneização cinemática de Hill-Mandel para o caso de sólidos porosos com vazios esféricos distribuídos aleatoriamente. O comportamento da matriz é descrito pelo critério de plasticidade ortotrópico de Plunkett *et al.* (2008) e são adotados dois tipos de campos de velocidade de ensaio: os de Rice e Tracey (1969); e os ditos campos do tipo Eshelby, baseados na solução para os pontos exteriores do problema da inclusão de Eshelby (1959). O potencial de taxa de deformação à microescala é um ingrediente fundamental da análise de homogeneização. O conjugado exato do potencial plástico não quadrático de Plunkett *et al.* (2008) é, portanto, inicialmente derivado.

A novidade desta contribuição assenta no facto dos potenciais macroscópicos deixarem de ser avaliados analiticamente, mas sim através da integração numérica dos campos locais que entram no problema de homogeneização. Assim, foi desenvolvido um método de integração numérica eficiente para as operações de cálculo da média sobre o volume do domínio esférico. O método proposto baseia-se na divisão dos integrais de volume em integrais de superfície sobre as superfícies esféricas e integrais unidimensionais sobre a direção radial. Os primeiros são determinados com base na teoria dos *designs* esféricos e os últimos através um esquema de integração adaptativo baseado em *splines* cúbicas. Demonstra-se que o custo computacional para a determinação dos potenciais desenvolvidos, com uma

tolerância compatível com a habitualmente utilizada no domínio da mecânica computacional não-linear, não é proibitivamente alto.

De modo a avaliar a precisão dos critérios desenvolvidos, realizam-se análises de elementos finitos em células unitárias esféricas. Os resultados mostram que os potenciais numéricos propostos estão em excelente concordância com os resultados das células unitárias e que o seu desempenho preditivo é muito superior ao dos critérios analíticos na literatura.

Os critérios de base numérica propostos neste trabalho foram formulados com o objetivo de serem facilmente incorporados em simulações de engenharia. Para demonstrar este procedimento, estes critérios são implementados no âmbito de uma formulação constitutiva de grandes deformações, baseada na decomposição multiplicativa elástico-plástica com uma lei hiperelástica, associada a uma lei de plasticidade associada baseada no potencial de taxa de deformação para descrever a dissipação plástica. O desempenho e a eficiência da formulação constitutiva proposta são avaliados através de exemplos de aplicação com relevância industrial.

Incontestavelmente, as soluções analíticas são preferíveis, tanto do ponto de vista conceptual como computacional. No entanto, se estas forem obtidas à custa de uma simplificação excessiva do problema subjacente, então a sua pertinência é questionável. Este trabalho mostra que os critérios analíticos para sólidos porosos existentes na literatura são incapazes de representar a complexa relação entre a plasticidade à micro- e macro- escala induzida pela porosidade. A principal conclusão é que estas limitações não são imputáveis à qualidade dos campos de teste utilizados, mas sim às hipóteses de simplificação assumidas nas respetivas análises analíticas que, em última análise, suprimem a capacidade de modelação inerente ao processo de homogeneização. Isto reforça claramente o interesse em adotar uma abordagem numérica, uma vez que, neste caso, a qualidade das previsões é tão exata quanto o permitido pela operação de transição de escala.

Palavras-chave: Potenciais plásticos, Sólidos porosos, Anisotropia plástica, Assimetria tração-compressão, Dano dúctil

Contents

List of Figures

List of Tables

List of Boxes

Notation

General convention of symbols

The mathematical meaning associated with adopted font styles is given in the following. Some exceptions do occur in the text; however, these are explicitly marked and no conflict arises.

a, A, α...	Scalars and scalar-valued functions in $\mathbb{R}$ and indices of tensorial quantities
$\underline{\boldsymbol{a}}, \underline{\boldsymbol{A}}, \underline{\boldsymbol{\alpha}}$...	Points, vectors and vector-valued functions in $\mathbb{R}^3$
$\boldsymbol{a}, \boldsymbol{A}, \boldsymbol{\alpha}$...	Second-order tensors and tensor-valued functions in $\mathbb{R}^3$
$\boldsymbol{\mathcal{A}}$...	Fourth-order tensors and tensor-valued functions in $\mathbb{R}^3$
$\mathcal{A}$...	Spaces, sets, groups or bodies
$\underline{\mathbf{a}}, \underline{\mathbf{A}}, \underline{\boldsymbol{\alpha}}$...	Computational column array representing vectors or the pseudo-vectorial representation of second-order tensors in Voigt notation
$\mathbf{a}, \mathbf{A}, \boldsymbol{\alpha}$...	Computational matrix array representing second-order tensors or the pseudo-matrix representation of fourth-order tensors in Voigt notation

Operators and functions

$\det(\cdot)$	Determinant operator
$\mathrm{div}_p(\cdot)$	Divergence operator with respect to p
$\nabla_p(\cdot)$	Gradient operator with respect to p
$\langle(\cdot)\rangle_{\mathcal{P}}$	Averaging over (the surface or volume) domain $\mathcal{P}$ of the field $(\cdot)$
$\mathrm{vol}(\cdot)$	Volume of a domain $(\cdot)$
$\bar{\mathcal{I}}_M(\cdot)$	Characteristic function of a subset M (convex analysis)
$\mathcal{L}_{\mathrm{LF}}(\cdot)$	Legendre-Fenchel transformation
$\mathcal{L}(\cdot)$	Lagrangian function
$\exp(\cdot)$	Exponential and tensor exponential
$\ln(\cdot)$	Natural logarithm and tensor logarithm
$\mathrm{diag}(\cdot)$	Assignment of a vector to a square diagonal second-order tensor or matrix
$\mathrm{eig}(\cdot)$	Diagonal tensor whose diagonal components are the eigenvalues of $(\cdot)$
$\mathrm{sgn}(\cdot)$	Signum function
$\min(\cdot)$	Minimum function

$\max(\cdot)$	Maximum function
$\inf(\cdot)$	Infimum function
$\sup(\cdot)$	Supremum function
$\cosh(\cdot)$	Hyperbolic cosine
$\text{skew}(\cdot)$	Skew-symmetric part of $(\cdot)$
$\text{sym}(\cdot)$	Skew-symmetric part of $(\cdot)$
$(\cdot)'$	Deviatoric part of $(\cdot)$
$(\cdot)_{\text{m}}$	Hydrostatic part of $(\cdot)$, i.e. $(\cdot)_{\text{m}} = \text{tr}(\cdot)/3$
$(\cdot)^{\text{T}}$	Transpose of $(\cdot)$
$(\cdot)^{-1}$	Inverse and tensor inverse
$(\cdot)^{-1}_{\text{dev}}$	Deviatoric inverse of an arbitrary tensor $(\cdot)$ or its pseudo-matrix notation
$\text{tr}(\cdot)$	Trace of $(\cdot)$
$\Delta(\cdot)$	Increment of $(\cdot)$ (typically a FE time increment)
$\delta(\cdot)$	Iterative (quasi)-Newton increment of $(\cdot)$
$D(\cdot)$	Increment of $(\cdot)$ within FE equilibrium iterations
$d(\cdot)$	Infinitesimal increment of $(\cdot)$
$\partial(\cdot)$	Boundary of the domain $(\cdot)$; Subdifferential operation (Chapter 4)
$\partial(\cdot)/\partial p$	Partial derivative with respect to p
$I(\cdot)$	Exact integral of $(\cdot)$
$Q_N(\cdot)$	Approximate integral of $(\cdot)$ with a positive weight quadrature rule with N points
$\dot{(\cdot)}$	Material time derivative of $(\cdot)$
$\underline{\boldsymbol{a}} \cdot \underline{\boldsymbol{b}}$	Single contraction of two arbitrary vectors $(\underline{\boldsymbol{a}}, \underline{\boldsymbol{b}})$
$\boldsymbol{a} : \boldsymbol{b}$	Double contraction of two arbitrary tensors $(\boldsymbol{a}, \boldsymbol{b})$
$\underline{\boldsymbol{a}} \times \underline{\boldsymbol{b}}$	Cross product of two arbitrary vectors $(\underline{\boldsymbol{a}}, \underline{\boldsymbol{b}})$
$\boldsymbol{a} \otimes \boldsymbol{b}$	Tensor product of two arbitrary tensors $(\boldsymbol{a}, \boldsymbol{b})$
$\lvert(\cdot)\rvert$	Norm (absolute value) of a scalar $(\cdot)$
$\lvert(\cdot)\rvert^p$	Element-wise absolute value operation to the power p of an arbitrary tensor $(\cdot)$
$\lVert\underline{\boldsymbol{a}}\rVert_p$	p-norm of an arbitrary vectors $\underline{\boldsymbol{a}}$
$\lVert\boldsymbol{a}\rVert_p$	p-norm of an arbitrary second-order tensor or matrix $\boldsymbol{a}$
$\lVert\boldsymbol{a}\rVert_{\text{vM}}$	von Mises norm of an arbitrary second-order tensor or matrix $\boldsymbol{a}$
$\mathcal{O}(\cdot)$	In the order of $(\cdot)$
$a := b$	Assignment operation in computational algorithms
$a \leftarrow b$	General assignment operation
$a \triangleq b$	a is by definition equal to b

$a \cong b$	a is approximately equal to b
$a \equiv b$	a is identical to b, i.e., an equality that holds regardless of the values of the variables

Indices

$(\cdot)_0$	Initial value; Relative to initial configuration (Chapter 7)
$(\cdot)_\mathrm{f}$	Final value
$(\cdot)_t$	Field at instant t
$(\cdot)_\mathrm{vM}$	Relative to the von Mises norm
$(\cdot)_\mathrm{Caz}$	Relative to Cazacu *et al.* (2010) criterion
$(\cdot)_\mathrm{iso}$	Relative the isotropic case
$(\cdot)^\mathrm{e}$	Elastic part/contribution of $(\cdot)$
$(\cdot)^\mathrm{p}$	Elastic part/contribution of $(\cdot)$
$(\cdot)_n$	Relative to the reference configuration of the incremental problem
$(\cdot)_{n+1}$	Relative to the current configuration of the incremental problem
$(\cdot)^+$	An upper-bound of $(\cdot)$
$(\cdot)^\mathrm{E}$	Relative to the Eshelby-type fields
$(\cdot)^\mathrm{RT}$	Relative to the Rice and Tracey (1969) fields
$(\cdot)^{(n)}$	Relative to the n-th orthotropic transformation of the Plunkett *et al.* (2008) criterion
$(\cdot)_\mathrm{m}$ or $(\cdot)_\mathrm{hid}$	Hydrostatic part of $(\cdot)$
$(\cdot)_\mathrm{dev}$	Deviatoric part of $(\cdot)$
$(\cdot)_\mathrm{eq}$	Equivalent quantity of $(\cdot)$
$(\cdot)_\mathrm{T}$	Relative to a uniaxial tensile loading
$(\cdot)_\mathrm{C}$	Relative to a uniaxial compressive loading
$(\cdot)_1^\mathrm{T}$	Relative to a uniaxial tensile loading along the 1-direction of orthotropy
$(\cdot)_1^\mathrm{C}$	Relative to a uniaxial compressive loading along the 1-direction of orthotropy
$(\cdot)^{(5)}$	Tensorial quantity in the auxiliary pentadimensional space (Appendix B)
$(\cdot)^*$	Unknown tensorial quantity to be determined
$(\cdot)_\mathrm{min}$	Minimum value of $(\cdot)$
$(\cdot)_\mathrm{max}$	Maximum value of $(\cdot)$
$(\cdot)_{\underline{\boldsymbol{v}}=\boldsymbol{D}\underline{\boldsymbol{x}}}$	Relative to uniform strain-rate boundary conditions
$(\cdot)_{\boldsymbol{\sigma}\underline{\boldsymbol{n}}=\boldsymbol{\Sigma}\underline{\boldsymbol{n}}}$	Relative to uniform stress boundary conditions

$(\bar{\cdot})$	Spatial tensor rotated to the intermediate configuration (Chapter 7)
$(\cdot)_{\text{tr}}$	Relative to the elastic trial state (Chapter 7)
$(\cdot)^{\text{tr}}$	Relative to a trial velocity field (Chapter 5)
$(\cdot)_k$ or $(\cdot)^{(k)}$	Relative to the k-th iteration of the (quasi)-Newton method
$(\cdot)^{\text{P}}$	Relative to the Predict stage of the Predict-Correct procedure

Constants

$\underline{\mathbf{0}}$	Null vector in $\mathbb{R}^3$ or null pseudo-vector in Voight notation
$\mathbf{0}$	Null tensor in $\mathbb{R}^3$
δ_{ij}	Kronecker delta
$\boldsymbol{I}$	Second-order identity tensor in $\mathbb{R}^3$ $I_{ij} = \delta_{ij},\ i,j = 1,2,3$
$\mathcal{I}$	Symmetric fourth-order identity tensor in $\mathbb{R}^3$ (maps a second-order tensor to itself) $\mathcal{I}_{ijkl} = \frac{1}{2}(\delta_{ik}\delta_{jl} + \delta_{il}\delta_{jk}),\ i,j,k,l = 1,2,3$
$\mathcal{K}$	Deviatoric fourth-order unit tensor in $\mathbb{R}^3$ (maps a second-order tensor to its deviator) $\mathcal{K} = \mathcal{I} - \frac{1}{3}\boldsymbol{I}\otimes\boldsymbol{I}$ or $\mathcal{K}_{ijkl} = \frac{1}{2}(\delta_{ik}\delta_{jl} + \delta_{il}\delta_{jk}) - \frac{1}{3}(\delta_{ij}\delta_{kl}),\ i,j,k,l = 1,2,3$

List of symbols

General variables

a	Inner radius of the spherical RVE
$A(r)$	Area of the spherical surface
$\mathcal{A}$	Chu and Needleman (1980) strain-controlled distribution function for void nucleation
$\boldsymbol{A}$	Uniform extension field tensor of the Eshelby-type trial fields
b	Outer radius of the spherical RVE
$\mathcal{B}$, $(\mathcal{B}_1, \mathcal{B}_2)$	Chu and Needleman (1980) stress-controlled distribution function for void nucleation
$\mathcal{B}_0$	Body in the reference configuration
$\mathcal{B}_t$	Body in the current configuration
$\boldsymbol{b}$	Transformed strain-rate tensor (Chapter 4); Left Cauchy-Green tensor (Chapter 7)
$\boldsymbol{b}_p$	Transformed strain-rate tensor in the principal transformed space
$\mathcal{B}_0$	Body in the reference configuration
C_{eq}	Gurson (1977) parameter for macroscopic yield criterion for cylindrical voids
$\boldsymbol{C}$	Right Cauchy-Green tensor
$\check{\boldsymbol{C}}^{\text{ep}}_{\text{tan}}$	Linear/tangent elastoplastic modulus

$\overleftarrow{\boldsymbol{\mathcal{C}}}^{\mathrm{ep}}_{\mathrm{alg}}$	Consistent (alias algorithmic) elastoplastic modulus
$\boldsymbol{d}$	Eulerian strain-rate tensor (or rate of deformation tensor)
$\overline{\boldsymbol{d}}$	Local/microscopic unitary (or normalized) plastic strain-rate tensor
$\boldsymbol{d}^{*}$	Uniform eigenstrain-rate tensor
$\boldsymbol{d}^{\mathrm{E},\infty}$	Strain rate tensor associated with the Eshelby (1959) exterior point solution
$\boldsymbol{d}(\underline{\boldsymbol{x}})$	Kinematically admissible Eulerian strain-rate tensor field in the RVE
$\boldsymbol{d}^{\mathrm{E}}(\underline{\boldsymbol{x}})$	Eshelby-type trial strain-rate field in the RVE
$\boldsymbol{d}^{\mathrm{RT}}(\underline{\boldsymbol{x}})$	Rice and Tracey (1969) trial strain-rate field in the RVE
D	Isotropic damage variable (CMD)
D_{c}	Critical value of the damage variable (uncoupled CMDM)
D_i^{-}, D_i^{+}	Domains of the Cazacu *et al.* (2010) criterion
$D_{(\underline{\boldsymbol{n}})}$	Anisotropic damage variable (CMD) in a plane normal to $\underline{\boldsymbol{n}}$
D_{vM}	Macroscopic von Mises equivalent strain-rate
$\tilde{D}_{\mathrm{e}}$	Macroscopic equivalent strain-rate quantity
$\dot{\mathcal{D}}$	Dissipation power per unit of volume in the intermediate configuration
$\mathcal{D}(\boldsymbol{d}^{\mathrm{p}})$	Dissipation function
$\boldsymbol{D}$	Macroscopic plastic strain rate; Lagrangian strain-rate tensor or rate of deformation tensor (Chapter 7)
$\overline{\boldsymbol{D}}$	Macroscopic unitary (or normalized) plastic strain-rate tensor
$\hat{\boldsymbol{\mathcal{D}}}(r)$	Tensor associated with the Eshelby exterior point solution in the spherical frame
e	Relative cubature error
$\mathcal{E}$	Set of elastic stress states at the microscale
$\overline{\mathcal{E}}$	Closure of $\mathcal{E}$
$\partial\mathcal{E}$	Boundary of $\mathcal{E}$
$\mathscr{E}$	Set of elastic stress states at the macroscale
$\overline{\mathscr{E}}$	Closure of $\mathscr{E}$
$\partial\mathscr{E}$	Boundary of $\mathscr{E}$
$(\underline{\boldsymbol{e}}_1, \underline{\boldsymbol{e}}_2, \underline{\boldsymbol{e}}_3)$	Orthotropy (or material) axes Orthonormal Cartesian base in the current configuration (Chapter 7)
$\boldsymbol{e}_{(n)}$	Generalized Eulerian strain tensors
$(\underline{\boldsymbol{e}}_r, \underline{\boldsymbol{e}}_\theta, \underline{\boldsymbol{e}}_\phi)$	Orthonormal spherical base
$\boldsymbol{E}$	FE unit cell macroscopic strain tensor
$\boldsymbol{E}_{(0)}$	Lagrangian logarithmic (or Hencky) strain tensor
$\boldsymbol{E}_{(n)}$	Generalized Lagrangian strain tensors
$(\underline{\boldsymbol{E}}_1, \underline{\boldsymbol{E}}_2, \underline{\boldsymbol{E}}_3)$	Orthonormal Cartesian base in the reference configuration (Chapter 7)

f	Void volume fraction or porosity
f_{c}	Critical porosity value for the onset of void coalescence
f_{f}	Void volume fraction at final failure
$\overline{f}$	Nahshon and Hutchinson (2008) damage parameter
$f^{*}(f)$	Effective porosity value (Tvergaard and Needleman, 1984)
$\dot{f}_{\mathrm{growth}}$	Growth rate of pre-existing voids
$\dot{f}_{\mathrm{nucl}}$	Growth rate of the nucleation of new voids
$f_{\sigma_{\mathrm{Y}}}^{\mathrm{e}}$, $f_{\sigma_{\mathrm{Y}}}^{\mathrm{p}}$	Threshold fractions of the yield condition (Chapter 7)
$f(\boldsymbol{\sigma},\tau)$	Local/microscopic yield function
$f(\boldsymbol{\sigma},\boldsymbol{\varepsilon}^{\mathrm{p}})$	Weighting function of damage (uncoupled CMDM)
F	Argument of the Plunkett *et al.* (2008) criterion
$\mathcal{F}$	Macroscopic yield function
$\mathcal{F}^{+}$	Approximate macroscopic yield function
$\underline{\boldsymbol{F}}$	Error function
$\boldsymbol{F}$	Deformation gradient tensor
$\boldsymbol{F}_{\Delta}$	Incremental deformation gradient tensor
g	Madou *et al.* (2013) void shape effect parameter
$g(f)$	Monchiet *et al.* (2011) analytical parameter
$g(\dot{\bar{\boldsymbol{\sigma}}},\sigma_{\mathrm{Y}})$	Yield condition in the strain-rate space (Bacroix and Gilormini, 1995)
G	Argument of the dual of the Plunkett *et al.* (2008) criterion
$\boldsymbol{G}_0$	Gradient of the incremental displacements with respect to the reference configuration
$\boldsymbol{G}_1$	Gradient of the incremental displacements with respect to the current configuration
H	Small-strain hardening modulus
$H_{\kappa}(\zeta)$	Isotropic hardening modulus of the overstress scalar
$H_{Y}(\overline{\epsilon}^{\mathrm{p}})$	Isotropic hardening modulus of the matrix equivalent plastic strain
$\boldsymbol{\mathcal{H}}(r)$	Tensor associated with the Eshelby exterior point solution in the Cartesian frame
$\hat{\boldsymbol{\mathcal{H}}}(r)$	Tensor associated with the Eshelby exterior point solution in the spherical frame
I_1^{Σ}	First invariant of the macroscopic stress tensor
J	Determinant of the deformation gradient tensor
j_2	Second invariant of the microscopic/local deviatoric stress tensor
j_3	Third invariant of the microscopic/local deviatoric stress tensor
J_2^{Σ}	Second invariant of the macroscopic deviatoric stress tensor
J_3^{Σ}	Third invariant of the macroscopic deviatoric stress tensor
J, $\boldsymbol{J}$, $\mathcal{J}$	Jacobian scalar, second-order tensor and forth-order tensor, respectively

$\mathcal{K}(\boldsymbol{D})$	Set of incompressible kinematically admissible microscopic strain-rate fields
$\mathcal{L}(\boldsymbol{\Sigma})$	Madou *et al.* (2013) linear term of the stress tensor
$\boldsymbol{l}$	Eulerian velocity gradient tensor
$\boldsymbol{L}$	Lagrangian velocity gradient tensor
$\boldsymbol{\mathcal{M}}^{\tilde{d}}_{\tilde{\boldsymbol{E}}_{(0)}}$	Mapping between the Lagrangian logarithmic and the Eulerian strain-rate spaces
n_{ex}	Number of orthotropic transformations
n_{gp}	Number of integration points of the FE unit cell model
n_{r}	Total number of partitions of the radial quadrature
$\bar{n}_{\text{r}}$	User-defined reference radial discretization parameter
n_{r}^{u}	Number of uniformly partitioned intervals of the radial quadrature
$n_{\text{r}}^{\text{arc}}(i)$	Uniform arc length-based partition of interval i
n_r^{FE}	FE unit cell number radial partitions
$\underline{\boldsymbol{n}}$	Unit normal vector; hydrostatic axis direction
$(\underline{\boldsymbol{n}}_1, \underline{\boldsymbol{n}}_2, \underline{\boldsymbol{n}}_3)$	Eulerian principal strain directions
$(\underline{\boldsymbol{N}}_1, \underline{\boldsymbol{N}}_2, \underline{\boldsymbol{N}}_3)$	Lagrangian principal strain directions
$\boldsymbol{n}$	Semi-infinite ray outward normal of the yield surface
$\tilde{\boldsymbol{n}}$	Unitary (or normalized) strain-rate tensor in the incremental problem
N	Number of quadrature points
N^{sym}	Number of non-equal antipodal quadrature points
$\mathcal{N}(\boldsymbol{\sigma})$	Normal cone with outward normals of the yield surface
$\mathbb{N}_0$	Naturals with zero
$\dot{\mathcal{P}}$	Stress power per unit of volume in the intermediate configuration
$\mathbb{P}_t(\mathbb{S}^2)$	Space of all spherical polynomials with degree of at most t
$\mathcal{Q}(\boldsymbol{\Sigma})$	Madou *et al.* (2013) quadratic term of the stress tensor
(r, θ, ϕ)	Spherical coordinate system (with $\theta \in [0, \pi]$, $\phi \in [0, 2\pi]$)
r_θ	r-value (Lankford coefficient) at an angle θ with the 1-direction of orthotropy
$\boldsymbol{R}$	Orthogonal rotation matrix
$\mathbb{R}$	Set of real numbers
$\mathbb{R}^3$	Three-dimensional Euclidean space
δS	Section area of an infinitesimal volume element
δS_0	Section area of micro-cracks and micro-voids
δS_{D}	Effective surface area of deterioration
δS^*	Net section area of resistance
$\delta \tilde{S}$	Effective section of resistance

$S(r)$	Spherical surface of radius $r \in [a,b]$
$\boldsymbol{s}$	Local/microscopic deviatoric stress tensor
$\overline{\boldsymbol{s}}$	Local/microscopic unitary (or normalized) deviatoric stress tensor
$\hat{\boldsymbol{s}}$	Transformed stress tensor
$\hat{\boldsymbol{s}}_p$	Transformed stress tensor in the principal transformed space
$\boldsymbol{\mathcal{S}}$	Eshelby tensor for a spherical inclusion
$\mathbb{S}^2$	Unit sphere
t	Degree of the polynomial (Chapter 5); Time/instant (Chapter 7)
T_D	Macroscopic strain-rate (or strain) triaxiality
T_Σ	Macroscopic stress triaxiality
$\mathcal{T}$	Time domain of the motion
$\boldsymbol{T}_{(0)}$	Logarithmic stress tensor or the generalized Kirchhoff stress tensor
$\overline{\boldsymbol{T}}_{\boldsymbol{b}}$	Transformation tensor between transformed strain-rate- and stress- tensor
$\boldsymbol{\mathcal{T}}(r)$	Tensor associated with the Eshelby exterior point solution in the Cartesian frame
$\hat{\boldsymbol{\mathcal{T}}}(r)$	Tensor associated with the Eshelby exterior point solution in the spherical frame
$\underline{\boldsymbol{u}}$	Displacement field vector
$\boldsymbol{U}$	Right stretch tensor
v_m	Volume fraction of the matrix phase of the porous aggregate
$\underline{\boldsymbol{v}}$	Velocity field of a particle
V	Volume of the RVE
dV	Differential volume element of the RVE
δV	Finite volume element
V_i	Volume associated with the integration point i of the FE unit cell model
V_Ω	Volume of the FE unit cell model
$\underline{\boldsymbol{v}}$	Local velocity field in the RVE
$\underline{\boldsymbol{v}}^\mathrm{A}$	Rice and Tracey (1969) radial/dilatational isotropic expansion velocity field
$\underline{\boldsymbol{v}}^\mathrm{B}$	Rice and Tracey (1969) uniform extension velocity field
$\underline{\boldsymbol{v}}^\infty$	Arbitrary expansion velocity field (not necessarily isotropic)
$\underline{\boldsymbol{v}}^\mathrm{RT}$	Rice and Tracey (1969) trial velocity field
$\underline{\boldsymbol{v}}^{\mathrm{E},\infty}$	Eshelby (1959) exterior-point solution (velocity field) for a spherical inclusion
$\underline{\boldsymbol{v}}^\mathrm{tr}(\underline{\boldsymbol{x}})$	Arbitrary trial velocity field in the RVE
$\boldsymbol{V}$	Left stretch tensor
$\boldsymbol{V}_{\boldsymbol{b}}$	Orthogonal matrix whose columns are the right eigenvectors of $\boldsymbol{b}$
$\boldsymbol{V}_{\hat{\boldsymbol{s}}}$	Orthogonal matrix whose columns are the right eigenvectors of $\hat{\boldsymbol{s}}$

w_i	Weight of point a i of the quadrature rule Q_N, $i=1,...,N$
$\mathcal{W}^{\mathrm{p}}$	Plastic power per unit of volume of the current configuration
$\boldsymbol{w}$	Eulerian spin tensor
$\boldsymbol{W}$	Lagrangian spin tensor
(x_1, x_2, x_3)	Cartesian coordinate systems
$\mathcal{X}_N$	Set of quadrature points in $\mathbb{S}^2$
$\mathcal{X}_N^{\mathrm{sym}}$	Set of symmetric (antipodal) quadrature points in $\mathbb{S}^2$
$\underline{\boldsymbol{x}}$	Point in the RVE (Chapter 5); Point in the current configuration (Chapter 7)
$\underline{\boldsymbol{X}}$	FE unit cell undeformed configuration (Chapter 6); Point in the reference configuration (Chapter 7)
$\boldsymbol{X}$	Macroscopic back-stress tensor
Y	Damage energy release rate
$Y(\cdot)$, $Y_\Delta(\cdot)$	Total and incremental isotropic hardening functions, respectively
$\underline{\boldsymbol{\alpha}}$	Set of scalars and tensorial internal variables of a model
$\dot{\boldsymbol{\alpha}}$	Arbitrary thermodynamic flux variable
$\boldsymbol{\beta}$	Rice and Tracey (1969) remote strain-rate field
$\boldsymbol{\beta}_D$	Arbitrary thermodynamic force
$\Gamma(\boldsymbol{D}, \boldsymbol{\zeta})$	Macroscopic plastic dissipation to be minimized in terms of $\boldsymbol{\zeta}$
$\bar{\epsilon}^{\mathrm{p}}$	Equivalent plastic strain of the matrix phase (Gurson, 1977)
$\bar{\varepsilon}^{\mathrm{p}}$	Equivalent plastic strain (general case and uncoupled CMDM)
$\bar{\varepsilon}_{\mathrm{f}}^{\mathrm{p}}$	Critical value of the equivalent plastic strain at fracture (uncoupled CMDM)
$\boldsymbol{\varepsilon}^{\mathrm{p}}$	Plastic strain tensor
ζ	Strain-like thermodynamic scalar internal variable
$\zeta(r)$	Natural spline based on piecewise polynomials of degree 3
$\boldsymbol{\zeta}$	Additional kinematic quantity entering the macroscopic dissipation function
θ	Generalised midpoint integration scheme parameter, $\theta \in [0,1]$.
κ	Overstress scalar
$\lambda_1, \lambda_2, \lambda_3$	Principal stretches
$\dot{\lambda}$	Local/microscopic plastic multiplier rate (or Lagrange multiplier)
$\dot{\lambda}_1^{\mathrm{T}}$	Effective plastic strain rate associated with σ_1^{T}
Λ	Accumulated equivalent plastic strain
$\dot{\Lambda}$	Macroscopic plastic multiplier rate (or Lagrange multiplier)
ξ	Positive multiplier of homogeneous functions
$\tilde{\boldsymbol{\xi}}$	Normalized (or unit) rotated stress tensor (Chapter 7)

$\boldsymbol{\xi}(\underline{\boldsymbol{X}},t)$	Arbitrary tensorial field in the material (or Lagrangian) frame
$\boldsymbol{\xi}(\underline{\boldsymbol{x}},t)$	Arbitrary tensorial field in the spatial (or Eulerian) frame
$\pi(\boldsymbol{d})$	Microscopic (or local) plastic dissipation rate associated with $\boldsymbol{d}$
$\Pi(\boldsymbol{D})$	Macroscopic plastic dissipation associated with $\boldsymbol{D}$
$\Pi^{+}(\boldsymbol{D})$	Approximate of $\Pi(\boldsymbol{D})$ associated with a subset of $\mathcal{K}(\boldsymbol{D})$
$\Pi^{+}_{\mathrm{dev}}(\boldsymbol{D})$	Deviatoric contribution of $\Pi^{+}(\boldsymbol{D})$
$\Pi^{+}_{\mathrm{hid}}(\boldsymbol{D})$	Hydrostatic contribution of $\Pi^{+}(\boldsymbol{D})$
$\Pi^{++}(\boldsymbol{D})$	Approximate of Π^{+}
$\Pi^{\mathrm{E},+}(\boldsymbol{D})$	Approximate of $\Pi(\boldsymbol{D})$ associated with the Eshelby-type trial fields
$\Pi^{\mathrm{RT},+}(\boldsymbol{D})$	Approximate of $\Pi(\boldsymbol{D})$ associated with the Rice and Tracey trial fields
ρ	Density of a porous aggregate
ρ_f	Error function of the incremental porosity
ρ_{m}	Density of the matrix phase of a porous aggregate
$\check{\boldsymbol{\rho}}_{\sigma}$	Error function of the (rotated) Cauchy stress
σ	True uniaxial stress (Kachanov, 1958)
$\tilde{\sigma}$	Effective uniaxial stress (Kachanov, 1958)
σ_0	Yield stress of an isotropic matrix
σ_{C}	Uniaxial compressive yield stress of an isotropic matrix
σ_{T}	Uniaxial tensile yield stress of an isotropic matrix
σ_1^{C}	Uniaxial compressive yield stress along the 1-direction of orthotropy of the matrix
σ_1^{T}	Uniaxial tensile yield stress along the 1-direction of orthotropy of the matrix
σ_{Y}	Current value of σ_1^{T} (Chapter 7)
$\bar{\sigma}_{\mathrm{Y}}$	Gurson (1977) hardening-type yield stress
$\boldsymbol{\sigma}$	Cauchy stress tensor at microscale (Chapter 5) Eulerian Cauchy stress tensor (Chapter 7)
$\tilde{\boldsymbol{\sigma}}$	Effective Cauchy stress tensor (CMD)
$\boldsymbol{\sigma}_p$	Plastically admissible stress states
$\boldsymbol{\sigma}(\underline{\boldsymbol{x}})$	Statically admissible stress field in the RVE
Σ_1, Σ_2	Leblond *et al.* (1995) isotropic strain hardening internal variables
Σ_{eq}, Σ_{vM}	Macroscopic von Mises equivalent stress
$\tilde{\Sigma}_{\mathrm{e}}$	Macroscopic equivalent stress
$\Sigma_{\gamma\gamma}$	Sum of the in-plane macroscopic stresses (Gurson, 1977)
$\boldsymbol{\Sigma}$	Macroscopic Cauchy stress tensor
$\bar{\boldsymbol{\Sigma}}$	Macroscopic unitary (or normalized) Cauchy stress tensor
$\hat{\boldsymbol{\Sigma}}$	Stewart and Cazacu (2011) transformed macroscopic stress tensor

τ	Positive scalar with the dimension of stress
$\boldsymbol{\tau}$	Kirchhoff stress tensor
γ	Orthotropic/effective strain-rate triaxiality
$\Upsilon(\boldsymbol{D},\boldsymbol{\zeta})$	Macroscopic strain-rate potential to be minimized in terms of $\boldsymbol{\zeta}$
$\Upsilon^{\mathrm{E}}(\boldsymbol{D},\boldsymbol{d}^{*\prime})$	Macroscopic strain-rate potential to be minimized in terms of $\boldsymbol{d}^{*\prime}$
φ	Stress potential or equivalent stress function
φ_{iso}	Arbitrary isotropic stress potential
$\varphi(\boldsymbol{\sigma})$	Local/microscopic stress potential or equivalent stress function
ϕ	Legendre-type convex thermodynamical dissipation potential (Chapter 4)
ϕ^{*}	Legendre-Fenchel transform of ϕ
$\phi(\underline{\boldsymbol{X}},t)$	Deformation map
Φ	Macroscopic stress potential or equivalent stress function
Φ^{+}	Approximate macroscopic stress potential or equivalent stress function
Φ^{E}	Macroscopic stress potential associated with the Eshelby-type fields
Φ^{RT}	Macroscopic stress potential associated with the Rice and Tracey trial fields
$\Phi^{\mathrm{G}}_{\mathrm{cyl}}$	Gurson (1977) macroscopic yield criterion for cylindrical voids
$\Phi^{\mathrm{G}}_{\mathrm{sph}}$	Gurson (1977) macroscopic yield criterion for spherical voids
$\Phi^{(\mathrm{P})}$	Hybrid analytical-numerical macroscopic stress potential
χ	FE unit cell scale factor
ψ	Strain-rate potential
ψ^{e}	Stored strain energy function
ψ_{H}	Helmholtz free energy per unit undeformed volume
$\psi^{\mathrm{p}}_{\mathrm{iso}}$	Stored energy due to isotropic hardening
$\psi(\boldsymbol{d}^{\mathrm{p}})$	Local/microscopic strain-rate potential (Chapter 5)
$\Psi(\boldsymbol{D})$	Macroscopic strain-rate potential (Chapter 5)
$\Psi^{+}(\boldsymbol{D})$	Approximate macroscopic strain-rate potential
$\Psi^{++}(\boldsymbol{D})$	Approximate of $\Psi^{+}(\boldsymbol{D})$
$\Psi^{\mathrm{E}}(\boldsymbol{D})$	Macroscopic strain-rate potential using the Eshely-type fields
$\Psi^{\mathrm{RT}}(\boldsymbol{D})$	Macroscopic strain-rate potential using the Rice and Tracey fields
$\Psi^{(\mathrm{P})}$	Hybrid analytical-numerical macroscopic strain-rate potential
ω	Void domain of the RVE; Eshelby ellipsoidal elastic inclusion
$\partial\omega$	Boundary of voids in the RVE
ω_1,ω_2	Madou *et al.* (2013) ellipsoidal void shape parameters
ω_i	Weight of the integration point i, of the FE unit cell model

$\omega(\boldsymbol{\Sigma})$	Nahshon and Hutchinson (2008) weight function
Ω	Total domain of the RVE
$\partial\Omega$	Boundary of the RVE

Constitutive tensors and parameters

a	Homogeneity degree/parameter of the CBP06 criterion
a, P, R, Q	Benallal (2017) functions for the non-quadratic isotropic porous criterion
$\boldsymbol{\mathcal{A}}$	Large-strain orthotropic elasticity tensor in the Lagrangian configuration
$\tilde{\boldsymbol{\mathcal{A}}}$	Large-strain weakened orthotropic elasticity tensor in the Lagrangian configuration
$\boldsymbol{\mathcal{A}}_{\text{iso}}$	Large-strain isotropic elasticity tensor in the Lagrangian configuration
$\boldsymbol{\mathcal{C}}$	Fourth-order orthotropic tensor of the CPB06 criterion
$\overleftarrow{\boldsymbol{\mathcal{C}}}^{\text{e}}$	Small-strain elasticity tensor
E	Isotropic modulus of elasticity (or Young modulus)
E_{11}, E_{22}, E_{33}	Youngs moduli in the 1-, 2-, and 3-direction of orthotropy, respectively
$\overline{E}$	Averaged Young modulus
$f_{\text{p}}, \sigma_{\text{p}}, s_{\text{p}}$	Chu and Needleman (1980) stress-controlled void nucleation parameters
$f_{\text{N}}, \overline{\epsilon}_{\text{N}}, s_{\text{N}}$	Chu and Needleman (1980) strain-controlled void nucleation parameters
G	Isotropic shear modulus
G_{23}, G_{13}, G_{12}	Shear moduli in the 2-3, 1-3 and 1-2 plane of orthotropy, respectively
$\overline{G}$	Averaged shear modulus
h, h^-, h^+	Anisotropy factor
$\boldsymbol{\mathcal{H}}$	Fourth-order strain-rate orthotropic transformation tensor of the CPB06 criterion
k	Tension-compression asymmetry parameter of the CPB06 criterion
k_ω	Nahshon and Hutchinson (2008) heuristic parameter
K, ε_0, n	Swift-type isotropic hardening power-law parameters
$\boldsymbol{\mathcal{L}}$	Fourth-order orthotropic stress transformation tensor of the CPB06 criterion (deviatoric projection of $\boldsymbol{\mathcal{C}}$)
$\boldsymbol{\mathcal{L}}_{\text{Hill'48}}$	Fourth-order orthotropic stress transformation tensor of the Hill (1948) criterion
m	Exponent of the non-quadratic Hershey-Hosford yield criterion; Richmond and Smelser (1985) heuristic parameter; Scaling parameter of the CPB06 and CPB06ex*n* criteria
n	Norton-law exponent for viscoplasticity
q_1, q_2	Tvergaard's (1982) fitting parameters for the criterion of Gurson (1977)
q_δ	Tvergaard and Needleman (1984) void coalescence acceleration factor/slope
R	Liao *et al.* (1997) anisotropy parameter

Y_0, Y_{sat}, C_Y	Voce isotropic hardening law parameters
$Y_{Voce}(\cdot)$	Voce isotropic hardening law
$Y_{Swift}(\cdot)$	Swift isotropic hardening law
z_s	Cazacu and Stewart (2009) SD ratio parameter
η	Monchiet and Bonnet (2013) void size effect coefficient
λ, μ	Lamé coefficients
υ	Isotropic Poisson ratio
υ_{ij}	Orthotropy Poisson ratios, $i, j = 1,2,3, \ i \neq j$
$\overline{\upsilon}$	Averaged/pseudo-isotropic Poisson ratio
Φ_i	Orthotropy components $\mathcal{L}_{ii11}$ of the CBP06 criterion
$\omega_\beta(f)$	Weakening factor of the elasticity modulus

Acronyms and Abbreviations

2-D	Two-Dimensional
3-D	Three-Dimensional
AI	Artificial Intelligence
AM	Additive Manufacturing
ASTM	American Society for Testing and Materials
bcc	body-centred cubic
CDM	Continuum Damage Mechanics
CDMM	Continuum Damage Mechanics Model
CH	Computational homogenization
CHM	Computational homogenization model
CP	Commercially Pure
CPB06	Cazacu-Plunkett-Barlat 2006 (Cazacu *et al.*, 2006)
CPB06ex*n*	Cazacu-Plunkett-Barlat 2006 with *n* linear transformations (Plunkett *et al.*, 2008)
CPU	Central Processing Unit
D	Direct Problem
DD3IMP	Deep Drawing 3D Implicit Finite Element Solver
DIC	Digital Image Correlation
E	Eshelby
fcc	face-centred cubic
FE	Finite Element

FEM	Finite Element Method
FFT	Fast Fourier Transform
GLD	Gologanu-Leblond-Devaux (Gologanu *et al.*, 1993)
GTN	Gurson-Tvergaard-Needleman
hcp	hexagonal close packed
HM	Heuristic model
HP	High Purity
I	Inverse Problem
MKL	Math Kernel Library
MTS	Mechanical Threshold Strength
ND	Normal direction
PBF	Powder Bed Fusion
RD	Rolling Direction
RT	Rice and Tracey
RVE	Representative Volume Element
SD	Strength-Differential
SEM	Scanning Electron Microscopy
SP	Stress Potential
SRI	Selective Reduced Integration
SRP	Strain-Rate Potential
TD	Transverse Direction
T-SRP	Transformed Strain-Rate Potential
VPSC	Visco-Plastic Self-Consistent polycrystal model
VR	Virtual Reality
XFEM	Extended Finite Element Method

Chapter 1

Introduction

This chapter presents a brief background on the framework of porous media in the context of ductility assessment of metals and alloys, highlighting the growing industrial interest on damage modelling and its current challenges. The main objectives of the thesis are identified with the aim of answering some of the raised research failings. The structure and contents of the thesis are also presented.

1.1 Motivation

It is well established that computational mechanics nowadays plays a major role at the design stage of many engineering components and industrial processes. This is particularly true in highly competitive industries, such as the automotive and aeronautical sectors, where cost-effectiveness and flexibility of the project of high value-added products benefit the most from such scientifically-based approach, as prototype development via experimental trial-and-error steps is considered either too costly or time-consuming. The increasing geometrical complexity and tight specifications on weight reduction, mechanical performance and reliability set by these industries on new, enhanced, components further contribute to the need for computational analyses, viz. simulation tools based on the Finite Element Method (FEM). In addition to its economical and industrial relevance, computational mechanics can facilitate the development new grades of materials with enhanced engineering properties.

Modelling the inelastic deformation and fracture of structural and functional materials is a long-standing problem in the field of solid mechanics. Ductile materials such as metals and alloys are characterized by their ability to dissipate large amounts of mechanical energy before fracture. Ductile fracture results from a gradual internal (i.e. microstructural) deterioration process, associated with high inelastic straining. Accurate prediction of the occurrence of ductile fracture is of particular relevance in the field of structural engineering. The interest is quite evident, especially in safe-critical applications, such as the nuclear and transport sectors, where accidental failure may entail catastrophic consequences beyond economic issues. Moreover, ecological-motivated ever-stringent standards on greenhouse gas emissions reduction continuously compel the automotive and aeronautical industries to implement materials with improved strength-to-weight ratio performance, while preserving the safety, (in particular, crash-worthiness) of the structural components. Unfortunately, these advanced materials typically present reduced ductility at room-temperature, and thus product and manufacturing design face increased

difficulties. Among these materials, one can emphasize the titanium and magnesium alloys which have been gaining increasing technological relevance due to their outstanding specific strength. The hexagonal crystal structure and, typically, strong basal texture of these materials lead to competing deformation mechanisms at the crystal level, which, in turn, manifest themselves in quite intricate forms of anisotropy and tension-compression asymmetry at the macroscale. Naturally, the reliability of a computational analysis rests, for the most part, on the predictive performance of the constitutive relations assumed to reproduce the underlying physical phenomena, particularly, the ability to translate the microstructural features to the macroscopic behaviour. It is therefore clear that the development of new, advanced, constitutive models for accurately describing the complex plasticity-damage couplings of such ductile materials constitutes a highly topical research field, both from the academic and industrial standpoint.

Traditionally, constitutive models are developed such that a closed-form expression is attained. The reasons are twofold: first, to minimize the computational cost; and second, to facilitate the implementation of the models within a numerical simulation scheme, e.g. the FEM. Unfortunately, due to mathematical limitations, obtaining closed-form expressions may entail the consideration of one or more, often detrimental, simplification hypotheses, or may even be impossible. Opportunely, advances in computational power/cost ratio have been enabling the adoption of mixed analytical-numerical and fully-numerical constitutive approaches, which, by design, bypass these problems, and, currently, permit numerical simulations to be carried out in a reasonable computational time. More crucially, the already impressive microprocessor development is due to accelerate in next few years, driven by the demand of emerging technologies such as virtual reality (VR) and artificial intelligence (AI), which renders the adoption of such type of formulation even more relevant.

In summary, the development and application of state-of-the-art material models, even if not in closed-form, implemented within and efficient numerical scheme should provide engineers an improved and more robust tool for dealing with ductile fracture in relevant industrial application, (e.g. sheet and/or bulk metal forming operations). The current processing power permits to consider fully-numerical constitutive models, which was deemed prohibitively expensive in a recent past. Ultimately, the usage of the latest scientific and technological tools should allow the automotive and aeronautical industrial sectors to maintain a competitive edge by innovating, developing and optimizing engineering components at lower costs.

1.2 Brief literature review and research-relevant issues

Most metals fail in a ductile fashion at room temperature. Ductile fracture is a physical process that results from the accumulation of plastic damage and leads to the formation and propagation of cracks. In turn, damage can be understood as the physical process of progressive deterioration of the material. At the microscopic level, damage is related to the mechanisms of nucleation, growth and coalescence of micro-cracks and micro-cavities (e.g., see Benzerga *et al.* (2004a); Hancock and Mackenzie (1976); McClintock (1968); Rice and Tracey (1969); Rousselier (1987); Tipper (1949)). At the macroscopic

level, damage translates into a decrease of the material stiffness, strength and a reduction of the remaining ductility. The void distribution in metallic materials originates from pre-existing voids (e.g., manufacturing defects) or from nucleation at second-phase particles, either by matrix-particle decohesion or by micro-cracking of second-phase particles (e.g. inclusions, impurities). Following nucleation, voids grow due to plastic deformation of the surrounding dense phase and eventually coalesce due to micro-necking of the ligaments between neighbouring voids. Fracture in ductile materials is thus a multi-scale phenomenon involving the generation and interaction of defects across several length scales.

Is this work one refers to a porous solid (or aggregate) to denote a material containing voids, which, upon mechanical handling, may grow or collapse. In practice, the porous aggregate may be viewed as a two-phase composite containing: the actual dense material, known as the matrix; and the pore network, known as the voids. While the application of the concept of porous media to deal with metallic foams, metal additive manufacturing (AM) parts and to natural materials such as rocks, soils and biological tissues (e.g. bones, wood, cork) is evident, considering more conventional engineering metals and alloys as porous media may not be so obvious, since (i) the initial porosity of the majority of structural metallic materials is extremely low, typically ranging between 10^{-5} and 10^{-2}; and (ii) the macroscopic softening induced by the void nucleation and void growth in the early deformation stages of these materials may be quite weak, as evidenced by numerical studies on unit cells (Pineau and Pardoen, 2007). Nevertheless, it turns out that constitutive modelling involving the coupling of porosity with the mechanical response of the material offers a powerful and quite natural approach for predicting ductile failure in these materials. This is closely related with the relationship between porosity, quantifying the accumulated damage of the material in the form of micro-voids, and ductile failure occurrence. Unfortunately, explicit tracking of the evolution of each micro-void in a sample, in the spirit of a bottom-up (alias inductive) approach, is still not viable from the computational standpoint. Instead, damage modelling typically follows a top-down (alias deductive) approach, where macroscopic (alias phenomenological) internal variables are defined in order to characterize the damage evolution of a thermomechanically equivalent homogeneous medium in a statistical fashion. The focus of this work is on modelling the void growth stage within the latter modelling framework, more specifically, following a micromechanical approach. In the following a brief literature review of this class of models is presented.

The first ductile damage models were developed by McClintock (1968) and Rice and Tracey (1969) to describe the growth of isolated cylindrical and spherical voids in a rigid perfectly plastic matrix. These pioneer works outlined the role of the stress triaxiality on the void growth. Inspired by these observations, Gurson (1977) carried out an upper bound limit load analysis of a single cylindrical and spherical void embedded in a cylindrical and spherical rigid-plastic matrix, respectively, obeying the classical von Mises criterion and developed approximate analytical criteria for ductile porous solids. The work in this dissertation follows the procedure originally outlined in Gurson (1977) hence a more comprehensive description of this subject is presented in a dedicated subsection. Gurson (1977) model is widely used to this day and has been shown to reproduce several experimentally-observed trends of ductile fracture (e.g. the cup-cone fracture of cylindrical tensile specimens (Tvergaard and Needleman,

1984); the formation of shear bands under plane-strain conditions (Tvergaard, 1981). Several modifications of empirical nature were later proposed to the spherical criterion of Gurson (1977) based on the results of finite element (FE) unit cell computations in order to improve the flexibility and accuracy of the original model (e.g., Koplik and Needleman (1988); Tvergaard (1981, 1982a, 1982b)). The proposal of Tvergaard and Needleman (1984) accounting for void interaction and void coalescence is, quite probably, the most popular extension of Gurson (1977) work and the corresponding model is usually referred in the literature as the Gurson-Tvergaard-Needleman (GTN) model. Despite the popularity of Gurson-type criteria, there are two main limitations associated with these models which stem from the underlying assumptions in the formulation. First, the assumption of isotropy of the plastic flow of the matrix. In practice, engineering metallic materials display a more or less pronounced texture as a result of their manufacturing process (e.g. cold-rolled metallic sheets), and thus display elastoplastic anisotropy. Second, the choice of the spherical geometry for the voids. In truth, even if nucleated voids are nearly spherical, spherical symmetry is violated under low triaxiality loadings as voids undergo rotation and shape change (Pardoen and Hutchinson, 2000; Thomason, 1990; Weck *et al.*, 2008). In order describe void shape effects, Gologanu *et al.* (1993, 1994, 1997) extended the analysis of Gurson (1977) by considering a spheroidal volume containing a confocal spheroidal cavity. Madou and Leblond (2012a, 2012b, 2013) and Madou *et al.* (2013) extended the analysis to the case of general ellipsoidal cavities. Plastic anisotropy of the matrix was first incorporated by Liao *et al.* (1997) based on Gurson's (1977) cylindrical model for transversely isotropic solids under plane stress conditions using Hill (1948) yield criterion. Benzerga and Besson (2001) later extended Gurson's (1977) spherical criterion for fully orthotropic metals subjected to triaxial loadings also assuming the using the Hill (1948) criterion for the matrix. Stewart and Cazacu (2011) proposed an approximate orthotropic criterion for orthotropic porous solids displaying tension-compression asymmetry (i.e., that have different yield strengths in tension and compression) based on a simplified and quadratic form of the Cazacu *et al.* (2006) (often referred to as the CPB06) yield criterion. These works have shown that the anisotropic behaviour of the matrix translates into the macroscopic scale in an intricate fashion (Cazacu *et al.*, 2019). The abovementioned orthotropic porous criteria result from a rigorous rework of Gurson's kinematic limit analysis. Conversely, orthotropy has also been modelled in a heuristic fashion via the straightforward substitution of the macroscopic von Mises equivalent stress by another orthotropic yield criterion. Heuristic extensions of this type were first proposed by Doege *et al.* (1995) considering the Hill (1948) criterion and more recently adopted, for instance, in Besson (2010); Bron and Besson (2006); Dæhli *et al.* (2017); Gruben *et al.* (2017); Shinohara *et al.* (2016); Steglich *et al.* (2010) regarding more advanced, non-quadratic, yield criteria. The task of combining the effects of void shape and matrix orthotropy was initiated in Benzerga *et al.* (2004b) and set the stage for other contributions accounting for more general loadings, void geometries and trial velocity fields (Keralavarma and Benzerga, 2008, 2010; Monchiet *et al.*, 2006, 2008; Morin, Leblond and Kondo, 2015), all of which considering the Hill (1948) yield criterion for the matrix phase.

In agreement with Gurson (1977) all the above works regarding the spherical void geometry are based on the Rice and Tracey (1969) velocity fields. Apart from the constitutive criteria considered for the matrix phase, the homogenization analysis can be modified by employing different velocity fields. Based on this idea, Monchiet *et al.* (2011) reworked the limit analysis of Gurson (1977) by replacing the Rice and Tracey (1969) local velocity fields with those of the exterior point solution of the well-known Eshelby inclusion problem for the particular case of a spherical inclusion Eshelby (1957, 1959). Later, Monchiet *et al.* (2014) extended the analysis for spheroidal voids (see also Monchiet *et al.*, 2007).

In addition to the analytical approach to the limit analysis problem of Gurson (1977), several studies have been devoted to numerical-based limit analysis (Alves *et al.*, 2014; Castañeda and Zaidman, 1994; Dæhli *et al.*, 2019; Fritzen *et al.*, 2012; Guo *et al.*, 2008; Lebensohn *et al.*, 2011; Lebensohn and Cazacu, 2012; Madou and Leblond, 2012b; Michel *et al.*, 2001; Morin *et al.*, 2014; Pastor *et al.*, 2009, 2012, 2013; Thoré *et al.*, 2011; Trillat and Pastor, 2005). Such computational analyses have proven useful in guiding the development and assessment of analytical criteria and play a key role for understanding the basic phenomenology governing ductile fracture at the mesoscale.

From what precedes, note that most efforts concerning the development of improved micromechanical models for porous metallic materials have been devoted to the description of the effects of void shape and orientation. In fact, in most contributions, the matrix material is assumed isotropic and described by the von Mises yield criterion or orthotropy is dealt with basic, rather primitive, criteria, viz. the Hill (1948) criterion. However, technologically advanced engineering metallic materials generally display pronounced texture, and thus a complex anisotropic behaviour. More critically, lightweight materials such as titanium, magnesium and their alloys have a hexagonal close-packed (hcp) crystal structure, which is known to promote strength differential (SD) effects due to the occurrence of twinning. The lack of representation of these features in porous criteria renders them virtually irrelevant in current engineering applications. In fact, the use of a state-of-the-art description of the void attributes (shape, orientation, size, void-particle interaction) seems questionable if the stress-strain history up to the point where these may actually play a part, typically at high porosities, is not properly captured by the model. Preliminary observations indicate the prevalence of plastic anisotropy over void morphology effects on the rate of void growth (e.g. Benzerga *et al.*, 2019; Pineau *et al.*, 2016). This is not to say that accounting for the shape of the voids, or, more generally, damage anisotropy, is a hopeless task. It just advocates that in order to do so, the description of the matrix properties should be of primary concern, as this should play a more important role, at least, in the early stages of the deformation process. Accordingly, more effort should be invested in the integration of the specific plastic flow characteristics of the matrix material, (viz. plastic anisotropy, isotropic and kinematic hardening, tension-compression asymmetry, etc.), and their evolution within the context of macroscopic porous models. This issue has already been tackled, but only to some extent. The task initiated by Cazacu and Stewart (2009) paved the way for the inclusion of tension-compression asymmetry in the analysis (see also Revil-Baudard *et al.*, 2012, 2016; Yoon, Stewart, *et al.*, 2011). As mentioned above, Stewart and Cazacu (2011) later extended their work to account for anisotropy based on the linear transformation method embedded in Cazacu *et al.* (2006)

yield criterion. Unfortunately, their proposal considers only six anisotropic coefficients (of which five are actually independent), i.e., the same number of those of the Hill (1948) criterion. Evidently, such formulations are not flexible enough to describe with appropriate accuracy the highly anisotropic behaviour of materials with hcp structure (e.g. the description of both tensile and compressive uniaxial yield stresses and Lankford/*r*-values in the context of thin metallic sheets). Moreover, existing orthotropic analytical criteria are restricted to quadratic yield functions for the matrix phase. However, theoretical, experimental, and numerical investigations have shown that some materials can be more accurately described by non-quadratic yield criteria (Hershey, 1954; Hosford, 1972; Lian and Chen, 1991), even in the isotropic case (e.g. some face-centred cubic (fcc) crystal structure materials such as aluminium alloys).

Accordingly, orthotropic criteria based on a single transformation and restricted to a quadratic form may not be able to capture with satisfactory accuracy the complex mechanical behaviour encountered in hcp metals (e.g. zirconium, uranium) and advanced structural engineering alloys (e.g. aluminium, magnesium and titanium alloys). In such cases, more anisotropic coefficients must be introduced in the formulation to increase the flexibility of the potentials. In this spirit, Plunkett *et al.* (2008) extended the general form of the CPB06 (Cazacu *et al.*, 2006) criterion to account for multiple linear transformations (see also Barlat *et al.*, 2005).

It is therefore clear that the development of Gurson-like criteria considering non-quadratic yield functions and/or a greater number of anisotropy coefficients is of paramount importance for the ductility assessment of advanced engineering materials. Moreover, the adoption of more flexible trial velocity fields in the homogenization process, such as the Eshelby-type ones, should lead to improved solutions. Unfortunately, for these complex velocity fields and microscale plasticity models, obtaining the respective macroscopic closed-form expression in the general case can be very challenging, if not impossible, and the problem must be tackled numerically.

1.3 Main objectives

The aim of this dissertation is to develop and implement improved plastic potentials for porous ductile solids containing spherical voids whose matrix behaviour is described by an advanced orthotropic criterion accounting both for tension-compression asymmetry and an arbitrary number of linear transformations. The non-quadratic form of the Plunkett *et al.* (2008) yield criterion is adopted for the matrix phase. Since the proposed problem does not admit a close-form analytical solution, the entire micromechanical-based homogenization must be solved numerically. Accordingly, a robust and efficient numerical integration scheme must be developed in order to evaluate the volume integrals involved in the expressions of the macroscopic plastic potentials and their respective derivatives. Two types of velocity fields will be considered in the kinematic homogenization problem: the Rice and Tracey (1969) fields; and the Eshelby-type fields (Eshelby, 1957, 1959). This work aims at comparing the predictions of these formulations, both from the constitutive and computational cost viewpoint. Moreover, the accuracy of

the developed macroscopic potentials is assessed through comparison with the results of finite element limit analyses on spherical unit cells.

The developed criteria and the associated numerical integration scheme must be suitable to the simulation of large-scale engineering problems. Accordingly, this work also intends to provide remarks on the implementation of the developed criteria in the context of finite element analyses. In order to demonstrate the applicability and to assess the cost-effectiveness of the proposed framework, a fully-implicit algorithm for large-strain elasto-plasticity based on a strain-rate plasticity formulation is formulated and application examples with industrial relevance are presented.

In summary, the successful development of such numerical-based constitutive framework should provide a more accurate description of the yielding behaviour of orthotropic porous solids under quasi-static conditions while bypassing the conventional simplification hypothesis (e.g. the Cauchy-Schwarz inequality) and miscellaneous heuristics (e.g. Tvergaard's load-dependent fitting parameters). Naturally, such models should yield 'sufficiently' accurate results in a reasonable computational time and be practical enough to be relevant in the fast-paced industrial environment.

1.4 Layout

This section presents a summary of the contents covered in this work. In line with the above objectives, the thesis is organized in eight chapters. Following the general introduction and motivation presented in this first chapter, the outline of the thesis is as follows.

Chapter 2 presents an overview of the physical mechanisms governing deformation and fracture of metals and alloys at room temperature. Emphasis in laid on micromechanisms involved in the ductile damage process and ensuing ductile crack formation.

Chapter 3 provides a literature review on damage constitutive modelling, particularly on micromechanical models describing the yielding behaviour of porous metallic materials during the void growth stage of the damage process.

Chapter 4 is devoted to the derivation of the expression for the strain-rate potential conjugated with the Plunkett *et al.* (2008) yield criterion. Some basic concepts regarding constitutive modelling of plastic deforming materials are firstly provided. An algorithm is proposed for evaluating the proposed strain rate potential numerically and some application examples are provided employing the dual formulation.

Chapter 5 presents the proposed three-dimensional orthotropic plastic potentials for porous media containing spherical voids. The mathematical framework regarding the variational characterization of porous solids is first recalled. This includes the kinematic homogenization approach of Hill-Mandel (Hill, 1967; Mandel, 1971) and the limit-analysis theory (Drucker *et al.*, 1952; Hill, 1951). The employed local velocity fields and respective strain rate tensors, viz. those of the Rice and Tracey (1969) analysis and the Eshelby-type approach (Eshelby, 1957, 1959), are described. The developed numerical integration methods are presented in detail. A method for evaluating the macroscopic stress potential, conjugate of the obtained macroscopic strain-rate potential, is provided. The algorithmic aspects of the computational homogenization scheme are summarized in pseudo-code format.

Chapter 6 is devoted to the comprehensive assessment of the developed potentials. Firstly, the predictions of the formulations using different trial velocity fields are compared. Then, both are compared with existing approximate analytical criteria, in particular for isotropic matrices with no tension-compression asymmetry (viz., Gurson, 1977; Monchiet *et al.*, 2011) and with tension-compression asymmetry (viz., the criterion of Cazacu and Stewart, 2009). Then, the accuracy of the developed macroscopic potentials is assessed through comparison with finite element limit analysis results on spherical unit cells. The employed finite element limit analysis scheme is briefly described. Lastly, some statistics regarding the computational performance and efficiency are provided.

Chapter 7 deals with the implementation of the proposed numerical homogenization scheme in the finite element method. A fully-implicit algorithm for large strain elasto-plasticity based on a hyperelastic formulation and strain-rate plasticity is developed. The constitutive formulation is described in detail and the algorithmic details of the implementation are provided. Two application examples are presented in order to discuss the applicability of the proposal and its computational performance in the context of finite element analyses.

Chapter 8 presents a summary of the issues addressed in the thesis, emphasising the main contributions of this work and the key conclusions withdrawn from it. The main advantages and limitations of the proposed approach are highlighted. Some recommendations for future work are suggested, mostly with the aim of further improving the developed criteria.

Chapter 2

Ductile fracture of metallic materials: fundamentals

This chapter presents an overview of general concepts regarding the mechanisms of deformation and fracture of metallic materials at room temperature. The main goal is to present a number of remarks in order to formulate and justify the hypothesis upon which the macroscopic phenomenological theories are often based.

2.1 Mechanical behaviour of metals and alloys: physical aspects of plasticity

This introductory subsection is devoted to a brief presentation of the physical mechanisms governing the irreversible deformation mechanisms of metallic solids. For a more comprehensive description of the metallurgical phenomena reviewed here, the reader is referred to dedicated books and articles, e.g., Cottrell (1961); Dieter and Bacon (1986); Hull and Bacon (2001); Kocks *et al.* (1998); Lemaitre and Chaboche (1994); McClintock and Argon (1966).

2.1.1 Structure of metals

The majority of metals and alloys used in engineering practice are found to consist of polycrystalline structures. Polycrystals are composed of a large number of crystallites (alias grains) of varying size and orientation, each having the structure of a crystal. The interface between adjacent grains is known as grain boundary. The crystalline state is characterized by a regular and repeating atomic arrangement of an elementary parallelepipedal pattern fully-defining the symmetry and the structure of the entire crystal – the lattice. The most common metallic lattices belong to one of the following: body centred cubic (bcc), face centred cubic (fcc) and hexagonal close packed (hcp). The crystalline lattice possesses axes and planes of symmetry. The slip planes denote the planes of greatest atomic planar density (in general, coincident with the symmetry planes of the lattice). Within each slip plane there are preferred slip directions which, in turn, correspond to the direction of highest linear density of atoms. A slip plane and a slip direction constitute a slip system. The faultless crystalline structure as described above (i.e., a crystal containing the exact number of the same type of atoms occupying their regular positions in the lattice), can only undergo reversible deformation and a so-called brittle fracture, in which loss of cohesion occurs without noticeable macroscopic deformation. However, this behaviour is not observed in

actual engineering metallic materials. This discrepancy is explained by the presence of defects that disturb the original lattice (see Figure 2.1), which emerge during crystal growth (solidification) or induced by subsequent handling. These imperfections can be classified as: (i) point defects (e.g. foreign atoms, vacancies); (ii) linear defects (e.g. edge and screw dislocations); (iii) surface defects (e.g. grain boundaries, twin crystal boundaries, stacking faults); and (iv) bulk defects, e.g. *voids* (clusters of vacancies), cracks and inclusions (e.g. phases, precipitates). Bulk defects occur on a much larger scale than their atomic-level counterparts. The bulk defects associated with presence of voids and cracks are a particularly relevant subject in this work, hence are explored later in a dedicated section.

Remark 2.1 The crystalline defects present in a crystal lattice are at the physical origin of irreversible (or inelastic) strains and, ultimately, the occurrence of ductile fracture.

The crystalline structure of metals and alloys is formed during solidification during cooling from the liquid state. As the temperature of the melt decreases, the interatomic distances become smaller and, eventually, nuclei of crystalline arrangements form in randomly distributed sites. Each nucleus develops into a crystal whose growth is limited by neighbouring ones. The result is a polycrystalline structure. The size and orientation of the monocrystals within the aggregate largely depend on the nature of the constitutive elements of the metal (or alloy), and on subsequent mechanical and thermal treatments. The distribution of the orientation of crystallites of a polycrystalline sample is known as *texture*. The absence of long-range order in a polycrystal due to the presence of defects greatly alters its physical properties when compared to those of the corresponding perfect monocrystalline structure.

Remark 2.2 A polycrystalline structure displaying randomly oriented grains and defects is said to have no texture. In this case, its properties at length scales sufficiently larger than the size of the grains can be regarded as isotropic, even if its constituent monocrystals essentially display anisotropic properties.

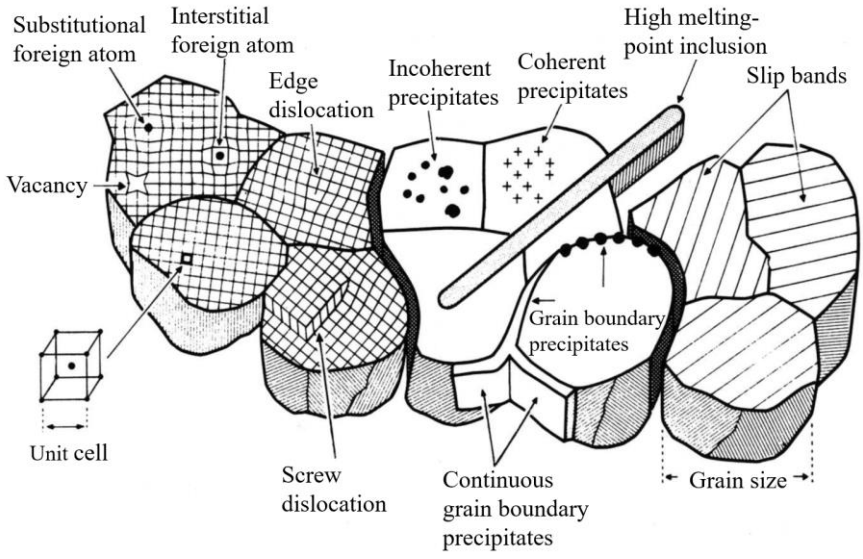

Figure 2.1 General structure of a polycrystalline metal containing several types of defects. The lattice spacing is largely exaggerated for illustrative purposes (after Engel and Klingele (1981).

In practice, engineering metals and alloys do not remain macroscopically isotropic when subjected to thermo-mechanical handling, viz. in the form of finite irreversible straining. This is due to the development of texture in the material, as the crystallographic orientations and distribution of lattice defects are no longer random but have preferred orientations. Depending on the proportion of grains having a given preferred orientation, the polycrystal can be classified has weak, moderate, or strongly textured. In such cases, the hypothesis of macroscopic isotropy is not accurate, and the aggregate should be regarded as macroscopically anisotropic.

2.1.2 Deformation mechanisms

This subsection intends to describe the role played by the crystalline structure and lattice defects on the basic deformation mechanisms of metals and alloys: reversible and permanent deformations.

Reversible deformation results from the expansion and compression of the interatomic bonds of the crystal lattice. Upon removal of the external load, the interatomic spacing returns to the original equilibrium state and no permanent microstructural rearrangements within the material occur. This self-reversing behaviour is often referred to as *elasticity*. An elastic deformation can also include reversible movement of dislocations.

Permanent deformation results from the irreversible movement of atoms in the crystal lattice under the effect of the external load. This irreversible behaviour is often referred to as *plasticity*. Irreversible deformation of monocrystals is mainly governed by two basic mechanisms: *slip* and *twinning*.

Slip refers to the gliding of successive rows of atoms in the form of dislocations along specific lattice planes and directions – the slip systems. In order to reduce the free energy of the deformation process, the dislocation movements on active slip planes tend to concentrate in low-energy regions in the form of slip bands (see Figure 2.2a). von Mises showed that five independent slip systems must be available at the single crystal level to accommodate an arbitrary plastic deformation only by slip (Mises, 1928; Taylor, 1938). The slip activity of any given system depends on the loading type and its relative orientation to the crystal axes. If five independent slip systems are not available, phase transformations or fracture at the crystal level may occur (Vitek *et al.*, 2004).

Deformation (or mechanical) twinning manifests by a simultaneous cooperative movement of blocks of atoms in a symmetrical fashion. Twinning occurs under local shear loadings and produces a two-part crystal with equal lattice structure, but different orientation: the parent crystal (associated with the original/undeformed atomic arrangement) and the twin denoting the sheared region (see Figure 2.2b). These regions differ in shape by a simple-shear type deformation (Clayton, 2011). The restoration of the twinned lattice to its original orientation is referred to as detwinning.

Remark 2.3 An important feature of twinning is that it is a polarized (or directional) deformation mechanism. This means that the crystal lattice can prevent the development of twins of equal shearing magnitude on opposite directions. It follows that the activation of a given twin mode in the crystal depends on the *sign* of the applied stress.

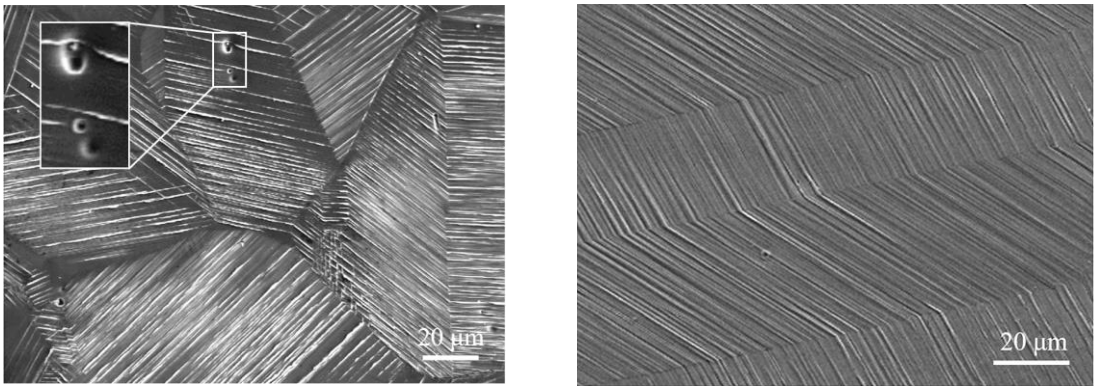

(a) (b)

Figure 2.2 Scanning electron microscopy (SEM) micrographs of the surface slip morphology of polycrystalline brass: (a) slip bands in a Cu-30wt.%Zn alloy (after Carstensen, 1998). Note the presence of voids within the crystal; (b) Twins and twin boundaries in a Cu-10wt.%Zn alloy. Several slip bands are activated both in the parent crystal and in the twins (after Zhang *et al.*, 2008).

Polarized deformation is not expected from the slip mechanism in close-packed crystal structures, viz. fcc and hcp, since, typically, the dislocation motions on a given slip plane can initiate with equal ease in opposite directions. In this case, slip in the single crystal is said to obey the Schmid law (Schmid, 1924). This law states that slip is triggered when the so-called resolved shear stress along a given slip system reaches a threshold value. However, this deformation theory does not hold for all crystal lattices. For instance, directional slip mechanisms can develop in bcc structures due to distorted or non-planar core structure of screw dislocations motions resulting from the so-called non-glide stresses (the stress components that do not lay in the slip planes) (Duesbery *et al.*, 1973; Knezevic *et al.*, 2014; Steinmann *et al.*, 1998). Crystal slip phenomena that do not obey the Schmid law are referred to as non-Schmid effects. Similarly to twinning, non-Schmid effects induce asymmetry of the mechanical response of single crystals regarding the sign of the applied stress (Christian, 1983; Duesbery and Vitek, 1998; Qin and Bassani, 1992; Vitek, Mrovec and Bassani, 2004; Vitek, Mrovec, Gröger, *et al.*, 2004).

Remark 2.4 The directional plastic deformation mechanisms of twinning and non-Schmid type slip lead to a difference between the tensile and compressive yield strengths at the single crystal level. This phenomenon is referred to as *tension-compression asymmetry* or *strength differential effect*.

While twinning-detwinning mechanisms are the main source of tension-compression asymmetry in low-symmetry lattice structures, such as hcp, the non-Schmid effects are the main cause of this type of asymmetry in bcc metals and alloys (Knezevic *et al.*, 2014). Mechanical twinning has also been reported in fcc and bcc cubic structures as a secondary deformation mechanism (Christian and Mahajan, 1995; Hosford and Allen, 1973; Richman, 1964; Venables, 1961), particularly for loadings with high strain rates or at very low temperatures (Hosford, 2010). However, the activation of twinning in these cubic lattices is rare due to the large number of "easy" slip systems available. Generally, this is not the case with hcp lattices where the number of such slip systems is scarce. Hence, mechanical twinning plays a crucial role in the deformation process of hcp materials, by relaxing the number of the required slip systems. As in the case of the cubic structures, twinning in hcp metals and alloys becomes increasingly

prominent with increasing strain rate and decreasing stacking-fault energy and temperature. In a broader sense, the plastic deformation process should be regarded as the interaction of several competitive and possibly coexisting deformation mechanisms at the single crystal level. For instance, slip-twinning interactions, twin-twin interactions, twinning-detwinning mechanisms, among others. The relevance of each mechanism on the final macroscopic response largely depends on the crystal structure, loading history and other conditions such as the temperature.

Remark 2.5 The irreversible nature of plastic deformation renders it a thermodynamically *dissipative* phenomenon. When metals and alloys experience a plastic deformation, most of the provided energy is dissipated as heat by the dislocations motions as the result of lattice friction. A residual energy fraction is retained internally associated with the purely elastic distortions of the lattice around the dislocation sites and of the grains due to residual stresses.

Regarding the deformation of polycrystalline materials, the physics governing deformation within the grains, i.e. the intragranular deformation, is virtually similar to those of single crystals. However, given the different lattice orientation of each grain of the polycrystal, upon macroscopic straining, intragranular slip occurs in stages, rather than simultaneously activated in all grains, since the Schmid-type slip condition is met heterogeneously in the sample. Moreover, the onset of slip in a crystallite must *a priori* satisfy the strain compatibility criteria on the grain boundary. This means that the intragranular deformation of each grain is, to some degree, constrained by its neighbours. This ensures that grain bonding, and ultimately the continuity of the aggregate, is preserved. This additional kinematic restriction partially explains the improved macroscopic resistance to plastic flow displayed by polycrystalline aggregates when compared to the response of a single crystal. The compatibility condition at the grain boundaries is guaranteed only by elastic micro-deformations (Lemaitre and Chaboche, 1994). The occurrence of twinning and/or non-Schmid slip at the grain level may also lead to a macroscopic tension-compression asymmetry at the polycrystalline level. Such behaviour is evident in the case of textured polycrystals, however, although it may not be so clear, it holds for texture-free ones (Hosford and Allen, 1973).

In the absence of phase transformations and other structural transformations (e.g. precipitation, recrystallization), plastic deformation of metallic polycrystals is virtually isochoric at the microscale, i.e., at level of the grains. This phenomenon, often referred to as plastic incompressibility, is explained by the insignificant volume change of the grains due to the increase of the density of dislocations (Lemaitre and Chaboche, 1994). This is not the case for the elastic deformation process where noticeable volume changes can take place due to the expansion and compression of the atomic bonds.

Remark 2.6 If bulk lattice defects such as micro-voids and/or micro-cracks are present in the polycrystal, the hypothesis of macroscopic plastic incompressibility is no longer adequate.

2.1.3 Hardening mechanisms

As discussed above, the ability of a polycrystalline material to undergo plastic deformation greatly depends on the ability of its lattice dislocations to move. This implies that the resistance to plastic deformation can be enhanced by restricting the motion of dislocations by acting on the degree of nucleation, propagation, and interaction of dislocations and mechanical twins, both at the intragranular and intergranular level. The *yield* (or *flow*) *stress* – the stress necessary to continue deformation at any stage of plastic strain – of a polycrystalline lattice can be increased via the so-called hardening mechanisms.

Hardening mechanisms, also known as strengthening mechanisms, describe how lattice defects (see §2.1.1) can act as barriers to dislocation motions. These include: (i) grain boundary hardening, associated with dependence of the initial flow stress on the average crystallite size of the aggregate, as expressed by the classical Hall-Petch relationship (Hall, 1951; Petch, 1953); (ii) strain hardening, alias work hardening, related with the increase of the density of dislocations and their ensuing interaction resulting a monotonic increase of the applied stress required to progress the plastic deformation of a crystal; (iii) solid solution hardening, related with the presence of punctual crystalline defects, both substitutional and/or interstitial; (iv) dispersion hardening promoted by the inclusion of finely dispersed particles in the polycrystal alloy (e.g. age or precipitation hardening of supersaturated solid solutions and/or from internal oxidation of the alloy (Hosford, 2010)); (v) martensitic phase hardening regarding a particular type of inclusion-based hardening of the lattice obtained by diffusionless transformations. These hardening mechanisms can coexist and interact with each other. Typically, the relative importance of each mechanism and the effect of its activation on the macroscopic response varies during the deformation process. The hardening characteristics of a given polycrystal crucially defines its ability to undergo irreversible deformation before mechanical failure – a property referred to as *ductility*. This topic will be revisited in forthcoming sections, where a comprehensive description of failure phenomena in metals and alloys is provided.

In general, the underlying hardening mechanisms governed by the interaction of lattice defects, as described above, remain valid at high temperatures. However, in this case, other thermally activated mechanisms, intrinsically time-dependent (viz. strain-rate dependent) due to the diffusion phenomena involved, are favoured. These include: viscoplasticity, restoration (or recovery), recrystallization, and other microstructural instabilities such as precipitation, phase and/or structural changes, static and/or dynamic aging (e.g. in the form of the so-called Piobert–Lüders bands and the Portevin-Le Chatelier effect), among others. The description of temperature and rate-effects on the behaviour of metals and alloys falls outside the scope of this thesis, thus no further discussion on the subject is provided.

2.2 Physics of the fracture of metals and alloys

This subsection provides an overview of the physics governing fracture phenomena in polycrystalline metallic solids. Emphasis is laid on ductile fracture, particularly under quasi-static loadings and at room temperature. The dynamic aspects of the crack formation and propagation are not covered as these do not concern the scope of the thesis. For a more detailed description of the phenomena reviewed here, the reader is referred to the works of Anderson (2017); Broek (2012); Garrison Jr and Moody (1987); Knott (1973); Lawn (1993); Pineau *et al.* (2016).

2.2.1 Fracture types

The reversible and permanent deformation mechanisms as described previously (§2.1) preserve the cohesion of the matter at the atomic and crystalline level, respectively. Fracture, in turn, refers to the destruction of this cohesion due to the irreversible rupture of interatomic bonds, ultimately resulting in the creation of surface and volume discontinuities within the solid. Accordingly, fracture encompasses mechanisms acting across different length scales. In a broad sense, the term damage describes the undesired evolution of one or more (micro)-structural features of a material that impair its engineering performance (Tekkaya *et al.*, 2020). Thus, regarding the study of fracture, one refers to damage to denote any local change in the microstructure of a material that leads to a reduction of its load-bearing capacity. The most representative example leading to such internal degradation process in ductile metals and alloys is the nucleation, growth, and coalescence of deformation-induced discontinuities in the material, namely in the form of microcracks and/or micro-voids.

Remark 2.7 The internal degradation of a material by the formation and propagation of micro-voids and/or micro-cracks is a plasticity-controlled irreversible thermodynamic process. Accordingly, *damage* can be regarded as a specific dissipative phenomenon.

Another important aspect regarding fracture phenomena in engineering applications is the concept of toughness. In essence, toughness is the ability of a material to absorb energy before fracturing. While a reasonable amount of ductility is required to deform metals and alloys into engineering parts, viz. in forming processes (e.g. forging, rolling, extrusion, stamping), toughness is required to prevent failure during service and to ensure the crashworthiness of a structure (Hosford, 2010). Naturally, absorbing energy entails plasticity. Accordingly, toughness associates the ductility and strength of a material. The polycrystalline structure (together with the density of built-in lattice defects), the deformation conditions, (viz. loading type, strain-rate, temperature), and any other features affecting the plastic flow of a material (e.g. geometric constrains), largely set the type of the fracture. A fracture is said *ductile* or *brittle* depending on the amount of irreversible deformation that precedes it.

Brittle fracture refers to the rupture of interatomic bonds without noticeable plastic deformation at the macroscale. Cleavage fracture is the most representative mechanism of transgranular brittle fracture. It consists in the direct separation of particular crystallographic planes – the cleavage planes, intrinsic to the crystal structure. In essence, cleavage fracture develops in a crystallite when the normal stress

across its cleavage planes reaches a critical value, i.e. when the installed strain energy reaches the energy necessary to pull the atomic layers apart (Hosford, 2010; Lemaitre and Chaboche, 1994). As one would expect, regions of high stress concentration in the lattice are preferred sites for triggering the nucleation of brittle microcracks, e.g., the stress developing at bulk lattice defects (e.g. inclusions, voids) and at dislocation pile-ups (e.g. at grain and/or twin boundaries) (Lemaitre and Chaboche, 1994; Pineau *et al.*, 2016; Stroh, 1954). Within a crystal, several cleavage facets can develop concurrently which, after joining with each other, provide the typical "stair-step" surface fracture (Figure 2.3a). Likewise, the cleavage facets must change direction at grain boundaries (and twin boundaries) in order to follow the crystallographic cleavage planes of the next crystal (or twin) (Lemaitre and Chaboche, 1994; Pineau, Benzerga and Pardoen, 2016). Cleavage fracture occurs most often in metallic materials with bcc and hcp lattice structures displaying high strength and very limited ductility (generally fcc metals do not exhibit a brittle behaviour due to 'recovery processes' at the crack tip, e.g. dislocation cross-slip and climb, inhibiting stress concentration at dislocation pile-ups (Ebrahimi *et al.*, 2006)). High strain-rates and low temperatures facilitate brittle fracture as plasticity is hindered. Fracture cannot occur totally by transgranular cleavage. The propagation of a microcrack to neighbouring grains requires the activation of an intergranular mechanism. Intergranular fracture is a particular type of cleavage that follows the grain boundaries (Figure 2.3b). The propagation of a brittle fracture after the nucleation of a microcrack is very rapid (approaching the speed of sound of the material) and virtually unstoppable (Mouritz, 2012). The presence of a smooth fracture surface whose orientation is perpendicular to the major applied stress is convincing evidence that the fracture in the material has a strong brittle component. The catastrophic and unanticipated nature of this type of fracture renders it particularly detrimental in engineering practice.

Ductile fracture involves extensive plastic deformation in the vicinity of microstructural bulk defects (§2.1.1) and results from a plasticity-controlled process often described by a three-stage process: the nucleation, growth and coalescence of voids (McClintock, 1968; Rousselier, 1987). Depending on the density of defects and the promptness of the damage accumulation process, a material may or may not display noticeable plastic deformation at the macroscopic scale (Lemaitre and Chaboche, 1994). The void distribution in a material can occur for several reasons. During solidification of the metallic melt, voids can form due to: (i) shrinkage of the solid (often referred to as cavitation); (ii) trapped gas bubbles (e.g. air and/or hydrogen); (iii) non-metallic impurities on the melt; (iv) defective or insufficient bonding in the grains (Pires, 2005). These are known as pre-existing voids. Additionally, during deformation, voids can nucleate at inclusions due to particle cracking and/or decohesion at the inclusion-matrix interface. The elastoplastic deformation of the material surrounding these cavities causes them to undergo volumetric and, possibly, shape changes. These phenomena are referred to as void growth and void distortion, respectively. Void coalescence marks the transition from the relatively diffuse plastic deformation surrounding the voids to a highly concentrated deformation mode within the intervoid ligaments (Pineau and Pardoen, 2007). In contrast to the growth stage, void coalescence necessarily involves strong interaction between voids. Intervoid linkage leads to the formation of microcracks in the lattice.

The propagation of a macroscopic crack takes place by several void coalescence events occurring at the crack tip, often involving the interaction of micro-void populations of varying size, spacing and/or orientation (Pineau *et al.*, 2016). Crack propagation in ductile media is a stable process since an external energy supply is required to growth an existing crack. This is in clear contrast with the brittle fracture where the energy needed to initiate a crack, largely stored as elastic energy, is higher than the one needed to propagate it. The stable nature of ductile crack propagation is intimately related with the dissipation of plastic energy in the vicinity of the crack tip of ductile metals, which constitutes a considerable part of the total energy released during fracture (Rice and Budiansky, 1973). Moreover, propagation occurs at a speed which is a function of the remote loading rate (Lemaitre and Chaboche, 1994), and material dependent. Of course, in both fracture types, the crack propagates along the path which minimizes the energy dissipated of the creation of new surfaces. Fractographic analyses under scanning electron microscopy (SEM) of metals exhibiting ductile failure reveal scooped out regions known as 'dimples' (see Figure 2.4). The dimpled surfaces result from the nucleation around pre-existing particles and the plasticity-controlled breaking of the ligaments of the voids during the coalescence stage. Under quasi-static loadings at room-temperature, fracture of most metals is of the ductile type (Pineau and Pardoen, 2007).

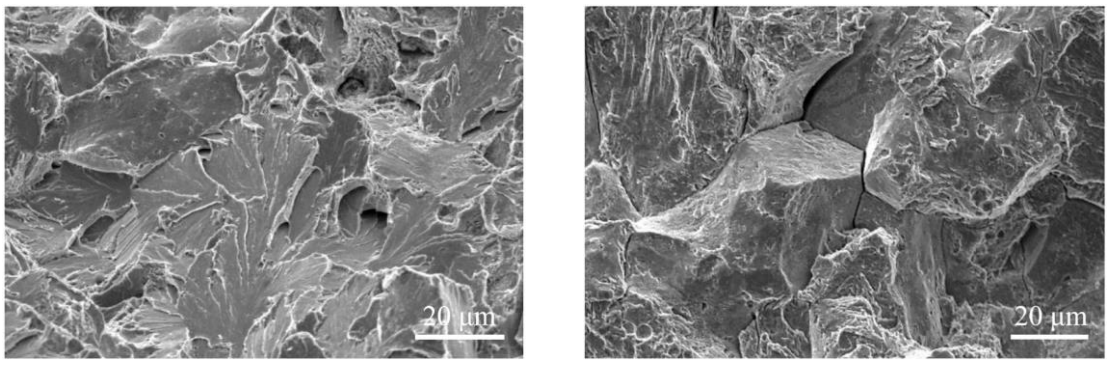

(a) (b)

Figure 2.3 SEM micrographs of the fracture surface of a low carbon steel that experienced temper-induced embrittlement (after Koneti *et al.* (2011)): (a) transgranular cleavage fracture; (b) intergranular fracture.

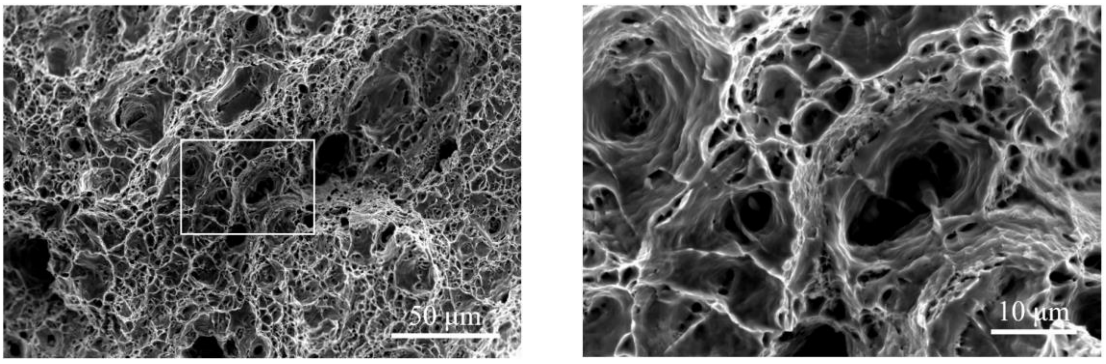

(a) (b)

Figure 2.4 SEM micrographs of the fracture surface of a Nb-micro-alloyed steel at different magnifications (after Wu *et al.* (2005)): (a) 500×; (b) 2000×. Note that dimples appear in a spectrum of length scales. The remaining part of the dimples (and possibly the inclusions that triggered them) are on the mating surface.

2.2.2 Ductile failure modes

Ductile fracture invariably results from the plasticity-controlled process of void nucleation, growth and coalescence. However, for practical purposes, it is convenient to distinguish two failure modes: (i) damage-controlled; and (ii) plastic localization-controlled (Pineau and Pardoen, 2007). In the former, the damage process evolves more or less evenly in homogenously deformed regions of the material until the onset of failure. Therefore, only at the very end of the process, macroscopically heterogenous deformation zones may arise due to coalescence events at void clusters and ensuing crack propagation in the solid by ductile tearing[1]. In the latter, a macroscopic plastic instability, viz. in the form of shear bands (often preceded by local 'necking'[2]), develops early in, or even prior to, the damage process. In such case, damage-induced softening may or may not be accountable for triggering the plastic instability (Pineau *et al.*, 2016). In engineering practice, the onset of strain localization in a material critically restricts its (remaining) ductility. Accordingly, localization it is often regarded as a standalone ductile failure mechanism. One cannot emphasize enough that the usual three-stage damage process still takes place within the localization band, being the ultimate responsible for the ductile fracture itself. Typically, the increasing stress constraint in the band accelerates the damage process and the final fracture follows rapidly (Pineau and Pardoen, 2007). Whether a ductile fracture is dominated by straightforward coalescence events or preceded by macroscopic plastic instability is a long-debated topic (Benzerga *et al.*, 2019; Keralavarma *et al.*, 2020; Morin *et al.*, 2019; Tekoğlu *et al.*, 2015). In short, the ductile failure mode strongly depends on the material behaviour, homogeneity, geometrical constraints and boundary conditions, viz. stress state history. For instance, ductile failure is typically coalescence-controlled in notched and pre-cracked specimens (Pineau *et al.*, 2016), i.e., geometries inducing multiaxial stress states. In contrast, planar geometries (e.g. thin sheets) and/or stress states approaching the uniaxial path are notorious for being conducive to a localization-controlled fracture (Benzerga *et al.*, 2019; Kõrgesaar *et al.*, 2014; Tasan *et al.*, 2009). Slant fracture denotes a ductile fracture mode associated with the occurrence of strain localization at the crack tip. The surface of a slant fracture can exhibit total or partial slanting and typically occurs in plane strain specimens and thin metal sheets (Benzerga and Leblond, 2010; Pineau *et al.*, 2016). A material may also experience a mixed ductile fracture mode. This is often the case of round smooth bars: the fracture is damage-controlled at the centre of the specimen, resulting in a flat fracture in this region; and localization-controlled at the outer rim, leading to the formation of so-called shear lips due to a slant fracture mode. Round tensile bars usually form a so-called cup-cone fracture, consisting of a flat part, which presents a quasi-equiaxed dimpled aspect; and of a slant part, displaying elongated dimples with a lower degree of roughness (Benzerga and Leblond, 2010). Material anisotropy can however lead to a full slant-type fracture in such specimens, as recently showed in Benzerga *et al.* (2019). Figure 2.5 represents a schematic of the two failure modes associated with the ductile fracture, as discussed above.

[1] The ductile tearing process denotes the mechanisms of void growth and coalescence ahead of the crack front.
[2] Localized necking is a strain localization phenomenon characterized by a non-uniform reduction of the cross section of a material during tensile stretching.

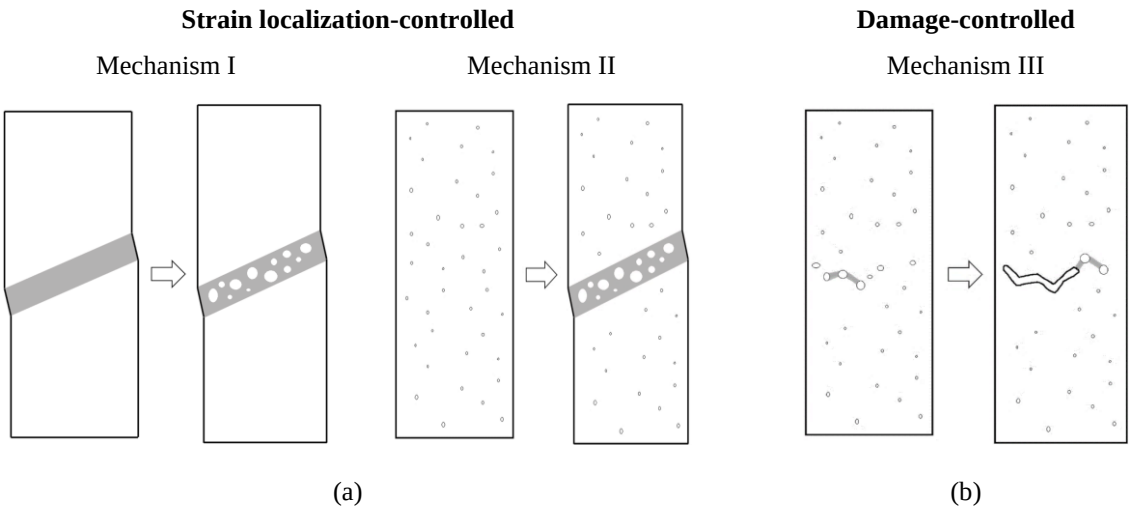

Figure 2.5 Two main modes of ductile failure: (a) strain localization-controlled (with damage playing either a primary – Mechanism I, or secondary – Mechanism II, role in the nucleation of a shear band); and (b) damage-controlled (Mechanism III). Adapted from Tekoğlu *et al.* (2015).

Strain localization (alias shear banding) denotes the formation of mesoscopic band-like planar zones of intense deformation developing from a more or less homogeneous deformation field (Raabe, 2014) (see Figure 2.5a). Strain localization is characterized by an intense dislocation (and/or twinning) activity within a narrow band, while the adjacent material undergoes comparably low and homogeneous plastic flow, or even elastic unloading (Raabe, 2014; Tekoğlu *et al.*, 2015). Accordingly, strain localization is a material instability since the homogeneity of the deformation of the solid cannot be restored after the nucleation of a shear band, which is preceded by a bifurcation of the trivial (or fundamental) equilibrium path (Bigoni, 2012). Strain localization can thus be regarded as an additional mesoscopic, (i.e. involving multiple grains), and non-crystallographic deformation mode. Although microstructural details of the crystalline lattice play a key role in the nucleation of the shear-band, the mesoscopic orientation of the band, typically oblique to the main deformation axis, does not follow a specific crystallographic direction (e.g. a slip or twinning system) (Benzerga *et al.*, 2019; Raabe, 2014). Instead, the band orientation is mainly defined by the specimen geometry, stress state and/or macroscopic material behaviour (e.g. anisotropy). Conversely, the band width is typically set by the microstructure, particularly, the grain size (Pineau and Pardoen, 2007).

Despite strain localization being one of the most frequently observed failure modes in ductile materials, the basic understanding of the microstructural features involved in this phenomenon remain somewhat elusive (Benzerga *et al.*, 2019; Raabe, 2014). Literature on strain localization phenomena, whether analytical (Anand and Spitzig, 1980, 1982; Hill, 1962; Hutchinson and Tvergaard, 1981; Leblond, Perrin and Devaux, 1994; Needleman and Rice, 1978; Rice, 1976; Rudnicki and Rice, 1975; Yamamoto, 1978) or computational (Becker and Needleman, 1986; Benzerga *et al.*, 2001, 2019; Al Kotob *et al.*, 2019; Kuroda and Tvergaard, 2007; Needleman, 1989; Tvergaard, 1987; Tvergaard *et al.*, 1981; Tvergaard and Needleman, 1995), primarily attempts to tackle the following problem: given a particular material behaviour and boundary conditions, viz. stress state, rationalize the occurrence of plastic strain

localization. This leads to the formulation of a collection of potentially sufficient conditions thought to be responsible for shear band formation (e.g. see Pineau *et al.* (2016) for a detailed description). These include, for instance: (i) pressure-sensitive plasticity (Rudnicki and Rice, 1975); (ii) anisotropic plasticity (Anand and Kalidindi, 1994; Benzerga *et al.*, 2019; Harren *et al.*, 1988; Kuroda and Tvergaard, 2007; Lloyd and Priddy, 2017; Steinmann *et al.*, 1998); (iii) thermal softening (Curran *et al.*, 1987; Needleman, 1989); (iv) non-associative flow (Anand and Spitzig, 1982; Greer *et al.*, 2013); (v) strain softening (Coleman and Hodgdon, 1987), viz., damage-induced (Benzerga *et al.*, 2001; Leblond, Perrin and Devaux, 1994; Tvergaard, 1981; Tvergaard and Needleman, 1995; Yamamoto, 1978). However, in engineering practice, the inverse problem is more realistic: given a structure experiencing strain localization, identify the (possibly competitive) features of the material that played a role in the nucleation of the shear band. Naturally, answering the inverse problem is more challenging since engineering materials can simultaneously meat several of the 'sufficient conditions' for shear banding described above. Moreover, the formation of shear bands in actual components (or specimens) is not solely governed by the material response. Material structural heterogeneity and geometrical constraints may also induce localization. Geometric-induced localization denotes the occurrence of localization as a result of local stress and strain gradients triggered by geometric constraints imposed to the specimen, rather than by the remote loading itself. The most representative example is the phenomena of necking in ductile metallic sheets (Rice, 1976). Geometry can facilitate or hinder the propagation of a shear band, and thus the propensity towards a slant fracture. In general, planar geometries, particularly with flat side surfaces and decreasing thickness are conducive to slant-type fractures (Asserin-Lebert *et al.*, 2005; Benzerga *et al.*, 2019; Pineau *et al.*, 2016; Rice, 1976). On the other hand, axisymmetric geometries (axisymmetric stress and strain states are extremely 'stiff' against localization, surface grooves, and planar geometries with high thickness values inhibit premature localization, thus promoting damage-controlled flat fractures (Figure 2.5b). Note that localization may still occur in these geometries, however in such cases, localization is triggered by material behaviour, e.g. anisotropy (Benzerga *et al.*, 2019), or strain hardening saturation (Asserin-Lebert *et al.*, 2005), rather than geometry.

Whether the presence of micro-voids and/or micro-cracks plays a primary or secondary role in the nucleation of plastic localization is often doubtful. This motivates the partition of the localization-controlled failure mode in two alternative mechanisms (Figure 2.5a). In some cases, damage-induced softening overrules strain hardening and leaves the possibility wide open for a macroscopic instability to set an effective limit on ductility (Keralavarma *et al.*, 2020) (Mechanism II, Figure 2.5a). In others, the pre-existing voids are, however, either not evident or decisive, and the plastic instability follows from a range of alternative mechanisms, many of which do not involve such microstructural defects (Mechanism I, Figure 2.5a). Strain localization phenomena is difficult to study experimentally given its unstable and abrupt nature (Benzerga *et al.*, 2019). The experimental work in Tasan *et al.* (2009) related the material microstructural homogeneity with the role played by ductile damage on strain localization. It was observed that, for a single-phase steel, damage did not display a significant role on strain localization; on the contrary, damage accumulation in a dual-phase steel was responsible for triggering plastic

localization. Moreover, recent high-resolution *in situ* synchrotron X-ray laminographic observations on an AA2198 (Al-Cu-Li) alloy revealed that the formation of shear bands ahead of a crack tip of a pre-cracked sheet specimen (by flat-to-slant crack transition) and final slant fracture were virtually unaffected by the accumulated damage before fracture (Morgeneyer *et al.*, 2014). In summary, the onset of plastic instability in the form of strain localization results from an intricate relationship between intrinsic (i.e. material) and non-intrinsic contributions.

2.2.3 Ductile crack formation

This subsection is devoted to a more in-depth discussion on the mechanisms of nucleation, growth, and coalescence of voids. The contents of this subsection are mainly based on the overarching works of Benzerga and Leblond (2010); Garrison Jr and Moody (1987); Pineau *et al.* (2016); Pineau and Pardoen (2007). The micromechanisms involved in the ductile damage process are initially discussed individually. To close, their collective manifestation for the ductile crack initiation is analysed.

Void nucleation

Early studies on ductile fracture of metals and alloys established that voids primarily nucleate at inclusions, through inclusion-matrix decohesion and particle cracking, either within the grains or along the grain boundaries (Argon *et al.*, 1975; Beremin, 1981; Fisher and Gurland, 1981; Goods and Brown, 1979; Puttick, 1959; Tipper, 1949; Wilsdorf, 1983). Nucleation phenomena are usually associated with strain incompatibility and stress concentration in the vicinity of lattice defects (Lemaitre and Chaboche, 1994; Tekkaya *et al.*, 2020). The local stress field leads to intense plastic deformation of the matrix material near the defects. The inclusions, often being more brittle than the matrix, ultimately experience decohesion (by microcrack propagation at the inclusion-matrix interface) or brittle-like fracture of the inclusion itself, typically, by cleavage. Factors favouring one mode of nucleation over the other include: the matrix flow properties, viz. yield strength and hardening behaviour; the particle shape and orientation (relative to the remote loading); the matrix-particle stiffness mismatch, and loading, (viz. the triaxiality) (Benzerga and Leblond, 2010). These factors and their trends on nucleation type are summarized in Table 2.1.

Table 2.1 Key parameters governing void nucleation and relative trends upon the increase of each parameter for the activation of a nucleation mode (after Benzerga and Leblond, 2010).

Parameter	Type	Nucleation trend	
		Decohesion	Cracking
Matrix yield strength		↘	↗
Matrix hardening exponent		↘	↗
Particle elongation		↘	↗
Matrix-particle stiffness mismatch		↗	↗
Relative loading orientation	Axial	↘	↗
	Transverse	↗	↘
Loading triaxiality		↗	↘

The ductility of structural alloys is strongly affected by their volume fraction of inclusions (Edelson, 1962). Some alloys involve several inclusion types. The existence of populations of particles of different size is particularly relevant regarding ductile fracture (Asserin-Lebert *et al.*, 2005; Bron *et al.*, 2004; Cox and Low, 1974; Hahn and Rosenfield, 1965). The size and shape of the voids mostly depend on the type of inclusions that originate them. In general, voids nucleated by particle cracking or by partial particle decohesion are initially flat and 'penny-shaped' (Lassance *et al.*, 2006), while the ones nucleated by complete particle decohesion are initially spherical (Pineau *et al.*, 2016). Likewise, elongated inclusions, typical in heavily rolled products, lead to the formation of channel-shaped voids (e.g. MnS inclusions in steel (Beremin, 1981)). As pointed out in Benzerga *et al.* (2016), it is still not clear what role, if any, the shape of the incipient voids plays on ensuing fracture events. In addition to particle decohesion and cracking, other microstructural surface and bulk defects, viz., interfaces, deformation-induced boundaries and other miscellaneous heterogeneities, may act as nucleation sites (Bieler *et al.*, 2009; Cuitino and Ortiz, 1996; Gardner *et al.*, 1977; Greenfield and Margolin, 1972; Inoue *et al.*, 2008; Kondori and Benzerga, 2014; Lemaitre and Chaboche, 1994; Lubarda *et al.*, 2004; Noell *et al.*, 2017, 2018; Rodriguez *et al.*, 2016; Tan *et al.*, 2007; Tasan *et al.*, 2009; Thompson and Williams, 1978)), yet these nucleation mechanisms are rarely observed in engineering alloys.

Void growth

Void growth and void distortion mechanisms denote, respectively, the volumetric enlargement and shape change of the nucleated (or pre-existing) voids by plastic deformation of the surrounding matrix. Early macroscopic observations on the ductile fracture of metals and alloys, as firstly reported in Hancock and Mackenzie (1976) and followed by many others (Becker *et al.*, 1988; Devaux *et al.*, 1985; Johnson and Cook, 1985; Marino *et al.*, 1985; Le Roy *et al.*, 1981), established that ductility deteriorates monotonically with increasing stress triaxiality. Such behaviour is intimately related to the exponential increase of the micro-void growth rate with increasing stress triaxiality of the remote loading (Rice and Tracey, 1969). Therefore, the hydrostatic stress, which has little to no influence on the plastic response of fully dense materials, exhibits a critical role on the behaviour of porous ones (i.e. containing voids), particularly on the void growth and coalescence stages (Nahshon and Hutchinson, 2008). Indeed, the stress triaxiality plays a major role in the ductile fracture formation. Under sufficiently high stress triaxiality loadings, volumetric enlargement of the voids dominates over the shape changing effect so that void growth is essentially spherical (Rice and Tracey, 1969). In such case, the micro-voids nucleated by particle cracking tend to open and become spherical with accumulated plastic deformation of the matrix material (Pineau and Pardoen, 2007). Conversely, under low stress triaxiality, void growth in the volumetric sense is relatively smaller (or even inexistent) and void distortion by large 'deviatoric' shape changes govern the damage process (Thomason, 1990). In the latter case, the initially quasi-spherical voids nucleated by particle decohesion tend to elongate in the principal loading direction (Pineau and Pardoen, 2007) (while contracting in the perpendicular directions). Accordingly, while the role played by the shape of the incipient voids is somewhat uncertain, thus often relegated, the micro-mechanics of void distortion and its role on the ductile damage process is a subject of ongoing research (Pineau *et al.*,

2016). At intermediate stress triaxialities there is a combined effect of volumetric and shape changes of the voids. Naturally, void distortion may also result from the presence of a shear component in the remote loading. If so, the elongated voids also undergo rotation. Void rotation can also take place if the void axis is not aligned with the principal loading direction, as shown in Benzerga *et al.* (2004a); Roth *et al.* (2018). In both cases, the rotation experienced by the voids can influence the interaction with the neighbouring voids in the coalescence stage (Pineau *et al.*, 2016; Tvergaard, 2012). In the absence of localization in the intervoid ligaments, an initially spherical void subjected to a shear stress field may elongate and rotate to the point where eventually it closes into a penny-shape crack (McClintock *et al.*, 1966; Tvergaard, 2012). This is referred to as void-rotation mediated closure. In practice, however, the particles responsible for void nucleation are still present within the voids. In turn, during the damage process, the kinetics of the void may be constrained by the particle itself. Void-particle interactions are particularly relevant at low stress triaxialities such as in uniaxial tension, compression and shear (Pineau *et al.*, 2016). The forced contact between the void and the particle is referred to as void locking (Lee and Mear, 1999; Siruguet and Leblond, 2004a, 2004b). Void locking leads to a net increase of the porosity, both in shear (Achouri *et al.*, 2013) and uniaxial loadings (Babout, Brechet, *et al.*, 2004) since the void collapse effect in the directions perpendicular to the direction of void elongation is precluded by the particle. In summary, the evolution of the size, shape and orientation of the voids is governed both by intrinsic (micro-structure) and by extrinsic factors (loading conditions).

State-of-the-art *in situ* 3-D X-ray tomographic (non-destructive) experiments have been allowing a more detailed characterization of the damage process, viz. the evolution of the size and morphology of the micro-voids (Babout *et al.*, 2001; Babout, Maire, *et al.*, 2004; Maire *et al.*, 2005; Weck *et al.*, 2008). Numerous other studies on void growth in metals and alloys were carried out using more tedious destructive methods, which allow to explore stress triaxiality effects and smaller porosity regimes on the void growth process, e.g. Benzerga *et al.* (2004a); Chae and Koss (2004); Pardoen and Delannay (1998).

Void coalescence

Void coalescence denotes the phenomenon of concentration of the plastic deformation within the ligaments of adjacent micro-voids, preceding their final linkage. Void coalescence governs the physical transition to fracture, i.e. the formation and propagation of discontinuities within the solid; ultimately controlling the resistance of the material to undergo ductile failure (Pineau and Pardoen, 2007). A significant part of the total energy associated with the damage process may be spent on the microscopic plasticity involved in this final stage (Besson, 2010). During the damage accumulation, void nucleation, growth and/or distortion leads to the reduction of the spacing between neighbouring voids. As the intervoid ligaments contract, the rather diffuse plastic deformation of the matrix that governs the void growth process is interrupted and plasticity concentrates within the intervoid ligaments. The first coalescence events often take place inside void clusters and/or at zones involving high stress triaxiality or large plastic deformation (Pineau *et al.*, 2016). Depending on the displayed strain concentration at the ligaments, two coalescence modes are often distinguished: (i) internal necking; (ii) internal shearing. A third mode, so-called ‘necklace’ coalescence, based on the conjectural evidence reported in Benzerga

(2000), may also be distinguished, yet this mode can be regarded as a particular case of the former coalescence mode.

The most commonly observed mode of void coalescence is internal necking (Benzerga and Leblond, 2010). In this mode, intervoid ligament contraction results in the formation of a neck-like plastic instability. After the onset of internal necking coalescence the involved micro-voids expand rapidly in the radial direction as the ligament necks down while their axial growth remains small. This often grants the voids a characteristic diamond shape, particularly when internal necking takes place near their equators (Pineau and Pardoen, 2007). Internal necking and final ligament failure may also occur away from the equators of the voids, due to prior void distortion events. Intervoid necking and ligament failure at the largest voids may be facilitated by the presence of a secondary population of smaller voids within the ligament (Bao, 2003), as reported in Benzerga (2000).

Internal shearing is driven by localization at the mesoscale and concerns voids that undergone void distortion and rotation in the growth stage. In contrast to internal necking, coalescence by internal shearing of large (primary) voids can be triggered while the voids are still quite apart (Benzerga and Leblond, 2010). The nucleation of a secondary population of smaller voids within a planar microshear band at the ligament or primary voids can facilitate intervoid linkage (Noell *et al.*, 2018). Internal shearing tends to produce a macroscopic crack along the shear band plane.

As in the void growth stage, the stress triaxiality displays a major role on the activated coalescence mode. Failure by internal necking of the ligaments mainly occurs at high stress triaxiality. As the stress triaxiality decreases and the deviatoric component of the stress state increases, shearing-based coalescence mechanisms are promoted (e.g. see work of Barsoum and Faleskog (2007), for experimental evidence). This is intimately related with the propensity to shear band formation at such stress states. At intermediate stress triaxialities there is a combined activation of internal necking and shearing mechanisms, i.e., the intermediate stress triaxiality range is a transition range (Bao, 2003). Again, one must stress that shearing-based coalescence modes are not limited to failure under shear-dominated loadings. Internal shearing coalescence has been observed under triaxial stress states developing inside the neck of a notched bar, due to void rotation during the damage process (Pineau *et al.*, 2016). This reinforces that the triggered coalescence mode is a statistical process, which depends on the relative position (viz. spacing and orientation) of the ligaments between neighbouring voids.

From damage to cracking

A material is said to be in a damaged state if it has progressively undergone the processes of void nucleation, growth (and/or distortion), as well as a few isolated and inconsequential void coalescence events (Pineau *et al.*, 2016). As damage accumulates either: (i) a crack initiates; (ii) a pre-existing crack propagates; or (iii) a plastic instability occurs. The latter outcome eventually leads to one of the former ones, i.e. either the nucleated shear band induces fracture in a crack-free specimen; or a crack propagating in a specimen undergoes transition from flat to slant mode. Typically, the onset of a macroscopic crack follows the coalescence of few of the largest voids (Benzerga *et al.*, 2004a). A coalescence event gives rise to a larger flat void resembling a microcrack. Further void coalescence events occurring near

the crack tip can then propagate the microcrack. A material can concurrently experience this process at other locations. Nevertheless, at some point, one main crack eventually develops and controls the remaining ductile fracture process, leading to the final loss of load-bearing capacity of the solid, while plasticity ceases elsewhere (Pineau *et al.*, 2016). The end of a coalescence process in metals usually involves the premature failure of the intervoid ligaments, rather than a plasticity-controlled radial void growth until void impingement, (alias void touching). Ligament failure mechanisms include (micro)-cleavage and crystallographic shearing, which may be additionally aided by the presence of a second population of smaller voids in the ligament (Pineau and Pardoen, 2007). To some extent, the transition between internal necking and internal shearing coalescence modes can be related to the transition between flat fracture to slant fracture surfaces (Figure 2.6a) (Pineau and Pardoen, 2007). The former characteristically exhibits a dull and fibrous aspect with quasi-equiaxed dimples (as in Figure 2.6b) whereas the latter exhibits parabolic elongated dimples, as represented in Figure 2.6b. In ductile materials, crack initiation usually occurs past the maximum macroscopic load, while in less ductile alloys, fracture may even initiate during the rising part of the load (Pineau and Pardoen, 2007).

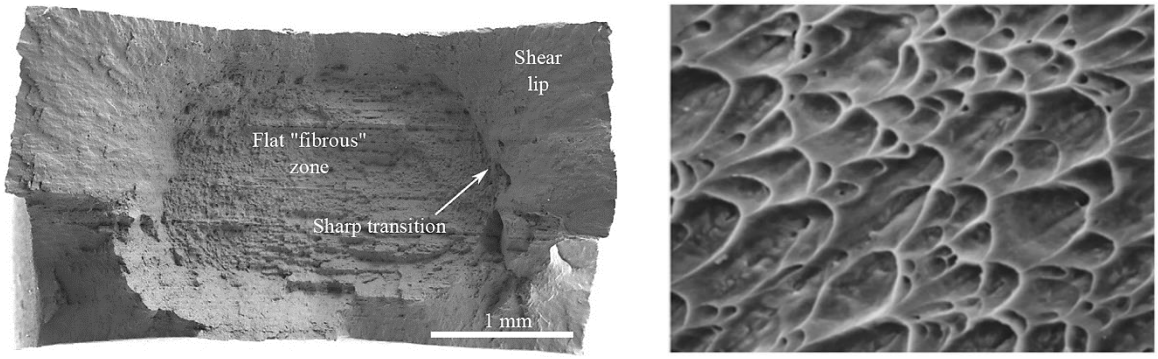

(a) (b)

Figure 2.6 Fracture morphology of a Ti-6Al-4V alloy: (a) two distinct fracture modes in a rectangular uniaxial tension specimen: a flat zone (mode I, plane strain) and a shear lip (mode II, plane stress) (Noell *et al.* 2018); (b) SEM micrograph of parabolic shear dimples after failure in torsion. Magnification of 1400× (Miller, 2002).

2.3 Concluding remarks

In this section, the main metallurgical phenomena governing the mechanical behaviour of poly-crystalline metals and alloys were described. The role of the microstructure, in particular the built-in lattice defects, was highlighted, demonstrating its crucial impact on the physical aspects of deformation, hardening, softening and fracture of these materials.

Remark 2.8 Plasticity and damage are strongly coupled dissipative phenomena that govern the occurrence of ductile fracture. A good understanding of the physics of the ductile fracture in metals and alloys relies on the proper appraisal of the theory of plasticity.

This implies the integration of the inherently heterogeneous phenomena, associated to *discrete* entities (viz. voids) at the microscopic level, with homogeneous *continuum* models, at the macroscopic level. In summary, such macroscopic models must fundamentally account for the following phenomena:

i. Elastoplastic flow (§2.1.2) and hardening (§2.1.3): the reversible and irreversible movement of atoms (slip, twinning and other dislocation motion mechanisms at the atomic level); the creation and interaction of slip and twinning systems;
ii. Texture (§2.1.1): initial preferred orientation of the grains; deformation-induced and twinning-induced crystallographic lattice reorientation relative to the loading direction;
iii. Strength differential effects (§2.1.2): mechanical twinning and/or non-Schmid type slip;
iv. Damage (§2.2.3): irreversible rupture of interatomic bonds and the nucleation and growth of deformation-induced discontinuities in the material, viz. voids.

These are strongly interdependent physical phenomena, involving complex couplings and interactions, from the diffuse deformation stage up to the onset of fracture. Hence, they should be modelled as such.

Chapter 3

Modelling ductile failure of metals and alloys

This chapter provides a literature review on damage constitutive modelling, continuum damage mechanics modelling schemes and a state-of-the-art review of the micromechanical-based void growth models for porous ductile solids, in particular, criteria of the Gurson-type.

3.1 Chapter introduction

Modelling is the approximation of reality. By definition a model is a simplified representation of a system and its features. Models are employed to identify, describe and better understand the fundamental principles and the cause-effect relationships between the features of the system which it represents. The proper rheological characterization of engineering materials by constitutive modelling contributes to a deeper understanding of the observed reality, in particular the intricate phenomena involved in the ductile fracture. Additionally, material models may also be applied for design proposes, viz. by improving the performance of mechanical components, both from the security and ecological point of view; and to aid the design of new grades of materials, by enhancing particular microstructural features (e.g. grain size, texture) in order to intrinsically improve their engineering performance (Besson *et al.*, 2009).

Continuum solid mechanics and thermodynamics constitute the basic theoretical tools and axioms for the formulation of the physical phenomena of deformation and fracture. In order to not overly extend this text, these general concepts are omitted here when possible and the focus is placed on the constitutive modelling concerning ductile damage. For a comprehensive description of such fundamental concepts, the reader is referred to 'classical' handbooks such as those of Besson (2010); Bonet and Wood (1997); De Borst *et al.* (2012); Germain (1973); Hill (1998); Jirásek and Bazant (2002); Lubarda (2002); Lubliner (2008); Mandel (1966); Simo and Hughes (2006); de Souza Neto *et al.* (2011); Zienkiewicz and Taylor (2005) on the framework of solid mechanics; and in particular to Benzerga and Leblond (2010); Cazacu *et al.* (2019); Lemaitre (2012); Lemaitre and Chaboche (1994); Lemaitre and Desmorat (2005); Saanouni (2013); Voyiadjis (2015) on damage modelling.

3.2 Overview of the possible modelling schemes

The local state method approach (Germain, 1973; Lemaitre and Chaboche, 1994) is remarkably well-suited for the formulation of constitutive equations involving several dissipative, often strongly coupled, phenomena. This approach is based on the assumption that the thermodynamic state at a given material point of the continuum can be fully defined at any instant of a thermokinetic deformation process by the knowledge of a finite number of *state variables*. Since no time derivatives of these variables are involved in the definition of the thermodynamic state, this approach implies that any evolution can be considered as a succession of equilibrium states (Lemaitre and Chaboche, 1994). The state variables, (alias independent/thermodynamic variables), in general, of scalar, vectorial or tensorial nature, may be grouped into two classes: observable and internal. For reversible phenomena (e.g. pure elasticity), the thermodynamic state depends at any instant uniquely on the observable variables[3]. In contrast, internal variables are introduced to account for dissipative phenomena (which are known to render the current state dependent on the history of the deformation). Each dissipative phenomenon envisioned to be modelled (e.g. plasticity, damage, etc.) entails the introduction of its own internal state variable, involving a more or less level of abstraction, in order to represent the current micro- or meso-structural state of the material (Lemaitre and Chaboche, 1994). By definition, an internal variable cannot be directly observed nor even directly measured (Saanouni, 2013).

Remark 3.1 The success of the constitutive model based on the local state method critically depends on the choice of an appropriate set of internal variables.

Naturally, for practical reasons, no plausible model may be general enough to describe the response of a wide range of materials under all types of applications. This way, the choice of internal variables must be guided not only by the envisioned class of materials but also by the (thermo)-kinetic processes under which the model is meant to describe the (thermo)-mechanical behaviour of the material (e.g. temperature range, strain-rate, etc.) (de Souza Neto *et al.*, 2011). For a more in-depth assessment on the local state method approach, refer for instance to Bataille and Kestin (1979); Kestin and Bataille (1977). In this work, this approach is adopted since it is appropriate for modelling the behaviour and fracture of deformable solids under large plasticity conditions.

Within the local state method, two particular approaches may be distinguished regarding the smallest scale which one intends to deal with in order to describe the desired reversible and/or dissipative phenomena: (i) the micromechanical; and (ii) the macroscopic phenomenological approach. Before briefly discussing these alternative approaches, it is of all interest to, at first, introduce and describe the concept of representative volume element (RVE). The existence of a RVE is intimately connected to the notion of separability of scales. The RVE defines the smallest volume holding, *a priori*, all the statistical (or deterministic, in the periodic case) information describing the distribution and the morphology of the heterogeneities of a material such that the volume element of matter can be regarded as a homogeneous

[3] In materially simple continua (e.g. Saanouni, 2013) one refers to observable variables, (alias external variables), to denote the following thermomechanical quantities: the deformation gradient (or any total strain measure tensor); the absolute temperature; and the temperature gradient. Naturally, time may be included in this definition.

continuum (Besson *et al.*, 2009; de Souza Neto *et al.*, 2011). Accordingly, by definition, any larger volume of material may be deduced through successive translations or additional realizations of the known statistical RVE. From the continuum solid mechanics viewpoint, the RVE must be large enough, with respect to the local material heterogeneities; and small enough, compared with the dimensions of the structure, for the classical mathematical operations (e.g. derivation and integration) at a spatial point of the continuum to be meaningful[4] (Lemaitre and Chaboche, 1994; Saanouni, 2013). In what follows, it is assumed that such RVE does exist. Returning to the previous topic, one distinguishes:

i. the micromechanical (alias bottom-up or inductive) approach, which describes the physical phenomena with state variables related to the nano- (viz. atomic, molecular) and/or microscopic (viz. crystalline) level. The basic idea behind this approach is the application of appropriate localization-homogenization techniques in order to deduce the 'macroscopic' behaviour of the RVE from the knowledge of the local (thermo)-mechanical fields of each of the elementary constituents of the RVE at lower length scales (Lemaitre and Chaboche, 1994; Saanouni, 2013; de Souza Neto *et al.*, 2011). This implies an explicit definition of the RVE *a priori*, viz. microstructural features (e.g., phases, grains and their size and orientations distribution for each phase);
ii. the macroscopic phenomenological (alias top-down or deductive) approach, which describes the behaviour of the RVE exclusively in a global fashion, totally disregarding the heterogeneities and specificities of the phenomena at lower length scales (Lemaitre and Chaboche, 1994; Saanouni, 2013; de Souza Neto *et al.*, 2011). Accordingly, the RVE is treated as a 'black box' during the task of determining the cause-effect relationship between input and output of the thermodynamic process under study. The dissipative behaviour observed at the macroscopic level, associated with microscopic physical phenomena, is modelled with macroscopic (alias phenomenological) internal variables. Such state variables should however, as far as possible, be related to the underlying microscopic dissipation mechanisms which they concern (de Souza Neto *et al.*, 2011).

In summary, while both approaches are based on the existence of a RVE, the idea behind the formulation of the continuum constitutive models is indeed distinct: the micromechanical approach aims to explicitly describe the 'true' physical mechanisms acting within the RVE; whereas the macroscopic phenomenological approach aims to directly couple continuum mechanics with phenomenology.

The micromechanical -based continuum models have, due to their very principle, a sounder physical background and are an undeniably promising and powerful approach. Nonetheless, it is unlikely that these may offer similar accuracy to the phenomenological, top-down, approach in the foreseeable future given the complexity involved in modelling the microscopic mechanisms of actual engineering materials (Benzerga and Leblond, 2010). Nevertheless, a growing number of studies are being devoted to the description of the behaviour of highly heterogeneous solids using this approach (see e.g. the books of Asaro and Lubarda (2006); Besson *et al.* (2009); Lubarda (2002); Raabe (1998); Tome and Lebensohn (2023)). On the other hand, the purely phenomenological approach to irreversible thermodynamics has

[4] In practice, from the numeric point of view, the RVE materializes as an integration point (often a Gauss point), when using the finite element method.

been historically successful in the field of solid mechanics, where numerous well-established models of elastoplastic solids have been developed. Indeed, despite its heuristic nature, the latter approach remains highly practical and efficient in the development of new constitutive equations (Saanouni, 2013). Developing constitutive laws with this modelling scheme entails the construction of the so-called state and dissipation *potentials*, which are closed, convex, scalar-valued functions of their arguments, as to be discussed in forthcoming sections. The constitutive laws developed in this work are based on the macroscopic phenomenological approach.

3.3 Damage constitutive modelling

The present subsection presents an overview concerning constitutive modelling within the damage mechanics framework. An introduction to this branch of continuum solid mechanics is provided, placing particular emphasis on the definition of damage variables. The section starts by distinguish the domains of application of the fields of damage mechanics and fracture mechanics (§3.3.1); following it, the framework of continuum damage mechanics (CDM) is presented and its two main branches, the phenomenological and the micromechanical approaches are described (§3.3.2). A first mathematical definition of the damage variable is provided. The section ends by describing a different scheme for modelling ductile damage, known as the uncoupled approach (§3.3.3).

3.3.1 Damage mechanics and fracture mechanics

The theory of *damage mechanics* is employed to describe the progressive deterioration of the matter, from the virgin state up to macroscopic fracture, within the continuum solid mechanics framework; viz. working with the RVE concept. In this context, the changes at the microstructural level due to the evolution of damage phenomena are incorporated in the continuum model by means of a set of scalars and/or tensor-valued internal state variables, either micromechanically or phenomenologically inspired, known as *damage variables* (Besson *et al.*, 2009; De Borst *et al.*, 2012; Lemaitre and Chaboche, 1994). Recall that, in a given material, damage (i.e. the irreversible rupture of interatomic bonds) may be triggered by a wide range of physical mechanisms, fundamentally depending on the type and rate of loading, temperature, as well as other environmental factors (e.g. oxidation, corrosive substances, radiation). Accordingly, damage mechanics must consider the material-process-environment triad, rather than the material alone (de Souza Neto *et al.*, 2011). Naturally, different damage variables, each describing a particular damage feature, can accumulate and interact with each other in a constitutive model. In any case, by knowing the stress and strain history of a given volume element of the structure, the evolution of a damage variable is provided by integration with respect to time of a *damage law*, consistent with the fundamental conservation and/or thermodynamic laws (Lemaitre and Chaboche, 1994). The final damage state is identified by the fulfilment of a failure criterion at a volume element of the continuum, representing the onset of a crack of the size of the RVE, often referred to as macrocrack (Figure 3.1). More specifically, as depicted in Figure 3.1, depending on the scale of the crack in a metallic material,

typically, one refers to a microcrack to denote a crack of an order of 0.01 – 0.1 mm (mesoscale); and to a macro-crack regarding length scales superior to the tenths of a millimetre (macroscale).

Remark 3.2 The growth of a micro- in to a macrocrack marks the transition of the domains of damage mechanics to fracture mechanics (Figure 3.1). While the notions of damage mechanics are often employed to predict the onset of a macrocrack in the continuum, the theory of fracture mechanics can be applied to study the propagation of this macrocrack up to the complete failure of the structure.

The theory of *fracture mechanics* (alias crack mechanics) deals with the description of the behaviour of solids with embedded macroscopic geometric discontinuities at the scale of the structure, viz. macrocracks. In the presence of these discontinuities, the crack geometry and dimensions must be directly taken into consideration in a fracture mechanics model as they modify the stress-strain fields on a scale that renders the assumption of a homogeneous medium no longer meaningful (Lemaitre and Chaboche, 1994).

An important remark is that damage and fracture mechanics are not incompatible nor mutually exclusive[5]. Fracture mechanics, which is often related to the study of concepts such as the fracture toughness, crack growth stability, intrinsic resistance to cracking, crack path prediction; does not exclude the possibility of studying the behaviour of a cracked medium within the theory of damage mechanics, thus staying in the framework of continuum mechanics. On the contrary, one should in fact account for the diffuse internal degradation of the solid both prior and during the fracture process, and thus adopt the theory of damage mechanics in the entire thermomechanical deformation process.

This work mainly concerns the framework of damage mechanics. Hereafter, one refers to continuum damage mechanics model (CDMM) to any continuum constitutive model that includes a set of internal variables representing, directly or indirectly, the density and/or distribution of the microscopic features that characterise the damage state of the solid, i.e., the damage variables. In the following subsection, the definition of these variables regarding their physical significance is addressed.

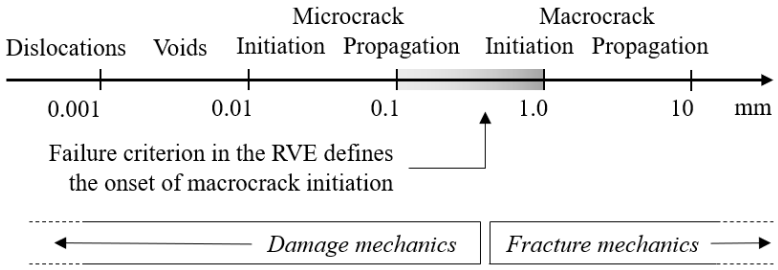

Figure 3.1 Bridge between the framework of damage mechanics and fracture mechanics, regarding the typical magnitude of the cracks in metals and alloys (adapted from Besson *et al.*, 2009). The gradient filled area represents the transition from micro- to macroscopic fracture. The domain of validity of each theory is defined somewhere in this zone.

[5] Figure 3.1 may suggest otherwise, however, the partition of these fields in it is merely based on the crack size.

3.3.2 Continuum damage mechanics: notions and general concepts

In practice, prior to fracture, there is virtually no macroscopic observable indication which allows to distinguish a highly damaged volume element and a virgin one (Lemaitre and Chaboche, 1994). The introduction of a damage variable which, by definition, cannot be directly observed nor measured, is thus necessary for representing the deteriorated state of the matter. CDMM are proposed to link field variables defining a current thermodynamic state (e.g. strain and/or stress tensors) to the material deterioration towards fracture, by means of damage laws. As with any internal state variable, the definition of the damage variables crucially sets the predictive ability and the domain of validity of the continuum model envisioned for the description of the dissipative phenomena regarding microstructural damage. Given the diversity of forms in which damage may manifest at the microscopic level, the definition of an adequate damage variable presents a difficult problem on itself (Lemaitre and Chaboche, 1994; de Souza Neto *et al.*, 2011). Depending on the proposed measurement method for evaluating the damage state of a volume element, one can classify it as a direct or an indirect method. The direct measurement method aims to describe the actual microstructural features of the matter, viz., the density and/or distribution of the lattice defects, e.g. the volume fraction and shape of the micro-voids in the case of ductile damage. Conversely, the indirect measurement method, inherently more phenomenological-biased, is based the couplings between the global behaviour of the material and its damaged state, in particular: (i) the modification of macroscopic *mechanical* properties (e.g. the elastic modulus); (ii) the modification of *physical* properties (e.g. density, resistivity, acoustic emission); (iii) *remaining lifetime* measurements (e.g. the well-know Palmgren-Miner rule (Miner, 1945) for fatigue damage modelling).

The direct and the indirect method based on macroscopic mechanical properties are, by far, the most renowned and pragmatic approaches for introducing damage variables within the framework of CDM. In fact, these lead to the distinction of the two main CDM theories: the so-called *micromechanical* and the *phenomenological* CDM models. Before describing these alternative theories, it is interesting to present an initial mathematical definition of the damage state variable and describe the concepts of effective stress, intimately related with the adopted damage description.

A first definition of the damage variable

Consider a damaged solid in which an element of finite volume δV, sufficiently large with respect to its heterogeneities (e.g. an RVE), as represented in Figure 3.2. Let δS be the area of a section of this volume element, defined by its normal, $\underline{\boldsymbol{n}}$; and δS_{D} define the 'effective' surface area of deterioration, concurrently accounting for: (i) the area of intersection of micro-cracks and micro-voids with the plane δS, denoted δS_0 (Figure 3.2); as well as (ii) possible correction terms accounting for stress concentration in the vicinity of the discontinuities and their interactions. Accordingly, one may instead define the net section of resistance, δS^* of the damaged solid as:

$$\delta S^* = \delta S - \delta S_0, \tag{3.1}$$

as well as the effective section of resistance, $\delta \tilde{S}$ as:

$$\delta\tilde{S} = \delta S - \delta S_{\mathrm{D}}, \tag{3.2}$$

the latter accounting for both the net section and the abovementioned possible corrections for the effects of stress concentration and microdefect interactions. Hence, one may define a mechanical measure of the local damage relative to the direction $\underline{\boldsymbol{n}}$ as (Lemaitre and Dufailly, 1987):

$$D_{(\underline{\boldsymbol{n}})} = \frac{\delta S - \delta\tilde{S}}{\delta S} = \frac{\delta S_{\mathrm{D}}}{\delta S}, \tag{3.3}$$

where $D_{(\underline{\boldsymbol{n}})}$ is the damage variable, denoting the *effective* (or corrected) surface density of discontinuities within the RVE, in the plane normal to $\underline{\boldsymbol{n}}$. From the mathematical point of view, the condition $D_{(\underline{\boldsymbol{n}})} = 0$ corresponds to undamaged (or virgin) state of the matter; $D_{(\underline{\boldsymbol{n}})} = 1$ corresponds to the fracture of the volume element along the plane normal to $\underline{\boldsymbol{n}}$; and $0 \le D_{(\underline{\mathbf{n}})} < 1$ characterizes an arbitrary damage state (Lemaitre and Chaboche, 1994). Being defined on the RVE, the damage variable represents a statistical information characterizing the density and distribution of defects associated with a given direction.

The above expression accounts for the general case of *anisotropic damage* which considers the possibility of the micro-cracks and/or micro-voids to have preferred orientations (e.g. the micro-cracks in metals tend to propagate in a direction normal to that of the maximum stress (Lemaitre and Chaboche, 1994). In practice, this feature may be introduced in a constitutive model via damage variables represented by second or fourth order tensors, depending on the adopted modelling scheme. Conversely, a damaged medium whose microdefects have a statistically random distribution of orientations is said to obey the hypothesis of *isotropic damage*. In such case, the directional nature of the variable is dropped, and the damaged state can be completely characterized by a single scalar, D:

$$D \equiv D_{(\underline{\mathbf{n}})}, \ \forall \underline{\boldsymbol{n}}. \tag{3.4}$$

This thesis is restricted to the case of isotropic damage. Recall from §2.2 that this assumption is actually reasonable given the typical random shape and distribution of the microstructural particles triggering damage initiation (viz. void nucleation).

Effective stress concept

The foundations of CDMM can be traced back to Kachanov (1958) who proposed a model for creep failure of isotropic metals under uniaxial loads. Specifically, in order to describe the plastic strain rate increase in the tertiary creep regime due to damage accumulation, Kachanov (1958) replaced the true uniaxial stress, σ with a uniaxial effective stress, $\tilde{\sigma}$:

$$\tilde{\sigma} = \frac{\sigma}{1 - D}, \tag{3.5a}$$

in the standard constitutive equation (Norton's law) for creep (de Souza Neto *et al.*, 2011). Kachanov's damage variable, D was originally introduced without a clear physical meaning. Only later, Rabotnov (1963) proposed an actual physical interpretation for this variable, assuming the reduction of the cross-section area due to microcracking, as a suitable measure of the state of internal damage.

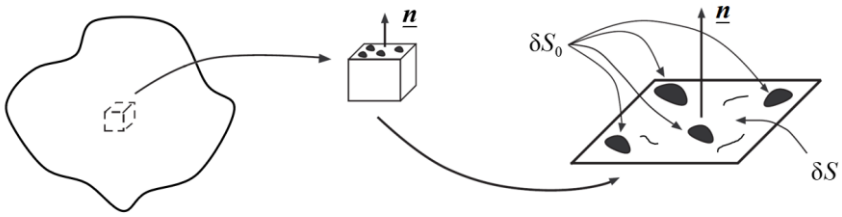

Figure 3.2 Idealization of a damaged solid. Adapted from Pires (2005).

As the name implies, the effective stress is defined over the section which effectively resists the loading in the RVE satisfying the equilibrium equation, i.e.:

$$\tilde{\sigma} = \frac{\delta S}{\delta \tilde{S}} \sigma, \tag{3.5b}$$

in the uniaxial case. Evidently, $\tilde{\sigma} = \sigma$ for a virgin material and $\tilde{\sigma} \to \infty$ at the onset of fracture of the RVE. In the case of multiaxial isotropic damage, the ratio $\delta S / \delta \tilde{S}$ does not depend on the orientation of the normal, $\underline{\boldsymbol{n}}$, of the RVE, hence the operator $(1 - D)$ (often referred to as material continuity or integrity) can be applied equally to all the components of a stress tensor, viz. the Cauchy stress tensor, $\boldsymbol{\sigma}$, i.e.:

$$\tilde{\boldsymbol{\sigma}} = \frac{\boldsymbol{\sigma}}{1 - D}, \tag{3.6}$$

where $\tilde{\boldsymbol{\sigma}}$ is the effective stress tensor.

The phenomenological and micromechanical approaches

The phenomenological approach to CDM is grounded on the replacement of the standard definition of damage in terms of the reduction of the (neither well-defined nor easily measurable) effective load-bearing section by the evaluation of the deterioration of a macroscopic, hence more easily measured, material property describing the overall behaviour of the damaged material. In view of this approach, the constitutive relations are formulated within the framework of irreversible thermodynamics. If the hypothesis of damage isotropy is not applicable, the generalization to multiaxiality of the effective stress concept (Eq. (3.5b)) can be achieved either by the so-called principle of strain equivalence (Chaboche, 1977; Lemaitre and Chaboche, 1978) or by the principle of energy equivalence (Cordebois and Sidoroff, 1979). In either case, the resulting effective stress tensor is employed in the constitutive equations in place of the actual stress tensor, in order to describe the impact of the damage on the material behaviour at the scale of the RVE.

Remark 3.3 Consistency and thermodynamic admissibility, i.e. the fulfilment of the conservation laws of materially simple continua and of the fundamental inequality of thermodynamics, respectively, is *not a sufficient condition* for a CDM model to be accurate.

If, in contrast, one aims to represent the internal damage as some average measurement describing, with a more or less level of abstraction, the actual microstructural damage features characterizing the current state of internal deterioration, one is referred to a micromechanical approach to CDM.

Remark 3.4 Micromechanical-based CDM models take advantage of the intimate relationship between the density and distribution of material microdefects and the onset of fracture: the ability to accurately describe the evolution of these microstructural features describing damage accumulation allows an accurate prediction of the mechanical failure of the material.

Unfortunately, at the present, computational constraints render explicit tracking of the evolution of each microdefect unreasonable in most engineering applications. Thus, as an alternative to the latter method, scale transition operations, viz. homogenization procedures, allow to translate the microstructural features into macroscopic (averaged) properties, entering some macroscopic constitute model. In this case, the damage variables describe, even if in an average fashion, some well-defined microstructural feature; as opposed to the 'hidden' internal state variables characteristic of the phenomenological approach to CDM. Moreover, their evolution is often explicitly set by physical considerations (e.g. conservation of mass and material continuity), rather than postulated by means of a somewhat arbitrary thermodynamic damage dissipation potential.

Following the pioneering work on creep failure of Kachanov-Rabotnov (Kachanov, 1958; Rabotnov, 1963) who established the framework of CDM, the concept of damage variable was soon adopted by a number of authors in order to model other types of damage and/or material behaviour, either following (what is here distinguished as) a phenomenological or micromechanical approach. Within the phenomenological approach to CDM, several theories describing a variety of materials and damage processes can be highlighted, e.g. creep damage (Chaboche, 1978, 1981, 1984; Leckie and Hayhurst, 1974; Saanouni *et al.*, 1989); fatigue damage (Chaboche, 1988; Janson, 1978), creep-fatigue interaction (Chaboche, 1988; Lemaitre, 1987); and ductile damage, both isotropic (Lemaitre, 1984, 1985a, 1985b; Marquis and Lemaitre, 1988) as well as anisotropic (Cordebois and Sidoroff, 1979; Lemaitre *et al.*, 2000; Simo and Ju, 1987). Regarding the micromechanical approach, the following are worth mentioning: creep damage (Krajcinovic and Selvaraj, 1984; Murakami and Ohno, 1981); brittle damage (Fonseka and Krajcinovic, 1981; Krajcinovic and Fonseka, 1981); and ductile damage, either with vectorial damage variables describing the distribution of planar penny-shaped micro-cracks (Krajcinovic, 1983, 1985), or with a scalar variable denoting the volume fraction of spherical micro-voids, according to the well-known *Gurson theory* (Gurson, 1977). Refer to the books of Lemaitre and Chaboche (1994) and de Souza Neto *et al.* (2011) for a further description of these.

This subsection intended to demonstrate that damage variables of different tensorial nature, hence, holding different physical meaning, viz. the reduction of load bearing area, loss of stiffness, distribution of micro-voids, have been employed in the description of damage under various areas of solid mechanics. In this work an analogous theory to that of Gurson (1977) is pursued in order model damage accumulation of ductile materials.

Before proceeding to next subsection, it is important to sort out two nomenclature-related aspects. The first is associated with the acronym CDM. This acronym is often applied in the literature to denote exclusively the phenomenological approach; this is however an ill-judged designation, since its micromechanical counterpart also relies on a continuous description of damage. The second remark is related

with the recurrence to the term 'micromechanical approach' in the previous (§3.2) and in the present subsection. It must be clear that these represent in fact distinct concepts. For instance, in theory, the micromechanical approach to CDM can be pursued both with a top-down and a bottom-up (alias micromechanical) approach, depending on the smallest scale which one intends to deal with. As stated in §3.2, this work focusses solely on the top-down approach. This does not impede one to describe damage phenomena by means of some statistical microstructural-based measurements, it simply means that such description must be provided via 'macroscopic' internal state variables, related with some constitutive laws written exclusively at the macroscopic level.

3.3.3 Other damage and failure criteria

This short subsection aims to present an alternative scheme for modelling ductile damage, known as the uncoupled approach. Some uncoupled models, alias failure criteria, are mentioned and briefly described.

As mentioned in the previous subsection, by definition, a damage model links the history of field variables (e.g. strain tensor, stress tensor, or their invariants) to the predicted damage state of the solid. In the literature, this connection is established either by means of the so-called *uncoupled* or *coupled* models. In the former there is no interaction between the damage variable(s) (hence the current damaged state) and the material behaviour; whereas in the latter the opposite holds true, i.e. damage is indeed incorporated in the constitutive equations of the material at some scale, and thus one or more properties of the material are considered to be related with the damage state, usually the macroscopic elastic and/or plastic behaviour. The CDM framework, as defined in §3.3, is based on the coupled approach.

According to the uncoupled approach, damage evolution laws are formulated empirically or semi-empirically through a scalar variable, D. Regarding ductile damage, one may write as general criterion:

$$D = \int_0^{\bar{\varepsilon}_f^p} f(\boldsymbol{\sigma}, \boldsymbol{\varepsilon}^p)\, d\bar{\varepsilon}^p \geq D_c, \tag{3.7}$$

where $\bar{\varepsilon}^p$ is an equivalent plastic strain, $\bar{\varepsilon}_f^p$ is the critical value of the equivalent plastic strain at fracture for a given loading path, $\boldsymbol{\sigma}$ is the Cauchy stress tensor and $\boldsymbol{\varepsilon}^p$ is the plastic strain tensor. The integrand, $f(\boldsymbol{\sigma}, \boldsymbol{\varepsilon}^p)$, is the so-called weighting function of damage, representing here an all-purpose function of the field variables. The weighting function can be phenomenologically- or micromechanically-inspired and may also account for thermal and/or strain rate effects (not represented in the integrand). According to the above expression, fracture is considered to occur when the damage variable exceeds a critical value, D_c. Several uncoupled criteria, i.e. weighting functions, have been proposed in the literature. Regarding the fully-empirical models, one may highlight the ones based on: the critical value of plastic work (Freudenthal and Geiringer, 1958); the maximum principal stress and/or stress triaxiality (Ayada, 1987; Brozzo *et al.*, 1972; Cockcroft and Latham, 1968); and the concept of 'fracture locus' in which a measurement of a 'strain to fracture', under proportional loadings, is explicitly defined as a function of some invariants of the stress state, viz. the stress triaxiality and the Lode angle (Bai and Wierzbicki, 2008; Bao and Wierzbicki, 2004, 2005; Mohr and Marcadet, 2015; Wierzbicki *et al.*, 2005). Regarding

the micromechanically-inspired models, special mention is given to the classical works of McClintock (1968) and Rice and Tracey (1969), which analytically described the combined role of the stress triaxiality and the plastic flow on the growth of isolated cylindrical and spherical voids, respectively, in an infinite rigid, perfectly plastic matrix subjected to a uniform remote strain field. More recently, semi-empirical micromechanically-motivated failure criteria have been developed (Lou *et al.*, 2012, 2014, 2017; Mohr and Marcadet, 2015), to concurrently account for the nucleation, growth and coalescence of voids on the explicit definition of the fracture locus concept.

In practice, within a numerical simulation scheme, the uncoupled approach evaluates the damage state of the matter exclusively at a post-processing stage of the final solution. Since these models do not modify the material behaviour, convergence issues characteristic of their coupled counterparts are hindered. As a result, uncoupled damage models do not *generally* lead to pathological mesh-dependent results. Given they relatively simpler formulation, implementation, and, usually, parameter calibration, uncoupled criteria are popular in the industrial community, especially in the early product development stages (Tekkaya *et al.*, 2020; Xue *et al.*, 2010). Nevertheless, it should be emphasized that, given the over-simplification of the mechanical behaviour of the materials, uncoupled models often display limited accuracy, hence predictive ability, specially, when applied to complex (e.g. non-proportional), loading paths. Moreover, the critical damage value D_c is often considered dependent on the loading path. This violates the notion of 'material parameter', thus further undermining the physical significance of this approach. As such, these models should be employed only in a qualitative fashion. In closing, note that, from the physical viewpoint, the uncoupled approach is, in part, counterintuitive: it intends to model a damage process (which is known to be governed by strongly coupled damage-plasticity dissipative phenomena), without actually taking into account the effect of damage on the material behaviour. This interpretation is in total disagreement with the modelling framework adopted in the present work; the uncoupled approach reviewed here was presented just for the sake of completeness.

3.4 State-of-the-art of micromechanical-based criteria for porous ductile solids

This section provides an overview of some recent developments concerning constitutive modelling within the continuum mechanics of porous ductile materials, regarding each of the three micromechanisms. Major emphasis is laid on the micromechanics-based framework originally proposed by Gurson (Gurson, 1977). A more in-depth review of the models described here is available in the extensive reviews of Benzerga and Leblond (2010); Besson (2010); Pineau *et al.* (2016); and Pineau and Pardoen (2007). The section starts by introducing the framework of porous media (§3.4.1). Following it, constitutive models representative of growth (§3.4.2), nucleation (§3.4.3) and coalescence (§3.4.4) stages are discussed in detail, with emphasis laid on the first (void growth models are intentionally presented at the outset with the intention to provide a clear reference framework in which the latter models can be more easily introduced).

3.4.1 Fundamentals of porous models

A porous solid (alias aggregate or medium) refers to a material containing pores which may grow or collapse when the solid is loaded. Two phases of the solid can be distinguished: the actual dense 'frame', known as the *matrix*; and the pore network/distribution, known as the *voids*. Constitutive models for porous elastic-(visco)plastic solids, (also known as dilatant plasticity models), adopt micromechanical-inspired internal variables to describe the state of the voids (e.g., size, shape, orientation) of the porous solid and form the basis of several ductile failure theories.

Constitutive models for porous solids have been proposed based both on micromechanical (e.g., Castañeda and Zaidman (1994); Gurson, (1977)) and phenomenological (e.g., Green (1972); Rousselier (1987); Schofield and Wroth (1968)) considerations. The basic idea behind these is the (either direct or indirect) introduction of a variable known as the *void volume fraction* (or *porosity*), f, defined as the ratio between the total volume of voids within the RVE and the total volume the RVE. Let Ω denote the total domain, ω the domain occupied by the voids and $\partial\Omega$ and $\partial\omega$ their respective boundaries (see Figure 3.4). Assuming that $\partial\Omega \bigcap \partial\omega = \varnothing,$ i.e. none of the void boundaries coincides with the external surface of the RVE, it follows that:

$$f = \frac{\mathrm{vol}(\omega)}{\mathrm{vol}(\Omega)}, \tag{3.8}$$

where $\mathrm{vol}(\cdot)$ denotes the volume of a domain.

The framework of Gurson (1977) is, quite possibly, the micromechanical-based approach currently receiving most attention in the literature (Pineau and Pardoen, 2007). As discussed in the forthcoming sections, its original form is, however, only representative of the void growth stage. Moreover, having a single scalar damage state variable, it can only represent an isotropic damage distribution. In theory, a more general model could include, in addition to the porosity (which accounts for the relative size of the voids), other microstructural-based internal state variables describing, for instance, the morphology, orientation and spacing of the voids within the RVE. This is exactly the idea followed by many works aiming to extend Gurson's theory in order to account for damage anisotropy (Gologanu *et al.*, 1993, 1994, 1997; Madou and Leblond, 2012b, 2012a; Morin, Leblond and Kondo, 2015). Whether damage anisotropy plays an important role on ensuing fracture events, in particular when compared to the role of the matrix plastic flow anisotropy, is a key question that, to the authors' knowledge, is still open.

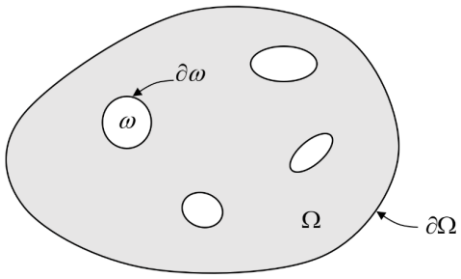

Figure 3.3 An arbitrary porous RVE with domain Ω, containing voids occupying a domain ω, at the reference temperature (adapted from Benzerga and Leblond, 2010).

Given the complexity of the micromechanisms of damage initiation and propagation, analytical models describing these phenomena inevitably rely on several simplifying hypothesis, especially if one aims to arrive at closed-form constructive expressions (and provided that scale separation is possible). In this context, computational micromechanical analyses, either finite element (FE)-based (Needleman, 1972a, 1972b; Tvergaard, 1981) or fast Fourier transform (FFT)-based (Lebensohn, 2001; Lebensohn *et al.*, 2011; Lebensohn and Cazacu, 2012; Michel *et al.*, 2001), have proven useful in guiding the development of improved ductile fracture models (Benzerga *et al.*, 2016; Benzerga and Leblond, 2010; Besson, 2010; Pineau *et al.*, 2016; Pineau and Pardoen, 2007). These computational analyses are based on so-called *unit cells*, in which the microstructure is idealized considering simple void and/or particle arrangements, on which proper boundary conditions are enforced to represent the full material (Figure 3.4). The term unit cell is occasionally coined in the literature as RVE. However, such nomenclature is not pursued here since, in general, a unit cell does not necessarily coincide with the concept of RVE, as defined in §3.1. In summary, cell model studies are a major tool for understanding the basic phenomenology governing ductile fracture at the mesoscale. Numerous lessons can be drawn from these, the ultimate goal being the development of improved closed-form, micromechanics-based constitutive models. Naturally, unit cell studies may also be useful to validate the derived analytical solutions and to provide a database for tuning possible phenomenological-based parameters present in the derived constitutive laws. The advent of ultra-high-resolution tomography may eventually complement these analyses, especially for dealing with fracture mechanisms that are poorly described by state-of-the-art computational micromechanics (e.g. intervoid crack propagation).

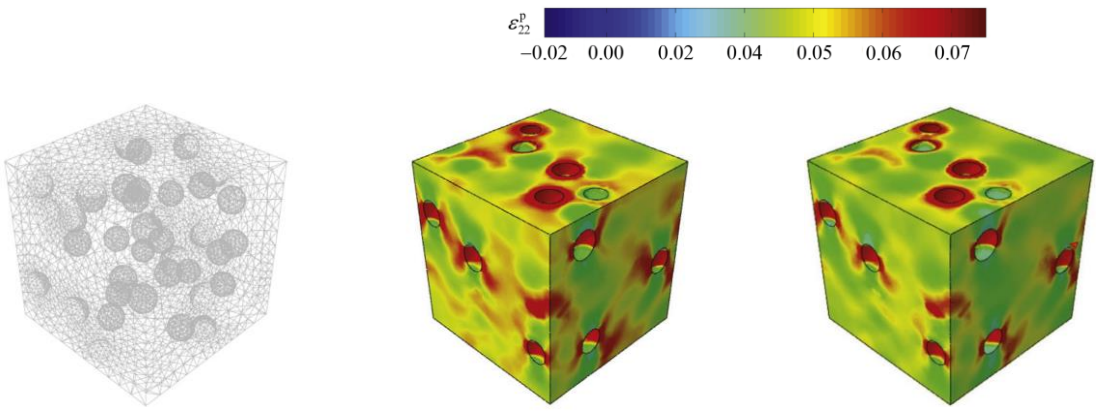

Figure 3.4 FE-based numerical micromechanical analyses of the cyclic response of porous ductile solids (adapted from Cheng *et al.*, 2017): (a) initial 3-D unit cell comprising 30 voids with a total porosity $f = 0.05$. Effect of the matrix elasticity on the local axial (x_2-) direction plastic strain distribution for a uniaxial load in the same direction: (b) $E/\sigma_0 = 300$; (c) $E/\sigma_0 = 1000$.

3.4.2 Void growth models

The first developments on micromechanical-based ductile damage modelling are coined to the uncoupled void growth criteria of McClintock (1968) and Rice and Tracey (1969). According to these, fracture is predicted when the normalized void radius has reached a critical value (cf. Eq.(3.7)). However, these models describe the growth of isolated voids, therefore these cannot take into account inter-void interactions, nor the effect of void growth on the material response (i.e. damage-induced softening) (Besson, 2010). In this context, two questions naturally arise: (i) for a given constitutive description at the microscale, i.e. the scale at which each void is resolved, what relationship exists between stress and strain at the macroscale, i.e. one which contains (a sufficiently) large number of voids; and (ii) how the microstructural information, viz. the void population characteristics and the matrix properties, entering in such macroscopic constitutive laws evolve (Benzerga and Leblond, 2010). This problem was first addressed by Gurson (1977) using homogenization, alias averaging, methods similar to those applied by Bishop *et al.* (1945). Its principle consisted in combining the classical theory of limit-analysis with the kinematic-type Hill-Mandel (Hill, 1967; Mandel, 1971) homogenization approach.

Other micromechanical-based models for porous elastic-(visco)-plastic media were also proposed, e.g., Castañeda and Zaidman (1994); Kailasam and Castaneda (1998) and, more recently, in Cheng *et al.* (2017); Danas and Castañeda (2009); and Vincent *et al.* (2009) based on alternative homogenization procedures, viz. the nonlinear variational approach of Castañeda (1991) (see also Michel and Suquet, 1992). The latter models are however known to underperform for high stress triaxiality loadings, given that damage growth is proposed to vary linearly with the stress triaxiality (Besson, 2010). Such assumption may be valid for viscous solids, but it is apparently erroneous for plastic materials, for which this dependence is known to be exponential, as considered in the criterion of Rice and Tracey (1969) and that of Gurson (1977). The latter approach, which this work concerns, suffers its own drawbacks, viz. poor results at low stress triaxialities and for high porosities (Benzerga and Besson, 2001) (e.g. in metallic foams, Ponte-Castañeda (Castañeda, 1991) approach is often preferred (Blazy *et al.*, 2004)). Nevertheless, a noteworthy, yet still incomplete, degree of convergence between recent developments within both micromechanical schemes has been pointed out in recent works (Benzerga *et al.*, 2016). The questions stated above were also tackled within the phenomenologically by Rousselier (1987) however such approach leads to a rather weak coupling between ductile damage and plasticity.

This thesis is heavily grounded on the framework established by Gurson (1977). Within this framework, expressions for the onset of plastic yielding of the porous aggregate, i.e. macroscopic flow potentials (in the form of yield functions in the rate-independent limit), as well as evolution laws for the microstructural-based variables are derived based on the variational characterization of porous media. The mathematical details regarding the backbone theories used in the development of such potentials, in particular, the homogenization and the limit-analysis theories are reviewed in Chapter 5. The criteria of Gurson (1977) and their more relevant extensions are now presented.

Original work of Gurson (1977)

Gurson (1977) developed closed-form criteria for ductile materials containing either randomly distributed spherical or cylindrical voids. A hollow sphere RVE and a cylindrical tube RVE were adopted for the spherical and for the cylindrical criterion, respectively. The matrix was assumed rigid-ideal plastic, obeying the classical von Mises criterion (j_2 flow theory), and the Prandtl-Reuss associated plastic flow rule; The criteria are based on an axisymmetric form of the velocity fields proposed by Rice and Tracey (1969). The porosity, f is the single microstructural variable. Gurson (1977) arrived at a macroscopic yield criterion for spherical voids, $\Phi^{\mathrm{G}}_{\mathrm{sph}}$, as:

$$\Phi^{\mathrm{G}}_{\mathrm{sph}}(\boldsymbol{\Sigma}, f) \triangleq \left(\frac{\Sigma_{\mathrm{eq}}}{\sigma_{\mathrm{T}}}\right)^2 + 2f\cosh\left(\frac{3}{2}\frac{\Sigma_{\mathrm{m}}}{\sigma_{\mathrm{T}}}\right) - 1 - f^2 = 0, \tag{3.9}$$

and for cylindrical voids, $\Phi^{\mathrm{G}}_{\mathrm{cyl}}$, as:

$$\Phi^{\mathrm{G}}_{\mathrm{cyl}}(\boldsymbol{\Sigma}, f) \triangleq C_{\mathrm{eq}}\left(\frac{\Sigma_{\mathrm{eq}}}{\sigma_{\mathrm{T}}}\right)^2 + 2f\cosh\left(\frac{\sqrt{3}}{2}\frac{\Sigma_{\gamma\gamma}}{\sigma_{\mathrm{T}}}\right) - 1 - f^2 = 0, \tag{3.10a}$$

with

$$C_{\mathrm{eq}} = \begin{cases} (1+3f+24f^6)^2 & \text{for plane strain,} \\ 1 & \text{for axisymmetry,} \end{cases} \tag{3.10b}$$

where Σ_{eq} is the macroscopic von Mises equivalent stress (von Mises norm of the deviator of $\boldsymbol{\Sigma}$), σ_{T} is the yield stress of the matrix in uniaxial tension (homogeneous in the matrix), and $\Sigma_{\gamma\gamma}$ is the sum of the in-plane stresses (e.g., $\Sigma_{\gamma\gamma} = (\Sigma_{11} + \Sigma_{22})$ if the 3-direction is the out-of-plane direction). Note that even with the matrix assumed to obey a standard j_2 flow theory, the homogenization of Gurson (1977) demonstrated that the overall behaviour of the porous solid depends not only on the second invariant of the macroscopic stress deviator tensor, $J_2^{\Sigma} = (\Sigma_{\mathrm{eq}})^2/3$, but also on the first invariant of the macroscopic Cauchy stress tensor, $I_1^{\Sigma} = \mathrm{tr}(\boldsymbol{\Sigma})$ (Stewart, 2009).

Remark 3.5. Regardless of the assumed plasticity model for the matrix, the presence of voids in a solid induces dependence on *all* invariants of the applied (i.e. macroscopic) stress state.

In order to simplify the volume integrals of the matrix plastic dissipation associated with the von Mises criterion and the assumed axisymmetric trial velocity field, Gurson approximated this dissipation function with a truncated one, which only depended on the radial coordinate of the RVE (thus obtaining and upper-bound estimate of an otherwise approximated plastic dissipation). Recently, Cazacu, *et al.* (2013) demonstrated that the insensitivity of Gurson's (1977) spherical void criterion to the third invariant of the macroscopic stress deviator, $J_3^{\Sigma} = \det(\boldsymbol{\Sigma}')$, is a consequence of this approximation. In the latter work, the authors solved the limit-analysis problem without assuming the truncation hypothesis of Gurson and derived an analytical, yet in parametric form, yield locus for porous solids obeying von Mises theory which, in this case, captured particular and non-trivial couplings between the signs of the macroscopic hydrostatic stress, Σ_{m}, and the third invariant of the stress deviator tensor, J_3^{Σ}, (for more details

see e.g. Alves *et al.* (2014)). Both numerical (Alves *et al.*, 2014; Alves and Cazacu, 2015; Cazacu and Stewart, 2009; Kim *et al.*, 2004; Zhang *et al.*, 2001) and experimental (Bao and Wierzbicki, 2004; Barsoum and Faleskog, 2007) studies seem to support this result.

Returning to the original work of Gurson (1977) it should be highlighted that: (i) in the absence of voids ($f = 0$), the above criteria reduce to that of the matrix, i.e. the von Mises criterion; (ii) for purely hydrostatic loadings ($\Sigma_{eq} = 0$), the yield locus regarding the spherical criterion coincides with the exact solution of the limit-analysis problem of a rigid-perfect plastic hollow sphere, viz. $|\Sigma_m| = (2/3)\sigma_T \ln(f)$ (see e.g. Cazacu *et al.* (2019) for a formal proof); (iii) for purely deviatoric loadings ($\Sigma_m = 0$), Gurson criteria predicts the macroscopic yield limit as $\Sigma_{eq} = (1-f)\sigma_T$.

The cylindrical void criterion of Gurson has received less attention in the literature than its sphere-based counterpart. This is partially explained by the restrictions related to the loading conditions in the former. This work intends to follow the spherical void framework. Nevertheless, it is worth noting that the cylinder-based homogenized model has been pointed out more appropriate to model metallic sheets containing elongated void-nucleating particles (Benzerga and Besson, 2001).

Extensions of the work of Gurson (1977)

The analysis leading to the previously stated 'minimal form' of the work of Gurson (1977) assumed a rigid, perfect-plastic, rate independent matrix. The first extensions to this framework are due to Gurson himself who included, in a heuristic fashion, the effects of elasticity and strain hardening, (Leblond *et al.*, 2018): (i) elasticity was incorporated by supplementing the macroscopic plastic strain rate, $\boldsymbol{D}$, with an elastic contribution $\boldsymbol{D}^e$, given by some weak-elasticity (viz. hypoelastic) law, i.e., $\boldsymbol{D} = \boldsymbol{D}^e + \boldsymbol{D}^p$, while disregarding the influence of the porosity on the elastic behaviour; and (ii) the isotropic hardening of the matrix was introduced preserving the analytic form of the criterion (Eq. (3.9)) and replacing the (constant) yield stress σ_T, of ideal plastic materials, by an 'average' yield stress value, $\bar{\sigma}_Y$, assumed to obey a relation of the type $\bar{\sigma}_Y = \bar{\sigma}_Y(\bar{\epsilon}^p)$; where $\bar{\sigma}_Y(\cdot)$ denotes a hardening-type function with respect to the equivalent plastic strain, $\bar{\epsilon}^p$, of some *fictitious material* that would deform *uniformly* in the RVE (cf. phenomenological approach to CDM) (Benzerga and Leblond, 2010). From the above reasoning, Gurson proposed a simple, yet elegant, expression for the evolution law of $\bar{\epsilon}^p$, as:

$$(1-f)\bar{\sigma}_Y\dot{\bar{\epsilon}}^p = \boldsymbol{\Sigma} : \boldsymbol{D}^p, \tag{3.11}$$

which expresses the heuristic assumption of equality of the plastic dissipation rate in the real, heterogeneous (i.e. with a spatially variable yield stress) porous aggregate and of the fictitious 'equivalent' homogeneous one. A noteworthy feature of the above equation is that it accounts for the hardening of the matrix arising from both the deviatoric and hydrostatic parts of $\boldsymbol{D}^p$ (Benzerga *et al.*, 2016).

The application of the original criteria of Gurson (1977) model the damage process of engineering metals and alloys whose mechanical behaviour greatly differs from that employed within his micromechanical analysis may be ill-judged. Following Gurson, many other authors have done a vast amount of research aimed at extending his framework, either heuristically or micromechanically, by reformulating the homogenization problem and modifying one or more of its basic 'ingredients', viz. the geometry of

the RVE, the plasticity criteria for the matrix material, and/or the subset of trial local velocity fields; as well as introducing additional microstructural variables accounting for void shape and distribution. In essence, such extensions attempt to tackle, directly or indirectly, three main limitations of the Gurson model, intimately related with each of the simplifying hypotheses assumed in the formulation of his original problem: (i) the spherical void geometry; (ii) the j_2 flow theory; and (iii) the basic (viz. axisymmetric and truncated) velocity fields. This thesis concerns the last two points. It turns out that the format of the extended models found in the literature remains basically the same as the criterion of Gurson. A brief review of some of these extensions is provided in Table 3.1. A further discussion on some of its elements is provided next, as necessary.

Table 3.1 Some extensions of the Gurson model (partially adapted from Pineau and Pardoen, 2007).

Purpose of the extension and respective references	Brief description
Improve global accuracy	
Tvergaard (1981, 1982b)	Better agreement toward FE unit cell computations can be achieved by adding some 'fitting parameters', q_1 and q_2, into the expression of the spherical-void yield criterion of Gurson: $$\Phi \triangleq \left(\frac{\Sigma_{\mathrm{eq}}}{\sigma_{\mathrm{T}}}\right)^2 + 2q_1 f \cosh\left(\frac{3}{2} q_2 \frac{\Sigma_{\mathrm{m}}}{\sigma_{\mathrm{T}}}\right) - 1 - \left(q_1 f\right)^2 = 0, \quad (3.12)$$ Recommended values of $q_1 = 1.5$ and $q_2 = 1$, based on the FE results;
Perrin and Leblond (1990)	Estimate of the fitting parameters based on a theoretical self-consistent scheme. Recommended values of $q_1 = 4/e \cong 1.47$ and $q_2 = 1$;
Koplik and Needleman (1988)	Estimate of the fitting parameters based on FE unit cell computations for the void growth rate, at fixed stress triaxiality. Recommended values of $q_1 = 1.25$ and $q_2 = 1$;
Faleskog *et al.* (1998)	Calibration of the fitting parameters toward FE unit cell computations. The best set (q_1,q_2) is thought to depend on some matrix flow properties, viz. a plastic hardening exponent, n, and the ratio of the yield stress over an elasticity modulus, σ_{T}/E. The product $q_1 q_2$ for the recommended values is approximately constant and equal to 1.5.
Vadillo *et al.* (2016)	Heuristically incorporate the effects of the third invariant of deviatoric stress tensor into the Gurson model, in the range of high stress triaxialities, by specifying the set (q_1,q_2) directly as a function of the stress triaxiality and Lode angle parameter.
Richmond and Smelser (1985); Spitzig *et al.* (1988)	Based on experimental tests on compacted iron specimens the following modified version of Gurson's spherical criterion is proposed: $$\Phi \triangleq \left(\frac{\Sigma_{\mathrm{eq}}}{\sigma_{\mathrm{T}}}\right)^2 + 2 f^m \cosh\left(\frac{3}{2} m \frac{\Sigma_{\mathrm{m}}}{\sigma_{\mathrm{T}}}\right) - 1 - f^{2m} = 0, \quad (3.13)$$ where m is a heuristic-based material parameter, ranging between 2/3 and unity, typically depending upon the strain hardening of the matrix.

Improved modelling of strain hardening

Leblond *et al.* (1995)

Based on an approximate analytical solution of the problem of a rigid-hardening hollow sphere, the following modification was proposed:

$$\Phi \triangleq \left(\frac{\Sigma_{\mathrm{eq}}}{\Sigma_1}\right)^2 + 2f\cosh\left(\frac{3}{2}\frac{\Sigma_{\mathrm{m}}}{\Sigma_2}\right) - 1 - f^2 = 0, \tag{3.14}$$

where Σ_1 and Σ_2 denote internal variables connected to the overall yield stresses, under purely deviatoric and purely hydrostatic loadings, respectively. Somewhat complex closed-form evolution equations for these are provided in the cited reference, under the assumption of positively proportional straining at the macroscale;

Lacroix *et al.* (2016)

The above hypothesis of positively proportional straining is relaxed. The analytical evaluation of Σ_1 and Σ_2 is no longer possible, hence numerical integration is necessary. This approach leads to an improved description of the distribution of hardening around the voids.

Kinematic hardening

Mear and Hutchinson (1985); Leblond *et al.* (1995); Arndt *et al.* (1997); Ristinmaa (1997); Besson and Guillemer-Neel (2003); Mühlich and Brocks (2003); Cheng *et al.* (2017); Morin *et al.* (2017)

Several extensions of the Gurson model to account for kinematic hardening of the matrix have been proposed in the literature. The typical yield criterion writes:

$$\Phi \triangleq \frac{\left(\boldsymbol{\Sigma} - \boldsymbol{X}_1\right)_{\mathrm{eq}}^2}{\sigma_{\mathrm{T}}^2} + 2f\cosh\left(\frac{3}{2}\frac{\Sigma_{\mathrm{m}} - X_2}{\sigma_{\mathrm{T}}}\right) - 1 - f^2 = 0, \tag{3.15}$$

where $(\boldsymbol{\Sigma} - \boldsymbol{X}_1)_{\mathrm{eq}}^2 = (3/2)(\boldsymbol{\Sigma}' - \boldsymbol{X}_1) : (\boldsymbol{\Sigma}' - \boldsymbol{X}_1)$ is a von Mises norm; $\boldsymbol{\Sigma}'$ denotes the deviator of the stress tensor; and $\boldsymbol{X}_1$ and X_2 denote a general traceless second-order tensor and a scalar, respectively, (often $X_2 = \mathrm{tr}(\boldsymbol{X}_1)/3$), describing the effect of the local back-stress tensor, i.e. in the matrix, at the macroscale. The model must be supplemented with evolution laws for these; see the references for further details.

Void shape and rotation effects

Gologanu *et al.* (1993, 1994, 1997); Pardoen and Hutchinson (2000); Gărăjeu *et al.* (2000); Madou and Leblond (2012a, 2012b, 2013); Madou *et al.* (2013); Scheyvaerts *et al.* (2011); Kailasam and Castaneda (1998); Castañeda and Zaidman (1994); Monchiet *et al.* (2014)

Several extensions of the Gurson model to account for non-spherical void shapes have been proposed in the literature (e.g. the so-called GLD model proposed in Gologanu *et al.* (1993, 1994, 1997). These are obtained by means of rigorous micromechanical analysis. The general form of the yield criterion writes (after Madou *et al.* (2013)):

$$\Phi \triangleq \frac{\mathcal{Q}(\boldsymbol{\Sigma})}{\sigma_{\mathrm{T}}^2} + 2(1+g)(f+g)\cosh\left(\frac{\mathcal{L}(\boldsymbol{\Sigma})}{\sigma_{\mathrm{T}}}\right) - (1+g)^2 - (f+g)^2 = 0, \tag{3.16}$$

where $\mathcal{Q}(\boldsymbol{\Sigma})$ is some quadratic term of the components of $\boldsymbol{\Sigma}'$; and $\mathcal{L}(\boldsymbol{\Sigma})$ is a linear term of the diagonal components of $\boldsymbol{\Sigma}$. In addition to the porosity, f, these entails, in the general case, two microstructural variables – the void shape parameters (alias aspect ratios), (w_1,w_2) – which describe the ratios of the size of the voids of two axes over a third one. $\mathcal{Q}(\boldsymbol{\Sigma})$, $\mathcal{L}(\boldsymbol{\Sigma})$ and g are analytical functions of the above state variables (see the reference for complete expressions). The evolution laws for the length, aspect ratios and orientation of the axes of the voids follow from micromechanical analysis, often heuristically augmented using numerical limit analysis studies on unit cells.

Rate dependency and viscoplasticity

Pan *et al.* (1983); Tvergaard (1989); Moran *et al.* (1991); Haghi and Anand (1992); Duva and Hutchinson (1984); Duva (1986); Licht and Suquet (1988); Michel and Suquet (1992); Cocks (1989); Leblond, Perrin and Suquet (1994)

A number of authors have proposed models for rigid, nonlinear viscous porous solids whose matrix obeys a standard Norton constitutive law. See e.g. Benzerga and Leblond (2010) for a detailed analysis of these. A notable contribution is that of Leblond, Perrin and Suquet (1994), who proposed a macroscopic flow potential for spherical voids, which recovers the exact solution of the problem of a viscous hollow sphere loaded hydrostatically, viz.:

$$\Phi \triangleq \left(1+\frac{2f}{3}\right)\Sigma_{\mathrm{eq}}^{2} + f\left[F\left(\Sigma_{\mathrm{m}}\right)+\frac{n-1}{n+1}\frac{1}{F\left(\Sigma_{\mathrm{m}}\right)}\right]-1-\frac{n-1}{n+1}f^{2}=0, \qquad \text{with } F\left(\Sigma_{\mathrm{m}}\right)=\left[1+\frac{1}{n}\left(\frac{3\left|\Sigma_{\mathrm{m}}\right|}{2}\right)^{\frac{n+1}{n}}\right]^{n}. \tag{3.17}$$

which reduces to the criterion of Gurson and the associated flow rule for an ideal-plastic matrix (i.e. n → +∞), *n* being the Norton exponent.

Klöcker and Tvergaard (2003)

Extension of the abovementioned rate-dependent spherical void model to spheroidal voids.

Flandi and Leblond (2005)

Improved spheroidal void model that no longer violates the Castañeda (1991) non-linear Hashin-Shtrikman bounds condition.

Improve accuracy at low or vanishing stress triaxiality

Nahshon and Hutchinson (2008)

Numerous extensions have been proposed in the literature in order to better describe the experimentally observed onset of fracture under shear-dominated loadings while retaining the Gurson-type form. In essence, these introduce a heuristic dependency of the damage evolution law on the third invariant of the stress deviator tensor, J_3^{Σ}, (as known as Lode angle dependence), in order to describe the material softening. Such extensions can be formulated based either on geometrical or on purely phenomenological considerations. Regarding the latter, the one of (Nahshon and Hutchinson, 2008) is highlighted here:

$$\dot{\bar{f}} = \dot{f} + k_{\omega} f\, \omega(\boldsymbol{\Sigma}) \frac{\boldsymbol{\Sigma}' : \boldsymbol{D}^{\mathrm{p}}}{\bar{\sigma}}, \quad \text{where } \omega(\boldsymbol{\Sigma}) = 1-\left(\frac{27 J_3^{\Sigma}}{2\Sigma_{\mathrm{eq}}^{3}}\right)^{2}, \tag{3.18}$$

where $\dot{f} = (1-f)\mathrm{tr}(\boldsymbol{D}^{\mathrm{p}})$, k_{ω} is a heuristic parameter to be calibrated, and $\omega(\boldsymbol{\Sigma})$ is a weight function of the applied stress state, ranging from zero for dominant tensile stress states to unity for shear dominant stress states. Note that the introduction of such heuristic term in the evolution law of the microstructural variable violates the axiom of mass conservation of the porous solid. As such, the physical meaning of the variable *f* is lost, hence porosity should, in this case, be treated as an arbitrary damage parameter, $\bar{f}$, such as in the phenomenological CDM approach, rather than a micromechanical variable as in Gurson (1977).

Nielsen and Tvergaard (2010)

A heuristic stress state-dependent linear scaling factor (as well as cut-off value) to the abovementioned additional shear term, in order to better represent damage evolution at moderate to high stress triaxialities, which is known to be well described by the Gurson model.

Dæhli *et al.* (2018); Jiang *et al.* (2016); Malcher *et al.* (2014)

An alternative scaling function, $\omega(\boldsymbol{\Sigma})$ in Eq. (3.18) for the damage law.

Xue (2008); Butcher *et al.* (2009)	A heuristic (yet, more physically-sound) shear damage term based on geometrical considerations, viz. the solution of McClintock (1968) for the coalescence of holes in a shear band.
Zhou *et al.* (2014)	A phenomenologically extended Gurson model based on two damage variables, distinguishing volumetric damage (govern by porosity) and shear-induced damage.
Highly dynamic material behaviour	
Addessio and Johnson (1993); Maudlin *et al.* (1999); Bronkhorst *et al.* (2006)	Modified model in order to deal with problems involving highly dynamic material behaviour (i.e. high strain rates and temperature effects). It uses Mie-Gruneisen equation of state (e.g. Burshtein, 2008) to specify the pressure and a mechanical threshold strength (MTS) model.
Two populations of voids	
Perrin and Leblond (2000); Enakoutsa *et al.* (2005); Morin and Michel (2018)	Reformulation of the homogenization scheme in order to derive macroscopic yield criteria to account for the presence of a second population of voids, (often nucleating on smaller particles and thus, at least, of one order of magnitude smaller than primary voids), on the ductility of the porous solid. In general, these account for the couplings between the growth of primary (larger) voids (as in Gurson original model) and the growth (and, possibly, nucleation and coalescence) of the small ones.
Void-particle interaction	
Siruguet and Leblond (2004a, 2004b)	The Gurson model intrinsically assumes that void growth is not influenced by the particle which served as nucleation site. Under low stress triaxiality conditions, the presence of a hard particles within the void prevents the void to contract in the direction transverse to the main loading direction (recall discussion in §2.2.3 on the 'void locking by the particle' phenomenon). Such interaction can only be accounted for within a model which incorporates void shape effects.
Void size effects	
Wen *et al.* (2005); Monchiet and Bonnet (2013)	When the size of the voids is comparable to or smaller than an internal length of the plastic solid, physically attributed to the generation and the storage of geometrically necessary dislocations, the application of the Gurson model appears to be questionable. In this context, closed-form models for ductile porous solids containing spherical micro- and/or submicron voids have been proposed in order to account for void size effects, e.g. in the form of Monchiet and Bonnet (2013): $$\Phi \triangleq \left(\frac{\Sigma_{\mathrm{eq}}}{\sigma_{\mathrm{T}}}\right)^2 + 2f\cosh\left(\frac{3}{2\eta}\frac{\Sigma_{\mathrm{m}}}{\sigma_{\mathrm{T}}}\right) - 1 - f^2 = 0, \tag{3.19}$$ where η is a coefficient, evaluated by the limit-analysis scheme for the particular case of a pure hydrostatic loading, which introduces the size effect, as a function of the current size of the voids and on some material intrinsic length. When the voids are large enough, the $\eta \to 1$ and Gurson's original criterion is recovered. These models predict that smaller voids growth slower than larger ones, as reported in numerous numerical studies in the literature (see e.g. Li and Steinmann (2006)).

Non-quadratic isotropic yield criterion for the matrix

Benallal (2017) Mixed analytical-numerical criterion for isotropic porous solids based on the non-quadratic Hershey-Hosford yield criterion (Hershey, 1954; Hosford, 1972):

$$\Phi \triangleq \left(\frac{a\Sigma_{\mathrm{eq}} + P}{R\sigma_{\mathrm{T}}} \right)^2 + 2f \cosh\left(\frac{\Sigma_{\mathrm{m}} - Q}{\sigma_{\mathrm{T}}} \right) - 1 - f^2 = 0, \tag{3.20}$$

where a, P, R, Q are functions of the macroscopic stress triaxiality, Lode angle, porosity and material and the matrix homogeneity exponent, *m*, are not generally available in closed-form, hence must be determined numerically.

Tension-compression asymmetry of the matrix

Cazacu and Stewart (2009) An approximate yield criterion of isotropic porous solids displaying tension-compression asymmetry. The matrix is considered rigid-plastic, containing randomly distributed spherical voids, and governed by the isotropic and quadratic form of the Cazacu *et al.* (2006) (alias CPB06) yield criterion The criterion is in the form:

$$\Phi \triangleq \left(\frac{m\sqrt{\sum_{i=1}^{3} \left(|\Sigma_i| - k\Sigma_i \right)^2}}{\sigma_{\mathrm{T}}} \right)^2 + 2f \cosh\left(z_s \frac{3}{2} \frac{\Sigma_{\mathrm{m}}}{\sigma_1^{\mathrm{T}}} \right) - 1 - f^2 = 0, \quad \text{with } z_s = \begin{cases} 1 & \text{if } \Sigma_{\mathrm{m}} < 0 \\ (\sigma_{\mathrm{T}}/\sigma_{\mathrm{C}}) & \text{if } \Sigma_{\mathrm{m}} > 0 \end{cases}, \tag{3.21}$$

where *k* is material parameter describing tension-compression asymmetry effect, σ_{C} is the uniaxial compression yield stress, Σ_i are the principal values of the macroscopic stress); *m* is a constant, function of *k*; and $(\sigma_{\mathrm{T}}/\sigma_{\mathrm{C}}) = \sqrt{(3k^2 + 2k + 3)/(3k^2 - 2k + 3)}$ is the SD ratio. The criterion predicts the exact solution of a hollow sphere with SD effects loaded in hydrostatic tension and compression.

Plastic anisotropy effects of the matrix

Liao *et al.* (1997) Semi-empirical spherical void-based porous model for transversely isotropic solids under plane stress conditions. The matrix is assumed to obey Hill (1948) associative plasticity criterion:

$$\Phi \triangleq \left(\frac{\tilde{\Sigma}_{\mathrm{e}}}{\sigma_{\mathrm{T}}} \right)^2 + 2f \cosh\left(3\sqrt{\frac{1+2R}{6(1+R)}} \frac{\Sigma_{\mathrm{m}}}{\sigma_{\mathrm{T}}} \right) - 1 - f^2 = 0, \tag{3.22}$$

where σ_{T} is the in-plane yield stress in uniaxial tension of the matrix; *R* is the anisotropy parameter, (or plastic strain ratio), characterizing the in-plane isotropy via the ratio of the transverse plastic strain rate to the through-thickness plastic strain rate of the metallic sheet under uniaxial loadings; $\tilde{\Sigma}_{\mathrm{e}}$ is the macroscopic equivalent stress associated with Hill (1948) criterion under plane stress (see reference for details). For isotropic materials, $R = 1$, Gurson's spherical criterion is recovered. An equivalent model for cylindrical voids is also proposed.

Benzerga and Besson (2001) Approximate yield criterion of orthotropic porous solids subjected to triaxial loadings. The matrix is assumed to obey Hill (1948) criterion and to contain randomly distributed spherical cavities (remaining spherical). The macroscopic yield criterion reads:

$$\Phi \triangleq \left(\frac{\tilde{\Sigma}_{\mathrm{e}}}{\sigma_1^{\mathrm{T}}}\right)^2 + 2f\cosh\left(\frac{3}{h}\frac{\Sigma_{\mathrm{m}}}{\sigma_1^{\mathrm{T}}}\right) - 1 - f^2 = 0, \qquad \text{with } \tilde{\Sigma}_{\mathrm{e}}{}^2 = \frac{3}{2}\boldsymbol{\Sigma}' : \boldsymbol{\mathcal{L}}_{\mathrm{Hill'48}} : \boldsymbol{\Sigma}', \tag{3.23}$$

where σ_1^{T} is the uniaxial tensile yield stress along an axis of orthotropy of the matrix, (e.g. the rolling direction of the metal sheet), denoted the 1-direction here; and h is the so-called *anisotropy factor* ($h = 2$ for isotropy) and is a function of the macroscopic fourth-rank anisotropy tensor, $\boldsymbol{\mathcal{L}}_{\mathrm{Hill'48}}$ (see reference for more details). An equivalent model for cylindrical voids was also proposed by the authors, which is shown to reduce to the analogous one of Liao *et al.* (1997), under the assumption of transverse isotropy and to the criterion of Gurson for cylindrical voids for an isotropic matrix ($\boldsymbol{\mathcal{L}}_{\mathrm{Hill'48}} = \boldsymbol{\mathcal{I}}$). In the case of a dense matrix ($f = 0$), these criteria reduce to Hill (1948) quadratic criterion.

Stewart and Cazacu (2011) An approximate yield criterion of orthotropic porous solids displaying tension-compression asymmetry. The matrix is considered rigid-plastic, containing randomly distributed spherical voids, and governed by the quadratic form of the Cazacu *et al.* (2006) (alias CPB06) orthotropic yield criterion The macroscopic yield criterion reads:

$$\Phi \triangleq \left(\frac{\hat{m}\sqrt{\sum_{i=1}^{3}\left(|\hat{\Sigma}_i| - k\hat{\Sigma}_i\right)^2}}{\sigma_1^{\mathrm{T}}}\right)^2 + 2f\cosh\left(\frac{3}{h}\frac{\Sigma_{\mathrm{m}}}{\sigma_1^{\mathrm{T}}}\right) - 1 - f^2 = 0, \qquad \text{with } \hat{\boldsymbol{\Sigma}} = \boldsymbol{\mathcal{C}} : \boldsymbol{\Sigma}, \tag{3.24}$$

where k is material parameter describing tension-compression asymmetry effects; $\boldsymbol{\mathcal{C}}$ is the macroscopic fourth-rank tensor describing the anisotropy; $\hat{\boldsymbol{\Sigma}}$ is the transformed stress tensor, (and $\hat{\Sigma}_i$ its principal values); and $\hat{m}$ is a constant, function of k and $\boldsymbol{\mathcal{C}}$. The scalars σ_1^{T} and h have the same meaning as in Eq. (3.23), (see the reference for more details on the explicit definition of the latter parameter, defined in terms of the plastic properties of the matrix). If the matrix is orthotropic (such that $\hat{\boldsymbol{\Sigma}}$ is deviatoric), and has no tension-compression asymmetry ($k = 0$), the above criterion reduces to that of Benzerga and Besson (2001); for an isotropic matrix (i.e., $\boldsymbol{\mathcal{C}} = \boldsymbol{\mathcal{I}}$), the criterion reduces to the one of Cazacu and Stewart (2009) for isotropic porous materials displaying SD effects (Eq. (3.21)); and to a particular case of the quadratic form of the CPB06 orthotropic yield criterion in the absence of voids ($f = 0$).

Combined plastic anisotropy and void shape effects

Benzerga *et al.* (2004b) Semi-empirical yield criterion, combining features of the porous model of Benzerga and Besson (2001) to describe plastic anisotropy and that of Gologanu *et al.* (2001) to account for morphological void anisotropy.

Monchiet *et al.* (2006, 2008) Extension of the model of Benzerga and Besson (2001) to the case of spheroidal void geometry, using the velocity fields considered in the earlier versions of the GLD model (see Gologanu *et al.*, 1993, 1994). The approximate criterion resulting from the homogenization analysis is restricted to axisymmetric loadings and microstructures for which the void axes are aligned with the material orthotropy axes.

Keralavarma and Benzerga (2008, 2010)	Deals with a similar homogenization scheme to the one of Monchiet *et al.* (2006, 2008), considering however a richer description of the trial velocity fields, viz. the ones discovered by Lee and Mear (1992). As such, the proposed yield criterion is applicable to non-axisymmetric loadings and to cases where the spheroidal void axis is no longer constrained to be aligned with a principal direction of orthotropy.
Morin, Leblond and Kondo (2015); Morin (2015)	Extension of the model of Madou *et al.* (2013); Madou and Leblond (2012a, 2012b) for general ellipsoidal (rather than spheroidal) voids, embedded in an orthotropic matrix obeying Hill (1948) criterion. No coincidence is assumed between the principal axes of the voids and those of the material. The obtained approximated criterion is formally analogous to that in Eq. (3.16), (albeit with different expressions for $\mathcal{Q}(\boldsymbol{\Sigma})$ and $\mathcal{L}(\boldsymbol{\Sigma})$).
Refined trial velocity fields	
Monchiet *et al.* (2007); Monchiet *et al.* (2011)	Consideration of Eshelby-like exterior point trial velocity fields in place of those of Rice and Tracey (1969) for the determination of the macroscopic plastic potentials for the particular case of a spherical inclusion (Eshelby, 1957, 1959). The approximate criterion is in the form: $$\Phi \triangleq \left(\frac{\Sigma_{\mathrm{eq}}}{\sigma_{\mathrm{T}}}\right)^2 + 2f\cosh\left(\sqrt{\frac{9}{4}\frac{\Sigma_{\mathrm{m}}^2}{\sigma_{\mathrm{T}}^2} + \frac{3}{2g(f)}\frac{\Sigma_{\mathrm{eq}}^2}{\sigma_{\mathrm{T}}^2}}\right) - 1 - f^2 = 0, \quad \text{with } g(f) = 1 - 4f\frac{\left(1-f^{2/3}\right)^2}{1-f}, \tag{3.25}$$ The authors showed that the obtained closed-form criterion provided a significant modification of the Gurson in the domain of low stress triaxialities. Later, Monchiet *et al.* (2014) extended the analysis for spheroidal voids.

As discussed previously, the FEM provides a powerful tool for solving the homogenization problem. Accordingly, in principle, heuristic modifications of existing closed form (approximate) criteria can be proposed based on such numerical analysis. Based on this idea, Tvergaard (1981, 1982b) proposed a modification of the spherical void criterion of Gurson (1977) by making use of the change of variables: $f \to q_1 f$ and $\Sigma_{\mathrm{m}} \to q_2 \Sigma_{\mathrm{m}}$, as defined in Eq. (3.12). The meaning of the q_i factors has been debated for some time (Pineau *et al.*, 2016). In theory, these allow a more accurate description of the observed void growth kinetics in unit cell computational analysis of periodic array of voids. As such, a classical interpretation of these is that they allow to account for the influence of neighbouring voids, i.e., for void interaction effects. A more recent interpretation is that the physical meaning of such heuristic factors is, however, multi-faceted, e.g. they may account for: void shape effects, heterogeneous hardening in the matrix, loading conditions, etc. (Benzerga *et al.*, 2016; Leblond and Morin, 2014). As such, the introduction of the q_i factors is likely to correct some inaccuracies occurring in the model itself (possibly due to the simplification hypotheses applied during its derivation), rather than being associated with a particular physical aspect. Note moreover that the exact solution for yielding of a hollow sphere under hydrostatic loadings is no longer recovered setting q_1 and q_2 different from unity.

Most engineering metallic materials display anisotropic plasticity. The roots of the plastic anisotropy and its role on the mechanical behaviour of the materials has long been recognized (recall §2.1). It is therefore of great interest to extend the isotropic model of Gurson to account for the plastic anisotropy of the matrix phase in the overall behaviour of the porous solid. A straightforward approach to tackle this problem would be the application of the conventional tools to extend existing isotropic yield criteria to orthotropy (viz., the linear transformation approach or the generalized invariants approach (Cazacu, 2018), and thus obtain some 'equivalent stress' quantity to replace that of Gurson (see Eq. (3.9)), while preserving the original form of the expression of the macroscopic criterion. Based on this purely heuristic approach, several authors, e.g. Brunet *et al.* (2005); Brunet and Morestin (2001); Doege *et al.* (1995); Grange *et al.* (2000); Rivalin *et al.* (2001) and more recently, Besson (2010); Dæhli *et al.* (2017); Gruben *et al.* (2017); Shinohara *et al.* (2016); Steglich *et al.* (2010), proposed extensions to account for plastic anisotropy within the framework of Gurson. It turns out that such crude formulations do not lead to any effect of the plastic anisotropy on the void evolution (hence on damage accumulation). Naturally, such outcome is totally irrational from the physical point of view, given the intrinsically coupled nature of these dissipative phenomena. This demonstrates that porous models cannot be postulated or obtained heuristically by simply modifying existing macroscopic models accounting for distinct plasticity criteria at the microscale (Cazacu *et al.*, 2019). A more physically sound alternative consists in entirely reworking the homogenization scheme, by assigning the anisotropic behaviour of the matrix to a closed-form expression of the local plastic dissipation to be integrated over the employed RVE. This rigorous approach was indeed followed in works highlighted in Table 3.1 (i.e. Eqs. (3.22)-(3.24)). Note that, in this case, the form of the resulting criteria differs from that of Gurson. Such modifications can be understood by the following change of variables: (i) the macroscopic von Mises equivalent stress is replaced with some counterpart, referred to a given anisotropic criterion, $\Sigma_{eq} \to \tilde{\Sigma}_e$; and (ii) a factor h, so-called anisotropy factor, arises in the argument of the hyperbolic cosine, such that $\Sigma_m \to (2/h)\Sigma_m$. More crucially, the anisotropic plastic flow of the matrix has a direct effect on the rate of void growth, in other words, plastic anisotropy induces damage evolution anisotropy. Despite the great number of phenomenological anisotropic plasticity criteria in the literature, note that the porous models described in Table 3.1 accounting for anisotropy consider the matrix material obeying either the criterion of Hill (1948) or the minimal form of that of Cazacu *et al.* (2006). This is explained by the fact that only for these the exact strain-rate plastic potential associated to the stress-based plastic potential of the matrix are known in closed-from. This renders the analytical derivation of improved porous criteria, i.e., accounting for more accurate/elaborated local plasticity criteria, extremely difficult or impossible. Moreover, even if these potentials are known, the evaluation of the macroscopic plastic dissipation may turn out to be impossible to carry out analytically, even for the simplest loading states, viz. hydrostatic loadings. This encourages the usage of a numerical approach to the problem, as pursued in this work. In closing, it should be noted that the focus here is on porous models for which the matrix is characterized by some phenomenological theory of plasticity, rather than within the crystal plasticity framework. For the latter approach refer e.g. to Cazacu *et al.* (2019); Han *et al.* (2013); Lebensohn and Cazacu (2012); and Paux *et al.* (2015).

3.4.3 Void nucleation models

Since most structural engineering metals and alloys display virtually no initial porosity, void nucleation criteria constitute the first essential ingredient in the formulation of a damage constitutive model. Models that fit within the void nucleation framework are now outlined. Depending on the size of the particles operating as nucleation sites, void nucleation criteria have been proposed based on the theory of dislocations and on pure continuum mechanics principles (Besson, 2010; Pineau and Pardoen, 2007). Here the focus is solely on the latter description, i.e. the size-independent regime (refer e.g. to Berdin (2004); Montheillet and Moussy (2012) for a review on the dislocation-based analysis).

As discussed in §2.2.3, void nucleation results from one of two competing events: particle fracture and fracture/debonding at the matrix-particle interface. If one considers the particles as purely elastic, brittle, and containing some form internal microdefects (as the size of the particle increases, so does the probability that the particle contains flaws (Goods and Brown, 1979)), a necessary condition for void nucleation by particle cracking can, in principle, be derived based on a simple one-parameter condition motivated from linear-elastic fracture mechanics arguments, similar to that of Griffith (1921). In this context, particle fracture is assumed to take place as soon as the elastic energy release rate equals or exceeds the particle fracture toughness, which can be also translated into an effective critical stress condition within the particle (Huber *et al.*, 2005). For relatively small, defect-free particles, a critical stress condition based on some material-dependent strength is also valid (Pineau and Pardoen, 2007). In contrast, in theory, such necessary conditions do not hold when predicting void nucleation by means of interface fracture. In this case, stress concentration mechanisms, generally involving plastic flow in the matrix and dislocation accumulation at the particle interface, render the critical stress for interface fracture not intrinsic to the particle, i.e. it also depends on the plastic features of the matrix. When a particle-strengthened material is loaded, the matrix material undergoes plastic deformation, while the particles deform mostly elastically (Goods and Brown, 1979). In this case, both the separation energy and the interface strength play a role in the problem. In particular, decohesion will not take place unless: (i) the elastic energy released by removing the stress (or some fraction of it) from the particle is at least equal to the surface energy created in forming the new internal surfaces; and (ii) the interfacial stress is sufficient to break the interface (or fracture the particle itself) (Goods and Brown, 1979). It turns out that the energy condition can be easily met, while plastic deformation must still be accumulated on the interface in order to raise the interfacial stress above its critical value (Pineau and Pardoen, 2007). Even if at the scale of the individual particles the necessary nucleation conditions are fundamentally based both on energetics and interfacial strength, several sufficient conditions for void nucleation have been proposed in the literature solely in terms of critical stresses (Pineau *et al.*, 2016). Moreover, while the attainment of a critical local strain is neither necessary nor sufficient for voids to nucleate, strain-based models have also been proposed based on the stress-based criteria (e.g. see Ashby (1966); Goods and Brown (1979); Tvergaard and Hutchinson (1992)). In fact, neither the critical-strain-based models nor the stress-based models are entirely physically-sound (Pineau and Pardoen, 2007). The formulation of local conditions for void nucleation by interface fracture via micromechanical considerations is a very

challenging topic, which remains open to further research. This problem is still largely tackled through phenomenological considerations (e.g. Chu and Needleman (1980)), involving both strain- and stress-controlled conditions, for which the critical stress and critical strains for nucleation are macroscopic values rather than their actual 'local' values in the particle or along the interface.

Micromechanical-inspired criteria describing the onset of particle cracking and interfacial debonding have been proposed both based on static and kinematic homogenization approaches. The analytical criteria of Argon and co-workers, (Argon, 1976; Argon *et al.*, 1975; Argon and Im, 1975), and Beremin (1981) and the hybrid numerical-analytical criterion of Lee and Mear (1999) deserve mention. Unit cell numerical simulations have also been performed in order to study void nucleation, e.g. the analysis in Wilner (1988) for spherical elastic particles, and in Lee and Mear (1999) for prolate spheroidal particles; and, later, the ones in Steglich *et al.* (1999); Steglich and Brocks (1997) to include particle damage and Needleman (1987, 1990); and Segurado and LLorca (2004) regarding interface decohesion, using cohesive zone models. More details on these works can be found in Benzerga (2000); Benzerga and Leblond (2010); Pineau *et al.* (2016); Pineau and Pardoen (2007). The focus is now shifted to the presentation of models that fall within the scope of the model for void nucleation using distribution functions, in particular, the one of Chu and Needleman (1980).

Continuum void nucleation models using distribution functions

Within the CDM framework for ductile porous solids based on a single damage variable, viz, the void volume fraction, *f*, as in the constitutive model of Gurson (1977), the nucleation of voids can be introduced through a rate equation of the form:

$$\dot{f} = \dot{f}_{\text{growth}} + \dot{f}_{\text{nucl}}, \tag{3.26}$$

where $\dot{f}$ is the total void volume fraction rate, $\dot{f}_{\text{growth}}$ denotes the growth rate of pre-existing voids and $\dot{f}_{\text{nucl}}$ represents the term related with the nucleation of new voids. Such formulation goes back to Gurson (1975) and was further developed by Chu and Needleman (1980). In the latter work, the authors proposed a general expression for the nucleation term, $\dot{f}_{\text{nucl}}$, consisting of two possible contributions:

$$\dot{f}_{\text{nucl}} = \mathcal{A}\dot{\bar{\epsilon}}^{\text{p}} + \left(\mathcal{B}_1\dot{\bar{\sigma}} + \mathcal{B}_2\dot{\Sigma}_{\text{m}}\right), \tag{3.27}$$

where the first term represents plastic strain-controlled nucleation, and the terms within the parentheses represent stress-controlled nucleation, under the condition $\mathcal{B}_1\dot{\bar{\sigma}} + \mathcal{B}_2\dot{\Sigma}_{\text{m}} \geq 0$. In the above expression, $\dot{\bar{\epsilon}}^{\text{p}}$ and $\dot{\bar{\sigma}}$ are the rates of the local 'effective' values of the flow stress and plastic strain of the matrix, respectively (Eq. (3.11)). $\mathcal{A}$ and $(\mathcal{B}_1, \mathcal{B}_2)$ are functions describing the nucleation rate of voids per unit of plastic strain, $\bar{\epsilon}^{\text{p}}$, and the dependence of the nucleation rate on the increment of the matrix flow stress, $\dot{\bar{\sigma}}$, and on the increment of macroscopic hydrostatic stress, $\dot{\Sigma}_{\text{m}}$, respectively. In general, both depend on the loading and deformation history (Chu and Needleman, 1980). One can adopt a formulation that assumes a purely strain-driven nucleation, $(\mathcal{B}_1, \mathcal{B}_2) = 0$, or a purely stress-driven nucleation, $\mathcal{A} = 0$. A 'mixed' formulation for describing the nucleation kinetics is also possible. In the latter case, one often assumes $\mathcal{A} \cdot \mathcal{B}_1 = 0$, since $\bar{\sigma} = f(\bar{\epsilon})$ and thus the first term of the stress controlled nucleation

law in Eq. (3.27) is equivalent (in the plastic case) to strain driven nucleation (Besson, 2010; Chu and Needleman, 1980). Based on earlier studies (Argon *et al.*, 1975; Goods and Brown, 1979) the authors suggested $\mathcal{A}$ to be a function of $\bar{\epsilon}^{\mathrm{p}}$ and that the stress-controlled nucleation can be described by a single parameter, $\mathcal{B}$, as a function of the arguments $(\bar{\sigma}+\Sigma_{\mathrm{m}})$, respectively. Chu and Needleman (1980) further assumed that $\mathcal{A}$ and $\mathcal{B}$ ought to follow a statistical expression, viz. in the form of a normal/Gaussian distribution. For plastic strain-controlled nucleation, the nucleation strain is thus distributed in a normal fashion about some average nucleation strain, $\bar{\epsilon}_{\mathrm{N}}$, in the form:

$$\mathcal{A}=\frac{f_{\mathrm{N}}}{s_{\mathrm{N}}\sqrt{2\pi}}\exp\left[-\frac{1}{2}\left(\frac{\bar{\epsilon}^{\mathrm{p}}-\bar{\epsilon}_{\mathrm{N}}}{s_{\mathrm{N}}}\right)^{2}\right], \tag{3.28}$$

provided that $\dot{\bar{\epsilon}}^{\mathrm{p}}>0$, otherwise $\mathcal{A}=0$ (Tvergaard, 1989). In the expression, s_{N} is the standard deviation of the distribution and f_{N} represents the volume fraction of strain-driven nucleating particles. Analogously, for plastic strain-controlled nucleation, one writes:

$$\mathcal{B}=\frac{f_{\mathrm{p}}}{s_{\mathrm{p}}\sqrt{2\pi}}\exp\left[-\frac{1}{2}\left(\frac{\left(\bar{\sigma}+\Sigma_{\mathrm{m}}\right)-\sigma_{\mathrm{p}}}{s_{\mathrm{p}}}\right)^{2}\right], \tag{3.29}$$

provided that $(\bar{\sigma}+\Sigma_{\mathrm{m}})$ is at its maximum over the deformation history and that $(\dot{\bar{\sigma}}+\dot{\Sigma}_{\mathrm{m}})>0$, otherwise $\mathcal{B}=0$ (Tvergaard, 1989). In the last equation, σ_{p} is the average nucleation stress; s_{p} and f_{p} represent the standard deviation and volume fraction of stress-driven void-nucleating particles, respectively. Note that the proposal of Chu and Needleman (1980) in Eqs. (3.26)-(3.29) rests on purely phenomenological evidence. The above nucleation parameters must be tuned based on experimental observations and/or via inverse identification in order to capture, as good as allowed by the distribution laws, the damage kinetics at inclusions.

While a stress-controlled formulation appears to be more comprehensive, strain-controlled void nucleation laws may present an expedient and reasonable way of representing the outcome of a more basic stress-based criterion (Needleman, 1987). Moreover, strain-controlled criteria can be more easily implemented in a numerical scheme, which further contributes to its prominence (note that if $\dot{f}_{\mathrm{nucl}}\propto\dot{\Sigma}_{\mathrm{m}}$, a strong non-normality of the macroscopic plastic flow rule arises, ultimately entailing a non-symmetric tangent matrix; this is not the case if a strain-controlled law, $\dot{f}_{\mathrm{nucl}}\propto\dot{\bar{\epsilon}}^{\mathrm{p}}$, is adopted). Unfortunately, the strain-controlled law does not capture the dependence of void nucleation upon stress triaxiality (a fact that has been noted both from analytical (Beremin, 1981) and numerical results (Lee and Mear, 1999; Needleman, 1987). More critically, such formulation tends to predict an increasing amount of nucleation with decreasing stress triaxiality, simply due to the larger accumulated plastic strain in the matrix under low stress triaxialities (Keralavarma and Benzerga, 2010). Studies on plastic strain localization within the framework of Rice (1976) indicate that strain-controlled and stress-controlled nucleation models may lead to quite different predictions of the macroscopic ductility, the latter approach potentially displaying a stronger destabilizing effect (Needleman and Rice, 1978; Saje *et al.*, 1982).

To close, one should note that the model described in Eqs. (3.26)-(3.29) does not refer to a specific nucleation mode nor it is able to distinguish particle debonding from particle cracking. Moreover, phenomena such as void-locking by the particles, particle shape effects, deformation-induced nucleation not involving particles (e.g. at twin boundaries), are merely regarded in an empirical fashion. In practice, one could formulate criteria similar to that of Chu and Needleman (1980) in order to account for several void populations (e.g. varying size, shape and/or orientation) in order to extend this framework to void growth models that allow to account for such features (hence, necessarily entailing additional damage variables) (Benzerga *et al.*, 2016). Despite its limitations, currently, the model of Chu and Needleman (1980) is, by far, the most well-established approach to account for void nucleation within the Gurson-type framework. Other proposals have attempted to account for more complex stress-state effects (Horstemeyer and Gokhale, 1999), damage initiation conditions (Hu and Ghosh, 2008), void shape effects (Tvergaard, 1989), though these have not yet been widely adopted. In general, there is still a need for more comprehensive and accurate micromechanical studies of void nucleation phenomena, as well as a need to employ such studies into the development of improved, more physically-sound, void nucleation criteria (Benzerga *et al.*, 2016).

3.4.4 Void coalescence models

If the stable growth of voids, as modelled within the framework of Gurson (§3.4.2), is assumed to hold during the entire deformation process, then a unitary porosity value would be required to reach the complete loss of load carrying capacity of the RVE. Such approach would lead to a significant overestimation of the ductility and associated fracture properties of actual porous media (Pineau *et al.*, 2016). Indeed, the volume fraction of voids at the onset of fracture of structural engineering metals and alloys need not to reach unity[6]. This suggests that, in general, void growth theory alone, even when accounting for the modifications in Table 3.1, is unable to deliver *quantitative* predictions of ductility of engineering materials (Pineau *et al.*, 2016). This is related to the fact that Gurson-like criteria are established on the hypothesis that plastic flow takes place in the entire RVE, i.e. a diffuse mode of plasticity. Nevertheless, it is well-established that void coalescence events govern the final stages of the ductile damage process, which, by definition, consists in the transition from a diffuse plastic deformation stage to a concentrated plasticity mode within the ligament separating two or more voids (see §2.2.3). From this point on, the velocity fields employed in the Gurson-like models are no longer accurate, as certain modes of concentrated plastic strain rate within the RVE can deliver a lower plastic dissipation of the matrix (Pineau *et al.*, 2016). Predicting the onset of this final stage of the damage process, as well as how it develops, in particular, by describing the gradual loss of stress-bearing capacity during the post-localization regime, is a crucial step in the quest for accurate constitutive models describing ductile fracture. In essence, void coalescence may be regarded as a particular case of a void growth process, in which voids growth under some restrained kinetics induced by intervoid interactions (Benzerga and Leblond, 2010). Thus,

[6] Observations on *post-mortem* failed sections, *in situ* experimental observations, as well as FE micromechanical studies, point that the porosity level at vanishing macroscopic stress typically ranges between 0.15 and 0.3 (Benzerga and Leblond, 2010).

modelling void coalescence should, in principle, entail the introduction of some microstructural information related to the geometry and size of the intervoid ligaments (e.g. the void spacing), in addition to the description of the void itself (Pineau and Pardoen, 2007).

Fundamentally, coalescence models can be categorized into two categories: (i) models to predict the onset of coalescence; and (ii) models to describe the coalescence process, (alias, post-coalescence models). As the terms suggest, the former is employed to predict the transition from diffuse to a concentrated plastic flow within the voids, whereas the latter describe the gradual loss of stress-bearing ability during the 'post-localization' regime. While models for the growth of voids of porous media have been developed with increasing degree of sophistication since the seminal work of Gurson, modelling void coalescence is, in part, still in its infancy (Morin, Leblond and Benzerga, 2015; Morin, Leblond, Benzerga, *et al.*, 2016). This is mainly explained by the major difficulties arising from the large interacting nature of the voids, intrinsic to the coalescence phenomenon.

Nonetheless, some micromechanical-inspired models the onset of void coalescence have been proposed in the past decades. The most promising approach was initiated by the novel work of Thomason (1985), who attempted to model the onset of internal necking by means of a semi-analytical criterion, providing the limit-load of coalescence of primary voids. Thomason formulated the problem of rigid-plastic limit analysis of a cylindrical cell of either square or circular section containing a coaxial void of finite height. Plastic flow in the matrix was described by an associated von Mises yield criterion and restricted to intervoid ligaments, the regions above and below the voids being taken as rigid. The concentration of the plastic strain rate in the ligaments was represented by some discontinuous, yet kinematically admissible, trial velocity fields (see e.g. Benzerga and Leblond (2010) for more details). In the past two decades, some extensions of the analysis of Thomason (1985) have been proposed, either heuristically or physically-inspired (Benzerga and Leblond, 2014; Gallican and Hure, 2017; Hure and Barrioz, 2016; Keralavarma, 2017; Keralavarma and Chockalingam, 2016; Morin, Leblond and Benzerga, 2015; Morin, Leblond, Benzerga, *et al.*, 2016; Scheyvaerts *et al.*, 2010; Torki *et al.*, 2015, 2017). These mainly aim to account for more realistic material behaviour, void shapes, as well as more general loading conditions, whose effects were oversimplified (or totally disregarded), in the original criterion. For a more in-depth overview of these contributions, the reader is referred to Benzerga *et al.* (2016); Benzerga and Leblond (2010); Morin, Leblond, Benzerga, *et al.* (2016); Pineau *et al.* (2016).

Unfortunately, models for the onset of void coalescence and post-coalescence regime derived based on micromechanical arguments, viz. Thomason-like criteria. have not received much attention in terms of critical assessment (Scheyvaerts *et al.*, 2010). Indeed, the current practice on coalescence modelling is still largely based on (more or less physically sound) alternative methods. These include: (i) the numerical reduction of the load-carrying capacity (e.g. ramping down the stress state by means of a cohesive zone-type model (Gao *et al.*, 1998; Gullerud *et al.*, 2000; Krüger *et al.*, 2019; Xia and Shih, 1995a, 1995b)); (ii) phenomenological acceleration of the void growth rate, while staying on the void growth framework. Details regarding the latter approach are described in the following, given its popularity in the literature.

Phenomenological void coalescence and post-coalescence models

The most commonly employed criterion for the onset of void coalescence states that coalescence initiates at a constant (unique) critical porosity value, f_c, characteristic of the material (d'Escatha and Devaux, 1979; McClintock, 1968, 1971). Based on a similar phenomenological viewpoint, Tvergaard and Needleman (1984) (see also Needleman and Tvergaard, 1984) proposed an augmented model to describe the post-coalescence regime. The authors replaced the actual void volume fraction, *f*, entering the spherical void growth yield criterion of Gurson with an 'effective' counterpart, $f^*(f)$, function of the former, such that the rate of void growth is artificially accelerated past some threshold value in order to mimic the strain concentration effects in the intervoid ligaments. Therefore, the framework of Gurson is retained after the onset of coalescence. The criterion reads:

$$f^* = \begin{cases} f & \text{if } f < f_c, \\ f_c + q_\delta (f - f_c) & \text{if } f \geq f_c, \end{cases} \tag{3.30a}$$

where the critical porosity, f_c, describes the onset of coalescence and q_δ, the acceleration factor/slope, is related to the actual porosity at complete macroscopic failure, f_f, as:

$$q_\delta = \frac{f_u^* - f_c}{f_f - f_c}, \tag{3.30b}$$

where f_u^* denotes the ultimate value of the effective void volume fraction, (e.g., $f_u^* = 1$ for the original Gurson model; and $(q_1 f)_u^* = 1$ if the fitting parameters of Tvergaard (1981, 1982b) in Eq. (3.12) are employed). The range of the acceleration parameter is, typically, $q_\delta \in [3,8]$ (Pineau and Pardoen, 2007). Equation (3.30a) combined with Gurson criterion (Eq. (3.9)) states that, as $f \to f_f$, thus $f^* \to f_u^*$, the material loses all stress-bearing capacity. Since the physics underlying the void growth acceleration are left unspecified, experiments are used to provide calibration of the involved parameters, f_c and q_δ at the smallest scale of relevance (Hutchinson and Evans, 2000). Note that such formulation is unable to distinguish the coalescence mode. In the literature, Tvergaard and Needleman (1984) proposal is often referred to as the "f^* approach". Moreover, if coupled with the q_i fitting parameters (Eq. (3.12)) and the description of the void nucleation after Chu and Needleman (1980) (Eqs. (3.26)-(3.29)), this framework is widely known as the Gurson-Tvergaard-Needleman (GTN) model. While the two-parameter criterion in Eq. (3.30a) is rather crude, it is very attractive from the numerical implementation point of view, as it allows to describe coalescence is an expedient and efficient fashion, which partially explains its extensive adoption. An equivalent expression to Eq. (3.30a) for void growth models accounting for void shape effects can also be heuristically formulated (Morin, Leblond and Tvergaard, 2016).

3.5 Concluding remarks

Given the growing understanding of the mechanisms of damage at the micro-scale, known to govern failure of materials at the macroscale, micromechanics has revealed to be a quite natural, yet powerful, framework for its modelling. Micromechanical models are built on the idea that a proper description of the phenomena at the micro- or meso- scale will strengthen the predictions of the model at larger scales (viz., actual components and structures). In the particular case of ductile damage modelling, the framework of 'porous solids' is often adopted. It turns out that viewing metals and alloys as porous media leads to an effective framework for deriving constitutive equations from micro-mechanical considerations. Being based on scale transition micromechanical models display an innate predictive capability as they directly account for the microstructural features of the matter and their effect on the plastic flow and damage state. On the contrary, Lemaitre-based phenomenological damage models rely on the measurement of some apparent elastic modulus to quantify the damage state. While this allows to obtain a lighter identification procedure, recent studies point out that the modification of the elastic modulus with increasing plastic strain in uniaxial tension tests go far beyond the effect of the accumulated damage (Hering and Tekkaya, 2020). This fundamentally weakens the principles on which such models are built. Moreover, the effect of damage on the overall elastic behaviour may also been accounted in an *ad hoc* fashion using the micromechanical counterparts. This dependence is however very often neglected (Besson, 2010).

One could argue that the micromechanical models reviewed in this work are already too cumbersome to be used by engineers. However, in fact these are in their early development stages. In the void growth models, the incorporation of void shape effects and of plastic anisotropy are, perhaps, the most interesting developments of the field in the past two decades (see Table 3.1). Meanwhile, more incremental, yet valuable, developments are needed to improve certain aspects of existing models, in order to better describe the ductility of engineering materials. One of the most, if not the most, relevant aspect is the improvement of the plasticity description of the matrix phase, which, as shown in this subsection, has been mainly dealt with isotropic or basic, rather unsophisticated, orthotropic plasticity criteria.

The current limitations of the micromechanical approach are far greater regarding the void nucleation and coalescence stages. This is in part explained by the increased difficulties inherent to modelling these phenomena: nucleation is a statistical process, strongly dependent on the geometry and properties of the inclusions and the inclusion/matrix interfaces; and void coalescence introduces problems of scale separability which render classical homogenization procedures not applicable. Accordingly, only relatively crude, phenomenological-inspired, void nucleation and coalescence criteria are often employed to supplement the (more sophisticated) void growth models. The development and implementation of advanced void nucleation and coalescence models falls outside the scope of this thesis, and the above topics were reviewed above just for the sake of completeness.

Chapter 4

Non-quadratic orthotropic strain-rate potential: development and implementation

This chapter deals with the development and implementation of a non-quadratic orthotropic strain-rate potential based on an arbitrary number of linear transformations. The proposed strain-rate potential is the exact work-conjugate of the stress potential of Plunkett *et al.* (2008). Similarly to the reference stress potential, the derived strain-rate potential is able to describe both the anisotropy and the tensile and compressive asymmetry of the plastic response of textured metals. These potentials are applied to describe the behaviour of dense materials with hexagonal crystal structure, viz. a commercially pure titanium and a AZ31B magnesium alloy, in order to highlight the flexibility of the model and to graphically illustrate the duality between the yield surface and strain-rate potential isovalue surfaces.

4.1 Chapter introduction

In order to model the elastic-plastic behaviour of metallic materials it is vital to accurately describe the plastic dissipation, i.e., the irreversible mechanical work. Based on the work equivalence principle, Ziegler (1977) and Hill (1987) shown that a meaningful strain-rate potential can be associated with any convex stress potential. Accordingly, one can use a strain-rate potential, in place of the classical stress potential, to describe the plastic dissipation response of a deforming solid. While the development of stress potentials has received a lot of attention, that of strain-rate potentials has been somewhat inactive (Kim *et al.*, 2007). The reasons are mainly twofold: (i) the derivation of a strain-rate potential from an existing stress potential can be very challenging, if not impossible; and (ii) in contrast to the yield function, the strain-rate potential does not provide an explicit definition of the boundary between elastic and plastic domain, thus the determination of the plastic loading/unloading conditions is more expensive from the computational viewpoint (Bacroix and Gilormini, 1995). However, without knowledge of the expression for the strain-rate potential associated with a given stress potential, it is not possible to derive the corresponding macroscopic stress potential for a *porous* solid by means of the kinematic homogenization approach, as in the theory of Gurson (1977). Furthermore, with the advent of full-field Digital Image Correlation (DIC) techniques, a strain-rate-based formulation can be advantageous from the experimental point of view given that, in truth, one measures strain and strain-rate fields rather than stress fields, and thus a constitutive model can be calibrated based on strain information in addition to (or in

place of) global stress measurements, which implicitly introduce dubious assumptions such as of stress homogeneity in the test specimens.

Strain-rate potentials can be defined based on the crystal plasticity theory or on purely phenomenological grounds. Within the former approach, a numerical crystallographic strain rate potential is approximated by a suitable analytical function. This approach was applied in Fortunier (1989) for face-centred cubic (fcc) single crystals and in Arminjon *et al.* (1994); van Bael and van Houtte (2003); Hiwatashi *et al.* (1997); van Houtte (1994); van Houtte and van Bael (2004) regarding body-centred cubic (bcc) polycrystals, and employed in finite-element simulations, for example, in Bacroix and Gilormini (1995); Hu *et al.* (1998); Li *et al.* (2001); Szabó and Jonas (1995); Zhou *et al.* (1998), among others. Within the phenomenological (macroscopic) approach, analytic expressions of the *exact* strain-rate potentials are only known for a few cases, among these, the classical yield criteria for materials with cubic crystal structure, viz. von Mises, Tresca and Hill (1948). Recently, an orthotropic strain-rate formulation for metals with hexagonal crystal structure, which are known to display tension-compression asymmetry, was proposed by Cazacu *et al.* (2010) as the exact dual of a simplified and quadratic form of the Cazacu *et al.* (2006) (alias CPB06) stress potential. In the same spirit as the Hill-type dual potentials, Cazacu *et al.* (2010) imposed a constrain to the fourth-order orthotropic tensor so that the transformed stress (and therefore strain-rate) tensor is deviatoric. While such restriction was introduced for mathematical convenience, this is not a necessary condition to ensure plastic incompressibility (see the discussing in Cazacu *et al.* (2006)) and, ultimately, hinders the flexibility of the general form of the CPB06 stress potential. In an effort to improve the description of the behaviour of textured polycrystals with cubic structure, Barlat and his co-workers proposed several non-quadratic orthotropic strain-rate potentials of heuristic nature based on the linear-transformation method using: one (Barlat *et al.*, 1993; Chung *et al.*, 1999; Kim *et al.*, 2003); two (Barlat and Chung, 2005; Kim *et al.*, 2007); and multiple (Rabahallah, Balan and Barlat, 2009) transformations of the plastic strain-rate tensor. None of these formulations are strictly dual (or work-conjugate) of the respective non-quadratic stress potential. Indeed, the transformation tensors of the stress and strain-rate space are actually independent, only agreeing in the number of coefficients. Nevertheless, these authors demonstrated that some of the above potentials can be regarded as pseudo-conjugates, since their description of the plastic anisotropy is similar to that of the respective stress potential. Phenomenological strain-rate potentials are more convenient and computationally time-efficient regarding finite-element simulations (e.g. Yoon *et al.* (1995) using the non-quadratic potential of Barlat *et al.* (1993); Rabahallah *et al.* (2009) using the dual of the Hill (1948) and the Barlat and Chung (2005) non-quadratic potential; and Yoon *et al.* (2011) and Balan and Cazacu (2013), using the Cazacu *et al.* (2010) strain-rate potential for fully-dense and porous solids, respectively). For a review of the majority of phenomenological strain-rate formulations mentioned in this paragraph, the reader is referred to the book of Cazacu *et al.* (2019).

The derivation of suitable strain-rate potentials for materials concurrently displaying anisotropy and tension-compression asymmetry was tackled in Cazacu *et al.* (2010), but only to some extent. Indeed, orthotropic stress and strain-rate potentials based on a single transformation and restricted to a quadratic

form may not be able to capture the complex mechanical behaviour encountered in strongly textured hexagonal crystal structure metals with satisfactory accuracy. In such cases, more coefficients must be introduced in the formulation to increase the flexibility of the potentials. In this spirit, Plunkett *et al.* (2008) extended the general form of the CPB06 criterion to account for multiple linear transformations.

The goal of this chapter is to provide the dual potential of the Plunkett *et al.* (2008) stress potential. It is shown that the proposed non-quadratic orthotropic strain-rate potential is an exact dual (rather than pseudo-conjugate). The strain-rate potential accounts for tension-compression asymmetry and assumes an arbitrary number of linear transformations on the (full 3-D) strain-rate space. Given the exact duality property, the material parameters are the same for the stress and strain-rate potentials.

4.2 Theoretical background

In the following, some basic concepts regarding constitutive modelling of plastic deforming materials using strain-rate potentials and orthotropic extensions using the linear transformation method are reviewed. The expression of the Cazacu *et al.* (2010) strain-rate potential and the stress potential of Plunkett *et al.* (2008), are also recalled, the latter being the starting point of the analysis.

4.2.1 Strain-rate potentials: definitions and review

Within the theory of thermodynamics a constitutive relation can be based on the existence of a scalar function, ϕ, known as dissipation potential, for which the thermodynamic force, $\boldsymbol{\beta}_D$, (e.g., stress-like variable), is defined by a tensor gradient relationship of the type:

$$\boldsymbol{\beta}_D = \frac{\partial \phi(\dot{\boldsymbol{\alpha}})}{\partial \dot{\boldsymbol{\alpha}}}, \tag{4.1}$$

where $\dot{\boldsymbol{\alpha}}$ denotes some flux variable (e.g. strain-like variable), dual of $\boldsymbol{\beta}_D$. If ϕ is non-negative, convex with respect to $\dot{\boldsymbol{\alpha}}$, and respects $\phi(\mathbf{0}) = 0$, then the model is thermodynamically admissible, in the sense that non-negative dissipation is guaranteed. The inverse relation can be written from the so-called *dual* dissipation potential, ϕ^* – the Legendre-Fenchel transformation (e.g. Fenchel (1949)) of ϕ, as:

$$\dot{\boldsymbol{\alpha}} = \frac{\partial \phi^*(\boldsymbol{\beta}_D)}{\partial \boldsymbol{\beta}_D}. \tag{4.2}$$

The above relationships often include state variables which are omitted here for readability. Let us now focus on the description of rate-independent perfect isochoric plasticity. Let $\boldsymbol{\sigma}$ denote the Cauchy stress tensor and $\boldsymbol{d}^{\mathrm{p}}$ the Eulerian (plastic) strain-rate tensor. In the rate-independent case, the dissipation potential $\phi^*(\boldsymbol{\sigma})$ is non-differentiable. Hence a convex yield function of the type $f(\boldsymbol{\sigma}) = \varphi(\boldsymbol{\sigma}) - \tau$ is introduced, where τ is a positive scalar with the dimension of stress and $\varphi(\boldsymbol{\sigma})$ an equivalent stress function. The elastic domain is therefore defined as the set of all the elastic stress states, i.e.:

$$\mathcal{E} = \left\{ \boldsymbol{\sigma} \in \mathcal{S}_2 \mid f(\boldsymbol{\sigma}) < 0 \right\}, \tag{4.3}$$

where $\mathcal{S}_2$ denotes all symmetric second-order tensors. Moreover one defines the closure of $\mathcal{E}$ as $\bar{\mathcal{E}}$, to describe the set of all the plastically admissible stress states, and its boundary as $\partial\mathcal{E}$, describing the set of stress states satisfying the yield condition, i.e. defining the yield surface, $f(\boldsymbol{\sigma}) = 0$ (Jirásek and Bazant, 2002). Based on the yield function, a dissipation potential in the stress space $\phi^*(\boldsymbol{\sigma})$, can be defined as the characteristic function[7], $\bar{\mathcal{I}}(\cdot)$, (reciprocal of the indicator function), of the set of all plastically admissible stress states, $\bar{\mathcal{E}}$, i.e.:

$$\phi^*(\boldsymbol{\sigma}) = \bar{\mathcal{I}}_{\bar{\mathcal{E}}}(\boldsymbol{\sigma}) = \begin{cases} 0 & \text{if } \boldsymbol{\sigma} \in \bar{\mathcal{E}} \\ \infty & \text{if } \boldsymbol{\sigma} \notin \bar{\mathcal{E}} \end{cases}. \tag{4.4}$$

Differentiation of this expression leads to the set (cf. Eq. (4.2)):

$$\boldsymbol{d}^{\mathrm{p}} \in \partial\phi^*(\boldsymbol{\sigma}) = \partial\bar{\mathcal{I}}_{\bar{\mathcal{E}}}(\boldsymbol{\sigma}) = \begin{cases} \{\mathbf{0}\} & \text{if } \boldsymbol{\sigma} \in \mathcal{E} \\ \mathcal{N}(\boldsymbol{\sigma}) & \text{if } \boldsymbol{\sigma} \in \partial\mathcal{E} \\ \varnothing & \text{if } \boldsymbol{\sigma} \notin \bar{\mathcal{E}} \end{cases}, \tag{4.5}$$

where $\partial(\cdot)$ denotes the subdifferential operation (generalization of the differential of smooth functions, see e.g. Moreau, (1970, 1966) for more details) and $\mathcal{N}(\boldsymbol{\sigma})$ the normal cone with outward normals of the yield surface, $\partial\mathcal{E}$, at point $\boldsymbol{\sigma}$. If the yield surface is regular (i.e. not a vertex) at point $\boldsymbol{\sigma}$ this cone reduces to the semi-infinite ray given by:

$$\mathcal{N}(\boldsymbol{\sigma}) = \left\{ \boldsymbol{n} \in \mathcal{S}_2 \mid \boldsymbol{n} = \dot{\lambda}\frac{\partial f(\boldsymbol{\sigma})}{\partial \boldsymbol{\sigma}}, \dot{\lambda} \geq 0 \right\}, \tag{4.6}$$

The last two expressions can be rewritten as:

$$\boldsymbol{d}^{\mathrm{p}} = \dot{\lambda}\frac{\partial f(\boldsymbol{\sigma})}{\partial \boldsymbol{\sigma}} = \dot{\lambda}\frac{\partial \varphi(\boldsymbol{\sigma})}{\partial \boldsymbol{\sigma}}, \tag{4.7}$$

for $\dot{\lambda} \geq 0$, $f \leq 0$, and $f\dot{\lambda} = 0$, which denotes the well-known associated flow rule as well as the loading-unloading (or Kuhn-Tucker) conditions, where $\dot{\lambda}$ is a Lagrange multiplier known as plastic multiplier rate. The dual potential of $\phi^*(\boldsymbol{\sigma})$, $\phi(\boldsymbol{d}^{\mathrm{p}})$, results from the Legendre-Fenchel transform as:

$$\phi(\boldsymbol{d}^{\mathrm{p}}) = \mathcal{L}_{\mathrm{LF}}\left(\phi^*(\boldsymbol{\sigma})\right) = \sup_{\boldsymbol{\sigma}_p \in \mathcal{S}_2}\left(\boldsymbol{\sigma}_p : \boldsymbol{d}^{\mathrm{p}} - \phi^*(\boldsymbol{\sigma}_p)\right), \tag{4.8}$$

where $\mathcal{L}_{\mathrm{LF}}(\cdot)$ and sup(·) denote the Legendre transformation and the supremum operations, respectively. This expression can be simplified since $\phi^*(\boldsymbol{\sigma}_p)$ vanishes for all $\boldsymbol{\sigma}_p \in \bar{\mathcal{E}}$ (see Eq. (4.4)) and $\phi^*(\boldsymbol{\sigma}_p) = \infty$ for $\boldsymbol{\sigma}_p \notin \bar{\mathcal{E}}$, hence it suffices to perform the supremum operation over $\bar{\mathcal{E}}$, i.e.:

$$\phi(\boldsymbol{d}^{\mathrm{p}}) = \sup_{\boldsymbol{\sigma}_p \in \bar{\mathcal{E}}}\left(\boldsymbol{\sigma}_p : \boldsymbol{d}^{\mathrm{p}}\right), \tag{4.9}$$

An important result is that, for the class of rate-independent models, the dissipation potential $\phi(\boldsymbol{d}^{\mathrm{p}})$ is a homogeneous function of degree one with respect to positive multipliers:

[7] Let X be a set and M a subset of X. In convex analysis the characteristic function $\bar{\mathcal{I}}_M : X \to \mathbb{R} \cup \{+\infty\}$ of a subset M, is defined as: $\bar{\mathcal{I}}_M(x) = 0$ if $x \in M$ and $\bar{\mathcal{I}}_M(x) = +\infty$ if $X \notin M$.

$$\phi(\xi \boldsymbol{d}^{\mathrm{p}}) = \sup_{\boldsymbol{\sigma}_p \in \bar{\mathcal{E}}} \left(\boldsymbol{\sigma}_p : \xi \boldsymbol{d}^{\mathrm{p}} \right) = \xi \sup_{\boldsymbol{\sigma}_p \in \bar{\mathcal{E}}} \left(\boldsymbol{\sigma}_p : \boldsymbol{d}^{\mathrm{p}} \right) = \xi \phi(\boldsymbol{d}^{\mathrm{p}}), \ \forall \xi \geq 0 , \tag{4.10}$$

and therefore, the dissipation potential $\phi(\boldsymbol{d}^{\mathrm{p}})$ is equal to the dissipation function, $\mathcal{D}(\boldsymbol{d}^{\mathrm{p}})$, i.e.:

$$\mathcal{D}(\boldsymbol{d}^{\mathrm{p}}) \triangleq \boldsymbol{\sigma} : \boldsymbol{d}^{\mathrm{p}} = \sup_{\boldsymbol{\sigma}_p \in \bar{\mathcal{E}}} \left(\boldsymbol{\sigma}_p : \boldsymbol{d}^{\mathrm{p}} \right) = \phi(\boldsymbol{d}^{\mathrm{p}}) , \tag{4.11}$$

where $\boldsymbol{\sigma}$ denotes the actual stress (resulting from the applied plastic strain-rate, $\boldsymbol{d}^{\mathrm{p}}$) and $\boldsymbol{\sigma}_p$ denotes all plastically admissible stress states. The last equation implicitly assumes the convexity and normality (the flow rule is associated) conditions. Note that the inequality $\mathcal{D}(\boldsymbol{d}^{\mathrm{p}}) = \boldsymbol{\sigma} : \boldsymbol{d}^{\mathrm{p}} \geq \boldsymbol{\sigma}_p : \boldsymbol{d}^{\mathrm{p}} \ \ \forall \boldsymbol{\sigma}_p \in \bar{\mathcal{E}}$ is no more than the postulate of maximum plastic dissipation. Unfortunately, under the classical flow rule in Eq. (4.7), the stress gradient of the yield function constrains the strain-rate in 'type' (or 'direction') but not in magnitude, and thus there is not a one-to-one relationship between stress and strain-rate, which precludes the determination of a dual potential, $\phi(\boldsymbol{d}^{\mathrm{p}})$, of the Legendre-type. Nevertheless, it turns out that, based on the work-equivalence principle, an alternative meaningful dual can be associated with any convex yield function (Chung and Richmond, 1993; Hill, 1987; Ziegler, 1977). If the yield function is homogeneous of degree one with respect to positive multipliers, i.e. $f(\xi\boldsymbol{\sigma}) = \xi f(\boldsymbol{\sigma}), \forall \xi \geq 0$, then, from the Euler theorem, $\boldsymbol{\sigma} : \partial f(\boldsymbol{\sigma}) / \partial \boldsymbol{\sigma} = \varphi(\boldsymbol{\sigma})$. Combining Eq. (4.7), Eq. (4.11) and the yield condition, $\varphi(\boldsymbol{\sigma}) = \tau$, results in:

$$\mathcal{D}(\boldsymbol{d}^{\mathrm{p}}) = \boldsymbol{\sigma} : \boldsymbol{d}^{\mathrm{p}} = \boldsymbol{\sigma} : \dot{\lambda} \frac{\partial f(\boldsymbol{\sigma})}{\partial \boldsymbol{\sigma}} = \dot{\lambda} \tau = \psi(\boldsymbol{d}^{\mathrm{p}}) \tau , \tag{4.12}$$

where the function $\psi(\boldsymbol{d}^{\mathrm{p}})$ in the strain-rate space, often referred to as the *strain-rate potential* (SRP), was defined as:

$$\psi(\boldsymbol{d}^{\mathrm{p}}) = \dot{\lambda} . \tag{4.13}$$

The scalar function $\psi(\boldsymbol{d}^{\mathrm{p}})$ acts as a work-equivalent strain-rate measure (as $\mathcal{D}(\boldsymbol{d}^{\mathrm{p}}) = \tau \psi(\boldsymbol{d}^{\mathrm{p}})$ and thus isovalue surfaces $\psi(\boldsymbol{d}^{\mathrm{p}})$ correspond to the same dissipation) and is always homogeneous of degree one with respect to positive multipliers. Based on geometrical considerations, Hill (1987) showed that the hypersurfaces $\varphi(\boldsymbol{\sigma}/\tau) = 1$ and $\psi(\boldsymbol{d}^{\mathrm{p}}/\dot{\lambda}) = 1$ are polar reciprocates with respect to the unit hypersphere, and thus $\psi(\boldsymbol{d}^{\mathrm{p}})$ is necessarily convex (since $\varphi(\boldsymbol{\sigma})$ is convex) and its gradient acts as a conventional dissipation potential (c.f. Eq. (4.1)), for which a constitutive relation for the stress can be stated as:

$$\boldsymbol{\sigma} = \tau \frac{\partial \psi(\boldsymbol{d}^{\mathrm{p}})}{\partial \boldsymbol{d}^{\mathrm{p}}} . \tag{4.14}$$

One refers to the strain-rate potential, $\psi(\boldsymbol{d}^{\mathrm{p}})$, as the *dual* of the equivalent stress function, $\varphi(\boldsymbol{\sigma})$, in turn also known as *stress potential*[8]. This duality is not of Legendre type but reflects a sound relationship based on the notion of polar reciprocity. Naturally, either potential is readily constructed from the other

[8] The dual potentials $\{\varphi(\boldsymbol{\sigma}), \psi(\boldsymbol{d}^{\mathrm{p}})\}$ must not be confounded with the dual potentials of the Legendre-type, i.e., $\{\phi^*(\boldsymbol{\sigma}), \phi(\boldsymbol{d}^{\mathrm{p}})\}$, respectively. Note moreover that these have, in fact, different physical dimensions.

since duality is a two-way relationship. The naming convention between the primal and dual potentials is simply a matter of preference.

Given a closed-form expression for the stress potential $\varphi(\boldsymbol{\sigma})$, the derivation of the expression of the associated strain-rate potential, $\psi(\boldsymbol{d}^{\mathrm{p}})$, entails a mathematical manipulation which can be summarised by a four-step procedure: (i) the strain-rate tensor, $\boldsymbol{d}^{\mathrm{p}}$, is determined from the associated flow rule (Eq. (4.7)), i.e. $\boldsymbol{d}^{\mathrm{p}} \equiv \boldsymbol{d}^{\mathrm{p}}(\boldsymbol{\sigma}, \dot{\lambda}, \tau)$; (ii) the obtained expression is inverted in order to isolate the stress tensor (or, more precisely, its deviator), $\boldsymbol{\sigma} \equiv \boldsymbol{\sigma}(\boldsymbol{d}^{\mathrm{p}}, \dot{\lambda}, \tau)$; (iii) the latter expression for the stress tensor is substituted in the scalar equation $\varphi(\boldsymbol{\sigma}) = \tau$ (yield condition), which leads to the elimination of τ; (iv) the plastic multiplier rate, $\dot{\lambda}$, is isolated from the latter equation resulting in a final expression for the SRP: $\psi(\boldsymbol{d}^{\mathrm{p}}) \triangleq \dot{\lambda} \equiv \dot{\lambda}(\boldsymbol{d}^{\mathrm{p}})$. In truth, this seemingly straightforward procedure can turn out to be quite challenging, if not impossible, when the reference (stress) potential involves complex forms, (e.g. eigenvalues, piecewise defined due to absolute values, exponentiation, etc.), namely in the abovementioned variable isolation tasks. This explains the limited number of *exact* dual formulations in the literature. In the following paragraphs the strain-rate potential function proposed in Cazacu *et al.* (2010), which is of special interest to the present work, is presented.

4.2.2 Review of the Cazacu *et al.* (2010) strain rate potential

Cazacu *et al.* (2010) derived the exact dual of the quadratic form of the CPB06 (Cazacu *et al.*, 2006) orthotropic stress potential. The quadratic form of the CPB06 yield criterion, acting as the primal potential, is given by:

$$f(\boldsymbol{\sigma}, k, \boldsymbol{\mathcal{L}}, \sigma_1^{\mathrm{T}}) \triangleq \varphi(\boldsymbol{\sigma}, k, \boldsymbol{\mathcal{L}}) - \sigma_1^{\mathrm{T}} = 0 \quad \text{with} \quad \varphi(\boldsymbol{\sigma}, k, \boldsymbol{\mathcal{L}}) = m\sqrt{\sum_{i=1}^{3}\left(|\hat{s}_i| - k\hat{s}_i\right)^2}\,, \tag{4.15}$$

where σ_1^{T} is the yield stress in uniaxial tension in along the 1-direction of the orthotropy axes (say, the rolling direction), $k \in [-1,1]$ is a material parameter describing the tension-compression asymmetry, $\boldsymbol{\mathcal{L}} = \boldsymbol{\mathcal{C}} : \boldsymbol{\mathcal{K}}$ is the deviatoric projection of a symmetric fourth-order orthotropic tensor $\boldsymbol{\mathcal{C}}$, $(\hat{s}_1, \hat{s}_2, \hat{s}_3)$ are the eigenvalues values of the transformed stress tensor $\hat{\boldsymbol{s}} = \boldsymbol{\mathcal{L}} : \boldsymbol{\sigma}$, and m is a constant defined such that $\varphi(\boldsymbol{\sigma})$ reduces σ_1^{T} for uniaxial tensile loadings (refer to Cazacu *et al.* (2006) for its expression). In relation to the original form of the stress potential, Cazacu *et al.* (2010) further assumed a constraint to the 'type' of orthotropy such that $\boldsymbol{\mathcal{L}}$ is (major) *symmetric*, and thus $\hat{\boldsymbol{s}}$ is traceless. The expression of Cazacu *et al.* (2010) orthotropic strain-rate potential is given by a piecewise function of the type:

$$\psi(\boldsymbol{d}^{\mathrm{p}}, k, \boldsymbol{\mathcal{L}}) = \begin{cases} \dfrac{1}{m(1-k)}\sqrt{b_1^2 + b_2^2 + \left(\dfrac{3k^2 - 10k + 3}{3k^2 + 2k + 3}\right) b_3^2} & \text{if } (b_1, b_2, b_3) \in D_3^- \\ \dfrac{1}{m(1+k)}\sqrt{b_1^2 + b_2^2 + \left(\dfrac{3k^2 + 10k + 3}{3k^2 - 2k + 3}\right) b_3^2} & \text{if } (b_1, b_2, b_3) \in D_3^+ \end{cases}, \tag{4.16}$$

where (b_1, b_2, b_3) are the eigenvalues of a deviatoric transformed strain-rate tensor: $\boldsymbol{b} = \boldsymbol{\mathcal{H}} : \boldsymbol{d}^{\mathrm{p}}$, $\boldsymbol{\mathcal{H}}$ is an orthotropic fourth-order symmetric tensor such that $\boldsymbol{\mathcal{H}} : \boldsymbol{\mathcal{L}} = \boldsymbol{\mathcal{K}}$ and $\boldsymbol{\mathcal{K}}$ is the deviatoric fourth order

unit tensor. Note that $\mathcal{H}$ is the counterpart of $\mathcal{L}$ in the strain-rate space. The domains D_3^- and D_3^+ in Eq. (4.16) are given as follows:

$$D_3^- = \left\{ (b_1, b_2, b_3) \,|\, \frac{b_3}{\sqrt{b_1^2 + b_1^2 + b_1^2}} \geq \frac{3k^2 - 2k + 3}{\sqrt{6\left(k^2 + 3\right)\left(3k^2 + 1\right)}} \right\},$$
$$D_3^- = \left\{ (b_1, b_2, b_3) \,|\, \frac{b_3}{\sqrt{b_1^2 + b_1^2 + b_1^2}} \leq \frac{-\left(3k^2 + 2k + 3\right)}{\sqrt{6\left(k^2 + 3\right)\left(3k^2 + 1\right)}} \right\}. \tag{4.17}$$

For brevity, Eq. (4.16) represents only two (out of six) branches of the potential. The expressions of the remaining branches of $\psi(\boldsymbol{d}^{\mathrm{p}})$ corresponding to the domains D_i^- and D_i^+, $i = 1, 2,$ are readily obtained from Eq. (4.16) by symmetry. The interested reader is referred to Cazacu *et al.* (2010) for the expression of the components of $\mathcal{H}$, the full piecewise representation of the potential and its first derivatives. For $k = 0,$ i.e., no tension-compression asymmetry, the Cazacu *et al.* (2010) strain-rate potential reduces to that of Hill (1987, 1979), the latter being the exact dual of the well-known orthotropic stress potential of Hill (1948).

4.3 Linear transformation-based criteria

Most orthotropic plastic potentials are developed based on isotropic criteria. This inherently ensures that the developed orthotropic functions are able to reduce to isotropy, which otherwise could lead to spurious anisotropic effects (Barlat *et al.*, 2005). Two rigorous formulations for extending to orthotropy existing isotropic criteria can be distinguished: (i) the generalized invariants approach; and (ii) the linear transformation approach. The former is based on the theory of tensor representation of orthotropic scalar functions (see e.g. Cazacu and Barlat, 2001, 2003) and is applicable for criteria that are written in terms of invariants of the deviatoric stress tensor, whereas the latter is based on the use of one or more linear transformations to the stress tensor (or its deviator), similarly to the criterion in Eq. (4.15). This work concerns the latter approach. Indeed, the linear transformation approach has received more attention in the literature. The reasons are twofold: first, linear transformations on the arguments of a convex isotropic function automatically preserves its convexity (which, in contrast, can be difficult to verify in the generalized invariants formulation); and second, it is a quite simple method, applicable to virtually any isotropic criterion. The main idea of this methodology is as follows. Let $\varphi_{\mathrm{iso}}(\boldsymbol{\sigma}) \triangleq \varphi_{\mathrm{iso}}(s_1, s_2, s_3)$ describe a convex isotropic potential, defined in terms of the eigenvalues of the deviatoric stress tensor, (s_1, s_2, s_3), and $\mathcal{L}^{(k)}$ denote the *k*-th fourth-order orthotropic transformation tensor defined such that: (i) orthotropic symmetry is preserved; and (ii) the condition of plastic incompressibility is satisfied. Therefore one can define a transformed stress tensor $\hat{\boldsymbol{s}}^{(k)}$, not necessarily traceless, as the *k*-th linear transformation of the actual stress tensor, $\boldsymbol{\sigma}$, i.e., $\hat{\boldsymbol{s}}^{(k)} = \mathcal{L}^{(k)} : \boldsymbol{\sigma}$. The orthotropic potential, φ, is then defined based on the isotropic (reference) counterpart, φ_{iso}, as:

$$\varphi = \varphi\left(\hat{\boldsymbol{s}}^{(1)},...,\hat{\boldsymbol{s}}^{(k)},...,\hat{\boldsymbol{s}}^{(n_{\text{ex}})}\right) = \sum_{n=1}^{n_{\text{ex}}} \varphi_{\text{iso}}^{(n)}(\hat{\boldsymbol{s}}^{(n)}) = \tau \text{ , with } 1 \le p \le n \tag{4.18}$$

when n_{ex} linear transformations are considered. An appropriate scaling factor should also enter the above expression such that $\varphi(\boldsymbol{\sigma}) \triangleq \tau$ for a given reference yield stress value, τ, usually the uniaxial tensile yield stress. Increasing the number of transformations potentially improves the mathematical flexibility of the model. For an overview of the criteria developed within this framework refer, for example, to the works of Barlat *et al.* (2005), Plunkett *et al.* (2008), Aretz and Barlat, (2013) and references therein. The general form of the stress potential of Plunkett *et al.* (2008) is now presented which operates as the primal potential for the strain-rate potential worked out in this chapter.

4.3.1 Review of the Plunkett *et al.* (2008) stress potential

Plunkett *et al.* (2008) orthotropic yield criterion is no more than an extension of Cazacu *et al.* (2006) (CBP06) criterion, by incorporating $n_{\text{ex}} \ge 1$ linear transformations (cf. Eq. (4.18)), i.e.:

$$\begin{aligned} &f(\boldsymbol{\sigma}, k^{(n)}, \mathcal{L}^{(n)}, a, \sigma_1^{\text{T}}) \triangleq \varphi(\boldsymbol{\sigma}, k^{(n)}, \mathcal{L}^{(n)}, a) - \sigma_1^{\text{T}} = 0, \quad n = 1,...,n_{\text{ex}}, \\ &\varphi = m\left(F\right)^{\frac{1}{a}} \text{, with } F = \sum_{n=1}^{n_{\text{ex}}} F^{(n)} \text{ and } F^{(n)} = \sum_{i=1}^{3}\left(\left|\hat{s}_{p_i}^{(n)}\right| - k^{(n)}\hat{s}_{p_i}^{(n)}\right)^a, \end{aligned} \tag{4.19}$$

where a is the homogeneity degree, $\hat{s}_{p_i}^{(n)}$, $i = 1,2,3$, are the eigenvalues of the *n*-th transformed stress tensor, $\hat{\boldsymbol{s}}^{(n)}$, $\mathcal{L}^{(n)} = \mathcal{C}^{(n)} : \mathcal{K}$ is the corresponding fourth-order deviatoric transformation tensor, and $\mathcal{C}^{(n)}$ is a major-symmetric orthotropic tensor whose Voigt 6x6-matrix notation, $\mathbf{C}^{(n)} \leftarrow \mathcal{C}^{(n)}$ is in the form:

$$\mathbf{C}^{(n)} = \begin{bmatrix} C_{11}^{(n)} & C_{12}^{(n)} & C_{13}^{(n)} & 0 & 0 & 0 \\ C_{12}^{(n)} & C_{22}^{(n)} & C_{23}^{(n)} & 0 & 0 & 0 \\ C_{13}^{(n)} & C_{23}^{(n)} & C_{33}^{(n)} & 0 & 0 & 0 \\ 0 & 0 & 0 & C_{44}^{(n)} & 0 & 0 \\ 0 & 0 & 0 & 0 & C_{55}^{(n)} & 0 \\ 0 & 0 & 0 & 0 & 0 & C_{66}^{(n)} \end{bmatrix}, \tag{4.20}$$

$k^{(n)}$ is tension-compression asymmetry parameter associated with the transformation *n*, and *m* is a material constant defined such that $\varphi(\boldsymbol{\sigma})$ reduces σ_1^{T} for uniaxial tensile loadings and it is given in terms of $\mathcal{L}^{(n)}$ and $k^{(n)}$ as:

$$m = \left(\sum_{i=1}^{n_{\text{ex}}} \bar{m}^{(n)}\right)^{-\frac{1}{a}} \text{, with } \bar{m}^{(n)} = \sum_{i=1}^{3}\left(\left|\Phi_i^{(n)}\right| - k^{(n)}\Phi_i^{(n)}\right)^a, \tag{4.21}$$

where $\Phi_i^{(n)}$, $i = 1,2,3$ are the components $\mathcal{L}_{ii11}^{(n)}$, $i = 1,2,3$ (no sum), respectively, (or, equivalently, the non-zero components of the first column of the 6x6-matrix form representation of $\mathcal{L}^{(n)}$, see Eq. (4.51) in §4.4.4). In Eq. (4.19), $F^{(n)}$, is the general form of the CBP06 criterion in Eq. (4.15), the latter being a particular case for $a = 2$. The criterion in Eq. (4.19) is often referred to as CPB06ex*n*, where *n* is replaced by the number of transformations adopted in the formulation (CPB06ex2, CPB06ex3, etc.). Plunkett *et al.* (2008) criterion reduces to that of Cazacu *et al.* (2006) if only one linear transformation

is used or if all n_{ex} transformations are equal (or multiples of each other). Convexity is guaranteed for any integer $a \geq 1$ and for $k^{(n)} \in [-1,1]$ (for the proof see Cazacu *et al.* (2006)). In the following the dual of the Plunkett *et al.* (2008) criterion is presented.

4.4 Derivation of the exact dual of the Plunkett *et al.* (2008) criterion

4.4.1 Definition of the strain rate potential

Let $a > 1$ and $k^{(n)} \in]-1,1[$. The expression for the proposed strain-rate potential, ψ , is in the form:

$$\psi(\boldsymbol{d}^{\mathrm{p}}, k^{(n)}, \boldsymbol{\mathcal{L}}^{(n)}, a) \triangleq \frac{1}{m}\left(G\right)^{\frac{a-1}{a}} = \dot{\lambda}_1^{\mathrm{T}}, \quad n = 1,...,n_{\mathrm{ex}} \text{ , with}$$
$$G(\boldsymbol{d}^{\mathrm{p}}, k^{(n)}, \boldsymbol{\mathcal{L}}^{(n)}, a) = \sum_{n=1}^{n_{\mathrm{ex}}} G^{(n)} \text{ and } G^{(n)} = \sum_{i=1}^{3}\left(\frac{|b_{p_i}^{(n)}|}{1-\mathrm{sgn}(b_{p_i}^{(n)})k^{(n)}}\right)^{\frac{a}{a-1}} \tag{4.22}$$

where $b_{p_i}^{(n)}$, $i = 1,2,3$ are the eigenvalues of the *n*-th, transformed strain rate tensor, $\boldsymbol{b}^{(n)}$. The scalar $\dot{\lambda}_1^{\mathrm{T}}$ is the effective plastic strain rate associated with the adopted equivalent stress, $\bar{\sigma} = \varphi(\boldsymbol{\sigma})$, entering the dual/stress potential, (in this case, the uniaxial tensile yield stress, see Eq. (4.19)), under the plastic work rate equivalence principle. The transformed strain tensors, $\boldsymbol{b}^{(n)}$, $n = 1,...,n_{\mathrm{ex}}$, are given by:

$$\boldsymbol{b}^{(n)} = \boldsymbol{\mathcal{H}}^{(n)} : \boldsymbol{d}^{\mathrm{p}}, \tag{4.23}$$

where $\boldsymbol{\mathcal{H}}^{(n)}$ is the fourth order plastic strain-rate transformation tensor[9] associated with transformation *n* and is given by:

$$\boldsymbol{\mathcal{H}}^{(n)} = \boldsymbol{\mathcal{T}}_{\boldsymbol{b}}^{(n)} : \boldsymbol{\mathcal{L}}^{(n)} : \left(\boldsymbol{\mathcal{T}}_{\boldsymbol{b}}\right)_{\mathrm{dev}}^{-1} \text{, with}$$
$$\boldsymbol{\mathcal{T}}_{\boldsymbol{b}} = \sum_{n}\left(\boldsymbol{\mathcal{L}}^{(n)\mathrm{T}} : \boldsymbol{\mathcal{T}}_{\boldsymbol{b}}^{(n)} : \boldsymbol{\mathcal{L}}^{(n)}\right) \tag{4.24}$$

where $(\cdot)_{\mathrm{dev}}^{-1}$ represents the 'deviatoric inverse' operation $\left(\boldsymbol{\mathcal{A}}\right)_{\mathrm{dev}}^{-1} : \boldsymbol{\mathcal{A}} = \boldsymbol{\mathcal{A}} : \left(\boldsymbol{\mathcal{A}}\right)_{\mathrm{dev}}^{-1} = \boldsymbol{\mathcal{K}}$ and $\boldsymbol{\mathcal{K}}$ the deviatoric fourth order unit tensor. The fourth order tensor $\boldsymbol{\mathcal{T}}_{\boldsymbol{b}}^{(n)}$ has the major symmetry and it is defined based on a symmetric second order tensor $\boldsymbol{T}_{\boldsymbol{b}}^{(n)}$ such that the following equality holds:

$$\boldsymbol{\mathcal{T}}_{\boldsymbol{b}}^{(n)} : \boldsymbol{a} = \boldsymbol{T}_{\boldsymbol{b}}^{(n)}\boldsymbol{a} = \boldsymbol{a}\boldsymbol{T}_{\boldsymbol{b}}^{(n)}, \text{ or, equivalently, } \mathcal{T}_{ijkl}^{(n)} a_{kl} = T_{ik}^{(n)} a_{kj} = a_{jk} T_{ki}^{(n)}, \; i, j = 1,2,3, \tag{4.25}$$

where $\boldsymbol{a}$ denotes an arbitrary symmetric second order tensor, and tensor $\boldsymbol{T}_{\boldsymbol{b}}^{(n)}$ is expressed as follows:

$$\boldsymbol{T}_{\boldsymbol{b}}^{(n)} = \boldsymbol{V}_{\boldsymbol{b}^{(n)}} \bar{\boldsymbol{T}}_{\boldsymbol{b}}^{(n)} \boldsymbol{V}_{\boldsymbol{b}^{(n)}}^{\mathrm{T}} \text{ , where}$$
$$\bar{\boldsymbol{T}}_{\boldsymbol{b}}^{(n)} = \left|\boldsymbol{D}^{(n)}\right|^{\frac{1}{a-1}} \left|\mathrm{eig}(\boldsymbol{b}^{(n)})\right|^{\frac{a-2}{a-1}}, \tag{4.26}$$

and

$$\boldsymbol{D}^{(n)} = \mathrm{diag}\left[\left(1-\mathrm{sgn}(b_i^{(n)})k^{(n)}\right)^a\right], \; i = 1,2,3, \tag{4.27}$$

[9] The term 'tensor' is, to some extent, abused in this text as it is also employed to describe mappings which, in truth, are not linear. Nevertheless, this tensor notation adopted here for numerical convenience.

where $\boldsymbol{V}_{\boldsymbol{b}^{(n)}}$ denotes the orthogonal matrix whose columns are the corresponding right eigenvectors of $\boldsymbol{b}^{(n)}$, (thus $\boldsymbol{b}^{(n)} = \boldsymbol{V}_{\boldsymbol{b}^{(n)}} \mathrm{eig}(\boldsymbol{b}^{(n)}) \boldsymbol{V}_{\boldsymbol{b}^{(n)}}^{\mathrm{T}}$, and, equivalently, $\mathrm{eig}(\boldsymbol{b}^{(n)}) = \boldsymbol{V}_{\boldsymbol{b}^{(n)}}^{\mathrm{T}} \boldsymbol{b}^{(n)} \boldsymbol{V}_{\boldsymbol{b}^{(n)}}$). In Eq. (4.27) $\mathrm{sgn}(\cdot)$ represents the sign function, $\mathrm{diag}(\cdot)$ represents the assignment of vector components to a square diagonal matrix, $\mathrm{eig}(\cdot)$ represents a diagonal square matrix whose diagonal components are the eigenvalues of the argument tensor (not necessarily ordered), and $|\cdot|^p$ represents the element-wise absolute value operation to the power p, (i.e. $|a|_{ij}^p = |a_{ij}|^p$). The physical meaning of $\boldsymbol{T}_{\boldsymbol{b}}^{(n)}$, $\bar{\boldsymbol{T}}_{\boldsymbol{b}}^{(n)}$, $\boldsymbol{D}^{(n)}$, and $\mathcal{T}_{\boldsymbol{b}}$ is discussed in the next subsection.

Remarks 4.1

(i) The strain rate potential expression given in Eq. (4.21) is the exact dual of the orthotropic non-quadratic stress potential of Plunkett *et al.* (2008) (see Eq. (4.19));

(ii) The SRP is convex and homogeneous of degree one with respect to positive multipliers, i.e., $\psi(\xi \boldsymbol{d}^{\mathrm{p}}) = \xi \psi(\boldsymbol{d}^{\mathrm{p}}), \quad \xi \geq 0$;

(iii) The material parameters $\{k^{(n)}, \mathcal{L}^{(n)}, a\}$ entering the SRP are those of the respective dual (stress) potential, rather than independent parameters. Hence, no specific parameter identification procedure is needed. This is a direct consequence of the exact dual nature of the potentials.

(iv) No constrains are imposed on the form of the fourth order orthotropic tensors $\mathcal{C}^{(n)}$ (see Eq. (4.20)) (hence $\mathcal{L}^{(n)}$) and thus the number of independent anisotropy coefficients is maximum;

(v) Equations (4.23)-(4.27) fully define the input of the SRP in Eq. (4.22), namely, the eigenvalues of the transformed strain rate tensors, $\boldsymbol{b}^{(n)}$. Note that generally $\boldsymbol{b}^{(n)}$ depends on the eigenvalues and eigenvectors of *all* equivalent isotropic spaces $n = 1, ..., n_{\mathrm{ex}}$, and on all $k^{(n)}$ and $\mathcal{L}^{(n)}$ (via the sum in Eq. (4.24)), and not only of those associated with transformation n, as is the case of the stress potential formulation;

(vi) The strong non-linear nature of Eqs. (4.23)-(4.27) precludes the explicit closed-form determination of the tensors $\boldsymbol{b}^{(n)}$ in the general case[10], (note that $\mathcal{H}^{(n)} = \mathcal{H}^{(n)}(\boldsymbol{d}^{\mathrm{p}})$). Numerical methods are therefore required to evaluate the SRP value and its derivatives. Nevertheless, it must be emphasized that these equations present a well-posed and mathematically sound problem for evaluating the potential.

(vii) Exact duality is preserved for any real number $a > 1$ for the homogeneity parameter. However, since the convexity of the stress potential was formally proven only for integer numbers $a \geq 1$, one should similarly adopt this restriction in the strain-rate potential in Eq. (4.22).

In the following, the proof and discussion of the presented expressions is in order.

4.4.2 Derivation of the expression

Departing from the associated flow rule (Eq. (4.7)) and applying the chain rule yields:

[10] Closed-form solutions do exist for some particular cases, as described in subsection §4.4.3.

$$\boldsymbol{d}^{\mathrm{p}} \triangleq \dot{\lambda}\frac{\partial\varphi}{\partial\boldsymbol{\sigma}} = \dot{\lambda}\sum_{n}\frac{\partial\varphi}{\partial\hat{\boldsymbol{s}}^{(n)}}:\frac{\partial\hat{\boldsymbol{s}}^{(n)}}{\partial\boldsymbol{s}}:\frac{\partial\boldsymbol{s}}{\partial\boldsymbol{\sigma}} = \sum_{n}\dot{\lambda}\frac{\partial\varphi}{\partial\hat{\boldsymbol{s}}^{(n)}}:\left(\mathcal{C}^{(n)}:\mathcal{K}\right) = \sum_{n}\boldsymbol{d}^{(n)}\text{, with}$$
$$\boldsymbol{d}^{(n)} = \mathcal{L}^{(n)\mathrm{T}}:\boldsymbol{b}^{(n)}, \tag{4.28}$$

where, for readability, $\dot{\lambda} \leftarrow \dot{\lambda}_1^{\mathrm{T}}$ and:

$$\boldsymbol{b}^{(n)} \triangleq \dot{\lambda}\frac{\partial\varphi}{\partial\hat{\boldsymbol{s}}^{(n)}}\text{, with } n=1,...,n_{\mathrm{ex}}. \tag{4.29}$$

The previous expression describes the normality principle between the transformed stress and the strain-rate tensors in the transformed space n (Figure 4.1) at the reference frame associated with the orthotropy axes, $(\underline{\boldsymbol{e}}_1, \underline{\boldsymbol{e}}_2, \underline{\boldsymbol{e}}_3)$. The local isotropy condition implies that the eigenvectors of $\boldsymbol{b}^{(n)}$ and $\hat{\boldsymbol{s}}^{(n)}$ are the same. Therefore, this expression can be recast to the principal transformed space as:

$$\boldsymbol{b}_p^{(n)} = \mathrm{eig}\left(\boldsymbol{b}^{(n)}\right) \triangleq \dot{\lambda}\frac{\partial\varphi}{\partial\hat{\boldsymbol{s}}_p^{(n)}}, \tag{4.30}$$

where $\hat{\boldsymbol{s}}_p^{(n)} = \mathrm{eig}(\hat{\boldsymbol{s}}^{(n)})$, i.e. $\hat{s}_{p_i}$ are the eigenvalues of the transformed stress tensor $\hat{\boldsymbol{s}}^{(n)}$. Differentiation of the expression of the Plunkett *et al.* (2008) stress potential, φ, (Eq. (4.19)), results in:

$$\boldsymbol{b}_p^{(n)} = \dot{\lambda}\frac{\partial\varphi}{\partial\hat{\boldsymbol{s}}_p^{(n)}} = \mathrm{diag}\left[\dot{\lambda}m^a\sigma_{\mathrm{T}}^{1-a}\left(\left|\hat{s}_{p_i}^{(n)}\right| - k^{(n)}\hat{s}_{p_i}^{(n)}\right)^{a-1}\left(\mathrm{sgn}\left(\hat{s}_{p_i}^{(n)}\right) - k^{(n)}\right)\right],\ i=1,2,3, \tag{4.31}$$

which can be more conveniently written as:

$$\boldsymbol{b}_p^{(n)} = \dot{\lambda}\frac{\partial\varphi}{\partial\hat{\boldsymbol{s}}_p^{(n)}} = \mathrm{diag}\left[\dot{\lambda}m^a\sigma_{\mathrm{T}}^{1-a}\left(1-\mathrm{sgn}\left(\hat{s}_{p_i}^{(n)}\right)k^{(n)}\right)^a\left|\hat{s}_{p_i}^{(n)}\right|^{a-2}\hat{s}_{p_i}^{(n)}\right],\ i=1,2,3. \tag{4.32}$$

Inverting the above expression, and assuming $a>1$ and $k^{(n)} \in]-1,1[$ leads to:

$$\hat{\boldsymbol{s}}_p^{(n)} = \mathrm{diag}\left(\frac{\sigma_{\mathrm{T}}}{\dot{\lambda}^{\frac{1}{a-1}}m^{\frac{a}{a-1}}}\mathrm{sgn}(b_{p_i}^{(n)})\left[\frac{\left|b_{p_i}^{(n)}\right|}{\left(1-\mathrm{sgn}(b_{p_i}^{(n)})k^{(n)}\right)^a}\right]^{\frac{1}{a-1}}\right),\ i=1,2,3. \tag{4.33}$$

where the property $\mathrm{sgn}(b_{p_i}^{(n)}) = \mathrm{sgn}(\hat{s}_{p_i}^{(n)})$, $i=1,2,3$, was employed, as trivially proven by examining Eq. (4.32) and noting that $(1-\mathrm{sgn}(\hat{s}_{p_i}^{(n)})k^{(n)}) \in]0,2[$, $a>1$, $\sigma_{\mathrm{T}}>0$, $m>0$, and $\dot{\lambda}>0$ if $\boldsymbol{d}^{\mathrm{p}} \neq \boldsymbol{0}$. Substitution of Eq. (4.33) for $\hat{s}_{p_i}^{(n)}$ into the stress potential in Eq. (4.19), and isolating the factor $\dot{\lambda}$, leads, finally, to Eq. (4.22).

Let us now focus on the determination of the $n_{\mathrm{ex}} \geq 1$ transformed strain tensors $\boldsymbol{b}^{(n)}$, given a total plastic strain rate tensor, $\boldsymbol{d}^{\mathrm{p}}$, entering in the SRP. Recalling the definition of $\boldsymbol{D}^{(n)}$ in Eq. (4.27), Eq. (4.32) can be written in matrix form as the product of the diagonal matrices:

$$\boldsymbol{b}_p^{(n)} = \dot{\lambda}\frac{\partial\varphi}{\partial\hat{\boldsymbol{s}}_p^{(n)}} = \dot{\lambda}m^a\sigma_{\mathrm{T}}^{1-a}\left(\boldsymbol{D}^{(n)}\left|\hat{\boldsymbol{s}}_p^{(n)}\right|^{a-2}\right)\hat{\boldsymbol{s}}_p^{(n)}. \tag{4.34}$$

Performing a similar rearrangement to Eq. (4.33), applying the $|\cdot|^p$ operator (defined in the text following Eq. (4.27), with $p=(a-2)$ and left multiplying by $\boldsymbol{D}^{(n)}$ leads to the equality:

$$\boldsymbol{D}^{(n)}\left|\hat{\boldsymbol{s}}_p^{(n)}\right|^{a-2}=\left(\dot{\lambda}m^a\sigma_{\mathrm{T}}^{1-a}\right)^{\frac{a-2}{1-a}}\left|\boldsymbol{D}^{(n)}\right|^{\frac{1}{a-1}}\left|\boldsymbol{b}_p^{(n)}\right|^{\frac{a-2}{a-1}}. \tag{4.35}$$

Combining the last two equations results in:

$$\boldsymbol{b}_p^{(n)}=\dot{\lambda}\frac{\partial\varphi}{\partial\hat{\boldsymbol{s}}_p^{(n)}}=\left(\frac{\dot{\lambda}^{\frac{1}{a-1}}m^{\frac{a}{a-1}}}{\sigma_{\mathrm{T}}}\right)\bar{\boldsymbol{T}}_{\boldsymbol{b}}^{(n)}\hat{\boldsymbol{s}}_p^{(n)}, \tag{4.36}$$

where $\bar{\boldsymbol{T}}_{\boldsymbol{b}}^{(n)}$ was defined in Eq. (4.26). The previous expression shows that $\bar{\boldsymbol{T}}_{\boldsymbol{b}}^{(n)}$ is the diagonal tensor which modifies the relationship between the principal stress and strain tensors in the eigenspace associated with the linear transformation n. Note that the operator $\bar{\boldsymbol{T}}_{\boldsymbol{b}}^{(n)}$ is not a linear mapping in the general case. Indeed, the above relationship is linear only for $a=2,$ i.e. for a quadratic stress potential. The diagonal tensor $\boldsymbol{D}^{(n)}$ holds the mathematical representation of the material behaviour associated with tension-compression asymmetry phenomena. Similarly, Eq. (4.36) can be recast to the orthotropy frame as:

$$\boldsymbol{b}^{(n)}\triangleq\dot{\lambda}\frac{\partial\varphi}{\partial\hat{\boldsymbol{s}}^{(n)}}=\left(\frac{\dot{\lambda}^{\frac{1}{a-1}}m^{\frac{a}{a-1}}}{\sigma_{\mathrm{T}}}\right)\boldsymbol{T}_{\boldsymbol{b}}^{(n)}\hat{\boldsymbol{s}}^{(n)}, \tag{4.37}$$

where $\boldsymbol{T}_{\boldsymbol{b}}^{(n)}$ was also defined in Eq. (4.26). Naturally, the symmetric tensor $\boldsymbol{T}^{(n)}$ holds the exact same physical interpretation as $\bar{\boldsymbol{T}}_{\boldsymbol{b}}^{(n)},$ only in a different base. Moreover, $\boldsymbol{T}_{\boldsymbol{b}}^{(n)}$ and $\hat{\boldsymbol{s}}^{(n)}$ commute. The mathematical manipulation when transforming Eq. (4.34) into Eq. (4.36) may seem detrimental since an explicit stress-strain relationship is converted to an implicit one. In fact, in the same spirit as $\bar{\boldsymbol{T}}_{\boldsymbol{b}}^{(n)},$ one could define an alternative formulation to Eq. (4.34), (henceforward denoted the stress-based formulation) as:

$$\boldsymbol{b}_p^{(n)}=\dot{\lambda}\frac{\partial\varphi}{\partial\hat{\boldsymbol{s}}_p^{(n)}}=\left(\dot{\lambda}m^a\sigma_{\mathrm{T}}^{1-a}\right)\boldsymbol{D}^{(n)}\left|\hat{\boldsymbol{s}}_p^{(n)}\right|^{a-2}\hat{\boldsymbol{s}}_p^{(n)}=\left(\dot{\lambda}m^a\sigma_{\mathrm{T}}^{1-a}\right)\bar{\boldsymbol{T}}_{\hat{\boldsymbol{s}}}^{(n)}\hat{\boldsymbol{s}}_p^{(n)}, \tag{4.38}$$

with $\bar{\boldsymbol{T}}_{\hat{\boldsymbol{s}}}^{(n)}=\boldsymbol{D}^{(n)}\left|\hat{\boldsymbol{s}}_p^{(n)}\right|^{a-2}$. However, the main idea here is to isolate and eventually cancel the hanging stress term in Eq. (4.37) so that, ultimately, no stress quantities appear in the formulation, which is not a straightforward task when working with $\bar{\boldsymbol{T}}_{\hat{\boldsymbol{s}}}^{(n)}$ instead of $\bar{\boldsymbol{T}}_{\boldsymbol{b}}^{(n)}$. Nevertheless, a formulation grounded on $\bar{\boldsymbol{T}}_{\hat{\boldsymbol{s}}}^{(n)}$ may be advantageous from the numerical point of view, as demonstrated later on in this work. Replacing Eq. (4.37) in Eq. (4.28) yields:

$$\boldsymbol{d}^{\mathrm{p}}=\sum_n\boldsymbol{\mathcal{L}}^{(n)\mathrm{T}}:\boldsymbol{b}^{(n)}=\left(\frac{\dot{\lambda}^{\frac{1}{a-1}}m^{\frac{a}{a-1}}}{\sigma_{\mathrm{T}}}\right)\sum_n\left(\boldsymbol{\mathcal{L}}^{(n)\mathrm{T}}:\boldsymbol{\mathcal{T}}_{\boldsymbol{b}}^{(n)}:\hat{\boldsymbol{s}}^{(n)}\right). \tag{4.39}$$

Recalling that $\boldsymbol{T}_{\boldsymbol{b}}^{(n)}\hat{\boldsymbol{s}}^{(n)}=\hat{\boldsymbol{s}}^{(n)}\boldsymbol{T}_{\boldsymbol{b}}^{(n)}\triangleq\boldsymbol{\mathcal{T}}_{\boldsymbol{b}}^{(n)}:\hat{\boldsymbol{s}}^{(n)}$ (Eq. (4.25)) and the definition $\hat{\boldsymbol{s}}^{(n)}=\boldsymbol{\mathcal{L}}^{(n)}:\boldsymbol{s},$ one obtains:

$$\boldsymbol{d}^{\mathrm{p}}=\sum_n\boldsymbol{\mathcal{L}}^{(n)\mathrm{T}}:\boldsymbol{b}^{(n)}=\left(\frac{\dot{\lambda}^{\frac{1}{a-1}}m^{\frac{a}{a-1}}}{\sigma_{\mathrm{T}}}\right)\sum_n\left[\boldsymbol{\mathcal{L}}^{(n)\mathrm{T}}:\boldsymbol{\mathcal{T}}_{\boldsymbol{b}}^{(n)}:\left(\boldsymbol{\mathcal{L}}^{(n)}:\boldsymbol{s}\right)\right]=\left(\frac{\dot{\lambda}^{\frac{1}{a-1}}m^{\frac{a}{a-1}}}{\sigma_{\mathrm{T}}}\right)\boldsymbol{\mathcal{T}}_{\boldsymbol{b}}:\boldsymbol{s}, \tag{4.40}$$

with $\mathcal{T}_{\boldsymbol{b}}$ being defined in Eq. (4.24). The previous expression shows that $\mathcal{T}_{\boldsymbol{b}}$ is the tensor that describes the pseudo-linear relationship (actually linear in the case of $a=2$), resulting from the normality principle between the deviatoric stress, $\boldsymbol{s}$, and the plastic strain rate tensor, $\boldsymbol{d}^{\mathrm{p}}$. For completeness, if $\bar{\boldsymbol{T}}_{\hat{\boldsymbol{s}}}^{(n)}$ is used instead of $\bar{\boldsymbol{T}}_{\boldsymbol{b}}^{(n)}$, then the alternative form of Eq. (4.40) writes:

$$\boldsymbol{d}^{\mathrm{p}} = \sum_{n} \mathcal{L}^{(n)\mathrm{T}} : \boldsymbol{b}^{(n)} = \left(\dot{\lambda} m^{a} \sigma_{\mathrm{T}}^{1-a}\right) \mathcal{T}_{\boldsymbol{s}} : \boldsymbol{s}, \tag{4.41}$$

with

$$\mathcal{T}_{\boldsymbol{s}} \triangleq \sum \left(\mathcal{L}^{(n)\mathrm{T}} : \mathcal{T}_{\boldsymbol{s}}^{(n)} : \mathcal{L}^{(n)}\right), \text{ and } \boldsymbol{T}_{\hat{\boldsymbol{s}}}^{(n)} = \boldsymbol{V}_{\hat{\boldsymbol{s}}^{(n)}} \bar{\boldsymbol{T}}_{\hat{\boldsymbol{s}}}^{(n)} \boldsymbol{V}_{\hat{\boldsymbol{s}}^{(n)}}^{\mathrm{T}}, \tag{4.42}$$

where the properties $\boldsymbol{T}_{\hat{\boldsymbol{s}}}^{(n)} \hat{\boldsymbol{s}}^{(n)} = \hat{\boldsymbol{s}}^{(n)} \boldsymbol{T}_{\hat{\boldsymbol{s}}}^{(n)} \triangleq \mathcal{T}_{\boldsymbol{s}}^{(n)} : \hat{\boldsymbol{s}}^{(n)}$ and $\boldsymbol{V}_{\hat{\boldsymbol{s}}^{(n)}} = \boldsymbol{V}_{\boldsymbol{b}^{(n)}}$ were applied. Tensor $\mathcal{T}_{\boldsymbol{s}}$ has thus the same physical reasoning as $\mathcal{T}_{\boldsymbol{b}}$.

Remark 4.2. The fourth-order $\mathcal{T}$ tensors (both $\mathcal{T}_{\boldsymbol{b}}$ or $\mathcal{T}_{\boldsymbol{s}}$) are major symmetric and enjoy the property $\mathcal{T} : \mathcal{K} = \mathcal{K} : \mathcal{T} = \mathcal{T}$, i.e., $\mathcal{T}_{ijkl} = \mathcal{T}_{klij}$, and $\mathcal{T}_{ijkk} = \mathcal{T}_{kkij} = 0$, $i, j, k, l = 1, 2, 3$, respectively. Thus, $\mathcal{T}$ admits a deviatoric inverse tensor, $(\mathcal{T})_{\mathrm{dev}}^{-1}$, such that $(\mathcal{T})_{\mathrm{dev}}^{-1} : \mathcal{T} = \mathcal{T} : (\mathcal{T})_{\mathrm{dev}}^{-1} = \mathcal{K}$. Moreover, $(\mathcal{T})_{\mathrm{dev}}^{-1}$ (denoting $(\mathcal{T}_{\boldsymbol{b}})_{\mathrm{dev}}^{-1}$ or $(\mathcal{T}_{\boldsymbol{s}})_{\mathrm{dev}}^{-1}$) is also major symmetric and enjoys the property $(\mathcal{T})_{\mathrm{dev}}^{-1} : \mathcal{K} = \mathcal{K} : (\mathcal{T})_{\mathrm{dev}}^{-1} = (\mathcal{T})_{\mathrm{dev}}^{-1}$.

Accordingly, one can invert Eq. (4.40) (and Eq. (4.41)) in order to determine the deviatoric stress tensor, $\boldsymbol{s}$, associated with $\boldsymbol{d}^{\mathrm{p}}$, resulting in:

$$\boldsymbol{s} = \left(\frac{\sigma_{\mathrm{T}}}{\dot{\lambda}^{\frac{1}{a-1}} m^{\frac{a}{a-1}}}\right) \left(\mathcal{T}_{\boldsymbol{b}}\right)_{\mathrm{dev}}^{-1} : \boldsymbol{d}^{\mathrm{p}}, \tag{4.43}$$

for the purely strain-based formulation and

$$\boldsymbol{s} = \left(\frac{1}{\dot{\lambda} m^{a} \sigma_{\mathrm{T}}^{1-a}}\right) \left(\mathcal{T}_{\boldsymbol{s}}\right)_{\mathrm{dev}}^{-1} : \boldsymbol{d}^{\mathrm{p}}, \tag{4.44}$$

for the stress-based counterpart. Note that Eq. (4.43) defines $\boldsymbol{s}$ in an explicit fashion, i.e., $\boldsymbol{s}$ is actually isolated. This does not hold true for Eq. (4.44), as stress terms appear in both sides of the expression. Nevertheless, from the numerical point of view, $\mathcal{T}_{\boldsymbol{b}}^{(n)}$ and $\mathcal{T}_{\hat{\boldsymbol{s}}}$ (and their respective inverse tensors) hold the same mapping, only differing by a scale factor. Substitution of Eq. (4.43) (and Eq. (4.44)) into Eq. (4.37) (and Eq. (4.38)), respectively, leads, at last, to Eq. (4.23) (rewritten here for readability purposes):

$$\boldsymbol{b}^{(n)} = \mathcal{H}^{(n)} : \boldsymbol{d}^{\mathrm{p}}, \tag{4.23}$$

where the factors $(\dot{\lambda}^{\frac{1}{a-1}} m^{\frac{a}{a-1}} \sigma_{\mathrm{T}}{}^{-1})$ and $(\dot{\lambda} m^{a} \sigma_{\mathrm{T}}^{1-a})$, appearing in Eq. (4.36) and Eq. (4.38), respectively, were cancelled out. The transformation tensor $\mathcal{H}^{(n)}$ can be determined either using $\mathcal{T}_{\boldsymbol{b}}^{(n)}$ (as defined in Eq. (4.24)) or with $\mathcal{T}_{\hat{\boldsymbol{s}}}^{(n)}$, i.e.:

$$\begin{gathered} \mathcal{H}^{(n)} = \mathcal{H}_{\boldsymbol{b}}^{(n)} = \mathcal{H}_{\hat{\boldsymbol{s}}}^{(n)}, \text{ with} \\ \mathcal{H}_{\boldsymbol{b}}^{(n)} = \mathcal{T}_{\boldsymbol{b}}^{(n)} : \mathcal{L}^{(n)} : \left(\mathcal{T}_{\boldsymbol{b}}\right)_{\mathrm{dev}}^{-1}, \text{ and } \mathcal{H}_{\hat{\boldsymbol{s}}}^{(n)} = \mathcal{T}_{\hat{\boldsymbol{s}}}^{(n)} : \mathcal{L}^{(n)} : \left(\mathcal{T}_{\hat{\boldsymbol{s}}}\right)_{\mathrm{dev}}^{-1}. \end{gathered} \tag{4.45}$$

The above equality is to be expected since the mapping between $\boldsymbol{d}^{\mathrm{p}}$ and $\boldsymbol{b}^{(n)}$ must be unique (in the same spirit to the one-to-one mapping between $\boldsymbol{s}$ and $\hat{\boldsymbol{s}}^{(n)}$) and corroborates the equivalence between the strain-based and stress-based formulations for the determination of $\boldsymbol{b}^{(n)}$.

Remarks 4.3

(i) In general, the transformed strain rate tensors, $\boldsymbol{b}^{(n)}$, and respective work-conjugate, $\hat{\boldsymbol{s}}^{(n)}$, are not deviatoric. This results from the fact that the restriction of major symmetry of the linear operator $\mathcal{L}^{(n)}$, i.e. $\mathcal{L}^{(n)}_{ijkl} = \mathcal{L}^{(n)}_{klij}$, $i,j,k,l = 1,2,3$, was *not* employed, contrary to the practice in the literature. In fact, such condition is not necessary to guarantee plastic incompressibility and it is application is uniquely motivated to define an orthotropic transformation tensor of the type $\mathcal{H} = (\mathcal{L}^{\mathrm{T}})^{-1}_{\mathrm{dev}}$, which exists if and only if $\mathcal{L}$ is major symmetric. In fact, if $\mathcal{L}$ is not major symmetric it still admits a deviatoric inverse, i.e. there exists a tensor $\mathcal{B}$ such that $\mathcal{B} : \mathcal{L} = \mathcal{K}$, however it is not possible to define an analogous inverse tensor for $\mathcal{L}^{\mathrm{T}}$, entering Eq. (4.28);

(ii) Similarly to $\mathcal{L}^{(n)}$, $\mathcal{H}^{(n)}$ are not major symmetric and enjoy the property $\mathcal{H}^{(n)} : \mathcal{K} = \mathcal{H}^{(n)}$, as $\mathcal{H}^{(n)}_{ijkk} = 0$, $i,j,k = 1,2,3$, (yet $\mathcal{H} : \mathcal{H}^{(n)} \neq \mathcal{H}^{(n)}$). This means that $\mathcal{H}^{(n)}$ admits some 'left' deviatoric inverse tensor, $(\mathcal{H}^{(n)})^{-1}_{\mathrm{dev}} : \mathcal{H}^{(n)} = \mathcal{K}$, but not an analogous 'right' inverse operator;

(iii) Recalling that the total plastic strain rate tensor, $\boldsymbol{d}^{\mathrm{p}}$, can be interpreted as the sum of the contribution of each transformation $\boldsymbol{d}^{(n)}$ (see Eq. (4.28) and Figure 4.1), one can define tensors $\mathcal{A}^{(n)}$, $n = 1,...,n_{\mathrm{ex}}$, such that:

$$\boldsymbol{d}^{(n)} = \mathcal{A}^{(n)} : \boldsymbol{d}^{\mathrm{p}}, \text{ where } \mathcal{A}^{(n)} = \mathcal{L}^{(n)\mathrm{T}} : \mathcal{H}^{(n)}. \tag{4.46}$$

$\mathcal{A}^{(n)}$ is not major symmetric however it is 'fully' (both right and left) deviatoric, i.e. it verifies $\mathcal{A}^{(n)} : \mathcal{K} = \mathcal{K} : \mathcal{A}^{(n)} = \mathcal{A}^{(n)}$, as $\mathcal{A}^{(n)}_{ijkk} = \mathcal{A}^{(n)}_{kkij} = 0$, $i,j,k,l = 1,2,3$. Therefore one can determine a non-symmetric tensor $(\mathcal{A}^{(n)})^{-1}_{\mathrm{dev}}$ such that $(\mathcal{A}^{(n)})^{-1}_{\mathrm{dev}} : \mathcal{A}^{(n)} = \mathcal{A}^{(n)} : (\mathcal{A}^{(n)})^{-1}_{\mathrm{dev}} = \mathcal{K}$, which verifies $(\mathcal{A}^{(n)\mathrm{T}})^{-1}_{\mathrm{dev}} = (\mathcal{A}^{(n)})^{-1\,\mathrm{T}}_{\mathrm{dev}}$. While the practical relevance of $\mathcal{A}^{(n)}$ is limited (as tensors $\boldsymbol{d}^{(n)}$ do not enter the SRP definition, but rather their transformed counterparts), it is worth noting that $\sum \mathcal{A}^{(n)} = \mathcal{K}$. Moreover, in the same spirit as the partition in $\boldsymbol{d}^{(n)}$, the deviatoric stress tensor, $\boldsymbol{s}$, can be subdivided in n_{ex} parts, $\boldsymbol{s}^{(n)}$, (not to be mistook with $\hat{\boldsymbol{s}}^{(n)}$). Combining Eq. (4.39), (4.43) and (4.46), one arrives at:

$$\boldsymbol{s} = \sum_n \boldsymbol{s}^{(n)}, \text{ with } \boldsymbol{s}^{(n)} = \mathcal{A}^{(n)\mathrm{T}} : \boldsymbol{s}. \tag{4.47}$$

The fourth-order tensor $\mathcal{A}^{(n)}$ can also be used to define scalars $\alpha^{(n)}$, $n = 1,...,n_{\mathrm{ex}}$, such that the total plastic work rate, $\dot{w}_{\mathrm{p}}$, can be written as the sum of parcels $\dot{w}^{(n)}_{\mathrm{p}}$ corresponding to each transformation *n* as:

$$\begin{aligned} \dot{w}_{\mathrm{p}} = \boldsymbol{s} : \boldsymbol{d}^{\mathrm{p}} = \sum_n \dot{w}^{(n)}_{\mathrm{p}} = \sum_n \left(\boldsymbol{s} : \mathcal{A}^{(n)} : \boldsymbol{d}^{\mathrm{p}} \right) = \sum_n \alpha^{(n)} \dot{w}_{\mathrm{p}}, \text{ with} \\ \alpha^{(n)} = \left(\frac{\boldsymbol{s}}{\sigma_{\mathrm{T}}} \right) : \mathcal{A}^{(n)} : \left(\frac{\boldsymbol{d}^{\mathrm{p}}}{\dot{\lambda}} \right), \; n = 1,...,n_{\mathrm{ex}}, \end{aligned} \tag{4.48}$$

where equality $\boldsymbol{s}:\boldsymbol{d}^{(n)}=\hat{\boldsymbol{s}}^{(n)}:\boldsymbol{b}^{(n)}$ was applied. Naturally, $0<\alpha^{(n)}\leq 1$ and $\sum\alpha^{(n)}=1$. Thus, $\alpha^{(n)}$ can be used to quantify the relative weight of each linear transformation, n, for a given stress-strain associated pair;

(iv) While for non-quadratic stress potentials (i.e. $a\neq 2$), $\mathcal{T}_{\hat{s}}$ (and thus $(\mathcal{T}_{\hat{s}})^{-1}_{\text{dev}}$) depend on the magnitude of the stress quantities $\hat{\boldsymbol{s}}^{(n)}$ through $\boldsymbol{s}$, the operation $\mathcal{T}^{(n)}_{\hat{s}}:\left(\mathcal{T}_{\hat{s}}\right)^{-1}_{\text{dev}}$ eliminates this dependence. Accordingly, $\mathcal{H}^{(n)}$ is indeed independent of the magnitude of $\boldsymbol{s}$, only depending on its 'direction', $\boldsymbol{s}/\varphi(\boldsymbol{s})$. In the particular case of $a=2$, the equality in Eq. (4.35) is trivial and $\bar{\boldsymbol{T}}^{(n)}\triangleq\bar{\boldsymbol{T}}^{(n)}_{\boldsymbol{b}}=\bar{\boldsymbol{T}}^{(n)}_{\hat{s}}$, (with $\bar{\boldsymbol{T}}^{(n)}=\left|\boldsymbol{D}^{(n)}\right|=\boldsymbol{D}^{(n)}$), i.e. the so-called strain- and stress-based formulations coincide as the stress-strain rate relationship becomes linear.

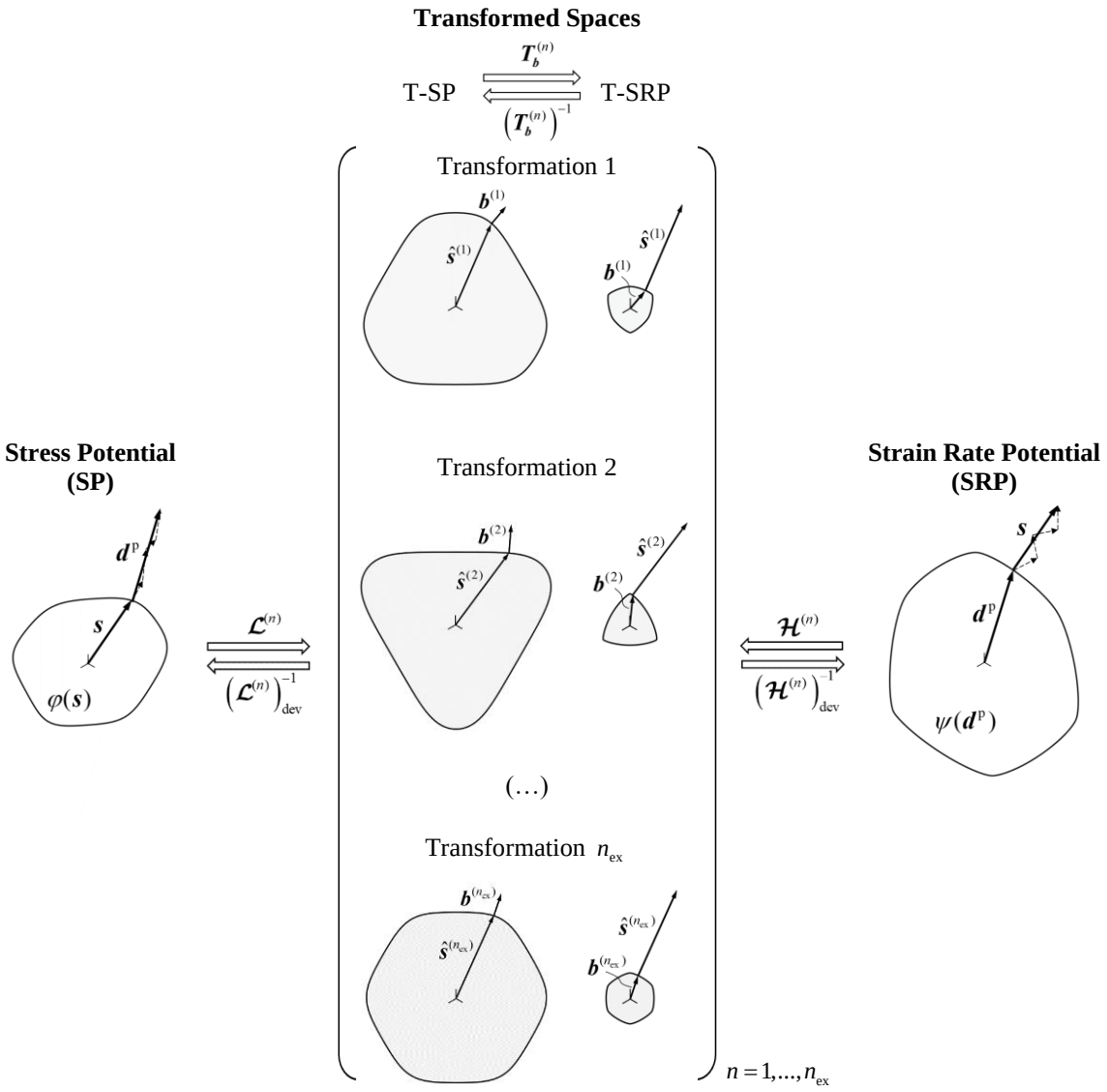

Figure 4.1 Schematic view of the principle of the equivalent 'isotropic' transformed spaces in the definition of the actual plastic stress potential, $\varphi(\boldsymbol{s})$, and the respective strain rate potential, $\psi(\boldsymbol{d}^{\text{p}})$, for a non-quadratic orthotropic criterion accounting for tension-compression asymmetry. The surfaces are projected in the orthogonal (π-) plane and are at scale. The dual relationship holds for each transformation, n. The dashed lines represent the contributions $\boldsymbol{s}^{(n)}$ and $\boldsymbol{d}^{(n)}$ to the total stress, $\boldsymbol{s}=\sum\boldsymbol{s}^{(n)}$, and strain-rate, $\boldsymbol{d}^{\text{p}}=\sum\boldsymbol{d}^{(n)}$ tensors, respectively.

4.4.3 Particular cases

Table 4.1 resumes the relevant particular cases of the strain-rate potential presented in the subsection §4.4.1. Some of these are now described.

If a single linear transformation is employed and the (unique) orthotropy tensor $\boldsymbol{\mathcal{C}} \leftarrow \boldsymbol{\mathcal{C}}^{(n)}$, is defined such that $\boldsymbol{\mathcal{L}} = \boldsymbol{\mathcal{C}} : \boldsymbol{\mathcal{K}}$ is symmetric, then the derived SRP expression reduces to that of Cazacu *et al.* (2010) (see §4.2.2). When comparing these formulations, the reader may question the increased complexity of the expressions presented in this work, which, in fact, do not lead to an explicit expression for the (unique) transformed strain rate tensor $\boldsymbol{b} \leftarrow \boldsymbol{b}^{(n)}$, even in this basic case. However, it is important to understand that these formulations originate from different approaches. The orthotropic form of the SRP of Cazacu *et al.* (2010) was obtained by a straightforward, yet sound, extension of its isotropic counterpart, in turn resulting from the application of the normality rule to an *isotropic* stress potential; conversely, in this work, one departs from the normality rule of a stress potential in which orthotropy (of the more general form) is assumed *a priori* (see Eqs. (4.28)-(4.29)). Consequently, in Cazacu *et al.* (2010) the tension-compression asymmetry information, quantified by $k \leftarrow k^{(n)}$, enters solely in the actual potential function (Eq. (4.16)), since the respective strain rate tensor, $\boldsymbol{b}|_{\text{Caz}}$, necessarily deviatoric, depends exclusively on the orthotropy coefficients. On the other hand, tension-compression asymmetry (and/or non-quadratic potentials) render $\boldsymbol{b}$, as defined in Eq. (4.23), *not* deviatoric, even if $\boldsymbol{\mathcal{L}}$ is symmetric. In summary, $\boldsymbol{b}|_{\text{Caz}}$ and $\boldsymbol{b}$ hold different physical meanings, yet $\psi_{\text{Caz}}(\boldsymbol{b}|_{\text{Caz}}) = \psi(\boldsymbol{b})$. A noteworthy remark is that $\boldsymbol{b}|_{\text{Caz}} = \boldsymbol{\mathcal{K}} : \boldsymbol{b}$, i.e. $\boldsymbol{b}|_{\text{Caz}}$ is the deviatoric part of $\boldsymbol{b}$, since $\boldsymbol{\mathcal{H}}_{\text{Caz}}| = (\boldsymbol{\mathcal{L}})^{-1}_{\text{dev}} = \boldsymbol{\mathcal{K}} : \boldsymbol{\mathcal{H}}$. Obviously, for this particular orthotropy case, the approach of in Cazacu *et al.* (2010) is much preferred from the computational point of view. Nevertheless, if one intends to increase the flexibility of the description of the plastic orthotropy, either by relaxing the restriction $\boldsymbol{\mathcal{L}} = \boldsymbol{\mathcal{L}}^{\text{T}}$, or by adding more transformation spaces, such formulation is not appropriate.

Under the condition of no tension-compression asymmetry, i.e. $k^{(n)} = 0$, the orthotropic strain rate potential proposed in this paper (Eq. (4.22)) does not reduce to any of the non-quadratic formulations presented in subsection §4.1. Recall that this is to be expected as the latter functions are, in fact, heuristic pseudo-conjugated forms of the respective stress-based potentials, and thus duality is not guaranteed. Moreover, note that, if more than one linear transformation is applied, the contribution of each transformation to the overall strain rate potential materialises implicitly in the definition of the tensors $\boldsymbol{b}^{(n)}$ and is not necessarily equal (see Eq. (4.48)). Figure 4.1 illustrates this idea by the size of the respective transformed strain rate spaces (T-SRP): the greater the surface, the greater its contribution to the overall SRP, and vice versa. This is in opposition to previous proposals (c.f. Barlat and Chung, 2005; Rabahallah *et al.*, 2009a), where the variable of the number of transformations, n_{ex}, is explicitly imposed in the respective SRP functions to average the contribution of each transformation by equal factor $1/n_{\text{ex}}$.

Table 4.1 Summary of particular forms of the derived expression for the strain-rate potential.

Description	Simplified expressions	Explicit form	Expression of $\boldsymbol{b}^{(n)}$
No tension-compression asymmetry $k^{(n)}=0$	$\boldsymbol{D}^{(n)}=\boldsymbol{I}$, $\bar{\boldsymbol{T}}_{\boldsymbol{b}}^{(n)}=\left\|\mathrm{eig}(\boldsymbol{b}^{(n)})\right\|^{\frac{a-2}{a-1}}$.	No	---
No tension-compression asymmetry and the stress potential is quadratic $k^{(n)}=0,\ a=2$	$\boldsymbol{D}^{(n)}=\boldsymbol{I},\ \bar{\boldsymbol{T}}_{\boldsymbol{b}}^{(n)}=\boldsymbol{I}$, $\mathcal{T}_{\boldsymbol{b}}^{(n)}=\mathcal{I}$.	Yes (1 branch)	$\boldsymbol{b}^{(n)}=\left[\mathcal{L}^{(n)}:\left(\sum_n\left(\mathcal{L}^{(n)\mathrm{T}}:\mathcal{L}^{(n)}\right)\right)_{\mathrm{dev}}^{-1}\right]:\boldsymbol{d}^{\mathrm{p}}$
No tension-compression asymmetry, the stress potential is quadratic and isotropic $k^{(n)}=0,\ a=2,\ \mathcal{C}^{(n)}=\mathcal{I}$	$\mathcal{L}=\mathcal{L}^{\mathrm{T}}=\mathcal{K}$, $\mathcal{T}_{\boldsymbol{b}}^{(n)}=\mathcal{I}$.	Yes (1 branch)	$\boldsymbol{b}^{(n)}=\left[\left(\frac{1}{n}\right)\mathcal{K}\right]:\boldsymbol{d}^{\mathrm{p}}$
A single transformation $n_{\mathrm{exp}}=1$	$\boldsymbol{D}^{(n)}\leftarrow\boldsymbol{D},\ \bar{\boldsymbol{T}}_{\boldsymbol{b}}^{(n)}\leftarrow\bar{\boldsymbol{T}}$, $\mathcal{H}^{(n)}\leftarrow\mathcal{H}$, $\mathcal{L}^{(n)}\leftarrow\mathcal{L}$, $\mathcal{H}^{\mathrm{T}}:\mathcal{L}=\mathcal{L}^{\mathrm{T}}:\mathcal{H}=\mathcal{K}$.	No	---
A single transformation, no tension-compression asymmetry and the stress potential is quadratic $k^{(n)}=0,\ a=2,\ n_{\mathrm{exp}}=1$	$\mathcal{T}_{\boldsymbol{b}}^{(n)}\leftarrow\mathcal{T}_{\boldsymbol{b}}=\mathcal{I}$.	Yes (1 branch)	$\boldsymbol{b}=\left[\mathcal{L}:\left(\mathcal{L}^{\mathrm{T}}:\mathcal{L}\right)_{\mathrm{dev}}^{-1}\right]:\boldsymbol{d}^{\mathrm{p}}$
A single transformation, no tension-compression asymmetry, the stress potential is quadratic, and the transformed space is deviatoric $k^{(n)}=0,\ a=2,\ n_{\mathrm{exp}}=1,$ $\mathcal{C}_{ijkk}^{(n)}=A,\ (A\in\mathbb{R}^{+})$	$\mathcal{T}_{\boldsymbol{b}}=\mathcal{I}$, $\mathcal{L}=\mathcal{L}^{\mathrm{T}}$, $\mathcal{H}=\mathcal{H}^{\mathrm{T}}$.	Yes (1 branch)	$\boldsymbol{b}=\left[\left(\mathcal{L}\right)_{\mathrm{dev}}^{-1}\right]:\boldsymbol{d}^{\mathrm{p}}$
The plastic strain rate tensor is in a principal frame (no shear terms) $\boldsymbol{V}_{\boldsymbol{b}^{(n)}}=\boldsymbol{I}$	$\boldsymbol{T}_{\boldsymbol{b}}^{(n)}=\bar{\boldsymbol{T}}_{\boldsymbol{b}}^{(n)}$	No	---
The strain rate tensor is in a principal frame (no shear terms) and the stress potential is quadratic $\boldsymbol{V}_{\boldsymbol{b}^{(n)}}=\boldsymbol{I},\ a=2$	$\boldsymbol{T}_{\boldsymbol{b}}^{(n)}=\bar{\boldsymbol{T}}_{\boldsymbol{b}}^{(n)}=\boldsymbol{D}^{(n)}$, 8 permutations of $\mathrm{sgn}(b_i^{(n)}),\ i=1,2,3.$	Yes (8^{n} branches)	$\boldsymbol{b}^{(n)}=\left[\mathcal{T}_{\boldsymbol{b}}^{(n)}:\mathcal{L}^{(n)}:\left(\sum_n\left(\mathcal{L}^{(n)\mathrm{T}}:\mathcal{T}_{\boldsymbol{b}}^{(n)}:\mathcal{L}^{(n)}\right)\right)_{\mathrm{dev}}^{-1}\right]:\boldsymbol{d}^{\mathrm{p}}$
The strain rate tensor is in a principal frame (no shear terms), the stress potential is quadratic, and the transformed space is deviatoric $\boldsymbol{V}_{\boldsymbol{b}^{(n)}}=\boldsymbol{I},\ a=2,\ \mathcal{C}_{ijkk}^{(n)}=A,$ $(A\in\mathbb{R})$	$\boldsymbol{T}_{\boldsymbol{b}}^{(n)}=\bar{\boldsymbol{T}}_{\boldsymbol{b}}^{(n)}=\boldsymbol{D}^{(n)}$ 6 permutations of $\mathrm{sgn}(b_i^{(n)}),\ i=1,2,3,$ $(\mathrm{tr}(\hat{\boldsymbol{s}}^{(n)})=0).$	Yes (6^{n} branches)	$\boldsymbol{b}^{(n)}=\left[\mathcal{T}_{\boldsymbol{b}}^{(n)}:\mathcal{L}^{(n)}:\left(\sum_n\left(\mathcal{L}^{(n)\mathrm{T}}:\mathcal{T}_{\boldsymbol{b}}^{(n)}:\mathcal{L}^{(n)}\right)\right)_{\mathrm{dev}}^{-1}\right]:\boldsymbol{d}^{\mathrm{p}}$

4.4.4 Numerical evaluation

As shown in subsection §4.4.1, the determination of the transformed strain-rate tensors $\boldsymbol{b}^{(n)}$ entering the strain rate potential function in Eq. (4.22) generally encompasses laborious mathematical operations (e.g., matrix eigendecomposition, tensorial product, deviatoric inversion, exponentiation) which render closed-form solutions virtually impossible and inevitably lead to a numerical approach to the problem. In this section an efficient algorithm for determining these tensors is presented.

Let us start by rewriting Eqs. (4.23)-(4.24) in a more computationally suitable fashion. Using Voigt notation, one arrives at:

$$\underline{\mathbf{b}}^{(n)} = \mathbf{H}^{(n)}\underline{\mathbf{d}}^{\mathrm{p}}, \tag{4.49}$$

with

$$\begin{gathered}\mathbf{H}^{(n)} = \mathbf{T}_{\boldsymbol{b}}^{(n)}\mathbf{L}^{(n)}\left(\mathbf{T}_{\boldsymbol{b}}\right)_{\mathrm{dev}}^{-1} = \mathbf{T}_{\boldsymbol{s}}^{(n)}\mathbf{L}^{(n)}\left(\mathbf{T}_{\boldsymbol{s}}\right)_{\mathrm{dev}}^{-1}, \text{ with} \\ \mathbf{T}_{\boldsymbol{b}} = \sum_{n}\left(\mathbf{L}^{(n)\mathrm{T}}\mathbf{T}_{\boldsymbol{b}}^{(n)}\mathbf{L}^{(n)}\right), \text{ and } \mathbf{T}_{\boldsymbol{s}} = \sum_{n}\left(\mathbf{L}^{(n)\mathrm{T}}\mathbf{T}_{\hat{\boldsymbol{s}}}^{(n)}\mathbf{L}^{(n)}\right),\end{gathered} \tag{4.50}$$

where $\mathbf{L}^{(n)}$ is the classical 6x6-matrix form of the orthotropic tensor $\mathcal{L}^{(n)}$:

$$\mathbf{L}^{(n)} = \begin{bmatrix} L_{11}^{(n)} & L_{12}^{(n)} & L_{13}^{(n)} & 0 & 0 & 0 \\ L_{21}^{(n)} & L_{22}^{(n)} & L_{23}^{(n)} & 0 & 0 & 0 \\ L_{31}^{(n)} & L_{32}^{(n)} & L_{33}^{(n)} & 0 & 0 & 0 \\ 0 & 0 & 0 & L_{44}^{(n)} & 0 & 0 \\ 0 & 0 & 0 & 0 & L_{55}^{(n)} & 0 \\ 0 & 0 & 0 & 0 & 0 & L_{66}^{(n)} \end{bmatrix}, \tag{4.51}$$

$\mathbf{H}^{(n)}$ is the 6x6-matrix form of $\mathcal{H}^{(n)}$ (non-symmetric, full matrix), $\underline{\mathbf{b}}^{(n)}$ and $\underline{\mathbf{d}}^{\mathrm{p}}$ are the pseudo-vectorial representation of tensors $\boldsymbol{b}^{(n)}$ and $\boldsymbol{d}^{\mathrm{p}}$, respectively, assuming the standard correction on the shear terms: $\underline{\mathbf{b}}^{(n)} = [b_{11}^{(n)} \;\; b_{22}^{(n)} \;\; b_{33}^{(n)} \;\; 2b_{23}^{(n)} \;\; 2b_{13}^{(n)} \;\; 2b_{12}^{(n)}]^{\mathrm{T}}$ and $\underline{\mathbf{d}}^{\mathrm{p}} = [d_{11}^{p} \;\; d_{22}^{p} \;\; d_{33}^{p} \;\; 2d_{23}^{p} \;\; 2d_{13}^{p} \;\; 2d_{12}^{p}]^{\mathrm{T}}$, such that the scalar invariance $\underline{\mathbf{s}} \cdot \underline{\mathbf{d}}^{\mathrm{p}} = \underline{\mathbf{s}}^{\mathrm{T}}\underline{\mathbf{d}}^{\mathrm{p}} = \boldsymbol{s} : \boldsymbol{d}^{\mathrm{p}}$ is preserved, where $\underline{\mathbf{s}} = [s_{11} \;\; s_{22} \;\; s_{33} \;\; s_{23} \;\; s_{13} \;\; s_{12}]^{\mathrm{T}}$ denotes the pseudo-vectorial representation of the deviatoric stress tensor, $\boldsymbol{s}$. In Eq. (4.50) the 6x6-matrices $\mathbf{T}_{\boldsymbol{b}}^{(n)}$ and $\mathbf{T}_{\hat{\boldsymbol{s}}}^{(n)}$ are obtained by the components of the second-order tensors $\boldsymbol{T}_{\boldsymbol{b}}^{(n)}$ (defined in Eq. (4.37)) and $\boldsymbol{T}_{\hat{\boldsymbol{s}}}^{(n)}$ (defined in Eq. (4.42)) and denote the 6x6-matrix notation of $\mathcal{T}_{\boldsymbol{b}}^{(n)}$ and $\mathcal{T}_{\hat{\boldsymbol{s}}}^{(n)}$, respectively (see Appendix A for details on their determination). The operator $(\cdot)_{\mathrm{dev}}^{-1}$ in Eq. (4.50) represents the deviatoric inverse of a 6x6-matrix, defined such that $(\mathbf{A})_{\mathrm{dev}}^{-1}\mathbf{A} = \mathbf{A}(\mathbf{A})_{\mathrm{dev}}^{-1} = \mathbf{K}$, where $\mathbf{K}$ is the 6x6-matrix Voigt representation of the fourth-order deviatoric unit tensor, $\mathcal{K}$. Adopting the above convention, tensors $\mathbf{T}_{\boldsymbol{b}}$ and $\mathbf{T}_{\boldsymbol{s}}$ are symmetric (and thus admit a symmetric deviatoric tensor). Accordingly, the constitutive relation in Eq. (4.40) and Eq. (4.41) can be rewritten in Voigt format as:

$$\underline{\mathbf{d}}^{\mathrm{p}} = \left(\frac{\dot{\lambda}^{\frac{1}{a-1}} m^{\frac{a}{a-1}}}{\sigma_{\mathrm{T}}}\right)\mathbf{T}_{\boldsymbol{b}}\,\underline{\mathbf{s}}, \tag{4.52}$$

for the strain-based formulation, and

$$\underline{\mathbf{d}}^{\mathrm{p}} = \left(\dot{\lambda} m^{a} \sigma_{\mathrm{T}}^{1-a}\right) \mathbf{T}_{\mathbf{s}}\, \underline{\mathbf{s}}, \tag{4.53}$$

for the stress-based formulation, respectively. Note that $\mathbf{T}_{\boldsymbol{b}}$ in Eq. (4.52) depends on *all* transformed tensors $\underline{\mathbf{b}}^{(n)}$, $n = 1,...,n_{\mathrm{ex}}$, i.e., $\mathbf{T}_{\boldsymbol{b}} = \mathbf{T}_{\boldsymbol{b}}(\underline{\mathbf{b}}^{(1)}, ..., \underline{\mathbf{b}}^{(n_{\mathrm{ex}})})$, which, in actual fact, are unknown *a priori*. This means that the construction of a numerical method grounded on such formulation would generally encompass the assumption of $6n_{\mathrm{ex}}$ variables, e.g., the independent components of each tensor $\boldsymbol{b}^{(n)}$, (or their eigendecomposition). On the other hand, irrespective of the number of linear transformations, $\mathbf{T}_{\mathbf{s}}$ in Eq. (4.53) can be completely determined knowing $\underline{\mathbf{s}}$, i.e., $\mathbf{T}_{\mathbf{s}} = \mathbf{T}_{\mathbf{s}}(\underline{\mathbf{s}})$, which has only 5 independent values $(\mathrm{tr}(\boldsymbol{s}) = 0)$. Both approaches are mathematically sound, however, it is clear that the latter should be more efficient from the computational point of view. In this view, the proposed numerical resolution scheme is grounded on the following non-linear system (c.f. Eq. (4.53)):

$$\begin{aligned} &\text{Find } \hat{\underline{\mathbf{s}}} \text{ such that: } \underline{\mathbf{F}}\left(\hat{\underline{\mathbf{s}}}\right) \triangleq \hat{\mathbf{T}}_{\mathbf{s}}\, \hat{\underline{\mathbf{s}}} - \underline{\mathbf{d}}^{\mathrm{p}} = \underline{\mathbf{0}}, \text{ with} \\ &\hat{\mathbf{T}}_{\mathbf{s}} = \mathbf{T}_{\mathbf{s}}\left(\hat{\underline{\mathbf{s}}}\right) = \sum_{n} \left[\mathbf{L}^{(n)\mathrm{T}} \left(\mathbf{T}_{\hat{\boldsymbol{s}}}^{(n)} \left(\hat{\underline{\mathbf{s}}} \right) \right) \mathbf{L}^{(n)} \right], \end{aligned} \tag{4.54}$$

where $\hat{\underline{\mathbf{s}}}$ is an auxiliary deviatoric pseudo-vector with the same physical interpretation of the actual deviatoric stress tensor, $\boldsymbol{s}$, obtained by the change of variable: $\hat{\underline{\mathbf{s}}} \triangleq \left(\dot{\lambda} m^{a} \sigma_{\mathrm{T}}^{1-a}\right) \underline{\mathbf{s}}$, $\hat{\mathbf{T}}_{\mathbf{s}}$ is the value of $\mathbf{T}_{\mathbf{s}}$ evaluated for $\boldsymbol{s} \leftarrow \hat{\boldsymbol{s}}$, and $\underline{\mathbf{F}}(\hat{\underline{\mathbf{s}}})$ is the error function. Note that the above system has six equations but only five are linear independent. To regularize the problem, the above system is mapped into the pentadimensional deviatoric space (see Appendix B for details) and obtain the, now unique, solution in this space, as the pentadimensional Jacobian is no longer singular. Following the constitutive relation in Eq. (4.38), once $\hat{\underline{\mathbf{s}}}$ is known, the eigenvalues of the transformed strain rate tensors, $\boldsymbol{b}_{p}^{(n)}$, are trivially determined using:

$$\boldsymbol{b}_{p}^{(n)} = \mathrm{eig}(\boldsymbol{b}^{(n)}) = \overline{\boldsymbol{T}}_{\hat{\boldsymbol{s}}}^{(n)}\, \hat{\boldsymbol{s}}_{p}^{(n)}, \tag{4.55}$$

where $\overline{\boldsymbol{T}}_{\hat{\boldsymbol{s}}}^{(n)}$ denotes the 3x3-tensor $\overline{\boldsymbol{T}}_{\hat{\boldsymbol{s}}}^{(n)}$ (see text definition following Eq. (4.38)) evaluated for $\boldsymbol{s} \leftarrow \hat{\boldsymbol{s}}$, and $\hat{\boldsymbol{s}}_{p}^{(n)} = \mathrm{eig}(\hat{\boldsymbol{s}}^{(n)})$ where $\hat{\boldsymbol{s}}^{(n)}$ denotes the transformed stress tensors replacing $\boldsymbol{s} \leftarrow \hat{\boldsymbol{s}}$, i.e. $\hat{\underline{\mathbf{s}}}^{(n)} = \mathbf{L}^{(n)} \hat{\underline{\mathbf{s}}}$. Box 4.1 and Box 4.2 resume the proposed numerical scheme in a pseudo-code format. The superscript $(\cdot)^{(5)}$ is employed to denote variables cast into the auxiliary pentadimensional space, as in Appendix B.

Remarks 4.4

i. A valued by-product of such formulation is the determination of the 'normalized' deviatoric stress tensor, $\overline{\boldsymbol{s}} = \partial \psi(\boldsymbol{d}^{\mathrm{p}}) / \partial \boldsymbol{d}^{\mathrm{p}}$, associated with $\boldsymbol{d}^{\mathrm{p}}$, which can be obtained with virtually no added computational cost as:

$$\overline{\boldsymbol{s}} \triangleq \frac{\partial \psi\left(\boldsymbol{d}^{\mathrm{p}}\right)}{\partial \boldsymbol{d}^{\mathrm{p}}} = \frac{\hat{\boldsymbol{s}}}{\varphi\left(\hat{\boldsymbol{s}}\right)}, \tag{4.56}$$

where the homogeneity of the stress potential, φ, was employed. Indeed, such expression is fundamental when using a strain-rate-based formulation to model (elasto-) plasticity.

ii. No deviatoric inversion operation is actually performed in the proposed stress-based numerical scheme. In fact, computation of the tensors $\mathbf{H}^{(n)}$ (see Eq. (4.50)) is not a mandatory step to determine the transformed strain rate tensors, $\boldsymbol{b}^{(n)}$, (or their eigenvalues, $\boldsymbol{b}_p^{(n)}$), as these can be directly determined from the normality relationship in each transformed space (as used in Eq. (4.55)), rather than from fractioning the actual deviatoric stress and/or strain-rate tensors in n_{ex} contributions (recall point (iii) in Remarks 4.3) which would imply the (computational costly) determination of $\left(\mathbf{T}_{\boldsymbol{s}}\right)_{\text{dev}}^{-1}$.

The algorithm in Box 4.1 inputs a plastic strain-rate tensor $\boldsymbol{d}^{\text{p}}$, and outputs the respective potential value, $\psi(\boldsymbol{d}^{\text{p}})$, and its first derivative (the normalized deviatoric stress tensor, $\bar{\boldsymbol{s}}$, Eq. (4.56)). In practice one can also formulate the inverse problem: given a deviatoric stress tensor, $\boldsymbol{s}$, determine its equivalent stress value, $\varphi(\boldsymbol{s})$, and the associated normalized plastic strain-rate tensor, $\bar{\boldsymbol{d}}^{\text{p}}$. Naturally, if the expression of the stress potential φ, is known in closed-form, them the stated problem is trivial. However, if only the expression of the SRP is known, the problem can be solved by the following non-linear system:

$$\text{Find } (\underline{\bar{\mathbf{d}}}^{\text{p}}, \tau) \text{ such that: } \underline{\mathbf{F}}(\underline{\bar{\mathbf{d}}}^{\text{p}}, \tau) \triangleq \begin{Bmatrix} \tau \dfrac{\partial \psi}{\partial \underline{\bar{\mathbf{d}}}^{\text{p}}} - \underline{\mathbf{s}} \\ \psi(\underline{\bar{\mathbf{d}}}^{\text{p}}) - 1 \end{Bmatrix} = \begin{Bmatrix} \underline{\mathbf{0}} \\ 0 \end{Bmatrix}, \tag{4.57}$$

where τ is the equivalent stress associated with $\boldsymbol{s}$ and $\bar{\boldsymbol{d}}^{\text{p}}$ is the plastic strain-rate tensor of unitary SRP value associated with $\boldsymbol{s}$ by the normality principle, i.e. $\bar{\boldsymbol{d}}^{\text{p}} = \partial\varphi/\partial\boldsymbol{s}$, and $\underline{\bar{\mathbf{d}}}^{\text{p}}$ its pseudo-vectorial notation. Note that both $\partial\psi/\partial\bar{\boldsymbol{d}}^{\text{p}}$ and $\psi(\bar{\boldsymbol{d}}^{\text{p}})$ in Eq. (4.57) are the outputs of the algorithm in Box 4.1, and thus no numerical derivatives are actually needed to evaluate the error function, $\underline{\mathbf{F}}$. The scalar expression in Eq. (4.57) is added to regularize the problem. Indeed, even if $\psi(\bar{\boldsymbol{d}}^{\text{p}})$ is homogeneous of degree one with respect to positive multipliers, $\partial\psi/\partial\bar{\boldsymbol{d}}^{\text{p}}$ is homogeneous of degree zero, i.e. $\partial\psi(\alpha\bar{\boldsymbol{d}}^{\text{p}})/\partial\bar{\boldsymbol{d}}^{\text{p}} = \partial\psi(\bar{\boldsymbol{d}}^{\text{p}})/\partial\bar{\boldsymbol{d}}^{\text{p}}$, $\forall\alpha \in \mathbb{R}^{+}$ and therefore $\bar{\boldsymbol{d}}^{\text{p}}$ must be 'constrained', otherwise the system would be singular. The system in Eq. (4.57) has seven equations but only six are linear independent, hence the vectorial equation of the error function is $\underline{\mathbf{F}}$ actually solved in the pentadimensional space. The proposed inverse problem is summarized in Box 4.3 and Box 4.4 in a pseudo-code format.

In the following, the developed strain rate potential is to describe the strong asymmetry and anisotropy observed in textured metallic sheets.

Box 4.1 A numerical resolution scheme for determination of the proposed orthotropic strain rate potential for dense materials: the direct problem.

0. Inputs: $\underline{\mathbf{d}}^{\mathrm{p}}$, $\{\mathbf{L}^{(n)}, k^{(n)}, a, m\}$

1. Compute the auxiliary tensor $\underline{\hat{\mathbf{s}}}$

1.1. Set initial guess $\underline{\hat{\mathbf{s}}}_0$ and relative convergence tolerances $\left\{\varepsilon_{\mathrm{tol}}^{\mathrm{fun}}, \varepsilon_{\mathrm{tol}}^{\Delta \mathrm{x}}\right\}$

- Transform $\underline{\hat{\mathbf{s}}}_0$ into the pentadimensional space: $\underline{\hat{\mathbf{s}}}_0 \rightarrow \underline{\hat{\mathbf{s}}}_0^{(5)}$ % (Appendix B)

1.2. Solve the system in Box 4.2 for $\underline{\hat{\mathbf{s}}}^{(5)}$ with a quasi-Newton method, such that:

- $\left(\dfrac{\left\|\underline{\mathbf{F}}^{(5)}\left(\underline{\hat{\mathbf{s}}}_{k+1}^{(5)}\right)\right\|_2}{\left\|\underline{\mathbf{d}}^{\mathrm{p}(5)}\right\|_2} < \varepsilon_{\mathrm{tol}}^{\mathrm{fun}}\right)$ and $\left(\dfrac{\left\|\underline{\hat{\mathbf{s}}}_{k+1}^{(5)} - \underline{\hat{\mathbf{s}}}_k^{(5)}\right\|_2}{\left\|\underline{\hat{\mathbf{s}}}_k^{(5)}\right\|_2} < \varepsilon_{\mathrm{tol}}^{\Delta \mathrm{x}}\right)$, where k is the number of the iteration

1.3. Pull-back to reference space $\underline{\hat{\mathbf{s}}}^{(5)} \rightarrow \underline{\hat{\mathbf{s}}}$ % (Appendix B)

2. Compute the eigenvalues of $\boldsymbol{b}^{(n)}$

for $n = 1 : n_{\mathrm{ex}}$ % loop over the number of transformations

- Compute stress transformations: $\underline{\hat{\mathbf{s}}}^{(n)} \rightarrow \mathbf{L}^{(n)} \underline{\hat{\mathbf{s}}}$
- Eigendecomposition of $\underline{\hat{\mathbf{s}}}^{(n)}$: $\hat{\boldsymbol{s}}_p^{(n)}$, $\boldsymbol{V}_{\hat{\boldsymbol{s}}^{(n)}}$
- Compute $\boldsymbol{D}^{(n)}\left(k^{(n)}, a\right)$ % (Eq. (4.27))
- Compute $\bar{\boldsymbol{T}}_{\hat{\boldsymbol{s}}}^{(n)} = \boldsymbol{D}^{(n)} \left|\hat{\mathbf{s}}_p^{(n)}\right|^{a-2}$
- Compute $\boldsymbol{b}_p^{(n)} = \bar{\boldsymbol{T}}_{\hat{\boldsymbol{s}}}^{(n)} \hat{\boldsymbol{s}}_p^{(n)}$

end

3. Compute the strain-rate potential

3.1. Compute the scalar G % (Eq. (4.22))

- Initialize $G := 0$

for $n = 1 : n_{\mathrm{ex}}$ % loop over the number of transformations

for $i = 1 : 3$

- Compute auxiliary scalar: $\beta_i = \left(1 - \operatorname{sgn}\left(\hat{\mathrm{s}}_{p,i}^{(n)}\right) k^{(n)}\right)^{-\frac{a}{a-1}}$
- Add to the sum: $G := G + \beta_i \left|b_{p,i}^{(n)}\right|^{\frac{a}{a-1}}$

end

end

3.2. Compute the SRP: $\psi = (1/m) G^{\frac{a-1}{a}}$

4. Compute the normalized deviatoric stress tensor

- Compute the equivalent stress associated with $\hat{\mathbf{s}}$: $\varphi\left(\hat{\boldsymbol{s}}, \mathbf{L}^{(n)}, k^{(n)}, a\right)$ % (Eq. (4.19))
- Compute $\bar{\boldsymbol{s}} = \hat{\boldsymbol{s}} / \varphi\left(\hat{\boldsymbol{s}}\right)$

5. Output: $\{\psi, \bar{\boldsymbol{s}}\}$

Box 4.2 Computation of the error function in the pentadimensional space for the determination of the proposed orthotropic strain rate potential for dense materials.

0. Inputs: $\underline{\mathbf{s}}^{(5)}$, $\underline{\mathbf{d}}^{\mathrm{p}}$, $\{\mathbf{L}^{(n)}, k^{(n)}, a\}$

1. Compute $\mathbf{T}_s$

- Pull-back to reference space: $\underline{\mathbf{s}}^{(5)} \rightarrow \underline{\mathbf{s}}$ % (Appendix B)
- Initialize $\mathbf{T}_s = \mathbf{0}$

for $n = 1 : n_{\mathrm{ex}}$ % loop over the number of transformations

- Compute stress transformations: $\hat{\underline{\mathbf{s}}}^{(n)} \rightarrow \mathbf{L}^{(n)}\underline{\mathbf{s}}$
- Eigendecomposition of $\hat{\underline{\mathbf{s}}}^{(n)}$: $\hat{\mathbf{s}}_p^{(n)}$, $\boldsymbol{V}_{\hat{s}^{(n)}}$
- Compute $\boldsymbol{D}^{(n)}(k^{(n)}, a)$ % (Eq. (4.27))
- Compute $\bar{\boldsymbol{T}}_{\hat{s}}^{(n)} = \boldsymbol{D}^{(n)} \left|\hat{\boldsymbol{s}}_p^{(n)}\right|^{a-2}$ and its rotation $\boldsymbol{T}_{\hat{s}}^{(n)} = \boldsymbol{V}_{\hat{s}^{(n)}} \bar{\boldsymbol{T}}_{\hat{s}}^{(n)} \boldsymbol{V}_{\hat{s}^{(n)}}^{\mathrm{T}}$ % (Eq. (4.42))
- Convert $\boldsymbol{T}_{\hat{s}}^{(n)}$ to the equivalent Voigt notation: $\boldsymbol{T}_{\hat{s}}^{(n)} \rightarrow \mathbf{T}_{\hat{s}}^{(n)}$ % (Appendix A)
- Perform the notation correction $\left(\mathrm{T}_{\hat{s}}^{(n)}\right)_{IJ} \leftarrow 2\left(\mathrm{T}_{\hat{s}}^{(n)}\right)_{IJ}$, $I = 4,5,6$, $J = 1,\ldots,6$
- Add to the sum: $\mathbf{T}_s := \mathbf{T}_s + \left(\mathbf{L}^{(n)\mathrm{T}} \mathbf{T}_{\hat{s}}^{(n)} \mathbf{L}^{(n)}\right)$

end

2. Determine the error function

- Transform $\mathbf{T}_s$ and $\underline{\mathbf{d}}^{\mathrm{p}}$ into the pentadimensional space: $\mathbf{T}_s \rightarrow \mathbf{T}_s^{(5)}$, $\underline{\mathbf{d}}^{\mathrm{p}} \rightarrow \underline{\mathbf{d}}^{\mathrm{p}(5)}$ % (Appendix B)
- Compute the error function: $\underline{\mathbf{F}}^{(5)} = \mathbf{T}_s^{(5)} \underline{\mathbf{s}}^{(5)} - \underline{\mathbf{d}}^{\mathrm{p}(5)}$ % (Eq. (4.54))

3. Output: $\underline{\mathbf{F}}^{(5)}$

Box 4.3 A numerical resolution scheme for the inverse problem of the proposed orthotropic strain rate potential for dense materials.

0. Inputs: $\underline{\boldsymbol{\sigma}}$, $\{\mathbf{L}^{(n)}, k^{(n)}, a\}$

1. Solve the system of equations

1.1. Compute the deviatoric stress tensor: $\underline{\mathbf{s}} \rightarrow \underline{\boldsymbol{\sigma}} - (1/3)\mathrm{tr}(\boldsymbol{\sigma})\underline{\mathbf{I}}$

1.2. Set initial guess $(\bar{\underline{\mathbf{d}}}_0, \tau_0)$ and relative convergence tolerances $\left\{\varepsilon_{\mathrm{tol}}^{\mathrm{fun}}, \varepsilon_{\mathrm{tol}}^{\Delta \mathrm{x}}\right\}$

1.3. Solve the system in Box 4.4 for $(\bar{\underline{\mathbf{d}}}^{(5)}, \tau)$ with a quasi-Newton method, such that:

- $\left(\dfrac{\left\|F_{(1:5)}(\bar{\underline{\mathbf{d}}}_{k+1}^{(5)}, \tau_{k+1})\right\|_2}{\left\|\underline{\mathbf{s}}\right\|_2} < \varepsilon_{\mathrm{tol}}^{\mathrm{fun}}\right)$ and $\left(\left|F_{(6)}(\bar{\underline{\mathbf{d}}}_{k+1}^{(5)}, \tau_{k+1})\right| < \varepsilon_{\mathrm{tol}}^{\mathrm{fun}}\right)$; and $\left(\dfrac{\left\|\bar{\underline{\mathbf{d}}}_{k+1}^{(5)} - \bar{\underline{\mathbf{d}}}_k^{(5)}\right\|_2}{\left\|\bar{\underline{\mathbf{d}}}_{k+1}^{(5)}\right\|_2} < \varepsilon_{\mathrm{tol}}^{\Delta \mathrm{x}}\right)$,

where k is the number of the iteration and $F_{(I:J)}$ denotes the I to J components of vector $\underline{\mathbf{F}}$ with $1 \le I \le J \le 6$.

1.4 Pull-back to reference space: $\bar{\underline{\mathbf{d}}}_{k+1}^{(5)} \rightarrow \bar{\underline{\mathbf{d}}}_{k+1}$ % (Appendix B)

2. Output: $\tau \leftarrow \tau_{k+1}$, $\bar{\underline{\mathbf{d}}}^{\mathrm{p}} \leftarrow \bar{\underline{\mathbf{d}}}_{k+1}^{\mathrm{p}}$

Box 4.4 Determination of the error function vector for the inverse problem of the proposed orthotropic strain rate potential for dense materials.

0. Inputs: $\underline{\mathbf{s}}$, $(\underline{\bar{\mathbf{d}}}^{(5)},\tau)$, $\{\mathbf{L}^{(n)},k^{(n)},a\}$

1. Compute the SRP and normalized deviatoric stress tensor

- Pull-back to reference space: $\underline{\bar{\mathbf{d}}}^{(5)}\rightarrow\underline{\bar{\mathbf{d}}}$ % (Appendix B)
- CALL Box 3.1 for $\underline{\bar{\mathbf{d}}}$ to get $\partial\psi/\partial\underline{\bar{\mathbf{d}}}$ and $\psi(\underline{\bar{\mathbf{d}}})$

2. Determine the error function

- Transform $\partial\psi/\partial\underline{\bar{\mathbf{d}}}$ and $\underline{\mathbf{s}}$ into the pentadimensional space: $\partial\psi/\partial\underline{\bar{\mathbf{d}}}\rightarrow(\partial\psi/\partial\underline{\bar{\mathbf{d}}})^{(5)}$, $\underline{\mathbf{s}}\rightarrow\underline{\mathbf{s}}^{(5)}$
- Compute the error function: $\underline{\mathbf{F}}\leftarrow\begin{Bmatrix}(\partial\psi/\partial\underline{\bar{\mathbf{d}}})^{(5)}-\underline{\mathbf{s}}^{(5)}\\ \psi(\underline{\bar{\mathbf{d}}})-1\end{Bmatrix}$ % (Eq. (4.57))

3. Output: $\underline{\mathbf{F}}$

4.5 Application examples

4.5.1 Remarks on parameter identification

The description of the constitutive behaviour of any class of materials involves essentially two main tasks. First, the formulation of appropriate mathematical functions; second, the development and selection of tests and calibration tools to determine the parameters entering these models. The goal of this chapter is on the first task (described in subsection §4.4). Nevertheless some comments regarding the second task are presented in the following.

Ideally, an identification procedure should have (at least) the same number of available experimental data as the number of coefficients to be fitted[11]. Given the considerable number of parameters allowed by the strain-rate (or, equivalently, stress) potential described in this work, extensive experimental characterization would be needed to take full advantage of the predictive capabilities of this model. This includes, but is not limited to, mechanical tests with monotonously proportional loadings along various directions of the orthotropic axes, e.g., uniaxial tensile and compressive yield stresses, *r*-values (alias strain-ratios or Lankford coefficients), balanced biaxial yield stress, simple shear tests, among others. In the particular case of thin metallic sheets, the out-of-plane experimental data is not readily available, and thus the determination of the corresponding orthotropic coefficients, (e.g. $C_{II}^{(n)}=L_{II}^{(n)},\ \ I=4,5$ (no sum) in Eq. (4.51)) is unfeasible. Alternatively, the identification of these parameters can be grounded on pseudo-experimental results based on the theory of crystal-plasticity (e.g. using the self-consistent polycrystal model (VPSC), Barlat *et al.* (2005)) if the texture or any other microstructural information is available. If this is not the case, one can assume, as a first approximation, that the out-of-plane orthotropic coefficients respect one of the following assumptions: (i) equal to their reference isotropic values, $(C_{44}^{(n)}=C_{55}^{(n)}=1)$; (ii) determined such that the out-of-plane pure shear response is isotropic (e.g. equal

[11] This is not however a sufficient condition for arriving at a quality identification.

to that of von Mises, $\tau = \sigma_T/\sqrt{3}$); (iii) equal to respective in-plane counterpart, (i.e. $C_{44}^{(n)} = C_{55}^{(n)} = C_{66}^{(n)}$). In summary, the use of texture-based predictions, combined with actual experimental data in a properly weighted objective function, allows the identification of virtually any number of orthotropic (as well as tension-compression asymmetry) coefficients.

According to the theorem of representation for orthotropic scalar functions, invariance with respect to the orthotropic group requires orthotropic yield criteria to involve at most seventeen independent orthotropic coefficients, (see e.g. Cazacu *et al.* (2019)). In the case of the linear transformation method, this constraint would correspond to the case of two linear transformations using tensors of the form $\mathbf{C}^{(n)}$ (see Eq. (4.20)). In this view, linear dependence between coefficients can take place when working with more than two transformation spaces and, as such, non-uniqueness, in the sense that the overall response can be replicated by a separate set of parameters, may follow. Nevertheless, it is important to emphasise that adding more transformations, hence coefficients, for a given number of available experimental data is not a fruitless task[12]. In practice, no orthotropic model is general enough to fit all possible convex sets. However, by increasing the number of coefficients, the flexibility of stress (or strain-rate) potentials is invariably increased, which allows for an improved identification. In other words, the addition of a new transformation space n can be viewed as a correction of the potential with $(n-1)$ transformations. This process is repeated until a desired level of accuracy in the description of the plastic behaviour is obtained (note that, in the limit, an infinite number of transformations would return the optimal fitting, similarly to a convergent series). In practice, the accuracy improvement resulting from each added transformation must be balanced with the inevitably increase of the computational cost, both in the identification task, and, more critically, in the subsequent numerical simulations. In the following application examples of the developed strain-rate potential using one, three and four transformations are presented.

4.5.2 Commercially pure titanium

Commercially pure (CP) titanium exhibits outstanding engineering properties, namely high strength and ductility, moderate weight, exceptional heat- and corrosion resistance, which explains its extensive application in the aerospace (viz. high-performance parts under extreme environments) and biomedical (viz. osseointegration) industries. Titanium and its alloys are found to have a hexagonal close-packed (hcp) crystal structure at ambient temperature and pressure. Twinning is known to play a crucial role in the plastic deformation process of hcp materials due to the lack of available slip systems, in particular those which can accommodate deformation along the *c*-axis of the hcp lattice. Being a polarized mechanism twinning leads to tension-compression asymmetry at the macroscopic level (recall Remark 2.4 and its adjacent discussion). Moreover, CP-Ti sheets usually have a pronounced basal texture as a result of processing operations. The competitive deformation mechanisms at the single crystal level and crystallographic texture from prior deformation history ultimately render CP-Ti sheets to display plastic anisotropy and tension-compression asymmetry. These properties can evolve during the deformation

[12] Practical examples of this statement are discussed in subsections §4.5.3 and §4.5.4.

process due to slip-twinning and twin-twin interactions, twinning-detwinning mechanisms and deformation-induced texture evolution. For insights on the mechanical behaviour of CP-Ti under quasi-static conditions at room temperature, the reader is referred to dedicated studies, e.g., Hama *et al.* (2015); Ma *et al.* (2019); Won *et al.* (2016); Yang *et al.* (2022); Yi *et al.* (2016) regarding crystallographic aspects and to those of Nixon *et al.* (2010) (on high-purity (HP)-Ti); Baral *et al.* (2018); Raemy *et al.* (2017); Revil-Baudard *et al.* (2016, 2021); Zhai *et al.* (2016) regarding the macroscopic aspects of deformation and phenomenological constitutive modelling. The latter works have shown that classic plasticity models, such as those of von Mises and the Hill (1948) cannot describe the plastic behaviour of hcp materials with adequate accuracy. The reason is twofold: firstly, these models cannot account for asymmetry of the material; and secondly, they lack the flexibility to describe the complex orthotropic behaviour associated with hcp crystal structures. Thus, modelling titanium (or its alloys) should involve a criterion which is sensitive to the asymmetry of the material, such as the potentials described in this work.

Let us now focus on the experimental investigation of the quasi-static room temperature behaviour reported in Baral *et al.* (2018), regarding a CP-Ti (Grade 2) hot-rolled plate. The reported data consists of uniaxial tension and compression and plane-strain tension tests at several angles between the rolling direction (RD) and the transverse direction (TD) (increments of 15º) and uniaxial tension and compression along the through-thickness (alias normal) direction (ND), the latter two using miniature specimens machined along of the 12.7 mm thickness plate. The authors used this experimental data to characterize the material according to the quadratic form of the CPB06 criterion (a single linear transformation) for six levels of plastic work, or, equivalently, 'equivalent' plastic deformation, $\bar{\varepsilon}^{\mathrm{p}}$, (work-conjugate of the equivalent stress, $\bar{\sigma}$, associated with the CPB06 stress potential). The coefficients are given Table 4.1. No data was available for the out-of-plane parameters. The authors recommended $C_{44}=C_{55}=1$. Note that the sum $\sum_{J=1}^{3}(C_{IJ})$ (fixed *I*), $I,J=1,2,3,$ when using the parameters in Table 4.1 is not constant, and thus the tensor $\mathbf{L}=\mathbf{CK}$ in Eq. (4.51) is *not* symmetric. This is in contrast with the parameters given in Cazacu *et al.* (2010) for describing the behaviour of a high-purity (HP) α-titanium using the same criterion, for which the restriction of the symmetry of $\mathbf{L}$ was employed, ultimately resulting in six (rather than nine) independent orthotropic coefficients. Figure 4.2 represents the yield, or stress potential (SP), loci and the respective strain-rate potential (SRP) loci (obtained by Eq. (4.22)) for several accumulated equivalent plastic deformation levels, as well as the relevant experimental yield data used to calibrate the potentials. The isovalue surfaces are represented in the π-plane[13] (alias deviatoric plane or octahedral plane) in a polar-like plot. The yield loci are normalized by the initial tensile yield stress along the 1-direction, i.e., $\bar{\boldsymbol{s}}=\boldsymbol{s}/(\sigma_1^T)_0$. The SRP loci are normalized such that the plastic power is unitary for each $\bar{\varepsilon}^{\mathrm{p}}$- level, i.e., $\bar{\boldsymbol{s}}:\bar{\boldsymbol{d}}^{\mathrm{p}}=1$. This representation convention is adopted in order to better picture the duality property and avoid overlapping surfaces (the innermost SP locus is associated with the out-most SRP locus, and vice-versa). Figure 4.2a shows that model is able to capture with reasonable accuracy the

[13] The plane normal to the hydrostatic axis, $\underline{\boldsymbol{n}}=(1/\sqrt{3})\underline{\boldsymbol{e}}_1+(1/\sqrt{3})\underline{\boldsymbol{e}}_2+(1/\sqrt{3})\underline{\boldsymbol{e}}_3$, where $(\underline{\boldsymbol{e}}_1,\underline{\boldsymbol{e}}_2,\underline{\boldsymbol{e}}_3)$ denote the Cartesian coordinate system associated with the orthotropy axes and $\underline{\boldsymbol{e}}_1$, $\underline{\boldsymbol{e}}_2$ and $\underline{\boldsymbol{e}}_3$ denote the rolling, transverse and normal directions, respectively.

experimental data in the principal stress space, both in tensile and compressive loadings. Note that for low strain levels the CP-Ti displays a mild asymmetric behaviour (deviates from the von Mises circle mainly due to anisotropy). In contrast, for larger plastic strain levels, the curvature of the locus tends towards a triangular shape as the tension-compression asymmetry effects became pronounced. Naturally, the same observation could be drawn from the SRP loci, as these are exact duals.

Table 4.2 Coefficients for the stress- and strain rate potentials for a CP titanium (after Baral *et al.*, 2018).

a	2.0							
$\bar{\varepsilon}^{\mathrm{p}}$	k	C_{11}	C_{12}	C_{13}	C_{22}	C_{23}	C_{33}	C_{66}
0.013	-0.0298	1.0000	1.1512	1.2907	1.7085	1.3913	1.7290	0.4299
0.026	-0.0347	1.0000	1.0343	1.3607	1.6453	1.3897	1.6886	0.4560
0.048	-0.0324	1.0000	1.0283	1.3220	1.6078	1.3583	1.6621	0.4350
0.088	-0.0691	1.0000	0.8224	0.8201	1.0612	0.8707	1.0491	0.2236
0.13	-0.1328	1.0000	0.8041	0.8017	1.0152	0.8254	0.9987	0.2143
0.20	-0.2534	1.0000	0.7922	0.7923	0.9938	0.7953	0.9784	0.2151

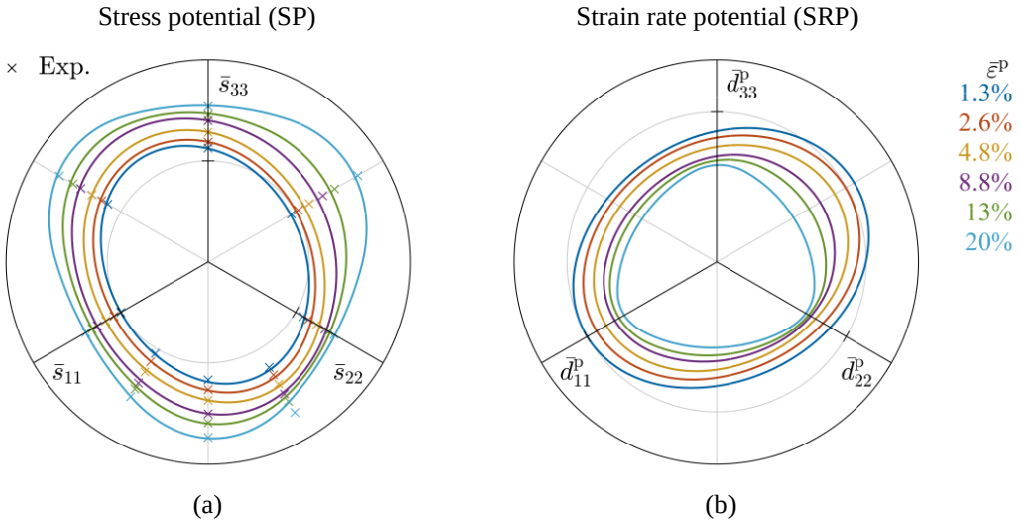

Figure 4.2 π-plane representation of the dual potentials of the CP-Ti for several values of equivalent plastic strain: (a) stress potential (SP) loci, as predicted by the CPB06 criterion; (b) strain-rate potential (SRP) loci, as predicted by the proposed potential in Eq. (4.22). A polar-like plot is adopted where the radial grid lines represent the unitary von Mises stress and strain-rate potential loci in (a) and (b), respectively.

4.5.3 AZ31B magnesium alloy

Magnesium (Mg) and its alloys have received a lot of attention in recent years due to its exceptional low density (about 1.75g/cm^3) when compared with more conventional structural materials (e.g., steel (7.8/cm^3), aluminium alloys (2.7/cm^3)). Moreover, magnesium materials display improved recycling potential. Despite these appealing properties, application in sheet metal forming lags far behind other lightweight design alternatives (viz. Al alloys). This is related to the poor ductility of Mg alloys at room temperature, in turn explained by its hcp crystal structure and, typically, strong basal texture, which lead to intricate forms of anisotropy and tension-compression asymmetry at the macroscale, (as briefly discussed above regarding the CP-Ti and in more detail in §2.1). For insights on the mechanical behaviour and constitutive modelling of magnesium alloys under quasi-static conditions at room temperature the reader is referred to dedicated works, for instance those of Abedini *et al.* (2017); Guo *et al.* (2013); Hama *et al.* (2016); Kondori and Benzerga (2017); Lou *et al.* (2007); Shi *et al.* (2017); Tari *et al.* (2014); Yoon *et al.* (2013). Let us now focus on the data reported in Tari *et al.* (2014) regarding a AZ31B-O (Mg+3%Al+1%Zn) sheet in annealed (O temper) condition. The experimental data consists of uniaxial tension and compression tests at several angles between the RD and TD and uniaxial compression in the ND. The Mg alloy was characterized using the non-quadratic form of the CPB06 potential for two ranges of equivalent plastic strain using one to four linear transformations (the same data was used for calibrating the model for all four cases). It was shown that the model with a single transformation (CPB06) was unable to capture the experimental yield loci; using two transformations (CPB06ex2) improved the fitting, yet with unsatisfactory accuracy; with three transformations (CPB06ex3) the data was fitted with reasonable accuracy; and the usage of four transformations (CPB06ex4) did not meaningfully improve the previous fitting. Table 4.3 summarizes the parameters of the CPB06ex3 model for six equivalent plastic strain levels. No data is available for the out-of-plane parameters. Figure 4.3 represents the π-plane projection of the yield loci and the respective strain-rate potential loci (obtained by Eq. (4.22)), as well as the experimental yield data used to calibrate the potentials assuming plastic incompressibility. Both surfaces are normalized in the same fashion as in Figure 4.2 (see details in §4.5.2). Figure 4.3 shows that a remarkable shape change of the yield locus (and, necessarily, SRP locus) takes place with the accumulated plastic deformation. This is a consequence of twinning-detwinning activation and texture evolution and demonstrates the importance of adopting a constitutive model accounting for evolving orthotropy when describing hcp materials.

Table 4.3 Coefficients for the stress- and strain rate potentials for the AZ31B Mg alloy. Three linear transformations ($n = 1, 2, 3$), are considered (after Tari *et al.*, 2014).

a	6.0								
$\bar{\varepsilon}^{\mathrm{p}}$	n	$k^{(n)}$	$C_{11}^{(n)}$	$C_{12}^{(n)}$	$C_{13}^{(n)}$	$C_{22}^{(n)}$	$C_{23}^{(n)}$	$C_{33}^{(n)}$	$C_{66}^{(n)}$
0	1	0.3230	1.0000	2.4710	3.5140	-0.0430	3.3763	0.4731	-2.6925
	2	0.3500	-0.1720	2.4086	1.1527	-0.1570	0.2129	-1.1634	-2.5011
	3	1.0000	-0.2172	1.6280	3.3118	-0.1054	3.3548	3.0409	-1.8000
0.02	1	0.0550	1.0000	2.5190	2.8260	0.2798	2.3902	1.0479	-2.1657
	2	0.3380	-0.1382	1.9415	0.7579	-0.1263	0.1685	-0.9345	-2.0114
	3	1.0000	0.0892	1.6116	2.8229	0.1766	2.6979	2.2805	-1.4476
0.04	1	-0.1774	1.0000	0.4562	-0.5860	0.3470	-0.7125	-0.7383	-0.6320
	2	0.3457	0.0408	1.4902	0.5287	0.0785	0.2802	2.0305	-1.4543
	3	0.5770	0.7173	1.9236	2.8231	0.8876	1.5836	3.4085	-1.2257
0.06	1	-0.1698	1.0000	1.0032	-0.8071	0.6919	-0.9020	-0.4525	-0.8719
	2	0.3627	0.0563	2.0530	0.7549	0.1142	0.4838	2.2563	-1.9831
	3	0.3659	1.6655	3.2411	4.3033	2.0108	2.6026	4.7192	-1.6884
0.08	1	-0.1639	1.0000	2.0851	-1.2937	1.4257	0.7289	-0.2619	-1.3997
	2	0.3798	0.0906	3.2907	1.2522	0.1917	0.9349	2.7644	-3.1459
	3	0.1549	3.7541	6.0765	7.5618	4.4816	5.7627	7.6025	-2.7061

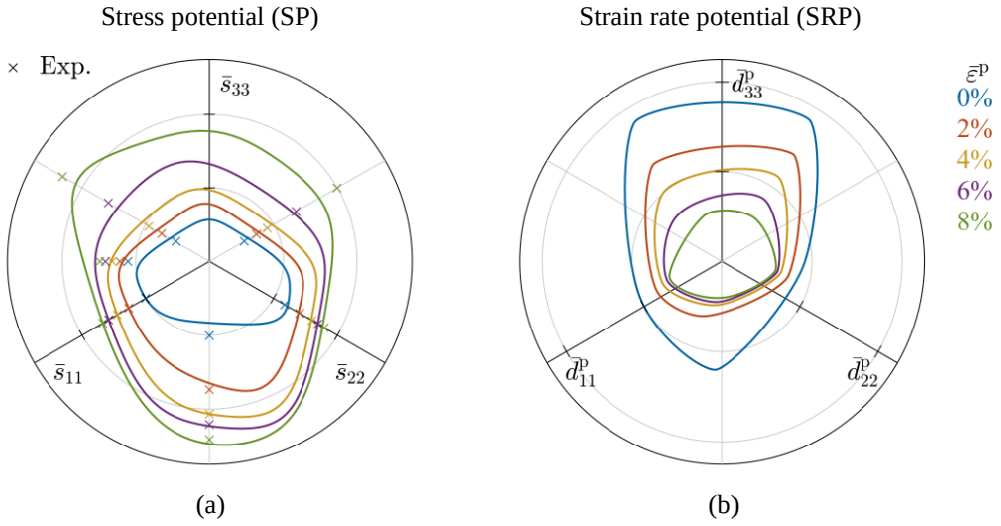

Figure 4.3 π-plane representation of the dual potentials of the AZ31B Mg alloy for several values of equivalent plastic strain: (a) stress potential (SP) loci, as predicted by the CPB06ex3 criterion; (b) strain-rate potential (SRP) loci, as predicted by the proposed potential in Eq. (4.22). A polar-like plot is adopted where the radial grid lines represent multiples of the unitary von Mises stress and strain-rate potential loci in (a) and (b), respectively.

4.5.4 2090-T3 aluminium alloy

While twinning-detwinning mechanisms are the main source of tension-compression asymmetry in low-symmetry lattice structures such as hcp, the activation of twinning in cubic lattices is rare due to the considerable number of 'easy' slip systems available. As such, the deformation mechanisms in tension and compression are not fundamentally different in aluminium alloys, which are known to have the fcc crystal structure. Nevertheless, some mild forms of tension-compression asymmetry may arise in the initial stages of deformation of these materials due to directional slip mechanisms (non-Schmid effect) and other micro-plasticity effects resulting from prior thermo-mechanical processing. Barlat *et al.* (1991,2003) reported the results of an experimental investigation of the quasi-static room temperature behaviour of a cold rolled 2090-T3 aluminium alloy. The experimental data consists of uniaxial tension and compression tests along several angles between the RD and TD (increments of 15º), including the tensile *r*-values, biaxial yield stress from the bulge test and the biaxial *r*-value from a disk compression test. The results shown that the material exhibits some tension-compression asymmetry. Plunkett *et al.* (2008) applied this data to characterize the yielding response of the 2090-T3 Al alloy with the non-quadratic form of the CPB06 potential using one to four transformations. The same number of data points was used for calibrating the model for all four cases. It was shown that, although the yield loci were captured with similar accuracy by all models, only those with three (CPB06ex3) and four transformations (CPB06ex4) were able to capture the trends of the experimental tensile *r*-values, the latter offering a considerable accuracy improvement over the former. The fitted parameters of the CPB06ex4 formulation are presented in Table 4.4. As in the previous examples, no data is available for the out-of-plane parameters. Figure 4.4 represents the biaxial projections of the plane-stress yield loci the and the respective strain-rate potential loci (obtained by Eq. (4.22)), as well as the experimental yield data used to calibrate the potentials. The axes of both figures coincide with the orthotropic axes. The yield loci are normalized by the tensile yield stress in the 1-direction, σ_1^T, and the SRP loci are normalized by its work-conjugate, $\dot{\lambda}_1^{\mathrm{T}}$, such that both potentials represent surfaces of unitary isovalue, $\varphi(\boldsymbol{\sigma}) = \psi(\boldsymbol{d}^p) = 1$. The contours represent 10% increments relative to the maximum value of the normalized shear component of each potential. Note that due to tension-compression asymmetry the location of the maximum shear stress, $\sigma_{12}^{\max}$, is not that of the pure shear loading $(\sigma_{11} = \sigma_{22} = 0)$. An analogous observation holds for the SRP loci. This phenomenon is thought to substantiate the occurrence of permanent axial deformation during monotonic free-end torsion (known as the Swift effect) of materials exhibiting tension-compression asymmetry (e.g. see Cazacu *et al.*, 2013; Guo *et al.*, 2013; Revil-Baudard *et al.*, 2014). It is important to note that the contour increments of the potentials in Figure 4.4 are not work conjugated, as these represent different loading conditions (in other words, a σ_{12}/σ_1^T isovalue contour in the stress biaxial plane does not generally imply a constant value of $d_{12}^{\mathrm{p}}/\dot{\lambda}$, by the normality rule, and vice versa).

Table 4.4 Coefficients for the stress- and strain rate potentials for the 2090-T3 aluminium alloy. Four linear transformations $(n = 1, 2, 3, 4)$, are considered (after Plunkett *et al.*, 2008).

a	12.0							
n	$k^{(n)}$	$C_{11}^{(n)}$	$C_{12}^{(n)}$	$C_{13}^{(n)}$	$C_{22}^{(n)}$	$C_{23}^{(n)}$	$C_{33}^{(n)}$	$C_{66}^{(n)}$
1	0.331	1.0000	-1.7002	-1.4101	0.6643	-2.5252	-4.6739	3.0576
2	-0.311	1.0000	-1.0600	-1.3165	-2.3381	-4.2998	-2.2158	-1.9664
3	0.063	1.0000	0.5132	3.1055	-0.1367	0.1559	-1.4964	4.6139
4	0.625	1.0000	-0.7122	2.0528	-1.3669	-0.3837	1.8585	2.2494

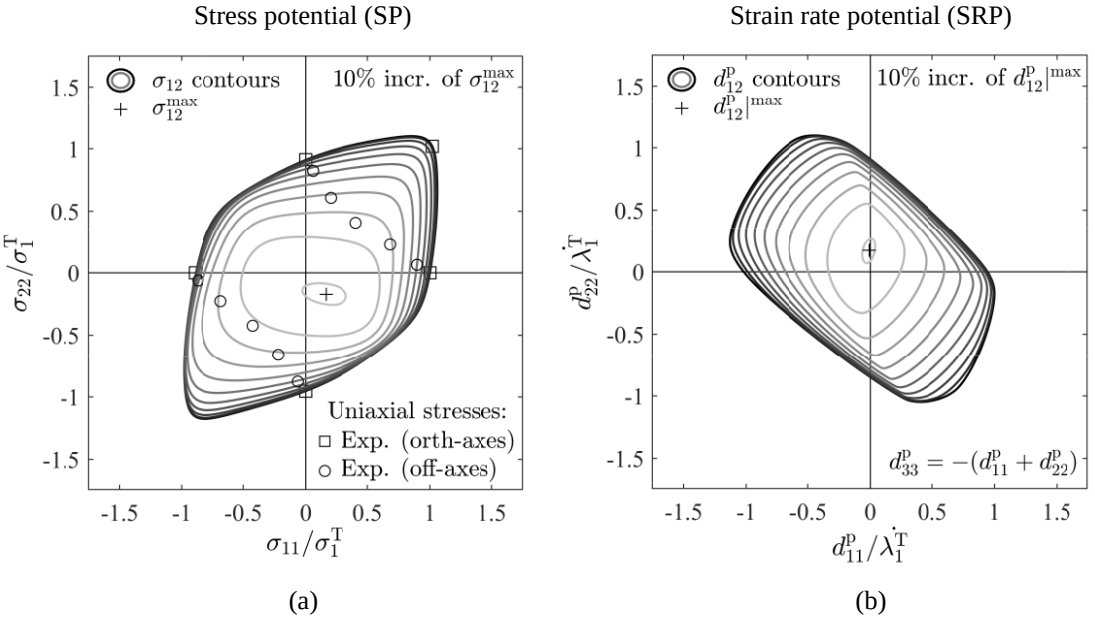

Figure 4.4 Biaxial representation of the dual potentials of 2090-T3 aluminium alloy for several increments of the in-plane shear component $(\sigma_{33} = 0)$: (a) stress potential (SP) locus, as predicted by the CPB06ex4 criterion; (b) strain-rate potential (SRP) locus, as predicted by the proposed potential in Eq. (4.22).

Figure 4.5 represents the model predictions for uniaxial loading conditions in the plane of the sheet. There is a remarkable agreement with the experimental data (the error is virtually zero in these points). This is a consequence of the high flexibility of the model given the considered number of transformations. More crucially for the present work, Figure 4.5 demonstrates that the predictions when using the CPB06ex4 stress potential or the respective SRP formulation proposed in Eq. (4.22) are equal[14]. This is to be expected as the potentials are exact duals, contrasting with the results of (Kim *et al.*, 2007) where the predictions where not identical due to the pseudo-conjugate nature of the latter.

[14] To determine the uniaxial yield stresses and *r*-values (or any other yield limit for that matter), one can solve the inverse problem described in Eq. (4.57) substituting $\boldsymbol{s}$ with the relevant deviatoric stress tensor. In this case the nonzero components are $s_{\theta,11}^{\text{trial}} = (\cos^2\theta - 1/3)$, $s_{\theta,22}^{\text{trial}} = (\sin^2\theta - 1/3)$, $s_{\theta,33}^{\text{trial}} = -1/3$, $s_{\theta,12}^{\text{trial}} = (\sin 2\theta)/2$. Let $(\bar{\boldsymbol{d}}_\theta^{\text{p}}, \tau_\theta)$ be the solution. Then, the normalized uniaxial stress is $\sigma_\theta/\sigma_1^{\text{T}} = (1/\tau_\theta)$ and the *r*-values are determined using the classical expression, $r_\theta = -(\sin^2\theta\,\bar{d}_{\theta,11}^{\text{p}} - \sin(2\theta)\bar{d}_{\theta,12}^{\text{p}} + \cos^2\theta\,\bar{d}_{\theta,22}^{\text{p}})/(\bar{d}_{\theta,11}^{\text{p}} + \bar{d}_{\theta,22}^{\text{p}})$.

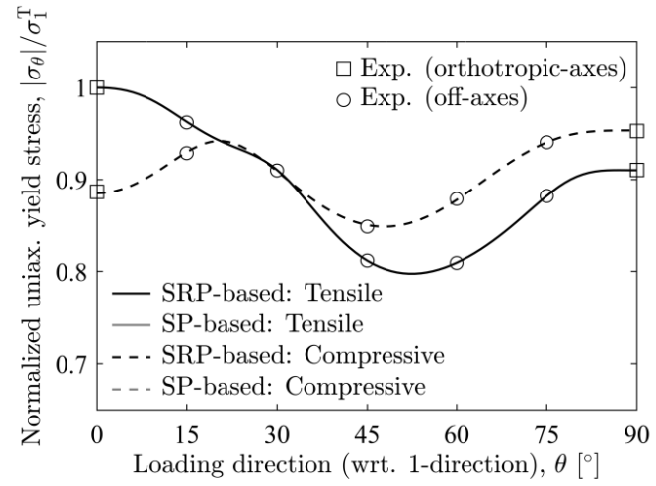

(a)

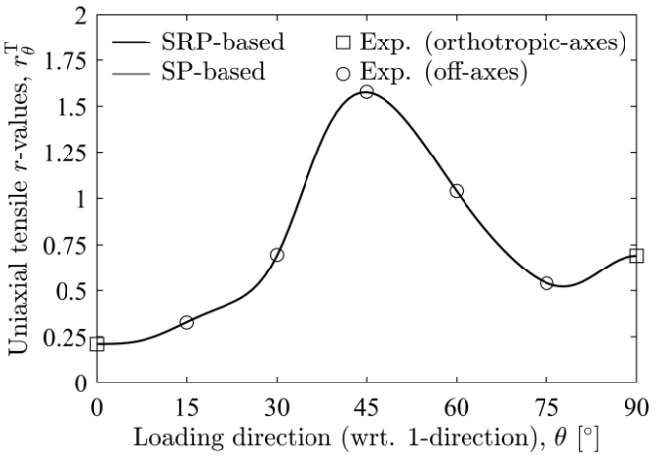

(b)

Figure 4.5 Uniaxial stress response in the plane of the sheet as predicted by the CPB06ex4 criterion and its proposed dual potential (Eq. (4.22)): (a) normalized tensile and compressive yield stresses; (b) tensile *r*-values.

4.6 Concluding remarks

In this chapter, the analytic expression for the orthotropic strain-rate potential conjugated with the non-quadratic stress potential of Plunkett *et al.* (2008) was derived. The strain-rate potential accounts for an arbitrary number of linear transformations and is an exact dual. Being the exact dual of a convex potential, it also enjoys convexity. Moreover, the material parameters are those of the stress potential, hence no specific parameter identification procedure is required. No constrains were imposed on the original form of the fourth order orthotropic tensors $\boldsymbol{\mathcal{C}}^{(n)}$, thus each transformation tensor holds nine independent anisotropic coefficients. If n_{ex} denotes the total number of linear transformations adopted in the model, then, under 3-D conditions, the proposed strain-rate potential involves: a single homogeneity parameter, a; n_{ex} parameters $k^{(n)}$ quantifying the tension-compression asymmetry; and $(9n_{\text{ex}}-1)$ independent anisotropy parameters associated with n_{ex} orthotropy tensors $\boldsymbol{\mathcal{C}}^{(n)}$, (note that, due to the homogeneity of the potentials, the parameter $C_{11}^{(1)}$ should be set to unity, or, equivalently, one should normalize all $\boldsymbol{\mathcal{C}}^{(n)}$ by $C_{11}^{(1)}$, or any other non-zero reference anisotropic parameter, $C_{ij}^{(n)}$, for that matter).

In contrast to the stress potential, the proposed potential does not lead to explicit expressions for the transformed strain-rate tensors (with the exception of a few particular cases, as discussed in §4.4.3). Therefore, an efficient numerical method was proposed in order to evaluate the potential and its gradient with respect to the deviatoric stress tensor. This method can be effortlessly included in a time integration algorithm for strain-rate-based elastic-plastic models within the finite element analysis. The presented application examples illustrated graphically the duality of the potentials and showed the exceptionally good description of the experimental data and its trends on cubic and hexagonal metals when a large number of linear transformations is employed. Naturally, the developed potential could also describe the anisotropic behaviour of materials whose tensile and compressive yield stresses are assumed equal, as is often the case with materials with cubic structure at large strains. The number of linear transformations in the model must account for the trade-in between model accuracy and accessibility: it must be simple enough to allow for efficient numerical handling and experimental characterization, while not disregarding the main trends of the observed mechanical behaviour.

A key accomplishment of this chapter is that it paves the way for the development of enhanced stress and strain-rate potentials for porous media based on the kinematic homogenization theory, by improving the description of the anisotropy and tension-compression asymmetry of the matrix (dense material). This task in tackled in the following chapter.

Chapter 5

Three-dimensional potentials for porous solids containing spherical voids

This chapter is devoted to the determination of approximate three-dimensional orthotropic plastic potentials for porous media containing randomly distributed spherical voids, as in the theory of Gurson (1977). The kinematic homogenization approach of Hill-Mandel (Hill, 1967; Mandel, 1971) and the limit-analysis theory (Drucker *et al.*, 1952; Hill, 1951), upon which macroscopic potentials are based, are first recalled. The employed local velocity fields and respective strain-rate tensors are presented. Efficient cubature methods of the volume averaging over the spherical RVE are proposed. A method for evaluating the macroscopic stress potential, conjugate of the obtained macroscopic strain-rate potential, is also provided. Lastly, the algorithmic aspects of the numerical homogenization scheme are summarized in pseudo-code format.

5.1 Fundamentals of porous solids and homogenization

In this subsection the mathematical framework regarding the variational characterization of porous ductile solids is reviewed. This includes results from the theories of homogenization, viz. Hill-Mandel lemma (Hill, 1967; Mandel, 1971) and the limit-analysis theory (Drucker *et al.*, 1952; Hill, 1951). The objective is to provide a general idea of the theories and assumptions employed in the derivation of the macroscopic potentials. For a comprehensive review of these topics, the reader is referred to specialized monographs (e.g. Prager and Hodge (1968); Suquet (1982); Nemat-Nasser and Hori (2013); Benzerga and Leblond (2010); Besson (2010); and Leblond *et al.* (2018).

5.1.1 Hill-Mandel homogenization

Let us consider representative volume element (RVE) of an arbitrary porous solid consisting of voids with traction-free boundaries embedded in a homogeneous rigid-plastic matrix. Following §3.4.1, let Ω denote the total domain, ω the domain occupied by the voids and $\partial\Omega$ and $\partial\omega$ their respective boundaries. Assuming that $\partial\Omega \bigcap \partial\omega = \varnothing$, then the porosity, f, is given by Eq. (3.8), i.e., $f = \mathrm{vol}(\omega)/\mathrm{vol}(\Omega)$. A Eulerian description is adopted to describe the problem. One defines $\boldsymbol{\sigma}$ as the Cauchy stress tensor and $\boldsymbol{d} \leftarrow \boldsymbol{d}^{\mathrm{p}}$ as the Eulerian (plastic) strain-rate tensor, (the superscript 'p' is omitted for readability). These tensors are defined at the microscopic scale, i.e. that of the voids. In the voids, ω, the local stress field is taken to be zero, i.e., $\forall \underline{\boldsymbol{x}} \in \omega,\ \boldsymbol{\sigma}(\underline{\boldsymbol{x}}) = \boldsymbol{0}$, consistent with the condition of traction-free boundaries, and

the local (alias microscopic) velocity field, $\underline{\boldsymbol{v}}$, associated with $\boldsymbol{d} \triangleq (1/2)(\nabla\underline{\boldsymbol{v}} + \nabla\underline{\boldsymbol{v}}^{\mathrm{T}})$ is extended in some arbitrary but C^1 manner.

Within the *kinematic* homogenization approach the boundary conditions are formulated in terms of a uniform strain-rate prescribed on the boundary of the RVE, i.e.

$$\underline{\boldsymbol{v}}(\underline{\boldsymbol{x}}) = \boldsymbol{D}\underline{\boldsymbol{x}}\ ,\ \forall\underline{\boldsymbol{x}} \in \partial\Omega\,. \tag{5.1}$$

where $\underline{\boldsymbol{v}}$ denotes the local velocity vector, $\underline{\boldsymbol{x}}$ a position vector and $\boldsymbol{D}$ a specified second-rank symmetric tensor. From the application of the Green's theorem and the extension of $\underline{\boldsymbol{v}}$ in the voids postulated above is possible to demonstrate that $\boldsymbol{D}$ is equal to the volume average of the microscopic deformation rate, $\boldsymbol{d}$, over the volume of the entire RVE (Benzerga and Leblond, 2010), i.e.:

$$\boldsymbol{D} = \langle \boldsymbol{d} \rangle_{\Omega}\,, \tag{5.2}$$

where the notation $\langle\cdot\rangle_V$ stands for volume averaging over V. Accordingly, $\boldsymbol{D}$ is the often referred to as the macroscopic strain-rate tensor. In the same spirit, one can define the macroscopic stress tensor, $\boldsymbol{\Sigma}$, as the volume average of the microscopic stress, $\boldsymbol{\sigma}$, i.e.:

$$\boldsymbol{\Sigma} = \langle \boldsymbol{\sigma} \rangle_{\Omega} = (1-f)\langle \boldsymbol{\sigma} \rangle_{\Omega\setminus\omega}\,, \tag{5.3}$$

where $\Omega\setminus\omega$ denotes the domain occupied by the dense phase of the RVE, i.e. the matrix, and the property $\langle \boldsymbol{\sigma} \rangle_{\omega} = \boldsymbol{0}$ was applied. In contrast, note that $\langle \boldsymbol{d} \rangle_{\omega}$ is generally not zero, as it is the sole responsible for the dilatational, alias hydrostatic, component of $\boldsymbol{D}$. Based on the boundary conditions in Eq. (5.1), one can define the set of incompressible kinematically admissible microscopic strain-rate fields consistent with a homogeneous strain rate, $\boldsymbol{d} \in \mathcal{K}(\boldsymbol{D})$, as:

$$\mathcal{K}(\boldsymbol{D}) = \left\{ \boldsymbol{d} \,|\, \exists\underline{\boldsymbol{v}}, \forall\underline{\boldsymbol{x}} \in \Omega,\ \boldsymbol{d} = \frac{1}{2}\left(\nabla\underline{\boldsymbol{v}} + \nabla^{\mathrm{T}}\underline{\boldsymbol{v}}\right),\ \text{and}\ \forall\underline{\boldsymbol{x}} \in \partial\Omega,\ \underline{\boldsymbol{v}} = \boldsymbol{D}\underline{\boldsymbol{x}},\ \text{and} \right.$$
$$\left. \forall\underline{\boldsymbol{x}} \in \Omega\setminus\omega,\ \mathrm{tr}(\boldsymbol{d}) = 0 \right\}, \tag{5.4}$$

the latter condition enforcing the incompressibility of the solid phase of the RVE. Provided that: (i) the local velocity field, $\underline{\boldsymbol{v}}(\underline{\boldsymbol{x}})$, imposing an arbitrary local strain-rate field, $\boldsymbol{d}(\underline{\boldsymbol{x}})$, is kinematically admissible with $\boldsymbol{D}$, i.e. it obeys Eq. (5.1); and (ii) the microscopic stress field, $\boldsymbol{\sigma}(\underline{\boldsymbol{x}})$, is statically admissible with $\boldsymbol{\Sigma}$, i.e. it obeys Eq. (5.4), as well as traction-free boundary conditions on the voids ($\forall\underline{\boldsymbol{x}} \in \Omega$, $\boldsymbol{\sigma}(\underline{\boldsymbol{x}})\underline{\boldsymbol{n}} = \underline{\boldsymbol{0}}$, where $\underline{\boldsymbol{n}}$ is the unit normal), then the Hill-Mandel Lemma (Hill, 1967; Mandel, 1971) applies, hence:

$$\langle \boldsymbol{\sigma} : \boldsymbol{d} \rangle_{\Omega} \triangleq \langle \boldsymbol{\sigma} \rangle_{\Omega} : \langle \boldsymbol{d} \rangle_{\Omega} = \boldsymbol{\Sigma} : \boldsymbol{D}\,, \tag{5.5}$$

Interestingly, the equalities in Eq. (5.2), (5.3) and (5.5) hold true in the case of the *static* homogenization approach, in which a uniform stress, $\boldsymbol{\Sigma}$, (rather than uniform strain-rate) is prescribed on the boundary of the RVE. In the latter case, the statically admissible stress field is defined as $\boldsymbol{\sigma} \in \mathcal{S}(\boldsymbol{\Sigma}) = \{\boldsymbol{\sigma} \,|\, \forall\underline{\boldsymbol{x}} \in \Omega,$ $\mathrm{div}(\boldsymbol{\sigma}(\underline{\boldsymbol{x}})) = 0,\ \boldsymbol{\sigma}\underline{\boldsymbol{n}} = \boldsymbol{\Sigma}\underline{\boldsymbol{n}}, \forall\underline{\boldsymbol{x}} \in \partial\Omega\}$, (rather than Eq. (5.3)), and the associated set of kinematically admissible fields consist of those obeying Eq. (5.2) (rather than Eq. (5.1)). Nevertheless, the focus is solely on the kinematic approach, the reasons being discussed in the following paragraphs.

5.1.2 Limit analysis

The limit analysis theory combined with the results from the Hill-Mandel homogenization is known to provide a suitable framework to formulate constitutive criteria for porous solids (e.g. Benzerga and Leblond (2010); Gurson (1977); and Leblond *et al.* (2018)). Indeed, these allow to conveniently perform the scale transition operation and conveying the signature of the microstructural information into the macroscopic constitutive behaviour.

Classical limit analysis theory is restricted to ideal plastic materials within a linearized (small strain) framework. The matrix material is therefore considered incompressible, ideal-plastic and obeying some rate-independent constitutive law, described by a convex stress-based plastic potential, $\varphi(\boldsymbol{\sigma})$, homogeneous of degree one in stresses with respect to positive multipliers, as well as obeying the associated flow rule. Let $f(\boldsymbol{\sigma},\tau) \triangleq (\varphi(\boldsymbol{\sigma}) - \tau)$ denote the yield function associated with $\varphi(\boldsymbol{\sigma})$, where τ is a positive scalar with the dimension of stress and $\varphi(\boldsymbol{\sigma})$ expresses the equivalent stress function. Hence, the constitutive relations described in §4.2.1 (Eqs. (4.7), (4.13), (4.14)) can be summarized as:

$$\boldsymbol{d} = \dot{\lambda}\frac{\partial f(\boldsymbol{\sigma})}{\partial \boldsymbol{\sigma}} = \dot{\lambda}\frac{\partial \varphi(\boldsymbol{\sigma})}{\partial \boldsymbol{\sigma}} \Leftrightarrow \begin{cases} \boldsymbol{\sigma} = \tau \dfrac{\partial \psi(\boldsymbol{d})}{\partial \boldsymbol{d}} \\ \psi(\boldsymbol{d}) = \dot{\lambda} \end{cases}, \quad \dot{\lambda} \geq 0, \ f \leq 0, \ f\dot{\lambda} = 0, \tag{5.6}$$

where the meaning for the variables was given in the abovementioned subsection. For a given microscopic strain-rate field, $\boldsymbol{d}$, the associated microscopic (or local) plastic dissipation rate, $\pi(\boldsymbol{d})$ is defined as (holds the same physical meaning as Eq. (4.11), yet renamed here to follow the literature practice):

$$\pi(\boldsymbol{d}) = \sup_{\boldsymbol{\sigma}^* \in \bar{\mathcal{E}}} \left(\boldsymbol{\sigma}^* : \boldsymbol{d} \right), \tag{5.7}$$

(cf. the principle of maximum plastic work, Hill, (1951), the supremum being taken over all microscopic stresses that fall within the microscopic convex domain of reversibility, $\bar{\mathcal{E}}$, (closure of the elastic domain, $\mathcal{E} = \{\boldsymbol{\sigma} \in \mathcal{S}_2 \mid f(\boldsymbol{\sigma}) < 0\}$, as defined in Eq. (4.3)). Note that $\boldsymbol{d}$ must be traceless, otherwise $\pi(\boldsymbol{d})$ would be infinite. If the velocity field, $\underline{\boldsymbol{v}}(\underline{\boldsymbol{x}})$, is kinematically admissible and the microscopic stress field $\boldsymbol{\sigma}(\underline{\mathbf{x}})$, is both statically and plastically admissible, the latter meaning that $\forall \mathbf{x} \in \Omega$, $\boldsymbol{\sigma}(\underline{\boldsymbol{x}}), \in \bar{\mathcal{E}}$, it follows from the application of the Hill-Mandel lemma (Eq. (5.5)), the definition of $\pi(\boldsymbol{d})$ in Eq. (5.7) and the assumed extensions for the stress and strain-rate fields in the voids that:

$$\forall \boldsymbol{d} \in \mathcal{S}_2, \ \ \boldsymbol{\Sigma} : \boldsymbol{D} \leq \left\langle \pi(\boldsymbol{d}) \right\rangle_{\Omega}. \tag{5.8}$$

This inequality holds true for arbitrary strain-rate fields. A tighter upper bound is therefore associated with the set of kinematically admissible microscopic strain-rate fields, $\boldsymbol{d} \in \mathcal{K}(\boldsymbol{D})$, (e.g. Eq. (5.4) for the kinematic approach) i.e.:

$$\boldsymbol{\Sigma} : \boldsymbol{D} \leq \Pi(\boldsymbol{D}) \triangleq \inf_{\boldsymbol{d} \in \mathcal{K}(\boldsymbol{D})} \left\langle \pi(\boldsymbol{d}) \right\rangle_{\Omega}. \tag{5.9}$$

where one introduces the function $\Pi(\boldsymbol{D})$ as the macroscopic plastic dissipation associated with $\boldsymbol{D}$. Based on the previous expression it is possible to define a macroscopic domain of elasticity, $\mathscr{E}$, bounded by the set:

$$\mathscr{E} = \left\{ \boldsymbol{\Sigma} \mid \forall \boldsymbol{D}, \boldsymbol{\Sigma} : \boldsymbol{D} \leq \Pi(\boldsymbol{D}) \right\} . \tag{5.10}$$

$\boldsymbol{D}$ being the independent variable (i.e. the parameter). Of particular interest is the boundary of this set, $\partial\mathscr{E}$, describing the envelope of the hyperplanes $\boldsymbol{\Sigma} : \boldsymbol{D} = \Pi(\boldsymbol{D})$ whose parametric equation is given as:

$$\begin{cases} \boldsymbol{\Sigma} : \boldsymbol{D} - \Pi(\boldsymbol{D}) = 0 \\ \boldsymbol{\Sigma} - \dfrac{\partial \Pi}{\partial \boldsymbol{D}}(\boldsymbol{D}) = \boldsymbol{0} \end{cases} . \tag{5.11}$$

Since $\Pi(\boldsymbol{D})$ is positively homogeneous of degree one, (i.e., $\Pi(\xi \boldsymbol{D}) = \xi \Pi(\boldsymbol{D}), \ \forall \xi > 0$), the theorem of Euler for homogeneous functions implies that the first expression in Eq. (5.10) is included in the second and, accordingly, the parametric equation of $\partial\mathscr{E}$ reduces to:

$$\boldsymbol{\Sigma} = \frac{\partial \Pi}{\partial \boldsymbol{D}}(\boldsymbol{D}) , \tag{5.12}$$

which, according to the classical results of limit analysis, defines the macroscopic yield surface of the porous solid. Since $\partial\Pi(\boldsymbol{D})/\partial\boldsymbol{D}$ is homogeneous of degree zero, elimination of $\boldsymbol{D}$ from the parametric form in Eq. (5.12) is, in theory, possible. Hence, $\partial\mathscr{E}$ can be written in a standard explicit fashion as:

$$\mathcal{F}(\boldsymbol{\Sigma}, \tau) \triangleq \Phi(\boldsymbol{\Sigma}) - \tau = 0 , \tag{5.13}$$

where $\mathcal{F}(\boldsymbol{\Sigma})$ denotes the macroscopic yield criterion, and $\Phi(\boldsymbol{\Sigma})$ plays the role of an equivalent stress function, coined in this work as macroscopic stress potential (yet not of the Legendre-type, recall discussion in §4.2.1). Moreover, according to the Hill-Mandel lemma it is possible to demonstrate that, if the microscopic plastic flow is assumed to obey Drucker's stability postulate (Drucker *et al.*, 1952), (or, equivalently, the principle of maximum plastic work (Hill, 1951)), then the same principle holds at the macroscale. Accordingly, (i) the macroscopic elastic domain $\mathscr{E}$ is necessarily convex; and (ii) given a limit load, $\boldsymbol{\Sigma}$, (i.e. lying on $\partial\mathscr{E}$), the corresponding macroscopic plastic strain rate, $\boldsymbol{D}$, belongs to the local hypercone of normals to $\partial\mathscr{E}$. If the boundary $\partial\mathscr{E}$ is smooth in the limit load $\boldsymbol{\Sigma}$, then it admits a local tangent hyperplane, i.e. the macroscopic flow rule obeys the normality rule, hence the yield criterion so derived indeed serves as a plastic potential and one can write (c.f. Eq. (5.6)):

$$\boldsymbol{D} = \dot{\Lambda} \frac{\partial \Phi}{\partial \boldsymbol{\Sigma}}(\boldsymbol{\Sigma}), \quad \dot{\Lambda} \geq 0 , \tag{5.14}$$

where the scalar $\dot{\Lambda}$ is the macroscopic plastic multiplier rate. In summary, if one assumes a microscopic flow rule obeying normality, such property is preserved at the macroscale, as shown in Hill (1967) and later in Gurson (1977) for the particular case of porous metals. From Eq. (5.9), it is clear that in order to derive the expression for $\Pi(\boldsymbol{D})$, one needs to evaluate the expression of the local plastic dissipation, $\pi(\boldsymbol{d})$. Following the reasoning of Eq. (4.12), one gets:

$$\pi(\boldsymbol{d}) = \boldsymbol{\sigma} : \boldsymbol{d} = \boldsymbol{\sigma} : \dot{\lambda} \frac{\partial \varphi(\boldsymbol{\sigma})}{\partial \boldsymbol{\sigma}} = \dot{\lambda} \varphi(\boldsymbol{\sigma}) = \psi(\boldsymbol{d}) \tau , \ \forall \underline{\boldsymbol{x}} \in \Omega \backslash \omega, \tag{5.15}$$

with $\pi(\boldsymbol{d}) = 0,\ \forall \underline{\boldsymbol{x}} \in \omega$. The previous expression shows that the determination of the microscopic plastic dissipation rate, $\pi(\boldsymbol{d})$, entails the evaluation of the strain-rate potential, $\psi(\boldsymbol{d})$, associated with the yield criterion of the matrix. Given that the yield function in Eq. (5.13) is homogeneous of degree one with respect to positive multipliers, based on the application of the work-equivalence principle at the macroscale, one can define a meaningful dual relationship as:

$$\begin{cases} \boldsymbol{\Sigma} = \tau \dfrac{\partial \Psi(\boldsymbol{D})}{\partial \boldsymbol{D}}, & \dot{\Lambda} \geq 0,\ \mathcal{F} \leq 0,\ \mathcal{F}\dot{\Lambda} = 0, \\ \Psi(\boldsymbol{D}) = \dot{\Lambda} \end{cases} \tag{5.16}$$

where $\Psi(\boldsymbol{D})$ is the macroscopic strain-rate potential, dual of the macroscopic stress potential, $\Phi(\boldsymbol{\Sigma})$, and is also homogeneous of degree one with respect to positive multipliers. Note that Eq. (5.16) is the macroscopic counterpart of Eq. (5.6). Combining Eq. (5.11), Eq. (5.16), the macroscopic yield condition, $\Phi(\boldsymbol{\Sigma}) = \tau$, and the application of Euler theorem for homogeneous functions allows to write:

$$\Pi(\boldsymbol{D}) = \boldsymbol{\Sigma} : \boldsymbol{D} = \left(\tau \frac{\partial \Psi(\boldsymbol{D})}{\partial \boldsymbol{D}} \right) : \boldsymbol{D} = \tau \Psi(\boldsymbol{D}) = \tau \dot{\Lambda}, \quad \dot{\Lambda} \geq 0,\ \mathcal{F} \leq 0,\ \mathcal{F}\dot{\Lambda} = 0, \tag{5.17}$$

The previous expression, representing the macroscopic counterpart of Eq. (5.15), shows that, within the adopted kinematical homogenization approach, the macroscopic strain-rate potential $\Psi(\boldsymbol{D})$, is related with the macroscopic plastic dissipation function $\Pi(\boldsymbol{D})$ via the same scalar as in the microscale (see Eq. (5.15)), viz. the scalar which defines the yield condition of the rigid-plastic matrix, $\varphi(\boldsymbol{\sigma}) = \tau$.

5.1.3 Principle of determination of the macroscopic criteria

In truth, the variational problem presented above is still ill-posed. The reason is twofold: first, the geometry of the RVE is only known statistically for most porous solids; and second, the actual boundary conditions to which such RVE is subjected when macroscopically loaded are unknown (Besson *et al.*, 2009). In order to bypass the first problem, one can assume the ergodic hypothesis[15], and thus a single realization of a RVE must be specified. Regarding the boundary conditions, as mentioned previously, one may choose to adopt a kinematic or a static homogenization approach[16]. Since the space of kinematically admissible velocity fields is smaller in the former, the resulting dissipation function, $\Pi(\boldsymbol{D})$, is greater, hence the macroscopic domain, $\bar{\mathscr{E}}$, is larger, i.e., $\bar{\mathscr{E}}_{\underline{\boldsymbol{v}}=\boldsymbol{D}\underline{\boldsymbol{x}}} \supset \bar{\mathscr{E}}_{\boldsymbol{\sigma}\underline{\boldsymbol{n}}=\boldsymbol{\Sigma}\underline{\boldsymbol{n}}}$, where the notation is self-explanatory. Although no formal proof is available, it is likely that the true yield locus of the porous solid $\bar{\mathscr{E}}$, lies between these, i.e. $\bar{\mathscr{E}}_{\underline{\boldsymbol{v}}=\boldsymbol{D}\underline{\boldsymbol{x}}} \supset \bar{\mathscr{E}} \supset \bar{\mathscr{E}}_{\boldsymbol{\sigma}\underline{\boldsymbol{n}}=\boldsymbol{\Sigma}\underline{\boldsymbol{n}}}$ (Benzerga and Leblond, 2010). In theory, regardless of the adopted homogenization approach, the minimization problem in Eq. (5.9) ought to be performed over the *complete* set of local velocity fields, $\underline{\boldsymbol{v}}$, compatible with the adopted boundary conditions. In practice this problem can be solved numerically, e.g. by application of the FEM in combination with convex optimization tools (Pastor *et al.*, 2013, 2009). However, given the computational cost of latter approach, analytical-based analyses are often preferred. In this context, the minimization procedure is

[15] According to ergodic hypothesis, all the statistical information is available in a single realization of the RVE.
[16] Other types of boundary conditions could be considered, viz. periodic and mixed boundary conditions, such as those used in the cell model studies, however these do not pertain to the Hill-Mandel homogenization theory.

relaxed and $\Pi(\boldsymbol{D})$ is evaluated based on some *partial* minimization over a reduced set of trial velocity fields, i.e. a subset of $\mathcal{K}(\boldsymbol{D})$, which inherently results in an upper bound estimate for the macroscopic plastic dissipation function, $\Pi^{+}(\boldsymbol{D})$. As a result, one obtains an *approximate* macroscopic yield locus, $\partial\bar{\mathscr{E}}_{\Pi^{+}(\boldsymbol{D})}$, exterior to the exact one, $\partial\bar{\mathscr{E}}$, i.e. $\bar{\mathscr{E}}_{\Pi^{+}(\boldsymbol{D})} \supset \bar{\mathscr{E}}$, which holds true for both static and kinematic boundary conditions. Accordingly, the kinematic approach is often preferred to the static one for the following reasons: first, the space of velocity fields is smaller, the search for a 'good' approximation of the infimum in Eq. (5.9) ought to be easier; and second, and more crucially, the use of kinematic boundary conditions ensures that $\bar{\mathscr{E}}^{\Pi^{+}(\boldsymbol{D})}_{\underline{\boldsymbol{v}}=\boldsymbol{D}\underline{\boldsymbol{x}}} \supset \bar{\mathscr{E}}$, i.e. it preserves the upper bound character of the macroscopic yield locus (whereas, on the contrary, the original lower bound character of the static approach can no longer be guaranteed). In fact, the kinematic homogenization approach is widely used to model metallic materials (Benzerga and Leblond, 2014; Benzerga and Besson, 2001; Gurson, 1977; Keralavarma and Benzerga, 2008; Keralavarma and Chockalingam, 2016; Monchiet *et al.*, 2008; Morin, Leblond and Kondo, 2015; Morin, Leblond, Benzerga, *et al.*, 2016; Stewart and Cazacu, 2011; Thomason, 1985), whereas the static homogenization is more prevalent for modelling porous geologic materials and polymers (Dormieux *et al.*, 2006; Hsu *et al.*, 2009; Salençon, 1983; Thoré *et al.*, 2011). In closing, is should be remarked that the fact that one aims to determine $\Pi^{+}(\boldsymbol{D})$ instead of $\Pi(\boldsymbol{D})$, i.e. disregarding the minimization procedure, does not imply that it is possible to derive an explicit expression for the approximate stress-based potential of the porous solid: a closed-form criterion may only be attainable in a parametric fashion (e.g. Alves *et al.*, 2014; Cazacu *et al.*, 2014); or it cannot be obtained at all. Issues related with the volume averaging of $\pi(\boldsymbol{d})$ over the RVE (recall Eq. (5.9)) may preclude the analytical determination of $\Pi^{+}(\boldsymbol{D})$. In such cases, either new upper bounds, $\Pi^{++}(\boldsymbol{D}) \geq \Pi^{+}(\boldsymbol{D})$, are postulated, (e.g. by means of the Cauchy-Schwarz inequality) such that the closed-form determination of a modified integral is possible; or else the integration must inevitably be performed numerically (e.g. Cazacu and Revil-Baudard, 2015; Leblond *et al.*, 2018; Morin *et al.*, 2017), which, naturally, does not allow for closed-form expressions for the macroscopic potentials. The present work falls into the latter case.

5.2 Statement of the problem

It follows from what precedes that the development of macroscopic plastic criteria for porous solids invariably requires the following to be defined: (i) the geometry of the RVE; (ii) a microscale plasticity model, necessary obeying an associated flow rule; and (iii) the kinematically admissible local velocity fields, $\underline{\boldsymbol{v}}(\underline{\boldsymbol{x}})$, $\forall \underline{\boldsymbol{x}} \in \Omega \backslash \omega$, (and the corresponding microscopic strain-rate tensor, $\boldsymbol{d}$) defining a subset of $\mathcal{K}(\boldsymbol{D})$ (c.f. Eq. (5.4)). In the following, each one of these basic elements is specified.

5.2.1 RVE geometry

In the spirit of Gurson's (1977) analysis, the RVE consists of a hollow sphere with outer radius b, containing a concentric spherical void of radius a. Figure 5.1 illustrates the spherical RVE and defines the adopted Cartesian, (x_1, x_2, x_3), and spherical, (r, θ, ϕ) (with $\theta \in [0, \pi]$, $\phi \in [0, 2\pi]$) coordinate systems associated with the orthonormal bases $(\underline{\boldsymbol{e}}_1, \underline{\boldsymbol{e}}_2, \underline{\boldsymbol{e}}_3)$ and $(\underline{\boldsymbol{e}}_r, \underline{\boldsymbol{e}}_\theta, \underline{\boldsymbol{e}}_\phi)$, respectively. The geometry of

the RVE is fully determined by the porosity, $f = a^3/b^3$, which is the unique microstructural-based variable of the analysis. The choice of this RVE is driven by the simplicity it affords both from the analytical (viz. the definition of boundary conditions within the Hill-Mandel homogenization framework and the local trial velocity fields); and the numerical (viz. integration scheme) standpoints. While the hollow sphere model in unable to represent true periodic microstructures (in the sense of space-filling configurations, as is the case with a cubic unit cell), it still offers a reasonable representation for the cases in which the voids are nearly spherical and uniformly distributed (Hsu *et al.*, 2009). Within the framework of damage mechanics, the adopted RVE is consistent with the hypothesis of isotropic damage, in which a damaged medium is assumed to have a random distribution of microdefect orientations, and thus the damaged state can be completely characterized by a single scalar, (in this work, f). In most cases this assumption is indeed reasonable given the typical random shape and distribution of the microstructural particles triggering damage initiation (viz. void nucleation).

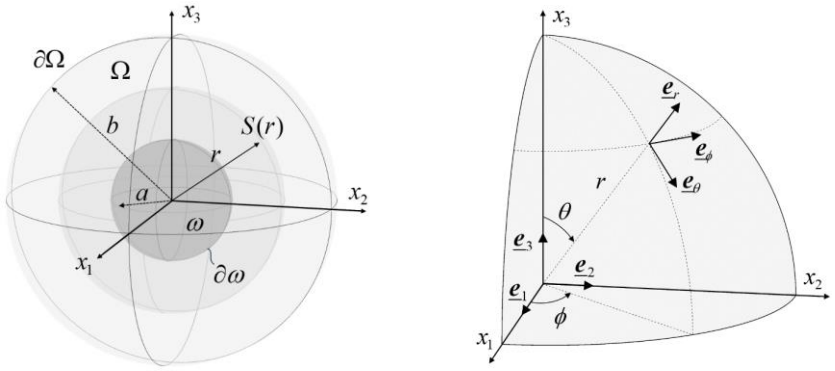

(a) (b)

Figure 5.1 Geometry of the spherical RVE: (a) definition of an arbitrary spherical surface of radius $r \in [a,b]$, $S(r)$; and the inner, $\partial\omega$, and outer, $\partial\Omega$, RVE boundaries; (b) the adopted Cartesian, $(\underline{\boldsymbol{e}}_1, \underline{\boldsymbol{e}}_2, \underline{\boldsymbol{e}}_3)$, and spherical, $(\underline{\boldsymbol{e}}_r, \underline{\boldsymbol{e}}_\theta, \underline{\boldsymbol{e}}_\phi)$, bases on one-eight of $S(r)$.

5.2.2 Microscale constitutive model

The matrix material is assumed rigid-plastic and obeying the (generally) non-quadratic orthotropic yield criterion of Plunkett *et al.* (2008), based on an arbitrary number of orthotropic transformations, as showed in Eq. (4.19). The associated dual potential is of paramount importance for the present analysis and was developed in Chapter 4 (see Eqs. (4.22)-(4.27), p. 67). Moreover, the numerical scheme in Box 4.1 to evaluate the SRP, $\psi(\boldsymbol{d})$, and its first derivative, $\partial\psi/\partial\boldsymbol{d}$, simultaneously, should also be kept in mind as it is the foundation of the numerical methods developed in the forthcoming subsection.

5.2.3 Local velocity fields and boundary conditions

As discussed in §5.1.3, the choice of relevant trial microscopic velocity fields is a crucial task in the development of approximate macroscopic criteria. Indeed, it is evident that the adoption of sophisticated velocity fields should favour the quality of the homogenization. Unfortunately, very few velocity fields compatible with uniform strain-rate boundary conditions are known. In the case of the hollow sphere

RVE considered here, to the best knowledge of the author, the only known velocity fields verifying the incompressibility property, compatible or not with such boundary conditions, are those proposed by: (i) Rice and Tracey (1969), Budiansky *et al.* (1982) and Huang (1991), (the last two being extensions of the first, based on the consideration of additional velocity field terms derived from a stream function those contribution ought to be determined by minimization of a functional); and by (ii) Monchiet *et al.* (2011), based on Eshelby's inclusion theory. In this work both formulations are considered in order to compare the results of each one. Their expressions and admissibility conditions are now discussed.

Rice and Tracey (1969) velocity fields

In agreement with Gurson (1977), a truncated form of the classical Rice and Tracey (1969) velocity fields, who studied the growth of an isolated void in an infinite rigid perfectly plastic medium obeying the von Mises criterion, is adopted. The velocity field in the matrix consists of a linear combination of two fundamental fields: an isotropic radial/dilatational expansion $\underline{\boldsymbol{v}}^{\mathrm{A}}$, inspired from the solution of the problem of a hollow sphere loaded hydrostatically; and a uniform extension $\underline{\boldsymbol{v}}^{\mathrm{B}}$, as:

$$\forall \underline{\boldsymbol{x}} \in \mathbb{R}^3 \backslash \omega,\ \ \underline{\boldsymbol{v}}^{\mathrm{RT},\infty}(\underline{\boldsymbol{x}}) = A\underline{\boldsymbol{v}}^{\mathrm{A}} + B\underline{\boldsymbol{v}}^{\mathrm{B}},\ \text{with}\ \underline{\boldsymbol{v}}^{\mathrm{A}} = \frac{1}{r^2}\underline{\boldsymbol{e}}_r,\ \text{and}\ \underline{\boldsymbol{v}}^{\mathrm{B}} = \boldsymbol{\beta}\underline{\boldsymbol{x}}, \tag{5.18}$$

where $\boldsymbol{\beta}$ is a symmetric second order tensor defining a remote strain-rate field, and A and B are arbitrary parameters supposed to be determined by a minimization procedure in the determination of the infimum in Eq. (5.9). In practice however, no minimization is actually needed since uniform strain-rate boundary conditions of the type $\underline{\boldsymbol{v}}(\underline{\boldsymbol{x}} = b\underline{\boldsymbol{e}}_r) = \boldsymbol{D}\underline{\boldsymbol{x}}$ (Eq. (5.1)) and the incompressibility condition, $\mathrm{div}\,\underline{\boldsymbol{v}}(\underline{\boldsymbol{x}}) = 0$, $\forall \underline{\boldsymbol{x}} \in \Omega\backslash\omega$, require that $A = b^3 D_{\mathrm{m}}$ and $B\boldsymbol{\beta} = \boldsymbol{D}'$, where $\boldsymbol{D}'$ and D_{m} represent the deviatoric and the hydrostatic part of the imposed macroscopic strain rate tensor $\boldsymbol{D}$, respectively, i.e., $\boldsymbol{D} = \boldsymbol{D}' + D_{\mathrm{m}}\boldsymbol{I}$, with $D_{\mathrm{m}} = \mathrm{tr}(\boldsymbol{D})/3$ and $\boldsymbol{I}$ is the second-order identity tensor. Hence, the Rice and Tracey microscopic velocity fields, $\underline{\boldsymbol{v}}^{\mathrm{RT}}$, in the (finite) RVE are given as:

$$\forall \underline{\boldsymbol{x}} \in \Omega\backslash\omega,\ \ \underline{\boldsymbol{v}}^{\mathrm{RT}}(\underline{\boldsymbol{x}}) = \boldsymbol{D}'\underline{\boldsymbol{x}} + D_{\mathrm{m}}\left(\frac{b^3}{r^2}\right)\underline{\boldsymbol{e}}_r\,. \tag{5.19}$$

Accordingly, the associated microscopic strain rate tensor, $\boldsymbol{d}^{\mathrm{RT}}$, is given as follows:

$$\forall \underline{\boldsymbol{x}} \in \Omega\backslash\omega,\ \ \boldsymbol{d}^{\mathrm{RT}}(\underline{\boldsymbol{x}}) = \boldsymbol{D}' + D_{\mathrm{m}}\left(\frac{b}{r}\right)^3\left(-2\underline{\boldsymbol{e}}_r \otimes \underline{\boldsymbol{e}}_r + \underline{\boldsymbol{e}}_\theta \otimes \underline{\boldsymbol{e}}_\theta + \underline{\boldsymbol{e}}_\phi \otimes \underline{\boldsymbol{e}}_\phi\right). \tag{5.20}$$

Note that both Cartesian and spherical coordinate system were used in Eqs. (5.19)-(5.20) for shortness. In practice, the determination of the plastic dissipation rate, $\pi(\boldsymbol{d})$, in Eq. (5.15) requires $\boldsymbol{d}^{\mathrm{RT}}$ to be expressed in Cartesian coordinates alone (those defining the orthotropy axes). This can be achieved by application of the rotation matrix relating the Cartesian and spherical basis, as described in Appendix C. Moreover, it must be remarked that $\boldsymbol{d}^{\mathrm{RT}}(\underline{\boldsymbol{x}}) = \boldsymbol{d}^{\mathrm{RT}}(-\underline{\boldsymbol{x}})$, i.e. $\boldsymbol{d}^{\mathrm{RT}}$ in Eq. (5.20) is an even function.

At this point one may question the hypothesis of the adoption of an 'isotropic' expansion field in order to represent the behaviour of solids assumed orthotropic. Indeed, for these materials, the isotropic expansion field (second term in Eq. (5.19)), obtained from the consideration of a plastically isotropic

medium, is no longer the exact for a hydrostatic loading. However, it is frequent practice in the literature to adopt this type of fields, even when considering orthotropic matrices (e.g., Benzerga and Besson, 2001; Keralavarma and Benzerga, 2010; Morin *et al.*, 2015; Stewart and Cazacu, 2011). Recent numerical studies (Pastor *et al.*, 2012; Morin *et al.*, 2014), suggest that criteria obtained in this fashion are still in good agreement with the 'exact' solutions, (those based on finite element method numerical limit-analyses), provided that the anisotropy is moderate (Morin, Leblond and Kondo, 2015). However, such numerical studies did not consider matrix materials displaying tension-compression asymmetry, and/or non-quadratic yield criteria. In Chapter 6, the latter case is considered, and it is shown that the adoption of such isotropic expansion fields still leads to reasonable estimates for the approximate yield loci of such porous solids. Nevertheless, it is interesting to assess if the analysis can benefit from adopting trial velocity fields which indeed admit 'anisotropic' expansion fields. An example of such field is presented in the following.

Eshelby-based velocity fields

Following Monchiet *et al.* (2014, 2011, 2007), the local velocity fields in the matrix can be postulated based on the results of the Eshelby inclusion problem (Eshelby, 1957, 1959). Eshelby demonstrated that the strain rate field of an ellipsoidal elastic inclusion subjected to a uniform arbitrary eigenstrain[17] rate, $\boldsymbol{d}^*$, embedded in an infinite linear medium is: (i) homogeneous inside the inclusion – the interior point solution; and (ii) heterogeneous outside the inclusion – the exterior point solution (e.g. see Mura, 2013). In the particular case of an inclusion occupying a finite subdomain ω with a spherical shape of radius a, and assuming the medium as incompressible, the Eshelby velocity fields, $\underline{\boldsymbol{v}}^{\mathrm{E},\infty}$, are in the form:

$$\underline{\boldsymbol{v}}^{\mathrm{E},\infty}(\underline{\boldsymbol{x}}) = \begin{cases} \left[\boldsymbol{\mathcal{T}}(a):\boldsymbol{d}^*\right]\underline{\boldsymbol{x}}, & \forall \underline{\boldsymbol{x}} \in \omega \\ \left[\boldsymbol{\mathcal{T}}(r):\boldsymbol{d}^*\right]\underline{\boldsymbol{x}} + \dfrac{a^3}{r^2}\left(1-\dfrac{a^2}{r^2}\right)\hat{d}^*_{rr}\underline{\boldsymbol{e}}_r, & \forall \underline{\boldsymbol{x}} \in \mathbb{R}^3\backslash\omega \end{cases}. \tag{5.21}$$

where the component $\hat{d}^*_{rr}$ in the spherical basis is given by $\hat{d}^*_{rr} = \boldsymbol{d}^* : (\underline{\boldsymbol{e}}_r \otimes \underline{\boldsymbol{e}}_r)$ and $\boldsymbol{\mathcal{T}}$ is a fourth order tensor containing the major symmetry ($\mathcal{T}_{ijkl} = \mathcal{T}_{ijkl}$) and both minor symmetries ($\mathcal{T}_{ijkl} = \mathcal{T}_{ijikl}, \mathcal{T}_{ijkl} = \mathcal{T}_{ijilk}$) whose non-zero components in the Cartesian coordinate system are given as:

$$\begin{aligned} \mathcal{T}_{1111} = \mathcal{T}_{2222} = \mathcal{T}_{3333} = \frac{3}{5}\frac{a^3}{r^5}, \\ \mathcal{T}_{1122} = \mathcal{T}_{1133} = \mathcal{T}_{2233} = \mathcal{T}_{1212} = \mathcal{T}_{1313} = \mathcal{T}_{2323} = \frac{a^3}{5r^5}, \end{aligned} \tag{5.22}$$

the remaining components being obtained by the abovementioned symmetries. Note that $\boldsymbol{\mathcal{T}}$ depends exclusively on the radial coordinate. Moreover, the second term in Eq. (5.21) for $\underline{\boldsymbol{x}} \in \mathbb{R}^3\backslash\omega$ vanishes at $r = a$, i.e. in the boundary of the spherical inclusion, which ensures the continuity of the velocity field. The strain rate tensor associated with the Eshelby velocity field in Eq. (5.21), $\boldsymbol{d}^{\mathrm{E},\infty}$, can be written as:

[17] Eigenstrain denotes a stress-free deformation strain, e.g. associated with thermal expansion, initial strain, phase transformation (e.g. see Ryu *et al.* (2019) and references therein).

$$\boldsymbol{d}^{\mathrm{E},\infty}(\underline{\boldsymbol{x}}) = \boldsymbol{\mathcal{D}} : \boldsymbol{d}^{*}, \text{ with } \boldsymbol{\mathcal{D}}(r) = \begin{cases} \boldsymbol{\mathcal{S}}, & \forall \underline{\boldsymbol{x}} \in \omega \\ \boldsymbol{\mathcal{T}}(r) + \boldsymbol{\mathcal{H}}(r) & \forall \underline{\boldsymbol{x}} \in \mathbb{R}^3 \backslash \omega \end{cases}, \tag{5.23}$$

where $\boldsymbol{\mathcal{S}} \leftarrow \boldsymbol{\mathcal{T}}(r=a)$ is the well-known Eshelby tensor for a spherical inclusion in an infinite elastic incompressible medium, given in the Cartesian coordinate system by the isotropic fourth order tensor:

$$\mathcal{S}_{ijkl} = \frac{1}{5}\left(\delta_{ij}\delta_{kl} + \delta_{ik}\delta_{jl} + \delta_{il}\delta_{jk}\right), \; i,j,k,l = 1,2,3, \tag{5.24}$$

where δ_{ij} denotes the Kronecker delta operator. Note that tensor $\boldsymbol{\mathcal{S}}$ does not depend on the inclusion radius due to the absence of a characteristic length scale in Eshelby's analysis. The fourth order tensor $\boldsymbol{\mathcal{H}}$ in Eq. (5.23) is more readily written in the spherical coordinate system, $(\underline{\boldsymbol{e}}_r, \underline{\boldsymbol{e}}_\theta, \underline{\boldsymbol{e}}_\phi)$ (see Figure 5.1), denoted $\hat{\boldsymbol{\mathcal{H}}}$, which has the minor symmetries and whose non-zero components are given as follows:

$$\begin{aligned}
\hat{\mathcal{H}}_{rrrr} &= -\frac{a^5}{r^5}\left(\frac{2r^2}{a^2} - 1\right), \\
\hat{\mathcal{H}}_{rr\theta\theta} &= \hat{\mathcal{H}}_{rr\phi\phi} = -\frac{a^5}{r^5}, \\
\hat{\mathcal{H}}_{\theta\theta rr} &= \hat{\mathcal{H}}_{\phi\phi rr} = -\frac{a^5}{r^5}\left(1 - \frac{r^2}{a^2}\right), \\
\hat{\mathcal{H}}_{r\phi r\phi} &= \hat{\mathcal{H}}_{r\theta r\theta} = -\frac{a^5}{r^5}\left(1 - \frac{r^2}{2a^2}\right).
\end{aligned} \tag{5.25}$$

In the same spirit, the relationship in Eq. (5.23) can be recast into the spherical coordinate system as:

$$\hat{\boldsymbol{d}}^{\mathrm{E},\infty}(\underline{\boldsymbol{x}}) = \hat{\boldsymbol{\mathcal{D}}} : \hat{\boldsymbol{d}}^{*}, \tag{5.26}$$

with $\hat{\boldsymbol{d}}^{\mathrm{E},\infty} = \boldsymbol{R}^T \boldsymbol{d}^{\mathrm{E},\infty} \boldsymbol{R}$ and $\hat{\boldsymbol{d}}^{*} = \boldsymbol{R}^T \boldsymbol{d}^{*} \boldsymbol{R}$, where $\boldsymbol{R}$ is the rotation matrix relating the Cartesian unit vectors to the spherical ones (see Appendix C). Noting that $\hat{\boldsymbol{\mathcal{T}}} = \boldsymbol{\mathcal{T}}$ due to its isotropic nature and combining Eqs. (5.22)-(5.23) and Eq. (5.25), the components of $\hat{\boldsymbol{\mathcal{D}}}$ result in:

$$\begin{aligned}
\hat{\mathcal{D}}_{rrrr} &= -2\hat{\mathcal{D}}_{\theta\theta rr} = -2\hat{\mathcal{D}}_{\phi\phi rr} = -2\frac{a^3}{r^3}\left(1 - \frac{4}{5}\frac{a^2}{r^2}\right), \\
\hat{\mathcal{D}}_{\theta\theta\theta\theta} &= \hat{\mathcal{D}}_{\phi\phi\phi\phi} = \frac{3}{5}\frac{a^5}{r^5}, \\
\hat{\mathcal{D}}_{rr\theta\theta} &= \hat{\mathcal{D}}_{rr\phi\phi} = -\frac{4}{5}\frac{a^5}{r^5}, \\
\hat{\mathcal{D}}_{\theta\theta\phi\phi} &= \hat{\mathcal{D}}_{\phi\phi\theta\theta} = \hat{\mathcal{D}}_{\theta\phi\theta\phi} = \frac{1}{5}\frac{a^5}{r^5}, \\
\hat{\mathcal{D}}_{r\theta r\theta} &= \hat{\mathcal{D}}_{r\phi r\phi} = \frac{1}{2}\frac{a^3}{r^3}\left(1 - \frac{8}{5}\frac{a^2}{r^2}\right).
\end{aligned} \tag{5.27}$$

$\hat{\boldsymbol{\mathcal{D}}}$ has minor symmetries but not the major one. Moreover, note that $\boldsymbol{I} : \hat{\boldsymbol{\mathcal{D}}} = \boldsymbol{0}$ due to the incompressibility condition, and $\hat{\boldsymbol{\mathcal{D}}} : \boldsymbol{I} = (a^3/r^3)[-2\underline{\boldsymbol{e}}_r \otimes \underline{\boldsymbol{e}}_r + \underline{\boldsymbol{e}}_\theta \otimes \underline{\boldsymbol{e}}_\theta + \underline{\boldsymbol{e}}_\phi \otimes \underline{\boldsymbol{e}}_\phi]$ (c.f. Eq. (5.20)), which corresponds to an isotropic expansion. The components of $\boldsymbol{\mathcal{D}}$ in the cartesian coordinate system (Eq. (5.23)) can be found in Ju and Sun, (1999); Li *et al.* (2007); Mura, (2013). These lead however to lengthy expressions

for $\boldsymbol{d}^{\mathrm{E},\infty}$, the spherical formulation being preferred here for practical reasons. Combining Eqs. (5.26)-(5.27), the components of $\hat{\boldsymbol{d}}^{\mathrm{E},\infty}$ are thus given by:

$$\begin{aligned}
\hat{d}_{rr}^{\mathrm{E},\infty} &= -2\frac{a^3}{r^3}\hat{d}_{rr}^{*} + \frac{4}{5}\frac{a^5}{r^5}\left(2\hat{d}_{rr}^{*} - \hat{d}_{\theta\theta}^{*} - \hat{d}_{\phi\phi}^{*}\right),\\
\hat{d}_{\theta\theta}^{\mathrm{E},\infty} &= \frac{a^3}{r^3}\hat{d}_{rr}^{*} + \frac{1}{5}\frac{a^5}{r^5}\left(-4\hat{d}_{rr}^{*} + \hat{d}_{\theta\theta}^{*} + 3\hat{d}_{\phi\phi}^{*}\right),\\
\hat{d}_{\phi\phi}^{\mathrm{E},\infty} &= \frac{a^3}{r^3}\hat{d}_{rr}^{*} + \frac{1}{5}\frac{a^5}{r^5}\left(-4\hat{d}_{rr}^{*} + 3\hat{d}_{\theta\theta}^{*} + \hat{d}_{\phi\phi}^{*}\right),\\
\hat{d}_{\theta\phi}^{\mathrm{E},\infty} &= \frac{2}{5}\frac{a^5}{r^5}\hat{d}_{\theta\phi}^{*},\quad \hat{d}_{r\theta}^{\mathrm{E}} = \frac{a^3}{r^3}\left(1-\frac{8}{5}\frac{a^2}{r^2}\right)\hat{d}_{r\theta}^{*},\quad \hat{d}_{r\phi}^{\mathrm{E}} = \frac{a^3}{r^3}\left(1-\frac{8}{5}\frac{a^2}{r^2}\right)\hat{d}_{r\phi}^{*}.
\end{aligned} \tag{5.28}$$

Let us return to the problem of the finite hollow sphere RVE. The RVE is concurrently subjected to a homogeneous strain rate and a heterogeneous expansion field due to the expansion of the cavity, such that, $\forall \underline{\boldsymbol{x}} \in \Omega\backslash\omega,\ \underline{\boldsymbol{v}}(\underline{\boldsymbol{x}}) = \boldsymbol{A}\underline{\boldsymbol{x}} + \underline{\boldsymbol{v}}^{\infty}(\underline{\boldsymbol{x}})$, where the term $\boldsymbol{A}\underline{\boldsymbol{x}}$ denotes the uniform extension field, $\boldsymbol{A}$ an arbitrary symmetric second order tensor and $\underline{\boldsymbol{v}}^{\infty}$ the dilatational expansion (not necessarily isotropic). The matrix incompressibility condition requires the tensor $\boldsymbol{A}$ to be traceless and $\mathrm{div}\,\underline{\boldsymbol{v}}^{\infty} = 0$. A particular case of $\underline{\boldsymbol{v}}(\underline{\boldsymbol{x}})$ was presented in Eq. (5.19), based on the Rice and Tracey fields, $\underline{\boldsymbol{v}}^{\mathrm{RT},\infty}$ in (5.18). In the same fashion, one can formulate an alternative field, $\underline{\boldsymbol{v}}^{\mathrm{E}}$, based on Eshelby results as:

$$\forall \underline{\boldsymbol{x}} \in \Omega\backslash\omega,\ \underline{\boldsymbol{v}}^{\mathrm{E}}(\underline{\boldsymbol{x}}) \triangleq \boldsymbol{A}\underline{\boldsymbol{x}} + \underline{\boldsymbol{v}}^{\mathrm{E},\infty}(\underline{\boldsymbol{x}}). \tag{5.29}$$

where $\underline{\boldsymbol{v}}^{\mathrm{E},\infty}$ was defined in Eq. (5.21). Therefore, the strain rate tensor associated with Eq. (5.29) is in the form:

$$\forall \underline{\boldsymbol{x}} \in \Omega\backslash\omega,\ \boldsymbol{d}^{\mathrm{E}}(\underline{\boldsymbol{x}}) = \boldsymbol{A} + \boldsymbol{d}^{\mathrm{E},\infty}(\underline{\boldsymbol{x}}), \tag{5.30}$$

where $\boldsymbol{d}^{\mathrm{E},\infty}$ was defined in Eq. (5.23). The determination $\boldsymbol{d}^{\mathrm{E}}$ in the Cartesian frame is readily achieved by successive application of the rotation matrix relating the Cartesian and spherical basis, as described in Appendix D. Likewise the Rice and Tracey case, it is possible of prove that the Eshelby-based field, $\boldsymbol{d}^{\mathrm{E}}$, is an even function, $\boldsymbol{d}^{\mathrm{E}}(\underline{\boldsymbol{x}}) = \boldsymbol{d}^{\mathrm{E}}(-\underline{\boldsymbol{x}})$. Combining Eq. (5.21) with Eq. (5.29) and the uniform strain-rate boundary condition on the sphere outer surface, $\underline{\boldsymbol{v}}(\underline{\boldsymbol{x}} = b\underline{\boldsymbol{e}}_r) = \boldsymbol{D}\underline{\boldsymbol{x}}$, leads to the following equation:

$$\boldsymbol{D}\underline{\boldsymbol{x}} = \boldsymbol{A}\underline{\boldsymbol{x}} + \left[\boldsymbol{\mathcal{T}}(b) : \boldsymbol{d}^{*}\right]\underline{\boldsymbol{x}} + bf\left(1 - f^{2/3}\right)\hat{d}_{rr}^{*}\underline{\boldsymbol{e}}_r. \tag{5.31}$$

While the first two terms on the right hand of the previous equation are proportional to $\underline{\boldsymbol{x}}$, hence comply with uniform strain rate boundary conditions, it is possible to demonstrate that the same does not hold true for the last term in the general case. In fact, the solution of Eq. (5.31) is: $\boldsymbol{A} = \boldsymbol{D}' \wedge \boldsymbol{d}^{*} = (D_{\mathrm{m}}/f)\boldsymbol{I}$, which corresponds to a purely hydrostatic eigenstrain, for which $\hat{d}_{rr}^{*} = D_{\mathrm{m}}/f$. Introducing the deviatoric-hydrostatic decomposition of the eigenstrain rate tensor as $\boldsymbol{d}^{*} = \boldsymbol{d}^{*\prime} + d_{\mathrm{m}}^{*}\boldsymbol{I}$, where $\boldsymbol{d}^{*\prime}$ and $d_{\mathrm{m}}^{*} = \mathrm{tr}(\boldsymbol{d}^{*})/3$ represent its deviatoric and hydrostatic part, respectively, it follows that the Eshelby-based trial velocity fields, $\underline{\boldsymbol{v}}^{\mathrm{E}}$, in Eq. (5.29) are compatible with uniform strain rate boundary conditions (Eq. (5.1)) if and only if $\boldsymbol{d}^{*\prime} = \boldsymbol{0}\ \wedge\ d_{\mathrm{m}}^{*} = D_{\mathrm{m}}/f$. Note that tensor $\boldsymbol{d}^{*\prime}$ is related with the shape change of the inclusion

(independent from the overall shape change of the hollow sphere, the latter associated with $\boldsymbol{A}$). Under this condition, the Eshelby-based velocity fields, $\underline{\boldsymbol{v}}^{\mathrm{E}}$ (Eq. (5.29)) reduce to those of Rice and Tracey, $\underline{\boldsymbol{v}}^{\mathrm{RT}}$, (Eq. (5.18)), since the term $\underline{\boldsymbol{v}}^{\mathrm{E},\infty}$, in Eq. (5.21) reduces to the expansion field considered by Rice and Tracey, $D_{\mathrm{m}}(b^3/r^2)\underline{\boldsymbol{e}}_r$ (Eq. (5.19)). In other words, the Rice and Tracey velocity fields can be viewed as a particular case of the Eshelby-based fields for a spherical inclusion subjected to an isotropic dilatational eigenstrain rate. It follows that the remaining velocity fields, i.e., those associated with $\boldsymbol{d}^{*\prime} \neq \boldsymbol{0}$, cannot verify Eq. (5.31).

Remark 5.1 In general, the Eshelby-based local velocity fields do not comply with uniform strain-rate boundary conditions on the spherical RVE (Eq. (5.1)).

According to Monchiet *et al.* (2014, 2011), the use of the complete Eshelby-based velocity field (in the sense that $\boldsymbol{d}^{*\prime} \neq \boldsymbol{0}$) within a kinematic limit analysis theory can be justified in the context of uniform stress boundary conditions, i.e., $\boldsymbol{\sigma}\underline{\boldsymbol{n}} = \boldsymbol{\Sigma}\underline{\boldsymbol{n}}, \forall \underline{\boldsymbol{x}} \in \partial\Omega$, (recall discussion in §5.1.3). Within the latter framework, the set of kinematically admissible velocity fields, $\boldsymbol{d} \in \mathcal{K}(\boldsymbol{D})$, is no longer based on the set in Eq. (5.4), and instead are defined based on the velocity fields that verify the strain-rate averaging rule, i.e.:

$$\boldsymbol{D} = \langle \boldsymbol{d} \rangle_{\Omega} = \frac{1}{\mathrm{vol}(\Omega)} \int_V \boldsymbol{d}\, dV \,. \tag{5.32}$$

Note that Eq. (5.32) and Eq. (5.2) hold the same mathematical operation, yet the former is adopted as a definition, whereas the latter is a theorem (result) from the kinematical homogenization approach. The opposite holds for the stress averaging rule, $\boldsymbol{\Sigma} = \langle \boldsymbol{\sigma} \rangle_{\Omega}$. In the author's view, the usage of Eshelby-based velocity field in the context of the kinematic limit analysis theory (Eq. (5.9)) has a weak mathematical rational: first, in view of the fact that uniform strain-rate boundary conditions are not met, and thus the upper-bound nature of the analysis (which motivated the choice a kinematic limit analysis in the first place) is lost; second, the application of the Hill-Mandel lemma (Eq. (5.5)) is questionable since neither uniform strain rate conditions nor uniform stress boundary conditions are actually being fulfilled. This implies that the obtained macroscopic yield surface should be interior to the upper-bound solution, viz. that using the Rice and Tracey fields, and exterior to the lower-bound counterpart. Despite the above-mentioned deficiencies, following the work of (Monchiet *et al.*, 2007, 2011), the Eshelby-based velocity fields are still employed in the context of the Gurson-type proposed homogenization scheme. Substitution of Eq. (5.30) in Eq. (5.32) leads to:

$$\boldsymbol{D} = \boldsymbol{A} + f\boldsymbol{\mathcal{S}} : \boldsymbol{d}^{*} = \boldsymbol{A} + f\left(\frac{2}{5}\boldsymbol{d}^{*\prime} + d^{*}_{\mathrm{m}}\boldsymbol{I}\right). \tag{5.33}$$

The previous expression is of major importance as it provides the link between the macroscopic strain rate tensor $\boldsymbol{D}$ and the two unknown kinematical tensors, $\boldsymbol{A}$ and $\boldsymbol{d}^{*}$, entering the definition of the microscopic strain-rate tensor in Eq. (5.30). Note that Eq. (5.33) provides six scalar equations for eleven unknown parameters: five independent parameters A_{ij}, $(\mathrm{tr}(\boldsymbol{A}) = 0)$; and six parameters d^{*}_{ij}. The deviatoric-hydrostatic decomposition of Eq. (5.33) results in:

$$D_{\mathrm{m}} = f d_{\mathrm{m}}^{*}, \text{ and } \boldsymbol{D}' = \boldsymbol{A} + \frac{2f}{5}\boldsymbol{d}^{*\prime}. \tag{5.34}$$

One can readily conclude that the hydrostatic eigenstrain rate is known from the outset in terms of the macroscopic hydrostatic strain rate, as $d_{\mathrm{m}}^{*} = D_{\mathrm{m}} / f$. This is to be expected as the expansion of the RVE results exclusively from the expansion of the void, due to matrix incompressibility. Conversely, the equation associated with the deviatoric part shows that five unknown parameters must be determined: either the parameters of $\boldsymbol{A}$ or those of $\boldsymbol{d}^{*\prime}$. In this work the latter formulation is adopted. In practice, these are determined by a minimization procedure on the macroscopic dissipation function (Eq. (5.9)), as discussed in more detail in the next chapter. One cannot emphasize enough that since, in general, the Eshelby-based velocity fields do not comply with uniform strain-rate boundary conditions, the upper-bound character of the analysis can no longer be guaranteed (recall discussion in §5.1.3). Nevertheless, the truncated nature of the analysis (in the sense that minimization is done over a subset of $\mathcal{K}(\boldsymbol{D})$) will inherently result in an upper-bound estimate of the macroscopic yield criterion in the context of uniform stress boundary conditions, i.e. $\bar{\mathscr{E}}_{\bar{\boldsymbol{\sigma}}\underline{\boldsymbol{n}}=\boldsymbol{\Sigma}\underline{\boldsymbol{n}}}^{\Pi^{+}(\boldsymbol{D})} \supset \bar{\mathscr{E}}_{\bar{\boldsymbol{\sigma}}\underline{\boldsymbol{n}}=\boldsymbol{\Sigma}\underline{\boldsymbol{n}}}^{\Pi(\boldsymbol{D})}$ (following the notation of §5.1.3), for which the Hill-Mandel lemma still applies. Unfortunately, one cannot *a priori* determine if the approximate yield locus is interior or exterior with respect to the exact one, i.e. whether $\bar{\mathscr{E}} \supset \bar{\mathscr{E}}_{\bar{\boldsymbol{\sigma}}\underline{\boldsymbol{n}}=\boldsymbol{\Sigma}\underline{\boldsymbol{n}}}^{\Pi^{+}(\boldsymbol{D})}$ or $\bar{\mathscr{E}}_{\bar{\boldsymbol{\sigma}}\underline{\boldsymbol{n}}=\boldsymbol{\Sigma}\underline{\boldsymbol{n}}}^{\Pi^{+}(\boldsymbol{D})} \supset \bar{\mathscr{E}}$. In any case, given the increased flexibility of the Eshelby-based fields, it is clear that the approximate macroscopic yield locus obtained from these, $\partial\bar{\mathscr{E}}_{\Pi^{+}(\boldsymbol{D})}^{\mathrm{E}}$, should always be interior to that obtained with the Rice and Tracey velocity fields, $\partial\bar{\mathscr{E}}_{\Pi^{+}(\boldsymbol{D})}^{\mathrm{RT}}$, i.e., $\bar{\mathscr{E}}_{\Pi^{+}(\boldsymbol{D})}^{\mathrm{RT}} \supset \bar{\mathscr{E}}_{\Pi^{+}(\boldsymbol{D})}^{\mathrm{E}}$, as the respective approximate macroscopic dissipation functions must verify the inequality $\Pi^{\mathrm{E},+}(\boldsymbol{D}) \leq \Pi^{\mathrm{RT},+}(\boldsymbol{D})$, given the additional minimization procedure and the fact that the former is able to reduce to the latter.

5.3 Approximate macroscopic potentials: definition

This subsection is devoted to the determination of approximate strain-rate potentials and the associated stress potentials of porous solids containing randomly distributed spherical voids for general 3-D states using the kinematic homogenization approach presented in §5.1. The assumed RVE, microscale plasticity model, and trial velocity fields are those presented in §5.2.

5.3.1 Approximate macroscopic plastic dissipation and strain-rate potential

Following the discussion in §5.1.3, an approximation of the macroscopic plastic dissipation in Eq. (5.9), $\Pi^{+}(\boldsymbol{D})$, associated with a specific trial velocity field, $\underline{\boldsymbol{v}}^{\mathrm{tr}}(\underline{\boldsymbol{x}})$, is defined as:

$$\Pi(\boldsymbol{D}) \leq \Pi^{+}(\boldsymbol{D}) = \left\langle \pi\left(\boldsymbol{d}^{\mathrm{tr}}(\underline{\boldsymbol{x}})\right)\right\rangle_{\Omega} = \frac{1}{V}\int_{\Omega} \pi\left(\boldsymbol{d}^{\mathrm{tr}}(\underline{\boldsymbol{x}})\right) dV = \frac{1}{V}\int_{\Omega\setminus\omega} \pi\left(\boldsymbol{d}^{\mathrm{tr}}(\underline{\boldsymbol{x}})\right) dV, \tag{5.35}$$

where the property $\pi(\boldsymbol{d}) = 0,\ \forall \underline{\boldsymbol{x}} \in \omega$ was applied, $\boldsymbol{d}^{\mathrm{tr}} \triangleq (1/2)[\nabla\underline{\boldsymbol{v}}^{\mathrm{tr}} + (\nabla\underline{\boldsymbol{v}}^{\mathrm{tr}})^{\mathrm{T}}]$ is the trial local strain-rate field, $V = \mathrm{vol}(\Omega) = (4/3)\pi b^3$ is the volume of the spherical RVE (Figure 5.1), with the differential volume element $dV = r^2 \sin\theta d\theta d\phi dr$. For convenience, the above triple integral is rewritten in the form:

$$\Pi^{+}\left(\boldsymbol{D}\right)=\frac{1}{V}\int_{a}^{b}A(r)\left\langle \pi\left(\boldsymbol{d}^{\mathrm{tr}}\right)\right\rangle_{S(r)}dr\,, \tag{5.36}$$

where $S(r)=\{\underline{\boldsymbol{x}}\in\mathbb{R}^{3}:\|\underline{\boldsymbol{x}}\|_{2}=r\}$ denotes the spherical surface of radius r and area $A(r)=4\pi r^{2}$, $\langle\cdot\rangle_{S(r)}$ denotes the averaging operation over $S(r)$, i.e.:

$$\left\langle g\right\rangle_{S(r)}=\frac{1}{4\pi}\int_{0}^{2\pi}\int_{0}^{\pi}g(\theta,\phi)\sin\theta d\theta d\phi\,, \tag{5.37}$$

where g denotes an arbitrary scalar field, continuous on $S(r)$. The case of tensorial fields is a trivial extension of the previous expression. In view of Eq. (5.15), Eq. (4.19), and the matrix rigid-perfectly plastic response, Eq. (5.35) can also be expressed as:

$$\Pi^{+}\left(\boldsymbol{D}\right)=\frac{1}{V}\int_{\Omega\setminus\omega}\sigma_{1}^{\mathrm{T}}\psi\left(\boldsymbol{d}^{\mathrm{tr}}\left(\underline{\boldsymbol{x}}\right)\right)dV=\sigma_{1}^{\mathrm{T}}\left(1-f\right)\left\langle \psi\left(\boldsymbol{d}^{\mathrm{tr}}\left(\underline{\boldsymbol{x}}\right)\right)\right\rangle_{\Omega\setminus\omega}, \tag{5.38}$$

where $\psi(\boldsymbol{d})$ is the local (or microscopic) strain-rate potential, given in Eq. (4.22). Combining Eq. (5.38) and Eq. (5.17) allow us to determine the approximate macroscopic strain-rate potential, $\Psi^{+}(\boldsymbol{D})$, associated with the trial velocity field, $\underline{\boldsymbol{v}}^{\mathrm{tr}}(\underline{\boldsymbol{x}})$, as:

$$\Psi^{+}\left(\boldsymbol{D}\right)=\left(1-f\right)\left\langle \psi\left(\boldsymbol{d}^{\mathrm{tr}}\left(\underline{\boldsymbol{x}}\right)\right)\right\rangle_{\Omega\setminus\omega}=\frac{1}{V}\int_{a}^{b}A(r)\left\langle \psi\left(\boldsymbol{d}^{\mathrm{tr}}\left(\underline{\boldsymbol{x}}\right)\right)\right\rangle_{S(r)}dr\,. \tag{5.39}$$

The previous expressions implicitly assume that the trial strain-rate fields, $\boldsymbol{d}^{\mathrm{tr}}$, in the integrand of Eq. (5.35) can be explicitly defined based on $\boldsymbol{D}$, i.e., $\boldsymbol{d}^{\mathrm{tr}}=\boldsymbol{d}^{\mathrm{tr}}\left(\underline{\boldsymbol{x}},\boldsymbol{D}\right)$. Conversely, if the determination of these local fields encompasses an additional set of kinematic quantities, say $\boldsymbol{\zeta}$, such that $\Pi=\Pi(\boldsymbol{D},\boldsymbol{\zeta})$, then, in view of Eq. (5.9), a minimization procedure on these unknown parameters is required in order to eliminate their dependence on Π. Accordingly, Eq. (5.35) and Eq. (5.39) are replaced with:

$$\begin{aligned}&\Pi^{+}\left(\boldsymbol{D}\right)=\inf_{\boldsymbol{\zeta}}\Gamma\left(\boldsymbol{D},\boldsymbol{\zeta}\right),\text{ with}\\&\Gamma\left(\boldsymbol{D},\boldsymbol{\zeta}\right)=\left\langle \pi\left(\boldsymbol{d}^{\mathrm{tr}}\left(\underline{\boldsymbol{x}},\boldsymbol{D},\boldsymbol{\zeta}\right)\right)\right\rangle_{\Omega}=\frac{1}{V}\int_{a}^{b}A(r)\left\langle \pi\left(\boldsymbol{d}^{\mathrm{tr}}\left(\underline{\boldsymbol{x}},\boldsymbol{D},\boldsymbol{\zeta}\right)\right)\right\rangle_{S(r)}dr\,,\end{aligned} \tag{5.40}$$

and

$$\begin{aligned}&\Psi^{+}\left(\boldsymbol{D}\right)=\inf_{\boldsymbol{\zeta}}\Upsilon\left(\boldsymbol{D},\boldsymbol{\zeta}\right),\text{ with}\\&\Upsilon\left(\boldsymbol{D},\boldsymbol{\zeta}\right)=\left(1-f\right)\left\langle \psi\left(\boldsymbol{d}^{\mathrm{tr}}\left(\underline{\boldsymbol{x}},\boldsymbol{D},\boldsymbol{\zeta}\right)\right)\right\rangle_{\Omega\setminus\omega}=\frac{1}{V}\int_{a}^{b}A(r)\left\langle \psi\left(\boldsymbol{d}^{\mathrm{tr}}\left(\underline{\boldsymbol{x}},\boldsymbol{D},\boldsymbol{\zeta}\right)\right)\right\rangle_{S(r)}dr\,,\end{aligned} \tag{5.41}$$

respectively. The specific forms of these expressions for the considered velocity fields is now presented. Hereafter, attention is set exclusively on the expressions of the approximate strain-rate potential. In the following, the particular cases of the Rice and Tracey and the Eshelby-based velocity fields are replaced in the above general expressions.

Rice and Tracey (1969) velocity fields

The Rice and Tracey velocity fields, $\underline{\boldsymbol{v}}^{\mathrm{RT}}$, (see Eq. (5.19)) fall in the context of Eq. (5.39), hence the respective strain-rate potential, $\Psi^{\mathrm{RT}}(\boldsymbol{D})$, is in the form:

$$\Psi^{\mathrm{RT}}\left(\boldsymbol{D}\right)=\left(1-f\right)\left\langle\psi\left(\boldsymbol{d}^{\mathrm{RT}}\right)\right\rangle_{\Omega\setminus\omega}=\frac{1}{V}\int_{a}^{b}A(r)\left\langle\psi\left(\boldsymbol{d}^{\mathrm{RT}}\right)\right\rangle_{S(r)}dr\,, \tag{5.42}$$

where the respective local strain-rate field $\boldsymbol{d}^{\mathrm{RT}}$ was defined in Eq. (5.20), (see Appendix C for its determination on the Cartesian frame).

Eshelby-based velocity fields

The Eshelby-based velocity fields, $\underline{\boldsymbol{v}}^{\mathrm{E}}$, (see Eq. (5.29)) fall in the domain of Eq.(5.41), in which the deviatoric part of the eigenstrain rate tensor, $\boldsymbol{d}^{*\prime}$, plays the role of the additional kinematic tensor. Accordingly, the approximate strain-rate potential associated with the Eshelby-based approach, $\Psi^{\mathrm{E}}(\boldsymbol{D})$, is given it terms of the following minimization scheme:

$$\begin{aligned}&\Psi^{\mathrm{E}}\left(\boldsymbol{D}\right)=\inf_{\boldsymbol{d}^{*\prime}}\Upsilon^{\mathrm{E}}\left(\boldsymbol{D},\boldsymbol{d}^{*\prime}\right),\ \text{with}\\&\Upsilon^{\mathrm{E}}\left(\boldsymbol{D},\boldsymbol{d}^{*\prime}\right)=\left(1-f\right)\left\langle\psi\left(\boldsymbol{d}^{\mathrm{E}}\left(\boldsymbol{D},\boldsymbol{d}^{*\prime}\right)\right)\right\rangle_{\Omega\setminus\omega}=\frac{1}{V}\int_{a}^{b}A(r)\left\langle\psi\left(\boldsymbol{d}^{\mathrm{E}}\left(\boldsymbol{D},\boldsymbol{d}^{*\prime}\right)\right)\right\rangle_{S(r)}dr\,,\end{aligned} \tag{5.43}$$

where the respective local strain-rate field $\boldsymbol{d}^{\mathrm{E}}$ was defined in Eq. (5.30) (see Appendix D for its determination on the Cartesian frame).

5.3.2 Approximate macroscopic yield criterion and macroscopic stresses

Combining Eqs. (5.12), (5.17) and (5.39), the macroscopic yield stress of the porous solid associated with the upper-bound estimate, Π^{+}, in turn related with a particular trial velocity field, can be expressed as:

$$\frac{\boldsymbol{\Sigma}}{\sigma_1^{\mathrm{T}}}=\frac{\partial\Psi^{+}}{\partial\boldsymbol{D}}\left(\boldsymbol{D}\right), \tag{5.44}$$

which is the parametric representation of the macroscopic yield locus in terms of the approximate strain-rate potential, Ψ^{+}, where $\partial\Psi^{+}(\boldsymbol{D})/\partial\boldsymbol{D}$ homogeneous of degree zero. As discussed in §5.1, in order to obtain an expression for the associated yield function, $\boldsymbol{D}$ must be eliminated from Eq. (5.44), such that an expression of the type of Eq. (5.13) is attained, in this case rewritten as:

$$\mathcal{F}^{+}(\boldsymbol{\Sigma},\sigma_1^{\mathrm{T}})\triangleq\Phi^{+}(\boldsymbol{\Sigma})-\sigma_1^{\mathrm{T}}=0\,, \tag{5.45}$$

where $\Phi^{+}(\boldsymbol{\Sigma})$ is the approximated macroscopic stress potential, conjugated (or dual) of $\Psi^{+}(\boldsymbol{D})$. If the abovementioned elimination is not possible, as is the case in this work, function $\Phi^{+}(\boldsymbol{\Sigma})$ (and therefore $\mathcal{F}^{+}(\boldsymbol{\Sigma},\sigma_1^{\mathrm{T}})$ in Eq. (5.45)) can still be evaluated in a numerical fashion based on the work-equivalence and normality principles applied to its dual potential, $\Psi^{+}(\boldsymbol{D})$ (Eq. (5.39)). This entails solving a non-linear equation system analogous to that in Eq. (4.57) regarding the case of dense, thus plastic isochoric,

materials. Let $\boldsymbol{\Sigma}$ denote an arbitrary macroscopic stress state and $(\boldsymbol{D}^*, \tau^*)$ the solution of the following system equation:

$$\boldsymbol{F}(\boldsymbol{D}^*, \tau^*) = \begin{Bmatrix} \boldsymbol{\Sigma} - \tau^* \dfrac{\partial \Psi^+(\boldsymbol{D}^*)}{\partial \boldsymbol{D}^*} \\ \Psi^+(\boldsymbol{D}^*) - \dot{\Lambda}_{\text{ref}} \end{Bmatrix} = \begin{Bmatrix} \boldsymbol{0} \\ 0 \end{Bmatrix}, \tag{5.46}$$

where $\dot{\Lambda}_{\text{ref}} \geq 0$ is an arbitrary reference value for the strain-rate potential. From Eq. (5.14), Eq. (5.17) and Eq. (5.44), it follows that:

$$\begin{gathered} \Phi^+(\boldsymbol{\Sigma}) \triangleq \tau^*, \text{ and} \\ \bar{\boldsymbol{D}} \triangleq \frac{\boldsymbol{D}^*}{\dot{\Lambda}_{\text{ref}}} = \frac{\partial \Phi^+(\boldsymbol{\Sigma})}{\partial \boldsymbol{\Sigma}}, \text{ with } \Psi^+(\bar{\boldsymbol{D}}) = 1. \end{gathered} \tag{5.47}$$

A natural choice for $\dot{\Lambda}_{\text{ref}}$ is the unity, such that the solution of Eq. (5.46) is coincides with the macroscopic strain-rate tensor of unitary strain-rate potential value, alias the 'normalized' strain-rate tensor, i.e. $\boldsymbol{D}^* \leftarrow \bar{\boldsymbol{D}}$, which is of special interest in the context of elastoplastic modelling using the stress-based formulation (see Eq. (5.14)). Note that, in contrast with Eq. (4.57), the tensorial equation in Eq. (5.46) has six (as opposed to five) independent coefficients, since plasticity now depends on the installed hydrostatic component of the stress tensor. The scalar equation in Eq. (5.46) is crucial to bound the problem. In fact, $\partial \Psi^+(\boldsymbol{D})/\partial \boldsymbol{D}$ is homogeneous of degree zero, i.e., $\partial \Psi^+(\xi \boldsymbol{D}^*)/\partial(\xi \boldsymbol{D}^*) = \partial \Psi^+(\boldsymbol{D}^*)/\partial(\boldsymbol{D}^*)$, $\forall \xi > 0$ and thus $\boldsymbol{D}^*$ must be somehow constrained otherwise the system would be singular in $\boldsymbol{D}^*$. Regarding the determination of $\partial \Psi^+(\boldsymbol{D})/\partial \boldsymbol{D}$ in Eq. (5.46) one takes advantage of the fact that the local SRP, $\psi(\boldsymbol{d})$, and its derivative, $\partial \psi(\boldsymbol{d})/\partial \boldsymbol{d}$, are obtained simultaneously in each quadrature point the RVE (see Remarks 4.4 in §4.4.4). In summary, Eq. (5.46) has seven independent equations. In line with Eq. (5.6) and Eq. (4.19), $\bar{\boldsymbol{s}}(\underline{\boldsymbol{x}}) = \partial \psi(\boldsymbol{d}(\underline{\boldsymbol{x}}))/\partial \boldsymbol{d}$ is actually the unitary (or normalized) microscopic (or local) deviatoric stress tensor field, obeying the local yield condition, i.e. $f(\bar{\boldsymbol{s}}(\underline{\boldsymbol{x}})) = 0$, $\varphi(\bar{\boldsymbol{s}}(\underline{\boldsymbol{x}})) = 1$, $\forall \underline{\boldsymbol{x}} \in \Omega \backslash \omega$. Accordingly, following Eq. (5.3) and Eq. (5.36), the deviatoric part of $\partial \Psi^+(\boldsymbol{D})/\partial \boldsymbol{D}$, denoted $(\partial \Psi^+(\boldsymbol{D})/\partial \boldsymbol{D})'$, can be defined based on the unitary macroscopic deviatoric stress tensor, $\bar{\boldsymbol{\Sigma}}'$, as the volume average of its microscopic counterpart, $\bar{\boldsymbol{s}}$, i.e.:

$$\left(\frac{\partial \Psi^+(\boldsymbol{D})}{\partial \boldsymbol{D}} \right)' \triangleq \bar{\boldsymbol{\Sigma}}'(\boldsymbol{D}) = \langle \bar{\boldsymbol{s}} \rangle_{\Omega} = (1 - f) \langle \bar{\boldsymbol{s}} \rangle_{\Omega \backslash \omega} = \frac{1}{V} \int_a^b 4\pi r^2 \langle \bar{\boldsymbol{s}}(\underline{\boldsymbol{x}}) \rangle_{S(r)} dr \,. \tag{5.48}$$

At this point, it remains to determine the hydrostatic part of function $\partial \Psi^+(\boldsymbol{D})/\partial \boldsymbol{D}$. Defining the deviatoric-hydrostatic decomposition of the macroscopic stress tensor as $\boldsymbol{\Sigma} = \boldsymbol{\Sigma}' + \Sigma_{\text{m}} \boldsymbol{I}$, where $\Sigma_{\text{m}} = \text{tr}(\boldsymbol{\Sigma})/3$ the macroscopic hydrostatic stress, the macroscopic plastic dissipation function $\Pi^+(\boldsymbol{D})$, can be thought as a contribution of a deviatoric, Π^+_{dev}, and hydrostatic, Π^+_{hid}, parts as:

$$\Pi^+(\boldsymbol{D}) = \boldsymbol{\Sigma} : \boldsymbol{D} = \Pi^+_{\text{dev}} + \Pi^+_{\text{hid}}, \text{ with } \begin{cases} \Pi^+_{\text{dev}} = \boldsymbol{\Sigma}' : \boldsymbol{D} = \boldsymbol{\Sigma} : \boldsymbol{D}' = \boldsymbol{\Sigma}' : \boldsymbol{D}' \\ \Pi^+_{\text{hid}} = \dfrac{\text{tr}(\boldsymbol{\Sigma})\text{tr}(\boldsymbol{D})}{3} = \text{tr}(\boldsymbol{\Sigma}) D_{\text{m}} = \Sigma_{\text{m}} \text{tr}(\boldsymbol{D}) \end{cases}. \tag{5.49}$$

Combining Eq. (5.17) and Eq. (5.57), it follows from the work-equivalence at the macroscale that:

$$\Sigma_{\mathrm{m}} = \frac{\Pi^{+}_{\mathrm{hid}}(\boldsymbol{D})}{\mathrm{tr}(\boldsymbol{D})} = \begin{cases} \dfrac{\tau\Psi^{+}(\boldsymbol{D}) - \boldsymbol{\Sigma}' : \boldsymbol{D}}{\mathrm{tr}(\boldsymbol{D})} & \text{if } \mathrm{tr}(\boldsymbol{D}) \neq 0 \\ 0 & \text{if } \mathrm{tr}(\boldsymbol{D}) = 0 \end{cases}, \text{ with } \Phi^{+}(\boldsymbol{\Sigma}) = \tau \,. \tag{5.50}$$

The term $\partial\Psi^{+}(\boldsymbol{D})/\partial\boldsymbol{D}$ is thus obtained with minimal computational effort. Of course, this tensor could be determined by numerical differentiation (e.g. via finite differences), yet this would entail conducting multiple homogenization tasks. The proposed method is therefore superior both from the computational efficiency and precision point of view.

Remark 5.2 Likewise the local constitutive formulation, the approximate macroscopic SRP, $\Psi^{+}(\boldsymbol{D})$, and its derivative, $\partial\Psi^{+}(\boldsymbol{D})/\partial\boldsymbol{D}$, are determined simultaneously, i.e., in a single homogenization task.

Conversely, the evaluation of the approximate macroscopic stress potential, $\Phi^{+}(\boldsymbol{\Sigma})$, (Eq. (5.45)) and its first derivative, $\partial\Phi^{+}(\boldsymbol{\Sigma})/\partial\boldsymbol{\Sigma}$, through the system in Eq. (5.46) requires the computation of a Jacobian tensor, $\mathcal{J}(\boldsymbol{D},\tau)$, when using a Newton (or quasi-Newton) method. Since close-form expressions are not available, the determination of the Jacobian is restricted to numerical differentiation, which entails multiple homogenization tasks to be performed (in theory, $\mathcal{O}(8i)$ using a forward or backwards finite difference scheme and $\mathcal{O}(14i)$ when using a central scheme, where i is the number of iterations of the solution of Eq. (5.46)). It follows that the usage of a stress-based constitutive formulation (Eqs. (5.13)-(5.14)) to describe the macroscopic plastic response of porous solids for which the stress potential is not known in closed-form is *not* recommended due to the massive computational overhead that such formulation entails. Given the adopted kinematic approach to the homogenization problem, one should instead use its dual relationship, i.e. the strain-rate-based formulation (Eq. (5.16)), for which the constitutive behaviour of the porous solid is determined in a single homogenization task. However, one should keep in mind that such approach does not provide an explicit definition of the boundary between elastic and plastic macroscopic domains, $\mathcal{F}$, (see Eq. (5.13)) , and thus solving Eq. (5.46) (or any other equivalent problem) is still necessary in order to determine the plastic loading-unloading conditions in the context of elastic-plastic modelling. This subject is explored in more detail in Chapter 7.

5.4 Computational homogenization

Unfortunately, the volume integral in Eq. (5.39) (and its particular forms in Eqs. (5.42)-(5.43)) does not admit an explicit analytical expression for general 3-D states. This is due to the dependence of the trial velocity fields on the azimuthal, $\phi \in [0, 2\pi]$, and polar, $\theta \in [0, \pi]$, coordinates in the surface integrals $\langle \psi(\boldsymbol{d}) \rangle_{S(r)}$. This issue holds even in the case there the expression for the local strain rate potential, $\psi(\boldsymbol{d})$, is known in closed form (e.g. von-Mises). In order to bypass this problem, it is common practice in the literature to restrict the analysis to macroscopic axisymmetric loading conditions in the principal basis (coincident with the orthotropic axes), and/or to define new upper bounds $\Psi^{++}(\boldsymbol{D}) \geq \Psi^{+}(\boldsymbol{D})$, viz. using the Cauchy-Schwarz inequality, $\langle \psi \rangle_{S(r)} \leq [\langle \psi^2 \rangle_{S(r)}]^{1/2}$, to simplify the integrands, as implicitly done in Gurson (1977), and later proposed in several works (Benzerga and Besson, 2001; Keralavarma and Benzerga, 2008, 2010; Morin, Leblond and Kondo, 2015; Stewart and Cazacu, 2011). Evidently, if

the integrand cannot be evaluated analytically, is not possible to provide an analytical expression for the respective integral. This work falls into the latter case. In fact, as discussed in Chapter 4, the considered local strain rate potential, $\psi(\boldsymbol{d})$, (Eq. (4.22)) does not admit a closed-form expression in the general case. Accordingly, the homogenization procedure must be performed numerically. The merit of this approach is that there is no need for modifying the integrands or to restrict the analysis to axisymmetry, which in theory should lead to more rigours results and tighter upper-bounds solutions, when compared with those based on the Cauchy-Schwarz inequality and/or other, (ideally, but not always upper-bound-preserving), approximations. On the other hand, the lack of closed-form expressions is disadvantageous from the computational point of view. 3-D numerical integration (alias cubature) necessarily entails the discretization of the RVE, which adds ambiguity to the problem. Thus, robust and efficient cubature rules must be employed in order to reduce the additional computational effort associated with such fully numerical homogenization framework. The objective is to minimize the number of function evaluations (and thus integration points) in Eq. (5.39), while guaranteeing a desired accuracy for the results. In the following this task is tackled.

5.4.1 Determination of the integrals over the spherical surface: $\langle\cdot\rangle_{S(r)}$

In this subsection the focus is on evaluating the surface averaging integrals in the form of Eq. (5.37). Let us first consider the more standard problem of numerical integration over the unit sphere $\mathbb{S}^2 \in \mathbb{R}^3$, where $\mathbb{S}^2 = \{\underline{\boldsymbol{x}} \in \mathbb{R}^3 : \|\underline{\boldsymbol{x}}\|_2 = 1\}$. The exact integral of an integrable function f defined on $\mathbb{S}^2$, $I(f)$, can be approximated by a positive weight quadrature rule based on a finite sum, $Q_N(f)$, in the form:

$$I(f) \triangleq \int_{\mathbb{S}^2} f(\underline{\boldsymbol{x}}) dA(\underline{\boldsymbol{x}}) \cong Q_N(f) \triangleq \sum_{i=1}^{N} w_i f(\underline{\boldsymbol{x}}_i), \tag{5.51}$$

where $dA(\underline{\boldsymbol{x}})$ denotes the differential surface area on $\mathbb{S}^2$, $\underline{\boldsymbol{x}}_i \in \mathbb{S}^2$, $0 < w_i \in \mathbb{R}$, $i = 1,...,N$. Of particular importance are the Gauss-type quadrature rules which integrate *exactly* all multivariate polynomials of maximal degree $t \in \mathbb{N}_0$, i.e.:

$$I(p) = Q_N(p), \quad \forall p \in \mathbb{P}_t(\mathbb{S}^2), \tag{5.52}$$

where $\mathbb{P}_t(\mathbb{S}^2)$ is the space of all spherical polynomials with degree of at most *t*, (e.g. Müller, 2006). If, additionally, all quadrature weights are postulated to be equal, i.e. $w_1 = ... = w_N = \frac{1}{N}\int dA$, the quadrature rule is said to be of Chebyshev-type. Gauss- and Chebyshev-type quadrature rules are called *optimal* if the identity in Eq. (5.52) is attained for the minimal number of quadrature points, *N*, for a given polynomial degree *t* (Gräf, 2013). It is clear that the integration on the unit sphere can be formulated based on extensions of well-known one-dimensional quadrature rules. However, by doing so, one is not making use of the symmetry of the integration domain. Indeed, more efficient methods can be achieved by applying schemes that consider the specificities of the spherical geometry domain *a priori*. The set of quadrature points $\mathcal{X}_N = \{\underline{\boldsymbol{x}}_1,...,\underline{\boldsymbol{x}}_N\} \in \mathbb{S}^2$ of a Chebyshev-type quadrature rule on $\mathbb{S}^2$ with polynomial degree of precision, *t*, is known as 'spherical *t*-design'. A spherical *t*-design is therefore a particular form of Eq. (5.51) with equal weights $w_i = 4\pi/N$, $i = 1,...,N$, i.e.:

$$\int_{\mathbb{S}^2} p(\underline{\boldsymbol{x}})\,dA(\underline{\boldsymbol{x}}) = \frac{4\pi}{N}\sum_{i=1}^{N} p(\underline{\boldsymbol{x}}_i)\,,\ \forall p \in \mathbb{P}_t\left(\mathbb{S}^2\right). \tag{5.53}$$

Spherical designs were introduced by Delsarte *et al.* (1977) in the context of algebraic combinatorics on spheres and its connection with different areas of mathematics, (viz. number theory, geometry, geometric combinatorics). The link with numerical integration on the sphere was soon made (Bannai and Bannai, 2009; Brauchart and Grabner, 2015). The platonic solids can be seen as spherical designs. The existence of spherical designs for arbitrary degree t if N is sufficiently large was shown in Seymour and Zaslavsky (1984). However, the smallest number N needed to construct a spherical design of degree t, i.e. the optimal rule, is still an open subject. It is commonly conjectured that spherical t-designs with $N \approx \frac{1}{2}t^2$ points do exist, yet there is no proof. In practice, spherical designs must be constructed based on numerical computation for large t values. The construction of efficient quadrature rules on $\mathbb{S}^2$ has been tackled by many authors after the seminal works of Sobolev (1962) and McLaren (1963). Here, the algebraic contribution due to Lebedev (1976) and the numerical constructions of Hardin and Sloane (2002, 1996), who derived spherical designs up to $t = 21$ are highlighted. Gräf (2013b, 2013a); Gräf *et al.* (2012) computed designs with high accuracy degree for values of t up to 1000 based on a fast Fourier transform (FFT) method. More recently, Womersley (2018, 2017) employed the Levenberg-Marquardt method to determine general spherical t-designs for $t = 1,...,180$ and symmetric (alias *antipodal*), i.e. $\underline{\boldsymbol{x}} \in \mathcal{X}_N \Leftrightarrow -\underline{\boldsymbol{x}} \in \mathcal{X}_N$, t-designs for odd degrees up to 325. The latter designs are of special interest to the present work. The idea is to exploit the symmetry of the antipodal sets to reduce (ideally in half) the number of function evaluations in Eq. (5.39) of an even function, $f : \mathbb{R}^3 \to \mathbb{R}$, $f(\underline{\boldsymbol{x}}) = f(-\underline{\boldsymbol{x}})$, $\forall \underline{\boldsymbol{x}} \in \mathbb{S}^2$ for a given polynomial degree of accuracy, t. The datasets containing the abovementioned numerical-based designs, including those used in this work, are available on the Web (see the respective citations). In order to justify the attractiveness of spherical t-designs in terms of efficiency (in the sense of McLaren (1963)) and of the convergence rate the works of Beentjes (2015) and of An and Chen (2016) are mentioned. These authors compared the spherical designs with different quadrature rules, including: the Gaussian product quadrature, the Lebedev quadrature, and the Monte Carlo quadrature, the bivariate trapezoidal rule, and the equal partition area points rule, on a set of test functions with distinct levels of smoothness. These authors concluded that the spherical designs generally perform the best, displaying the best attenuation to absolute error and convergence rate with increasing number of points. Figure 5.2 shows examples of spherical t-designs for three accuracy degrees. Note the uniformly spread nature of these (no point clustering near the poles, as is the case with Gaussian longitude-latitude grids).

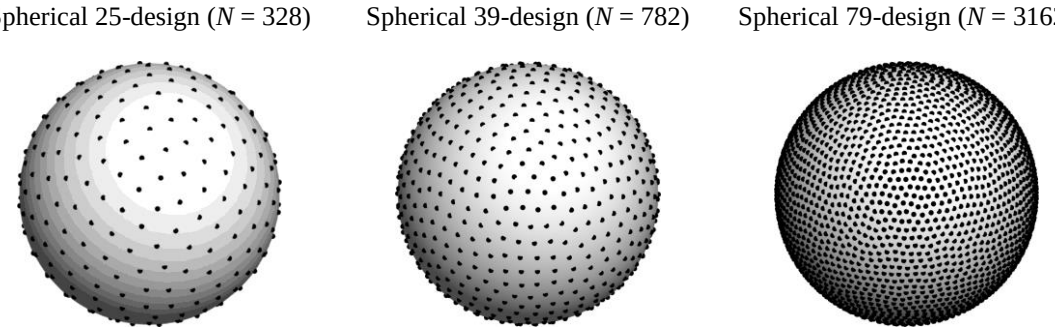

Figure 5.2 Womersley (2018) symmetric (antipodal) spherical *t*-designs on $\mathbb{S}^2$ for three polynomial degrees: (a) $t = 25$; (b) $t = 39$; and (c) $t = 79$. The total number of points, *N*, necessarily even, is $N = \frac{1}{2}t^2 + \frac{1}{2}t + \mathcal{O}(1)$.

Returning to the problem at hand, following Eq. (5.39), the task is on determining the surface average $\langle \psi(\boldsymbol{d}^{\mathrm{tr}}(\underline{\boldsymbol{x}}))\rangle_{S(r)}$, with ψ given in Eq. (4.22). Since function ψ is not a spherical polynomial, i.e. $\psi \notin \mathbb{P}_t(\mathbb{S}^2)$, one arrives at an *approximation* of this surface integral when using spherical designs with a given degree *t*. Combining Eq. (5.39), Eq. (5.51) and Eq. (5.53) one obtains:

$$\left\langle \psi\left(\boldsymbol{d}^{\mathrm{tr}}\left(\underline{\boldsymbol{x}}\right)\right)\right\rangle_{S(r)} \cong \frac{1}{N}\sum_{i=1}^{N}\psi\left(\boldsymbol{d}^{\mathrm{tr}}\left(\underline{\boldsymbol{x}}_i\right)\right), \underline{\boldsymbol{x}}_i \in S(r) \text{ and } \underline{\boldsymbol{x}}_i/\left\|\underline{\boldsymbol{x}}_i\right\|_2 \in \mathcal{X}_N . \tag{5.54}$$

In other words, the surface averaging integral $\langle \psi(\boldsymbol{d}^{\mathrm{tr}}(\underline{\boldsymbol{x}}))\rangle_{S(r)}$ is simply determined by the average of the function values $\psi(\boldsymbol{d}^{\mathrm{tr}}(\underline{\boldsymbol{x}}_i))$, $i = 1,...,N$, at the points of a spherical design of radius $r = \|\underline{\boldsymbol{x}}_i\|_2$. This expression is valid of all spherical *t*-design formulations. In view of the even symmetry of the fields considered in this work (see §5.2.3), i.e. $\boldsymbol{d}^{\mathrm{tr}}(\underline{\boldsymbol{x}}) = \boldsymbol{d}^{\mathrm{tr}}(-\underline{\boldsymbol{x}})$, working with symmetric (antipodal) point sets, $\mathcal{X}_N^{\mathrm{sym}} \leftarrow \mathcal{X}_N$, provides a key computational advantage. Assuming $\mathcal{X}_N^{\mathrm{sym}} = \{\underline{\boldsymbol{x}}_1,...,\underline{\boldsymbol{x}}_{N/2},...,\underline{\boldsymbol{x}}_N\} \in \mathbb{S}^2$ with $\underline{\boldsymbol{x}}_{N/2+j} = -\underline{\boldsymbol{x}}_j$, for $j = 1,...,N/2$, allows us to effectively half the number of function evaluations of Eq. (5.54), i.e.:

$$\left\langle \psi\left(\boldsymbol{d}^{\mathrm{tr}}\left(\underline{\boldsymbol{x}}\right)\right)\right\rangle_{S(r)} \cong \frac{1}{N/2}\sum_{i=1}^{N/2}\psi\left(\boldsymbol{d}^{\mathrm{tr}}\left(\underline{\boldsymbol{x}}_i\right)\right), \underline{\boldsymbol{x}}_i \in S(r) \text{ and } \underline{\boldsymbol{x}}_i/\left\|\underline{\boldsymbol{x}}_i\right\|_2 \in \mathcal{X}_N^{\mathrm{sym}} . \tag{5.55}$$

It flows that the usage of antipodal spherical *t*-designs, such as those reported in Womersley (2018), is highly recommend. Figure 5.3 represents a proof of concept of the integration scheme proposed in Eq. (5.55). Note that the brightened points in Figure 5.3 (a) are not used in the cubature. For the considered spherical design formulation these correspond to the $N^{\mathrm{sym}} = \frac{1}{4}t^2 + \frac{1}{4}t + \mathcal{O}(1)$ points on a single hemisphere (either northern or southern). An example of the local field $\psi(\boldsymbol{d}(\underline{\boldsymbol{x}}))$ distribution on the outer surface, $r = b$, is represented in Figure 5.3 (b)-(c) in a Cartesian and spherical plot, respectively. These figures were obtained by 2-D interpolation of the reduced set of quadrature points $(\theta_i \leq \pi/2)$ and applying the appropriate symmetry and periodicity properties.

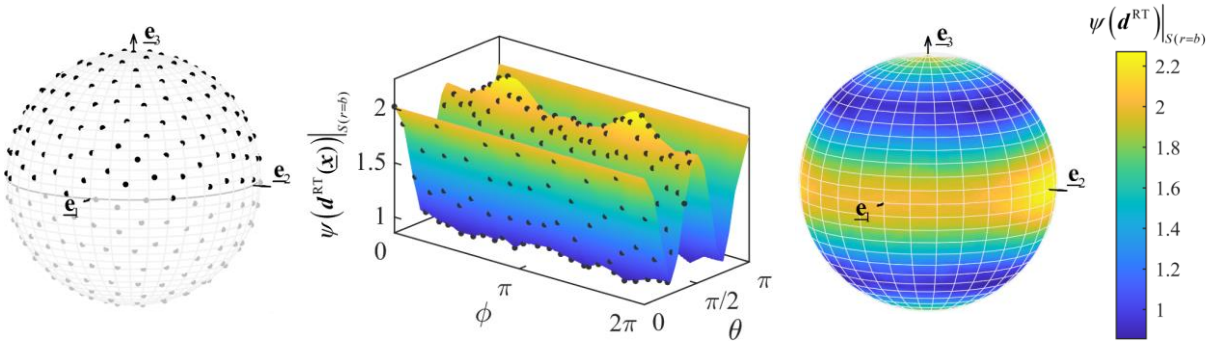

(a) (b) (c)

Figure 5.3 Principle of determination of the average surface integral over the spherical surface $S(r)$: (a) antipodal spherical 25-design with only half points considered, $N^{\text{sym}} = N/2 = 164$; (b) and (c): integrand distribution on the outer RVE surface, $S(r=b)$, for a purely hydrostatic compression loading, $\boldsymbol{D} = -\boldsymbol{I}$, using the Rice and Tracey local fields for a CP-Ti matrix (constitutive data in §4.5.2).

At this point, the question arises as to what is the minimum polynomial degree, *t*, (or, equivalently, the minimum number of points, *N*) of the design which guarantees a desired accuracy for the integrals $\langle \psi(\boldsymbol{d}^{\text{tr}}(\underline{\boldsymbol{x}})) \rangle_{S(r)}$. Evidently, the answer depends on the integrand, more specifically, on the particular trial strain-rate field, $\boldsymbol{d}^{\text{tr}}(\underline{\boldsymbol{x}})$ and the complexity of the constitutive relations of the material. In order to tackle this problem, a convergence rate analysis is performed. The results are shown in Figure 5.4. For the matrix phase, the three orthotropic models presented in Chapter 4 in the context of dense materials are recalled. The respective (local) plastic potentials involve three different homogeneity degrees: $a = 2$ for the CP titanium (§4.5.2); $a = 6$ for the AZ31B magnesium alloy (§4.5.3); and $a = 12$ for the 2090-T3 aluminium alloy (§4.5.4). The analysis is carried out on a sample of $n_s = 10^4$ macroscopic strain-rate states, $\boldsymbol{D}$, with random deviatoric components $D'_{ij} \in [-1,1]$ and superimposed macroscopic strain triaxiality[18], $T_D \in [10^{-8}, 10^{1}]$, considering the trial strain-rate fields of Rice and Tracey, $\boldsymbol{d}^{\text{RT}}(\underline{\boldsymbol{x}}, \boldsymbol{D})$ (Eq. (5.20)), on porous solids with porosity $f = 10^{-6}$. For each loading of the sample, a quadrature error, $e = (I(f) - Q_N(f))/I(f)$, (c.f. Eq. (5.51)), $f(\underline{\boldsymbol{x}}) \leftarrow \psi(\boldsymbol{d}(\underline{\boldsymbol{x}}))$ is determined. The approximations, Q_N of $\langle \psi(\boldsymbol{d}^{\text{RT}}(\underline{\boldsymbol{x}})) \rangle_{S(r)}$ are determined using the antipodal spherical designs of Womersley (2018) with $t = 1,...,99$, for which $N \in [2, 4952]$. The 'exact' integrals, I, are computed using a spherical design with $t = 245$ ($N = 30138$). Figure 5.4 shows the decrease of the average quadrature error with increasing number of quadrature points, *N*, (or degree *t*), as well as the associated error bars depicting 2 corrected sample standard deviations, 2*s*. The analysis was carried out for the inner, $S(r=a)$, (Figure 5.4a) and outer, $S(r=b)$, (Figure 5.4b) surfaces of the RVE. It is concluded that the average quadrature error is greater at $S(r=a)$ (the variance is however inferior in the latter). This is thought to be explained by the increased heterogeneity of the trial strain-rate fields, $\boldsymbol{d}^{\text{RT}}(\underline{\boldsymbol{x}})$, (and therefore of $\psi(\boldsymbol{d}^{\text{RT}}(\underline{\boldsymbol{x}}))|_{S(r)}$), for the spherical surfaces approaching the inner RVE surface, due to the second term of Eq. (5.20). Moreover, the material homogeneity parameter, *a*, has major influence on the quadrature error of the surface integrals. This is attributed to the increasing number of local maxima and minima of the

[18] The macroscopic strain triaxiality is defined as $T_D = D_{\text{m}}/D_{\text{vM}}$, where D_{vM} is the macroscopic von Mises equivalent strain-rate associated with $\boldsymbol{D}$, $D_{\text{vM}} = \frac{2}{3}\|\boldsymbol{D}\|_{\text{vM}} = \sqrt{\frac{2}{3}\boldsymbol{D}' : \boldsymbol{D}'}$.

integrand, $\psi(\boldsymbol{d}^{\mathrm{RT}}(\underline{\mathbf{x}}))|_{S(r)}$, (as in Figure 5.3b-c), with increasing homogeneity parameter, in particular, near the inner surface, $S(r=a)$. For a given accuracy level, one must then select a spherical design based on the guidelines of Figure 5.4a, since the average quadrature error on any other surface $S(r)$ is lower (from the statistic standpoint). For example, in order to fulfil a relative error $e=10^{-6}$, in the worst-case scenario, i.e. at $S(r=a)$ and for porous media with vanishing porosity, viz. $f=\mathcal{O}(10^{-6})$, a minimum number of points $N=328$ ($t=25$), $N=782$ ($t=39$), and $N=3162$ ($t=79$) are required for the matrices with $a=2$, $a=6$, $a=12$, respectively. These designs correspond to those represented in Figure 5.4. If one is satisfied with a relative error $e=10^{-5}$ then the number of points reduces to $N=156$ ($t=17$), $N=380$ ($t=27$), and $N=1130$ ($t=47$), respectively, which corresponds to about half of the computational effort. Regarding computational aspects, it is worth mentioning that the CPU time of the surface averaging operations scales quasi-linearly with the number of quadrature points, N, (as expected given the sum in Eq. (5.55)). Lastly, it should be noted that the surface average $\langle\overline{\boldsymbol{s}}(\underline{\mathbf{x}})\rangle_{S(r)}$ in Eq. (5.48) regarding the local deviatoric stress field is determined using spherical t-designs similarly to Eq. (5.54) (or its particular form Eq. (5.55), using Womersley (2018) antipodal sets). Adopting the latter, one arrives at a straightforward cubature expression in the form:

$$\left\langle\overline{\boldsymbol{s}}(\underline{\boldsymbol{x}})\right\rangle_{S(r)} \cong \frac{1}{N/2}\sum_{i=1}^{N/2}\overline{\boldsymbol{s}}\left(\underline{\boldsymbol{x}}_i\right),\ \underline{\boldsymbol{x}}_i \in S(r) \text{ and } \underline{\boldsymbol{x}}_i/\left\|\underline{\boldsymbol{x}}_i\right\|_2 \in \mathcal{X}_N^{\mathrm{sym}}. \tag{5.56}$$

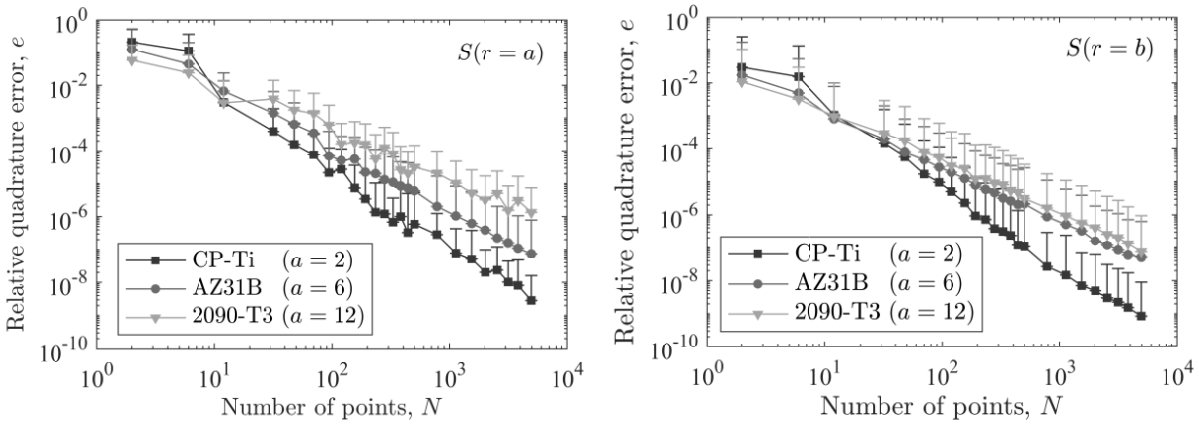

Figure 5.4 Average and two standard deviations of the relative quadrature error of $\langle\psi(\boldsymbol{d}^{\mathrm{RT}})\rangle_{S(r)}$ using spherical t-designs with N points for a sample with $n_{\mathrm{s}}=10^4$ random loading states, $\boldsymbol{D}$, on the boundary surfaces of an RVE with $f=10^{-6}$: (a) $S(r=a)$; (b) $S(r=b)$; for three orthotropic matrices with tension-compression asymmetry and varying homogeneity degree, a (see §4.5) and adopting the Rice and Tracey fields. The lower error bar is omitted due to the limitations of the logarithmic scale.

5.4.2 Determination of the 1-D integral over the radial coordinate

The focus of this subsection is on the determination of the one-dimensional definite integral in Eq. (5.39). Given that the integrand, $A(r)\langle\psi(\boldsymbol{d}^{\mathrm{tr}}(\underline{\mathbf{x}}))\rangle_{S(r)}$, is obtained in a numerical fashion (Eq. (5.55)), this integral is restricted to numerical evaluation. The goal here is to optimize the 1-D quadrature, both in number of points and location, in order to comply with a given accuracy for the radial integrals while minimizing the number of function evaluations (hence surface averaging operations). It is proposed the

usage of piecewise polynomial-based integration methods built on a non-uniform partition of the integration domain, $r \in [a,b]$. In fact, the hydrostatic expansion fields of the considered local strain-rate fields (recall Eq. (5.20) and Eq. (5.30), for the Rice and Tracey and Eshelby-based fields, respectively), depend on the radial coordinate, its contribution being proportional to $\delta_r \triangleq (b/r)^3 = (a/r)^3/f$. This is in contrast with the uniform extension field, which, by definition, does not depend on any spherical coordinate. Accordingly, for loadings with $D_{\mathrm{m}} \neq 0$, the gradient of function $\langle \psi(\boldsymbol{d}^{\mathrm{tr}}(\underline{\mathbf{x}}))\rangle_{S(r)}$ increases as $r \to a$, since $\delta_r \to 1/f$, (in the limit, $f \to 0$, it becomes an asymptote). Depending on the porosity level, *f*, and the contribution of the hydrostatic part, D_{m}, to the overall macroscopic loading, $\boldsymbol{D}$, a finer discretization in this zone may be required. The latter can be quantified by an unitless scalar $D_{\mathrm{m}}/\|\boldsymbol{D}\|_{\beta}$, where $\|\cdot\|_{\beta}$ denotes any matrix norm, (e.g. the *p*-norm, $p = 1, 2, \infty$). Defining the von Mises norm as $\|\cdot\|_{\mathrm{vM}} = \sqrt{3J_2(\cdot)}$, with $J_2(\boldsymbol{D}) = \frac{1}{2}\boldsymbol{D}' : \boldsymbol{D}'$, one can adopt the macroscopic strain triaxiality, $T_D = D_{\mathrm{m}}/D_{\mathrm{vM}}$, (see Footnote 18) to quantify the abovementioned contribution. Figure 5.5 depicts the typical shape of the functions $\langle \psi(\boldsymbol{d}^{\mathrm{tr}}(\underline{\mathbf{x}}))\rangle_{S(r)}$ and $A(r)\langle \psi(\boldsymbol{d}^{\mathrm{tr}}(\underline{\mathbf{x}}))\rangle_{S(r)}$ for porosities, *f*, of different orders of magnitude and macroscopic loadings with varying hydrostatic contribution, viz. vanishing, $T_D \to 0$, intermediate, $T_D = \mathcal{O}(10^{-2})$, and dominant, $T_D = \mathcal{O}(1)$. Note that, in fact, an asymptotic behaviour of $\langle \psi(\boldsymbol{d}^{\mathrm{tr}}(\underline{\mathbf{x}}))\rangle_{S(r)}$ is found with decreasing porosity and increasing hydrostatic contribution, viz. macroscopic strain triaxiality.

In order to capture the zones of high gradients of the 1-D integrals in Eq. (5.39) and/or Eq. (5.48) a three-step discretization method is employed. Firstly, the integration domain $[a,b]$ is uniformly partitioned in $n_{\mathrm{r}}^{\mathrm{u}}$ intervals and the functions $\langle \psi(\boldsymbol{d}^{\mathrm{tr}}(\underline{\mathbf{x}}))\rangle_{S(r)}$ and $A(r)\langle \psi(\boldsymbol{d}^{\mathrm{tr}}(\underline{\mathbf{x}}))\rangle_{S(r)}$ concerning the local SRP field are evaluated at the $(n_{\mathrm{r}}^{\mathrm{u}} + 1)$ equidistant points. The integer $n_{\mathrm{r}}^{\mathrm{u}}$ is given by $n_{\mathrm{r}}^{\mathrm{u}}(f) = \mathcal{O}((1 - f^{1/3})\bar{n}_{\mathrm{r}})$, where $\bar{n}_{\mathrm{r}} \in \mathbb{N}$ is a used-defined reference radial discretization parameter. This way, a regular distance between points is maintained regardless of the span of the radial domain $r \in [a,b]$ (otherwise, note that the usage of a fixed number of partitions $n_{\mathrm{r}}^{\mathrm{u}}$ would result in the decrease of the average distance between points with decreasing $(b-a)$, i.e. increasing *f*, and vice-versa). Secondly, each (uniform) partition is subdivided in $n_{\mathrm{r}}^{\mathrm{arc}}(i)$, $i = 1, ..., n_{\mathrm{r}}^{\mathrm{u}}$ intervals such that the arc length distribution of each curve is quasi-uniform, i.e., $n_{\mathrm{r}}^{\mathrm{arc}}(i) = \mathcal{O}(l_i/l_i^{\max}) \in \mathbb{N}_0$, where l_i is the arc length between adjacent points, $l_i^{\max} = (L/\bar{n}_{\mathrm{r}})$ is its threshold value and $L = \sum l_i$ the arc-length of the entire curve. In practice, the arc lengths are simply approximated using Euclidean norms of a normalized set of points, hence there is no need to parametrize the curve. Note that $n_{\mathrm{r}}^{\mathrm{arc}}(i)$ can be less than or equal to unity in which case no points are actually added to the original uniformly partitioned discretization. The integrand is then evaluated for the new set of radial points, resulting from the arc length distribution method of $\langle \psi(\boldsymbol{d}^{\mathrm{tr}}(\underline{\mathbf{x}}))\rangle_{S(r)}$ and/or $A(r)\langle \psi(\boldsymbol{d}^{\mathrm{tr}}(\underline{\mathbf{x}}))\rangle_{S(r)}$. Finally, the above-mentioned arc length-based reparameterization is repeated for each component of the local deviatoric stress field counterparts: $\langle \bar{\boldsymbol{s}}(\underline{\mathbf{x}})\rangle_{S(r)}$ and $A(r)\langle \bar{\boldsymbol{s}}(\underline{\mathbf{x}})\rangle_{S(r)}$. This step is motived by anecdotal evidence: while abrupt curvature changes near $r \to a$ are often predicted concurrently in both the local- SRP and deviatoric stress integrands, these are found at slightly different radii, (viz., that of $\langle \psi(\boldsymbol{d}^{\mathrm{tr}}(\underline{\mathbf{x}}))\rangle_{S(r)}$ tends to precede that of $\langle \bar{\boldsymbol{s}}(\underline{\mathbf{x}})\rangle_{S(r)}$, see e.g. the last plot in Figure 5.5b). If one intends to determine the macroscopic SRP, $\Psi^{+}(\boldsymbol{D})$, (Eq. (5.39)) alone, then the abovementioned

third radial discretization step (the second arc-length-based reparameterization) is actually redundant and can be disregarded. However, if one is also interested in the determination of its first derivative, $\bar{\boldsymbol{\Sigma}} = \partial\Psi^{+}(\boldsymbol{D})/\partial\boldsymbol{D}$, (Eq. (5.44)) then the full three-step procedure is highly recommended. Indeed, in view of Eq. (5.50), the determination of the stress field integral in Eq. (5.48) with appropriate accuracy is as important as the SRP field integral in Eq. (5.39), especially for loadings with vanishing macroscopic triaxiality $(\mathrm{tr}(\boldsymbol{D}) \to 0)$. Figure 5.5 represents the sample radial points obtained using the proposed adaptative discretization method. The unique user-defined parameter is the reference radial discretization parameter, here taken as $\bar{n}_{\mathrm{r}} = 10$. Note that the actual number of points ranges between $n_{\mathrm{r}} \in [6,17]$. The function $\langle \psi(\boldsymbol{d}^{\mathrm{RT}}(\underline{\mathbf{x}})\rangle_{S(r)}$ (right ordinate in Figure 5.5) displays an asymptotic nature near the inner surface of the RVE, hence the arc-length method adds quadrature points in this zone. The point clustering near the inner RVE surface, $r = a$, increases with decreasing porosity due to the increasing severity of curvature changes. Nevertheless, the radial increments near the outer surface, $r = b$, are similar, being controlled solely by $\bar{n}_{\mathrm{r}}$ (i.e. radial increments of the order $\mathcal{O}((b/\bar{n}_{\mathrm{r}}))$. This is due to the fact that both $\langle \psi(\boldsymbol{d}^{\mathrm{tr}}(\underline{\mathbf{x}})\rangle_{S(r)}$ and $\langle \bar{\boldsymbol{s}}(\underline{\mathbf{x}})\rangle_{S(r)}$, tend to stabilize as $r \to b$. An important remark is that, for a given macroscopic loading, $\boldsymbol{D}$, function $\langle \psi(\boldsymbol{d}^{\mathrm{RT}}(\underline{\mathbf{x}})\rangle_{S(r)}$, (and thus $A(r)\langle \psi(\boldsymbol{d}^{\mathrm{RT}}(\underline{\mathbf{x}})\rangle_{S(r)}$), is the same for all porosity values, the difference being its domain, $r \in [f^{1/3},1]b$. Moreover, the curves $\langle \psi(\boldsymbol{d}^{\mathrm{RT}}(\underline{\mathbf{x}})\rangle_{S(r)}$ in Figure 5.5, (i.e. with increasing hydrostatic contribution), have essentially the same shape, for a given porosity value, f, only varying in magnitude. The magnitude of $\langle \psi(\boldsymbol{d}^{\mathrm{RT}}(\underline{\mathbf{x}})\rangle_{S(r)}$, largely controlled by the second term in Eq. (5.20), ultimately defines the overall shape of the integrand, $A(r)\langle \psi(\boldsymbol{d}^{\mathrm{RT}}(\underline{\mathbf{x}})\rangle_{S(r)}$: for vanishing triaxialities ((a)), the integrand was a parabolic shape, i.e., $A(r)\langle \psi(\boldsymbol{d}\rangle_{S(r)} \propto r^2$; whereas for predominantly hydrostatic states (Figure 5.5c), the integrand approximates a rectangular hyperbola, i.e., $A(r)\langle \psi(\boldsymbol{d}\rangle_{S(r)} \propto 1/r$. For intermediates triaxialities (Figure 5.5b), an hybrid behaviour is found: hyperbolic as $r \to a$, and parabolic as $r \to b$. Indeed, the latter loading type appears to be the most computational demanding, not only due to the shape change of $A(r)\langle \psi(\boldsymbol{d}\rangle_{S(r)}$ but also due to the presence of gradients of the components of the local deviatoric stress tensor $\langle \bar{\boldsymbol{s}}(\underline{\mathbf{x}})\rangle_{S(r)}$ (not shown here, yet note the extra circle markers in Figure 5.5b). In summary, the proposed discretization scheme has a variable number of sample points, $n_{\mathrm{r}} = n_{\mathrm{r}}(f,\bar{n}_{\mathrm{r}}) = (n_{\mathrm{r}}^{\mathrm{u}} + \sum n_{\mathrm{r},i}^{\mathrm{arc}} + 1)$. For a given reference discretization parameter, $\bar{n}_{\mathrm{r}}$, the total number of points, n_{r}, increases with decreasing porosity (no analogous connection can be drawn regarding the triaxiality). In fact, the more computational demanding case is that of extremely low porosity values, viz. $f = \mathcal{O}(10^{-6})$, characteristic of undamaged metallic materials. Given its adaptative nature, such discretization scheme circumvents the need for *ad hoc* discretization rules based on the RVE geometry and loading state.

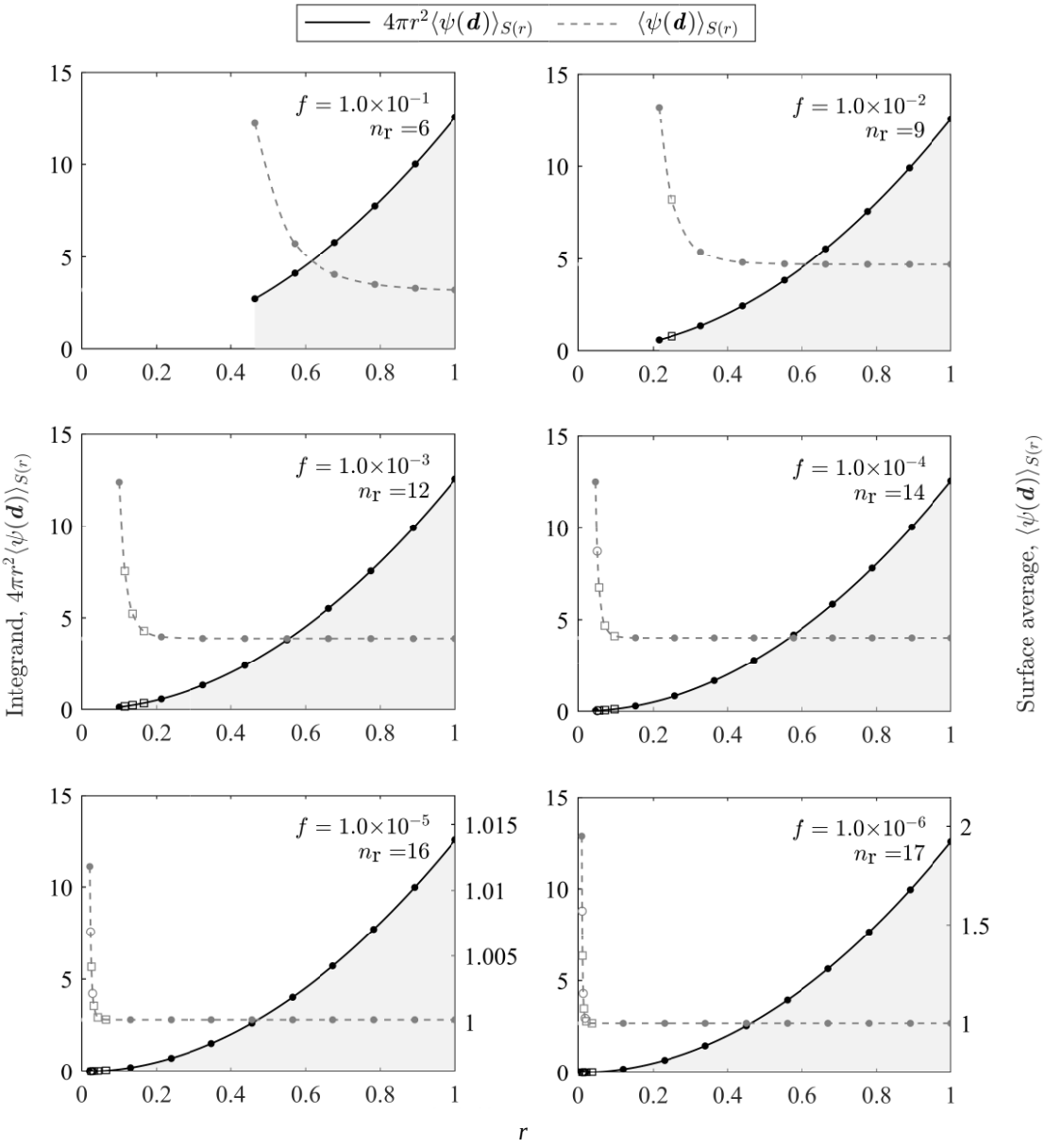
$4\pi r^2\langle\psi(\boldsymbol{d})\rangle_{S(r)}$
$\langle\psi(\boldsymbol{d})\rangle_{S(r)}$
$f = 1.0\times10^{-1}$
$n_{\mathrm{r}} = 6$
$f = 1.0\times10^{-2}$
$n_{\mathrm{r}} = 9$
$f = 1.0\times10^{-3}$
$n_{\mathrm{r}} = 12$
$f = 1.0\times10^{-4}$
$n_{\mathrm{r}} = 14$
$f = 1.0\times10^{-5}$
$n_{\mathrm{r}} = 16$
$f = 1.0\times10^{-6}$
$n_{\mathrm{r}} = 17$
Integrand, $4\pi r^2\langle\psi(\boldsymbol{d})\rangle_{S(r)}$
Surface average, $\langle\psi(\boldsymbol{d})\rangle_{S(r)}$
r

(a)

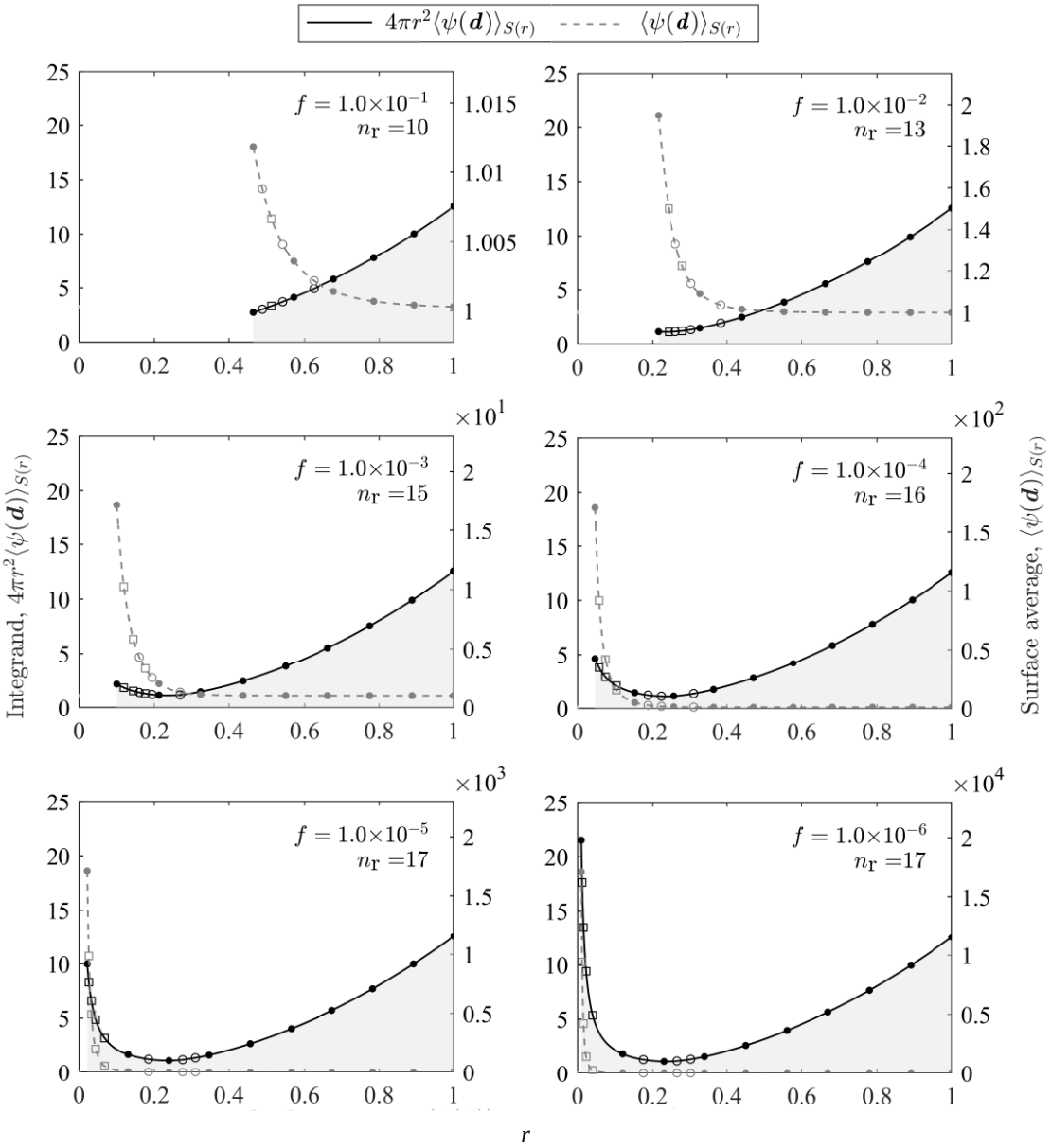
$4\pi r^2\langle\psi(\boldsymbol{d})\rangle_{S(r)}$
$\langle\psi(\boldsymbol{d})\rangle_{S(r)}$
$f = 1.0\times10^{-1}$
n_r =10
$f = 1.0\times10^{-2}$
n_r =13
$f = 1.0\times10^{-3}$
n_r =15
$f = 1.0\times10^{-4}$
n_r =16
$f = 1.0\times10^{-5}$
n_r =17
$f = 1.0\times10^{-6}$
n_r =17
$\times10^{1}$
$\times10^{2}$
$\times10^{3}$
$\times10^{4}$
Integrand, $4\pi r^2\langle\psi(\boldsymbol{d})\rangle_{S(r)}$
Surface average, $\langle\psi(\boldsymbol{d})\rangle_{S(r)}$
r

(b)

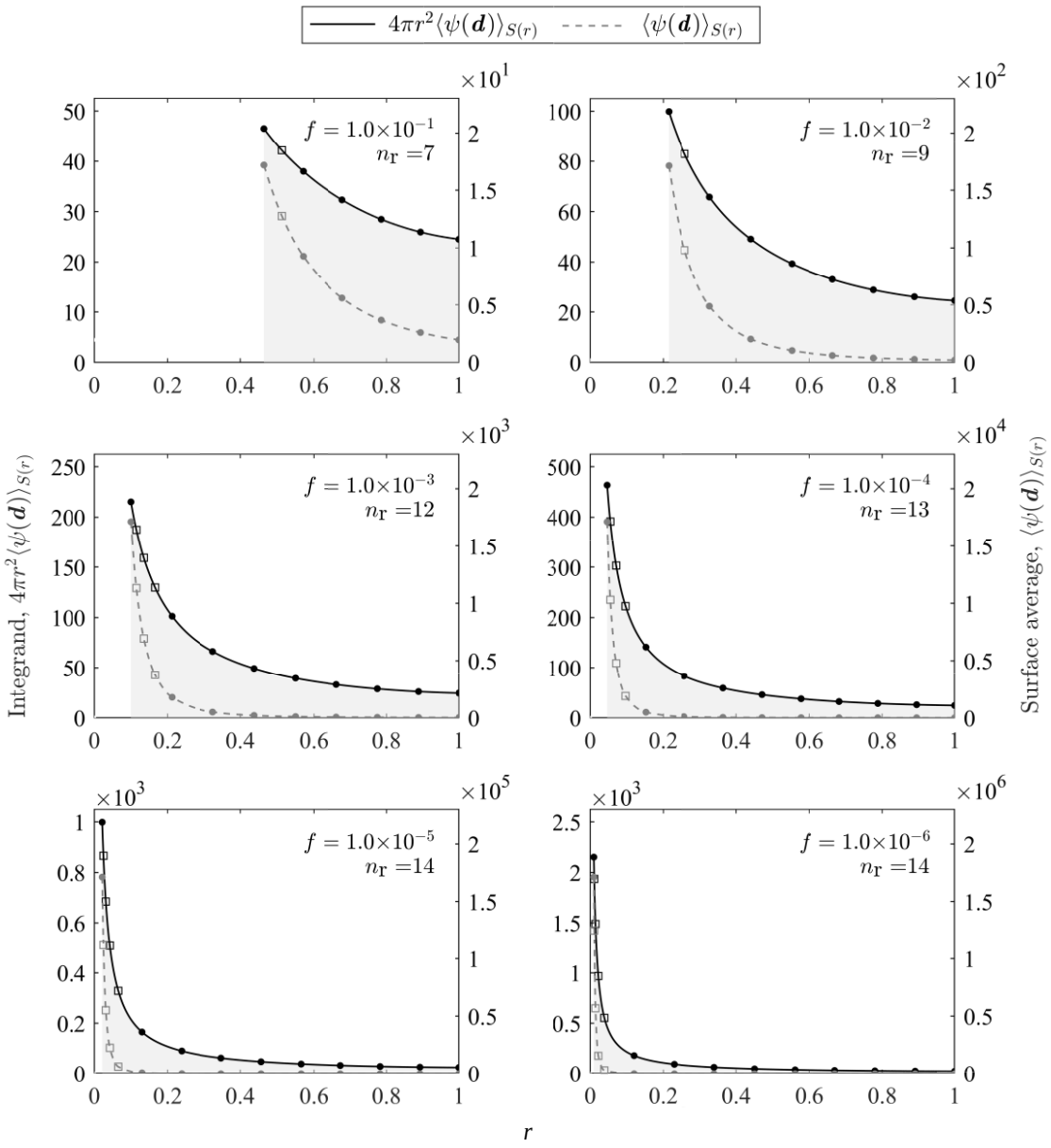

(c)

Figure 5.5 Principle of determination of the 1-D integrals over the radial direction (Eq. (5.39)): adaptative discretization based on the porosity and loading with varying macroscopic strain-rate triaxiality (a) $T_D = 10^{-6}$; (b) $T_D = 10^{-2}$; (c) $T_D = 1$. The point markers denote the reference uniform discretization ($\bar{n}_\mathrm{r} = 10$). The square and circle markers indicate the points added based on the quasi-uniform arc-length criterion on the local SRP and deviatoric stress tensor fields, respectively. Rice and Tracey fields are adopted and along with a CP-Ti matrix (constitutive data in §4.5.2). The right ordinate labels of the first four plots of (a) were omitted (the relative variations of $\langle\psi(\boldsymbol{d}^{\mathrm{RT}}(\underline{\mathbf{x}}))\rangle_{S(r)}$ are in the order $\mathcal{O}(10^{-10},10^{-8},10^{-6},10^{-4})$, respectively, i.e. virtually straight lines).

Given the set of n_r data points (r_i, y_i), where $y_i = 4\pi r_i^2\langle\psi(\boldsymbol{d}^{\mathrm{tr}}(\underline{\mathbf{x}}))\rangle_{S(r_i)}$, and $a = r_0 < r_1 < \ldots < r_{n_\mathrm{r}-1} = b$, a spline $\zeta(r) \in C^2[a,b]$ is constructed based on piecewise polynomials of degree 3, i.e., for each interval $[r_{i-1}, r_i]$, one has:

$$\zeta(r)=\begin{cases} P_1(r), & r_0 \le r \le r_1 \\ \dots & \\ P_i(r), & r_{i-1} \le r \le r_i \\ \dots & \\ P_{n_r-1}(r), & r_{n_r-2} \le r \le r_{n_r-1} \end{cases}, \text{ with } P_i(r)=a_i+b_i r+c_i r^2+d_i r^3,\ \ i=1,\dots,n_r-1. \tag{5.57}$$

The $4(n_r-1)$ polynomial coefficients (a_i,b_i,c_i,d_i) are determined solving a tridiagonal linear equation system based on $4(n_r-1)$ boundary conditions: (i) $P_i(r_{i-1})=y_{i-1}$ and $P_i(r_i)=y_i$, $i=1,\dots,n_r-1$; (ii) $P_i^{'}(r_i)=P_{i+1}^{'}(r_i)$ and $P_i^{''}(r_i)=P_{i+1}^{''}(r_i)$, $i=1,\dots,n_r-2$; (iii) the not-a-knot endpoint condition (i.e. the third derivative of the cubic spline is continuous at r_1 and r_{n_r-2}: $P_1^{'''}(r_1)=P_2^{'''}(r_1)$, $P_{n_r-2}^{'''}(r_{n_r-2})=P_{n_r-1}^{'''}(r_{n_r-2})$ (De Boor, 1978). Once the interpolation spline is defined, one can compute an approximation of the 1-D integral in Eq. (5.39) as:

$$\Psi^{+}\left(\boldsymbol{D}\right)=\frac{1}{V}\int_a^b 4\pi r^2\left\langle\psi\left(\boldsymbol{d}^{\mathrm{tr}}(\underline{\boldsymbol{x}})\right)\right\rangle_{S(r)}dr\cong\frac{1}{V}\int_a^b\zeta\left(r\right)dr\,, \tag{5.58}$$

where the exact integration of the piecewise cubic polynomials is trivial and can be performed either analytically using the integration expressions for polynomials or via a Gauss-type quadrature rule (cf. Eq. (5.51) and Eq. (5.52)). In practice, the spline construction is performed using build-in optimized libraries routines, e.g., the `spline` (or `interp1`) function within MATLAB® platform, and the data fitting family of routines in Intel® Math Kernel Library (MKL) for Fortran (e.g. `dfdinterpolate1d` and `dfdintegrate1d`). Analogously to Eq. (5.58), an approximation of the 1-D integral in Eq. (5.48) is determined based on the integration of cubic splines of the (non-symmetric) components of the integrand $4\pi r^2\langle\bar{\boldsymbol{s}}(\underline{\boldsymbol{x}})\rangle_{S(r)}$.

A convergence rate analysis is now performed regarding the reference discretization parameter, $\bar{n}_r$, implicitly entering the quadrature rule in Eq. (5.58). A quadrature error, $e=(I(f)-Q_N(f))/I(f)$, (c.f. Eq. (5.51)), $f(\underline{\boldsymbol{x}})\leftarrow A(r)\langle\psi(\boldsymbol{d}^{\mathrm{tr}}(\underline{\boldsymbol{x}})\rangle_{S(r)}$, is determined for each approximation by varying the discretization parameter, $\bar{n}_r\in[4,50]$. The 'exact' integrals, I, are determined setting $\bar{n}_r=200$. The 1-D integrands are evaluated using a very refined surface discretization, viz. spherical 201-design ($N=20304$), in order to minimize error propagation an ensure that the obtained quadrature errors depend on the radial discretization alone. The analysis is carried out for the same matrix materials, pseudo-random macroscopic loading sample and local velocity fields type as in the equivalent analysis in subsection §5.4.1 (recall Figure 5.4 and its concerning text). Figure 5.6 shows the obtained results for porous solids with porosity, $f=10^{-6}$ (Figure 5.6a), and $f=10^{-2}$ (Figure 5.6b). It is concluded that the average quadrature is practically independent of the porosity degree. This highlights the robustness of the developed adaptative discretization scheme. In contrast with the findings in Figure 5.4 regarding the quadrature error of the surface integrals, the matrix constitutive model, namely the material homogeneity parameter, a as a minor influence on the convergence rate of the radial integrals. Depending on the desired degree of accuracy, the radial discretization parameter, $\bar{n}_r$, should be chosen based on the guidelines of Figure 5.6. For example, in order to satisfy a relative error $e=10^{-6}$, a discretization with at least $\bar{n}_r=16$ must be selected, whereas for an relative error $e=10^{-5}$, it suffices $\bar{n}_r=10$. It should be emphasised that $\bar{n}_r$

is not actually the number of quadrature points. As previously mentioned, the total number of points, n_r, depends on the span of the radial domain and, possibly, on the arc-length-based adaptative refinement method. Figure 5.7 illustrates this observation. The results revealed that the total number of quadrature points is virtually independent of the material, thus only one curve, (that of the CP-Ti) is shown in Figure 5.7. Regarding computational aspects, it is concluded that the CPU time of the radial averaging operation scales quasi-linearly with the total number of quadrature points, n_r, since the determination of the spline coefficients (see Eq. (5.57)) and the polynomial integration tasks have a negligible CPU time when compared with that expended in the computation of the local fields.

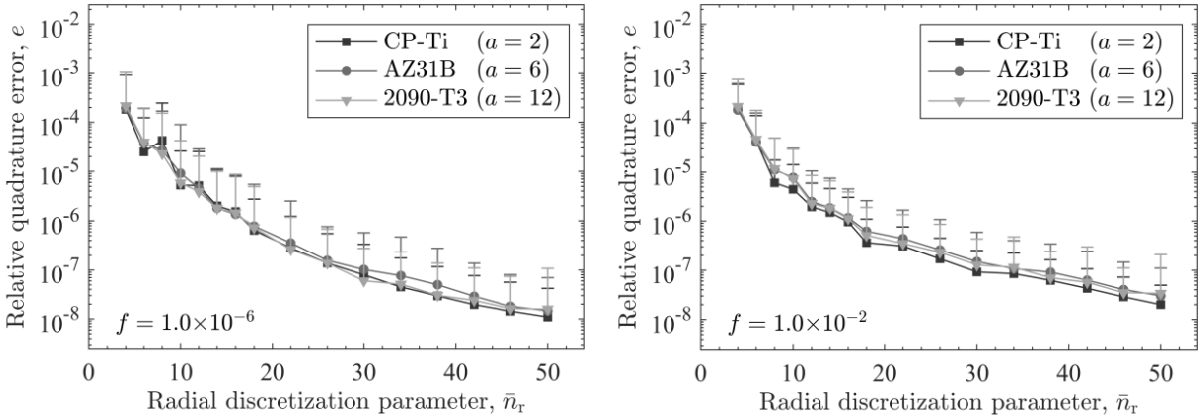

Figure 5.6 Average and two standard deviations of the relative error of $\Psi^+(\boldsymbol{D})$ (Eq. (5.39)) using a radial discretization parameter $\bar{n}_r$, for a sample with $n_s = 10^4$ random loading states, $\boldsymbol{D}$, and porosity values: (a) $f = 10^{-6}$; (b) $f = 10^{-2}$. The analysis is carried out for three orthotropic matrices with tension-compression asymmetry and varying homogeneity degree, a (see §4.5) and adopting the Rice and Tracey fields. The lower error bar is omitted due to the limitations of the logarithmic scale.

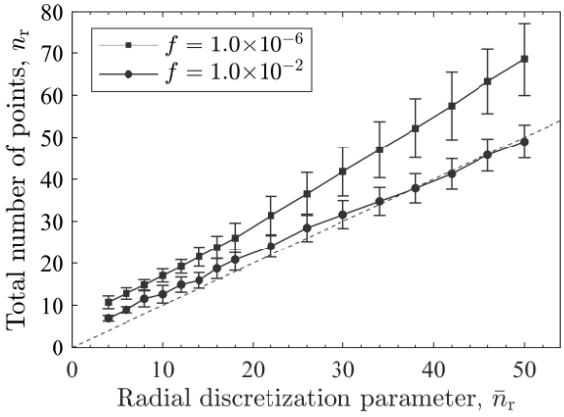

Figure 5.7 Averaged and two standard deviations of the total number of points, $n_r = n_r(\bar{n}_r, \boldsymbol{D}, f)$, employed in the radial quadrature of $\Psi^+(\boldsymbol{D})$ (Eq. (5.39)) for a sample with $n_s = 10^4$ random loading states on a CP-Ti matrix (constitutive data in §4.5.2). The dashed line has unitary slope $(n_r = \bar{n}_r)$.

5.5 Numerical implementation

The focus of this subsection is on the algorithmic aspects of the computational homogenization task described in §5.4. In the following, Voigt pseudo-vectorial and matrix notations are adopted on second order and forth order tensors, respectively, as well as the pentadimensional representation of symmetric deviatoric tensors (see Appendix B). As elucidated previously, one can distinguish two types of problems: (i) given a macroscopic strain-rate tensor, $\boldsymbol{D}$, determine its respective potential value, $\Psi(\boldsymbol{D})$, and its first derivative, $\partial\Psi(\boldsymbol{D})/\partial\boldsymbol{D}$; and (ii) given a macroscopic stress tensor $\boldsymbol{\Sigma}$, determine its respective potential value, $\Phi(\boldsymbol{\Sigma})$, and its first derivative, $\partial\Phi(\boldsymbol{\Sigma})/\partial\boldsymbol{\Sigma}$. Henceforth one refers to the 'direct problem' to denote the former and to 'inverse problem' to denote the latter. Naturally, these are duals. The naming convention is explained by the kinematic, rather than static, homogenization approach adopted in this work (it would be the opposite otherwise). The algorithms for the implementation of both problems are represented in pseudo-code format in: Box 5.1 and Box 5.2 for the direct problem; and Box 5.3 and Box 5.4 for the inverse problem. These apply for both the Rice and Tracey (Eq. (5.20)) and the Eshelby-type trial velocity fields (Eq. (5.30)). Note that for the latter an additional computational task is in order due the infimum in Eq. (5.30), viz. the determination of the deviatoric part of the eigenstrain-rate tensor, $\boldsymbol{d}^{*\prime}$. For details on the determination of this kinematical tensor refer to Appendix E. As mentioned in §5.3.2, solving the inverse problem (Box 4.3) implies determining a Jacobian matrix, which renders it more computationally demanding (a comparison of the relative computational cost is later presented in subsection §6.3). A similar problem holds regarding the determination of the eigenstrain-rate tensor for the Eshelby-type fields (see Appendix E). In practice, the associated computational overhead of these can be alleviated by adopting computational strategies, e.g.: (i) updating the Jacobian matrix in explicit fashion, rather than fully computing it in every iteration; and (ii) using a cruder RVE discretization to get an approximate solution, only then to be corrected by the actual (more refined) one. Fortran 90 code for the algorithms described here is provided in Appendix F.

Box 5.1 Computational homogenization scheme: the direct problem.

0. Inputs: $\{\underline{\mathbf{D}}, \underline{\mathbf{d}}^{*(5)}\}$, $\{f, b\}$, $\{\mathbf{L}^{(n)}, k^{(n)}, a\}$

1. Define the RVE discretization parameters

- Load the spherical *t*-design with *N* points: $X_N = \{\underline{\mathbf{x}}_1, ..., \underline{\mathbf{x}}_N\} \in \mathbb{S}^2$
- Set the radial discretization parameter, $\bar{n}_{\mathrm{r}}$

2. Reference solution

- Uniform partition of the radial coordinate, $r_{\mathrm{ref}} = \{r_0, ..., r_{n_{\mathrm{r}}^{\mathrm{u}}}\} \in [a, b]$
- Compute local fields in the surfaces of r_{ref} : CALL Box 5.2
- Compute reference surface averages: $\langle \psi(\underline{\mathbf{x}}) \rangle_{S(r_i)} = \sum_{j=1}^{N} \psi(\underline{\mathbf{x}}_j)/N, \quad i = 1, ..., n_{\mathrm{r}}^{\mathrm{u}}$ % (Eq. (5.54))
- Compute reference 1-D radial integrand: $4\pi r_i^2 \langle \psi(\underline{\mathbf{x}}) \rangle_{S(r_i)}, \quad i = 1, ..., n_{\mathrm{r}}^{\mathrm{u}}$

3. Arc-length based reparameterization

- Determine approximate arc-lengths of the set: $\{r_i, 4\pi r_i^2 \langle \psi(\underline{\mathbf{x}}) \rangle_{S(r_i)}\}, \quad i = 1, ..., n_{\mathrm{r}}^{\mathrm{u}}$
- Determine number of new partitions for each $[r_i, r_{i+1}]$: $n_{\mathrm{r}}^{\mathrm{arc}}(i)$

if $\mathrm{sum}(n_{\mathrm{r}}^{\mathrm{arc}}(i)) \neq 0$

- Define new points, $r_{\mathrm{arc}} = \{r_0, ..., r_{n_{\mathrm{r}}^{\mathrm{arc}}}\} \in]a, b[$
- Compute local fields in the surfaces of r_{arc} : CALL Box 5.2
- Update surface averages: $\langle \psi(\underline{\mathbf{x}}) \rangle_{S(r_i)} = \sum_{j=1}^{N} \psi(\underline{\mathbf{x}}_j)/N, \quad i = 1, ..., (n_{\mathrm{r}}^{\mathrm{u}} + n_{\mathrm{r}}^{\mathrm{arc}} + 1)$ % (Eq. (5.54))
- Update 1-D radial integrand: $4\pi r_i^2 \langle \psi(\underline{\mathbf{x}}) \rangle_{S(r_i)}, \quad i = 1, ..., (n_{\mathrm{r}}^{\mathrm{u}} + n_{\mathrm{r}}^{\mathrm{arc}} + 1)$

end if

4. Deviatoric stress integrand

- Compute surface averages: $\langle \bar{\boldsymbol{s}}(\underline{\mathbf{x}}) \rangle_{S(r_i)} = \sum_{j=1}^{N} \bar{\boldsymbol{s}}(\underline{\mathbf{x}}_j)/N, \quad i = 1, ..., (n_{\mathrm{r}}^{\mathrm{u}} + n_{\mathrm{r}}^{\mathrm{arc}} + 1)$
- Compute 1-D radial integrand: $4\pi r_i^2 \langle \bar{\boldsymbol{s}}(\underline{\mathbf{x}}) \rangle_{S(r_i)}, \quad i = 1, ..., (n_{\mathrm{r}}^{\mathrm{u}} + n_{\mathrm{r}}^{\mathrm{arc}} + 1)$
- Repeat Step 3 based on the arc-lengths of the set: $\{r_i, 4\pi r_i^2 \langle \bar{\boldsymbol{s}}(\underline{\mathbf{x}}) \rangle_{S(r_i)}\}, \quad i = 1, ..., (n_{\mathrm{r}}^{\mathrm{u}} + n_{\mathrm{r}}^{\mathrm{arc}} + 1)$

5. Spline construction and integration

- Construct spline for the SRP: $\zeta_{\psi}(r) \leftarrow 4\pi r_i^2 \langle \psi(\underline{\mathbf{x}}) \rangle_{S(r_i)}$ % (Eq. (5.57))
- Construct spline for the stress components: $\zeta_{\bar{\boldsymbol{s}}}(r) \leftarrow 4\pi r_i^2 \langle \bar{\boldsymbol{s}}(\underline{\mathbf{x}}) \rangle_{S(r_i)}$
- Integrate splines: $\Psi^{+} = (1/V)\int_a^b \zeta_{\psi}(r)dr$ and $\bar{\underline{\boldsymbol{\Sigma}}}' = (\partial \Psi^{+}/\partial \underline{\mathbf{D}})' = (1/V)\int_a^b \zeta_{\bar{\boldsymbol{s}}}(r)dr$ % (Eq. (5.48))

6. First derivative

- $\mathrm{tr}(\boldsymbol{D}) = 3D_{\mathrm{m}} = \mathrm{sum}(\underline{\mathbf{D}}(1:3))$
- Hydrostatic part: $\bar{\Sigma}_{\mathrm{m}} = (\Psi^{+} - \bar{\underline{\boldsymbol{\Sigma}}}' \cdot \underline{\mathbf{D}})/(3D_m)$ % (Eq. (5.50))
- Normalized macroscopic Cauchy stress tensor: $\bar{\underline{\boldsymbol{\Sigma}}} = \partial \Psi^{+}/\partial \underline{\mathbf{D}} = \bar{\underline{\boldsymbol{\Sigma}}}' + \bar{\Sigma}_{\mathrm{m}} \begin{bmatrix} 1 & 1 & 1 & 0 & 0 & 0 \end{bmatrix}^{\mathrm{T}}$

7. Output:

if (Rice and Tracey)

$\{\Psi^{+}(\underline{\mathbf{D}}), \partial \Psi^{+}(\underline{\mathbf{D}})/\partial \underline{\mathbf{D}}\}$ % (Eq.(5.39))

elseif (Eshelby)

$\{\Upsilon(\underline{\mathbf{D}}, \underline{\mathbf{d}}^{*(5)}), \partial \Upsilon(\underline{\mathbf{D}}, \underline{\mathbf{d}}^{*(5)})/\partial \underline{\mathbf{D}}\}$ % (Eq. (5.41))

end

Box 5.2 Determination of the local fields in the RVE.

0. Inputs: $\{\underline{\mathbf{D}}, \underline{\mathbf{d}}^{*(5)}\}$, $\{f, b\}$, $\{\mathbf{L}^{(n)}, k^{(n)}, a\}$ $\{\mathcal{X}_N, n_r, r_i\}$

▪ Transform the spherical *t*-design X_N into spherical coordinates (θ_j, ϕ_j), $j = 1:N$

1. Determine microscopic/local fields in the cubature points

for $i = 1:n_r$ % (loop over the radial set $r_i \in [a,b]$, $i = 1,...,n_r$)

▪ Spherical surface $S(r_i)$

for $j = 1:N$ % (loop over the spherical design points: $\mathcal{X}_N = \{\underline{\mathbf{x}}_1, ..., \underline{\mathbf{x}}_N\} \in \mathbb{S}^2$)

▪ Compute local strain-rate fields:

if (Rice and Tracey)

CALL Box C.1: $\underline{\mathbf{d}} \leftarrow \boldsymbol{d}^{\mathrm{tr}}(\underline{\mathbf{D}}, r_i, \theta_j, \phi_j)$ % (Eq. (5.20))

elseif (Eshelby)

CALL Box D.1: $\underline{\mathbf{d}} \leftarrow \boldsymbol{d}^{\mathrm{tr}}(\underline{\mathbf{D}}, \underline{\mathbf{d}}^{*(5)}, r_i, \theta_j, \phi_j)$ % (Eq. (5.30))

end

▪ Compute local SRP and its first derivative

CALL Box 4.1: $\psi(\underline{\mathbf{d}}, \mathbf{L}^{(n)}, k^{(n)}, a)$ and $\partial\psi/\partial\underline{\mathbf{d}}$

$\psi(i, j) = \psi(\underline{\mathbf{d}}, \mathbf{L}^{(n)}, k^{(n)}, a)$ % (Eq. (4.22))

$\bar{s}(i, j, :) = \partial\psi/\partial\underline{\mathbf{d}}$

end

end

2. Output: $\{\psi_{ij}, \bar{s}_{ijk}\}$, $i = 1,...,n_r$, $j = 1,...,N$, $k = 1,...,6$

Box 5.3 Determination of the macroscopic stress potential and its first derivative: the inverse problem

0. Inputs: $\underline{\boldsymbol{\Sigma}}$, $\{f, b\}$, $\{\mathbf{L}^{(n)}, k^{(n)}, a\}$

1. Solve the system of equations

▪ Set initial guess $(\bar{\underline{\mathbf{D}}}_0, \tau_0^*)$, and relative convergence tolerances for the system: $\{\varepsilon_{\mathrm{tol}}^{\mathrm{fun}}, \varepsilon_{\mathrm{tol}}^{\Delta x}\}$

▪ Solve the system in Box 5.4 for $(\bar{\underline{\mathbf{D}}}, \tau^*)$, with a quasi-Newton method, such that:

$$\left(\frac{\left\| F_{(1:6)}(\bar{\underline{\mathbf{D}}}_{k+1}, \tau_{k+1}^*) \right\|_2}{\tau_{k+1}^*} < \varepsilon_{\mathrm{tol}}^{\mathrm{fun}} \right), \text{ and } \left(\left| F_{(7)}(\bar{\underline{\mathbf{D}}}_{k+1}, \tau_{k+1}^*) \right| < \varepsilon_{\mathrm{tol}}^{\mathrm{fun}} \right) \text{ and } \left(\frac{\left\| \bar{\underline{\mathbf{D}}}_{k+1} - \bar{\underline{\mathbf{D}}}_k \right\|_2}{\left\| \bar{\underline{\mathbf{D}}}_k \right\|_2} < \varepsilon_{\mathrm{tol}}^{\Delta x} \right),$$

where k is the number of the iteration and $F_{(I:J)}$ denotes the I to J components of vector $\underline{\mathbf{F}}$ with $1 \le I \le J \le 6$.

2. Output: $\Phi(\underline{\boldsymbol{\Sigma}}) \leftarrow \tau_{k+1}^*$, $\partial\Phi(\underline{\boldsymbol{\Sigma}})/\partial\underline{\boldsymbol{\Sigma}} \leftarrow \bar{\underline{\mathbf{D}}}_{k+1}$

Box 5.4 Error function vector of the inverse homogenization problem.

0. Inputs: $\{\underline{\boldsymbol{\Sigma}}, \underline{\bar{\mathbf{D}}}, \tau^*\}$, $\{f, b\}$, $\{\mathbf{L}^{(n)}, k^{(n)}, a\}$

1. Perform the direct homogenization problem

▪ Determine $\Psi^+(\underline{\bar{\mathbf{D}}})$ and $\partial\Psi^+(\underline{\bar{\mathbf{D}}})/\partial\underline{\bar{\mathbf{D}}}$

if (Rice and Tracey)

CALL Box 5.1 % (Eq.(5.39))

elseif (Eshelby)

CALL Box E.1 % (Eq. (5.41))

end

2. Construct the error pseudo-vector function

▪ $\underline{\mathbf{F}} \leftarrow \begin{Bmatrix} \underline{\boldsymbol{\Sigma}} - \tau^* \left(\partial\Psi^+(\underline{\bar{\mathbf{D}}})/\partial\underline{\bar{\mathbf{D}}} \right) \\ \Psi^+(\underline{\bar{\mathbf{D}}}) - 1 \end{Bmatrix}$

3. Output: $\underline{\mathbf{F}}$

Chapter 6

Assessment of the proposed numerical potentials

The objective of this chapter is to compare the numerical-based potentials developed in Chapter 5 with existing analytical criteria and to assess their accuracy through numerical limit analyses using FE unit cell computations. An application example is initially presented in order to discuss some general trends of the developed macroscopic potentials when describing the behaviour of porous solids whose matrices display both tension-compression asymmetry and anisotropy. Next, the predictions using the Rice and Tracey and the Eshelby-type trial fields are compared considering isotropic matrices whose microscale plastic behaviour is described by quadratic and non-quadratic yield functions accounting for different tension-compression yield strength ratios. To close, remarks on the computational performance of the numerical homogenization are provided.

6.1 Application example: AZ31B magnesium alloy matrix

In order to discuss some features of the developed model, macroscopic potentials for porous solids are now evaluated considering the initial yield response of an AZ31B-O (Mg+3%Al+1%Zn) Mg alloy for the matrix. The matrix plastic behaviour is adopted following the experimental and constitutive data reported in Tari *et al.* (2014), presented in Figure 4.3 and Table 4.3 (§4.5.3), respectively, in the context of dense materials. The plastic behaviour of the matrix is thus described by the non-quadratic form of the Plunkett *et al.* (2008) orthotropic yield criterion (Eqs. (4.19)-(4.21)) using three transformations and a homogeneity parameter $a = 6$. Figure 6.1 represents the unitary isovalue loci of the respective macroscopic stress potential (SP), $\Phi^{\mathrm{RT}}(\boldsymbol{\Sigma}, f)$, (coincident with the macroscopic yield surface, Eq. (5.45)), and the macroscopic strain-rate potential (SRP), $\Psi^{\mathrm{RT}}(\boldsymbol{D}, f)$, based on the Rice and Tracey formulation (Eq. (5.42)), for porous solids with varying porosity, viz. $f = \{10^{-3}, 10^{-2}, 10^{-1}\}$. The surfaces are represented in a cylindrical coordinate system coaxial with the hydrostatic axis (recall Footnote 13, p.83). Figure 6.1 shows that the SP isosurface *contracts* along the hydrostatic axis as porosity increases, evolving from a capsule-like shape to an ellipsoidal one. Conversely, the conjugated SRP locus *expands* along the hydrostatic axis and develops an oblate ellipsoidal shape departing from a penny-shape one. Moreover, note that the macroscopic potentials exhibit asymmetric hydrostatic limits (more easily perceived in the SP loci). This is a result of the tension-compression asymmetry at the local (i.e. matrix), level, as shown in Stewart (2009) and Cazacu and Stewart (2009) in the context of isotropic matrices.

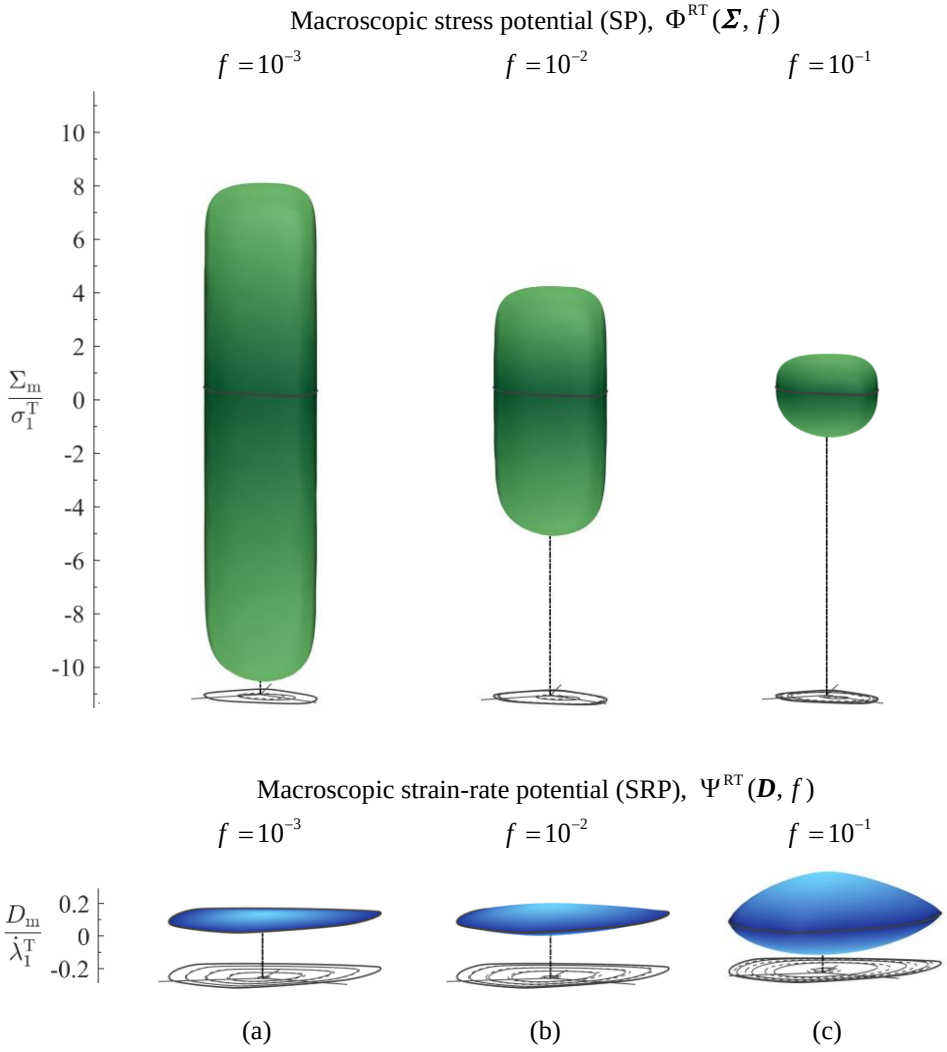

Figure 6.1 3-D representation of the macroscopic stress potential (Eq. (5.45)) and strain-rate potential (Eq. (5.29)) unitary isovalue surfaces in their respective principal space for porous solids with porosity: (a) $f = 10^{-3}$; (b) $f = 10^{-2}$; (c) $f = 10^{-1}$, with a AZ31B Mg alloy matrix (constitutive data after Tari *et al.* (2014)). Rice and Tracey local fields are considered. A cylindrical coordinate system coaxial with the hydrostatic axis is adopted. For illustrative purposes, the height coordinate (hydrostatic part) is not at scale with the radial (deviatoric part) one (2.5:1 ratio for the SP loci and 1:2.5 ratio for the SRP loci).

With the aim of better analysing the features of the developed potentials, Figure 6.2 represents π-plane (alias deviatoric plane) projections of the isovalue surfaces in Figure 6.1. Cross-sections of constant hydrostatic value are plotted based on the fractions $\overline{f}_i = \{0, 0.25, 0.5, 0.75, 0.985\}$ of the maximum and minimum hydrostatic values. Figure 6.2 shows that, as the porosity increases, the SP locus also contracts on the deviatoric plane. As expected from the duality property, the opposite holds for the SRP locus. More crucially, the shape of the π-plane projections changes drastically along the hydrostatic axis, departing from a shape reminiscent to that of the dense phase and resolving to a smoother, rounder one (i.e., approaching isotropy) near the poles. Note that existing closed-form criteria for porous solids cannot capture this shape changing behaviour as the underlying shape (but not size) in the purely deviatoric plane is maintained throughout the hydrostatic axis. Moreover, one can observe in Figure 6.2 that the shape of the cross-sections near the extreme hydrostatic values is about the same, irrespective of the

porosity. In contrast, porosity plays a key role on the rate of the shape change along the hydrostatic axis: the greater the porosity, the sooner, hence smoother, the shape change takes place, and vice versa. Similar trends were documented in the literature regarding isotropic matrix behaviours, viz. Revil-Baudard and Cazacu (2014) who performed a numerical homogenization study considering the Tresca and von Mises matrix behaviours; and Dæhli *et al.* (2019) who conducted FE limit analyses on non-quadratic isotropic matrices based on the Hershey-Hosford yield criterion. However, in contrast to the previous numerical studies, a novel result is that:

Remark 6.1 If the matrix is orthotropic, the loci of the extreme hydrostatic values (minima and maxima) of the respective macroscopic potentials *is not* on the hydrostatic axis.

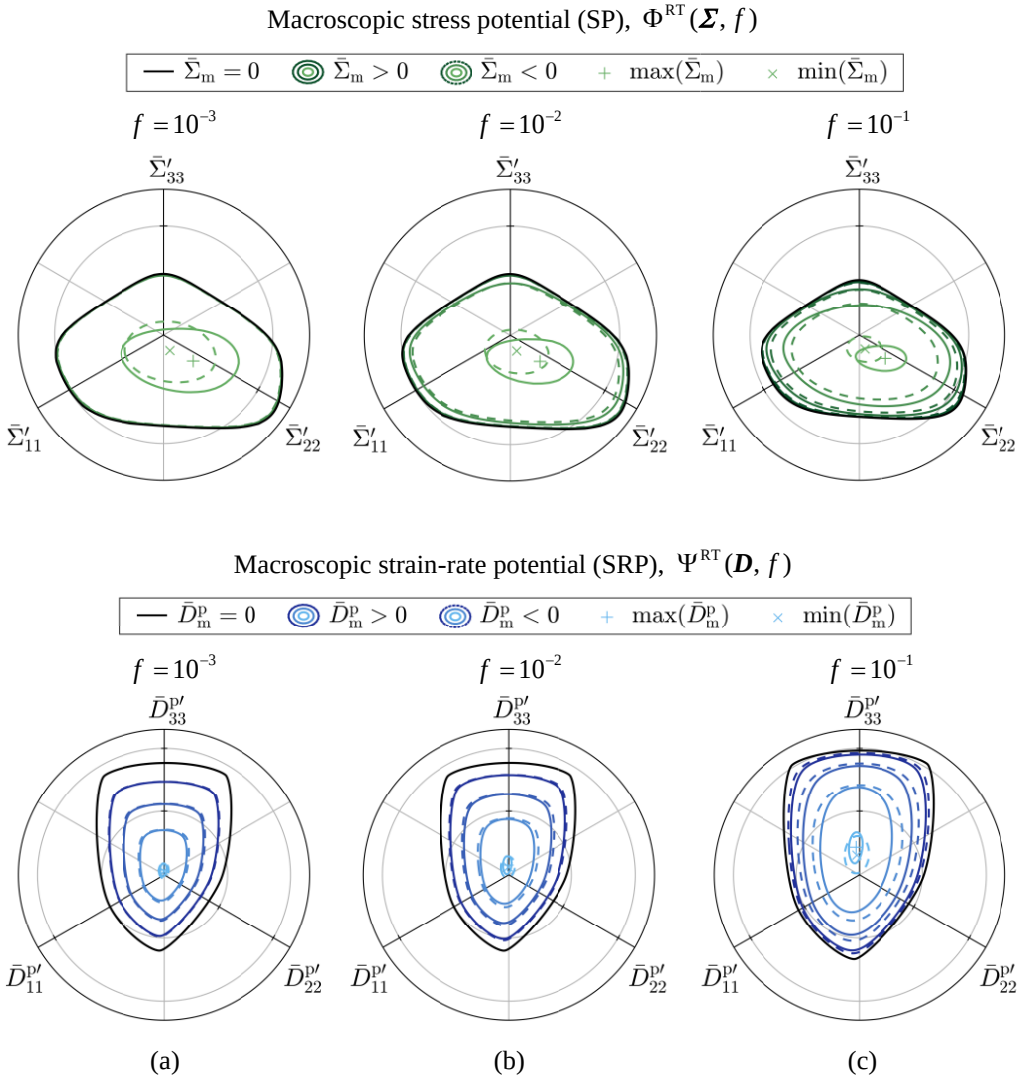

Figure 6.2 π-plane representation of the macroscopic stress potential (Eq. (5.45)) and strain-rate potential (Eq. (5.29)) unitary isovalue surfaces in their respective principal space for porous solids with porosity: (a) $f = 10^{-3}$; (b) $f = 10^{-2}$; (c) $f = 10^{-1}$, with a AZ31B Mg alloy matrix (constitutive data after Tari *et al.*, 2014). Rice and Tracey local fields are considered. Cross sections with varying hydrostatic fraction are plotted, with increments of 25% with respect to the tensile and compressive hydrostatic extreme values. The location of the latter is represented with markers. A polar-like plot is adopted, where the radial grid lines represent multiples of the respective unitary von Mises potential.

Figure 6.2 depicts this result with the marker points. This means that, for an orthotropic matrix, a purely hydrostatic macroscopic stress on the porous solid does not lead to a purely hydrostatic macroscopic strain-rate, and vice versa. Such behaviour cannot be replicated with existing closed-form orthotropic porous criteria, e.g., Benzerga and Besson (2001); Stewart and Cazacu (2011), which further motivates the usage of a numerical homogenization scheme.

6.2 Evaluation and validation

In the following, the developed approximate macroscopic potentials are evaluated for *isotropic* matrices whose microscale plastic behaviour is described by quadratic and non-quadratic yield functions accounting for different tension-compression yield strength ratios: no tension-compression asymmetry $(\sigma_1^{\mathrm{T}}/\sigma_1^{\mathrm{C}}=1)$, yield strength in tension greater than in compression $(\sigma_1^{\mathrm{T}}/\sigma_1^{\mathrm{C}}>1)$, and yield strength in tension lower than in compression $(\sigma_1^{\mathrm{T}}/\sigma_1^{\mathrm{C}}<1)$, where σ_1^{T} and σ_1^{C} are the uniaxial tensile and compressive yield stresses, respectively. The choice of restricting this subsection to isotropic conditions is justified by the large number of anisotropy coefficients (recall Eq. (4.20)) regarding general orthotropy, which would render the analysis untraceable. Nonetheless, the key observations of this subsection hold for the orthotropic case.

6.2.1 Approximate plastic potentials: evaluation and discussion

Nine matrix materials are considered based on the isotropic form of the microscale criterion (Eqs. (4.19)-(4.21) with a single transformation $\mathcal{C}=\mathcal{I}$, $(\mathcal{L}=\mathcal{K})$), by the combination of three homogeneity degrees: $a=\{2,8,12\}$ and three strength-differential (SD) ratios: $\sigma_1^{\mathrm{T}}/\sigma_1^{\mathrm{C}}=\{1,\ 1.21,\ 0.83\}$. These ratios are adopted following Hosford and Allen (1973) who showed that for a fully-dense body-centred cubic (bcc) polycrystal whose constituent grains deform exclusively by $\{112\}\langle 111\rangle$ twinning[19] the macroscopic yield stress in uniaxial tension is greater than in compression with a SD ratio $\sigma_1^{\mathrm{T}}/\sigma_1^{\mathrm{C}}=1.21$; and, conversely, for a fully-dense face-centred cubic (fcc) polycrystal deforming at the single-crystal level solely by $\{111\}\langle 112\rangle$ twinning, the reciprocal ratio holds, i.e., $\sigma_1^{\mathrm{T}}/\sigma_1^{\mathrm{C}}=0.83$ (see also Lebensohn and Cazacu (2012) on an assessment of these values). In the isotropic case, the (single) tension-compression parameter, *k*, entering the microscale criterion has a clear physical meaning and can be explicitly determined based on the SD ratio and homogeneity degree, i.e., $k\leftarrow k(\sigma_1^{\mathrm{T}}/\sigma_1^{\mathrm{C}},a)$ (see Cazacu *et al.* (2006) for its expression).

Figure 6.3 and Figure 6.4 represent π-plane projections of the unitary macroscopic stress potential isosurfaces for porous media with porosity $f=10^{-2}$ whose matrix behaviour is defined by each of the nine materials described above, as predicted by: the Rice and Tracey (Eq. (5.42)) and the Eshelby-type (Eq. (5.43)) formulations, respectively. The results are organized in a two-input table format, varying the homogeneity degree, *a*, row-wise and the SD ratio, $\sigma_1^{\mathrm{T}}/\sigma_1^{\mathrm{C}}$, column-wise. Cross-sections of constant hydrostatic value are plotted based on the fractions $\bar{f}_i=\{0,0.75,0.90,0.985\}$ of the hydrostatic tensile and compressive extreme values. As expected, the presence of a void phase induces dependence

[19] The notation { } and ⟨ ⟩ denotes the twinning plane and direction type, respectively.

on all invariants of the macroscopic stress state[20]: $(I_1, J_2^{\Sigma}, J_3^{\Sigma})$. This holds true even for the limit case of a j_2- plasticity[21] model at the microscale, viz., the von Mises criterion (see Figure 6.3 (a)), corroborating with the results of Cazacu and Revil-Baudard (2015); Revil-Baudard and Cazacu (2014). Naturally, if the microscale constitutive model is j_3- dependent, then such dependence automatically conveys into the macroscale, even for purely deviatoric states (e.g. Figure 6.3 (b-c)). More crucially, it must be emphasized that, for both trial field formulations, such J_3^{Σ}- dependence is not static. Indeed, it is shown that both predict a strong shape changing behaviour along the hydrostatic axis. Moreover, this shape change follows similar trends in both formulations (cf. Figure 6.3 and Figure 6.4): with increasing hydrostatic fraction, the macroscopic yield loci evolve from a shape that is identical to that of the yield locus of the respective dense phase to a nearly circular shape regarding predominant hydrostatic states, i.e. near the poles of the isosurface. Moreover, both formulations predict that the extreme hydrostatic values are along the hydrostatic axis. This is in clear contrast to the case of an orthotropic matrix (cf. Figure 6.2), and shows that, if the matrix is isotropic, a purely hydrostatic stress on the porous solid results in a purely hydrostatic strain-rate, and vice-versa, irrespective of the homogeneity degree, a, and tension-compression asymmetry effects, $\sigma_1^{\mathrm{T}}/\sigma_1^{\mathrm{C}}$, active at the microscale. Note however that the hydrostatic macroscopic stress (and strain-rate) limit values on the hydrostatic axis actually depend on the latter. This statement will be substantiated in ensuing figures, yet, in advance, it is disclosed that all porous solids in Figure 6.3 and Figure 6.4 have the same hydrostatic compressive limit, but not the same hydrostatic tensile limit, which, in fact, depends on (and only on) the matrix SD ratio. A close comparison of Figure 6.3 and Figure 6.4 shows that the isosurfaces of the Eshelby type tend to magnify void-induced J_3^{Σ} effects (i.e., angular dependence) of the porous aggregates when compared to those of Rice and Tracey (e.g., compare the isosurfaces in Figure 6.3a and Figure 6.4a, regarding the von Mises matrix). This is explained by the additional degrees of freedom available in the former homogenization approach. It should be remarked however that the fact that J_3^{Σ} effects are amplified does not entail that the respective approximate potential is an improved estimate of the exact potential (Eq. (5.9)). Indeed, in a following subsection, the opposite effect is encountered, since the Eshelby-type fields do not guarantee the rigorous upper-bound nature of the homogenization analysis (recall Remark 5.1, p.102). In any case, while hardly perceptible, the cross sections of the yield loci for the Eshelby-type formulation (Figure 6.4) are, in fact, interior to those of the Rice and Tracey counterpart (Figure 6.3), the lone exception being for purely hydrostatic loadings, for which the surfaces intercept (as later shown in Figure 6.7).

In the following, the FE limit analysis scheme employed to assess the accuracy of the macroscopic potentials of Figure 6.3 and Figure 6.4 is briefly described.

[20] Recall that in π-plane projections, the radial coordinate is related to J_2^{Σ}, whereas the angular azimuthal coordinate is related with J_3^{Σ}. The dependence on J_3^{Σ} is also referred in the literature as "Lode angle dependence".
[21] Majuscule invariants refer to the macroscale model, whereas minuscule invariants to the microscale counterpart.

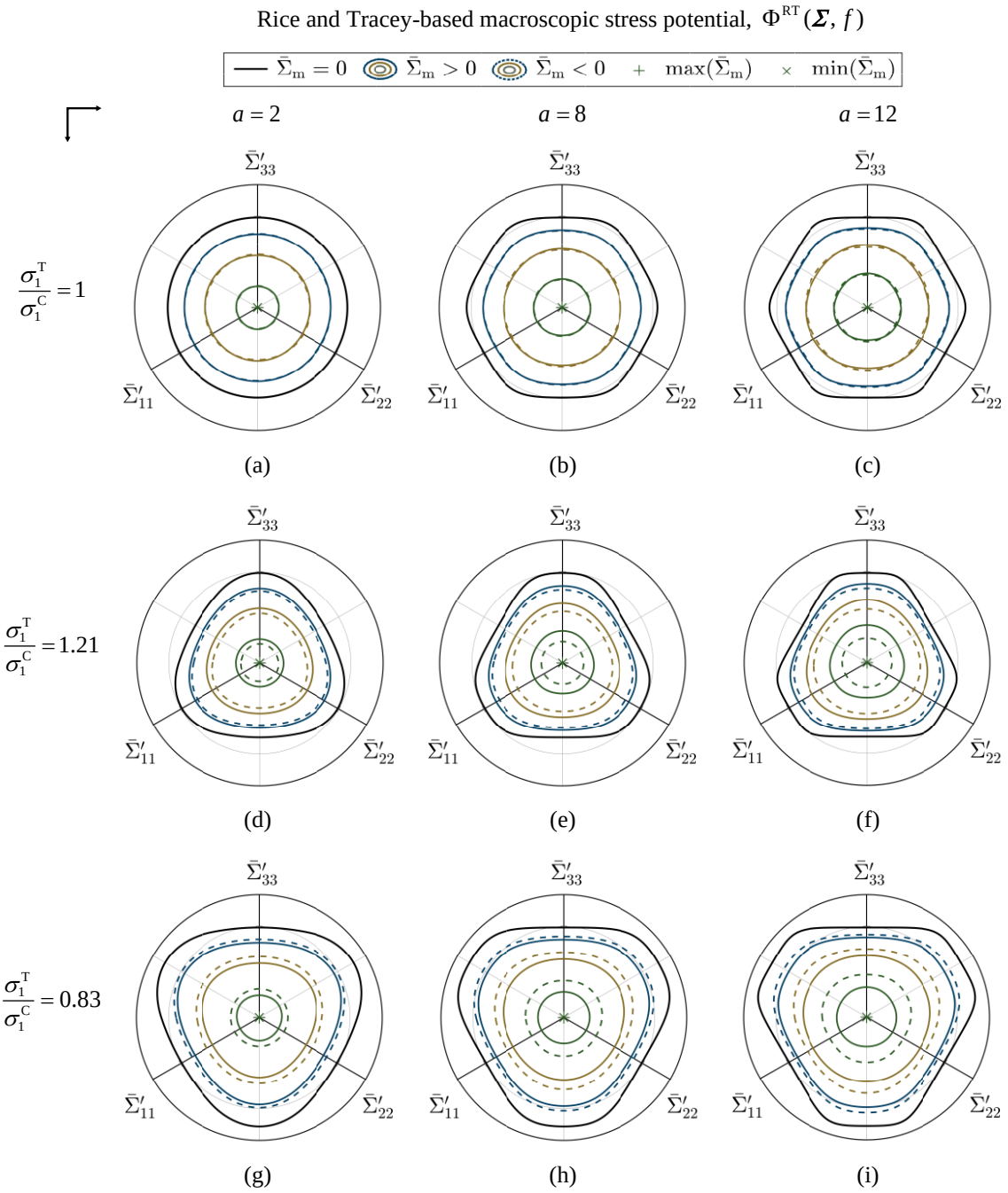

Figure 6.3 π-plane representation of the macroscopic stress potential (Eq. (5.45)) unitary isovalue surfaces using the Rice and Tracey trial velocity fields (Eq. (5.20)) for porous media with porosity $f = 10^{-2}$ and an isotropic matrix with a homogeneity degree $a = \{2,8,12\}$ and SD ratio: (a)-(c) $\sigma_1^{\mathrm{T}}/\sigma_1^{\mathrm{C}} = 1$; (d)-(f) $\sigma_1^{\mathrm{T}}/\sigma_1^{\mathrm{C}} = 1.21$; (g)-(i) $\sigma_1^{\mathrm{T}}/\sigma_1^{\mathrm{C}} = 0.83$. Cross sections of varying hydrostatic fraction, $\bar{f}_i = \{0, 0.75, 0.90, 0.985\}$ of the purely tensile and compressive hydrostatic values are represented. The items are organized in a two-input data table format.

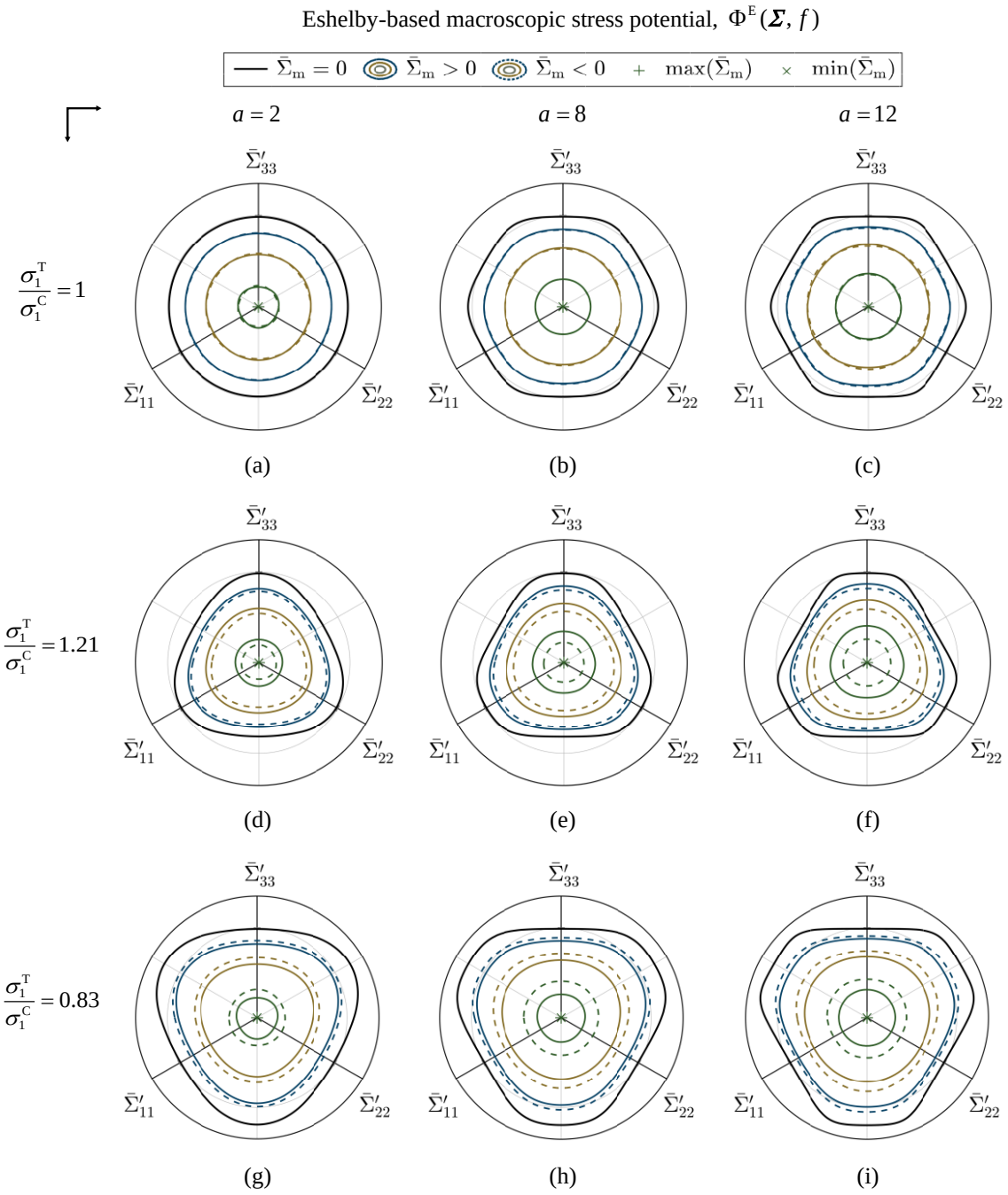

Figure 6.4 π-plane representation of the macroscopic stress potential (Eq. (5.45)) unitary isovalue surfaces using the Eshelby-type trial velocity fields (Eq. (5.30)) for porous media with porosity $f = 10^{-2}$ and an isotropic matrix with a homogeneity degree $a = \{2, 8, 12\}$ and SD ratio: (a)-(c) $\sigma_1^{\mathrm{T}}/\sigma_1^{\mathrm{C}} = 1$; (d)-(f) $\sigma_1^{\mathrm{T}}/\sigma_1^{\mathrm{C}} = 1.21$; (g)-(i) $\sigma_1^{\mathrm{T}}/\sigma_1^{\mathrm{C}} = 0.83$. Cross sections of varying hydrostatic fraction, $\bar{f}_i = \{0, 0.75, 0.90, 0.985\}$ of the purely tensile and compressive hydrostatic values are represented. The items are organized in a two-input data table format.

6.2.2 Overview of the unit cell finite element model

The criteria in Eqs. (5.42)-(5.43) are based on a particular trial velocity field. It is crucial to assess to what extent these fields represent the actual kinematics of the porous solid. In FE-based unit cell computations of porous media the actual microstructural features (viz., void boundaries, $\partial\omega$) are discretized and boundary conditions are imposed in order to represent the full material (e.g., periodic). The matrix material is assumed (elastic)-plastic with the plastic response governed by a given stress (or strain-rate) potential. The main idea is that, since the minimization of the macroscopic plastic dissipation (Eq. (5.9)) is performed over a larger set of kinematically admissible velocity fields (those complying with local equilibrium conditions, i.e. $\mathrm{div}(\boldsymbol{\sigma}(\underline{\boldsymbol{x}})) = 0,\ \forall \underline{\boldsymbol{x}} \in \Omega \backslash \omega$), the FE solution is a better estimate for the minimization problem, and thus can be used to assess the accuracy of analytical criteria established on some postulated trial velocity fields (Stewart, 2009).

In this work, the unit cell is taken as a hollow sphere, identical to the RVE adopted in the envisioned homogenization problem (§5.2.1). While such unit cell cannot represent a true periodic material structure (in the sense of space-filling), the main goal here is to compare the postulated trial fields with those predicted by the FE analysis for the same RVE geometry, rather than studying the underlying micromechanical features of porous media of at the mesoscale, which, indeed, ought to benefit from taking into account a more realistic periodic microstructure (e.g., the cubic unit cell). Recently, Dæhli *et al.* (2019), conducted a numerical study assessing the effect of the unit cell geometry, viz. cubic and spherical, on the FE limit analyses results, and showed that the obtained yield loci are qualitatively similar, yet the cubic unit cell model always provides lower plastic limit loads than the spherical counterpart, i.e., the hollow sphere model is an upper-bound of true periodic microstructures. In any case, the hollow sphere unit cell adopted in the following can be thought as an approximation of a periodic assemblage of cubic unit cells.

Full three-dimensional FE computations are conducted. The cell is subjected to homogeneous strain boundary conditions, i.e.:

$$\underline{\boldsymbol{u}}(\underline{\boldsymbol{X}}) = \boldsymbol{E}\underline{\boldsymbol{X}}\ ,\ \forall \underline{\boldsymbol{X}} \in \partial\Omega \tag{6.1}$$

where $\underline{\boldsymbol{u}}$ is the displacement vector with respect to the undeformed configuration, $\underline{\boldsymbol{X}} = b\underline{\boldsymbol{e}}_r$ is the initial position vector on the outer surface, $\boldsymbol{E}$ the imposed macroscopic strain tensor and $\partial\Omega$ the outer boundary of the spherical cell domain, Ω, while the void surface is traction-free. If one restricts the analysis to: (i) macroscopic strain tensors, $\boldsymbol{E}$, having the principal directions coincident with those of the spherical cell, i.e. $\boldsymbol{E} = E_{11}(\underline{\boldsymbol{e}}_1 \otimes \underline{\boldsymbol{e}}_1) + E_{22}(\underline{\boldsymbol{e}}_2 \otimes \underline{\boldsymbol{e}}_2) + E_{33}(\underline{\boldsymbol{e}}_3 \otimes \underline{\boldsymbol{e}}_3)$, and (ii) to isotropic matrices; then symmetry conditions in the three mutually orthogonal planes apply and therefore one-eighth of the unit cell can be considered to represent the entire model, as illustrated in Figure 6.5. The mesh generation is automated and depends on the prescribed porosity value, as described in the following. Recall from §5.4.2 that an asymptotic dissipation near the void is predicted with decreasing porosity. Accordingly, a radial discretization based on an exponential decay expression is employed: $r_n = ae^{-\lambda n},\ n = 0,...,n_r^{\mathrm{FE}}$, where λ is the decay constant and n_r^{FE} the total number of radial partitions to be considered. The boundary

condition $r_n(n_r^{\mathrm{FE}}) = b$, allows one to determine the decay constant as $\lambda = \frac{1}{3}\log(f)/n_{\mathrm{r}}^{\mathrm{e}}$, and, in the line with the discretization scheme in §5.4.2, $n_r^{\mathrm{FE}}(f) = \mathcal{O}((1-f^{1/3})\bar{n}_r^{\mathrm{FE}}) \in \mathbb{N}$, where $\bar{n}_r^{\mathrm{FE}}$ is user defined. The spherical unit surface, $\mathbb{S}^2$, is partitioned in N_{s} four-node elements of quasi-equal area, $T_j \in \mathbb{S}^2$, $j = 1,...,N_{\mathrm{s}}$, $\bigcup_{j=1}^{N_{\mathrm{s}}} \overline{T}_j \approx \mathbb{S}^2$, and extruded to each of the $(n_r^{\mathrm{FE}}+1)$ radii r_n, $n = 0,...,n_r^{\mathrm{FE}}$, in order to generate a 3-D mesh with 8-node hexahedral (tri-linear) elements with a total of $(n_r^{\mathrm{FE}} N_{\mathrm{s}})$ elements. A mesh refinement study was conducted beforehand to ensure converged results. The details of the mesh convergence study are omitted here. The discretization parameter pair $(\bar{n}_r^{\mathrm{FE}}, N_{\mathrm{s}}) = (30, 432)$ is satisfactory for envisioned numerical computations. Figure 6.6 shows the generated FE meshes of the one-eighth spherical cell for the porosity values $f = \{0.01, 0.05, 0.1\}$, and contains 10368, 8208, 6912 elements and 11725, 9380, 7973 nodes, respectively. The computations are performed using an academic FE code (DD3IMP, Menezes and Teodosiu, 2000; Oliveira *et al.*, 2008) in a quasi-static elastoplastic framework, using an updated Lagrangian and a fully-implicit time integration scheme. A selective reduced integration (SRI) technique is employed, with eight and one integration points for the deviatoric and hydrostatic parts of the velocity field gradient, respectively. Notice that such updated Lagrangian elastoplastic FE framework is, in theory, incompatible with the upper-bound limit analysis framework, which, as shown in §5.1, is based on the small strain theory and concerns rigid-plastic materials. In order to bypass these limitations, two assumptions are made: (i) the macroscopic homogeneous strain tensor, $\boldsymbol{E}$, is scaled by a factor $\chi = \min(10^{-6}, 10^{-4} f)$, thus the reference and the current configurations are virtually the same, given the extremely small magnitude of the prescribed displacements (Eq. (6.1)); and (ii) the rigid behaviour is replicated within a hypoelastic formulation of the generalized isotropic Hooke's by employing a huge Young's isotropic elastic modulus to tensile yield strength ratio, viz. $E/\sigma_1^{\mathrm{T}} = 10^{10}$, (with a Poisson ratio $\upsilon = 1/3$), such that the elastic strains are negligible, and the perfect-plastic behaviour is replicated considering an isotropic hardening power-law of the Swift-type, $Y(\bar{\varepsilon}^{\mathrm{p}}) = K(\varepsilon_0 + \bar{\varepsilon}^{\mathrm{p}})^n$, with an inconsequential hardening exponent, viz. $n = 10^{-4}$ with $K = \varepsilon_0 = 1$. The plastic behaviour is governed by the Plunkett *et al.* (2008) criterion (§4.3.1), adopting the associative flow rule (Eq. (4.7)). Test computations showed that this set of parameters leads in fact to a quasi-rigid-plastic response of the unit cell model without encountering numerical instability problems.

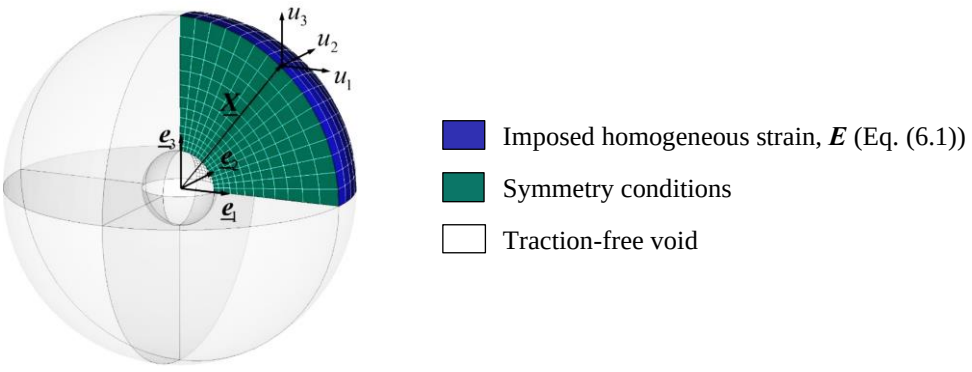

Figure 6.5 Geometry and boundary conditions of the FE unit cell model of the one-eighth hollow sphere. Symmetry conditions in the three orthogonal planes are imposed. The outer surface is subjected to homogeneous strain boundary conditions and the void is traction-free (adapted from Dæhli *et al.*, 2019).

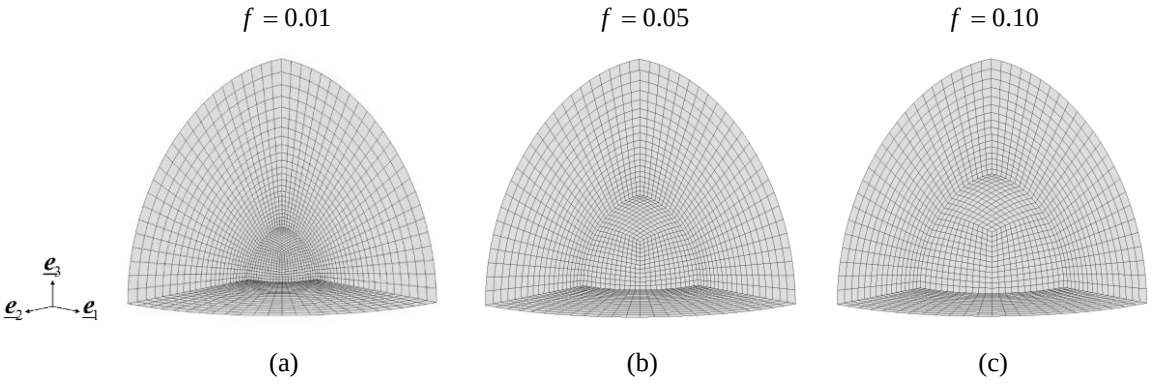

Figure 6.6 FE meshes employed in the unit cell computations of porous media with: (a) $f = 0.01$; (b) $f = 0.05$; (c) $f = 0.10$. Observe the concentration of elements near the void with decreasing porosity.

Given the rate-independent nature of the matrix material, the numerical values of the components of the macroscopic strain tensor $\boldsymbol{E}$ (Eq. (6.1)) defining the boundary conditions of the time-discretized FE problem correspond those of the macroscopic strain-rate tensor $\boldsymbol{D}$ (Eq. (4.1)) employed in the linearized analytical limit-analysis problem (see also Morin *et al.* (2014) for a proof of this equivalence). Within the FE analysis, the volume averaged quantities are determined using standard FE quadrature rules, e.g., letting ω denote a kinematic or internal variable determined in the integration points for the FE model, its macroscopic (homogenized) quantity is readily given by:

$$\langle \omega \rangle_{\Omega} = \frac{1}{V_{\Omega}} \sum_{i=1}^{n_{\text{gp}}} \omega_i V_i \,, \tag{6.2}$$

where n_{gp} is the total number of integration points, ω_i denotes the value of ω at the integration point i, V_i is the volume associated with the integration point i, and V_{Ω} denotes the volume of the unit cell (including the void), which can be determined by the sum of volumes of the tetrahedra defined by the 3-D Delaunay triangulation of the unit cell outer boundary points including the centre point (in this case the origin). The elastic-plastic evolution problem is solved until the normalized measure of the macroscopic plastic equivalent strain, $\varepsilon_{ij}^{\text{p}} = \int_0^t d_{ij}^{\text{p}} dt$, $\langle \varepsilon_{ij}^{\text{p}} \rangle_{\Omega} / \langle \overline{\varepsilon}^{\text{p}} \rangle_{\Omega}$ becomes constant, where $\overline{\varepsilon}^{\text{p}}$ is the equivalent plastic strain entering the hardening law and t is the pseudo-time variable (note that $\langle \varepsilon_{ij}^{\text{p}} \rangle_{\Omega} \cong t E_{ij}$, since elasticity is negligible and the unit cell geometry is quasi-spherical; and that $\langle \overline{\varepsilon}^{\text{p}} \rangle_{\Omega}$ is the FE counterpart to macroscopic SRP value $\Psi(t\boldsymbol{D})$, regarding the analytical limit-analysis problem in Eq. (5.39)). At this instant, t_{lim}, the limit-load is considered to be reached and is normalized value is determined as $\langle \sigma_{ij} \rangle_{\Omega} / \langle \sigma_1^T \rangle_{\Omega}$. In practice, the limit load is reached in the very beginning of the FE simulation.

In summary, the above FE analysis determines a tensor pair $\{\langle \varepsilon_{ij}^{\text{p}} \rangle_{\Omega} / \langle \overline{\varepsilon}^{\text{p}} \rangle_{\Omega}, \langle \sigma_{ij} \rangle_{\Omega} / \langle \sigma_1^T \rangle_{\Omega}\}$, which allows the construction of unitary macroscopic potentials in the strain and stress spaces. In the particular case of macroscopic loadings in the principal frame, one can take advantage of the dual nature of this pair, (i.e., one is the gradient of the other) and interpolate the discrete point cloud of the 3-D macroscopic isovalue potentials using a Nagata patch interpolation scheme (Nagata, 2005). This allows to accurately obtain the FE solution for any other loading 'direction', both in the stress and strain space. This technique is employed in the next paragraphs to represent the FE-based macroscopic yield loci.

6.2.3 Comparison with FE results and existing analytical criteria

The developed numerical criteria are now assessed under the particular case of macroscopic axisymmetric stress loadings, as usually performed in the literature. Let $(\underline{\boldsymbol{e}}_1, \underline{\boldsymbol{e}}_2, \underline{\boldsymbol{e}}_3)$ denote the orthogonal frame associated with the material axes. An macroscopic axisymmetric stress loading about $\underline{\boldsymbol{e}}_3$ is defined as $\boldsymbol{\Sigma} = \Sigma_{11}(\underline{\boldsymbol{e}}_1 \otimes \underline{\boldsymbol{e}}_1 + \underline{\boldsymbol{e}}_2 \otimes \underline{\boldsymbol{e}}_2) + \Sigma_{33}(\underline{\boldsymbol{e}}_3 \otimes \underline{\boldsymbol{e}}_3)$, for which the macroscopic von Mises equivalent stress reduces to $\Sigma_{\text{eq}} = |\Sigma_{33} - \Sigma_{11}|$, and $J_3^{\Sigma} = \frac{2}{27}(\Sigma_{33} - \Sigma_{11})^3$. In a similar way as the macroscopic strain triaxiality, $T_D = D_{\text{m}}/D_{\text{vM}}$, (see Footnote 18, p.111), one can define the macroscopic stress triaxiality, $T_{\Sigma} = \Sigma_{\text{m}}/\Sigma_{\text{vM}}$, (with $\Sigma_{\text{vM}} = \|\boldsymbol{\Sigma}\|_{\text{vM}} = \sqrt{\frac{3}{2}\boldsymbol{\Sigma}' : \boldsymbol{\Sigma}'}$, the macroscopic von Mises equivalent stress), to be employed in the following paragraphs.

In a first analysis, let us consider the isotropic matrices with no tension-compression asymmetry, i.e. $\sigma_1^{\text{T}}/\sigma_1^{\text{C}} = 1$, and homogeneity degree $a = \{2,8,12\}$, i.e., those employed in Figure 6.3 and Figure 6.4. Figure 6.7 represents the projection of the macroscopic stress potential unitary isosurfaces (i.e., yield locus) in the axisymmetric plane for porous solids with the above three matrices and for porosity values $f = \{0.01, 0.05, 0.1, 0.2\}$, as predicted by the Rice and Tracey (Eq. (5.42)) and the Eshelby-type (Eq. (5.43)) formulations, as well as the results of the FE kinematic limit analysis scheme described in subsection §6.2.2, under axisymmetric loadings with $T_{\Sigma} = \pm\{0, 2/3, 1, 2, 3, 5, \infty\}$. The data in Figure 6.7 was obtained by the intersection of the 3-D potentials in the principal space with the plane $\Sigma_{11} = \Sigma_{22}$. Note that the ordinate in Figure 6.7 is actually a measure of the macroscopic von Mises equivalent stress under axisymmetric conditions, viz., $(\Sigma_{33} - \Sigma_{11})/\sigma_1^{\text{T}} = \text{sgn}(J_3^{\Sigma})(\Sigma_{\text{vM}}/\sigma_1^{\text{T}})$, hence $J_3^{\Sigma} > 0$ for the first and second quadrants, and $J_3^{\Sigma} < 0$ for the third and fourth ones. Let us start by pointing out the overall trends regarding the effect of the homogeneity degree of the matrix, *a*, on the macroscopic behaviour of the porous solid. Figure 6.7a-c shows that with increasing parameter *a*, the isosurfaces tend to square along the hydrostatic axis and, in turn, to flatten their poles. This indicates that the contraction of the macroscopic yield loci along the hydrostatic axis is delayed, yet more abrupt near the hydrostatic limits for these materials. A comparison of the predictions of the developed potentials demonstrates that the isosurfaces of the Eshelby-type approach are interior to those of Rice and Tracey. This is to be expected given that the former must be less dissipative than the latter, i.e., $\Pi^{\text{E}}(\boldsymbol{D}) \leq \Pi^{\text{RT}}(\boldsymbol{D})$, due to the additional minimization scheme carried out in the Eshelby-type approach (recall discussion in §5.2.3). The lone exception occurs for purely hydrostatic loadings for which these formulations coincide. In other words, the Eshelby fields reduce to those of Rice and Tracey, as the deviatoric part of the inclusion eigenstrain rate tensor vanishes, i.e., $\boldsymbol{d}^{*\prime} = \boldsymbol{0}$ is the solution of the minimization problem. The isosurfaces in Figure 6.7 are symmetric with respect to origin, i.e., $\Phi^{\text{RT}}(\boldsymbol{\Sigma}, f) = \Phi^{\text{RT}}(-\boldsymbol{\Sigma}, f)$, and $\Phi^{\text{E}}(\boldsymbol{\Sigma}, f) = \Phi^{\text{E}}(-\boldsymbol{\Sigma}, f)$. The centrosymmetric nature is to be expected since one assumes the porous aggregate to have randomly distributed spherical voids and the matrix criteria to be isotropic and given by an even function (see e.g. Alves *et al.* (2014); Cazacu *et al.* (2013) a proof). Moreover, note that the hydrostatic limits do not depend on the homogeneity degree, *a*, (thus on the j_3 microscale behaviour). In fact, the predicted hydrostatic limits are unique for the considered (j_2, j_3) isotropic matrices, and coincide with the exact solution of the limit-analysis problem of an hollow sphere loaded hydrostatically: $\Sigma_{\text{m}}/\sigma_1^{\text{T}} = \pm(2/3)\ln f$.

This independence is also in agreement with theorical results (see, for instance, Cazacu *et al.*, 2019). The maxima of the macroscopic von Mises equivalent stress, $\Sigma_{vM}/\sigma_1^T = |\Sigma_{33} - \Sigma_{11}|/\sigma_1^T$, occur for purely macroscopic deviatoric loadings $(\Sigma_m = 0)$, however the Rice and Tracey, $\Phi^{RT}(\boldsymbol{\Sigma}, f)$, and the Eshelby-type, $\Phi^{E}(\boldsymbol{\Sigma}, f)$, formulations predict different values for these quantities. In the former, the local strain-rate field is uniform in the RVE (as later illustrated in Figure 6.10), hence it is straightforward to verify that yielding for purely deviatoric axisymmetric loadings occurs for $\Sigma_{eq}/\sigma_1^T = (1-f)$, regardless of the homogeneity degree, *a*; conversely, for the Eshelby-type approach, it is verified that the deviatoric limit actually depends on the (j_2, j_3) matrix behaviour, yet, to the best of the author's knowledge, there is no close-form expression for its value. Regarding the macroscopic J_3^Σ- dependence, it is observed that the J_3^Σ- effects are more pronounced for the Eshelby-type criterion (as previously observed in §6.2.1). More crucially, Figure 6.7 shows that the J_3^Σ- effects increase with increasing homogeneity degree of the matrix, *a*, (especially observed for the Eshelby-type criterion). In other words, the macroscopic J_3^Σ- effects appear to be more prominent for porous aggregates whose matrix materials are j_3 - dependent at the microscale. An important remark is that the differences between the Rice and Tracey (Eq. (5.42)) and the Eshelby-type (Eq. (5.43)) predictions vanish with decreasing porosity. Indeed, only for extremely high porosity values, say, $f = \mathcal{O}(0.1)$, these clearly depart. This results from the fact that the porosity acts as a weighting factor on the role of the deviatoric eigenstrain rate tensor, $\boldsymbol{d}^{*\prime}$, on the uniform strain-rate field in the matrix, $\boldsymbol{A} \neq \boldsymbol{D}'$, (recall Eqs. (5.30) and (5.34)). Accordingly, in practice, for vanishing porosities, $f \to 0$, the Eshelby-type fields lead to virtually equal results to those of Rice and Tracey. Regarding the unit cell computations, Figure 6.7 shows that the Rice and Tracey formulation is in overall good agreement with the FE results for all matrix materials and porosity values considered. More importantly, the isosurfaces are indeed exterior to those of the FE limit analysis, given the upper-bound nature of this formulation. In contrast, it is shown that the Eshelby-type isosurfaces exhibit an excessively low dissipation for high porosity values under predominantly deviatoric loadings, when compared with the respective FE results. Moreover, the amplified J_3^Σ- effects predicted by this formulation along the hydrostatic axis aggravate the discrepancy between the (pseudo)-analytical and the FE results (viz., see Figure 6.7b-c). This confirms that the upper-bound character of homogenization cannot be guaranteed when using the Eshelby-type fields, since these do not comply with uniform strain-rate boundary conditions in the general case.

In order to better picture and compare the J_3^Σ- dependence predicted by each formulation, Figure 6.7a is rearranged by applying the absolute operation to the ordinate and rescaling the isosurfaces along this axis. Figure 6.8 and Figure 6.9 represent the obtained isosurfaces for the Rice and Tracey criterion and the Eshelby-type criterion, respectively. It is concluded that both formulations predict the trends of the FE results regarding the effect of J_3^Σ on macroscopic yielding, viz., for axisymmetric loadings with $\Sigma_m > 0$ the response is softer for $J_3^\Sigma > 0$ than for $J_3^\Sigma < 0$, while the opposite holds true for loadings with $\Sigma_m < 0$. The exceptions are the purely deviatoric and hydrostatic points, for which the results are independent of J_3^Σ, as in agreement with the FE results. Note however that for the Eshelby-type criterion (Figure 6.9) the J_3^Σ- effects clearly increase with the increase of the porosity, which contrasts with

the predictions regarding the Rice and Tracey fields (Figure 6.8). In any case, both formulations appear to underestimate the J_3^{Σ}- dependence revealed by the FE results. Nevertheless, it is important to highlight that, while the predicted J_3^{Σ}- dependence on yielding (in the sense of (I_1, J_2^{Σ})) is limited, the normals to the macroscopic yield surfaces also depend on J_3^{Σ}. Therefore, in agreement with the macroscopic flow rule (Eq. (5.14)), a J_3^{Σ}- dependent plastic flow is predicted, which, in the context of evolving porosity, mass conservation ($\dot{f} = (1-f)\mathrm{tr}(\boldsymbol{D})$) implies that the porosity is, in fact, J_3^{Σ}- dependent (e.g. see Alves *et al.* (2014) on the effects of J_3^{Σ} on void evolution with a von Mises matrix).

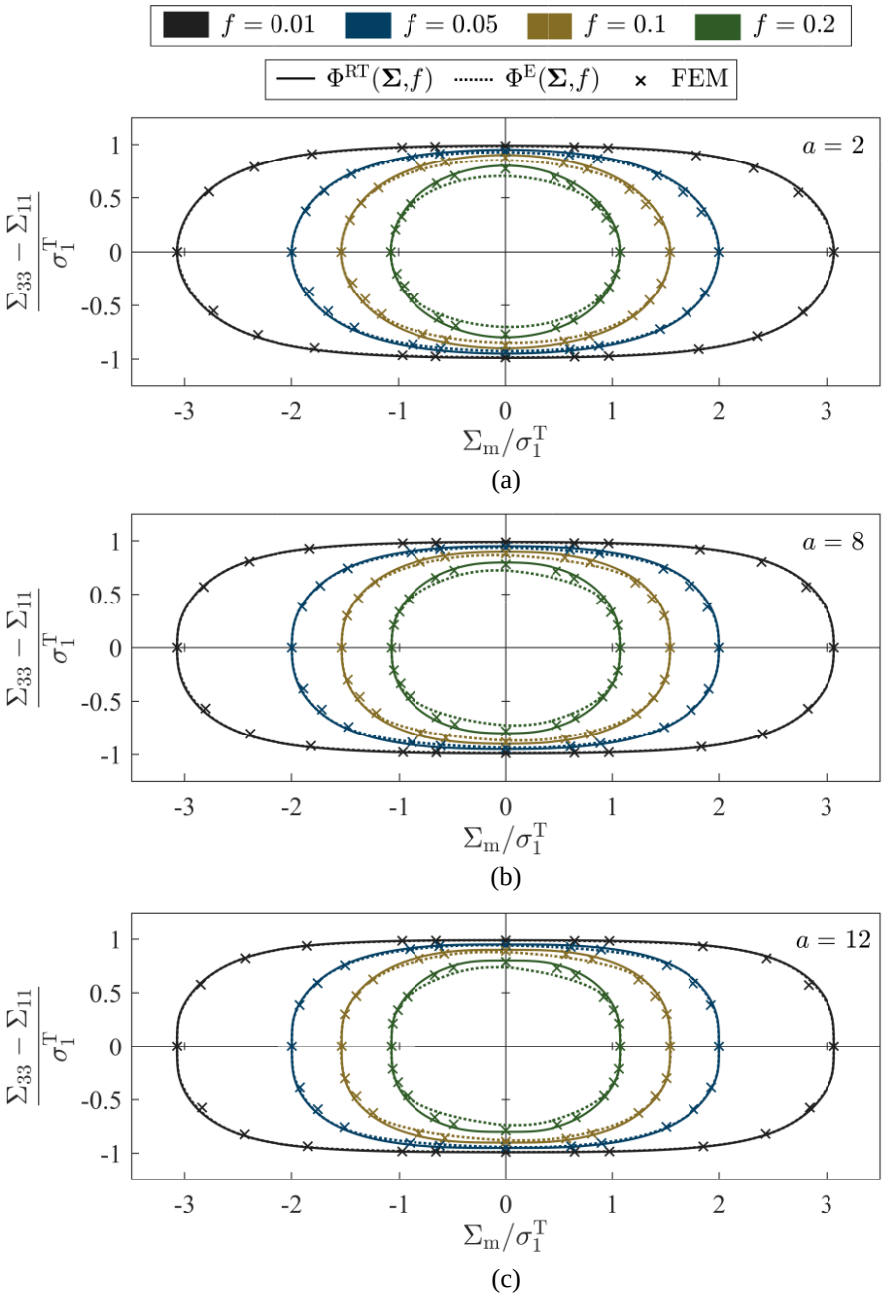

Figure 6.7 Axisymmetric projection of the macroscopic stress potential (Eq. (5.45)) unitary isovalue surfaces as obtained by the Rice and Tracey formulation (Eq. (5.42)), $\Phi^{\mathrm{RT}}(\boldsymbol{\Sigma}, f)$, the Eshelby-type formulation (Eq. (5.43)), $\Phi^{\mathrm{E}}(\boldsymbol{\Sigma}, f)$, and the FE limit analysis, for porous media with varying porosity and an isotropic matrix with a homogeneity degree: (a) $a = 2$ (von Mises); (b) $a = 8$; (c) $a = 12$; and no SD effects ($\sigma_1^{\mathrm{T}}/\sigma_1^{\mathrm{C}} = 1$). The FE results are plotted for the stress triaxiality values: $T_{\Sigma} = \pm\{0, 2/3, 1, 2, 3, 5, \infty\}$. The axes are at scale.

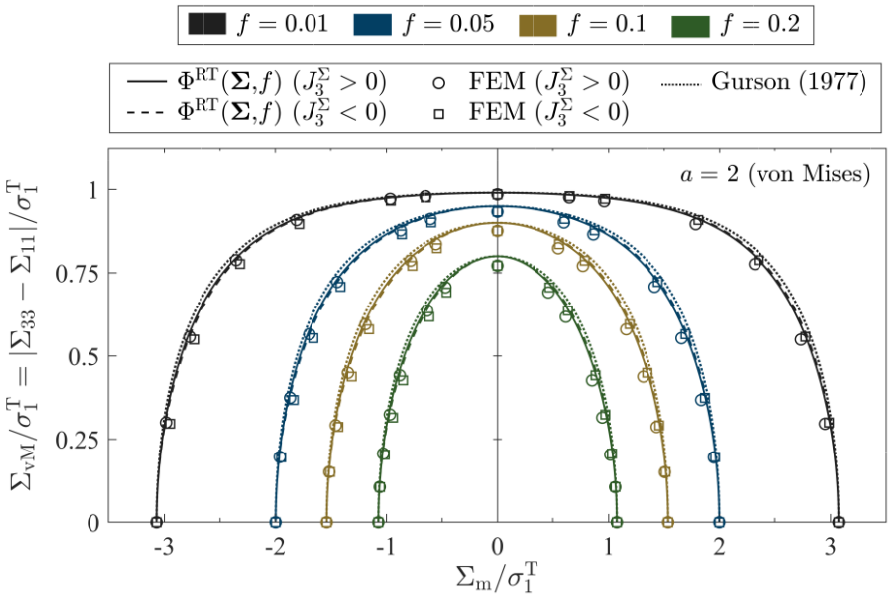

Figure 6.8 Axisymmetric projection of the macroscopic stress potential (Eq. (5.45)) unitary isovalue surfaces as obtained by the Rice and Tracey formulation (Eq. (5.42)), $\Phi^{\mathrm{RT}}(\boldsymbol{\Sigma}, f)$, the Gurson (1977) criterion, and the FE limit analysis, for porous media with a von Mises matrix and varying porosity. The FE results are plotted for the stress triaxiality values: $T_{\Sigma} = \pm\{0, 2/3, 1, 2, 3, 5, \infty\}$. The axes are not at scale.

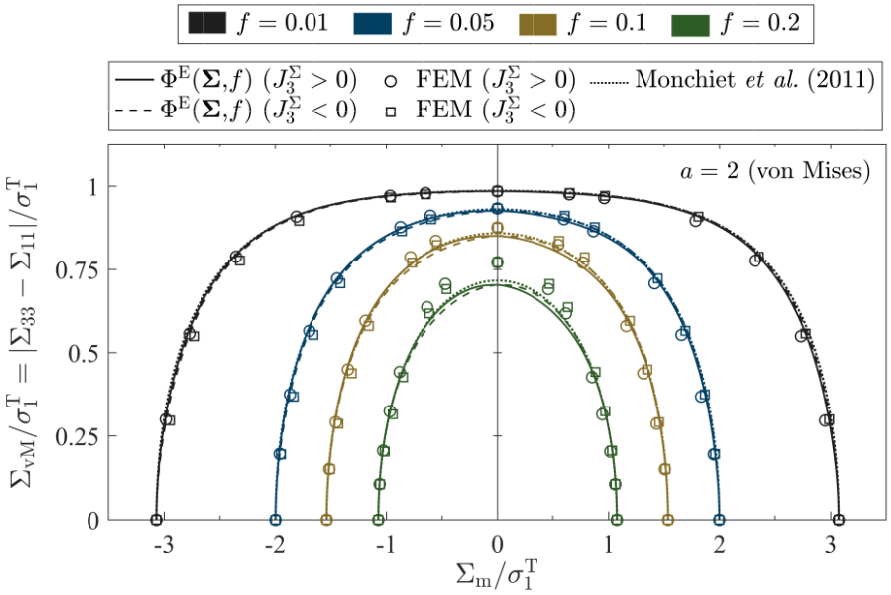

Figure 6.9 Axisymmetric projection of the macroscopic stress potential (Eq. (5.45)) unitary isovalue surfaces as obtained by the Eshelby-type formulation (Eq. (5.43)), $\Phi^{\mathrm{E}}(\boldsymbol{\Sigma}, f)$, the Monchiet *et al.* (2011) criterion, and the FE limit analysis, for porous media with a von Mises matrix and varying porosity. The FE results are plotted for the stress triaxiality values: $T_{\Sigma} = \pm\{0, 2/3, 1, 2, 3, 5, \infty\}$. The axes are not at scale.

At this point, it is also interesting to determine how the developed criteria compare with those in the literature. As far as the author is aware, no closed-form criteria (excluding those heuristic-based) exist for describing the behaviour of porous solids whose matrix phase obeys non-quadratic yield criteria, hence, the analysis is restricted to porous solids with a von Mises matrix ($a = 2$). Figure 6.8 and Figure 6.9 compare the yield loci in Figure 6.7a with the well-known Gurson (1977) criterion (Eq. (3.9)) and with the Monchiet *et al.* (2011) criterion (Eq. (3.25)), respectively. Recall that the former concerns the

Rice and Tracey fields, whereas the latter is grounded on the Eshelby-type fields. One can conclude that the Gurson (1977) criterion is, in fact, an upper-bound of the developed "exact" macroscopic yield potentials, i.e., $\Psi^{G}(\boldsymbol{D}) \geq \Psi^{RT}(\boldsymbol{D})$. This is a result of the application of the Cauchy-Schwarz inequality (recall discussion in §5.1.3), which is known to preserve the upper bound nature of the homogenization. Unfortunately, application of the Cauchy-Schwarz inequality implicitly erases any dependence of the local strain-rate potential on the polar and azimuthal spherical coordinates of the RVE, i.e., $\psi = \psi(r)$, which eliminates the couplings between $(\Sigma_{m}, \Sigma_{eq})$ and, ultimately, precludes J_3^{Σ}- effects to be captured[22]. This implies that the Gurson (1977) criterion is unable to predict the different void growth (and collapse) behaviour depending on the sign of J_3^{Σ}, as observed in unit cell studies (e.g., see Alves *et al.*, 2014). The same holds true for the Monchiet *et al.* (2011) criterion (Figure 6.9) which is shown to be independent of J_3^{Σ}, also due to the application of the Cauchy-Schwarz inequality. More crucially, note that that the Monchiet *et al.* (2011) criterion is not actually an upper bound with respect to its associated 'exact' potential, $\Phi^{E}(\boldsymbol{\Sigma}, f)$, (Eq. (5.43)). This theorical weakness, in advance recognised by Monchiet *et al.* (2011), is a consequence of the usage of "uncontrolled" (i.e. not upper-bound preserving) approximations in the homogenization analysis with the aim of simplifying the expressions.

In order to understand the differences of the predictions observed at the macroscale, (viz. Figure 6.8 and Figure 6.9), let us shift the attention to the microscale. Figure 6.10 and Figure 6.11 represent the distribution of the local strain-rate potential, $\psi(\boldsymbol{d}(r,\theta,\phi))$, in the adopted RVE as predicted by the Rice and Tracey fields (Eq. (5.20)), the Eshelby-type fields (Eq. (5.30)), and the FE limit analysis (§6.2.2) for porous solids with porosity $f = 0.01$ and $f = 0.1$, respectively, under imposed macroscopic axisymmetric strain-rates with $J_3^{\Sigma} \leq 0$ and for various levels of strain-rate triaxiality: (a)-(c) a purely deviatoric state, i.e., $T_D = 0$; (d)-(f) an intermediate state, viz., $T_D = 1/200$, (for which $T_{\Sigma} = \mathcal{O}(2/3)$); and (g)-(i) a purely hydrostatic state, i.e., $T_D = \infty$. For simplicity, the matrix is assumed to obey the von Mises criterion (Figure 6.7a). It is concluded that the distributions of the Eshelby-type are more heterogeneous than those of Rice and Tracey. In the particular case of purely deviatoric loadings, the Rice and Tracey criterion predicts an uniform dissipation field (see Figure 6.10a and Figure 6.11a), whereas the Eshelby-type one predicts an heterogeneous distribution. Moreover, observe that the latter criterion predicts a higher dissipation near the void (Eshelby's inclusion phase), which is counteracted with zones of lower dissipation (with respect to Rice and Tracey) farther from the void. Indeed, by definition, the overall, (i.e., volume averaged) local strain-rate potential of the Eshelby-type must be lower than that of Rice and Tracey, i.e., $\langle \psi(\boldsymbol{d}^{E}) \rangle \leq \langle \psi(\boldsymbol{d}^{RT}) \rangle$. The differences between the fields of these formulations decrease with increasing (stress or strain-rate) triaxiality. In the limit, under purely hydrostatic loadings, these coincide. Indeed, for this case, both analytical distributions coincide with those of the FE computations since the analytical solution is the exact solution of the problem, thus, in addition to obeying the uniform strain-rate conditions, the trial local fields verify the equilibrium condition: $\mathrm{div}(\boldsymbol{\sigma}(\underline{\boldsymbol{x}})) = 0, \ \forall \underline{\boldsymbol{x}} \in \Omega \backslash \omega$,

[22] Cazacu *et al.* (2013) later revisited Gurson's (1977) analysis and showed that the macroscopic plastic dissipation associated with a von Mises matrix can actually be obtained analytically (yet in parametric form) without applying the Cauchy-Schwarz inequality, i.e., an analytical solution of the surfaces $\Phi^{RT}(\boldsymbol{\Sigma}, f)$, in Figure 6.8.

which holds exclusively for this loading type. For the remaining loadings, the trends of the distributions regarding the FE computations are remarkably well reproduced by the Eshelby-type criterion, yet the latter appears to overestimate the dissipation near the void, regardless of the porosity. In contrast, with increasing porosity, the latter criterion tends to underestimate the local dissipation near the outer boundary when compared to the FE results (see Figure 6.11). This is thought to stem from the violation of the uniform strain-rate conditions, which is more severe for high porosity values and ultimately leads to the deterioration of the quality of the predictions for these porous solids, as shown in Figure 6.9. In closing, note that the FE results are able to predict regions of zero dissipation. Such behaviour cannot be captured by either analytical homogenization schemes since plasticity is enforced throughout the matrix domain from the outset (see §5.1.2).

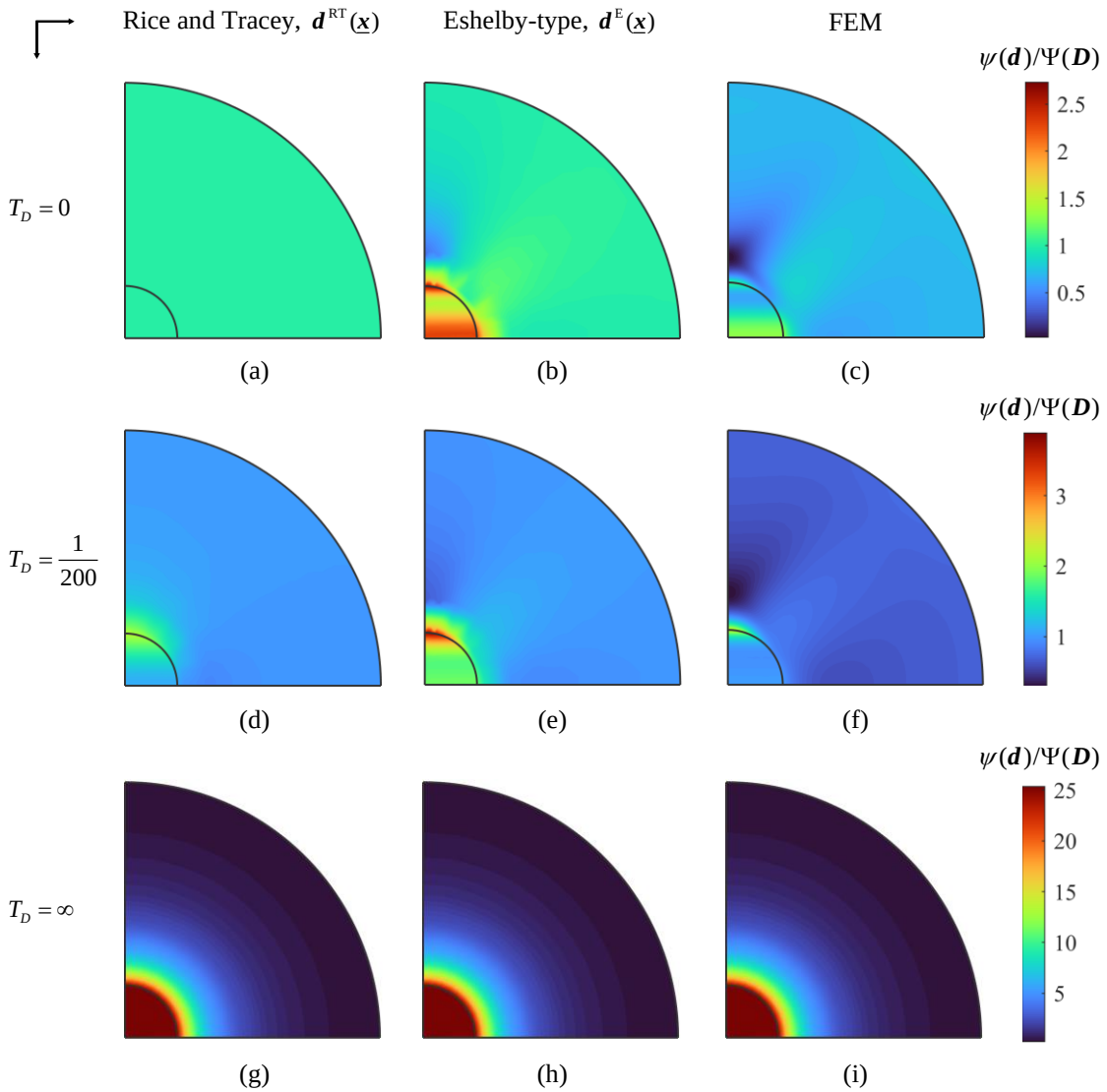

Figure 6.10 Distribution of the local strain-rate potential for porous media with porosity $f = 0.01$ and the von Mises matrix as predicted by the Rice and Tracey fields (Eq. (5.20)), the Eshelby-type fields (Eq. (5.30)), and the FE limit analysis under imposed macroscopic axisymmetric strain-rate state with $J_3^{\Sigma} \leq 0$ and varying triaxiality: (a)-(c) $T_D = 0$; (d)-(f) $T_D = 1/200$; (g)-(i) $T_D = \infty$. The figures represent sections on the (1-3) plane of one eighth of the RVE. The items are organized in a two-input table format.

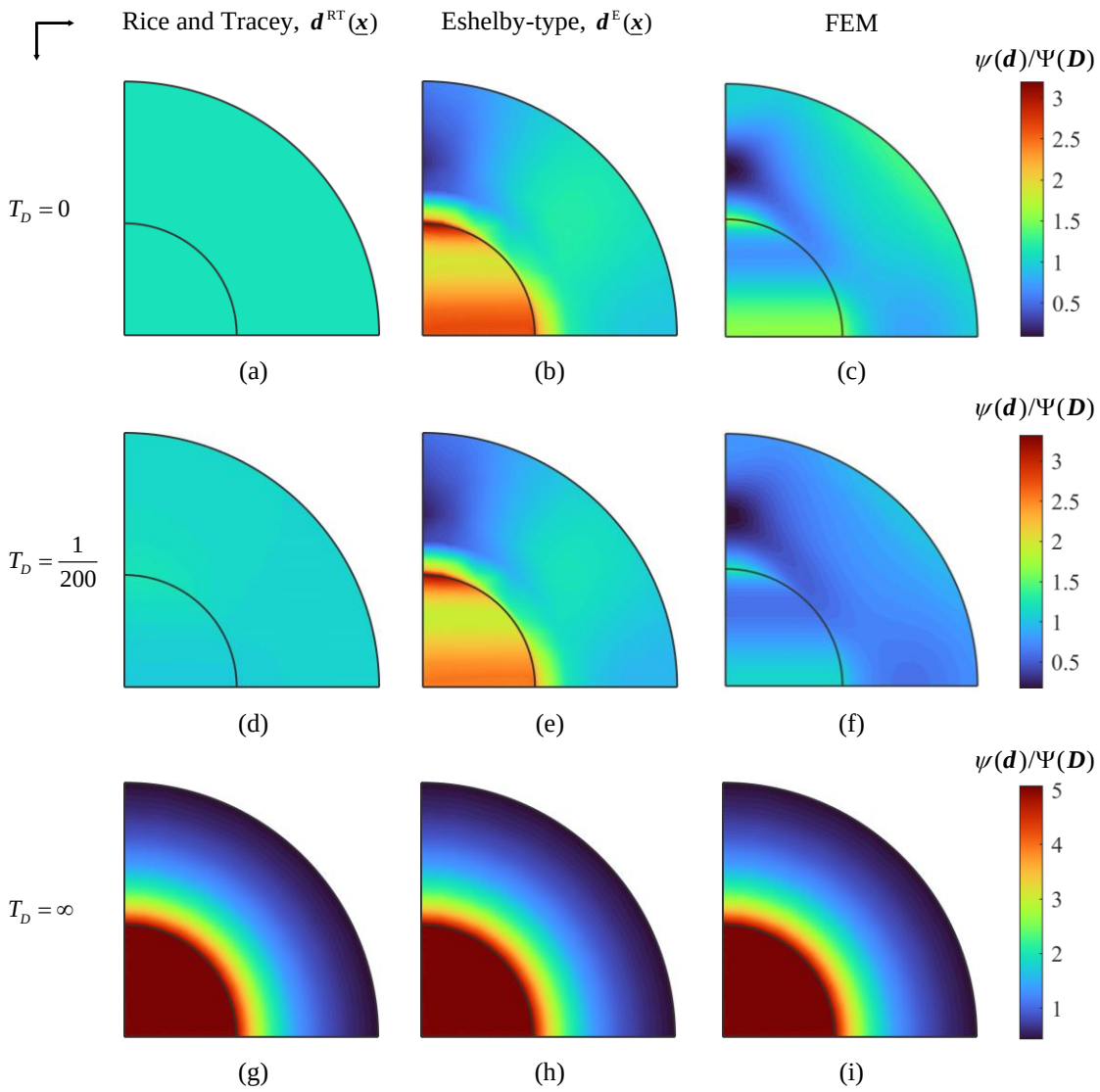

Figure 6.11 Distribution of the local strain-rate potential for porous media with porosity $f = 0.1$ and the von Mises matrix as predicted by the Rice and Tracey fields (Eq. (5.20)), the Eshelby-type fields (Eq. (5.30)), and the FE limit analysis under imposed macroscopic axisymmetric strain-rate state with $J_3^{\Sigma} \leq 0$ and varying triaxiality: (a)-(c) $T_D = 0$; (d)-(f) $T_D = 1/200$; (g)-(i) $T_D = \infty$. The figures represent sections on the (1-3) plane of one eighth of the RVE. The items are organized in a two-input table format.

In the following, the focus is on the isotropic matrices exhibiting tension-compression asymmetry, i.e., $\sigma_1^{\mathrm{T}}/\sigma_1^{\mathrm{C}} \neq 1$. Figure 6.12 and Figure 6.13 represent projections of the macroscopic stress potential unitary isosurfaces in the axisymmetric plane as predicted by the Rice and Tracey (Eq. (5.42)) and the Eshelby-type (Eq. (5.43)) formulations, respectively, for porous solids with porosity $f = \{0.01, 0.1\}$, whose matrices exhibit different types of tension-compression asymmetry, viz., $\sigma_1^{\mathrm{T}}/\sigma_1^{\mathrm{C}} = \{1, 1.21, 0.83\}$. For conciseness, the present analysis is restricted to matrices whose microscale potentials are quadratic $(a = 2)$, i.e., those employed in Figure 6.3 and Figure 6.4 (a),(d),(g). The corresponding results of the FE limit analysis scheme (§6.2.2) are also plotted in these figures. It is verified that that the macroscopic loci are no longer symmetric with respect to the origin for matrix materials displaying SD effects. The asymmetry at the microscale, deviatoric in nature due to the matrix incompressibility, conveys into the

macroscale in the form of asymmetry of the hydrostatic response. Moreover, the predicted hydrostatic limits coincide with the exact solution for a hydrostatically loaded isotropic hollow sphere exhibiting SD effects (see Stewart (2009) and Cazacu and Stewart (2009)): for tensile hydrostatic loadings yielding occurs for $\Sigma_m/\sigma_1^T = -(2/3)(\sigma_1^C/\sigma_1^T)\ln f$, whereas for compressive hydrostatic loadings yielding takes place for $\Sigma_m/\sigma_1^T = (2/3)\ln f$. Note the curious result that yielding of the porous solid depends on the matrix SD ratio for tensile hydrostatic loadings but not for compressive loadings. The former analytical solutions were obtained considering the matrix to have a quadratic yield function. However, inspection of the 3-D isovalues surfaces in Figure 6.3 and Figure 6.4 showed that these still hold true for porous solids whose matrix obey non-quadratic criteria. In other words, in the same fashion as Figure 6.7, the hydrostatic limits for matrices displaying SD effects *do not* depend on the homogeneity degree, *a*, of the matrix. Comparison of the predictions of the developed potentials with the FE computations leads to similar observations to those outlined regarding the case of the von Mises matrix (in Figure 6.7): the predictions using the Rice and Tracey formulation (Figure 6.12) are in very good agreement with the FE results for both porosities, whereas the predictions regarding the Eshelby-type formulation tend to underestimate the overall plastic dissipation for high porosity values (see Figure 6.13 (b)).

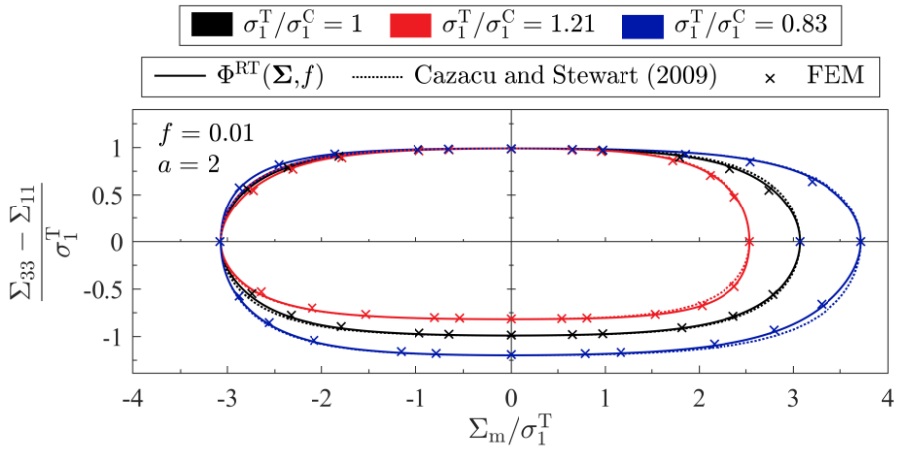

(a)

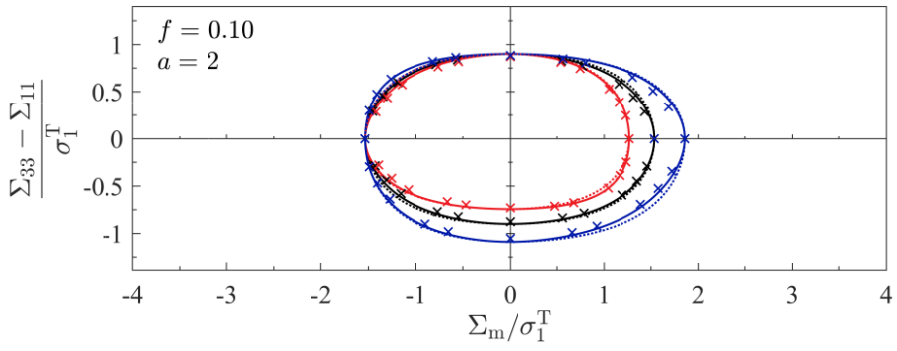

(b)

Figure 6.12 Axisymmetric projection of the macroscopic stress potential (Eq. (5.45)) unitary isovalue surfaces as obtained by the Rice and Tracey formulation (Eq. (5.42)) , $\Phi^{RT}(\boldsymbol{\Sigma}, f)$, the criterion of Cazacu and Stewart (2009), and the FE limit analysis, for porous media with porosity: (a) $f = 0.01$; (b) $f = 0.1$; and an isotropic matrix with SD ratio: $\sigma_1^T/\sigma_1^C = \{1, 1.21, 0.83\}$ and homogeneity degree $a = 2$. The FE results are plotted for the stress triaxiality values: $T_\Sigma = \pm\{0, 2/3, 1, 2, 3, 5, \infty\}$. The axes are at scale.

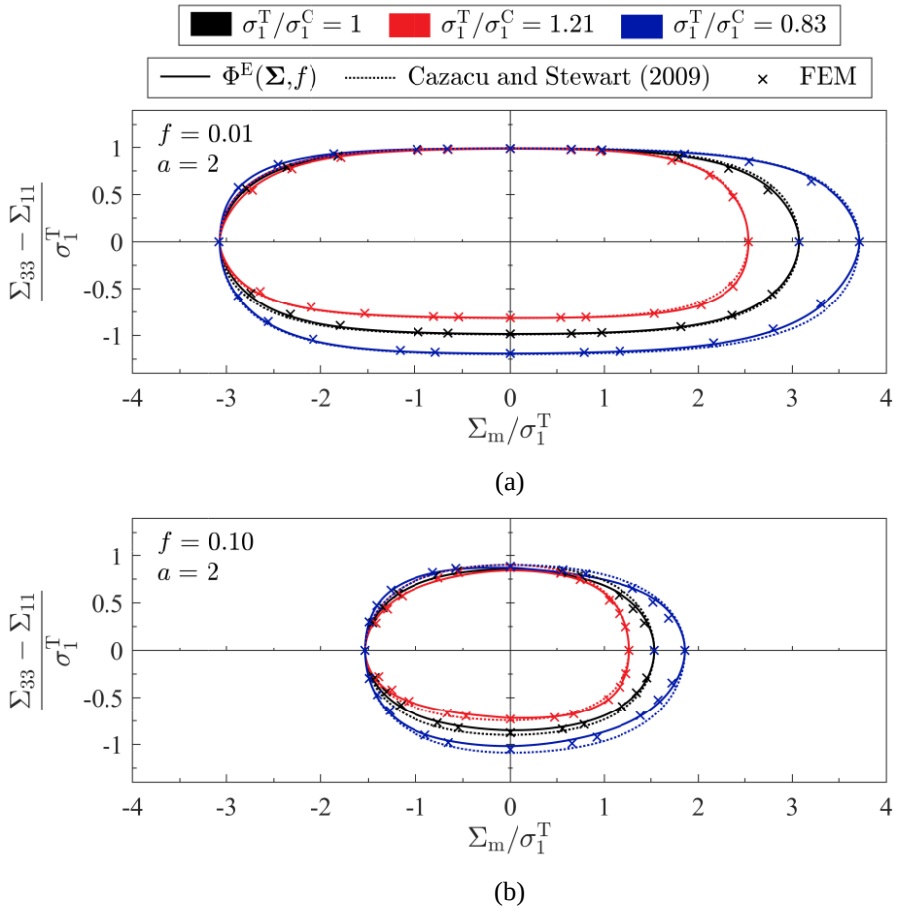

Figure 6.13 Axisymmetric projection of the macroscopic stress potential (Eq. (5.45)) unitary isovalue surfaces as obtained by the Eshelby-type formulation (Eq. (5.30)), $\Phi^E(\boldsymbol{\Sigma}, f)$, the criterion of Cazacu and Stewart (2009), and the FE limit analysis, for porous media with porosity: (a) $f = 0.01$; (b) $f = 0.1$; and an isotropic matrix with SD ratio: $\sigma_1^T/\sigma_1^C = \{1, 1.21, 0.83\}$ and homogeneity degree $a = 2$. The FE results are plotted for the stress triaxiality values: $T_\Sigma = \pm\{0, 2/3, 1, 2, 3, 5, \infty\}$. The axes are at scale.

In the following, the predictions of the development criteria are compared with those of closed-form criteria in the literature. As mentioned in the introductory chapter, Cazacu and Stewart (2009) proposed a closed-form plastic potential for porous materials with randomly distributed spherical voids assuming the matrix to obey the quadratic and isotropic form of the Cazacu *et al.* (2006) (CPB06) yield criterion, (see Eq. (3.21) and concerning text). Figure 6.12 and Figure 6.13 also represent the analytical criterion of Cazacu and Stewart (2009), which, as described in §3.4.2, is grounded on the Rice and Tracey fields. Figure 6.12 (a) shows that the former analytical criterion is not actually an upper-bound of the "exact" macroscopic potential, $\Phi^{RT}(\boldsymbol{\Sigma}, f)$, (Eq. (5.42)). This is a consequence of the truncation of the general form of the local strain-rate potential in terms of the applied macroscopic strain-rate, $\boldsymbol{D}$, to the particular case of purely deviatoric and purely hydrostatic loadings, $\psi(\boldsymbol{D}) \cong \psi(D_m, D_e)$, with the intention of simplifying the integrand expression. In addition, the authors applied the Cauchy-Schwartz inequality to evaluate the integrals in closed-form. Accordingly, the Cazacu and Stewart (2009) criterion is, in fact, unable to predict void-induced J_3^Σ- effects. The J_3^Σ- dependency observed at the macroscale is solely

a result of the j_3- dependency at the microscale due to the SD effects. This leads to a weak coupling between j_3- (micro) and J_3^{Σ}- (macro) effects on the overall response of the porous solid. For example, consider the second quadrant of the axisymmetric projections in Figure 6.12. The criterion of Cazacu and Stewart (2009) predicts that the response of the three porous solids is identical (the same as Gurson, 1977), irrespective of the SD ratio of the matrix. This is in contrast to the behaviour predicted by the developed potential, $\Phi^{\mathrm{RT}}(\boldsymbol{\Sigma}, f)$, which accurately replicates the FE results. Moreover, the yield loci in the fourth quadrant as predicted by the Cazacu and Stewart (2009) criterion are homothetic transformations of each other, scaled by the factor $\sigma_1^{\mathrm{C}}/\sigma_1^{\mathrm{T}}$ (see Brito (2018) for more details). By the normality principle, this implies that the direction of the macroscopic plastic strain increment, $\partial\Phi/\partial\boldsymbol{\Sigma}$, and thus, the porosity evolution, are insensitive of the SD ratio of the matrix. This is in clear contrast with the findings of micromechanical studies on the dilatational response of porous media (e.g. Alves and Cazacu, 2015), where void growth is indeed J_3^{Σ}- dependent and is strongly influenced by the SD effects of the matrix. Conversely, the numerically obtained criterion, $\Phi^{\mathrm{RT}}(\boldsymbol{\Sigma}, f)$, (Eq. (5.42)) clearly displays different normals to the yield loci regarding the nature of the SD effects of the matrix, which would necessarily lead to different void growth (and collapse) rates. The main conclusion of this paragraph is that the limitations of the studied close-form criterion are not imputable to the quality of the employed trial velocity fields (viz., those of Rice and Tracey), but rather to the simplification hypotheses, whether or not upper-bound preserving, employed in the respective homogenization. This further advocates the importance of adopting a numerical homogenization framework, as accomplished in this work.

6.3 Remarks on computational performance

In the context of constitutive modelling, *exact* closed-formed expressions are always preferable. This holds both from the computational standpoint, given their minor computational cost; and for mathematical accessibility, e.g., the definition of the derivatives to employ in parameter identification formulations and/or FE analyses. However, unfortunately, it is not always possible to derive exact solutions, in particular, for the problem of the limit-analysis of a hollow sphere addressed in this thesis (recall §5.1.3). The previous subsection demonstrated that although approximate analytical solutions do exist for some matrix materials, given their simplified character, these often fail to capture intricate micro-macro plasticity couplings associated with the originally sound homogenization problem. In this work, a numerical homogenization approach was proposed in Chapter 5 as an alternative of the standard Gurson-like fully-analytical one. In the following, the computational performance of such numerical scheme is evaluated using the code provided in Appendix F (in turn based on the algorithms described in subsection §5.5).

Given that the proposed homogenization scheme is grounded on numerical integration methods, it is evident that its computational cost depends on the accuracy degree intended for the analysis, in turn controlled by the RVE discretization. Figure 6.14 represents the average relative CPU time required to compute the macroscopic strain-rate potential using the Rice and Tracey trial fields, $\Psi^{\mathrm{RT}}(\boldsymbol{D}, f)$, (Eq. (5.42)) and its derivative, $\partial\Psi/\partial\boldsymbol{D}$, with a prescribed tolerance, normalized by the CPU time associated with the computation of the Gurson (1977) analytical counterpart. The RVE discretization parameter

pair, $(N,\bar{n}_r)$ (recall §5.4.1 and §5.4.2), employed in the computations of Figure 6.14 are selected based on the convergence study in Figure 5.4 and Figure 5.6, respectively, regarding the case of a quadratic yield function for the dense phase, viz, $(N,\bar{n}_r)=\{(48,6),(94,8),(156,10),(328,16)\}$, for the considered tolerances, i.e., $e=\{10^{-3},10^{-4},10^{-5},10^{-6}\}$, respectively. Recall that the radial integration is adaptative, hence a different number of integration points is employed depending on the loading state and the porosity. Accordingly, similarly to the convergence studies in §5.4.1 and §5.4.2, the computational performance statistics reported in the present subsection refer to the average of a sample of $n_s=10^4$ macroscopic loadings with a random deviatoric and hydrostatic contribution. Figure 6.14 shows that the proposed homogenization scheme is $\mathcal{O}(10^2)$ to $\mathcal{O}(10^3)$ times more costly than evaluation a (single) Gurson-type expression. Of course, the computational cost is proportional to the number of quadrature points, hence increases with decreasing tolerance and decreasing porosity. Moreover, for a given tolerance, the computational cost associated with the numerical homogenization roughly halves when the porosity increases from $f=10^{-6}$ to $f=10^{-1}$, (whereas the CPU time for the analytical case is virtually independent of the porosity and loading). Since surface averaging of local quantities on the RVE is more challenging for non-quadratic microscale potentials (see Figure 5.4), more points are needed to guarantee a given cubature tolerance, when compared with the quadratic case. One can thus anticipate more severe numerical-to-analytical time ratios when dealing with non-quadratic functions. However, a quantitative analysis (as in Figure 6.14) concerning non-quadratic microscale potentials, is impossible given the inexistence of analytical porous criteria for non-quadratic matrix models.

At first glance, the CPU time ratios in Figure 6.14 may appear overwhelming, however, the proposed computational homogenization scheme is actually $\mathcal{O}(10^5)$ to $\mathcal{O}(10^6)$ times faster than solving the corresponding elastoplastic FE-based limit analysis problem (similar to that in §6.2.2) with the same accuracy degree. In other words, the computational cost of the developed homogenization scheme is much closer to that of closed-form analytical criteria than to that multiscale FE-based constitutive formulations.

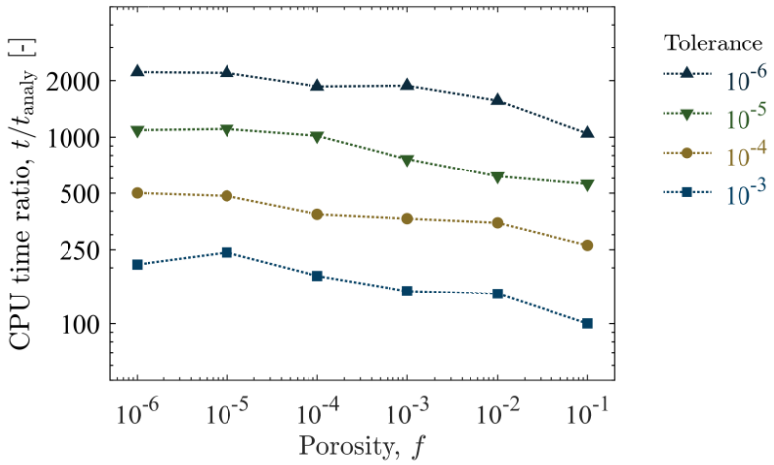

Figure 6.14 Comparison of the average computational cost for the evaluation of the macroscopic strain-rate potential, $\Psi^{RT}(\boldsymbol{D},f)$ (Eq. (5.42)), and its first derivative relative to the associated analytical expressions of Gurson (1977), assuming an average cubature error $e=\{10^{-3},10^{-4},10^{-5},10^{-6}\}$, and a sample of $n_s=10^4$ random loading states, $\boldsymbol{D}$, on porous media with a von Mises matrix and varying porosity.

Throughout this chapter, the predictions of the computational homogenization using two alternative trial fields, those of Rice and Tracey (Eq. (5.20)) and of the Eshelby-type (Eq. (5.30)), have been compared. As remarked in §5.2.3, the latter formulation entails the determination of an additional kinematical tensor in the deviatoric space (see also Appendix E). Figure 6.15 presents the average absolute and relative single-core CPU time of both formulations when evaluating the respective macroscopic strain-rate potentials. It is concluded that the Eshelby-type formulation is $\mathcal{O}(50)$ times more expensive than the Rice and Tracey counterpart. Recalling that these formulations virtually coincide for vanishing porosity values (§6.2.3), the usage of the Eshelby-type fields within a numerical homogenization analysis is therefore not recommended to model porous solids with such porosity degree (e.g. undamaged sheet or bulk metals and alloys). Conversely, for high porosities, found in metal additive manufacturing (AM), (e.g., powder bed fusion (PBF) manufactured parts), differences between formulations are evident and the usage of the Eshelby-type fields is reasonable.

In the context of elasto-plastic modelling, a macroscopic yield function value, $\mathcal{F}$, (Eq. (5.45)), associated with a given macroscopic Cauchy stress tensor, $\boldsymbol{\Sigma}$, must be evaluated in order to determine if the loading is elastic or elastoplastic. As mentioned in §5.5, in view of the fact that a kinematic homogenization approach was adopted, the determination of an equivalent strain-rate quantity was coined the 'direct problem' (Box 5.1), whereas the determination of an equivalent *stress* quantity was coined the 'inverse problem' (Box 5.3). Figure 6.16 presents the average single-core CPU time and the ratio the cost between the inverse (I) and the direct (D) problems. One can conclude that the inverse problem is $\mathcal{O}(25)$ times more expensive than the direct one. This clearly justifies the pertinence of a SRP-based formulation (Eq. (5.16)), (in place of the more usual stress-based counterpart, Eqs. (5.13)-(5.14)), when employing constitutive criteria based on a kinematic computational homogenization scheme within a FE analysis. In fact, the implementation of such strain-rate-based constitutive formulation using the criteria presented in Chapter 5 is undertook in the following chapter.

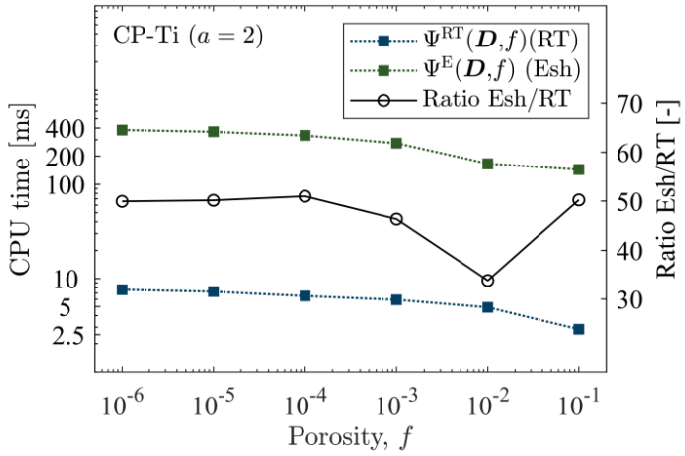

Figure 6.15 Comparison of the computational cost using the Rice and Tracey (RT), $\Psi^{RT}(\boldsymbol{D}, f)$ (Eq. (5.42)), and the Eshelby-type (Esh), $\Psi^{E}(\boldsymbol{D}, f)$ (Eq. (5.30)), fields. The plots represent the average single-core CPU time (Intel® Core™ i7-8700K) for the evaluation of the macroscopic strain-rate potentials with a relative cubature error $e = 10^{-5}$ on a sample of $n_s = 10^4$ random loading states, $\boldsymbol{D}$, of porous media with varying porosity and with a CP-Ti matrix (constitutive data in §4.5.2).

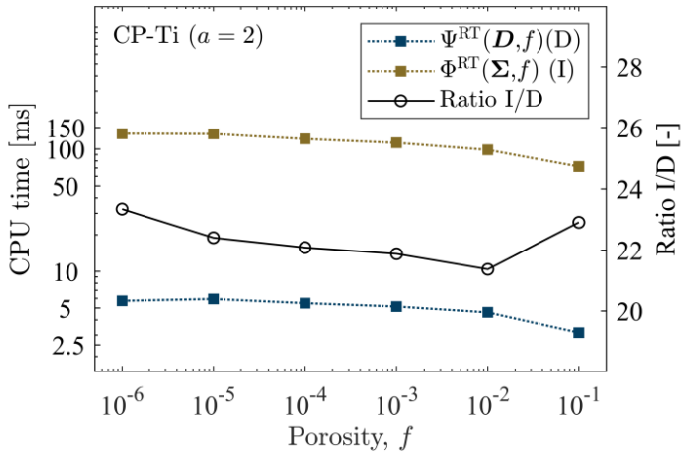

Figure 6.16 Comparison of the computational cost of the direct (D) and the inverse (I) homogenization schemes using the Rice and Tracey (RT), $\Psi^{\mathrm{RT}}(\boldsymbol{D}, f)$ (Eq. (5.42)) fields. The plots represent the average single-core CPU time (Intel® Core™ i7-8700K) for the evaluation of the macroscopic strain-rate potentials with a relative cubature error $e = 10^{-5}$ on a sample of $n_s = 10^4$ random loading states, $\boldsymbol{D}$, of porous media with varying porosity and with a CP-Ti matrix (constitutive data in §4.5.2).

Chapter 7

Implementation in the FEM framework

This chapter deals with the integration of the numerical-based porous criteria developed in Chapter 5 into large-strain rate-independent elastoplastic problems compatible with engineering applications. The proposed constitutive flamework is grounded on an orthotropic hyperelastic-based multiplicative plasticity formulation coupled a strain-rate potential for describing plastic dissipation. The outline of the chapter is as follows. First, the governing equations of the constitutive initial value problem are presented. Then, the respective incremental (i.e., time-discretized) problem, compatible with computational implementation, is developed based on fully-implicit time integration algorithms in the context of the finite-element method. Lastly, as a proof-of-concept, a numerical example is provided employing the developed constitutive formulation.

7.1 Constitutive theory: definition of the initial value problem

As discussed in §3.2, in the scope of engineering applications, the assumption of the existence of a RVE allows the description of the behaviour of a solid in terms of the continuum theory. The constitutive framework developed in this subsection is grounded on the mechanics and thermodynamics of continuous media. The general concepts of these theories are omitted when possible, and the focus is set solely on the kinematic and kinetic expressions actually employed in the envisioned analysis. For a more detailed description of the axioms and modelling hypothesis employed in the following, refer, for instance, to the books of Besson (2010); Bonet and Wood (1997); De Borst *et al.* (2012); Germain (1973); Hill (1998); Jirásek and Bazant (2002); Lubarda (2002); Lubliner (2008); Mandel (1966); Simo and Hughes (2006); de Souza Neto *et al.* (2011); Zienkiewicz and Taylor (2005).

7.1.1 Kinematics of deformation: preliminaries

This subsection sets out the basic kinematic quantities of material simple continua (micro-polar and micromorphic continua do not concern the present work) entering the proposed finite strain elastoplasticity constitutive framework. The notation and arrangement of the present subsection primarily follow that of Bonet and Wood (1997) and de Souza Neto *et al.* (2011).

Configurations and motion of a continuum body

Let $\mathcal{B}_0 \subset \mathbb{R}^3$ denote a body embedded in the three-dimensional Euclidean space in its *reference* configuration, here assumed coincident with the *initial* configuration. A one-to-one (and thus invertible) deformation map:

$$\phi(\underline{\boldsymbol{X}},t):\mathcal{B}_0\times\mathcal{T}\rightarrow\mathbb{R}^3,\ \text{with}\ \underline{\boldsymbol{x}}=\phi(\underline{\boldsymbol{X}},t)\,, \tag{7.1}$$

is introduced, which maps points $\underline{\boldsymbol{X}}\in\mathcal{B}_0$ of the reference configuration, $\mathcal{B}_0$, with respect to a Cartesian basis $\underline{\boldsymbol{E}}_i$, onto points $\underline{\boldsymbol{x}}\in\mathcal{B}_t\subset\mathbb{R}^3$ of the *current* configuration, $\mathcal{B}_t$, with respect to a Cartesian basis $\underline{\boldsymbol{e}}_i$, at time $t\in\mathcal{T}=[0,T]$. This mapping is illustrated in Figure 7.1. For a fixed time, *t*, Eq. (7.1) represents a mapping between the undeformed (initial) and deformed (current) bodies, whereas for a fixed particle $\underline{\boldsymbol{X}}$, Eq. (7.1) describes the motion (or trajectory) of this particle as a function of time. The displacement field $\underline{\boldsymbol{u}}$ at the instant *t* of a particle $\underline{\boldsymbol{X}}$ is the difference of the position of the particle between the current and reference configurations, i.e.:

$$\underline{\boldsymbol{u}}(\underline{\boldsymbol{X}},t)=\phi(\underline{\boldsymbol{X}},t)-\underline{\boldsymbol{X}}\,. \tag{7.2}$$

In finite deformation analysis a careful distinction has to be made between the coordinate systems adopted to describe the behaviour of the body whose motion is under consideration. Depending on the considered Euclidean space, one may distinguish: the material (alias Lagrangian) description; and the spatial (alias Eulerian) description. Let $\boldsymbol{\xi}$ denote an arbitrary tensorial (or scalar) field. In the material description, $\boldsymbol{\xi}=\boldsymbol{\xi}(\underline{\boldsymbol{X}},t)$, whereas in the spatial description, $\boldsymbol{\xi}=\boldsymbol{\xi}(\underline{\boldsymbol{x}},t)$. An analogous nomenclature holds for other mathematical operations (e.g. material and spatial gradients). It turns out that, even if the deformation process is assumed rate independent it is nevertheless convenient to establish the equilibrium equations in terms of virtual velocities and associated virtual time-dependant quantities (Bonet and Wood, 1997). According, based on the time derivative of the deformation map (Eq. (7.1)) one arrives at the velocity of a particle in terms of the material coordinates of a particle $\underline{\boldsymbol{X}}$:

$$\underline{\boldsymbol{v}}(\underline{\boldsymbol{X}},t)=\frac{\partial\phi(\underline{\boldsymbol{X}},t)}{\partial t}\,. \tag{7.3}$$

The velocity vector can be more consistently expressed in terms of the spatial position, $\underline{\boldsymbol{x}}$, as:

$$\underline{\boldsymbol{v}}(\underline{\boldsymbol{x}},t)=\underline{\boldsymbol{v}}(\phi^{-1}(\underline{\boldsymbol{x}},t),t)\,. \tag{7.4}$$

The deformation gradient

Based on Eq. (7.1), one defines the deformation gradient tensor, ***F***, as:

$$\boldsymbol{F}=\nabla_0\phi(\underline{\boldsymbol{X}},t)=\frac{\partial\phi(\underline{\boldsymbol{X}},t)}{\partial\underline{\boldsymbol{X}}}=\sum_{i,I=1}^{3}F_{iI}\ \underline{\boldsymbol{e}}_i\otimes\underline{\boldsymbol{E}}_i\,,\ \text{with}\ F_{iI}=\frac{\partial x_i}{\partial X_I},\ \ i,I=1,2,3\,, \tag{7.5}$$

where $\nabla_0(\cdot)$ denotes the gradient operation with respect to the material configuration (alias material derivative or gradient). In view of Eq. (7.2), the previous expression can be rewritten as:

$$\boldsymbol{F}=\boldsymbol{I}+\nabla_0\boldsymbol{u}(\underline{\boldsymbol{X}},t)\,. \tag{7.6}$$

Note that ***F*** transforms vectors in the initial or reference configuration into vectors in the current configuration, i.e., $d\underline{\boldsymbol{x}}=\boldsymbol{F}d\underline{\boldsymbol{X}}$, and is thus said to be a *two-point* tensor (it is neither material nor spatial). The inverse operation can also be defined:

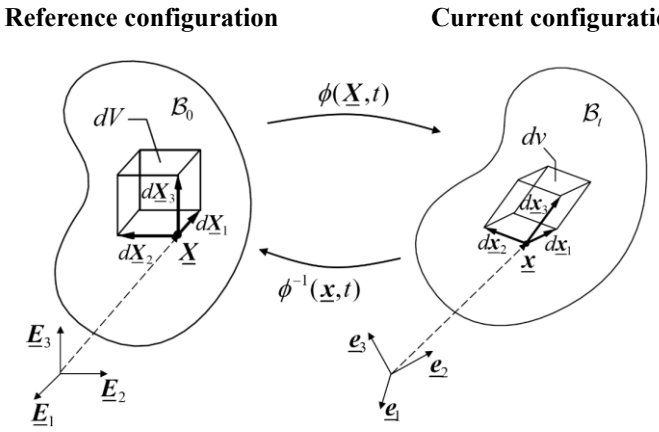

Figure 7.1 Reference, $\mathcal{B}_0$, and current, $\mathcal{B}_t$, configurations of a deformable body as defined by the deformation map, ϕ, and its inverse, ϕ^{-1} at instant $t \in \mathcal{T} = [0,T]$. Note that $d\underline{\boldsymbol{x}} = \boldsymbol{F} d\underline{\boldsymbol{X}}$ and $dv = \det(\boldsymbol{F})dV$, where $\boldsymbol{F}$ is the deformation gradient associated with ϕ. Adapted from de Souza Neto *et al.* (2011).

$$\boldsymbol{F}^{-1} = \nabla \phi^{-1}(\underline{\boldsymbol{x}},t) = \frac{\partial \phi^{-1}(\underline{\boldsymbol{x}},t)}{\partial \underline{\boldsymbol{x}}} = \sum_{i,I=1}^{3} F_{Ii}\ \underline{\boldsymbol{E}}_i \otimes \underline{\boldsymbol{e}}_I, \text{ with } F_{Ii} = \frac{\partial X_i}{\partial x_I},\ \ i,I = 1,2,3, \tag{7.7}$$

where $\nabla(\cdot)$ denotes the gradient operation with respect to the spatial configuration (alias spatial derivative or gradient), and ϕ^{-1} is the inverse mapping of that in Eq. (7.1), i.e., $\phi^{-1}(\underline{\boldsymbol{x}},t) : \mathcal{B} \times \mathcal{T} \to \mathbb{R}^3$, with $\underline{\boldsymbol{X}} = \phi^{-1}(\underline{\boldsymbol{x}},t)$. Of special importance is the determinant of $\boldsymbol{F}$, which quantifies the volume change as:

$$J = \frac{dv}{dV} = \det(\boldsymbol{F}), \tag{7.8}$$

where dv and dV are the infinitesimal volume elements in the current and reference configurations, respectively, arising from the application of a deformation gradient $\boldsymbol{F}$ at a material particle $\underline{\boldsymbol{X}}$ and time t (see Figure 7.1). Any physically sound deformed configuration must satisfy $J > 0$. Note that an isochoric deformation implies $J = 1$.

The velocity gradient, strain-rate and spin tensors

The velocity gradient tensor, $\boldsymbol{l}$, is defined based on the spatial derivative of the velocity, $\underline{\boldsymbol{v}}(\underline{\boldsymbol{x}},t)$, in Eq. (7.4) as:

$$\boldsymbol{l} = \nabla \boldsymbol{v} = \frac{\partial \underline{\boldsymbol{v}}(\underline{\boldsymbol{x}},t),}{\partial \underline{\boldsymbol{x}}}. \tag{7.9}$$

Combining Eqs. (7.3), (7.5) and (7.15), the time derivative of the deformation gradient tensor, $\boldsymbol{F}$, is given as:

$$\dot{\boldsymbol{F}} = \frac{d}{dt}\left(\frac{\partial \phi(\underline{\boldsymbol{X}},t)}{\partial \underline{\boldsymbol{X}}}\right) = \frac{\partial}{d\underline{\boldsymbol{X}}}\left(\frac{\partial \phi(\underline{\boldsymbol{X}},t)}{\partial t}\right) = \nabla_0 \boldsymbol{v} = \boldsymbol{l}\boldsymbol{F}\ , \tag{7.10}$$

which, in turn, allows Eq. (7.9) to be rewritten in the form:

$$\boldsymbol{l} = \dot{\boldsymbol{F}}\boldsymbol{F}^{-1}. \tag{7.11}$$

The split of the velocity gradient tensor, $\boldsymbol{l}$, into its symmetric and skew (antisymmetric) parts leads to two important kinematical quantities:

$$\boldsymbol{l} = \boldsymbol{d} + \boldsymbol{w}\,, \text{ with } \boldsymbol{d} = \boldsymbol{d}^{\mathrm{T}}\,, \text{ and } \boldsymbol{w}^{\mathrm{T}} = -\boldsymbol{w}\,, \tag{7.12}$$

where

$$\boldsymbol{d} = \mathrm{sym}(\boldsymbol{l})\,, \tag{7.13}$$

is known as the rate of deformation tensor, (or, simply, Eulerian strain-rate tensor, as identified throughout this work), and

$$\boldsymbol{w} = \mathrm{skew}(\boldsymbol{l})\,, \tag{7.14}$$

is the spin tensor (alias vorticity tensor). In the previous equations, the following notation has employed: $\mathrm{sym}(\cdot) = \frac{1}{2}[(\cdot) + (\cdot)^{\mathrm{T}}]$, and $\mathrm{skew}(\cdot) = \frac{1}{2}[(\cdot) - (\cdot)^{\mathrm{T}}]$.

Polar decomposition, stretches and rotation

It is often useful to decompose the deformation gradient in two components, one accounting for the stretch of the solid and another for its rotation. According to the polar decomposition theorem, the deformation gradient can be expressed as:

$$\boldsymbol{F} = \boldsymbol{R}\boldsymbol{U} = \boldsymbol{V}\boldsymbol{R}\,, \tag{7.15}$$

where $\boldsymbol{U}$ and $\boldsymbol{V}$ are the so-called right and left stretch tensors, respectively, by definition, symmetric positive definite; and $\boldsymbol{R}$ is a (orthogonal) rotation tensor. Note that $\boldsymbol{U}$ is a material tensor, whereas $\boldsymbol{V}$ is a spatial tensor. For convenience, one defines the right, $\boldsymbol{C}$, and left, $\boldsymbol{b}$, Cauchy-Green tensors are their respective spectral decomposition as:

$$\begin{aligned} \boldsymbol{C} = \boldsymbol{F}^{\mathrm{T}}\boldsymbol{F} = \boldsymbol{U}^2 = \sum_{\alpha=1}^{3} \lambda_\alpha^2 \; \underline{\boldsymbol{N}}_\alpha \otimes \underline{\boldsymbol{N}}_\alpha\,, \text{ and} \\ \boldsymbol{b} = \boldsymbol{F}\boldsymbol{F}^{\mathrm{T}} = \boldsymbol{V}^2 = \sum_{\alpha=1}^{3} \bar{\lambda}_\alpha^2 \; \underline{\boldsymbol{n}}_\alpha \otimes \underline{\boldsymbol{n}}_\alpha\,, \end{aligned} \tag{7.16}$$

respectively, where $\underline{\boldsymbol{N}}_\alpha$ and $\underline{\boldsymbol{n}}_\alpha$, $\alpha = 1,2,3,$ denote the (orthogonal) eigenvector triads of $\boldsymbol{C}$ and $\boldsymbol{b}$, respectively, and λ_α^2 and $\bar{\lambda}_\alpha^2$, $\alpha = 1,2,3,$ their corresponding eigenvalues. It is possible to demonstrate that the expressions in Eq. (7.16) are related via $\lambda_\alpha^2 = \bar{\lambda}_\alpha^2$ and that $\underline{\boldsymbol{n}}_\alpha = \boldsymbol{R}\underline{\boldsymbol{N}}_\alpha$, $\alpha = 1,2,3$ (e.g. see Bonet and Wood, 1997). Hence, from Eq. (7.16) and the aforementioned identities, is follows that the right, $\boldsymbol{U}$, and left, $\boldsymbol{V}$, stretch tensors are given by:

$$\begin{aligned} \boldsymbol{U} = \sqrt{\boldsymbol{C}} = \sum_{\alpha=1}^{3} \lambda_\alpha \; \underline{\boldsymbol{N}}_\alpha \otimes \underline{\boldsymbol{N}}_\alpha\,, \text{ and} \\ \boldsymbol{V} = \sqrt{\boldsymbol{b}} = \sum_{\alpha=1}^{3} \lambda_\alpha \; \underline{\boldsymbol{n}}_\alpha \otimes \underline{\boldsymbol{n}}_\alpha = \sum_{\alpha=1}^{3} \lambda_\alpha \; (\boldsymbol{R}\underline{\boldsymbol{n}}_\alpha) \otimes (\boldsymbol{R}\underline{\boldsymbol{n}}_\alpha)\,. \end{aligned} \tag{7.17}$$

respectively, where the (unique) λ_α, $\alpha = 1,2,3,$ are known as the principal stretches, and $\underline{\boldsymbol{N}}_\alpha$ and $\underline{\boldsymbol{n}}_\alpha$, $\alpha = 1,2,3,$ are coined the Lagrangian and Eulerian triads and define the Lagrangian and Eulerian principal strain directions, respectively. The previous equation implies any local stretching from a material

particle can be expressed as a superposition of stretches along three mutually orthogonal directions. Once the stretch tensors are known, the (unique) rotation tensor, $\boldsymbol{R}$, can be readily evaluated inverting Eq. (7.15) as follows:

$$\begin{aligned} \boldsymbol{R} &= \boldsymbol{F}\boldsymbol{U}^{-1}, \text{ with } \boldsymbol{U}^{-1} = \sum_{\alpha=1}^{3} \frac{1}{\lambda_\alpha} \underline{\boldsymbol{N}}_\alpha \otimes \underline{\boldsymbol{N}}_\alpha \text{ , or} \\ \boldsymbol{R} &= \boldsymbol{V}^{-1}\boldsymbol{F} \text{ , with } \boldsymbol{V}^{-1} = \sum_{\alpha=1}^{3} \frac{1}{\lambda_\alpha} \underline{\boldsymbol{n}}_\alpha \otimes \underline{\boldsymbol{n}}_\alpha , \end{aligned} \tag{7.18}$$

where the spectral decomposition of $\boldsymbol{U}$ and $\boldsymbol{V}$ was employed in order to compute the tensor inverse.

Generalized strain tensors

The stretch tensors defined above characterize the distance between material particles between the reference and the current configuration. In order to quantify *straining*, i.e., to evaluate how much $\boldsymbol{U}$ (or $\boldsymbol{V}$) departs from $\boldsymbol{I}$ (a rigid deformation), some strain measure must be defined. The definition of a strain measure is therefore somewhat arbitrary, and a specific choice is usually dictated by mathematical and physical convenience. It is common to distinguish two families of strain tensors: the generalized Lagrangian strain tensors, and the generalized Eulerian strain tensors. As the name suggests, the former is based on Lagrangian triad, whereas the latter is based on the Eulerian triad, $\underline{\boldsymbol{n}}_\alpha$, $\alpha = 1,2,3$. The generalized Lagrangian strain tensors, $\boldsymbol{E}_{(n)}$, are defined in terms of the right stretch tensor, $\boldsymbol{U}$, in the form:

$$\boldsymbol{E}_{(n)} = \begin{cases} \dfrac{1}{n}(\boldsymbol{U}^n - \boldsymbol{I}) & n \neq 0 \\ \ln(\boldsymbol{U}) & n = 0 \end{cases}, \tag{7.19}$$

where n is a real number and $\ln(\cdot)$ denotes the tensor logarithm operator. The previous expression is more conveniently written terms of its spectral decomposition using the Lagrangian triad, $\underline{\boldsymbol{N}}_\alpha$, as:

$$\boldsymbol{E}_{(n)} = \sum_{\alpha=1}^{3} f(\lambda_\alpha, n)\, \underline{\boldsymbol{N}}_\alpha \otimes \underline{\boldsymbol{N}}_\alpha, \tag{7.20}$$

with

$$f(\lambda_\alpha, n) = \begin{cases} \dfrac{1}{n}(\lambda_\alpha^n - 1) & n \neq 0 \\ \ln(\lambda_\alpha) & n = 0 \end{cases}, \quad \alpha = 1,2,3. \tag{7.21}$$

Some particular cases are worth mentioning: the Green-Lagrange $(n = 2)$, Biot $(n = 1)$, Hencky $(n = 0)$ and Almansi $(n = -2)$ strain tensors. Note that, regardless of n, the associated strain tensor vanishes if (and only if) the deformation gradient represents a rigid deformation, i.e.: $\boldsymbol{E}_{(n)} = \boldsymbol{0} \Leftrightarrow \boldsymbol{F} = \boldsymbol{R} \Leftrightarrow \boldsymbol{U} = \boldsymbol{I}$. Analogously, it is possible to define the Eulerian counterpart to Eqs. (7.19)-(7.20), coined generalized Eulerian strain tensors, $\boldsymbol{e}_{(n)}$, is this case defined in terms of the right stretch tensor, $\boldsymbol{V}$, in the form:

$$\boldsymbol{e}_{(n)} = \begin{cases} \dfrac{1}{n}(\boldsymbol{V}^n - \boldsymbol{I}) & n \neq 0 \\ \ln(\boldsymbol{V}) & n = 0 \end{cases}, \tag{7.22}$$

or, equivalently, written in the Eulerian principal strain space using the triad $\underline{\boldsymbol{n}}_\alpha$, $\alpha = 1,2,3$:

$$\boldsymbol{e}_{(n)} = \sum_{\alpha=1}^{3} f(\lambda_\alpha, n)\, \underline{\boldsymbol{n}}_\alpha \otimes \underline{\boldsymbol{n}}_\alpha, \tag{7.23}$$

where $f(\lambda_\alpha, n)$ was defined in Eq. (7.21). Note moreover that the Lagrangian and Eulerian strain differ by the rotation of the polar decomposition in Eq. (7.15): $\boldsymbol{e}_{(n)} = \boldsymbol{R}\boldsymbol{E}_{(n)}\boldsymbol{R}^{\mathrm{T}} \Leftrightarrow \boldsymbol{E}_{(n)} = \boldsymbol{R}^{\mathrm{T}}\boldsymbol{e}_{(n)}\boldsymbol{R}$.

7.1.2 Multiplicative decomposition

This subsection is concerned with the fundamental hypothesis underlying the proposed finite strain elastoplasticity constitutive framework: the multiplicative split of the deformation gradient (Eq. (7.5)) into elastic and plastic parts. Motivated by micromechanical observations regarding the slip theory of crystals (Asaro, 1983; Rice, 1971), the multiplicative decomposition hypothesis was introduced by Lee and Liu (1967) and Lee (1969), and later developed by many authors (Dafalias, 1985, 1998; Kroner and Teodosiu, 1974; Lubarda and Lee, 1981; Mandel, 1972, 1973). According to this theory the deformation gradient is decomposed as:

$$\boldsymbol{F} = \boldsymbol{F}^{\mathrm{e}}\boldsymbol{F}^{\mathrm{p}}, \tag{7.24}$$

where $\boldsymbol{F}^{\mathrm{e}}$ and $\boldsymbol{F}^{\mathrm{p}}$ are coined the *elastic* and *plastic* deformation gradients, respectively. The previous expression implicitly assumes the existence of an unstressed intermediate configuration, where $\boldsymbol{F}^{\mathrm{p}}$ defines the deformation map from the reference to the intermediate configuration. It must be observed that, the unstressed (unloaded) intermediate configuration concept is only valid in the local (pointwise) sense. In fact, in general, locally unloaded regions of a body cannot be reassembled to give an *overall* stress-free configuration since these are not necessarily geometrically compatible with each (Bonet and Wood, 1997). The non-uniqueness of the decomposition in Eq. (7.24) is a well-known weakness of this theory. Indeed, as it stands, tensors $\boldsymbol{F}^{\mathrm{e}}$ and $\boldsymbol{F}^{\mathrm{p}}$ cannot be uniquely defined since arbitrary rotations can be superposed to the intermediate configuration, preserving it unstressed, and thus not unique. It follows that an additional assumption to the form of $\boldsymbol{F}^{\mathrm{e}}$ or $\boldsymbol{F}^{\mathrm{p}}$ (or any other kinematic quantity related with these) must be made so that Eq. (7.24) is uniquely defined. A more detailed discussion on the issue of uniqueness and the choice of the intermediate configuration can be found e.g. in Casey and Naghdi (1980); Dafalias (1985, 1998); Naghdi (1990).

Based on the considered multiplicative decomposition of $\boldsymbol{F}$, the determinant, J, in Eq. (7.8) is split into an elastic, J^{e}, and plastic, J^{p}, contribution as follows:

$$J = \det(\boldsymbol{F}^{\mathrm{e}}\boldsymbol{F}^{\mathrm{p}}) = J^{\mathrm{e}}J^{\mathrm{p}}, \text{ with } \begin{cases} J^{\mathrm{e}} = \det(\boldsymbol{F}^{\mathrm{e}}), \\ J^{\mathrm{p}} = \det(\boldsymbol{F}^{\mathrm{p}}). \end{cases} \tag{7.25}$$

In the literature it is often assumed that $J^{\mathrm{p}}=1$ (and thus $J=J^{\mathrm{e}}$) due to the constrain of plastic incompressibility. However, in the context of porous solids which this work concerns, plasticity is not isochoric, and, therefore, the plastic- and elastic-based determinants must actually be distinguished.

Elastic and plastic stretch and rotation tensors

In the spirit of the polar decomposition of the (total) deformation gradient, $\boldsymbol{F}$, (see Eq. (7.15)), the stretches and rotations associated with its elastic and plastic part are as follows:

$$\boldsymbol{F}^{\mathrm{e}}=\boldsymbol{R}^{\mathrm{e}}\boldsymbol{U}^{\mathrm{e}}=\boldsymbol{V}^{\mathrm{e}}\boldsymbol{R}^{\mathrm{e}}\ \text{, and}\ \boldsymbol{F}^{\mathrm{p}}=\boldsymbol{R}^{\mathrm{p}}\boldsymbol{U}^{\mathrm{p}}=\boldsymbol{V}^{\mathrm{p}}\boldsymbol{R}^{\mathrm{p}}\,, \tag{7.26}$$

where $\boldsymbol{U}^{\mathrm{e}}$ ($\boldsymbol{U}^{\mathrm{p}}$), $\boldsymbol{V}^{\mathrm{e}}$ ($\boldsymbol{V}^{\mathrm{p}}$), $\boldsymbol{R}^{\mathrm{e}}$ ($\boldsymbol{R}^{\mathrm{p}}$), denote the elastic (plastic) right stretch tensor, the elastic (plastic) left stretch tensor and the elastic (plastic) rotation tensor, respectively. The physical meaning of these tensors is equivalent to the respective counterparts regarding the total deformation gradient, as described following Eq. (7.15). However, care should be taken regarding the different basis of these: note that $\boldsymbol{U}^{\mathrm{e}}$ refers to the intermediate configuration, whereas $\boldsymbol{U}^{\mathrm{p}}$ refers to the reference configuration. Analogously, $\boldsymbol{V}^{\mathrm{e}}$ refers to the current configuration and $\boldsymbol{V}^{\mathrm{p}}$ to the intermediate configuration.

Additive split of the velocity gradient

In agreement with the assumed multiplicative split of $\boldsymbol{F}$, application of the differentiation product rule to Eq. (7.11) with definition Eq. (7.26), results in the following *additive* decomposed for the spatial velocity gradient (Eqs. (7.9)), into an elastic and a plastic part as:

$$\boldsymbol{l}=\boldsymbol{l}^{\mathrm{e}}+\boldsymbol{l}^{\mathrm{p}}\ , \tag{7.27}$$

where the tensors $\boldsymbol{l}^{\mathrm{e}}$ and $\boldsymbol{l}^{\mathrm{p}}$ are the *spatial* elastic and plastic velocity gradient, respectively, given by:

$$\boldsymbol{l}^{\mathrm{e}}=\dot{\boldsymbol{F}}^{\mathrm{e}}(\boldsymbol{F}^{\mathrm{e}})^{-1}\ \text{, and}\ \boldsymbol{l}^{\mathrm{p}}=\boldsymbol{F}^{\mathrm{e}}\boldsymbol{L}^{\mathrm{p}}(\boldsymbol{F}^{\mathrm{e}})^{-1}, \tag{7.28}$$

with

$$\boldsymbol{L}^{\mathrm{p}}=\dot{\boldsymbol{F}}^{\mathrm{p}}(\boldsymbol{F}^{\mathrm{p}})^{-1}. \tag{7.29}$$

$\boldsymbol{L}^{\mathrm{p}}$ is also a plastic velocity gradient, yet it operates in the intermediate configuration[23]. The split of Eq. (7.27) into its symmetric and skew (antisymmetric) parts leads to the decomposition of the spatial strain-rate tensor into elastic and plastic parts as follows:

$$\boldsymbol{d}=\boldsymbol{d}^{\mathrm{e}}+\boldsymbol{d}^{\mathrm{p}}\text{, with}\ \boldsymbol{d}^{\mathrm{e}}=\mathrm{sym}(\boldsymbol{l}^{\mathrm{e}})\ \text{and}\ \boldsymbol{d}^{\mathrm{p}}=\mathrm{sym}(\boldsymbol{l}^{\mathrm{p}})\,, \tag{7.30}$$

and the spatial spin tensor as:

$$\boldsymbol{w}=\boldsymbol{w}^{\mathrm{e}}+\boldsymbol{w}^{\mathrm{p}}\text{, with}\ \boldsymbol{w}^{\mathrm{e}}=\mathrm{skew}(\boldsymbol{l}^{\mathrm{e}})\ \text{and}\ \boldsymbol{w}^{\mathrm{p}}=\mathrm{skew}(\boldsymbol{l}^{\mathrm{p}})\,. \tag{7.31}$$

Moreover, in the scope of the envisioned analysis, it is also relevant to decompose $\boldsymbol{L}^{\mathrm{p}}$ in Eq. (7.29) in its symmetric, $\boldsymbol{D}^{\mathrm{p}}$, and skew, $\boldsymbol{W}^{\mathrm{p}}$, parts as:

[23] Henceforward a convention is adopted regarding kinematical and kinetic tensorial quantities: majuscule letters refer to Lagrangian tensors defined in the *intermediate* (unstressed) configuration; whereas minuscule letters refer to Eulerian tensors defined in the *current* configuration.

$$\boldsymbol{L}^{\mathrm{p}} = \boldsymbol{D}^{\mathrm{p}} + \boldsymbol{W}^{\mathrm{p}}, \text{ with } \boldsymbol{D}^{\mathrm{p}} = \mathrm{sym}(\boldsymbol{L}^{\mathrm{p}}) \text{ and } \boldsymbol{W}^{\mathrm{p}} = \mathrm{sym}(\boldsymbol{L}^{\mathrm{p}}), \tag{7.32}$$

where $\boldsymbol{D}^{\mathrm{p}}$ and $\boldsymbol{W}^{\mathrm{p}}$ are the plastic strain-rate tensor and the plastic spin tensor in the *intermediate* configuration, respectively[24].

Definition of the intermediate configuration

In this work, the plastic spin tensor in Eq. (7.32), representing the instantaneous rate of rigid spinning of the intermediate configuration, is postulated to be null, i.e.:

$$\boldsymbol{W}^{\mathrm{p}} \triangleq \boldsymbol{0}. \tag{7.33}$$

This implies that the principal orthotropic directions do not change during plastic deformation. This is in opposition with the discussion in §2.1.2, where it was started that texture evolution and/or twinning-detwinning activation actually led to an evolving anisotropic behaviour. However, in order to consider plastic spin effects one must provide a suitable constitutive equation (dissipation potential) for its evolution, which not in scope of the present work (Dafalias, 1985, 1998; Kaiser *et al.*, 2020; Montáns *et al.*, 2012; Montáns and Bathe, 2007). Moreover, the relevance of plastic spin effects is controversial, particularly when compared with other elements of a constitutive formulation as the representation of the initial anisotropy and hardening aspects (Dafalias, 1998). Nevertheless, texture evolution effects can still be reproduced in a heuristic fashion by prescribing an evolution law for the anisotropy coefficients entering a given orthotropic plastic potential (e.g., see Abedini *et al.*, 2017; Plunkett *et al.*, 2006; Revil-Baudard *et al.*, 2014, 2016; Yoon *et al.*, 2013). It follows from the definition in Eq. (7.32) and the hypothesis of Eq. (7.33) and that the plastic velocity gradient in the intermediate configuration, $\boldsymbol{L}^{\mathrm{p}}$, is symmetric and reduces to:

$$\boldsymbol{L}^{\mathrm{p}} \equiv \boldsymbol{D}^{\mathrm{p}}. \tag{7.34}$$

If Eq. (7.33), (or, equivalently, Eq. (7.34)) is supplied with a constitutive equation for $\boldsymbol{D}^{\mathrm{p}}$, the evolution of $\boldsymbol{F}^{\mathrm{p}}$ is completely defined, and thus the intermediate configuration is unique.

7.1.3 Hyperelastic-based elastoplastic constitutive model

Introduction hyperelastic-based large strain elastoplasticity

Ealy works on large-strain elastoplasticity (e.g. Hill (1958) and Green and Naghdi (1965)) relied on hypoelastic-based approaches in which existing infinitesimal elastoplasticity models are extended to the finite strain range by an additive decomposition of a strain-rate tensor into elastic and plastic parts and recasting the original evolution equations in terms of *ad hoc* objective (or frame-invariant) stress rates. Despite their apparent simplicity, hypoelastic-based formulations have been the subject of intense

[24] The distinction of majuscule and minuscule variables was employed in Chapter 3 to Chapter 6 to distinguish the micro- and the macro- scalar and tensorial quantities in the context of homogenization of porous media (e.g., $(\boldsymbol{d}^{\mathrm{p}}, \boldsymbol{\sigma}, j_2, j_3)$ *vs.* $(\boldsymbol{D}^{\mathrm{p}}, \boldsymbol{\Sigma}, J_2, J_3)$). In the present chapter this convention is dropped and replaced with the convention in Footnote 23.

debate related with issues including (de Souza Neto *et al.*, 2011): (i) the arbitrariness of the objective stress rates to employ in the constitutive equations; (ii) objectivity issues of the incremental (algorithmic) constitutive laws; (iii) numerical errors in the time integration of the rate quantities, (even if algorithmic objectivity is preserved), which require a large number of integration steps; (iv) the oscillatory stress response under monotonic loadings; and (v) the non-conservative response in purely elastic cyclic motions (viz. in the form of non-physical residual stresses). While the latter two points may be considered negligible when both the elastic strains and strain-rates are small, these are clearly undesirable phenomena.

Owing to the issues described above, hyperelastic-based elastoplasticity models emerged. Initial developments in this field are attributed to Simo (1985) and Simo and Ortiz (1985). These rely on a more physically motivated multiplicative elastoplastic split of the deformation gradient into elastic and plastic parts (Eq. (7.24)) and a hyperelastic constitutive equation for describing the reversible behaviour. Such theory presents clear advantages over the hypoelastic-based counterpart, both from a conceptual viewpoint, since a dissipative response becomes impossible within the elastic range given the characteristic path-independence; and from the algorithmic viewpoint since incremental objectivity is trivially satisfied, and lager time (or pseudo-time) integration steps can be employed since it is a total (rather than rate-type) constitutive approach. This justifies the widespread acceptance of the hyperelastic-based multiplicative approach in the past two decades, which this work is concerned.

In closing, it should be noted that the abovementioned non-physical dissipative and oscillatory behaviour associated with the hypoelastic theory is usually negligible in metal plasticity, where the contribution of the elastic strains is small. Indeed, a recent numerical study in Brepols *et al.* (2014) showed that even if the hypo- and hype-elastic formulations lead to remarkably different results in an academic shear-dominated deformation test, the simulations of engineering forming processes (viz. deep drawing, draw bending and thermoforming) delivered very similar results of both global measurement and local fields, which suggests that both formulations are well-suited for dealing with elastoplastic modelling of common engineering metals and alloys. Note however that this may not hold in situations where elastic deformations become considerable. A comprehensive presentation of the theoretical aspects of and differences between the hypoelastic and hyperelastic formulations can be found in Xiao *et al.* (2006) and Simo and Hughes (2006), the latter also concerns algorithmic aspects.

Hyperelastic-based finite strain elastoplastic constitutive models are grounded on the formalism of thermodynamics with internal variable approach (recall §3.2). In essence, for the isothermal case, these are built by postulating (de Souza Neto *et al.*, 2011): (i) a free-energy potential, from which the hyperelastic constitutive law is derived; (ii) a yield function defining the onset of plastic yielding; and (iii) a dissipation potential from which the plastic flow rule and the evolution laws for the internal variables are derived. The mathematical details and intermediate steps of this approach (e.g. thermodynamic determinism, the Clausius-Duhem inequality, material objectivity, principle of maximum dissipation) are omitted here, and the focus is solely on the final results of the analysis. The elastoplastic constitutive framework presented in this subsection is based on the works Eterovic and Bathe (1990), Montáns and

Bathe (2007) and Caminero *et al.* (2011). The reared is referred to these for more details regarding the presented hyperelastic-based constitutive relationships. The output of each of the three points listed above are described in the following.

Orthotropic hyperelasticity based on logarithmic strains

When modelling small-strain elasticity, there is no theoretical reason to prefer one strain tensor over another one, and the same holds true for the stress tensors (Neff *et al.*, 2016). However, in the context of large-strain elastoplasticity, formulations based on elastic *logarithmic* (alias *natural* or *Hencky*) strain tensors provide a number of unique, favourable properties, both conceptually and computationally: the former is related with their intuitive and meaningful physical interpretation (Malvern, 1969; de Souza Neto *et al.*, 2011), viz., under uniaxial loadings; the latter is due to the fact that incremental schemes formulated in terms of logarithmic strains and exponential integration preserve the desired structure of the standard return mapping algorithms of classical elastoplastic models, thus providing a simple computational framework suitable for nonlinear FE analysis (Simo, 1992). Moreover, it has been shown that hyperelastic relations in terms of logarithmic strains with constant coefficients yield a simple and accurate description of the elastic behaviour of metals for moderate elastic strains (Anand, 1979, 1985; Weber and Anand, 1990). For these reasons, elastoplastic models based on logarithmic strains and their work-conjugate stresses have been used extensively (Anand, 1979; Caminero *et al.*, 2011; Eterovic and Bathe, 1990; Hill, 1950, 1979b; Hoger, 1987; Lehmann, 1991; Montáns *et al.*, 2012; Montáns and Bathe, 2007; Perić *et al.*, 1992; Raniecki and Nguyen, 1984; Simo, 1992; Xiao *et al.*, 1997) and successfully extended to soil mechanics in Borja and Tamagnini (1998).

As discussed in §2.1, engineering polycrystals often display texture, i.e. a non-uniform orientation distribution of crystal orientations. The consideration of the effects of texture in the plastic deformation of these materials (in the form of plastic anisotropy) is well recognized in the literature. However, texture can cause the alteration of other macroscopic properties, both mechanical, viz. *elasticity*, and physical (e.g. thermal, elastic, magnetic) (Bunge, 1969; Kocks *et al.*, 2000). Elastoplastic models of metallic materials generally account for orthotropic plasticity; however, the elastic properties are frequently considered isotropic. The reasons are two-fold: (i) the contribution of elastic strains is relatively small in large-strain deformations; and (ii) the hypothesis of elastic isotropy simplifies the material models since stress-and elastic strain- tensors commute. However, the influence of elastic anisotropy of textured polycrystals can be of interest. Examples include modelling of elastic recovery processes, viz., the springback analysis for metal forming processes and modelling wave propagation is solids (Böhlke and Bertram, 2001). Elastic anisotropy has been reported in metallic materials with cubic (Alekseyenko and Liu, 1966; Böhlke and Bertram, 2001; Bunge *et al.*, 1969, 2000; Deng and Korkolis, 2018; Huang and Man, 2003; Ledbetter and Austin, 1985; Zeng and Ericsson, 1996) and hcp (e.g. the uniaxial tensile results of Nixon *et al.* (2010) on a textured high-purity α-titanium) structures. Consideration of elastic anisotropy when modelling the large-strain deformation behaviour of hcp metals can be particularly relevant since these can display a lower stiffness-to-strength $(E/\sigma_1^{\mathrm{T}})$ ratio when compared with steels, hence the contribution of elastic strains to the total strain is greater. In this work, the hypothesis of

elastic isotropy is relaxed, and orthotropic elasticity is considered. As shown in Sumikawa *et al.* (2016), such approach should improve the accuracy of spring-back analyses.

Following the definition of the generalized Lagrangian strain tensors (Eq. (7.19)) and the polar decomposition of the elastic part of the deformation gradient, $\boldsymbol{F}^{\mathrm{e}} = \boldsymbol{R}^{\mathrm{e}}\boldsymbol{U}^{\mathrm{e}}$, (Eq. (7.26)), the Lagrangian elastic logarithmic (or Hencky) strain tensor, $\boldsymbol{E}^{\mathrm{e}}_{(0)}$, is given by:

$$\boldsymbol{E}^{\mathrm{e}}_{(0)} = \ln \boldsymbol{U}^{\mathrm{e}} = \frac{1}{2}\ln \boldsymbol{C}^{\mathrm{e}} = \sum_{\alpha=1}^{3} \ln(\lambda^{e}_{\alpha})\, \underline{\boldsymbol{N}}_{\alpha} \otimes \underline{\boldsymbol{N}}_{\alpha}, \tag{7.35}$$

where λ^{e}_{α} are the principal elastic stretches (eigenvalues), $\underline{\boldsymbol{N}}_{\alpha}$, $\alpha = 1,2,3,$ are the Lagrangian principal strain directions (eigenvectors), and

$$\boldsymbol{C}^{\mathrm{e}} = (\boldsymbol{F}^{\mathrm{e}})^{\mathrm{T}}\boldsymbol{F}^{\mathrm{e}}, \tag{7.36}$$

is the elastic right Cauchy-Green tensor (cf. (7.16)). Motivated by the work of Caminero *et al.* (2011). the following quadratic stored strain energy function, (alias elastic potential), ψ^{e}, is considered:

$$\psi^{\mathrm{e}}(\boldsymbol{E}^{\mathrm{e}}_{(0)}) = \frac{1}{2}\boldsymbol{E}^{\mathrm{e}}_{(0)} : \boldsymbol{\mathcal{A}} : \boldsymbol{E}^{\mathrm{e}}_{(0)}, \tag{7.37}$$

where $\boldsymbol{\mathcal{A}}$ is a (constant) fourth-order orthotropic elasticity tensor, with the same physical interpretation as in the small strain framework. Let $\{\underline{\boldsymbol{e}}_1, \underline{\boldsymbol{e}}_2, \underline{\boldsymbol{e}}_3\}$ denote three mutually orthogonal directions defining the orthotropy (alias material) axes. Tensor $\boldsymbol{\mathcal{A}}$ is more conveniently written in terms of is inverse, the compliance tensor, $\boldsymbol{\mathcal{A}}^{-1}$, whose Voigt 6x6-matrix notation, $\boldsymbol{A}^{-1} \leftarrow \boldsymbol{\mathcal{A}}^{-1}$ is given as (Jones, 1998):

$$\boldsymbol{A}^{-1} = \begin{bmatrix} 1/E_{11} & -\upsilon_{12}/E_{11} & -\upsilon_{13}/E_{11} & 0 & 0 & 0 \\ -\upsilon_{21}/E_{22} & 1/E_{22} & -\upsilon_{23}/E_{22} & 0 & 0 & 0 \\ -\upsilon_{31}/E_{33} & -\upsilon_{32}/E_{33} & 1/E_{33} & 0 & 0 & 0 \\ 0 & 0 & 0 & 1/G_{23} & 0 & 0 \\ 0 & 0 & 0 & 0 & 1/G_{13} & 0 \\ 0 & 0 & 0 & 0 & 0 & 1/G_{12} \end{bmatrix}, \tag{7.38}$$

where E_{11}, E_{22}, E_{33} are the Young's moduli in the 1-, 2-, and 3-directions, respectively, υ_{ij}, $i, j = 1,2,3,$ $i \neq j,$ are the Poisson's ratios[25], and G_{23}, G_{31}, G_{12} are the shear moduli in the 2-3, 1-3 and 1-2 planes, respectively. These elasticity parameters are not arbitrary. Indeed, thermodynamic consistency implies that the compliance matrix in Eq. (7.38), (and its inverse, the elastic stiffness matrix, $\boldsymbol{A} \leftarrow \boldsymbol{\mathcal{A}}$) must be symmetric:

$$\upsilon_{ij}/E_{ii} = \upsilon_{ji}/E_{jj}, \quad i, j = 1,2,3, \; i \neq j, \tag{7.39}$$

and positive-definite, which, in turn, requires that (see e.g. Jones (1998) for a proof):

$$E_{11}, E_{22}, E_{33}, G_{23}, G_{13}, G_{12} > 0, \tag{7.40}$$

[25] $\upsilon_{ij} = -d\varepsilon_{jj}/d\varepsilon_{ii}$, i.e. the negative of the transverse elastic strain in the *j*-direction over the axial elastic strain in the *i*-direction when a uniaxial stress state is applied in the *i*-direction.

$$(1-\upsilon_{23}\upsilon_{32}-\upsilon_{13}\upsilon_{31}-\upsilon_{12}\upsilon_{21}-2\upsilon_{32}\upsilon_{13}\upsilon_{21})>0, \text{ and}$$

$$(1-\upsilon_{23}\upsilon_{32})>0,\ (1-\upsilon_{13}\upsilon_{31})>0,\ (1-\upsilon_{12}\upsilon_{21})>0.$$

In the general case, tensor $\boldsymbol{\mathcal{A}}$ (and therefore $\boldsymbol{\mathcal{A}}^{-1}$), has nine independent coefficients. With the compliance matrix in Eq. (7.38) defined, the Voigt matrix form of the orthotropic elasticity tensor, $\boldsymbol{\mathcal{A}}$, is determined by matrix inversion. Analytical expressions for its the nonzero components of $\boldsymbol{\mathcal{A}}$ can be found, for instance, in the book of Jones (1998). Under isotropic conditions, i.e., $E \leftarrow E_{ii}$ (no sum), $\upsilon \leftarrow \upsilon_{ij}$, and $G \leftarrow G_{ij}$, $i, j = 1,2,3$, $i \neq j$, the number of independent coefficients reduces to two; e.g., in terms of the first, λ, and second, $\mu \equiv G$, Lamé coefficients, the isotropic form, $\boldsymbol{\mathcal{A}}_{\text{iso}}$, of the (generally) orthotropic tensor $\boldsymbol{\mathcal{A}}$ is given by:

$$\boldsymbol{\mathcal{A}}_{\text{iso}} = 2\mu\boldsymbol{\mathcal{I}} + \lambda \boldsymbol{I} \otimes \boldsymbol{I}\,, \tag{7.41}$$

where $\boldsymbol{\mathcal{I}}$ and $\boldsymbol{I}$ are the fourth- and second-order identity tensors, respectively.

An appropriate invariant stress tensor can be defined by imposing elastic work-rate conjugacy with the elastic logarithmic strain tensor, in the intermediate configuration (Eterovic and Bathe, 1990), i.e.:

$$\boldsymbol{T}_{(0)} : \boldsymbol{E}^{\text{e}}_{(0)} = \boldsymbol{\tau} : \boldsymbol{d}^{\text{e}}\,, \tag{7.42}$$

where $\boldsymbol{d}^{\text{e}}$ is the elastic part of the spatial strain-rate tensor, defined in Eq. (7.30), and $\boldsymbol{\tau}$ is the Kirchhoff stress tensor with respect to the intermediate configuration, i.e.:

$$\boldsymbol{\tau} = J^{\text{e}}\boldsymbol{\sigma}\,, \tag{7.43}$$

where $\boldsymbol{\sigma}$ is the Cauchy stress tensor and J^{e} the determinant of the elastic deformation gradient, quantifying the volume change of associated with the elastic deformation (see Eq. (7.25)). In Eq. (7.42), $\boldsymbol{T}_{(0)}$ is the stress conjugate of the logarithmic strain tensor $\boldsymbol{E}^{\text{e}}_{(0)}$, thus is coined the logarithmic stress tensor or the generalized Kirchhoff stress tensor. The latter term is due by the equivalence between $\boldsymbol{T}_{(0)}$ and the rotated Kirchhoff stress tensor, $\bar{\boldsymbol{\tau}} = (\boldsymbol{R}^{\text{e}})^{\text{T}}\boldsymbol{\tau}\boldsymbol{R}^{\text{e}}$, in the isotropic elasticity case (Eq. (7.41)), as shown in Caminero *et al.* (2011).

Hyperelastic-based constitutive models are grounded on an underlying free energy potential. Based on the principle of material objectivity, the Helmholtz free energy per unit undeformed volume in the intermediate configuration, ψ_{H}, is assumed to have the form:

$$\psi_{\text{H}} = \psi_{\text{H}}(\boldsymbol{E}^{\text{e}}_{(0)}, \zeta) = \psi^{\text{e}}(\boldsymbol{E}^{\text{e}}_{(0)}) + \psi^{\text{p}}_{\text{iso}}(\zeta)\,, \text{ with } \psi^{\text{p}}_{\text{iso}} = \tfrac{1}{2}H_{\kappa}\zeta^{2} \tag{7.44}$$

where ψ^{e} is the elastic strain-energy function in Eq. (7.37), $\psi^{\text{p}}_{\text{iso}}$ is the plastic contribution related with the stored energy due to isotropic hardening of the material and ζ is some strain-like thermodynamic scalar internal variable representing the accumulated plastic strain. Its conjugated thermodynamic force, κ, (often referred to as overstress scalar) is defined as (Montáns and Bathe, 2007; de Souza Neto *et al.*, 2011)):

$$\kappa \triangleq \frac{\partial \psi_{\text{iso}}^{\text{p}}(\zeta)}{\partial \zeta} \equiv \kappa(\zeta), \text{ and } \dot{\kappa} = H_{\kappa}\dot{\zeta} \tag{7.45}$$

where $\dot{\zeta}$ and $\dot{\kappa}$ are the rates of ζ and κ, respectively, and

$$H_{\kappa} = H_{\kappa}(\zeta) \tag{7.46}$$

is the isotropic hardening modulus. Refer to Rice (1971) for a micromechanical motivation of the additive split of the Helmholtz free energy in Eq. (7.44). By employing the isothermal version of the Clausius-Duhem inequality and the axiom of thermodynamic determinism, it is possible to demonstrate that a hyperelastic-type constitutive relationship of the type:

$$\boldsymbol{T}_{(0)} = \frac{\partial \psi^{\text{e}}(\boldsymbol{E}_{(0)}^{\text{e}})}{\partial \boldsymbol{E}_{(0)}^{\text{e}}}, \tag{7.47}$$

is arrived. In view of Eq. (7.37), the previous expression leads to a standard linear constitutive law:

$$\boldsymbol{T}_{(0)} = \boldsymbol{\mathcal{A}} : \boldsymbol{E}_{(0)}^{\text{e}}. \tag{7.48}$$

The previous equation is the Lagrangian counterpart of the logarithmic Hencky (1933) model, extended to orthotropy.

In the context of the finite element method, the determination of the element internal force vectors is often performed based on the current configuration (recall Figure 7.1). Accordingly, the state-update procedure of a material model encompasses the determination of a Cauchy stress tensor, $\boldsymbol{\sigma}$. One must therefore map the logarithmic stress tensor, $\boldsymbol{T}_{(0)}$ into the Cauchy stress tensor, $\boldsymbol{\sigma}$. This is achieved based on work-rate-conjugacy considerations, as demonstrated in Latorre and Montans (2016). Let $\dot{\boldsymbol{E}}_{(0)}$ denote a Lagrangian logarithmic strain rate tensor, projected from the (reference) orthotropy frame, $\underline{\boldsymbol{e}}_{\alpha}$, $\alpha = 1,2,3$, into the Lagrangian principal strain directions, $\underline{\boldsymbol{N}}_{\alpha}$, with principal stretches, λ_{α}, $\alpha = 1,2,3$, (cf. last term of Eq. (7.35)) and $\bar{\boldsymbol{d}} = \boldsymbol{R}^{\text{T}}\boldsymbol{d}\boldsymbol{R}$ a rotated Eulerian strain rate tensor, also projected into the abovementioned Lagrangian principal strain frame. Latorre and Montans (2016) demonstrated that there is a one-to-one relation between these kinematic quantities which can be described with a mapping of the type:

$$\dot{\boldsymbol{E}}_{(0)} = \boldsymbol{\mathcal{M}}_{\dot{\boldsymbol{E}}_{(0)}}^{\bar{\boldsymbol{d}}} : \bar{\boldsymbol{d}}, \tag{7.49}$$

where $\boldsymbol{\mathcal{M}}_{\dot{\boldsymbol{E}}_{(0)}}^{\bar{\boldsymbol{d}}}$ is a fourth-order full-symmetric tensor given as follows:

$$\begin{aligned} &\boldsymbol{\mathcal{M}}_{\dot{\boldsymbol{E}}_{(0)}}^{\bar{\boldsymbol{d}}} = \sum_{i=1}^{3} \boldsymbol{M}_i \otimes \boldsymbol{M}_i + \sum_{i=1}^{3}\sum_{j\neq i} \frac{\lambda_j^2 - \lambda_i^2}{2\lambda_i\lambda_j\left(\ln\lambda_j - \ln\lambda_i\right)} \boldsymbol{M}_{ij} \otimes \boldsymbol{M}_{ij}, \text{ with} \\ &\begin{cases} \boldsymbol{M}_i = \underline{\boldsymbol{N}}_i \otimes \underline{\boldsymbol{N}}_i \ \text{ (no sum)}, \\ \boldsymbol{M}_{ij} = \dfrac{1}{2}\left(\underline{\boldsymbol{N}}_i \otimes \underline{\boldsymbol{N}}_j + \underline{\boldsymbol{N}}_j \otimes \underline{\boldsymbol{N}}_i\right), \end{cases} \end{aligned} \tag{7.50}$$

whose Voigt 6x6-matrix notation is actually a diagonal matrix. An important result is that the respective conjugated stress tensors are related via the same mapping, i.e.:

$$\boldsymbol{T}_{(0)} = \boldsymbol{\mathcal{M}}^{\dagger d}_{\dot{\boldsymbol{E}}_{(0)}} : \dot{\bar{\boldsymbol{\tau}}} \;\Leftrightarrow\; \dot{\bar{\boldsymbol{\tau}}} = \left(\boldsymbol{\mathcal{M}}^{\dagger d}_{\dot{\boldsymbol{E}}_{(0)}} \right)^{-1} : \boldsymbol{T}_{(0)} . \tag{7.51}$$

Projecting $\boldsymbol{T}_{(0)}$ in the Lagrangian principal *strain* directions, $\underline{\boldsymbol{N}}_{\alpha}$, $\alpha = 1,2,3,$ i.e.:

$$\boldsymbol{T}_{(0)} = \sum_{i=1}^{3} \sum_{j=1}^{3} T_{ij} \; \underline{\boldsymbol{N}}_i \otimes \underline{\boldsymbol{N}}_j , \tag{7.52}$$

(note that $\boldsymbol{T}_{(0)}$ is not necessarily diagonal in the orthotropic case since the principal strain and principal stress directions do not coincide), the components of the rotated Kirchhoff stress tensor, $\dot{\bar{\boldsymbol{\tau}}}$, in the principal strain frame, i.e.:

$$\dot{\bar{\boldsymbol{\tau}}} = \sum_{i=1}^{3} \sum_{j=1}^{3} \dot{\bar{\tau}}_{ij} \; \underline{\boldsymbol{N}}_i \otimes \underline{\boldsymbol{N}}_j , \tag{7.53}$$

are given as follows:

$$\dot{\bar{\tau}}_{ij} = \begin{cases} T_{ij} & \text{if } i = j, \\ \dfrac{2\lambda_i \lambda_j \left(\ln \lambda_j - \ln \lambda_i \right)}{\lambda_j^2 - \lambda_i^2} T_{ij} & \text{if } i \neq j. \end{cases} \tag{7.54}$$

The previous expression advocates the term 'generalized' Kirchhoff stress tensor to describe $\boldsymbol{T}_{(0)}$ since the diagonal components of $\boldsymbol{T}_{(0)}$ and $\dot{\bar{\boldsymbol{\tau}}}$ coincide when these are represented in the Lagrangian principal strain frame. Moreover, in the limit case of two principal stretches being equal:

$$\lim_{\lambda_j \to \lambda_j} \frac{2\lambda_i \lambda_j \left(\ln \lambda_j - \ln \lambda_i \right)}{\lambda_j^2 - \lambda_i^2} = 1 , \tag{7.55}$$

hence $\boldsymbol{T}_{(0)} = \dot{\bar{\boldsymbol{\tau}}}$, even in the orthotropic case. Under isotropic conditions, $\boldsymbol{T}_{(0)}$ in Eq. (7.52) is diagonal hence the mapping in Eq. (7.54) leads trivially to $\boldsymbol{T}_{(0)} = \dot{\bar{\boldsymbol{\tau}}}$. Once $\dot{\bar{\boldsymbol{\tau}}}$ is known, it is rotated back from the principal strain space, $\underline{\boldsymbol{N}}_{\alpha}$, $\alpha = 1,2,3,$ to the reference orthotropic (or material) frame, $\{\underline{\boldsymbol{e}}_1, \underline{\boldsymbol{e}}_2, \underline{\boldsymbol{e}}_3\}$:

$$\dot{\bar{\boldsymbol{\tau}}} = \sum_{i=1}^{3} \sum_{j=1}^{3} \dot{\bar{\tau}}_{ij} \; \underline{\boldsymbol{e}}_i \otimes \underline{\boldsymbol{e}}_j . \tag{7.56}$$

Finally, the Cauchy stress tensor is determined rotating $\dot{\bar{\boldsymbol{\tau}}}$ to the current configuration, and applying the appropriate relationship between the Cauchy and the Kirchhoff stress measures as follows:

$$\boldsymbol{\sigma} = (1/J)\boldsymbol{\tau}, \text{ with } \boldsymbol{\tau} = \boldsymbol{R}\dot{\bar{\boldsymbol{\tau}}}\boldsymbol{R}^{\mathrm{T}} , \tag{7.57a}$$

or, equivalently,

$$\boldsymbol{\sigma} = \boldsymbol{R}\dot{\bar{\boldsymbol{\sigma}}}\boldsymbol{R}^{\mathrm{T}}, \text{ with } \dot{\bar{\boldsymbol{\sigma}}} = (1/J)\dot{\bar{\boldsymbol{\tau}}} . \tag{7.57b}$$

The notation adopted in this paragraph holds for an arbitrary deformation gradient, $\boldsymbol{F}$. However, in the scope of the envisioned constitutive formulation, grounded on the multiplicative split in Eq. (7.24) and the hypothesis in Eq. (7.33), the material frame $\{\underline{\boldsymbol{e}}_1, \underline{\boldsymbol{e}}_2, \underline{\boldsymbol{e}}_3\}$ coincides with the intermediate configuration (since $\boldsymbol{F}^{\mathrm{p}} = \boldsymbol{U}^{\mathrm{p}}$, i.e., $\boldsymbol{R}^{\mathrm{p}} = \boldsymbol{0}$), hence the kinematic quantities in Eqs. (7.49)-(7.50) and Eq. (7.57a) are

actually their elastic parts, i.e. $\dot{\boldsymbol{E}}_{(0)} \leftarrow \dot{\boldsymbol{E}}^{\mathrm{e}}_{(0)}$, $\vec{\boldsymbol{d}} \leftarrow \vec{\boldsymbol{d}}^{\mathrm{e}}$, $\lambda_\alpha \leftarrow \lambda^{\mathrm{e}}_\alpha$, $\alpha = 1,2,3$, $\boldsymbol{R} \leftarrow \boldsymbol{R}^{\mathrm{e}}$, and $J \leftarrow J^{\mathrm{e}}$, respectively. For more details on the mapping between generalized stress and strain measures (in the sense of Eq. (7.19)), refer to Latorre and Montans (2016).

As noted in §3.4.2 (p. 42), the original framework of Gurson (1977) on porous media disregards the influence of the damage variable, the porosity, on the elastic behaviour of the aggregate, since only the plastic response depends on the current damaged state. In the spirit of Lemaitre's phenomenologically CDM theory (Lemaitre, 1985a; Lemaitre and Chaboche, 1994), where internal degradation of the matter, (in turn associated with the reduction of the resisting cross-section area due to void growth and/or microcracking), is reproduced by the degradation of the (macroscopic) elastic modulus, a correction to the orthotropic elasticity tensor, $\boldsymbol{\mathcal{A}}$, in Eq. (7.37) is proposed as follows:

$$\tilde{\boldsymbol{\mathcal{A}}} = \omega_\beta(f)\boldsymbol{\mathcal{A}}, \tag{7.58}$$

where $\tilde{\boldsymbol{\mathcal{A}}}$ denotes the respective effective elasticity tensor, and ω_β is a dimensionless heuristically-motivated function, here coined the weakening factor, given by:

$$\omega_\beta(f) = 1 - f^\beta \ , \ \beta \in \mathbb{R} \ , \ \beta \geq 1 \, . \tag{7.59}$$

$\tilde{\boldsymbol{\mathcal{A}}}$ is therefore used in lieu of $\boldsymbol{\mathcal{A}}$ in the constitutive law in Eq. (7.48). Figure 7.2 plots the shape of the weakening factor for several user-defined parameters β. For a finite parameter β, in the absence of damage, ($f = 0$), $\tilde{\boldsymbol{\mathcal{A}}} = \boldsymbol{\mathcal{A}}$; whereas for a completely damaged state ($f = 1$), $\tilde{\boldsymbol{\mathcal{A}}} = \boldsymbol{0}$, corresponding to a total loss of the overall stiffness. If a weakening factor with $\beta = 1$ is chosen, $\omega_1(f) = (1 - f)$, thus the particular case of the Lemaitre's softening of the elastic modulus is attained, i.e.:

$$\tilde{\boldsymbol{\mathcal{A}}} = (1 - f)\boldsymbol{\mathcal{A}} \, . \tag{7.60}$$

In the limit, $\beta \to \infty$, $\omega_\infty = 1$, and the effective elasticity modulus of the porous aggregate equals that of the virgin (matrix) material, $\tilde{\boldsymbol{\mathcal{A}}} = \boldsymbol{\mathcal{A}}$, i.e., elastic softening is neglected. In closing, it must be emphasized that while the adopted naming and notation for $\tilde{\boldsymbol{\mathcal{A}}}$ are reminiscent of the concept of Lemaitre's 'effective' stress tensor (see Eq. (3.6)), the proposed modification for the elasticity tensor in Eq. (7.58) provides a weak elasticity-damage coupling since the evolution of the variable *f* will not be governed by thermodynamical considerations (viz., the definition of a damage energy release rate, $Y \equiv \partial \psi_H / \partial f$, as in Lemaitre's framework), and, instead, follows from the principle of mass conservation, as later discussed in the present subsection. In other words, porosity, *f*, enters Eq. (7.58) (and therefore Eq. (7.48)) as a parameter and not as a thermodynamical internal variable.

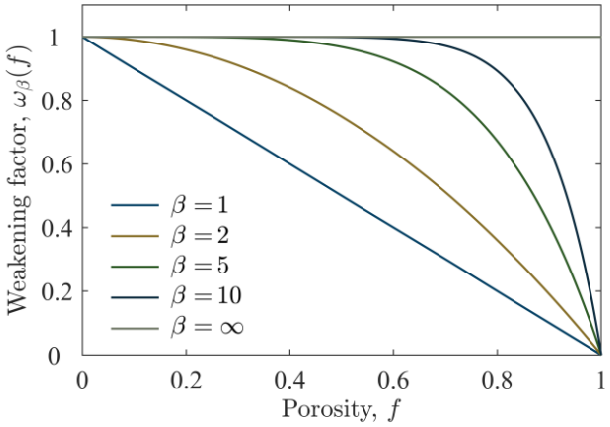

Figure 7.2 Weakening factor function, $\omega_\beta(f)$, for the elastic modulus for several parameters β.

The yield function

Considering the objectives set for this work, the yield function is probably the most important feature of the developed elastoplastic model. In the context of porous solids, it follows from Eq. (5.10), Eq. (5.13) (particularly, its approximated-form, Eq. (5.45)) and Eq. (7.44) that the elastic domain is defined as the set of Cauchy stress states:

$$\mathscr{E} = \left\{ \bar{\boldsymbol{\sigma}} \in \mathcal{S}_2 \mid \mathcal{F}(\bar{\boldsymbol{\sigma}}, f, \kappa, \sigma_1^{\mathrm{T}}) < 0 \right\}, \tag{7.61}$$

with the yield function, $\mathcal{F}$, given as (henceforth the superscript '+' related with the approximated nature of the potentials is omitted for readability):

$$\mathcal{F}(\bar{\boldsymbol{\sigma}}, f, \kappa, \sigma_1^{\mathrm{T}}) = \Phi(\bar{\boldsymbol{\sigma}}, f) - \sigma_{\mathrm{Y}}, \tag{7.62}$$

with

$$\sigma_{\mathrm{Y}}(\zeta) = \sigma_1^{\mathrm{T}} + \kappa(\zeta) \tag{7.63}$$

where $\bar{\boldsymbol{\sigma}}$ denotes the Cauchy stress tensor in the material (orthotropy) frame, $\bar{\boldsymbol{\sigma}} = (\boldsymbol{R}^{\mathrm{e}})^{\mathrm{T}} \boldsymbol{\sigma} \boldsymbol{R}^{\mathrm{e}}$, with $\boldsymbol{\sigma}$ in the current configuration given in Eq. (5.55) from the hyperelastic-law, Φ is the stress potential (an equivalent stress function) determined via Eqs. (5.46)-(5.47), κ is the overstress scalar in Eq. (7.44); σ_1^{T} is the initial tensile uniaxial yield stress of the virgin material along the 1-direction of orthotropy, hence $\sigma_{\mathrm{Y}} = (\sigma_1^{\mathrm{T}} + \kappa)$ denotes the current uniaxial yield stress of the matrix material. Note that, in line with the convention introduced in Footnote 24 (p. 156), the Cauchy stress tensor in Eq. (7.61) refers to the *macroscopic* behaviour of the porous solid, i.e. $\bar{\boldsymbol{\sigma}} \leftarrow \boldsymbol{\Sigma}$. The boundary of $\mathscr{E}$, $\partial\mathscr{E}$ defines the yield (hyper-)surface, which given the condition:

$$\mathcal{F}(\bar{\boldsymbol{\sigma}}, f, \kappa, \sigma_1^{\mathrm{T}}) = 0, \tag{7.64}$$

As discussed in §5.3.2 and then corroborated in §6.3, evaluation of the yield function is not efficient since the expression of its associated stress potential is unknown in the general case (recall Figure 6.16). Conversely, the determination of its dual, the SRP, is a straightforward task given the considered kinematic homogenization formulation. Accordingly, the goal is to follow a SRP-based constitutive formula-

tion for characterizing the plastic behaviour of the porous solid. Since the SRP cannot explicitly define the elastic domain (as in Eq. (7.61)), an alternative condition must need to be considered. Based on the principle of maximum work Bacroix and Gilormini (1995) proposed a SRP-based yield condition using the following function:

$$g(\bar{\boldsymbol{\sigma}}, f, \sigma_{\mathrm{Y}}) = \inf_{\hat{\boldsymbol{d}}} \left(\sigma_{\mathrm{Y}} \Psi(\hat{\boldsymbol{d}}, f) - \bar{\boldsymbol{\sigma}} : \hat{\boldsymbol{d}} \right), \ \hat{\boldsymbol{d}} \in \mathcal{S}_2, \ \|\hat{\boldsymbol{d}}\|_2 = 1, \tag{7.65}$$

where $\hat{\boldsymbol{d}}$ is a kinematic tensor with the physical interpretation of a rotated Eulerian plastic strain-rate, to be eliminated from the previous expression following the minimization of the argument of the infimum, and $\Psi(\hat{\boldsymbol{d}}, f)$ is the strain-rate potential in Eq. (5.39). Three cases can be distinguished based on the sign of function g:

$$g(\bar{\boldsymbol{\sigma}}, f, \sigma_{\mathrm{Y}}) \begin{cases} < 0 & \text{if } \bar{\boldsymbol{\sigma}} \text{ is outside the yield surface,} \\ = 0 & \text{if } \bar{\boldsymbol{\sigma}} \text{ is on the yield surface,} \\ > 0 & \text{if } \bar{\boldsymbol{\sigma}} \text{ is inside the yield surface.} \end{cases} \tag{7.66}$$

Inherently, the minimization of g is associated with the solution of the tensorial equation:

$$\frac{\partial g(\bar{\boldsymbol{\sigma}}, f, \sigma_{\mathrm{Y}})}{\partial \hat{\boldsymbol{d}}} = \boldsymbol{0}, \tag{7.67}$$

More details on this method can be found in Rabahallah *et al.* (2009). The merit of this approach is that the minimization can be stopped as soon as the argument of the infimum in Eq. (7.65) becomes negative, which is a sufficient condition for the increment to be elastoplastic, hence there is no need to determine the exact value of the unknown $\hat{\boldsymbol{d}}$. By applying the gradient in Eq. (7.67) to Eq. (7.65) and the Euler theorem for homogeneous functions one can easily verify that the minimization problem in Eq. (7.65) is equivalent to solving the equation system in Eq. (5.46) for the unknown $\hat{\boldsymbol{d}}$, rewritten here adopting the notational conventions of the present chapter as:

$$\underline{\boldsymbol{F}}(\hat{\boldsymbol{d}}, \bar{\sigma}) = \begin{Bmatrix} \bar{\boldsymbol{\sigma}} - \bar{\sigma} \dfrac{\partial \Psi(\hat{\boldsymbol{d}}, f)}{\partial \hat{\boldsymbol{d}}} \\ \Psi(\hat{\boldsymbol{d}}) - 1 \end{Bmatrix} = \begin{Bmatrix} \boldsymbol{0} \\ 0 \end{Bmatrix}, \ \hat{\boldsymbol{d}} \in \mathcal{S}_2 \tag{7.68}$$

where the scalar of the solution vector is no more than the equivalent stress, i.e. $\bar{\sigma} \equiv \Phi(\bar{\boldsymbol{\sigma}}, f)$ (cf. Eq. (5.47)), entering the standard yield function in Eq. (7.62). It turns out that solving Eq. (7.68) in lieu of Eq. (7.65) appears to be more robust when the SRP is not known in closed-form, as is the case of this work. This is thought to be due to the distinct regularization criterion of the unknown, $\hat{\boldsymbol{d}}$ of adopted in each system: $\Psi(\hat{\boldsymbol{d}}) = 1$ in Eq. (7.68) and $\|\hat{\boldsymbol{d}}\|_2 = 1$ in Eq. (7.62). The algorithmic aspects of the solution of Eq. (7.68) were provided in Box 5.3 and Box 5.4.

Evolution equation for the plastic deformation gradient, $\boldsymbol{F}^{\mathrm{p}}$

Inverting Eq. (7.29), the evolution of the plastic deformation gradient tensor, $\boldsymbol{F}^{\mathrm{p}}$, is given by:

$$\dot{\boldsymbol{F}}^{\mathrm{p}} = \boldsymbol{L}^{\mathrm{p}} \boldsymbol{F}^{\mathrm{p}}. \tag{7.69}$$

Given the hypothesis in Eq. (7.34), in turn due to $\boldsymbol{W}^{\mathrm{p}} = \boldsymbol{0}$, the previous expression reduces to:

$$\dot{\boldsymbol{F}}^{\mathrm{p}} = \boldsymbol{D}^{\mathrm{p}}\boldsymbol{F}^{\mathrm{p}} \tag{7.70}$$

where it should be stressed that $\boldsymbol{D}^{\mathrm{p}}$ is a *Lagrangian* quantity in the intermediate configuration (see Eq. (7.32)). The Clausius-Duhem entropy inequality for isothermal processes can be written as:

$$\dot{\mathcal{D}} = \dot{\mathcal{P}} - \dot{\psi}_{\mathrm{H}} \geq 0\,, \tag{7.71}$$

where $\dot{\psi}_{\mathrm{H}}$ is the rate of the Helmholtz free energy in Eq. (7.44), $\dot{\psi}_{\mathrm{H}} = \dot{\psi}^{\mathrm{e}} + \dot{\psi}^{\mathrm{p}}_{\mathrm{iso}}$, and $\dot{\mathcal{P}}$ is the (total) stress power per unit of volume in the intermediate configuration, i.e.:

$$\dot{\mathcal{P}} = \boldsymbol{T}_{(0)}:\dot{\boldsymbol{E}}_{(0)} = \bar{\boldsymbol{\tau}}:\bar{\boldsymbol{d}} = J_e\bar{\boldsymbol{\sigma}}:\bar{\boldsymbol{d}} = J_e\boldsymbol{\sigma}:\boldsymbol{d}\,. \tag{7.72}$$

where $\dot{\boldsymbol{E}}_{(0)}$ is the rate form of $\boldsymbol{E}_{(0)}$ in Eq. (7.35). Combining Eq. (7.44) and Eqs. (7.71)-(7.72) the reduced (plastic) dissipation, $\dot{\mathcal{D}}^{\mathrm{p}}$, inequality is then (refer to Montáns and Bathe (2007) for more details):

$$\dot{\mathcal{D}}^{\mathrm{p}} = \bar{\boldsymbol{\sigma}}:\bar{\boldsymbol{d}}^{\mathrm{p}} + \kappa\dot{\zeta} \geq 0\,, \tag{7.73}$$

now expressed per unit of current volume (see Figure 7.1). Let $\mathcal{F}(\bar{\boldsymbol{\sigma}},\kappa) \leq 0$ denote the plastically admissible stress states. In view of the principle of maximum plastic dissipation, (e.g., Lubliner (1984, 1986), for a fixed $(\bar{\boldsymbol{d}}^{\mathrm{p}},\kappa)$ the actual stress state, $\bar{\boldsymbol{\sigma}}$, maximizes the dissipation $\dot{\mathcal{D}}^{\mathrm{p}}$ in Eq. (7.73), subject to the constraint $\mathcal{F} \leq 0$. The constrained dissipation function can be written as the Lagrangian:

$$\mathcal{L}(\bar{\boldsymbol{\sigma}},\kappa) = \dot{\mathcal{D}}^{\mathrm{p}} - \dot{\Lambda}\mathcal{F}\,, \tag{7.74}$$

where $\dot{\Lambda}$ is the Lagrange multiplier, alias consistency parameter or plastic multiplier rate. The condition of extremum is thus given by:

$$\nabla\mathcal{L}(\bar{\boldsymbol{\sigma}},\kappa) = \boldsymbol{0} \Leftrightarrow \begin{cases} \dfrac{\partial\mathcal{L}}{\partial\bar{\boldsymbol{\sigma}}} = \boldsymbol{0} \Rightarrow \bar{\boldsymbol{d}}^{\mathrm{p}} = \dot{\Lambda}\dfrac{\partial\mathcal{F}}{\partial\bar{\boldsymbol{\sigma}}} \\ \dfrac{\partial\mathcal{L}}{\partial\kappa} = 0 \Rightarrow \dot{\zeta} = -\dot{\Lambda}\dfrac{\partial\mathcal{F}}{\partial\kappa} = \dot{\Lambda} \end{cases}, \tag{7.75}$$

and the complementary Kuhn-Tucker conditions:

$$\dot{\Lambda} \geq 0\,,\ \mathcal{F} \leq 0\,,\ \mathcal{F}\dot{\Lambda} = 0\,, \tag{7.76}$$

and the consistency condition:

$$\dot{\Lambda}\dot{\mathcal{F}} = 0\,. \tag{7.77}$$

Equations $(7.75)_1$ and $(7.75)_2$ provide, respectively, the flow rule and hardening rule consistent with the principle of maximum dissipation, and, accordingly, are coined the associated (or associative) plastic flow and the associated hardening rule for general large-strain elasto-plasticity Caminero *et al.* (2011).

Based on the results of §5.1.2, the plastic flow rule in Eq. $(7.75)_1$ can be rewritten as follows:

$$\begin{cases} \bar{\boldsymbol{\sigma}} = \sigma_{\mathrm{Y}}\dfrac{\partial\Psi}{\partial\bar{\boldsymbol{d}}^{\mathrm{p}}} \\ \Psi(\bar{\boldsymbol{d}}^{\mathrm{p}}, f) = \dot{\Lambda} \end{cases}, \tag{7.78}$$

where $\Psi(\bar{\boldsymbol{d}}^{\mathrm{p}}, f)$, defined in Eq. (5.39), is the dual (polar reciprocate) of $\Phi(\bar{\boldsymbol{\sigma}}, f)$ in Eq. (7.62). Moreover, in view of Eq. (5.17), the plastic power is given by:

$$\mathcal{W}^{\mathrm{p}} = \overset{\leftarrow}{\boldsymbol{\sigma}} : \overset{\leftarrow}{\boldsymbol{d}}^{\mathrm{p}} = \Phi(\overset{\leftarrow}{\boldsymbol{\sigma}}, f)\Psi(\overset{\leftarrow}{\boldsymbol{d}}^{\mathrm{p}}, f) = \sigma_{\mathrm{Y}}\dot{\Lambda}\,, \tag{7.79}$$

under the conditions Eq. (7.76). Note that *two* constitutive laws are available for determining the rotated Cauchy stress tensor, $\overset{\leftarrow}{\boldsymbol{\sigma}}$: (i) the hyperelastic relationship in Eq. (7.48) (along its mathematical manipulation to arrive at Eq. (7.57)); and (ii) the plastic flow rule in Eq. $(7.78)_1$. Of course, these must be equal, which provides the basic tensorial equation of the state-update algorithm, as shown in ensuing subsection.

The crucial evolution equation of the plastic deformation gradient tensor in Eq. (7.70) is written in terms of the Lagrangian kinematic variable, $\boldsymbol{D}^{\mathrm{p}}$, whereas Eq. (7.78) is written in terms of its Eulerian counterpart, $\overset{\leftarrow}{\boldsymbol{d}}^{\mathrm{p}}$. However, it turns out that formulating the constitutive problem in terms of the variable $\boldsymbol{D}^{\mathrm{p}}$ (in place of $\overset{\leftarrow}{\boldsymbol{d}}^{\mathrm{p}}$) is advantageous when deriving the respective incremental equations. Accordingly, a kinematical relationship between $\boldsymbol{D}^{\mathrm{p}}$ and $\overset{\leftarrow}{\boldsymbol{d}}^{\mathrm{p}}$ must be provided. Combining Eqs. (7.26), (7.28) and (7.30) results in a mapping $\boldsymbol{D}^{\mathrm{p}} \rightarrow \overset{\leftarrow}{\boldsymbol{d}}^{\mathrm{p}}$ given as follows:

$$\overset{\leftarrow}{\boldsymbol{d}}^{\mathrm{p}} = (\boldsymbol{R}^{\mathrm{e}})^{\mathrm{T}}\boldsymbol{d}^{\mathrm{p}}\boldsymbol{R}^{\mathrm{e}} = (\boldsymbol{R}^{\mathrm{e}})^{\mathrm{T}}\mathrm{sym}(\boldsymbol{F}^{\mathrm{e}}\boldsymbol{D}^{\mathrm{p}}(\boldsymbol{F}^{\mathrm{e}})^{-1})\boldsymbol{R}^{\mathrm{e}} = \mathrm{sym}(\boldsymbol{U}^{\mathrm{e}}\boldsymbol{D}^{\mathrm{p}}(\boldsymbol{U}^{\mathrm{e}})^{-1})\,. \tag{7.80}$$

Closed-form expression for the inverse mapping is challenging if not impossible, yet it is not needed in the present analysis.

Evolution equations for the hardening variables

In view of Eq. (7.45) and the associated hardening rule (Eq. $(7.75)_2$), the equation for the evolution of the isotropic hardening should follow: $\dot{\kappa} = H(\Lambda)\dot{\Lambda}$. However, in the in the context of porous solids, hardening is typically not governed via thermodynamical considerations (viz. Eq. $(7.75)_2$) and, instead, results from the phenomenological-based hypothesis of the equality of the plastic dissipation rate in the micro- and macro-scale, as proposed by Gurson (1977) (recall Eq. (3.11), p. 42 and concerning text). In this spirit, the definition of σ_{Y} in terms of the thermodynamic conjugates (ζ, κ) (Eq. (7.63)) is abandoned (it was used at the outset just for motivation purposes), and a new state variable, $\bar{\epsilon}^{\mathrm{p}}$, is introduced to describe isotropic hardening as:

$$\sigma_{\mathrm{Y}}(\bar{\epsilon}^{\mathrm{p}}) = \sigma_1^{\mathrm{T}} + Y_{\Delta}(\bar{\epsilon}^{\mathrm{p}})\,, \text{ with } Y_{\Delta}(0) = 0\,, \tag{7.81a}$$

where $Y_{\Delta}(\cdot)$ has the physical interpretation of the overstress scalar, $Y_{\Delta} \equiv \kappa$, yet with no thermodynamic basis, or, equivalently, in a 'total' fashion as:

$$\sigma_{\mathrm{Y}}(\bar{\epsilon}^{\mathrm{p}}) = Y(\bar{\epsilon}^{\mathrm{p}}), \text{ with } Y(0) = \sigma_1^{\mathrm{T}}. \tag{7.81b}$$

Close-form expressions for the isotropic hardening functions $Y_{\Delta}(\cdot)$ (and $Y(\cdot)$) are available in the literature. These can be of the linear-type, power-type (e.g. Swift (1952))), saturation-type (Voce (1948), or any linear or non-linear combination of these. Applying the phenomenological-based micro-macro plastic power balance (Eq. (3.11)), the yield condition, $\Phi(\overset{\leftarrow}{\boldsymbol{\sigma}}, f) = \sigma_{\mathrm{Y}}$, (Eq. (7.62)), and the Euler theorem for homogeneous functions, one arrives at the evolution equation of $\bar{\epsilon}^{\mathrm{p}}$ as:

$$\dot{\bar{\epsilon}}^{\mathrm{p}} = \frac{\dot{\Lambda}}{(1-f)}\,, \tag{7.82}$$

with $\dot{\Lambda}$ given in Eq. (7.78)$_2$. It follows that:

$$\dot{\sigma}_{\mathrm{Y}} = H_Y \dot{\bar{\epsilon}}^{\mathrm{p}}, \;\; H_Y = \frac{\partial Y_{\Delta}(\bar{\epsilon}^{\mathrm{p}})}{\partial \bar{\epsilon}^{\mathrm{p}}} = \frac{\partial Y(\bar{\epsilon}^{\mathrm{p}})}{\partial \bar{\epsilon}^{\mathrm{p}}} \tag{7.83}$$

where $\dot{\bar{\epsilon}}^{\mathrm{p}}$ and $\dot{\sigma}_{\mathrm{Y}}$ are the rates of $\bar{\epsilon}^{\mathrm{p}}$ and σ_{Y}, respectively, and $H_Y = H_Y(\bar{\epsilon}^{\mathrm{p}})$ is the hardening modulus associated with $Y_{\Delta}(\cdot)$ (or $Y(\cdot)$).

Evolution equation for the porosity

Similarly to the isotropic hardening variables, $(\bar{\epsilon}^{\mathrm{p}}, \sigma_{\mathrm{Y}})$, the evolution of the (unique) microstructural inspired variable – the porosity, *f*, is not directly associated with a dissipative mechanism, (hence with a thermodynamic dissipation potential), and, instead, follows from the axiom of mass conservation. In the following, two cases are considered for the evolution equation for *f*: (i) the neglect of void nucleation effects; and (ii) the consideration of void nucleation. Let us start with the former case.

Let ρ denote the density of a porous aggregate with a void volume fraction, *f*, (see Eq. (3.8), p. 38) and ρ_{m} the density of the matrix phase, both referred to the current configuration. These related as:

$$\rho = \rho_{\mathrm{m}} v_{\mathrm{m}}, \text{ with } v_{\mathrm{m}} = (1 - f), \tag{7.84}$$

where v_{m} is the volume fraction of the matrix. Time differentiation of this formula results in:

$$\dot{\rho} = \dot{\rho}_{\mathrm{m}}(1 - f) - \rho_{\mathrm{m}} \dot{f}. \tag{7.85}$$

If the elastic hydrostatic strains in the matrix are neglected, in view of the plastic incompressibility:

$$\dot{\rho}_{\mathrm{m}} = 0, \tag{7.86}$$

hence, combination of the last three equations leads to:

$$\dot{f} = -\frac{\dot{\rho}}{\rho_{\mathrm{m}}} = -\frac{\dot{\rho}}{\rho}(1 - f). \tag{7.87}$$

The axiom of mass conservation, $\dot{\rho} + \rho \mathrm{div}(\underline{\boldsymbol{u}}(\underline{\boldsymbol{x}})) = 0$, where $\mathrm{div}(\cdot)$ denotes the divergence in the spatial configuration and $\underline{\boldsymbol{u}}(\underline{\boldsymbol{x}})$ is the displacement field in spatial coordinates (cf. Eq. (7.2)) requires that (de Souza Neto *et al.*, 2011):

$$\mathrm{tr}(\boldsymbol{d}) = \mathrm{tr}(\bar{\boldsymbol{d}}) = \frac{\dot{v}}{v} = -\frac{\dot{\rho}}{\rho}, \tag{7.88}$$

where $v = \mathrm{vol}(\Omega)$ is the current volume of the porous aggregate (notation consistent with Eq. (3.8)) and $\dot{v}$ its time derivative. Combination of the last two equations results in:

$$\dot{f} = (1 - f)\mathrm{tr}(\bar{\boldsymbol{d}}). \tag{7.89}$$

Again, if the neglect of the elastic hydrostatic strains is invoked, in this case regarding the overall behaviour of the porous solid, the previous equation reduces to the well-known Gurson (1977) form:

$$\dot{f} = (1 - f)\mathrm{tr}(\bar{\boldsymbol{d}}^{\mathrm{p}}). \tag{7.90}$$

The attractiveness of Eq. (7.90) is that it allows to explicitly describe the evolution of porosity in terms of the kinematical variable $\bar{\boldsymbol{d}}^{\mathrm{p}}$ alone. As described in the following, if void nucleation is included in the formulation, this mathematical advantage is lost.

In light of Eqs. (3.26)-(3.29) (pp. 52-53), the consideration of a (continuum) void nucleation model implies an additional term for $\dot{f}$ as :

$$\dot{f} = (1-f)\mathrm{tr}(\bar{\boldsymbol{d}}^{\mathrm{p}}) + (\mathcal{A}\dot{\bar{\epsilon}}^{\mathrm{p}} + \mathcal{B}\dot{\sigma}_{\mathrm{m}}) \,, \tag{7.91}$$

where $\mathcal{A}$ and $\mathcal{B}$ are the normal distributions functions of Chu and Needleman (1980) regarding strain- and stress-controlled void nucleation, respectively; $\dot{\bar{\epsilon}}^{\mathrm{p}}$ is given in Eq. (7.79) and $\dot{\sigma}_{\mathrm{m}}$ is the rate of the hydrostatic part of the Cauchy stress tensor, $\dot{\sigma}_{\mathrm{m}} = \mathrm{tr}(\dot{\boldsymbol{\sigma}})/3$. Note that the added void nucleation terms in Eq. (7.91) preclude the incremental form of the state variable f, $\Delta f = \int_{t_0}^{t} \dot{f}\,dt$, to determined explicitly in terms of the variables $(\bar{\boldsymbol{d}}, \dot{\Lambda})$ entering the constitutive rule in Eq. (7.78). Ultimately, this requires that an additional equation for the state-update of the porosity must be provided. Conversely, if void nucleation is neglected, i.e., $\mathcal{A} = \mathcal{B} = 0$, then Eq. (7.91) reduces to Eq. (7.90) and an explicit incremental form for the evolution equation of f can be written, which is advantageous from the computational viewpoint. These issues are more clearly elucidated in the next subsection, regarding the computational implementation of these evolution laws in an incremental fashion.

7.1.4 Summary of the constitutive initial value problem

The quasi-static finite-strain elastoplastic constitutive initial value problem based on the multiplicative decomposition of the deformation gradient (§7.1.2) and hyperelastic-based elastoplasticity (§7.1.3) developed in the previous subsections to describe the behaviour of orthotropic porous solids is summarized in Box 7.1. Note that the choice of the *primary* kinematical unknow is not unique when formulation a differential equation system to solve the problem in Box 7.1. For example, one may choose any of the following: $\boldsymbol{F}^{\mathrm{e}}$, $\boldsymbol{F}^{\mathrm{p}}$, $\boldsymbol{D}^{\mathrm{p}}$, $\bar{\boldsymbol{d}}^{\mathrm{p}}$ as the primary kinematical unknow. In principle, these must lead to equivalent problems, hence, to the same solution. In the next subsection (§7.2) the incremental form of the problem in Box 7.1 will be derived assuming $\boldsymbol{D}^{\mathrm{p}}$ (or, more precisely, an incremental form of it) as the primary unknown, since this kinematical tensor leads to a straightforward integration scheme when using the exponential map operator along with an elastic predictor/return-mapping algorithm.

Box 7.1. Definition of the finite-strain constitutive elastoplastic initial value problem.

Given the initial values of $\boldsymbol{F}^{\mathrm{e}}(t_0)$ (or, equivalently, $\boldsymbol{F}^{\mathrm{p}}(t_0)$) and of the internal state variables, $\underline{\boldsymbol{\alpha}}(t_0) = \{f(t_0), \bar{\epsilon}^{\mathrm{p}}(t_0)\}$, and the history of the deformation gradient, $\boldsymbol{F}(t)$, $t \in [t_0, T]$, find the functions $\boldsymbol{F}^{\mathrm{e}}(t)$, (or equivalently, $\boldsymbol{F}^{\mathrm{p}}(t)$), $\underline{\boldsymbol{\alpha}}(t) = \{f(t), \bar{\epsilon}^{\mathrm{p}}(t)\}$, and $\dot{\Lambda}(t)$ that satisfy:

$$\begin{aligned} \Psi(\bar{\boldsymbol{d}}^{\mathrm{p}}(t), f(t)) &= \dot{\Lambda}(t)\,, \\ \bar{\boldsymbol{\sigma}}(t) &= \sigma_{\mathrm{Y}}(t)\frac{\partial \Psi}{\partial \bar{\boldsymbol{d}}^{\mathrm{p}}(t)}(\bar{\boldsymbol{d}}^{\mathrm{p}}(t), f(t))\,, \end{aligned} \tag{7.92}$$

subjected to the constrains:

$$\dot{\Lambda}(t) \geq 0\,,\ \mathcal{F}(\bar{\boldsymbol{\sigma}}(t), f(t), \sigma_{\mathrm{Y}}(t)) \leq 0\,,\ \mathcal{F}(\bar{\boldsymbol{\sigma}}(t), f(t), \sigma_{\mathrm{Y}}(t)) \cdot \dot{\Lambda}(t) = 0\,, \tag{7.93}$$

for each instant $t \in [t_0, T]$, with

$$\begin{aligned} \boldsymbol{T}_{(0)}(t) &= \tilde{\boldsymbol{\mathcal{A}}}(f(t)) : \boldsymbol{E}^{\mathrm{e}}_{(0)}(t)\,, \\ \tilde{\boldsymbol{\mathcal{A}}}(f(t)) &= (1 - f(t)^{\beta})\boldsymbol{\mathcal{A}}\,, \end{aligned} \tag{7.94}$$

and

$$\sigma_{\mathrm{Y}}(t) = \sigma_1^{\mathrm{T}} + Y_{\Lambda}(\bar{\epsilon}^{\mathrm{p}}(t))\,, \tag{7.95}$$

and the evolution equations:

$$\begin{aligned} \dot{f}(t) &= (1 - f(t))\mathrm{tr}(\bar{\boldsymbol{d}}^{\mathrm{p}}(t)) + \mathcal{A}(\bar{\epsilon}^{\mathrm{p}}(t)) \cdot \dot{\bar{\epsilon}}^{\mathrm{p}}(t) + \mathcal{B}(\sigma_{\mathrm{Y}}(t), \bar{\boldsymbol{\sigma}}(t)) \cdot \dot{\sigma}_{\mathrm{m}}(t)\,, \\ \dot{\bar{\epsilon}}^{\mathrm{p}}(t) &= \frac{\dot{\Lambda}(t)}{(1 - f(t))}\,; \end{aligned} \tag{7.96}$$

as well as the kinematic relations:

$$\boldsymbol{F}^{\mathrm{p}}(t) = (\boldsymbol{F}^{\mathrm{e}}(t))^{-1}\boldsymbol{F}(t) \ \text{ (or, equivalently, } \ \boldsymbol{F}^{\mathrm{e}}(t) = \boldsymbol{F}(t)(\boldsymbol{F}^{\mathrm{p}}(t))^{-1})\,, \tag{7.97}$$

$$\begin{aligned} \boldsymbol{U}^{\mathrm{e}}(t) &= \sqrt{\boldsymbol{C}^{\mathrm{e}}(t)} = \sqrt{(\boldsymbol{F}^{\mathrm{e}}(t))^{\mathrm{T}}(\boldsymbol{F}^{\mathrm{e}}(t))}\,, \\ \boldsymbol{E}^{\mathrm{e}}_{(0)}(t) &= \ln \boldsymbol{U}^{\mathrm{e}}(t)\,, \\ \boldsymbol{R}^{\mathrm{e}}(t) &= \boldsymbol{F}^{\mathrm{e}}(t)(\boldsymbol{U}^{\mathrm{e}}(t))^{-1}\,, \\ J^{\mathrm{e}}(t) &= \det \boldsymbol{F}^{\mathrm{e}}(t)\,, \end{aligned} \tag{7.98}$$

$$\begin{aligned} \dot{\boldsymbol{F}}^{\mathrm{p}}(t) &= \boldsymbol{D}^{\mathrm{p}}(t)\boldsymbol{F}^{\mathrm{p}}(t)\,, \\ \bar{\boldsymbol{d}}^{\mathrm{p}}(t) &= \mathrm{sym}(\boldsymbol{U}^{\mathrm{e}}(t)\boldsymbol{D}^{\mathrm{p}}(t)(\boldsymbol{U}^{\mathrm{e}}(t))^{-1})\,; \end{aligned} \tag{7.99}$$

and the kinetic relations:

$$\begin{aligned} \bar{\boldsymbol{\tau}}(t) &= \left(\boldsymbol{\mathcal{M}}^{\bar{\boldsymbol{d}}}_{\boldsymbol{E}_{(0)}}(t)\right)^{-1} : \boldsymbol{T}_{(0)}(t)\,, \\ \bar{\boldsymbol{\sigma}}(t) &= \frac{1}{J^{\mathrm{e}}(t)}\bar{\boldsymbol{\tau}}(t)\,. \end{aligned} \tag{7.100}$$

7.2 Computational implementation: the incremental problem

In this subsection an incremental version of the quasi-static finite-strain initial value problem presented in §7.1, compatible with an updated Lagrangian finite element scheme, is developed. Some basic considerations regarding the considered finite element formulation are initially provided. The interested reader is referred to the seminal books of Zienkiewicz and Taylor (2005), Belytschko *et al.* (2014), de Souza Neto *et al.* (2011) and Simo and Hughes (2006) for details regarding the finite element method and its spatial and time integration schemes.

7.2.1 Introductory remarks and the Updated Lagrangian formulation

The finite element method (FEM) is the most popular numerical technique to solve boundary value problems in the field of solid mechanics. The FEM is grounded on temporal and spatial discretization methods. The former defines time (or pseudo-time) increments of the (possibly) path-dependent deformation process, along with some hypothesis on the deformation path between time increments, ultimately providing an incremental (or time-discrete) version of the originally time-continuum initial value problem. The latter divides the domain in a finite number of elements and, after appropriate interpolation of the field variables, allows to establish a weak equilibrium equation on the nodal points. The problem then reduces to a root finding process for the discretized (generally non-linear) weak equilibrium equations for each (pseudo-)time increment of the initial value problem. This subsection is concerned exclusively with the time discretization scheme.

Let $\boldsymbol{\sigma}$ denote a stress tensor and $\underline{\boldsymbol{\alpha}} = \{\boldsymbol{\alpha}_1, \boldsymbol{\alpha}_2, ...\boldsymbol{\alpha}_k\}$ the set of (scalar and/or tensorial) internal variables of a given model. Considering the (pseudo)-time interval $[t_n, t_{n+1}]$, $\Delta t = t_{n+1} - t_n$, where n denotes the number of the increment, the axiom of thermodynamic determinism implies that:

$$\begin{cases} \boldsymbol{\sigma}_{n+1} = \hat{\boldsymbol{\sigma}}(\underline{\boldsymbol{\alpha}}_n, \boldsymbol{F}_{n+1}) \\ \underline{\boldsymbol{\alpha}}_{n+1} = \hat{\boldsymbol{\alpha}}(\underline{\boldsymbol{\alpha}}_n, \boldsymbol{F}_{n+1}) \end{cases}, \tag{7.101}$$

where $(\cdot)_n$ and $(\cdot)_{n+1}$ denote the value of the tensorial quantity at t_n and t_{n+1}, respectively, $\hat{\boldsymbol{\sigma}}$ and $\hat{\boldsymbol{\alpha}}$ are some (generally nonlinear) incremental functions of $\boldsymbol{\sigma}$ and $\underline{\boldsymbol{\alpha}}$, respectively, defined by means of a particular numerical integration algorithm of the constitutive equations of the model; and $\boldsymbol{F}_{n+1}$ is the deformation gradient prescribed at the end of the time interval, t_{n+1}.

In this work an updated Lagrangian scheme is considered. Within this formulation, given a (pseudo)-time interval $[t_n, t_{n+1}]$, the last admissible configuration satisfying equilibrium is known at instant t_n, is regarded as the reference configuration of the body, whereas the configuration at t_{n+1} is interpreted as the current configuration. As the solution is determined at successive time intervals, the new reference configuration is taken as the last (equilibrated) current configuration. Accordingly, $\mathcal{B}_0$ in Eq. (7.1) now describes the *initial* configuration (defined at t_0), and $\mathcal{B}_n$ (defined at t_n) is the new *reference* configuration. An incremental deformation map, ϕ_{n+1}, associated with the configuration at t_{n+1} is then defined by:

$$\phi_{n+1}(\underline{\boldsymbol{X}}_n) : \mathcal{B}_n \to \mathbb{R}^3, \text{ with } \underline{\boldsymbol{x}}_{n+1} = \phi(\underline{\boldsymbol{X}}_n), \tag{7.102}$$

which maps points $\underline{\boldsymbol{X}}_n \in \mathcal{B}_n$ with respect to a Cartesian basis $\underline{\boldsymbol{E}}_i$, onto points $\underline{\boldsymbol{x}}_{n+1} \in \mathcal{B}_{n+1}$ of the *current* configuration, $\mathcal{B}_{n+1}$, with respect to a Cartesian basis $\underline{\boldsymbol{e}}_i$, at time t_{n+1}. The associated displacement field $\underline{\boldsymbol{u}}_{n+1}$ at t_{n+1} of a particle $\underline{\boldsymbol{X}}_n$ is therefore given by:

$$\underline{\boldsymbol{u}}_{n+1}(\underline{\boldsymbol{X}}_n) = \phi_{n+1}(\underline{\boldsymbol{X}}_n) - \underline{\boldsymbol{X}}_n \,. \tag{7.103}$$

Based on the incremental deformation map, ϕ_{n+1}, in Eq. (7.102) the 'total' deformation gradient tensor, $\boldsymbol{F}_{n+1}$, at t_{n+1} can be defined as:

$$\boldsymbol{F}_{n+1} = \nabla_0 \phi_{n+1}(\underline{\boldsymbol{X}}_n) = \frac{\partial \phi_{n+1}(\underline{\boldsymbol{X}}_n)}{\partial \underline{\boldsymbol{X}}_n} = \boldsymbol{I} + \nabla_0 \boldsymbol{u}_{n+1}(\underline{\boldsymbol{X}}_n) \,, \tag{7.104}$$

where $\nabla_0(\cdot)$ denotes the gradient operation with respect to the initial (t_0) configuration, $\mathcal{B}_0$. However, in the context of the updated Lagrangian scheme, it is more interesting to define the deformation map using the *incremental* deformation gradient, $\boldsymbol{F}_\Delta$, associated with the time increment $\Delta t = t_{n+1} - t_n$, as:

$$\boldsymbol{F}_\Delta = \boldsymbol{F}_{n+1}(\boldsymbol{F}_n)^{-1} = \boldsymbol{I} + \boldsymbol{G}_0 \,, \tag{7.105a}$$

where

$$\begin{aligned} \boldsymbol{G}_0 &= \nabla_{\underline{\boldsymbol{X}}_n} \boldsymbol{u}_{n+1}(\underline{\boldsymbol{X}}_n) = (\boldsymbol{I} - \boldsymbol{G}_1)^{-1} \boldsymbol{G}_1 \,, \text{ with} \\ \boldsymbol{G}_1 &= \nabla_{\boldsymbol{x}_{n+1}} \boldsymbol{u}_{n+1}(\phi_{n+1}^{-1}(\underline{\boldsymbol{x}}_{n+1})) = (\boldsymbol{I} - \boldsymbol{G}_0)^{-1} \boldsymbol{G}_0 \end{aligned} \tag{7.105b}$$

where $\boldsymbol{G}_0$ and $\boldsymbol{G}_1$ denote the gradient of the incremental displacements with respect to the reference, $\underline{\boldsymbol{X}}_n \in \mathcal{B}_n$ and the current, $\underline{\boldsymbol{x}}_{n+1} \in \mathcal{B}_{n+1}$ configurations, respectively. It follows that $\boldsymbol{F}_{n+1}$ in Eq. (7.104) can rewritten as:

$$\boldsymbol{F}_{n+1} = \boldsymbol{F}_\Delta \boldsymbol{F}_n \,. \tag{7.106}$$

7.2.2 Time integration algorithms

In this subsection defines the numerical methods used for the integration of the differential equations (Eq. (7.92)), constrains (Eq. (7.93)) and evolution equations for the state variables (Eq. (7.96)). In view of the previous discussion (§7.2.1), the notation $(\cdot)_n$ and $(\cdot)_{n+1}$ is used to denote the value of a tensorial quantity in the reference, (t_n) and current, (t_{n+1}), configurations, respectively. Additionally, the operation $\Delta(\cdot)$ is defined as the difference (or *increment*) between configuration, i.e.:

$$\Delta(\cdot) = (\cdot)_{n+1} - (\cdot)_n \,. \tag{7.107}$$

Fully-implicit (alias backwards) numerical integration schemes are considered in the following. Given a (pseudo)-time interval $[t_n, t_{n+1}]$, within a fully implicit scheme the arguments of the rate quantities of a given differential equation are replaced by their corresponding incremental values at the *end* of the interval, $(\cdot)_{n+1}$. Fully-implicit schemes are known to be first-order accurate and unconditionally stable[26] (Ortiz and Popov, 1985; Simo and Govindjee, 1991; Simo and Taylor, 1985), which are necessary and

[26] Refer e.g. to de Souza Neto *et al.* (2011) and references therein for an insight on the concepts of accuracy order, finite step accuracy and stability.

sufficient conditions for the numerical (approximate) solution to converge to the exact solution as the increment size, $\Delta t = t_{n+1} - t_n$, tends to zero. Naturally, other mixed-schemes can be employed (e.g. the generalised trapezoidal rule and/or midpoint rules), the goal here is just to provide an example.

Integration of the plastic deformation gradient, $\boldsymbol{F}^{\mathrm{p}}$

The form of the differential equation for the evolution of the plastic deformation gradient, $\dot{\boldsymbol{F}}^{\mathrm{p}}$, (see Eq. (7.70)), renders the algorithms based on exponential mapping ideal for numerical integration. The notion of exponential map is review in Appendix G (note the similarly between Eq. (7.70), or, equivalently, Eq. $(7.99)_1$, and the general differential equation in Eq. (G.12)). In agreement with the previous discussion, a fully-implicit (alias backward) exponential integrator is used (setting $\theta = 1$ in Eq. (G.14)). Accordingly, the time discretisation of Eq. (7.70) by means of the resulting scheme leads to the following update formula for the plastic deformation gradient:

$$\boldsymbol{F}^{\mathrm{p}}_{n+1} = \exp(\Delta t \boldsymbol{D}^{\mathrm{p}}_{n+1}) \boldsymbol{F}^{\mathrm{p}}_{n} \,. \tag{7.108}$$

It is emphasized that this operator satisfies the consistency conditions and is first-order accurate in Δt, i.e. (Eterovic and Bathe, 1990):

$$\lim_{\Delta t \to 0} \boldsymbol{F}^{\mathrm{p}}_{n+1} = \boldsymbol{F}^{\mathrm{p}}_{n} \,, \tag{7.109}$$

and

$$\lim_{\Delta t \to 0} \frac{d}{d\Delta t} (\boldsymbol{F}^{\mathrm{p}}_{n+1}) = \dot{\boldsymbol{F}}^{\mathrm{p}}_{n} = \boldsymbol{D}^{\mathrm{p}}_{n} \boldsymbol{F}^{\mathrm{p}}_{n} \,. \tag{7.110}$$

The exponential map integrator has been shown to perform exceptionally well, both in terms of accuracy and robustness. For example, Vladimirov *et al.* (2008) performed a numerical study in order to compare the performance of the backward Euler-type scheme with the backward exponential map and concluded that the latter provided the best accuracy, even when large time increments were considered, for which the Euler integration scheme was underperforming. The (possibly unique) drawback of the exponential map is the need for solving an addition eigenvalue problem in each local iteration (see Eq. (G.5)), (note however, that this has a negligible effect when compared with the computational cost of the numerical homogenization considered in this work, therefore the possibility of using larger steps is very welcome).

In agreement with the update scheme adopted for the plastic deformation gradient, the corresponding update equation for the *elastic* deformation gradient is in the form:

$$\boldsymbol{F}^{\mathrm{e}}_{n+1} = \boldsymbol{F}_{n+1} (\boldsymbol{F}^{\mathrm{p}}_{n})^{-1} \exp(-\Delta t \boldsymbol{D}^{\mathrm{p}}_{n+1}) \,, \tag{7.111}$$

or, in view of the adopted updated Lagrangian scheme, more conveniently written as:

$$\boldsymbol{F}^{\mathrm{e}}_{n+1} = \boldsymbol{F}_{\Delta} \boldsymbol{F}^{\mathrm{e}}_{n} \exp(-\Delta t \boldsymbol{D}^{\mathrm{p}}_{n+1}) \,, \tag{7.112}$$

where the following relationships were used: the incremental deformation gradient: $\boldsymbol{F}_{n+1} = \boldsymbol{F}_{\Delta} \boldsymbol{F}_{n}$, (Eq. (7.106)); the multiplicative elastoplastic split in the reference, $\boldsymbol{F}_{n} = \boldsymbol{F}^{\mathrm{e}}_{n} \boldsymbol{F}^{\mathrm{p}}_{n}$, and current, $\boldsymbol{F}_{n+1} = \boldsymbol{F}^{\mathrm{e}}_{n+1} \boldsymbol{F}^{\mathrm{p}}_{n+1}$, configurations; and the property of the exponential map in Eq. (G.8).

Integration of the constitutive relations and loading-unloading conditions

In the following, the elastoplastic constitutive laws and the associated loading-unloading constraints (Eqs. (7.92)-(7.94)) are discretized. Henceforth, the conventional backward (fully-implicit) Euler integration scheme is employed. In line with the exponential integrator in Eq. (7.108), the Lagrangian plastic strain-rate tensor, $\boldsymbol{D}^{\mathrm{p}}$, is assumed constant over (pseudo)-time increment $[t_n, t_{n+1}]$, and equal to its value at t_{n+1}, i.e.:

$$\boldsymbol{D}^{\mathrm{p}}(t) \equiv \boldsymbol{D}^{\mathrm{p}}_{n+1},\ t \in [t_n, t_{n+1}]\,. \tag{7.113}$$

For convenience, an Lagrangian plastic strain tensor increment, $\Delta\boldsymbol{E}^{\mathrm{p}}$, is defined as[27]:

$$\Delta\boldsymbol{E}^{\mathrm{p}} = \int_{t_n}^{t_{n+1}} \boldsymbol{D}^{\mathrm{p}}(t)\, dt, \tag{7.114}$$

where, similarly to $\boldsymbol{D}^{\mathrm{p}}$, $\Delta\boldsymbol{E}^{\mathrm{p}}$ denotes a material tensor referred to the intermediate (unstressed) configuration, (in turn defined with respect to the reference, $\mathcal{B}_n$, and the current, $\mathcal{B}_{n+1}$, configurations of the increment $[t_n, t_{n+1}]$). Given the hypothesis Eq. (7.113), it follows that:

$$\Delta\boldsymbol{E}^{\mathrm{p}} \cong \Delta t \cdot \boldsymbol{D}^{\mathrm{p}}_{n+1} \tag{7.115}$$

is the *estimate* of the integral in Eq. (7.114) using the backward Euler scheme. In view of the kinematical relationship in Eq. $(7.99)_2$, one has:

$$\overleftarrow{\boldsymbol{d}}^{\mathrm{p}}_{n+1} = \mathrm{sym}(\boldsymbol{U}^{\mathrm{e}}_{n+1}\boldsymbol{D}^{\mathrm{p}}_{n+1}(\boldsymbol{U}^{\mathrm{e}}_{n+1})^{-1})\,. \tag{7.116}$$

Defining an Eulerian plastic strain tensor increment, $\Delta\overleftarrow{\boldsymbol{\varepsilon}}^{\mathrm{p}}$, as:

$$\Delta\overleftarrow{\boldsymbol{\varepsilon}}^{\mathrm{p}} = \int_{t_n}^{t_{n+1}} \overleftarrow{\boldsymbol{d}}^{\mathrm{p}}(t)\, dt, \tag{7.117}$$

where, similarly to $\overleftarrow{\boldsymbol{d}}^{\mathrm{p}}$, $\Delta\overleftarrow{\boldsymbol{\varepsilon}}^{\mathrm{p}}$ denotes a spatial (referred to the current configuration, $\mathcal{B}_{n+1}$) tensor rotated to the material axes, it follows from Eq. (7.113) and the last three expressions that:

$$\Delta\overleftarrow{\boldsymbol{\varepsilon}}^{\mathrm{p}} \cong \mathrm{sym}[\boldsymbol{U}^{\mathrm{e}}_{n+1}(\Delta t\boldsymbol{D}^{\mathrm{p}}_{n+1})(\boldsymbol{U}^{\mathrm{e}}_{n+1})^{-1}] = \mathrm{sym}[\boldsymbol{U}^{\mathrm{e}}_{n+1}(\Delta\boldsymbol{E}^{\mathrm{p}})(\boldsymbol{U}^{\mathrm{e}}_{n+1})^{-1}] = \Delta t \cdot \overleftarrow{\boldsymbol{d}}^{\mathrm{p}}_{n+1} \tag{7.118}$$

defines an *estimate* of the integral in Eq. (7.117) using the backward Euler scheme, where, in the same spirit as Eq. (7.113), it was considered that:

$$\boldsymbol{U}^{\mathrm{e}}(t) \equiv \boldsymbol{U}^{\mathrm{e}}_{n+1},\ t \in [t_n, t_{n+1}]\,. \tag{7.119}$$

It is straightforward to verify that with hypotheses Eq. (7.113) and Eq. (7.119), one implicitly assumes:

$$\overleftarrow{\boldsymbol{d}}^{\mathrm{p}}(t) \equiv \overleftarrow{\boldsymbol{d}}^{\mathrm{p}}_{n+1},\ t \in [t_n, t_{n+1}]\,. \tag{7.120}$$

Given that the strain-rate potential, $\Psi(\overleftarrow{\boldsymbol{d}}^{\mathrm{p}}, f)$, is first-order homogeneous with respect to positive scalar multipliers, one can write the incremental form of Eq. $(7.92)_1$ in any of the following equivalent forms:

$$\Delta\Lambda = \Delta t \cdot \Psi(\overleftarrow{\boldsymbol{d}}^{\mathrm{p}}_{n+1}, f_{n+1}) = \Psi(\Delta t \cdot \overleftarrow{\boldsymbol{d}}^{\mathrm{p}}_{n+1}, f_{n+1}) = \Psi(\Delta\overleftarrow{\boldsymbol{\varepsilon}}^{\mathrm{p}}, f_{n+1})\,. \tag{7.121}$$

[27] Tensor $\Delta\boldsymbol{E}^{\mathrm{p}}$ should not be confused with the logarithmic-type strain tensors denoted with subscript (0): $\boldsymbol{E}_{(0)}$.

Conversely, the first derivative of Ψ is homogeneous of degree zero, therefore:

$$\overleftarrow{\boldsymbol{\xi}}_{n+1} = \frac{\partial \Psi(\overleftarrow{\boldsymbol{d}}^{\mathrm{p}}_{n+1},\, f_{n+1})}{\partial \overleftarrow{\boldsymbol{d}}^{\mathrm{p}}_{n+1}} = \frac{\partial \Psi(\Delta \overleftarrow{\boldsymbol{\varepsilon}}^{\mathrm{p}},\, f_{n+1})}{\partial \Delta \overleftarrow{\boldsymbol{\varepsilon}}^{\mathrm{p}}} \,. \tag{7.122}$$

where $\overleftarrow{\boldsymbol{\xi}}_{n+1} = \overleftarrow{\boldsymbol{\xi}}_{n+1}(\overleftarrow{\boldsymbol{d}}^{\mathrm{p}}_{n+1}, f_{n+1}) = \partial \Psi_{n+1} / \partial \overleftarrow{\boldsymbol{d}}^{\mathrm{p}}_{n+1}$ denotes the (unique) normal to the strain-rate potential convex hypersurface at t_{n+1}, with $\Psi_{n+1} = \Psi(\overleftarrow{\boldsymbol{d}}^{\mathrm{p}}_{n+1},\, f_{n+1})$. Note that $\overleftarrow{\boldsymbol{\xi}}_{n+1}$ is actually the normalized (or unit) stress tensor, i.e., it has an unitary equivalent stress value, $\Phi(\overleftarrow{\boldsymbol{\xi}}_{n+1},\, f_{n+1}) = 1$. Following Eq. (7.92)$_2$, the updated rotated Cauchy stress tensor, $\overleftarrow{\boldsymbol{\sigma}}_{n+1}$ is given by:

$$\overleftarrow{\boldsymbol{\sigma}}_{n+1} = \sigma_{\mathrm{Y}\,n+1} \cdot \overleftarrow{\boldsymbol{\xi}}_{n+1} \,. \tag{7.123}$$

Analogously, the time-discretized version of the hyperelastic constitutive law in Eq. (7.94) is given by:

$$\begin{aligned} &\overleftarrow{\boldsymbol{\sigma}}_{n+1} = (J^{\mathrm{e}}_{n+1})^{-1} \left(\boldsymbol{\mathcal{M}}^{\overleftarrow{d}}_{\dot{\boldsymbol{E}}_{(0)}} \right)^{-1}_{n+1} : \boldsymbol{T}_{(0)\,n+1}, \text{ with } J^{\mathrm{e}}_{n+1} = \det \boldsymbol{F}^{\mathrm{e}}_{n+1}, \text{ and} \\ &\boldsymbol{T}_{(0)\,n+1} = \frac{\partial \phi^{\mathrm{e}}_{n+1}}{\partial \boldsymbol{E}^{\mathrm{e}}_{(0)\,n+1}} = \tilde{\boldsymbol{\mathcal{A}}}(f_{n+1}) : \boldsymbol{E}^{\mathrm{e}}_{(0)\,n+1} \,, \end{aligned} \tag{7.124}$$

where $\phi^{\mathrm{e}}_{n+1} = \phi^{\mathrm{e}}_{n+1}(\boldsymbol{E}^{\mathrm{e}}_{(0)\,n+1},\, f_{n+1})$ is the quadratic stored elastic strain energy function in Eq. (7.37), with the heuristic modification in Eq. (7.58). Note that no stress increments, $\Delta \overleftarrow{\boldsymbol{\sigma}}_{n+1}$, appear in the incremental constitutive formulation presented above, as all stress tensors are 'total' quantities.

The discrete version of the (Kuhn-Tucker) constrains in Eq. (7.93) is straightforwardly obtained as:

$$\Delta\Lambda \geq 0 \,, \quad \mathcal{F}(\overleftarrow{\boldsymbol{\sigma}}_{n+1},\, f_{n+1}, \sigma_{\mathrm{Y}\,n+1}) \leq 0 \,, \quad \Delta\Lambda \cdot \mathcal{F}(\overleftarrow{\boldsymbol{\sigma}}_{n+1},\, f_{n+1}, \sigma_{\mathrm{Y}\,n+1}) = 0 \,. \tag{7.125}$$

Integration of the state variables and the loading-unloading conditions

The time continuous evolution equations of the state variables in Eq. (7.96) are discretised using the conventional backward Euler scheme. The incremental version of the evolution of the hardening internal variable (Eq. (7.96)$_1$), is thus in the form:

$$\Delta \bar{\epsilon}^{\mathrm{p}} = \frac{\Delta\Lambda}{(1 - f_{n+1})} \Leftrightarrow \bar{\epsilon}^{\mathrm{p}}_{n+1} = \bar{\epsilon}^{\mathrm{p}}_{n} + \frac{\Delta\Lambda}{(1 - f_{n+1})} \,, \tag{7.126}$$

with $\Delta\Lambda$ given in Eq. (7.121). The current uniaxial yield stress of the matrix material (identical to the overall equivalent stress under elastoplastic loading), is therefore given by:

$$\sigma_{\mathrm{Y}\,n+1} = \sigma^{\mathrm{T}}_{1} + Y_{\Delta}(\bar{\epsilon}^{\mathrm{p}}_{n+1}) \,. \tag{7.127}$$

The porosity evolution equation (Eq. (7.96)$_2$) is transformed into the following incremental counterpart:

$$f_{n+1} = f_n + \Delta f \,, \text{ with } \Delta f = \Delta f_{\mathrm{growth}} + \Delta f_{\mathrm{nuc}} \,, \tag{7.128}$$

where

$$\begin{aligned} \Delta f_{\mathrm{growth}} &= (1 - f_{n+1}) \mathrm{tr}(\Delta t \cdot \overleftarrow{\boldsymbol{d}}^{\mathrm{p}}_{n+1}) = (1 - f_{n+1}) \mathrm{tr}(\Delta \overleftarrow{\boldsymbol{\varepsilon}}^{\mathrm{p}}) \,, \\ \Delta f_{\mathrm{nuc}} &= \mathcal{A}(\bar{\epsilon}^{\mathrm{p}}_{n+1}) \cdot \Delta \bar{\epsilon}^{\mathrm{p}} + \mathcal{B}(\sigma_{\mathrm{Y}\,n+1}, \overleftarrow{\boldsymbol{\sigma}}_{n+1}) \cdot \Delta \overleftarrow{\sigma}_{\mathrm{m}} \end{aligned} \tag{7.129}$$

and

$$\Delta\bar{\sigma}_{\mathrm{m}} = \mathrm{tr}(\bar{\boldsymbol{\sigma}}_{n+1})/3 - \mathrm{tr}(\bar{\boldsymbol{\sigma}}_{n})/3\,, \tag{7.130}$$

denotes the increment of the hydrostatic stress in the increment (pseudo)-time increment $[t_n, t_{n+1}]$. Note that Eq. (7.130) implies that equilibrated stress of the previous increment, $\bar{\boldsymbol{\sigma}}_n$ must be saved in memory for the update of the current state. $\Delta\bar{\sigma}_{\mathrm{m}}$ is the unique stress increment quantity entering the envisioned elastoplastic model. Note moreover that this quantity arises directly from the form of the heuristic stress-controlled void nucleation function and is in total contradiction to the adopted 'total' (hence inherently objective) stress formulation, in turn arising from the adopted hyperelastic (in lieu of hypoelastic) formulation. It is possible to show that the term $\mathcal{B}(\sigma_{\mathrm{Y}\,n+1}, \bar{\boldsymbol{\sigma}}_{n+1}) \cdot \Delta\bar{\sigma}_{\mathrm{m}}$ renders the elastoplastic moduli non-symmetric. More critically, the presence of void nucleation in Eq. $(7.129)_2$ precludes the explicit update of f_{n+1} in Eq. (7.128) in terms of $\Delta\bar{\boldsymbol{\varepsilon}}^{\mathrm{p}}$ alone (note the interdependency between $f_{n+1} \equiv f(\bar{\boldsymbol{d}}^{\mathrm{p}}_{n+1}, \bar{\boldsymbol{\sigma}}_{n+1})$, $\Delta\bar{\epsilon}^{\mathrm{p}} \equiv \Delta\bar{\epsilon}^{\mathrm{p}}(\Delta\bar{\boldsymbol{\varepsilon}}^{\mathrm{p}},\, f_{n+1})$ and $\bar{\boldsymbol{\sigma}}_{n+1} \equiv \bar{\boldsymbol{\xi}}(\bar{\boldsymbol{d}}^{\mathrm{p}}_{n+1},\, f_{n+1})$, entering the strain- and stress- controlled terms, respectively). If void nucleation is *neglected*, i.e. $\mathcal{A} = \mathcal{B} = 0 \Rightarrow \Delta f_{\mathrm{nuc}} = 0$, combining Eqs. (7.128)-(7.129), one arrives at:

$$f_{n+1} = \frac{f_n + \mathrm{tr}(\Delta\bar{\boldsymbol{\varepsilon}}^{\mathrm{p}})}{1 + \mathrm{tr}(\Delta\bar{\boldsymbol{\varepsilon}}^{\mathrm{p}})}, \text{ if } \mathcal{A} = \mathcal{B} = 0\,, \tag{7.131}$$

which is now provides an *explicit* update of the porosity state variable in terms of tensor $\Delta\bar{\boldsymbol{\varepsilon}}^{\mathrm{p}}$.

7.2.3 Summary of the incremental boundary value problem

Based on the above defined time discretised constitutive laws, evolution equations and kinematical and kinetic relations, the incremental counterpart of the initial value problem in Box 7.1 is summarized in Box 7.2. Note that Box 7.1 sets out a system of *differential* equations which, by means of time integration considerations, reduce to a system of *algebraic* equations of Box 7.2.

Once the problem in Box 7.2 is solved for $\Delta\boldsymbol{E}^{\mathrm{p}}$ (or $\boldsymbol{F}^{\mathrm{e}}_{n+1}$), the updated plastic deformation gradients can be determined promptly from the multiplicative elastoplastic split as:

$$\boldsymbol{F}^{\mathrm{p}}_{n+1} = (\boldsymbol{F}^{\mathrm{e}}_{n+1})^{-1}\boldsymbol{F}_{\Delta}\boldsymbol{F}_{n}\ , \tag{7.132}$$

(or Eq. (7.108) if $\boldsymbol{F}^{\mathrm{p}}_{n}$ in lieu of $\boldsymbol{F}_n$). Note however that the determination of this quantity is not actually needed within the proposed update Lagrangian scheme, since the elastic-plastic state is fully-defined knowing $\boldsymbol{F}_{\Delta}$ and $\boldsymbol{F}^{\mathrm{e}}_{n+1}$ alone. The evaluation of $\boldsymbol{F}^{\mathrm{p}}_{n+1}$ is thus only used for post-processing purposes.

Box 7.2. Definition of the incremental version of the finite-strain constitutive elastoplastic initial value problem.

Given $\boldsymbol{F}_n^{\mathrm{e}}$ (or, equivalently, $\boldsymbol{F}_n^{\mathrm{p}}$) and the set of internal state variables, $\underline{\boldsymbol{\alpha}}_n = \{f_n, \bar{\epsilon}_n^{\mathrm{p}}\}$, at the beginning at a (pseudo)-time increment $t \in [t_n, t_{n+1}]$, and given the prescribed incremental deformation gradient, $\boldsymbol{F}_{\Delta}$, of this increment, solve the following system of algebraic equations for the unknowns $\Delta\boldsymbol{E}^{\mathrm{p}} \equiv (\Delta t \boldsymbol{D}_{n+1}^{\mathrm{p}})$, (or $\boldsymbol{F}_{n+1}^{\mathrm{e}}$, or $\boldsymbol{F}_{n+1}^{\mathrm{p}}$), $\underline{\boldsymbol{\alpha}}_{n+1} = \{f_{n+1}, \bar{\epsilon}_{n+1}^{\mathrm{p}}\}$, and $\Delta\Lambda$:

$$\begin{aligned} &\Psi(\Delta\check{\boldsymbol{\varepsilon}}^{\mathrm{p}},\, f_{n+1}) = \Delta\Lambda\,, \\ &\check{\boldsymbol{\sigma}}_{n+1} = \sigma_{\mathrm{Y}\,n+1} \cdot \check{\boldsymbol{\xi}}_{n+1} = \sigma_{\mathrm{Y}\,n+1} \frac{\partial \Psi(\Delta\check{\boldsymbol{\varepsilon}}^{\mathrm{p}},\, f_{n+1})}{\partial \Delta\check{\boldsymbol{\varepsilon}}^{\mathrm{p}}}\,, \end{aligned} \tag{7.133}$$

subjected to the constrains

$$\Delta\Lambda \geq 0\,,\ \mathcal{F}(\check{\boldsymbol{\sigma}}_{n+1},\, f_{n+1}, \sigma_{\mathrm{Y}\,n+1}) \leq 0\,,\ \Delta\Lambda \cdot \mathcal{F}(\check{\boldsymbol{\sigma}}_{n+1},\, f_{n+1}, \sigma_{\mathrm{Y}\,n+1}) = 0\,, \tag{7.134}$$

with

$$\begin{aligned} &\boldsymbol{T}_{(0)\,n+1} = \tilde{\boldsymbol{\mathcal{A}}}(f_{n+1}) : \boldsymbol{E}_{(0)\,n+1}^{\mathrm{e}}\,, \\ &\tilde{\boldsymbol{\mathcal{A}}}(f_{n+1}) = [1 - (f_{n+1})^{\beta}]\boldsymbol{\mathcal{A}}\,, \end{aligned} \tag{7.135}$$

and

$$\sigma_{\mathrm{Y}\,n+1} = \sigma_1^{\mathrm{T}} + Y_{\Delta}(\bar{\epsilon}_{n+1}^{\mathrm{p}})\,, \tag{7.136}$$

and the incremental evolution equations:

$$\begin{aligned} f_{n+1} &= f_n + (1 - f_{n+1})\mathrm{tr}(\Delta\check{\boldsymbol{\varepsilon}}^{\mathrm{p}}) + \mathcal{A}(\bar{\epsilon}_{n+1}^{\mathrm{p}}) \cdot \Delta\bar{\epsilon}^{\mathrm{p}} + \mathcal{B}(\sigma_{\mathrm{Y}\,n+1}, \check{\boldsymbol{\sigma}}_{n+1}) \cdot \Delta\check{\sigma}_{\mathrm{m}}\,, \\ \bar{\epsilon}_{n+1}^{\mathrm{p}} &= \bar{\epsilon}_n^{\mathrm{p}} + \frac{\Delta\Lambda}{(1 - f_{n+1})}\,; \end{aligned} \tag{7.137}$$

as well as the kinematic relations:

$$\begin{aligned} \boldsymbol{U}_{n+1}^{\mathrm{e}} &= \sqrt{\boldsymbol{C}_{n+1}^{\mathrm{e}}} = \sqrt{(\boldsymbol{F}_{n+1}^{\mathrm{e}})^{\mathrm{T}}\, \boldsymbol{F}_{n+1}^{\mathrm{e}}}\,, \\ \boldsymbol{E}_{(0)\,n+1}^{\mathrm{e}} &= \ln \boldsymbol{U}_{n+1}^{\mathrm{e}}\,, \\ \boldsymbol{R}_{n+1}^{\mathrm{e}} &= \boldsymbol{F}_{n+1}^{\mathrm{e}} (\boldsymbol{U}_{n+1}^{\mathrm{e}})^{-1}\,, \\ J_{n+1}^{\mathrm{e}} &= \det \boldsymbol{F}_{n+1}^{\mathrm{e}}\,, \end{aligned} \tag{7.138}$$

$$\begin{aligned} &\boldsymbol{F}_{n+1}^{\mathrm{e}} = \boldsymbol{F}_{\Delta}\, \boldsymbol{F}_n^{\mathrm{e}} \exp(-\Delta\boldsymbol{E}^{\mathrm{p}}) \ \text{(or, equivalently, } \boldsymbol{F}_{n+1}^{\mathrm{p}} = \exp(\Delta\boldsymbol{E}^{\mathrm{p}})\boldsymbol{F}_n^{\mathrm{p}})\,, \\ &\Delta\check{\boldsymbol{\varepsilon}}^{\mathrm{p}} = \mathrm{sym}(\boldsymbol{U}_{n+1}^{\mathrm{e}} \Delta\boldsymbol{E}^{\mathrm{p}} (\boldsymbol{U}_{n+1}^{\mathrm{e}})^{-1})\,, \end{aligned} \tag{7.139}$$

and the kinetic relations:

$$\begin{aligned} \check{\boldsymbol{\tau}}_{n+1} &= \left(\boldsymbol{\mathcal{M}}_{\boldsymbol{E}_{(0)}}^{\mathrm{d}} \right)_{n+1}^{-1} : \boldsymbol{T}_{(0)\,n+1}\,, \\ \check{\boldsymbol{\sigma}}_{n+1} &= (J_{n+1}^{\mathrm{e}})^{-1} \check{\boldsymbol{\tau}}_{n+1}\,. \end{aligned} \tag{7.140}$$

7.2.4 Elastic predictor/return-mapping scheme

This subsection is devoted to the development of an computational algorithm for solving the finite-strain incremental problem postulated in Box 7.2. Motivated by the complementarity condition $\Delta\Lambda \geq 0$, in Eq. $(7.134)_1$, a two-step algorithm is considered. Indeed, note that condition $\Delta\Lambda \geq 0$ allows for two mutually exclusive possibilities: (i) a null incremental plastic multiplier, $\Delta\Lambda = 0$; and (ii) a strictly positive plastic multiplier, $\Delta\Lambda > 0$. In the former, the increment is purely elastic, therefore the dissipation (internal) state variables do not evolve and the constrain Eq. $(7.134)_3$ is automatically verified, thus only Eq. $(7.134)_2$, i.e., $\mathcal{F}(\bar{\boldsymbol{\sigma}}_{n+1}, \underline{\boldsymbol{\alpha}}_{n+1}) \leq 0$, must be tested. In the latter, Eq. $(7.134)_2$ combined with Eq. $(7.134)_3$ result in the constraint $\mathcal{F}(\bar{\boldsymbol{\sigma}}_{n+1}, \underline{\boldsymbol{\alpha}}_{n+1}) = 0$, which ultimately defines the magnitude of the plastic increment, $\Delta\Lambda$. The well-known elastic predictor/plastic corrector algorithm is a conceptually simple two-step algorithm grounded on the above reasoning (Simo and Hughes, 2006; de Souza Neto *et al.*, 2011). This strategy is adopted in this work and is described in the following. The proposed state-update computational procedure is developed in a rotated spatial configuration. The final quantities are then transformed to the current or intermediate configurations as needed.

Trial state: elastic predictor

The first step in the algorithm is the evaluation of the elastic trial state where, by definition, the time increment $[t_n, t_{n+1}]$ is assumed purely elastic, and thus the internal variables are 'frozen' at instant t_n. Henceforward, scalar or tensorial quantities concerning the trial state are represented with the notation $(\cdot)_{\text{tr}}$. The elastic trial state is obtained by solving Eq. $(7.139)_1$ for $\Delta\Lambda = 0$. Given $\boldsymbol{F}_\Delta$ and the set of state variables $\underline{\boldsymbol{\alpha}}_n = \{f_n, \bar{\epsilon}^{\text{p}}_n\}$, at t_n, the *trial* (elastic) deformation gradient tensor is given by:

$$\boldsymbol{F}^{\text{e}}_{\text{tr}} = \boldsymbol{F}_\Delta \boldsymbol{F}^{\text{e}}_n \ . \tag{7.141}$$

Moreover, condition $\Delta\Lambda = 0$ implies that the trial state variables are those of the previous increment, $(\cdot)_{\text{tr}} \equiv (\cdot)_n$. For the present constitutive equations one has:

$$\underline{\boldsymbol{\alpha}}_{\text{tr}} = \underline{\boldsymbol{\alpha}}_n \Rightarrow \begin{cases} f_{\text{tr}} = f_n \\ \bar{\epsilon}^{\text{p}}_{\text{tr}} = \bar{\epsilon}^{\text{p}}_n \end{cases} . \tag{7.142}$$

Once $\boldsymbol{F}^{\text{e}}_{\text{tr}}$ and $\underline{\boldsymbol{\alpha}}_{\text{tr}}$ are known, their associated kinematical quantities (cf. (7.138)):

$$\begin{aligned} \boldsymbol{U}^{\text{e}}_{\text{tr}} &= \sqrt{\boldsymbol{C}^{\text{e}}_{\text{tr}}} = \sqrt{(\boldsymbol{F}^{\text{e}}_{\text{tr}})^{\text{T}} \boldsymbol{F}^{\text{e}}_{\text{tr}}} \, , \\ \boldsymbol{E}^{\text{e}}_{(0)\,\text{tr}} &= \ln \boldsymbol{U}^{\text{e}}_{\text{tr}} \, , \\ \boldsymbol{R}^{\text{e}}_{\text{tr}} &= \boldsymbol{F}^{\text{e}}_{\text{tr}} (\boldsymbol{U}^{\text{e}}_{\text{tr}})^{-1} \, , \\ J^{\text{e}}_{\text{tr}} &= \det \boldsymbol{F}^{\text{e}}_{\text{tr}} \, . \end{aligned} \tag{7.143}$$

and hyperelastic constitutive quantities (cf. Eq. (7.135) and Eq. (7.140)):

$$\begin{aligned} \boldsymbol{T}_{(0)\,\text{tr}} &= \tilde{\boldsymbol{\mathcal{A}}}(f_{\text{tr}}) : \boldsymbol{E}^{\text{e}}_{(0)\,\text{tr}} \, , \\ \bar{\boldsymbol{\sigma}}_{\text{tr}} &= (J^{\text{e}}_{\text{tr}})^{-1} (\boldsymbol{\mathcal{M}}^{\check{\boldsymbol{d}}}_{\check{\boldsymbol{E}}_{(0)}})^{-1}_{\text{tr}} : \boldsymbol{T}_{(0)\,\text{tr}} \, , \end{aligned} \tag{7.144}$$

are determined, where $\overleftarrow{\boldsymbol{\sigma}}_{\mathrm{tr}}$ is the trial (elastic) rotated Cauchy stress tensor. The next step of the algorithm is to check the trial state in plastically admissible, i.e., if

$$\mathcal{F}(\overleftarrow{\boldsymbol{\sigma}}_{\mathrm{tr}},\, f_{\mathrm{tr}}, \sigma_{\mathrm{Y\,tr}}) = \Phi(\overleftarrow{\boldsymbol{\sigma}}_{\mathrm{tr}},\, f_{\mathrm{tr}}) - \sigma_{\mathrm{Y\,tr}} \leq 0\,, \tag{7.145}$$

where $\sigma_{\mathrm{Y\,tr}} = \sigma_1^{\mathrm{T}} + Y_{\Lambda}(\bar{\epsilon}_{\mathrm{tr}}^{\mathrm{p}})$ is the trial yield stress. If $\mathcal{F}(\overleftarrow{\boldsymbol{\sigma}}_{\mathrm{tr}}, f_{\mathrm{tr}}, \sigma_{\mathrm{Y\,tr}}) \leq 0$ the elastic trial state is plastically admissible and the process is indeed elastic within the (pseudo)-time increment $[t_n, t_{n+1}]$. The trial state is therefore accepted as the actual state, i.e.: $(\cdot)_{n+1} \equiv (\cdot)_{\mathrm{tr}}$. In such case, one sets:

$$\begin{gathered} \boldsymbol{F}_{n+1}^{\mathrm{e}} = \boldsymbol{F}_{\mathrm{tr}}^{\mathrm{e}}\,, \\ \underline{\boldsymbol{\alpha}}_{n+1} = \underline{\boldsymbol{\alpha}}_{\mathrm{tr}} \Rightarrow\ \bar{\epsilon}_{n+1}^{\mathrm{p}} = \bar{\epsilon}_{\mathrm{tr}}^{\mathrm{p}}\,,\ f_{n+1} = f_{\mathrm{tr}}\,,\ \sigma_{\mathrm{Y}\,n+1} = \sigma_{\mathrm{Y\,tr}}\,, \\ \overleftarrow{\boldsymbol{\sigma}}_{n+1} = \overleftarrow{\boldsymbol{\sigma}}_{\mathrm{tr}}\,. \end{gathered} \tag{7.146}$$

Otherwise, the process is in truth elastoplastic, hence it is necessary to apply a *plastic correction* (alias return mapping) whose procedure is described in the following.

Plastic correction (return-mapping algorithm)

As the name suggests, the plastic correction phase modifies the elastic trial state definition above in order to finding a solution $\overleftarrow{\boldsymbol{\sigma}}_{n+1},\ \{f_{n+1}, \bar{\epsilon}_{n+1}^{\mathrm{p}}\},\ \Delta\Lambda,$ that satisfies $\mathcal{F}(\overleftarrow{\boldsymbol{\sigma}}_{n+1}, f_{n+1}, \sigma_{\mathrm{Y}\,n+1}) = 0$ and $\Delta\Lambda > 0$. In view of the definition of the trial state (Eq. (7.141)) and the update formula Eq. (7.139), $\boldsymbol{F}_{n+1}^{\mathrm{e}}$ is updated as follows:

$$\boldsymbol{F}_{n+1}^{\mathrm{e}} = \boldsymbol{F}_{\mathrm{tr}}^{\mathrm{e}} \exp(-\Delta\boldsymbol{E}^{\mathrm{p}})\,, \tag{7.147}$$

Once $\boldsymbol{F}_{n+1}^{\mathrm{e}}$ is corrected, its associated kinematical quantities are determined by Eq. (7.138). Applying the exponential map integrator and developing the Taylor expansion series on the resulting expression for the logarithmic elastic strain tensor (Eq. $(7.138)_2$), it is possible to show that the previous equation leads to the approximation:

$$\boldsymbol{E}_{(0)\,n+1}^{\mathrm{e}} \cong \boldsymbol{E}_{(0)\,\mathrm{tr}}^{\mathrm{e}} - \Delta\boldsymbol{E}^{\mathrm{p}}\,, \tag{7.148}$$

which holds for moderately small elastic strains and incremental steps, i.e., $\|\boldsymbol{E}_{(0)\,\mathrm{tr}}^{\mathrm{e}}\|_2 \ll 1$. Note that Eq. (7.148) is the large strain incremental counterpart of the small strain additive decomposition of the strain rates: $\boldsymbol{d}^{\mathrm{e}} = \boldsymbol{d} - \boldsymbol{d}^{\mathrm{p}}$. This is a direct result of using logarithmic strains and the exponential mapping. This expression involves logarithmic and non-logarithmic strain tensors, yet, under the above condition, the approximation is reasonable. In this work the general correction expression Eq. (7.147) is considered, (the particular case in Eq. (7.148) was presented just for discussion purposes).

A valuable advantage of considering a SRP-based plasticity constitutive formulation is that its associated flow rule (Eq. $(7.133)_2$): $\overleftarrow{\boldsymbol{\sigma}}_{n+1} = \sigma_{\mathrm{Y}\,n+1} \cdot \overleftarrow{\boldsymbol{\xi}}_{n+1}$ automatically verifies plastic admissibility, i.e., verifies $\mathcal{F}_{n+1} = 0$. Indeed, given that $\Phi(\overleftarrow{\boldsymbol{\xi}}_{n+1}, f_{n+1}) \triangleq 1,\ \Phi(\overleftarrow{\boldsymbol{\sigma}}_{n+1}, f_{n+1}) = \sigma_{\mathrm{Y}\,n+1}$ and is therefore trivial to check that $\mathcal{F}_{n+1} = \Phi(\overleftarrow{\boldsymbol{\sigma}}_{n+1}, f_{n+1}) - \sigma_{\mathrm{Y}\,n+1} = 0$.

In Eq. (7.147) $\boldsymbol{F}_{\mathrm{tr}}^{\mathrm{e}}$ is a constant, and $\Delta\boldsymbol{E}^{\mathrm{p}}$ is the (unique) parameter. The plastic correction scheme presented in the following assumes $\Delta\boldsymbol{E}^{\mathrm{p}}$ as the *primary unknown* of the problem. Note that $\Delta\boldsymbol{E}^{\mathrm{p}}$ fully defines the elastoplastic multiplicative split via Eq. (7.147). Given the adopted hyperelastic formulation,

the elastic behaviour is fully-defined by $\boldsymbol{F}^{\mathrm{e}}_{n+1}$ which allows the definition of an 'elastic' Cauchy stress tensor (i.e. due to elasticity), $\bar{\boldsymbol{\sigma}}^{\mathrm{e}}_{n+1}$, as (combining Eq. (7.135) and Eq. (7.140)):

$$\bar{\boldsymbol{\sigma}}^{\mathrm{e}}_{n+1} = (J^{\mathrm{e}}_{n+1})^{-1} (\boldsymbol{\mathcal{M}}^{\check{\boldsymbol{d}}}_{\check{\boldsymbol{E}}_{(0)}})^{-1}_{n+1} : [\tilde{\boldsymbol{\mathcal{A}}}(f_{n+1}) : \boldsymbol{E}^{\mathrm{e}}_{(0)\,n+1}]. \tag{7.149}$$

Moreover, from the SRP-based flow rule in Eq. $(7.133)_2$, one can define a 'plastic' Cauchy stress tensor, (i.e. due to plasticity), $\bar{\boldsymbol{\sigma}}^{\mathrm{p}}_{n+1}$, as:

$$\bar{\boldsymbol{\sigma}}^{\mathrm{p}}_{n+1} = \sigma_{\mathrm{Y}\,n+1}(\bar{\epsilon}^{\mathrm{p}}_{n+1}) \cdot \bar{\boldsymbol{\xi}}_{n+1}(\Delta\bar{\boldsymbol{\varepsilon}}^{\mathrm{p}}, f_{n+1}) = \sigma_{\mathrm{Y}\,n+1}(\bar{\epsilon}^{\mathrm{p}}_{n+1}) \cdot \frac{\partial \Psi(\Delta\bar{\boldsymbol{\varepsilon}}^{\mathrm{p}}, f_{n+1})}{\partial \Delta\bar{\boldsymbol{\varepsilon}}^{\mathrm{p}}}, \tag{7.150}$$

where $\Delta\bar{\boldsymbol{\varepsilon}}^{\mathrm{p}}$ is given in terms of $\Delta\boldsymbol{E}^{\mathrm{p}}$ via Eq. (7.139). Naturally, Eq. (7.149) and Eq. (7.150) must be equal, which leads to the following non-linear tensorial equation in terms of the unknown $\Delta\boldsymbol{E}^{\mathrm{p}}$:

$$\begin{aligned} \bar{\boldsymbol{\rho}}_{\sigma}(\Delta\boldsymbol{E}^{\mathrm{p}}) &= (\bar{\boldsymbol{\sigma}}^{\mathrm{p}}_{n+1} - \bar{\boldsymbol{\sigma}}^{\mathrm{e}}_{n+1}) \\ &= \sigma_{\mathrm{Y}\,n+1}(\bar{\epsilon}^{\mathrm{p}}_{n+1}) \cdot \frac{\partial \Psi(\Delta\bar{\boldsymbol{\varepsilon}}^{\mathrm{p}}, f_{n+1})}{\partial \Delta\bar{\boldsymbol{\varepsilon}}^{\mathrm{p}}} - (J^{\mathrm{e}}_{n+1})^{-1} (\boldsymbol{\mathcal{M}}^{\check{\boldsymbol{d}}}_{\check{\boldsymbol{E}}_{(0)}})^{-1}_{n+1} : [\tilde{\boldsymbol{\mathcal{A}}}(f_{n+1}) : \boldsymbol{E}^{\mathrm{e}}_{(0)\,n+1}], \end{aligned} \tag{7.151}$$

where the residual function, $\bar{\boldsymbol{\rho}}_{\sigma}(\Delta\boldsymbol{E}^{\mathrm{p}})$ has the dimension of a (spatial) Cauchy stress tensor rotated to the intermediate configuration (material axes). Note that all entities entering the previous expression depend on the unknown, $\Delta\boldsymbol{E}^{\mathrm{p}}$. The plastic correction procedure consists of solving this system for the primary unknown, i.e., $\bar{\boldsymbol{\rho}}_{\sigma}(\Delta\boldsymbol{E}^{\mathrm{p}}) = \boldsymbol{0}$. Due to symmetry, system $\bar{\boldsymbol{\rho}}_{\sigma}(\Delta\boldsymbol{E}^{\mathrm{p}})$ has six independent non-linear equations for the six independent coefficients of $\Delta\boldsymbol{E}^{\mathrm{p}}$.

Remark 7.1 The evaluation of $\bar{\boldsymbol{\rho}}_{\sigma}(\Delta\boldsymbol{E}^{\mathrm{p}})$ requires the computation of the SRP value, $\Psi(\Delta\bar{\boldsymbol{\varepsilon}}^{\mathrm{p}}, f_{n+1})$ and its first derivative, $\bar{\boldsymbol{\xi}}_{n+1}(\Delta\bar{\boldsymbol{\varepsilon}}^{\mathrm{p}}, f_{n+1}) = \partial\Psi / \partial\Delta\bar{\boldsymbol{\varepsilon}}^{\mathrm{p}}$.

Recall that, within the present work on numerical-based plastic potentials for porous media, these quantities are actually determined simultaneously (see Remark 5.2, p. 107 and adjacent text).

Remark 7.2 The system $\bar{\boldsymbol{\rho}}_{\sigma}(\Delta\boldsymbol{E}^{\mathrm{p}}) = \boldsymbol{0}$ fully defines the plastic correction problem if and only if all the state variables entering the expression, in this case, $\underline{\boldsymbol{\alpha}}_{n+1} = \{f_{n+1}, \bar{\epsilon}^{\mathrm{p}}_{n+1}\}$, can be written *explicitly* in terms of the unknown $\Delta\boldsymbol{E}^{\mathrm{p}}$ (or explicit operations thereof, viz. $\Delta\bar{\boldsymbol{\varepsilon}}^{\mathrm{p}}$, $\Psi(\Delta\bar{\boldsymbol{\varepsilon}}^{\mathrm{p}})$).

Unfortunately, the condition in Remark 7.2 does not hold in the general case. While the isotropic hardening internal variable, $\bar{\epsilon}^{\mathrm{p}}_{n+1}$, can be explicitly updated in terms of $\Delta\Lambda = \Psi(\Delta\bar{\boldsymbol{\varepsilon}}^{\mathrm{p}}, f_{n+1})$ (Eq. $(7.137)_2$), in general, the equation for the current porosity, f_{n+1}, (Eq. $(7.137)_1$), cannot be explicitly defined in terms of the incremental plastic strain tensor alone, as discussed in the text following Eq. (7.128). The exception of the latter is in the case of void nucleation being neglected: $\mathcal{A}(\bar{\epsilon}^{\mathrm{p}}_{n+1})=\mathcal{B}(\sigma_{\mathrm{Y}\,n+1}, \bar{\boldsymbol{\sigma}}_{n+1}) = 0$. In this case, f_{n+1} can be explicitly defined (see Eq. (7.131)), and the solution of system $\bar{\boldsymbol{\rho}}_{\sigma}(\Delta\boldsymbol{E}^{\mathrm{p}})$ in Eq. (7.151) is solution of the plastic correction problem. Otherwise, an additional equation for f_{n+1}, $\rho_f(\Delta\boldsymbol{E}^{\mathrm{p}}, f_{n+1})$, must be added to Eq. (7.151) to describe the incremental porosity evolution. In view of Eqs. (7.128)-(7.130), the residual scalar function for the correction of the porosity, $\rho_f(\Delta\boldsymbol{E}^{\mathrm{p}}, f_{n+1})$, is in the form:

$$\begin{aligned}\rho_f(\Delta\boldsymbol{E}^{\mathrm{p}}, f_{n+1}) &= (f_{n+1} - f_n) - (\Delta f_{\mathrm{growth}} + \Delta f_{\mathrm{nuc}}) \\ &= (f_{n+1} - f_n) - ((1 - f_{n+1})\mathrm{tr}(\Delta\bar{\boldsymbol{\varepsilon}}^{\mathrm{p}}) + \mathcal{A}(\bar{\epsilon}^{\mathrm{p}}_{n+1}) \cdot \Delta\bar{\epsilon}^{\mathrm{p}} + \mathcal{B}(\sigma_{\mathrm{Y}\,n+1}, \bar{\boldsymbol{\sigma}}_{n+1}) \cdot \Delta\bar{\sigma}_{\mathrm{m}}).\end{aligned} \tag{7.152}$$

From the above, it is convenient to distinguish two types of problems regarding the modelling of the elastoplastic behaviour of porous media: (i) void nucleation effects neglected; (ii) the general case, i.e. including void nucleation effects. These are associated with the solution of the problems:

$$\underline{\boldsymbol{F}}(\Delta\boldsymbol{E}^{\mathrm{p}}) = \bar{\boldsymbol{\rho}}_{\sigma}(\Delta\boldsymbol{E}^{\mathrm{p}}) = \boldsymbol{0}, \tag{7.153}$$

for the former, and

$$\underline{\boldsymbol{F}}(\Delta\boldsymbol{E}^{\mathrm{p}}, f_{n+1}) = \begin{Bmatrix} \bar{\boldsymbol{\rho}}_{\sigma}(\Delta\boldsymbol{E}^{\mathrm{p}}, f_{n+1}) \\ \rho_f(\Delta\boldsymbol{E}^{\mathrm{p}}, f_{n+1}) \end{Bmatrix} = \begin{Bmatrix} \boldsymbol{0} \\ 0 \end{Bmatrix}, \tag{7.154}$$

for the latter. The solution of the non-linear system in Eq. (7.153) (or, more generally, in Eq. (7.154)) is solved using a quasi-Newton procedure with a numerical finite-difference differentiation scheme. Note that usage of the actual Newton-Raphson procedure is precluded since, in general, no analytical expression exists for $\Psi(\Delta\bar{\boldsymbol{\varepsilon}}^{\mathrm{p}}, f_{n+1})$, (hence $\bar{\boldsymbol{\xi}}_{n+1}(\Delta\bar{\boldsymbol{\varepsilon}}^{\mathrm{p}}, f_{n+1}) = \partial\Psi / \partial\Delta\bar{\boldsymbol{\varepsilon}}^{\mathrm{p}}$).

Let us consider the general problem in Eq. (7.154). Given an initial value for the solution 'vector' $\{\Delta\boldsymbol{E}^{\mathrm{p}(0)}, f_{n+1}^{(0)}\}$, the corresponding value at iteration $(k+1)$, $\{\Delta\boldsymbol{E}^{\mathrm{p}(k+1)}, f_{n+1}^{(k+1)}\}$, is determined correcting the current solution, $\{\Delta\boldsymbol{E}^{\mathrm{p}(k)}, f_{n+1}^{(k)}\}$, via:

$$\begin{Bmatrix} \Delta\boldsymbol{E}^{\mathrm{p}(k+1)} \\ f_{n+1}^{(k+1)} \end{Bmatrix} = \begin{Bmatrix} \Delta\boldsymbol{E}^{\mathrm{p}(k)} \\ f_{n+1}^{(k)} \end{Bmatrix} + \begin{Bmatrix} \delta(\Delta\boldsymbol{E}^{\mathrm{p}(k+1)}) \\ \delta f_{n+1}^{(k+1)} \end{Bmatrix}, \tag{7.155}$$

where $\{\delta\Delta\boldsymbol{E}^{\mathrm{p}(k+1)}, \delta f_{n+1}^{(k+1)}\}$ is correction term of iteration $(k+1)$, given as:

$$\begin{Bmatrix} \delta(\Delta\boldsymbol{E}^{\mathrm{p}(k+1)}) \\ \delta f_{n+1}^{(k+1)} \end{Bmatrix} = -\begin{bmatrix} \boldsymbol{\mathcal{J}}^{(k)}_{\partial\bar{\boldsymbol{\rho}}_{\sigma}/\partial\Delta\boldsymbol{E}^{\mathrm{p}}} & \boldsymbol{J}^{(k)}_{\partial\bar{\boldsymbol{\rho}}_{\sigma}/\partial f} \\ \boldsymbol{J}^{(k)}_{\partial\rho_f/\partial\Delta\boldsymbol{E}^{\mathrm{p}}} & J^{(k)}_{\partial\rho_f/\partial f} \end{bmatrix}^{-1} : \begin{Bmatrix} \bar{\boldsymbol{\rho}}_{\sigma}(\Delta\boldsymbol{E}^{\mathrm{p}(k)}, f_{n+1}^{(k)}) \\ \rho_f(\Delta\boldsymbol{E}^{\mathrm{p}(k)}, f_{n+1}^{(k)}) \end{Bmatrix}, \tag{7.156}$$

where

$$\begin{aligned} \boldsymbol{\mathcal{J}}^{(k)}_{\partial\bar{\boldsymbol{\rho}}_{\sigma}/\partial\Delta\boldsymbol{E}^{\mathrm{p}}} &= \frac{\partial\bar{\boldsymbol{\rho}}_{\sigma}(\Delta\boldsymbol{E}^{\mathrm{p}(k)}, f_{n+1}^{(k)})}{\partial(\Delta\boldsymbol{E}^{\mathrm{p}(k)})}, \\ \boldsymbol{J}^{(k)}_{\partial\bar{\boldsymbol{\rho}}_{\sigma}/\partial f} &= \frac{\partial\bar{\boldsymbol{\rho}}_{\sigma}(\Delta\boldsymbol{E}^{\mathrm{p}(k)}, f_{n+1}^{(k)})}{\partial f_{n+1}^{(k)}}, \\ \boldsymbol{J}^{(k)}_{\partial\rho_f/\partial\Delta\boldsymbol{E}^{\mathrm{p}}} &= \frac{\partial\rho_f(\Delta\boldsymbol{E}^{\mathrm{p}(k)}, f_{n+1}^{(k)})}{\partial(\Delta\boldsymbol{E}^{\mathrm{p}(k)})}, \\ J^{(k)}_{\partial\rho_f/\partial f} &= \frac{\partial\rho_f(\Delta\boldsymbol{E}^{\mathrm{p}(k)}, f_{n+1}^{(k)})}{\partial f_{n+1}^{(k)}} \end{aligned} \tag{7.157}$$

are the Jacobian tensors of the system $\underline{\boldsymbol{F}}(\Delta\boldsymbol{E}^{\mathrm{p}}, f_{n+1})$ in Eq. (7.154), to be estimated by finite differences at each iteration, (k). Note that $\boldsymbol{\mathcal{J}}^{(k)}_{\partial\bar{\boldsymbol{\rho}}_{\sigma}/\partial\Delta\boldsymbol{E}^{\mathrm{p}}}$ is a fourth-order tensor, $\boldsymbol{J}^{(k)}_{\partial\bar{\boldsymbol{\rho}}_{\sigma}/\partial f}$ and $\boldsymbol{J}^{(k)}_{\partial\rho_f/\partial\Delta\boldsymbol{E}^{\mathrm{p}}}$ are second-order tensors, and $J^{(k)}_{\partial\rho_f/\partial f}$ is a scalar. In practice, Voigt pseudo-vectorial notation is adopted to write the

residual function $\bar{\boldsymbol{\rho}}_\sigma(\Delta\boldsymbol{E}^{\mathrm{p}}, f_{n+1})$ (Eq. (7.151)), i.e., $\underline{\bar{\rho}}_\sigma(\Delta\underline{\mathbf{E}}^{\mathrm{p}}, f_{n+1}) \leftarrow \bar{\boldsymbol{\rho}}_\sigma(\Delta\boldsymbol{E}^{\mathrm{p}}, f_{n+1})$, as a six-element vector hence Eq. (7.156) simplifies to a more computationally convenient matrix form as:

$$\begin{Bmatrix} \delta(\Delta\underline{\mathbf{E}}^{\mathrm{p}\,(k+1)}) \\ \delta f_{n+1}^{(k+1)} \end{Bmatrix} = -\underbrace{\begin{bmatrix} \mathbf{J}^{(k)}_{\partial\underline{\bar{\rho}}_\sigma/\partial\Delta\underline{\mathbf{E}}^{\mathrm{p}}} & \underline{\mathbf{J}}^{(k)}_{\partial\underline{\bar{\rho}}_\sigma/\partial f} \\ \underline{\mathbf{J}}^{\mathrm{T}\,(k)}_{\partial\rho_f/\partial\Delta\underline{\mathbf{E}}^{\mathrm{p}}} & J^{(k)}_{\partial\rho_f/\partial f} \end{bmatrix}}_{\mathbf{J}^{(k)}}{}^{-1} \begin{Bmatrix} \underline{\bar{\rho}}_\sigma(\Delta\underline{\mathbf{E}}^{\mathrm{p}\,(k)}, f_{n+1}^{(k)}) \\ \rho_f(\Delta\underline{\mathbf{E}}^{\mathrm{p}\,(k)}, f_{n+1}^{(k)}) \end{Bmatrix}, \tag{7.158}$$

where $\mathbf{J}^{(k)}_{\partial\underline{\bar{\mathbf{p}}}_\sigma/\partial\Delta\underline{\mathbf{E}}^{\mathrm{p}}} \leftarrow \boldsymbol{\mathcal{J}}^{(k)}_{\partial\bar{\boldsymbol{\rho}}_\sigma/\partial\Delta\boldsymbol{E}^{\mathrm{p}}}$ is a 6×6 invertible matrix, $\underline{\mathbf{J}}^{(k)}_{\partial\underline{\bar{\mathbf{p}}}_\sigma/\partial f} \leftarrow \boldsymbol{J}^{(k)}_{\partial\bar{\boldsymbol{\rho}}_\sigma/\partial f}$ and $\underline{\mathbf{J}}^{(k)}_{\partial\rho_f/\partial\Delta\underline{\mathbf{E}}^{\mathrm{p}}} \leftarrow \boldsymbol{J}^{(k)}_{\partial\rho_f/\partial\Delta\boldsymbol{E}^{\mathrm{p}}}$ are 6-element vectors, and thus $\mathbf{J}^{(k)}$ is a 7×7 invertible matrix. The above solution scheme allows for supra-linear convergence rates, (quadratic if analytical expressions for the Jacobian tensors are provided).

The solution of the problem in Eq. (7.153), i.e. disregarding void nucleation, is no more than a particular case of the above procedure. In this case, one provides an initial value for $\Delta\boldsymbol{E}^{\mathrm{p}}$, $\Delta\boldsymbol{E}^{\mathrm{p}\,(0)}$, to be iteratively corrected, $\Delta\boldsymbol{E}^{\mathrm{p}\,(k+1)} = \Delta\boldsymbol{E}^{\mathrm{p}\,(k)} + \delta(\Delta\boldsymbol{E}^{\mathrm{p}\,(k+1)})$, with $\delta(\Delta\boldsymbol{E}^{\mathrm{p}\,(k+1)}) = (\boldsymbol{\mathcal{J}}^{(k)}_{\partial\bar{\boldsymbol{\rho}}_\sigma/\partial\Delta\boldsymbol{E}^{\mathrm{p}}})^{-1} : \bar{\boldsymbol{\rho}}_\sigma(\Delta\boldsymbol{E}^{\mathrm{p}\,(k)})$ (cf. Eq. (7.156)) where, as in Eq. (7.157), $\boldsymbol{\mathcal{J}}^{(k)}_{\partial\bar{\boldsymbol{\rho}}_\sigma/\partial\Delta\boldsymbol{E}^{\mathrm{p}}} = \partial\bar{\boldsymbol{\rho}}_\sigma(\Delta\boldsymbol{E}^{\mathrm{p}\,(k)})/\partial(\Delta\boldsymbol{E}^{\mathrm{p}\,(k)})$ is the Jacobian of the system $\bar{\boldsymbol{\rho}}_\sigma(\Delta\boldsymbol{E}^{\mathrm{p}}) = \mathbf{0}$, whose Voigt representation is in form:

$$\left\{\delta(\Delta\underline{\mathbf{E}}^{\mathrm{p}\,(k+1)})\right\} = \left[\mathbf{J}^{(k)}\right]^{-1}\left\{\underline{\bar{\rho}}_\sigma(\Delta\underline{\mathbf{E}}^{\mathrm{p}\,(k)})\right\}, \text{ with } \mathbf{J}^{(k)} = \mathbf{J}^{(k)}_{\partial\underline{\bar{\mathbf{p}}}_\sigma/\partial\Delta\underline{\mathbf{E}}^{\mathrm{p}}}, \tag{7.159}$$

where the overall Jacobian, $\mathbf{J}^{(k)}$, is now a 6×6 invertible matrix.

The iterative correction scheme is conducted until a given tolerance is met. Regarding the (general) problem in Eq. (7.154) the iterative process stops as soon as:

$$\begin{gathered} \left(\frac{\left\|\underline{\bar{\rho}}_\sigma(\Delta\underline{\mathbf{E}}^{\mathrm{p}\,(k+1)}, f_{n+1}^{(k+1)})\right\|_2}{\sigma_{\mathrm{Y}\,n+1}^{(k+1)}} < \varepsilon_{\mathrm{tol}}^{\mathrm{fun}} \wedge \frac{\rho_f(\Delta\underline{\mathbf{E}}^{\mathrm{p}\,(k+1)}, f_{n+1}^{(k+1)})}{f_{n+1}^{(k+1)}} < \varepsilon_{\mathrm{tol}}^{\mathrm{fun}} \right), \\ \text{and/or} \quad \left(\frac{\left\|\delta(\Delta\underline{\mathbf{E}}^{\mathrm{p}\,(k+1)})\right\|_2}{\left\|\Delta\underline{\mathbf{E}}^{\mathrm{p}\,(k+1)}\right\|_2} < \varepsilon_{\mathrm{tol}}^{\Delta\mathrm{x}} \wedge \frac{\delta f_{n+1}^{(k+1)}}{f_{n+1}^{(k+1)}} < \varepsilon_{\mathrm{tol}}^{\Delta\mathrm{x}} \right) \end{gathered} \tag{7.160}$$

where $\sigma_{\mathrm{Y}\,n+1}^{(k+1)}$ is the current yield stress regarding iteration $(k+1)$, and $\varepsilon_{\mathrm{tol}}^{\mathrm{fun}}$ and $\varepsilon_{\mathrm{tol}}^{\Delta\mathrm{x}}$ are the prescribed relative tolerances for the residual norm and increment norm, respectively. Regarding the reduced problem in Eq. (7.153), only the first inequality in each parenthesis of the previous expressions needs to be satisfied. The Jacobian matrix $\mathbf{J}^{(k+1)}_{\partial\underline{\bar{\mathbf{p}}}_\sigma/\partial\Delta\underline{\mathbf{E}}^{\mathrm{p}}}(\Delta\underline{\mathbf{E}}^{\mathrm{p}\,(k+1)}, f_{n+1}^{(k+1)})$, associated with the solution $(\Delta\underline{\mathbf{E}}^{\mathrm{p}\,(k+1)}, f_{n+1}^{(k+1)})$, of the problem Eq. (7.154), (or, similarly, $\mathbf{J}^{(k+1)}_{\partial\underline{\bar{\mathbf{p}}}_\sigma/\partial\Delta\underline{\mathbf{E}}^{\mathrm{p}}}(\Delta\underline{\mathbf{E}}^{\mathrm{p}\,(k+1)})$, associated with the solution $(\Delta\underline{\mathbf{E}}^{\mathrm{p}\,(k+1)})$ of Eq. (7.153)) is stored in memory for determining an estimate of the consistent/algorithmic elastoplastic modulus, as later shown in §7.2.6.

Once the plastic correction problem has been solved, i.e. Eq. (7.160) is satisfied: $\Delta\boldsymbol{E}^{\mathrm{p}} \leftarrow \Delta\boldsymbol{E}^{\mathrm{p}\,(k+1)}$ in the case of problem Eq. (7.153) and $\{\Delta\boldsymbol{E}^{\mathrm{p}}, f_{n+1}\} \leftarrow \{\Delta\boldsymbol{E}^{\mathrm{p}\,(k+1)}, f_{n+1}^{(k+1)}\}$, in the case of Eq. (7.154); the kinematical and kinetic tensors of the current (elastoplastic) increment are updated in a post-processing step following the definitions in Box 7.2. In addition to these, some auxiliary quantities are also computed, viz.: (i) the (non-rotated) updated Cauchy stress tensor:

$$\boldsymbol{\sigma}_{n+1} = \boldsymbol{R}^{\mathrm{e}}_{n+1}\bar{\boldsymbol{\sigma}}_{n+1}(\boldsymbol{R}^{\mathrm{e}}_{n+1})^{\mathrm{T}}, \tag{7.161}$$

required to assemble the internal finite element force vector: (ii) the rotated plastic strain-rate 'direction' (alias unitary plastic strain-rate tensor), $\overleftarrow{\boldsymbol{n}}^{\mathrm{p}}_{n+1}$, by definition, coincident with the gradient of the plastic stress potential, $\overleftarrow{\boldsymbol{n}}^{\mathrm{p}}_{n+1} \triangleq \partial\Phi(\overleftarrow{\boldsymbol{\sigma}}_{n+1}, f_{n+1})/\partial\overleftarrow{\boldsymbol{\sigma}}_{n+1}$:

$$\overleftarrow{\boldsymbol{n}}^{\mathrm{p}}_{n+1} = \frac{\Delta\overleftarrow{\boldsymbol{\varepsilon}}^{\mathrm{p}}}{\Delta\Lambda} = \frac{\Delta\overleftarrow{\boldsymbol{\varepsilon}}^{\mathrm{p}}}{\Psi(\Delta\overleftarrow{\boldsymbol{\varepsilon}}^{\mathrm{p}}, f_{n+1})} \equiv \frac{\overleftarrow{\boldsymbol{d}}^{\mathrm{p}}_{n+1}}{\Psi(\overleftarrow{\boldsymbol{d}}^{\mathrm{p}}_{n+1}, f_{n+1})}; \tag{7.162}$$

where the last equality results from the homogeneity property of the SRP, Ψ, and the adopted fully-implicit integration scheme $(\Delta\overleftarrow{\boldsymbol{\varepsilon}}^{\mathrm{p}} = \Delta t \cdot \overleftarrow{\boldsymbol{d}}^{\mathrm{p}}_{n+1})$. Note that $\overleftarrow{\boldsymbol{n}}^{\mathrm{p}}_{n+1}$ is a spatial quantity rotated to the intermediate configuration; (iii) an estimate of the hardening modulus scalar, *H*, obtained from the elastoplastic $(\dot{\Lambda} > 0)$ consistency condition $\dot{\mathcal{F}} = 0 \Leftrightarrow \dot{\overleftarrow{\boldsymbol{\sigma}}} : \overleftarrow{\boldsymbol{n}}^{\mathrm{p}} - \dot{\Lambda} H = 0.$ Integration of this expression in the context of the adopted fully-implicit incremental scheme results in the estimate $H \equiv H_{n+1}$:

$$\Delta\overleftarrow{\boldsymbol{\sigma}} : \overleftarrow{\boldsymbol{n}}^{\mathrm{p}}_{n+1} - \Delta\Lambda \cdot H_{n+1} = 0 \Leftrightarrow H_{n+1} = \frac{\Delta\overleftarrow{\boldsymbol{\sigma}} : \overleftarrow{\boldsymbol{n}}^{\mathrm{p}}_{n+1}}{\Delta\Lambda}, \tag{7.163}$$

where $\Delta\overleftarrow{\boldsymbol{\sigma}} = (\overleftarrow{\boldsymbol{\sigma}}_{n+1} - \overleftarrow{\boldsymbol{\sigma}}_{n})$ is the rotated Cauchy stress increment and $\overleftarrow{\boldsymbol{n}}^{\mathrm{p}}_{n+1}$ was defined in Eq. (7.162).

Sufficient conditions for determining the incremental loading-unloading conditions

The lack of an explicit expression defining the boundary between the elastic and plastic domains is the major drawback of SRP-based plasticity formulations. In Eq. (7.145) the plastic admissibility of the trial state was verified by determining the respective stress potential value, $\Phi(\overleftarrow{\boldsymbol{\sigma}}_{\mathrm{tr}}, f_{\mathrm{tr}})$, a priori. Recall that this can be achieved by performing the 'inverse' homogenization problem, as summarized in Box 4.3. However, this process is computationally extremely expensive and, if possible, should be avoided. Note that, in fact, the adopted SRP-based return mapping scheme does not require the computation of any equivalent stress quantity, $\bar{\sigma} = \Phi(\overleftarrow{\boldsymbol{\sigma}}, f)$. Indeed, the final equivalent stress, $\bar{\sigma}_{n+1} \equiv \sigma_{\mathrm{Y}\,n+1}$ is a mere output of the plastic correction scheme and is set in the post-processing phase. Following the work of (Hughes, 1984) on the numerical aspects of rate-independent associative flow rules, a sufficient condition to guarantee that the current increment is elastoplastic based on a deformation history is:

$$(\overleftarrow{\boldsymbol{\sigma}}_{\mathrm{tr}} - \overleftarrow{\boldsymbol{\sigma}}_{n}) : \overleftarrow{\boldsymbol{n}}^{\mathrm{p}}_{n} \geq 0 \text{ , if } \mathcal{F}(\overleftarrow{\boldsymbol{\sigma}}_{n}, f_{n}) = 0, \tag{7.164}$$

(thus $\overleftarrow{\boldsymbol{n}}^{\mathrm{p}}_{n} \neq \mathbf{0}$), i.e. the previous increment was elastoplastic, where $\overleftarrow{\boldsymbol{\sigma}}_{\mathrm{tr}}$ is the (current) trial elastic stress, and $\overleftarrow{\boldsymbol{\sigma}}_{n}$ and $\overleftarrow{\boldsymbol{n}}^{\mathrm{p}}_{n}$ are the rotated Cauchy stress tensor and the rotated unitary plastic strain-rate tensor, respectively, of the previous increment. The usage of Eq. (7.164) renders the evaluation of the yield condition Eq. (7.145) unnecessary in most cases (Rabahallah *et al.*, 2009), thus providing a major computational improvement. Indeed the computational cost of Eq. (7.164) is insignificant and simply requires storing $\overleftarrow{\boldsymbol{\sigma}}_{n}$ and $\overleftarrow{\boldsymbol{n}}^{\mathrm{p}}_{n}$ in memory for usage in the next increment.

If the previous increment (associated with $\overleftarrow{\boldsymbol{\sigma}}_{n}$), is not elastoplastic then Eq. (7.164) does not apply. In this case, *ad hoc* criteria can still be used to bypass the computationally expensive determination of the yield function. For example: (i) if a *p*-norm of the current trial stress tensor normalized by the last known yield stress is smaller than a user-defined threshold fraction, $f^{\mathrm{e}}_{\sigma_{\mathrm{Y}}}$, (say, $f^{\mathrm{e}}_{\sigma_{\mathrm{Y}}} = 0.1$),

$$\frac{\|\bar{\boldsymbol{\sigma}}_{\mathrm{tr}}\|_p}{\sigma_{\mathrm{Y}n}} < f^{\mathrm{e}}_{\sigma_{\mathrm{Y}}}\,; \tag{7.165}$$

then the increment is clearly elastic; and/or, (ii) if a p-norm (or the von Misis norm) of the deviatoric part of the current trial stress tensor normalized by the last known yield stress is greater than a user-defined threshold fraction, $f^{\mathrm{p}}_{\sigma_{\mathrm{Y}}}$, (say, $f^{\mathrm{p}}_{\sigma_{\mathrm{Y}}}=10$),

$$\frac{\|\bar{\boldsymbol{\sigma}}'_{\mathrm{tr}}\|_2}{\sigma_{\mathrm{Y}n}} > f^{\mathrm{p}}_{\sigma_{\mathrm{Y}}}\,, \tag{7.166}$$

then the increment is clearly elastoplastic; among others. Of course, these being based on heurist rules, such criteria should be used with discretion since ill-judged threshold fractions may lead to an incorrect conclusion (particularly in the context of porous solids given the dependence on all invariants of the stress tensor). Nevertheless, if conservative conditions are employed, these provide a reliable tool for reducing the computational cost associated with the determination of the loading-unloading conditions of the incremental problem.

7.2.5 Summary of the computational procedure

The complete computational procedure of the developed fully-implicit elastic predictor/return-mapping scheme for integration of the large-strain elastoplastic constitutive equations is summarized in Box 7.3-Box 7.7 in pseudo-code format. In line with the previous discussion, two cases are distinguished: (i) the general case; and (ii) a particular case due to the neglect of void nucleation, which was shown to considerably simply the governing equation system of the plastic correction phase.

Box 7.3 Elastic predictor/return mapping algorithm for the incremental finite-strain elastoplastic porous model.

0. Inputs: $\boldsymbol{G}_1,\ \boldsymbol{F}_n^{\mathrm{e}},\ \underline{\boldsymbol{\alpha}}_n = \{f_n, \bar{\epsilon}_n^{\mathrm{p}}\},\ \underline{\tilde{\boldsymbol{\sigma}}}_n,\ \underline{\tilde{\mathbf{n}}}_n^{\mathrm{p}}$

- Compute the incremental displacement gradient: $\boldsymbol{F}_\Delta = \boldsymbol{I} + (\boldsymbol{I} - \boldsymbol{G}_1)^{-1}\boldsymbol{G}_1$ % (Eq. (7.105))

1. Elastic trial state

- Compute the trial elastic deformation gradient $\boldsymbol{F}_{\mathrm{tr}}^{\mathrm{e}} = \boldsymbol{F}_\Delta \boldsymbol{F}_n^{\mathrm{e}}$ % (Eq. (7.141))
- Compute the trial elastic right Cauchy-Green deformation tensor its spectral decomposition:

$$\boldsymbol{C}_{\mathrm{tr}}^{\mathrm{e}} = (\boldsymbol{F}_{\mathrm{tr}}^{\mathrm{e}})^{\mathrm{T}}\boldsymbol{F}_{\mathrm{tr}}^{\mathrm{e}} = \textstyle\sum_{i=1}^{3}(\lambda_i^{\mathrm{e}})_{\mathrm{tr}}(\boldsymbol{N}_i)_{\mathrm{tr}} \otimes (\boldsymbol{N}_i)_{\mathrm{tr}}$$

- Compute the trial logarithmic strain tensor:

$$\boldsymbol{E}_{(0)\,\mathrm{tr}}^{\mathrm{e}} = \ln \boldsymbol{U}_{\mathrm{tr}}^{\mathrm{e}} = \tfrac{1}{2}\ln \boldsymbol{C}_{\mathrm{tr}}^{\mathrm{e}} = \textstyle\sum_{i=1}^{3}\ln(\lambda_i^{\mathrm{e}})_{\mathrm{tr}}(\boldsymbol{N}_i)_{\mathrm{tr}} \otimes (\boldsymbol{N}_i)_{\mathrm{tr}}$$

- Compute the trial logarithmic strain tensor and trial elastic determinant:

$$J_{\mathrm{tr}}^{\mathrm{e}} = \det \boldsymbol{F}_{\mathrm{tr}}^{\mathrm{e}} = \textstyle\prod_{i=1}^{3}(\lambda_i^{\mathrm{e}})_{\mathrm{tr}}$$

- Set trial state variables: $\underline{\boldsymbol{\alpha}}_{\mathrm{tr}} = \underline{\boldsymbol{\alpha}}_n \Rightarrow f_{\mathrm{tr}} = f_n,\ \bar{\epsilon}_{\mathrm{tr}}^{\mathrm{p}} = \bar{\epsilon}_n^{\mathrm{p}};\ \sigma_{\mathrm{Y\,tr}} = \sigma_{\mathrm{Y}n}$
- Transform to pseudo-vector Voigt notation: $\boldsymbol{E}_{(0)\,\mathrm{tr}}^{\mathrm{e}} \rightarrow \underline{\mathbf{E}}_{(0)\mathrm{tr}}^{\mathrm{e}}$ % (Appendix A)
- Compute the trial logarithmic stress tensor and the trial rotated trial Cauchy stress tensor:

$$\underline{\mathbf{T}}_{(0)\,\mathrm{tr}} = \tilde{\mathbf{A}}(f_{\mathrm{tr}})\underline{\mathbf{E}}_{(0)\,\mathrm{tr}}^{\mathrm{e}}, \text{ and } \underline{\tilde{\boldsymbol{\sigma}}}_{\mathrm{tr}} = (J_{\mathrm{tr}}^{\mathrm{e}})^{-1}(\mathbf{M}_{\underline{\tilde{\boldsymbol{d}}}_{(0)}}^{\tilde{\boldsymbol{d}}})_{\mathrm{tr}}^{-1}\underline{\mathbf{T}}_{(0)\,\mathrm{tr}}$$

2. Check plastic admissibility of the trial state

- Check sufficient condition % (cf. Eq. (7.164))

if $(\underline{\tilde{\mathbf{n}}}_n^{\mathrm{p}} \cdot \underline{\tilde{\mathbf{n}}}_n^{\mathrm{p}}) \neq 0$ then

if $(\underline{\tilde{\boldsymbol{\sigma}}}_{\mathrm{tr}} - \underline{\tilde{\boldsymbol{\sigma}}}_n)\cdot\underline{\tilde{\mathbf{n}}}_n^{\mathrm{p}} \geq 0$

- The process is elastoplastic: GOTO **3.**

end

end

- Determine the equivalent stress (i.e. the plastic stress potential):

CALL Box 5.3 (the 'inverse' homogenization problem): $\Phi_{\mathrm{tr}} \leftarrow \Phi(\underline{\tilde{\boldsymbol{\sigma}}}_{\mathrm{tr}}, f_{\mathrm{tr}})$

- Determine $\mathcal{F}(\underline{\tilde{\boldsymbol{\sigma}}}_{\mathrm{tr}}, f_{\mathrm{tr}}, \sigma_{\mathrm{Y\,tr}}) = \Phi_{\mathrm{tr}} - \sigma_{\mathrm{Y\,tr}}$

if $\mathcal{F}(\underline{\tilde{\boldsymbol{\sigma}}}_{\mathrm{tr}}, f_{\mathrm{tr}}, \sigma_{\mathrm{Y\,tr}}) \leq 0$ then

- The process is elastic. Set $(\cdot)_{n+1} \equiv (\cdot)_{\mathrm{tr}},\ \Delta\underline{\tilde{\boldsymbol{\varepsilon}}}^{\mathrm{p}} = \underline{\mathbf{0}},\ \Delta\underline{\mathbf{E}}^{\mathrm{p}} = \underline{\mathbf{0}},$ and GOTO **4.**

else

- The process is elastoplastic: GOTO **3.**

end

3. Return mapping

- Solve the plastic correction problem:

if (general problem) then % (void nucleation considered: 7-element system)

CALL Box 7.4 to solve $\underline{\mathbf{F}}(\Delta\underline{\mathbf{E}}^{\mathrm{p}}, f_{n+1}) = [\underline{\mathbf{0}}\ \ 0]^{\mathrm{T}}$ % (Eq. (7.154))

else % (void nucleation neglected: 6-element system)

CALL Box 7.5 to solve $\underline{\mathbf{F}}(\Delta\underline{\mathbf{E}}^{\mathrm{p}}) = \underline{\mathbf{0}}$ % (Eq. (7.153))

end

4. Update auxiliary variables and the Cauchy stress tensor

- Unitary rotated plastic strain-rate tensor: $\tilde{\boldsymbol{n}}_{n+1}^{\mathrm{p}} = \Delta\tilde{\boldsymbol{\varepsilon}}^{\mathrm{p}}/\Delta\Lambda$ % Eq. (7.162)
- Hardening scalar estimate: $H_{n+1} = (\underline{\tilde{\boldsymbol{\sigma}}}_{n+1} - \underline{\tilde{\boldsymbol{\sigma}}}_n)\cdot\underline{\tilde{\mathbf{n}}}_{n+1}^{\mathrm{p}}/\Delta\Lambda$; % Eq. (7.163)
- Voigt notation to matrix notation: $\tilde{\boldsymbol{\sigma}}_{n+1} \leftarrow \underline{\tilde{\boldsymbol{\sigma}}}_{n+1}$; and $\boldsymbol{\sigma}_{n+1} = \boldsymbol{R}_{n+1}^{\mathrm{e}}\tilde{\boldsymbol{\sigma}}_{n+1}(\boldsymbol{R}_{n+1}^{\mathrm{e}})^{\mathrm{T}}$ % Eq. (7.161))

5. Output: $\boldsymbol{F}_{n+1}^{\mathrm{e}},\ \underline{\boldsymbol{\alpha}}_{n+1} = \{f_{n+1}, \bar{\epsilon}_{n+1}^{\mathrm{p}}\},\ \underline{\boldsymbol{\sigma}}_{n+1}, (\underline{\tilde{\boldsymbol{\sigma}}}_{n+1}, \underline{\tilde{\mathbf{n}}}_{n+1}^{\mathrm{p}}, H_{n+1}),\ \mathbf{J}_{\partial\underline{\mathbf{P}}_\sigma/\partial\Delta\underline{\mathbf{E}}^{\mathrm{p}}}$

Box 7.4 The plastic correction problem (the general case).

0. Inputs: $\boldsymbol{G}_1$, $\boldsymbol{F}_n^{\mathrm{e}}$, $\underline{\boldsymbol{\alpha}}_n = \{f_n, \overline{\epsilon}_n^{\mathrm{p}}\}$, $\underline{\bar{\boldsymbol{\sigma}}}_n$

1. Solve the system of equations

- Set initial guess $\{\Delta\underline{\mathbf{E}}^{\mathrm{p}\,(0)}, f_{n+1}^{(0)}\}$, and the relative convergence tolerances for the system: $\{\varepsilon_{\mathrm{tol}}^{\mathrm{fun}}, \varepsilon_{\mathrm{tol}}^{\Delta\mathrm{x}}\}$
- Solve the system in Box 7.6 for $\{\Delta\underline{\mathbf{E}}^{\mathrm{p}}, f_{n+1}\}$ with a quasi-Newton method, such that:

$$\left(\frac{\left\| F_{(1:6)}(\Delta\underline{\mathbf{E}}^{\mathrm{p}\,(k+1)}, f_{n+1}^{(k+1)}) \right\|_2}{\sigma_{\mathrm{Y}\,n+1}^{(k+1)}} < \varepsilon_{\mathrm{tol}}^{\mathrm{fun}} \wedge \frac{F_{(7)}(\Delta\underline{\mathbf{E}}^{\mathrm{p}\,(k+1)}, f_{n+1}^{(k+1)})}{f_{n+1}^{(k+1)}} < \varepsilon_{\mathrm{tol}}^{\mathrm{fun}} \right) \quad \text{and}$$

$$\left(\frac{\left\| \delta(\Delta\underline{\mathbf{E}}^{\mathrm{p}\,(k+1)}) \right\|_2}{\left\| \Delta\underline{\mathbf{E}}^{\mathrm{p}\,(k+1)} \right\|_2} < \varepsilon_{\mathrm{tol}}^{\Delta\mathrm{x}} \wedge \frac{\delta f_{n+1}^{(k+1)}}{f_{n+1}^{(k+1)}} < \varepsilon_{\mathrm{tol}}^{\Delta\mathrm{x}} \right),$$

where k is the number of the iteration and $F_{(I:J)}$ denotes the I to J components of vector $\underline{\mathbf{F}}$ with $1 \le I \le J \le 7$.

2. Output: $\Delta\underline{\mathbf{E}}^{\mathrm{p}} \leftarrow \Delta\underline{\mathbf{E}}^{\mathrm{p}\,(k+1)}$, $\Delta\Lambda \leftarrow \Delta\Lambda^{(k+1)}$, $\{f_n, \overline{\epsilon}_n^{\mathrm{p}}\} \leftarrow \{f_{n+1}^{(k+1)}, \overline{\epsilon}_{n+1}^{\mathrm{p}(k+1)}\}$,

$\underline{\bar{\boldsymbol{\sigma}}}_{n+1} \leftarrow \underline{\bar{\boldsymbol{\sigma}}}_{n+1}^{\mathrm{p}(k+1)}$, $\mathbf{J}_{\partial\underline{\hat{\mathbf{p}}}_\sigma / \partial\Delta\underline{\mathbf{E}}^{\mathrm{p}}} \leftarrow \mathbf{J}_{\partial\underline{\hat{\mathbf{p}}}_\sigma / \partial\Delta\underline{\mathbf{E}}^{\mathrm{p}}}^{(k+1)}$

Box 7.5 The plastic correction problem for the particular case of the neglect of void nucleation effects.

0. Inputs: $\boldsymbol{G}_1$, $\boldsymbol{F}_n^{\mathrm{e}}$, $\underline{\boldsymbol{\alpha}}_n = \{f_n, \overline{\epsilon}_n^{\mathrm{p}}\}$

1. Solve the system of equations

- Set initial guess $\Delta\underline{\mathbf{E}}^{\mathrm{p}\,(0)}$ and the relative convergence tolerances for the system: $\{\varepsilon_{\mathrm{tol}}^{\mathrm{fun}}, \varepsilon_{\mathrm{tol}}^{\Delta\mathrm{x}}\}$
- Solve the system in Box 7.7 for $\Delta\underline{\mathbf{E}}^{\mathrm{p}}$ with a quasi-Newton method, such that:

$$\left(\frac{\left\| \underline{\mathbf{F}}(\Delta\underline{\mathbf{E}}^{\mathrm{p}\,(k+1)}) \right\|_2}{\sigma_{\mathrm{Y}\,n+1}^{(k+1)}} < \varepsilon_{\mathrm{tol}}^{\mathrm{fun}} \right) \quad \text{and} \quad \left(\frac{\left\| \delta(\Delta\underline{\mathbf{E}}^{\mathrm{p}\,(k+1)}) \right\|_2}{\left\| \Delta\underline{\mathbf{E}}^{\mathrm{p}\,(k+1)} \right\|_2} < \varepsilon_{\mathrm{tol}}^{\Delta\mathrm{x}} \right),$$

where k is the number of the iteration.

2. Output: $\Delta\underline{\mathbf{E}}^{\mathrm{p}} \leftarrow \Delta\underline{\mathbf{E}}^{\mathrm{p}\,(k+1)}$, $\Delta\Lambda \leftarrow \Delta\Lambda^{(k+1)}$, $\{f_n, \overline{\epsilon}_n^{\mathrm{p}}\} \leftarrow \{f_{n+1}^{(k+1)}, \overline{\epsilon}_{n+1}^{\mathrm{p}(k+1)}\}$,

$\underline{\bar{\boldsymbol{\sigma}}}_{n+1} \leftarrow \underline{\bar{\boldsymbol{\sigma}}}_{n+1}^{\mathrm{p}(k+1)}$, $\mathbf{J}_{\partial\underline{\hat{\mathbf{p}}}_\sigma / \partial\Delta\underline{\mathbf{E}}^{\mathrm{p}}} \leftarrow \mathbf{J}_{\partial\underline{\hat{\mathbf{p}}}_\sigma / \partial\Delta\underline{\mathbf{E}}^{\mathrm{p}}}^{(k+1)}$

Box 7.6 Error function vector of the plastic correction problem (general case).

0. Inputs: $\boldsymbol{G}_1$, $\boldsymbol{F}_n^{\mathrm{e}}$, $\underline{\boldsymbol{\alpha}}_n = \{f_n, \bar{\epsilon}_n^{\mathrm{p}}\}$, $\underline{\tilde{\boldsymbol{\sigma}}}_n$, $\{\Delta\underline{\mathbf{E}}^{\mathrm{p}}, f_{n+1}\}$

- Compute the incremental displacement gradient: $\boldsymbol{F}_{\Delta} = \boldsymbol{I} + (\boldsymbol{I} - \boldsymbol{G}_1)^{-1}\boldsymbol{G}_1$ % (Eq. (7.105))

1. Correction of the elastic tensors

- Transform to matrix notation from Voigt notation: $\underline{\mathbf{E}}_{(0)n+1}^{\mathrm{e}} \rightarrow \boldsymbol{E}_{(0)n+1}^{\mathrm{e}}$ % (Appendix A)
- Correction of the elastic deformation gradient $\boldsymbol{F}_{n+1}^{\mathrm{e}} = \boldsymbol{F}_{\mathrm{tr}}^{\mathrm{e}} \exp(-\Delta\boldsymbol{E}^{\mathrm{p}})$ % (Eq. (7.139)$_1$)
- Compute the elastic right Cauchy-Green deformation tensor its spectral decomposition:

$$\boldsymbol{C}_{n+1}^{\mathrm{e}} = (\boldsymbol{F}_{n+1}^{\mathrm{e}})^{\mathrm{T}}\boldsymbol{F}_{n+1}^{\mathrm{e}} = \sum_{i=1}^{3}(\lambda_i^{\mathrm{e}})_{n+1}(\boldsymbol{N}_i)_{n+1} \otimes (\boldsymbol{N}_i)_{n+1}$$

- Compute the logarithmic strain tensor:

$$\boldsymbol{E}_{(0)n+1}^{\mathrm{e}} = \ln \boldsymbol{U}_{n+1}^{\mathrm{e}} = \tfrac{1}{2}\ln \boldsymbol{C}_{n+1}^{\mathrm{e}} = \sum_{i=1}^{3}\ln(\lambda_i^{\mathrm{e}})_{n+1}(\boldsymbol{N}_i)_{n+1} \otimes (\boldsymbol{N}_i)_{n+1}$$

- Compute the logarithmic strain tensor and trial elastic determinant:

$$J_{n+1}^{\mathrm{e}} = \det \boldsymbol{F}_{n+1}^{\mathrm{e}} = \prod_{i=1}^{3}(\lambda_i^{\mathrm{e}})_{n+1}$$

2. Rotated Cauchy stress tensor from elasticity

- Compute the logarithmic stress tensor and the rotated trial Cauchy stress tensor from elasticity:

$$\underline{\mathbf{T}}_{(0)n+1} = \tilde{\mathbf{A}}(f_{n+1})\underline{\mathbf{E}}_{(0)n+1}^{\mathrm{e}}, \text{ and } \underline{\tilde{\boldsymbol{\sigma}}}_{n+1}^{\mathrm{e}} = (J_{n+1}^{\mathrm{e}})^{-1}(\mathbf{M}_{\boldsymbol{E}_{(0)}}^{\tilde{d}})_{n+1}^{-1}\underline{\mathbf{T}}_{(0)n+1}$$ % (Eq. (7.140))

3. Spatial rotated plastic strain increment

- Compute $\Delta\tilde{\boldsymbol{\varepsilon}}^{\mathrm{p}} = \mathrm{sym}(\boldsymbol{U}_{n+1}^{\mathrm{e}}\Delta\boldsymbol{E}^{\mathrm{p}}(\boldsymbol{U}_{n+1}^{\mathrm{e}})^{-1})$ % (Eq. (7.139)$_2$)
- Transform to pseudo-vector Voigt notation: $\Delta\tilde{\boldsymbol{\varepsilon}}^{\mathrm{p}} \rightarrow \Delta\underline{\tilde{\boldsymbol{\varepsilon}}}^{\mathrm{p}}$ % (Appendix A)

4. Strain rate potential and plastic flow rule

- Compute the SRP and its first derivative:

CALL Box 5.1 (the 'direct' homogenization problem) to obtain:

$$\Delta\Lambda \leftarrow \Psi(\Delta\underline{\tilde{\boldsymbol{\varepsilon}}}^{\mathrm{p}}, f_{n+1}) \text{ and } \underline{\tilde{\boldsymbol{\xi}}}_{n+1} = \partial\Psi(\Delta\underline{\tilde{\boldsymbol{\varepsilon}}}^{\mathrm{p}}, f_{n+1}) / \partial\Delta\underline{\tilde{\boldsymbol{\varepsilon}}}^{\mathrm{p}}$$ % (Eq. (7.133))

5. Update the explicit-type state variables

- $\bar{\epsilon}_{n+1}^{\mathrm{p}} = \bar{\epsilon}_n^{\mathrm{p}} + \Delta\Lambda / (1 - f_{n+1})$ % (Eq. (7.137)$_2$)
- Determine the current yield stress: $\sigma_{\mathrm{Y}n+1} = \sigma_{\mathrm{Y}n+1}(\bar{\epsilon}_{n+1}^{\mathrm{p}})$ % (Eq. (7.127))

6. Rotated Cauchy stress tensor from plasticity

- Compute $\underline{\tilde{\boldsymbol{\sigma}}}_{n+1}^{\mathrm{p}} = \sigma_{\mathrm{Y}n+1} \cdot \underline{\tilde{\boldsymbol{\xi}}}_{n+1}$ % (Eq. (7.150))

7. Construct the (pseudo-) vector error function

- Compute the stress residual vector: $\underline{\tilde{\boldsymbol{\rho}}}_{\sigma} = (\underline{\tilde{\boldsymbol{\sigma}}}_{n+1}^{\mathrm{p}} - \underline{\tilde{\boldsymbol{\sigma}}}_{n+1}^{\mathrm{e}})$ % (Eq. (7.151))
- Auxiliary scalars:

$$\Delta\bar{\epsilon}^{\mathrm{p}} = \Delta\Lambda / (1 - f_{n+1}),$$

$$\Delta\tilde{\varepsilon}_{\mathrm{m}}^{\mathrm{p}} = \mathrm{sum}(\Delta\underline{\tilde{\boldsymbol{\varepsilon}}}^{\mathrm{p}}(1:3))$$

$$\Delta\tilde{\sigma}_{\mathrm{m}} = \mathrm{sum}(\underline{\tilde{\boldsymbol{\sigma}}}_{n+1}^{\mathrm{p}}(1:3) - \underline{\tilde{\boldsymbol{\sigma}}}_n(1:3))/3$$

- Compute the porosity residual scalar:

$$\rho_f = (f_{n+1} - f_n) - ((1 - f_{n+1})\Delta\tilde{\varepsilon}_{\mathrm{m}}^{\mathrm{p}} + \mathcal{A}(\bar{\epsilon}_{n+1}^{\mathrm{p}}) \cdot \Delta\bar{\epsilon}^{\mathrm{p}} + \mathcal{B}(\sigma_{\mathrm{Y}n+1}, \underline{\tilde{\boldsymbol{\sigma}}}_{n+1}^{\mathrm{p}}) \cdot \Delta\tilde{\sigma}_{\mathrm{m}}).$$ % (Eq. (7.152))

- Assemble the error vector: $\underline{\mathbf{F}} \leftarrow \begin{Bmatrix} \underline{\tilde{\boldsymbol{\rho}}}_{\sigma} \\ \rho_f \end{Bmatrix}$

8. Output: $\underline{\mathbf{F}}$, $\Delta\Lambda$, $\underline{\boldsymbol{\alpha}}_{n+1} = \{f_{n+1}, \bar{\epsilon}_{n+1}^{\mathrm{p}}\}$, $\underline{\tilde{\boldsymbol{\sigma}}}_{n+1}^{\mathrm{p}}$

Box 7.7 Error function vector of the plastic correction problem for the particular case of the neglect of void nucleation effects.

0. Inputs: $\boldsymbol{G}_1,\ \boldsymbol{F}_n^{\mathrm{e}},\ \underline{\boldsymbol{\alpha}}_n = \{f_n, \bar{\epsilon}_n^{\mathrm{p}}\},\ \Delta\underline{\mathbf{E}}^{\mathrm{p}}$

- Compute the incremental displacement gradient: $\boldsymbol{F}_{\Delta} = \boldsymbol{I} + (\boldsymbol{I} - \boldsymbol{G}_1)^{-1}\boldsymbol{G}_1$ % (Eq. (7.105))

1. Correction of the elastic tensors

- Transform to matrix notation from Voigt notation: $\underline{\mathbf{E}}^{\mathrm{e}}_{(0)n+1} \rightarrow \boldsymbol{E}^{\mathrm{e}}_{(0)n+1}$ % (Appendix A)
- Correction of the elastic deformation gradient $\boldsymbol{F}^{\mathrm{e}}_{n+1} = \boldsymbol{F}^{\mathrm{e}}_{\mathrm{tr}} \exp(-\Delta\boldsymbol{E}^{\mathrm{p}})$ % (Eq. (7.139)$_1$)
- Compute the elastic right Cauchy-Green deformation tensor its spectral decomposition:

$$\boldsymbol{C}^{\mathrm{e}}_{n+1} = (\boldsymbol{F}^{\mathrm{e}}_{n+1})^{\mathrm{T}}\boldsymbol{F}^{\mathrm{e}}_{n+1} = \sum_{i=1}^{3}(\lambda^{\mathrm{e}}_i)_{n+1}(\boldsymbol{N}_i)_{n+1} \otimes (\boldsymbol{N}_i)_{n+1}$$

- Compute the logarithmic strain tensor:

$$\boldsymbol{E}^{\mathrm{e}}_{(0)n+1} = \ln \boldsymbol{U}^{\mathrm{e}}_{n+1} = \tfrac{1}{2}\ln \boldsymbol{C}^{\mathrm{e}}_{n+1} = \sum_{i=1}^{3}\ln(\lambda^{\mathrm{e}}_i)_{n+1}(\boldsymbol{N}_i)_{n+1} \otimes (\boldsymbol{N}_i)_{n+1}$$

- Compute the logarithmic strain tensor and trial elastic determinant:

$$J^{\mathrm{e}}_{n+1} = \det \boldsymbol{F}^{\mathrm{e}}_{n+1} = \prod_{i=1}^{3}(\lambda^{\mathrm{e}}_i)_{n+1}$$

2. Spatial rotated plastic strain increment

- Compute $\Delta\bar{\boldsymbol{\varepsilon}}^{\mathrm{p}} = \mathrm{sym}(\boldsymbol{U}^{\mathrm{e}}_{n+1}\Delta\boldsymbol{E}^{\mathrm{p}}(\boldsymbol{U}^{\mathrm{e}}_{n+1})^{-1})$ % (Eq. (7.139)$_2$)
- Transform to pseudo-vector Voigt notation: $\Delta\bar{\boldsymbol{\varepsilon}}^{\mathrm{p}} \rightarrow \Delta\bar{\underline{\boldsymbol{\varepsilon}}}^{\mathrm{p}}$ % (Appendix A)

3. Explicit update of the porosity variable

- $\Delta\bar{\varepsilon}^{\mathrm{p}}_{\mathrm{m}} = \mathrm{sum}(\Delta\bar{\underline{\boldsymbol{\varepsilon}}}^{\mathrm{p}}(1:3))$
- $f_{n+1} = \dfrac{f_n + \Delta\bar{\varepsilon}^{\mathrm{p}}_{\mathrm{m}}}{1 + \Delta\bar{\varepsilon}^{\mathrm{p}}_{\mathrm{m}}}$ % (Eq. (7.131))

4. Rotated Cauchy stress tensor from elasticity

- Compute the logarithmic stress tensor and the rotated trial Cauchy stress tensor from elasticity:

$$\underline{\mathbf{T}}_{(0)n+1} = \tilde{\mathbf{A}}(f_{n+1})\underline{\mathbf{E}}^{\mathrm{e}}_{(0)n+1}, \text{ and } \bar{\underline{\boldsymbol{\sigma}}}^{\mathrm{e}}_{n+1} = (J^{\mathrm{e}}_{n+1})^{-1}(\mathbf{M}^{\hat{\boldsymbol{d}}}_{\hat{\boldsymbol{E}}_{(0)}})^{-1}_{n+1}\underline{\mathbf{T}}_{(0)n+1}$$ % (Eq. (7.140))

5. Strain rate potential and plastic flow rule

- Compute the SRP and its first derivative:

CALL Box 5.1 (the 'direct' homogenization problem) to obtain:

$$\Delta\Lambda \leftarrow \Psi(\Delta\bar{\underline{\boldsymbol{\varepsilon}}}^{\mathrm{p}}, f_{n+1}) \text{ and } \bar{\underline{\boldsymbol{\xi}}}_{n+1} = \partial\Psi(\Delta\bar{\underline{\boldsymbol{\varepsilon}}}^{\mathrm{p}}, f_{n+1}) / \partial\Delta\bar{\underline{\boldsymbol{\varepsilon}}}^{\mathrm{p}}$$ % (Eq. (7.133))

6. Update the remaining state variables

- $\bar{\epsilon}^{\mathrm{p}}_{n+1} = \bar{\epsilon}^{\mathrm{p}}_n + \Delta\Lambda / (1 - f_{n+1})$ % (Eq. (7.137)$_2$)
- Determine the current yield stress: $\sigma_{\mathrm{Y}n+1} = \sigma_{\mathrm{Y}n+1}(\bar{\epsilon}^{\mathrm{p}}_{n+1})$ % (Eq. (7.127))

7. Rotated Cauchy stress tensor from plasticity

- Compute $\bar{\underline{\boldsymbol{\sigma}}}^{\mathrm{p}}_{n+1} = \sigma_{\mathrm{Y}n+1} \cdot \bar{\underline{\boldsymbol{\xi}}}_{n+1}$ % (Eq. (7.150))

8. Construct the (pseudo-) vector error function

- Compute the stress residual vector: $\bar{\underline{\boldsymbol{\rho}}}_{\sigma} = (\bar{\underline{\boldsymbol{\sigma}}}^{\mathrm{p}}_{n+1} - \bar{\underline{\boldsymbol{\sigma}}}^{\mathrm{e}}_{n+1})$ % (Eq. (7.151))
- Assign the error vector: $\underline{\mathbf{F}} \leftarrow \bar{\underline{\boldsymbol{\rho}}}_{\sigma}$

9. Output: $\underline{\mathbf{F}},\ \Delta\Lambda,\ \underline{\boldsymbol{\alpha}}_{n+1} = \{f_{n+1}, \bar{\epsilon}^{\mathrm{p}}_{n+1}\},\ \bar{\underline{\boldsymbol{\sigma}}}^{\mathrm{p}}_{n+1}$

7.2.6 Elastoplastic moduli estimates

In the context of the finite element method, the state-update procedure must also provide appropriate elastoplastic moduli estimates defining the tangent relationship between the (infinitesimal- or finite-) stress increments and strain increments, which are used in the assemblage of the finite element stiffness matrix. The goal of this subsection is to present estimates for the so-called (linear) tangent elastoplastic modulus and the algorithmic (or consistent) elastoplastic modulus. Here, the focus is solely on obtaining approximations for these fourth-order tensors. Indeed, in view of the adopted modelling approach, the definition of exact elastoplastic moduli a challenging task, if not impossible. The reasons are twofold: (i) one lacks the definition of the analytical expressions of the plastic potentials (hence of their derivatives); and (ii) defining the elastoplastic moduli in the spatial configuration (or any other configuration) is conceptually complex: the elastic constitutive rule is defined in the intermediate configuration based on Lagrangian logarithmic tensors, whereas the plastic behaviour is written in the current (rotated) configuration in terms of Eulerian tensors. Relating these tensors implies the use of mapping tensors similar to that in Eq. (7.50) (e.g. see Caminero *et al.* (2011)). In order to facilitate the analysis, the elastoplastic moduli present in this subsection are based on three simplifying conditions: (i) small strain framework, $\boldsymbol{\varepsilon} \cong \boldsymbol{E}_{(n)} \cong \boldsymbol{e}_{(n)}$, where $\boldsymbol{E}_{(n)}$ and $\boldsymbol{e}_{(n)}$ denote any Lagrangian- and Eulerian- strain tensors (see Eq. (7.20)-(7.22)); (ii) the postulate of elastoplastic additive decomposition of the strain rate tensor, $\bar{\boldsymbol{d}} = \bar{\boldsymbol{d}}^{\mathrm{e}} + \bar{\boldsymbol{d}}^{\mathrm{p}}$, where $(\bar{\cdot})$ denotes that the tensor is written in the material/orthotropy axes; (iii) hypoelastic formulation of the type $\dot{\bar{\boldsymbol{\sigma}}} = \bar{\boldsymbol{\mathcal{C}}}^{\mathrm{e}} : \bar{\boldsymbol{d}}^{\mathrm{e}}$, where $\dot{\bar{\boldsymbol{\sigma}}}$ is the rotated Cauchy stress rate. Under these conditions the finite-strain hyperelastic law Eq. (7.94) can be rewritten in rate form as: $\dot{\boldsymbol{T}}_{(0)} = \tilde{\boldsymbol{\mathcal{A}}}(f) : \dot{\boldsymbol{E}}^{\mathrm{e}}_{(0)} \Rightarrow \dot{\bar{\boldsymbol{\sigma}}} = \tilde{\boldsymbol{\mathcal{A}}}(f) : \bar{\boldsymbol{d}}^{\mathrm{e}}$, where it was implicitly assumed that:

$$\begin{aligned} \dot{\bar{\boldsymbol{\sigma}}} &\cong \dot{\bar{\boldsymbol{\tau}}} \cong \dot{\boldsymbol{T}}_{(0)}, \\ \bar{\boldsymbol{d}}^{\mathrm{e}} &\cong \dot{\boldsymbol{E}}^{\mathrm{e}}_{(0)}, \\ J^{\mathrm{e}} &\cong 1, \end{aligned} \tag{7.167}$$

and the convention for the (orthotropic) fourth-order elasticity tensor:

$$\bar{\boldsymbol{\mathcal{C}}}^{\mathrm{e}} \cong \tilde{\boldsymbol{\mathcal{A}}}(f). \tag{7.168}$$

Additionally, the associative plastic flow is described by the standard rate-independent dual constitutive laws: $\bar{\boldsymbol{d}}^{\mathrm{p}} = \dot{\Lambda} \bar{\boldsymbol{n}}^{\mathrm{p}}$ with $\bar{\boldsymbol{n}}^{\mathrm{p}} = \partial \Phi(\bar{\boldsymbol{\sigma}}, \underline{\boldsymbol{\alpha}}) / \partial \bar{\boldsymbol{\sigma}}$; and $\bar{\boldsymbol{\sigma}} = \sigma_{\mathrm{Y}} \bar{\boldsymbol{\xi}}$ with $\bar{\boldsymbol{\xi}} = \partial \Psi(\bar{\boldsymbol{d}}^{\mathrm{p}}, \underline{\boldsymbol{\alpha}}) / \partial \bar{\boldsymbol{d}}^{\mathrm{p}}$, where $\Psi(\bar{\boldsymbol{d}}^{\mathrm{p}}, \underline{\boldsymbol{\alpha}}) = \dot{\Lambda}$ and $\Phi(\bar{\boldsymbol{\sigma}}, \underline{\boldsymbol{\alpha}}) = \sigma_{\mathrm{Y}}$, (thus $\Psi(\bar{\boldsymbol{n}}^{\mathrm{p}}, \underline{\boldsymbol{\alpha}}) = \Phi(\bar{\boldsymbol{\xi}}, \underline{\boldsymbol{\alpha}}) = 1$), with an yield function $\mathcal{F}(\bar{\boldsymbol{\sigma}}, \underline{\boldsymbol{\alpha}}, \sigma_{\mathrm{Y}}) = \Phi(\bar{\boldsymbol{\sigma}}, \underline{\boldsymbol{\alpha}}) - \sigma_{\mathrm{Y}}$, where $\underline{\boldsymbol{\alpha}}$ is set of internal variables (viz. $\{\bar{\epsilon}^{\mathrm{p}}, f\}$), assumed to evolve in the general form $\dot{\underline{\boldsymbol{\alpha}}} = \dot{\Lambda} \underline{\boldsymbol{h}}(\underline{\boldsymbol{\alpha}})$. Note that plastic compressibility is considered. The small-strain moduli presented in the following are therefore estimates of their large-strain counterparts.

Approximate spatial linear/tangent elastoplastic modulus

Under elastoplastic loading $(\dot{\Lambda} > 0,\ \mathcal{F} = 0)$ it is possible to demonstrate that the consistency condition, $\dot{\Lambda} \dot{\mathcal{F}} = 0$, leads to:

$$\dot{\mathcal{F}} = \bar{\boldsymbol{n}}^{\mathrm{p}} : \dot{\bar{\boldsymbol{\sigma}}} - \dot{\Lambda} H = 0 \text{, with } \bar{\boldsymbol{n}}^{\mathrm{p}} = \frac{\partial \mathcal{F}}{\partial \bar{\boldsymbol{\sigma}}} = \frac{\partial \Phi(\bar{\boldsymbol{\sigma}}, \underline{\boldsymbol{\alpha}})}{\partial \bar{\boldsymbol{\sigma}}} \text{ and } H = -\frac{\partial \mathcal{F}}{\partial \underline{\boldsymbol{\alpha}}} : \underline{\boldsymbol{h}}, \tag{7.169}$$

where H is the (small-strain) hardening modulus. Combining the previous expression with the hypoplastic law, $\dot{\bar{\boldsymbol{\sigma}}} = \bar{\boldsymbol{\mathcal{C}}}^{\mathrm{e}} : \bar{\boldsymbol{d}}^{\mathrm{e}}$, and the small-strain addictive decomposition $\bar{\boldsymbol{d}} = \bar{\boldsymbol{d}}^{\mathrm{e}} + \bar{\boldsymbol{d}}^{\mathrm{p}}$, leads to:

$$\dot{\Lambda} = \frac{\bar{\boldsymbol{n}}^{\mathrm{p}} : \bar{\boldsymbol{\mathcal{C}}}^{\mathrm{e}} : \bar{\boldsymbol{d}}}{\bar{\boldsymbol{n}}^{\mathrm{p}} : \bar{\boldsymbol{\mathcal{C}}}^{\mathrm{e}} : \bar{\boldsymbol{n}}^{\mathrm{p}} + H}, \tag{7.170}$$

and, consequently, the plastic loading condition $\dot{\Lambda} > 0$, becomes $\bar{\boldsymbol{n}}^{\mathrm{p}} : \bar{\boldsymbol{\mathcal{C}}}^{e} : \bar{\boldsymbol{d}} > 0$, which is valid both in the hardening regime $H > 0$ as well as in softening $H < 0$, provided that no "snap-back" behaviour takes place, i.e. the denominator of Eq. (7.170) must remain positive (Besson *et al.*, 2004). Replacing Eq. (7.170) in the hypoplastic law, $\dot{\bar{\boldsymbol{\sigma}}} = \bar{\boldsymbol{\mathcal{C}}}^{e} : (\bar{\boldsymbol{d}} - \dot{\Lambda} \bar{\boldsymbol{n}}^{\mathrm{p}})$, results in the following tangent relation between the stress rate tensor and the (total) strain rate tensor:

$$\dot{\bar{\boldsymbol{\sigma}}} = \bar{\boldsymbol{\mathcal{C}}}^{\mathrm{ep}}_{\mathrm{tan}} : \bar{\boldsymbol{d}}, \tag{7.171}$$

where $\bar{\boldsymbol{\mathcal{C}}}^{\mathrm{ep}}_{\mathrm{tan}}$ is the linear/tangent elastoplastic modulus, given as follows:

$$\bar{\boldsymbol{\mathcal{C}}}^{\mathrm{ep}}_{\mathrm{tan}} = \begin{cases} \bar{\boldsymbol{\mathcal{C}}}^{\mathrm{e}} & \text{if } \mathcal{F} < 0 \vee \{\mathcal{F} = 0 \ \wedge \ \bar{\boldsymbol{n}}^{\mathrm{p}} : \bar{\boldsymbol{\mathcal{C}}}^{e} : \bar{\boldsymbol{d}} \leq 0\}, \\ \bar{\boldsymbol{\mathcal{C}}}^{\mathrm{e}} - \dfrac{(\bar{\boldsymbol{\mathcal{C}}}^{\mathrm{e}} : \bar{\boldsymbol{n}}^{\mathrm{p}}) \otimes (\bar{\boldsymbol{n}}^{\mathrm{p}} : \bar{\boldsymbol{\mathcal{C}}}^{\mathrm{e}})}{\bar{\boldsymbol{n}}^{\mathrm{p}} : \bar{\boldsymbol{\mathcal{C}}}^{\mathrm{e}} : \bar{\boldsymbol{n}}^{\mathrm{p}} + H} & \text{if } \{\mathcal{F} = 0 \ \wedge \ \bar{\boldsymbol{n}}^{\mathrm{p}} : \bar{\boldsymbol{\mathcal{C}}}^{e} : \bar{\boldsymbol{d}} > 0\}. \end{cases} \tag{7.172}$$

This expression holds for both stress- and strain-rate-based elastoplastic models. Eq. (7.172) is associated with the recently introduced small-strain framework. In view of the approximations in Eqs. (7.167)-(7.168), one can define an *estimate* for the spatial elastoplastic tangent modulus of the large-strain incremental constitutive problem in Box 7.2, to be evaluated after the solution of the state-update problem (Box 7.3), as:

$$\bar{\boldsymbol{\mathcal{C}}}^{\mathrm{ep}}_{\mathrm{tan}} \cong \tilde{\boldsymbol{\mathcal{A}}}(f_{n+1}) - \alpha \frac{(\tilde{\boldsymbol{\mathcal{A}}}(f_{n+1}) : \bar{\boldsymbol{n}}^{\mathrm{p}}_{n+1}) \otimes (\bar{\boldsymbol{n}}^{\mathrm{p}}_{n+1} : \tilde{\boldsymbol{\mathcal{A}}}(f_{n+1}))}{\bar{\boldsymbol{n}}^{\mathrm{p}}_{n+1} : \tilde{\boldsymbol{\mathcal{A}}}(f_{n+1}) : \bar{\boldsymbol{n}}^{\mathrm{p}}_{n+1} + H_{n+1}} \text{, with } \alpha = \begin{cases} 1 & \text{if } \Delta\Lambda > 0, \\ 0 & \text{if } \Delta\Lambda = 0. \end{cases} \tag{7.173}$$

where $\bar{\boldsymbol{n}}^{\mathrm{p}}_{n+1}$ and H_{n+1} are determined via Eq. (7.162) and Eq. (7.163), respectively, based on the solution of the return mapping scheme (Box 7.4).

Estimate of the spatial consistent elastoplastic modulus

In order to achieve (quasi-)quadratic rates of asymptotic convergence in the iterative solution of the displacement-based finite element equilibrium equations, a tangent operator consistent with the underlining incremental (time-discretized) constitutive problem must be defined. The consistent (alias algorithmic) elastoplastic tangent modulus, $\bar{\boldsymbol{\mathcal{C}}}^{\mathrm{ep}}_{\mathrm{alg}}$, defines the tangent relation between the increments of the updated stress, $D\bar{\boldsymbol{\sigma}}_{n+1}$, (defined by a given return mapping procedure), and the increment of the (total) strain increment, $D(\Delta\bar{\boldsymbol{\varepsilon}})$, between FE equilibrium iterations, i.e.:

$$\bar{\boldsymbol{\mathcal{C}}}^{\mathrm{ep}}_{\mathrm{alg}} \triangleq \frac{\partial (D\bar{\boldsymbol{\sigma}}_{n+1})}{\partial (D(\Delta\bar{\boldsymbol{\varepsilon}}))}, \tag{7.174}$$

where

$$D\overset{\leftarrow}{\boldsymbol{\sigma}} = (\overset{\leftarrow}{\boldsymbol{\sigma}}_{n+1}^{(j+1)} - \overset{\leftarrow}{\boldsymbol{\sigma}}_{n+1}^{(j)}), \text{ and } D(\Delta\overset{\leftarrow}{\boldsymbol{\varepsilon}}) = (\Delta\overset{\leftarrow}{\boldsymbol{\varepsilon}}^{(j+1)} - \Delta\overset{\leftarrow}{\boldsymbol{\varepsilon}}^{(j)}), \tag{7.175}$$

and j is iteration number of the equilibrium iterations regarding the (pseudo)-time increment $[t_n, t_{n+1}]$. The derivation of the consistent elastoplastic modulus requires the definition of an incremental version of the small strain hypoelastic-based (with non-isochoric plasticity) constitutive problem postulated in the introductory paragraph of the present subsection. Using the backward Euler scheme, the small-strain state-update is in the form:

$$\begin{aligned}
\Delta\overset{\leftarrow}{\boldsymbol{\varepsilon}} \triangleq \Delta t \cdot \overset{\leftarrow}{\boldsymbol{d}}_{n+1} = \Delta t \cdot (\overset{\leftarrow}{\boldsymbol{d}}^{\mathrm{e}}_{n+1} + \overset{\leftarrow}{\boldsymbol{d}}^{\mathrm{p}}_{n+1}) = \Delta\overset{\leftarrow}{\boldsymbol{\varepsilon}}^{\mathrm{e}} + \Delta\overset{\leftarrow}{\boldsymbol{\varepsilon}}^{\mathrm{p}}\,, \\
\overset{\leftarrow}{\boldsymbol{\sigma}}_{n+1} = \overset{\leftarrow}{\boldsymbol{\sigma}}_{n} + \overset{\leftarrow}{\boldsymbol{\mathcal{C}}}^{\mathrm{e}} : \Delta\overset{\leftarrow}{\boldsymbol{\varepsilon}}^{\mathrm{e}}\,, \\
\Psi(\Delta\overset{\leftarrow}{\boldsymbol{\varepsilon}}^{\mathrm{p}}, \underline{\boldsymbol{\alpha}}_{n+1}) = \Delta\Lambda\,, \\
\overset{\leftarrow}{\boldsymbol{\sigma}}_{n+1} = \sigma_{\mathrm{Y}\,n+1}\overset{\leftarrow}{\boldsymbol{\xi}}_{n+1} = \sigma_{\mathrm{Y}\,n+1}\dfrac{\partial\Psi(\Delta\overset{\leftarrow}{\boldsymbol{\varepsilon}}^{\mathrm{p}}, \underline{\boldsymbol{\alpha}}_{n+1})}{\partial(\Delta\overset{\leftarrow}{\boldsymbol{\varepsilon}}^{\mathrm{p}})}\,, \\
\underline{\boldsymbol{\alpha}}_{n+1} = \underline{\boldsymbol{\alpha}}_{n} + \Delta\Lambda\underline{\boldsymbol{h}}_{n+1}\,.
\end{aligned} \tag{7.176}$$

The solution of the return mapping (plastic correction) scheme of the above problem is associated with the solution of the residual function system (cf. Eq. (7.151)):

$$\overset{\leftarrow}{\boldsymbol{\rho}}_{\sigma}(\Delta\overset{\leftarrow}{\boldsymbol{\varepsilon}}^{\mathrm{p}}) = \sigma_{\mathrm{Y}\,n+1}\frac{\partial\Psi(\Delta\overset{\leftarrow}{\boldsymbol{\varepsilon}}^{\mathrm{p}}, \underline{\boldsymbol{\alpha}}_{n+1})}{\partial(\Delta\overset{\leftarrow}{\boldsymbol{\varepsilon}}^{\mathrm{p}})} - (\overset{\leftarrow}{\boldsymbol{\mathcal{C}}}^{\mathrm{e}} : \Delta\overset{\leftarrow}{\boldsymbol{\varepsilon}}^{\mathrm{e}} + \overset{\leftarrow}{\boldsymbol{\sigma}}_{n}) = \mathbf{0}\,, \tag{7.177}$$

where it was implicitly assumed that the set of state variables can be explicitly written in terms of $\Delta\overset{\leftarrow}{\boldsymbol{\varepsilon}}^{\mathrm{p}}$ alone. Differentiation of the previous expression leads to:

$$\mathcal{J} \triangleq \frac{\partial\overset{\leftarrow}{\boldsymbol{\rho}}_{\sigma}(\Delta\overset{\leftarrow}{\boldsymbol{\varepsilon}}^{\mathrm{p}})}{\partial(\Delta\overset{\leftarrow}{\boldsymbol{\varepsilon}}^{\mathrm{p}})} = \left(\frac{\partial\sigma_{\mathrm{Y}\,n+1}}{\partial\Psi_{n+1}}\overset{\leftarrow}{\boldsymbol{\xi}}_{n+1}\right)\otimes\overset{\leftarrow}{\boldsymbol{\xi}}_{n+1} + \sigma_{\mathrm{Y}\,n+1}\frac{\partial\overset{\leftarrow}{\boldsymbol{\xi}}_{n+1}}{\partial(\Delta\overset{\leftarrow}{\boldsymbol{\varepsilon}}^{\mathrm{p}})} + \overset{\leftarrow}{\boldsymbol{\mathcal{C}}}^{\mathrm{e}}\,, \tag{7.178}$$

where $\Psi_{n+1} = \Psi(\Delta\overset{\leftarrow}{\boldsymbol{\varepsilon}}^{\mathrm{p}}, \underline{\boldsymbol{\alpha}}_{n+1})$, $\overset{\leftarrow}{\boldsymbol{\xi}}_{n+1} = \partial\Psi(\Delta\overset{\leftarrow}{\boldsymbol{\varepsilon}}^{\mathrm{p}}, \underline{\boldsymbol{\alpha}}_{n+1})/\partial(\Delta\overset{\leftarrow}{\boldsymbol{\varepsilon}}^{\mathrm{p}})$ and $\sigma_{\mathrm{Y}\,n+1} = \sigma_{\mathrm{Y}\,n+1}(\Delta\overset{\leftarrow}{\boldsymbol{\varepsilon}}^{\mathrm{p}}, \underline{\boldsymbol{\alpha}}_{n+1})$. Based on the three previous expressions, it is possible to demonstrate that (Rabahallah *et al.*, 2009):

$$\mathcal{J} : D(\Delta\overset{\leftarrow}{\boldsymbol{\varepsilon}}^{\mathrm{p}}) = \overset{\leftarrow}{\boldsymbol{\mathcal{C}}}^{\mathrm{e}} : D(\Delta\overset{\leftarrow}{\boldsymbol{\varepsilon}})\,, \tag{7.179}$$

which, can be inverted resulting in:

$$D(\Delta\overset{\leftarrow}{\boldsymbol{\varepsilon}}^{\mathrm{p}}) = \mathcal{J}^{-1} : \overset{\leftarrow}{\boldsymbol{\mathcal{C}}}^{\mathrm{e}} : D(\Delta\overset{\leftarrow}{\boldsymbol{\varepsilon}})\,. \tag{7.180}$$

In view of the definition of the consistent elastoplastic tangent modulus, $\overset{\leftarrow}{\boldsymbol{\mathcal{C}}}^{\mathrm{ep}}_{\mathrm{alg}}$, (Eq. (7.174)) one obtains:

$$D\overset{\leftarrow}{\boldsymbol{\sigma}}_{n+1} = \overset{\leftarrow}{\boldsymbol{\mathcal{C}}}^{\mathrm{ep}}_{\mathrm{alg}} : D(\Delta\overset{\leftarrow}{\boldsymbol{\varepsilon}})\,. \tag{7.181}$$

Finally, combining the previous expression with Eq. (7.180) and the incremental form of the hypoplastic law with the addictive elastoplastic split, i.e., $D\overset{\leftarrow}{\boldsymbol{\sigma}}_{n+1} = \overset{\leftarrow}{\boldsymbol{\mathcal{C}}}^{\mathrm{e}} : (D(\Delta\overset{\leftarrow}{\boldsymbol{\varepsilon}}) - D(\Delta\overset{\leftarrow}{\boldsymbol{\varepsilon}}^{\mathrm{p}}))$, the elastoplastic consistent modulus associated with the small-strain incremental problem in Eq. (7.176) is given as follows:

$$\overset{\leftarrow}{\boldsymbol{\mathcal{C}}}^{\mathrm{ep}}_{\mathrm{alg}} = \overset{\leftarrow}{\boldsymbol{\mathcal{C}}}^{\mathrm{e}} - \overset{\leftarrow}{\boldsymbol{\mathcal{C}}}^{\mathrm{e}} : \mathcal{J}^{-1} : \overset{\leftarrow}{\boldsymbol{\mathcal{C}}}^{\mathrm{e}}\,, \tag{7.182}$$

which holds for elastoplastic loadings. In view of the approximations in Eqs. (7.167)-(7.168), one can define an *estimate* for the spatial elastoplastic consistent modulus of the large-strain incremental constitutive problem in Box 7.2, to be evaluated after the solution of the state-update scheme (Box 7.3), as:

$$\bar{\boldsymbol{\mathcal{C}}}^{\mathrm{ep}}_{\mathrm{alg}} \cong \tilde{\boldsymbol{\mathcal{A}}}(f_{n+1}) - \alpha \tilde{\boldsymbol{\mathcal{A}}}(f_{n+1}) : (\boldsymbol{\mathcal{J}}_{\partial \bar{\boldsymbol{\rho}}_\tau / \partial \Delta \boldsymbol{E}^{\mathrm{p}}})^{-1} : \tilde{\boldsymbol{\mathcal{A}}}(f_{n+1}) \text{, with } \alpha = \begin{cases} 1 & \text{if } \Delta\Lambda > 0, \\ 0 & \text{if } \Delta\Lambda = 0, \end{cases} \tag{7.183}$$

where the Jacobian $\boldsymbol{\mathcal{J}}_{\partial \bar{\boldsymbol{\rho}}_\tau / \partial \Delta \boldsymbol{E}^{\mathrm{p}}}$ is that of Eq. (7.157) and is really available from the solution of the return-mapping procedure in Box 7.4 (or Box 7.5). Note that the fourth-order tensor in Eq. (7.183) is conceptually remarkably simple and computationally efficient since it does not require any kinematic or kinetic tensor to be evaluated. Of course, being a straightforward extension of a small-strain hypoelastic constitutive law, one should expect supra-linear rates of asymptotic convergence. Nevertheless, preliminary results have shown excellent convergence rates when employing Eq. (7.183).

The spatial elastoplastic moduli presented above are defied in the material (orthotropy) axes. In the context of the finite element method, these must be rotated back to current configuration axes to define the element stiffness matrices. This operation is given by the rotation operation as follows:

$$\mathcal{C}^{\mathrm{ep}}_{ijkl} = (R^{\mathrm{e}}_{n+1})_{im} (R^{\mathrm{e}}_{n+1})_{jn} \overleftarrow{\bar{C}}^{\mathrm{ep}}_{mnrs} (R^{\mathrm{e}}_{n+1})_{kr} (R^{\mathrm{e}}_{n+1})_{ls} \text{ , } i,j,k,l,m,n = 1,2,3 \tag{7.184}$$

where $\boldsymbol{R}^{\mathrm{e}}_{n+1}$ denotes the updated elastic rotation matrix (Eq. $(7.138)_3$) and $\overleftarrow{\bar{\boldsymbol{\mathcal{C}}}}^{\mathrm{ep}}$ a fourth-order elastoplastic modulus (either tangent or the consistent), and $\boldsymbol{\mathcal{C}}^{\mathrm{ep}}$ the respective tensor represented in the current configuration.

7.2.7 Predict-Correct procedure

As shown in the computational performance study (§6.3), the adoption of a numerical homogenization approach entails to a much higher computational cost compared to analytical counterparts. In this subsection an algorithmic procedure is proposed in order to reduce and, ideally, minimize, the effective computational overhead associated with the adoption of such approach in the context of the FEM framework. The fundamental idea is to approximate the actual macroscopic plastic potentials with heuristically-formulated mixed analytical-numerical functions of the Gurson-type, to be employed in the initial FE equilibrium iterations of a given a (pseudo)-time increment, $[t_n, t_{n+1}]$, in in lieu of the fully-numerical homogenization procedure. Therefore, each time increment involves two stages, in turn associated with two different material models, henceforward coined the *Predict-Correct* procedure. Given a time increment, $[t_n, t_{n+1}]$, and the reference configuration, $\mathcal{B}_n$, the strategy is summarized as follows:

i. The *Predict* (P) phase solves the FE equilibrium problem in order to determine an estimate of the current configuration, $\mathcal{B}^{(\mathrm{P})}_{n+1}$, using a Gurson-type expression as an estimate of the 'actual' plastic behaviour of the porous solid;

ii. The *Correct* (C) phase solves (i.e., corrects) the FE equilibrium problem departing from the approximate configuration $\mathcal{B}^{(\mathrm{P})}_{n+1}$, in order to obtain the current configuration, $\mathcal{B}^{(\mathrm{C})}_{n+1} \equiv \mathcal{B}_{n+1}$, using the numerical-based homogenization model.

The total number of iterations of the increment is therefore the sum of the iterations of the two phases. In practice, only two Correction (C) iterations are typically needed. Based on the work of Benzerga and Besson (2001) and Stewart and Cazacu (2011) on approximate analytical criteria for orthotropic porous solids (Table 3.1), an hybrid analytical-numerical strain-rate potential, to be employed in the Predict phase, $\Psi^{(\mathrm{P})}$, is heuristically formulated as follows[28]:

$$\Psi^{(\mathrm{P})}(\boldsymbol{D}, f) = 2h\left|D_{\mathrm{m}}\right|\left[\frac{\sqrt{1+\gamma^2}-\sqrt{f^2+\gamma^2}}{\gamma}+\ln\left(\frac{1}{f}\frac{\gamma+\sqrt{f^2+\gamma^2}}{\gamma+\sqrt{1+\gamma^2}}\right)\right],\ \text{with}\ \gamma=\frac{h\left|D_{\mathrm{m}}\right|}{\tilde{D}_{\mathrm{e}}} \tag{7.185}$$

where $\tilde{D}_{\mathrm{e}} = \psi(\boldsymbol{D})$ is an equivalent strain-rate quantity, ψ is the dual of the Plunkett *et al.* (2008) criterion (Eq. (4.22)), and h is an upper-bound anisotropy factor estimate, given by:

$$h=\begin{cases} h^{-} & \text{if } \Sigma_{\mathrm{m}}<0 \\ h^{+} & \text{if } \Sigma_{\mathrm{m}}\geq 0 \end{cases}, \tag{7.186}$$

where h^{-} and h^{+} are material parameters evaluated from the purely hydrostatic strain-rate states as:

$$h^{-}=-\frac{\Psi^{+}(-\boldsymbol{I}, f_0)}{\ln(f_0)},\ h^{+}=-\frac{\Psi^{+}(\boldsymbol{I}, f_0)}{\ln(f_0)}, \tag{7.187}$$

and $\Psi^{+}(\cdot)$ is the macroscopic strain-rate potential associated with a given trial field (e.g. Eq. (5.42)) to be determined numerically by computational homogenization (i.e. the direct problem, Box 5.1), f_0 is an arbitrary porosity value, e.g. the initial porosity, and $\boldsymbol{I}$ is the second order identity tensor. It must be emphasised that h depends solely on the plastic behaviour of the matrix, (viz. via $\{k^{(n)}, \boldsymbol{\mathcal{L}}^{(n)}\}$ concerning the Plunkett *et al.* (2008) criterion, Eq. (4.19)), and not on the porosity of the porous solid. The exact dual of the heuristic strain-rate potential in Eq. (7.185) is the Gurson-type potential given by:

$$\Phi^{(\mathrm{P})}(\boldsymbol{\Sigma}, f)=\left(\frac{\tilde{\Sigma}_{\mathrm{e}}}{\sigma_1^{\mathrm{T}}}\right)^2+2f\cosh\left(\frac{3}{h}\frac{\Sigma_{\mathrm{m}}}{\sigma_1^{\mathrm{T}}}\right)-f^2-1, \tag{7.188}$$

where $\Phi^{(\mathrm{P})}$ is the hybrid analytical-numerical macroscopic stress potential and $\tilde{\Sigma}_{\mathrm{e}} = \varphi(\boldsymbol{\Sigma})$ is an equivalent stress obtained from the Plunkett *et al.* (2008) stress potential function, φ (Eq. (4.19)). Since $\Phi^{(\mathrm{P})}$ is known in closed-form, the determination of the macroscopic equivalent stress is trivial and thus there is no need to solve an inverse problem based on $\Psi^{(\mathrm{P})}$ (see Box 5.3) in order to determine if the current stress state is elastic or elastoplastic. Nevertheless, in view of the adopted return-mapping scheme (e.g. Eq. (7.151)), the plastic correction problem of the Predict phase is grounded on $\Psi^{(\mathrm{P})}$ (rather than $\Phi^{(\mathrm{P})}$).

If the matrix plastic behaviour is considered constant (e.g. no texture or SD effects evolution), then h must be evaluated only once, at the beginning of simulation, and saved as a material constant. If, on the contrary, the constitutive parameters evolve during the simulation, e.g., as a function of an accumulated plastic work or strain quantity, $\bar{\epsilon}$, $\{k^{(n)}(\bar{\epsilon}), \boldsymbol{\mathcal{L}}^{(n)}(\bar{\epsilon})\}$, then $h = h(\bar{\epsilon})$ can be readily determined by fitting piecewise polynomials, (or any other fitting function for that matter), to the discrete number of

[28] Exceptionally, the notation of Chapter 5 is again recovered in the following in order to distinguish micro- and macroscopic quantities in the context of porous media.

points $h_i(\bar{\epsilon}_i)$, $i=1,...,N$, determined *a priori* by simply performing $2N$ homogenizations (Eq. (7.187)) at the beginning of the simulation. The proposed Predict-Correct procedure is especially advantageous (but not limited to) FE analyses with frictional contact (mixed system of equations) where the majority of equilibrium iterations are due to the equilibrium of the bodies in contact. In this case, the usage of a simplified, much less computationally demanding, material model in the initial equilibrium iterations is recommended. In the following, two application examples show that this strategy greatly speeds up FE analyses grounded on numerical homogenization of porous media.

7.3 Numerical examples

In this subsection the applicability of the proposed strain-rate-based computational homogenization formulation to model the damage process of ductile porous solids is demonstrated. The robustness and performance of the algorithms developed in §7.2 is assessed. It should be emphasized that the goal here is not to predict fracture accurately[29], but to demonstrate the pertinence and the merits of the numerical approach followed in this work. Two application examples of distinct complexity are analysed. The first example, of introductory character, consists of a quasi-static uniaxial tensile test. The second example, of more industrial interest, deals with a cylindrical cup-drawing test. To that end, the hyperelastic-based orthotropic elastoplastic model presented in the previous subsection (§7.2) has been implemented into an academic FE research code (DD3IMP, University of Coimbra). A selective reduced integration technique, alias $\bar{B}$ -method, is used (e.g. de Souza Neto *et al.*, 2011). In this subsection the focus is solely on the homogenization formulation based on the Rice and Tracey (1969) fields (Eq. (5.42)). All numerical simulations are executed on a computer equipped with an Intel® Core™ i7-8700K (6C/12T) CPU on a 64-bit Windows 10 Pro for Workstations operating system.

7.3.1 Uniaxial tensile test

The uniaxial tensile test simulations are performed based on the sub-sized ASTM E8 specimen. Due to geometrical symmetry conditions and the assumption of orthotropy, only one eighth of the specimen is modelled. The geometry, coordinate system and relevant dimensions of the employed dogbone specimen are depicted in Figure 7.3. The length of the grip section of the actual ASTM E8 specimen was truncated for computational efficiency. Symmetry boundary conditions in the three mutually orthogonal planes are applied. A quasi-static axial displacement $u_x = 1.5$ mm is prescribed to the nodes of the grip section free surface and the displacement of these is constrained along the transverse directions ($u_y = u_z = 0$). This ensures that the stress and strain fields are homogeneous in the gauge section until the initiation of localized neck. The specimen gauge area is discretized with a structured regular mesh (see Figure 7.3). Conversely, the adjacent area is discretized with a coarse unstructured mesh given the small plastic deformation in this region. The structured zone is discretized with 50×12 (length × width) partitions in the plane of the sheet. Two through-thickness layers are considered. The FE mesh consists of a total of 1388 eight-node hexahedral SRI finite elements and a total of 2313 nodes.

[29] Indeed, this would imply the usage of some void coalescence criterion and a regularization method. This topic is discussed in more detail in the concluding remarks of the present chapter (§7.4).

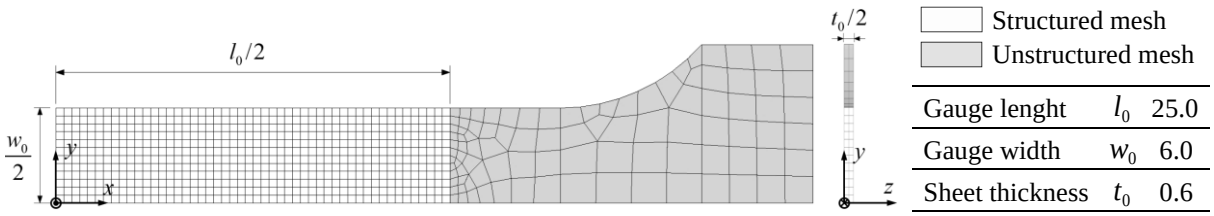

Gauge lenght	l_0	25.0
Gauge width	w_0	6.0
Sheet thickness	t_0	0.6

Figure 7.3 FE mesh of the tension test specimen in the reference configuration, $\mathcal{B}_0$.

The Ti-6Al-4V titanium alloy is selected in the present example. This is the most prevalent Ti alloy, applied in many industrial fields (viz., aerospace, military/defence and biomedical, see also §4.5.2). The elastic and plastic constitutive data is adapted from Tuninetti *et al.* (2015). These authors performed a thorough characterization of the quasi-static room temperature mechanical behaviour of a weakly-textured Ti-6Al-4V alloy ingot. Both tension and compression uniaxial tests were performed in the three material orthotropy directions. Tuninetti *et al.* (2015) applied the experimental data to characterize plastic yielding according to the quadratic form of the CPB06 criterion (a single linear transformation) for five of plastic work levels in order to capture texture evolution and twinning-detwinning effects. Here, the focus is on the initial yielding behaviour of the alloy. In addition to plastic anisotropy, these authors also reported anisotropic elastic properties (recall discussion in §7.1.3 on the occurrence of anisotropic elasticity in hcp structure metals). No experimental data is available for the orthotropic Poisson ratios, υ_{ij}, and shear moduli, G_{ij}, $i,j=1,2,3,\ i\neq j$. Estimates for these are therefore estimated as follows: the former are determined such that the non-diagonal terms of the orthotropic compliance tensor $(-\upsilon_{ij}/E_{ii}$, $i,j=1,2,3,$ Eq. (7.38)) are equal to a pseudo-isotropic term: $-\overline{\upsilon}/\overline{E},$ where $\overline{E}=(E_{11}+E_{22}+E_{33})/3$ is an averaged Young modulus and $\overline{\upsilon}$ is a prescribed pseudo-isotropic Poisson ratio. In the same vein, an averaged shear modulus, $\overline{G}=\overline{E}/2(1+\overline{\upsilon})$ is defined and assigned to the shear moduli G_{ij}, $i,j=1,2,3.$ The degradation of the elastic proprieties is modelled with a linear weakening factor, $\omega_1(f),$ (see Eq. (7.59)). The isotropic hardening of the matrix is described by a combined Swift-Voce law as follows:

$$Y(\overline{\epsilon}^{\mathrm{p}}_{\mathrm{M}})=\alpha Y_{\mathrm{Swift}}(\overline{\epsilon}^{\mathrm{p}}_{\mathrm{M}})+(1-\alpha)Y_{\mathrm{Voce}}(\overline{\epsilon}^{\mathrm{p}}_{\mathrm{M}})\,, \tag{7.189}$$

with

$$Y_{\mathrm{Swift}}(\overline{\epsilon}^{\mathrm{p}}_{\mathrm{M}})=K(\varepsilon_0+\overline{\epsilon}^{\mathrm{p}}_{\mathrm{M}})^n,\ Y_{\mathrm{Voce}}(\overline{\epsilon}^{\mathrm{p}}_{\mathrm{M}})=Y_0+(Y_{\mathrm{sat}}-Y_0)(1-e^{-C_{\mathrm{Y}}\overline{\epsilon}^{\mathrm{p}}_{\mathrm{M}}})\text{, and } Y(0)=\sigma_1^{\mathrm{T}}, \tag{7.190}$$

where α is the linear weighting factor of the mixture rule, $\{K,\varepsilon_0,n\}$ are the Swift law parameters, and $\{Y_0,Y_{\mathrm{sat}},C_{\mathrm{Y}}\}$ are the Voce law parameters. The initial porosity and nucleation parameters are based on those typically found in the literature (Aravas, 1987; Benseddiq and Imad, 2008; Tvergaard and Needleman, 1984). Stress-controlled nucleation is neglected. Table 7.1 summarizes the employed material parameters. Following the guidelines of Figure 5.4 and Figure 5.6, the spherical RVE is discretized with $(N,\overline{n}_{\mathrm{r}})=(328,16)$ in order to verify a cubature error in the order of $e=10^{-6}$.

Table 7.1 Material coefficients for the Ti-6Al-4V alloy (partially after Tuninetti *et al.*, 2015).

Elasticity (orthotropic)

Young moduli [GPa]			Shear moduli [GPa]	Poisson ratios [-]			
E_{11}	E_{22}	E_{33}	$G_{23}=G_{13}=G_{12}$	υ_{23}	υ_{13}	υ_{12}	$\bar{\upsilon}$
108	111	113	41.3	0.341	0.332	0.332	(0.34)

Plasticity: *matrix behaviour*

CPB06 parameters ($a=2$)

k	C_{11}	C_{12}	C_{13}	C_{22}	C_{23}	C_{33}	$C_{44}=C_{55}=C_{66}$
-0.136	1.0	-2.495	-2.928	-2.283	1.284	-2.446	4.015

Isotropic hardening

Weighting factor	Swift type law			Voce type law			
α [-]	K [MPa]	ε_0 [-]	n [-]	Y_0 [MPa]	Y_{sat} [MPa]	C_Y [-]	$Y(0)$ [MPa]
0.6154	1174.4	0.0154	0.038	806.7	1084.8	12.045	927

Porosity

Initial porosity	Critical porosity	Strain-controlled nucleation		
f_0	f_C	f_N	$\bar{\epsilon}_N$	s_N
0.0001	0.1	0.01	0.3	0.1

Figure 7.4 depicts several cross sections of the macroscopic yield surface in the principal stress space with varying hydrostatic level as predicted by the mixed numerical-analytical heuristic model (HM) and the computational homogenization model (CHM). Due to the weak texture and tention-compression assymetry of the studied Ti-6Al-4V alloy, the yield surface exhibits only mild asymmetry with respect to the origin. Furthermore, the shape change along the hydrostatic axis of the latter criterion is small.

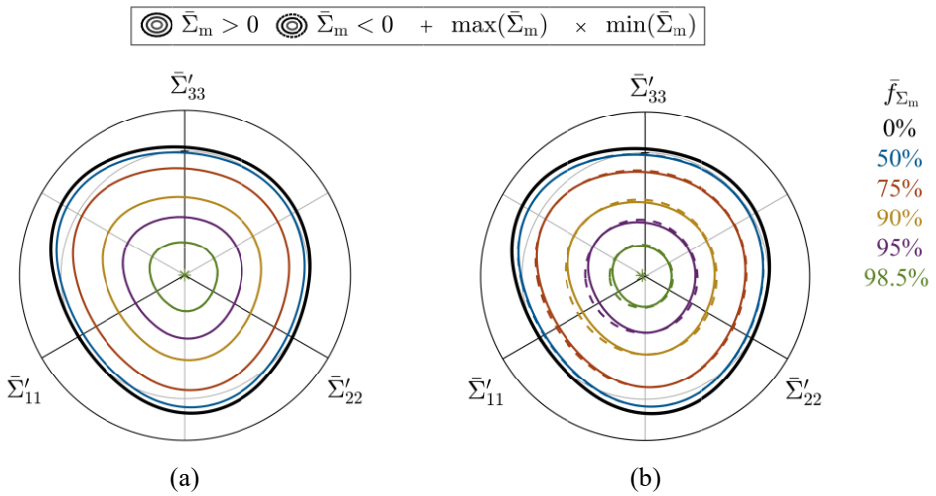

Figure 7.4 π-plane representation of the macroscopic stress potential (Eq. (5.45)) unitary isovalue surface in the principal stress space of the Ti-6Al-4V porous alloy with $f_0 = 0.01$ according to: (a) HM; (b) CHM. Cross sections with varying hydrostatic fraction are plotted with a fraction $\bar{f}_{\Sigma_m} = \{0.5, 0.75, 0.9, 0.95, 0.985\}$ with respect to the tensile and compressive hydrostatic extreme values. The location of the latter is represented with markers.

Uniaxial tensile test simulations are carried out along the three orthotropic directions (RD, TD, ND) considering four plasticity formulations: (i) the dense model (Eq. (4.22)), for which plastic incompressibility holds and thus the macroscopic behaviour is that of the matrix phase (i.e., the particular case of no porosity); (ii) the Gurson (1977) spherical-void-based model (Eq. (3.9)); (iii) the mixed numerical-analytical heuristic model (HM) (Eq. (7.185)); and (iv) the computational homogenization (CH) model (CHM) developed in Chapter 5, using the Predict-Correct strategy described in §7.2.7. The hyperelastic strain-rate-based state-update formulation described in the previous subsection (§7.2) is used in all four models. The Gurson model was purposely implemented as a particular case of the HM, viz., using the quadratic form of the Cazacu *et al.* (2006) criterion to compute the von Mises equivalent stress measure.

Table 7.2 compares the computational performance of the simulations for each material model. It is concluded that the simulation using the CH model is about 85 times more expensive than that using the mixed numerical-analytical model (HM). This is actually a reasonable ratio since the underlying state-update scheme of the former model is $\mathcal{O}(1000)$ times more costly than that of latter (recall the study in §6.3, viz., Figure 6.14). Note moreover that the computational time using the (orthotropic) HM is virtually the same than that using the (isotropic) Gurson model. This is due to the fact that the matrix phase behaviour is modelled via the quadratic form of the Cazacu *et al.* (2006) criterion, using a single orthotropic transformation. It is shown that under these conditions orthotropy and tension-compression asymmetry of the matrix have a negligible impact on the convergence rate, and thus the computational time of the simulation[30].

Table 7.2 Computational performance measurements of the uniaxial tensile test simulations along the RD for the four plasticity models: dense (CPB06) (Eq. (4.22)); Gurson (1977) (Eq. (3.9)); heuristic model (HM) (Eq. (7.185)); and the computational homogenization model (CHM) (Chapter 5).

		Dense	Gurson	HM	CHM
No. of increments		52	53	53	53
Computational time	Absolute [s]	22	47	47	4030
	Relative	0.47	1.0	1.0	85.74

Figure 7.5 represents the pre-necking true stress-strain curves of the monotonic uniaxial tensile tests in the three orthotropy directions (RD, TD, ND) as predicted by the CHM. The onset of necking (final value of the curve) was estimated applying the Considère criterion. The results of the CHM are in good agreement with the experimental data. It should be noted that the experimental curve was obtained on axisymmetric specimens which are less prone to localization and thus are able to achieve a higher axial strain before the occurrence of a localized neck. While the anisotropy of the elastic moduli is mild, the elastic strains reached in the Ti-6Al-4V alloy are actually significant given the relatively low stiffness-to-strength ratio of these materials. Therefore, it may be appropriate to account for elastic anisotropy if one intends to model elastic recovery processes, e.g. springback analyses.

[30] A completely opposite finding will be encountered in the second example of this subsection which concerns a non-quadratic plasticity model with multiple linear transformations.

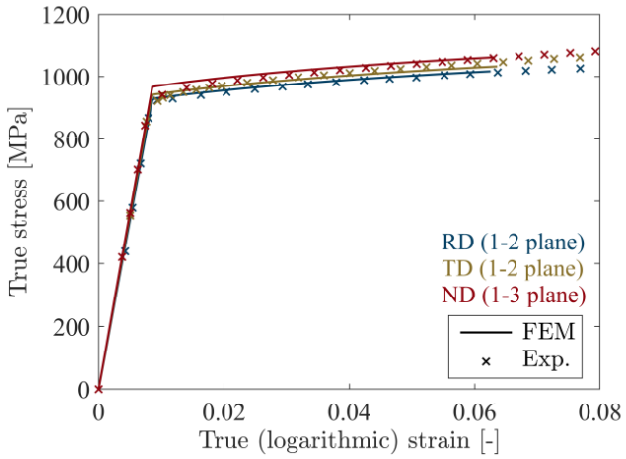

Figure 7.5 FE results of the true stress-strain curves for the uniaxial tensile response of the Ti-6Al-4V alloy in the three orthogonal material directions (RD, TD, ND) using the CHM. Experimental data on axisymmetric specimens at room temperature with a constant 10^{-3} s^{-1} strain rate (after Tuninetti *et al.*, 2015).

Figure 7.6 represents engineering stress-strain curves of the monotonic uniaxial tensile tests along the RD as predicted by each plasticity model. It is shown that the models predict a similar evolution. This is due to the small initial porosity of the alloy. Only in the post-necking regime the porous criteria predict a more severe softening due to the increase of the void growth and nucleation rates in the localization band, in turn resulting from the development of a triaxial stress state in this zone.

In order to further assess the predictions of the considered plasticity models, the distribution of some important fields is analysed Figure 7.7 represents the distribution of the porosity in the gauge section of the uniaxial specimen at a displacement $u_x = 1.4$ mm (with respect to $l_0/2$) as predicted by the Gurson (1977) model, the HM and the CHM. It is shown that these formulations lead to remarkably similar results regarding the distribution of the porosity. In fact, consistent with the results in Figure 7.6, the Gurson (1977) model predicts the greatest porosity in the centre of the specimen, which suggests that the (weak) anisotropy and/or tension-compression asymmetry of the Ti alloy is actually hindering damage accumulation at this stage. Of all models, the HM predicts the lowest porosity in the centre of the specimen, which is also in agreement with the trends of Figure 7.6.

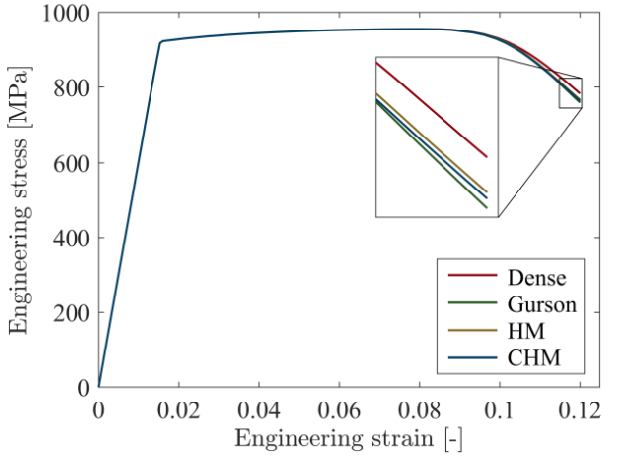

Figure 7.6 FE results of the engineering stress-strain curves (normalized force-displacement curves) for the uniaxial tensile tests along RD (1-2 plane) using: the dense model (CPB06); the Gurson (1977) model; the heuristic model (HM); and the computational homogenization model (CHM).

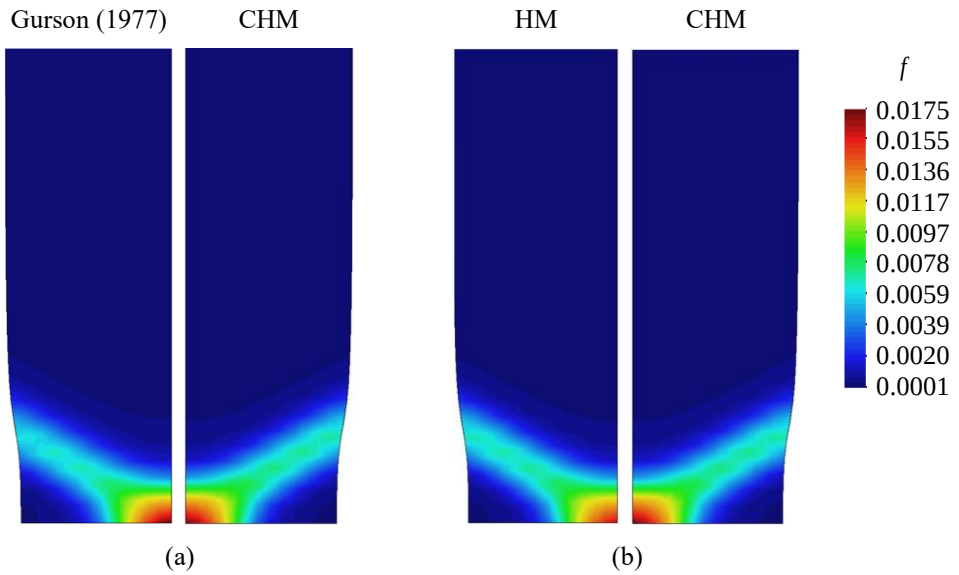

Figure 7.7 Comparison of the porosity isocontours at the gauge section of the specimen ($z = 0$), at instant $u_x = 1.4$ mm, as predicted by: (a) the Gurson (1977) model; and (b) the heuristic model (HM), with the results using the computational homogenization model (CHM).

The distribution of the normalized hydrostatic stress (normalized by the initial yield stress, $\sigma_1^T = Y(0)$), is represented in Figure 7.8, as predicted by the dense model (dual of the CPB06 criterion), the HM and the CHM. It is concluded that while the HM and the CHM display identical results, the dense model predicts a much higher hydrostatic stress (thus strain-rate) state within the localization band. This is related with the plastic incompressibility condition in the dense model, as the total hydrostatic/volumetric deformation must be accommodated exclusively by elasticity. In contrast, porous solids are plastic compressible, thus the volumetric component of the deformation gradient tensor can be distributed into elastic (reversible) and plastic (dissipated) parts, ultimately reducing the stored elastic energy.

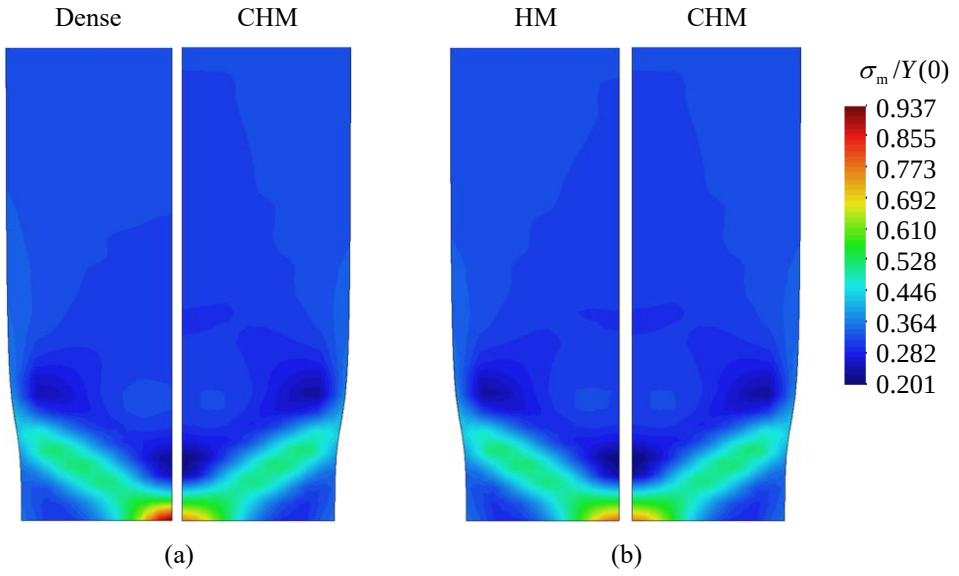

Figure 7.8 Comparison of the normalized hydrostatic stress isocontours at the gauge section of the specimen ($z = 0$), at instant $u_x = 1.4$ mm, as predicted by: (a) the Gurson (1977) model; and (b) the heuristic model (HM), with the results using the computational homogenization model (CHM).

This behaviour is illustrated in Figure 7.9 and Figure 7.10, which represent isovalue distributions of the determinants of the elastic, J^{e}, plastic, J^{p}, and the total deformation gradient, $J = J^{p}J^{e}$, (Eq. (7.25)) for the dense model and the CHM, respectively, Note that the predicted J^{e} of the dense model is indeed larger than that of the CHM in the centre of the specimen. Nevertheless, the total volume deformation, quantified by $J = J^{p}J^{e}$, is much larger for the CHM, due to the volumetric plastic deformation.

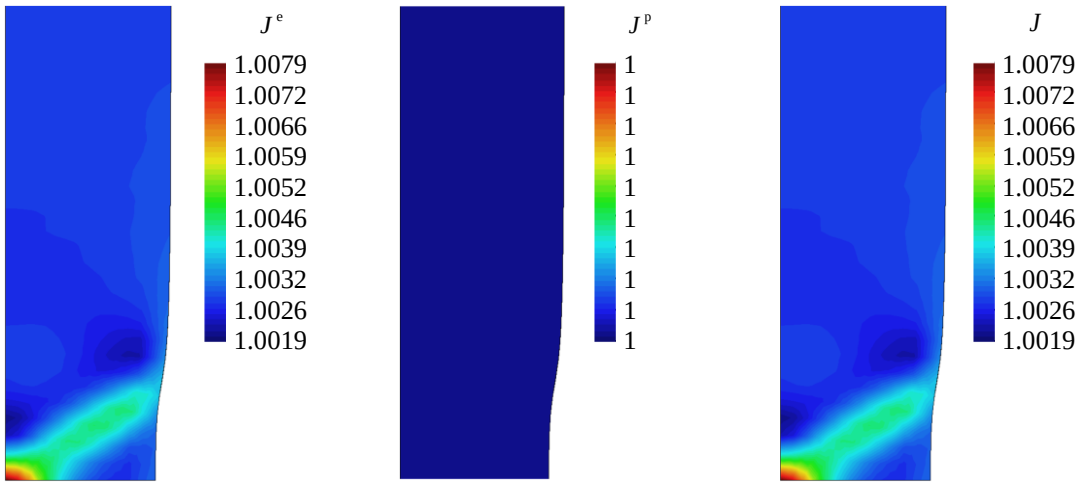

(a) (b) (c)

Figure 7.9 Isocontours of the determinant of the elastic, plastic, and total deformation gradients, J^{e}, J^{p}, and $J = J^{p}J^{e}$, respectively, at the gauge section of the specimen $(z = 0)$, at instant $u_x = 1.4$ mm, as predicted by the dense model (CPB06).

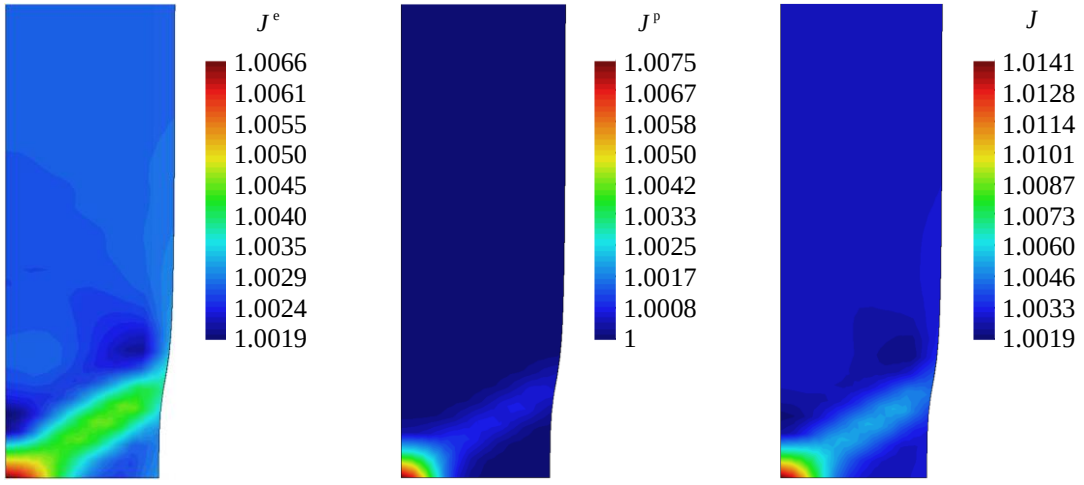

(a) (b) (c)

Figure 7.10 Isocontours of the determinant of the elastic, plastic, and total deformation gradients, J^{e}, J^{p}, and $J = J^{p}J^{e}$, respectively, at the gauge section of the specimen $(z = 0)$, at instant $u_x = 1.4$ mm, as predicted by the computational homogenization model (CHM).

The present application example showed that the HM in Eq. (7.185) led to quite similar results when compared to those of the full homogenization solution obtained with the CHM (Chapter 5), while being much less demanding from the computational viewpoint. It must be point out however that this example dealt with a weakly textured material for which the HM shown a good fit to the actual behaviour of the porous alloy (see Figure 7.4). Moreover, the considered monotonic uniaxial stress states are not representative of most loading paths found in engineering applications. The next application example deals with more complex material behaviour and loading conditions in order to better assess the accuracy of the HM with respect to the CHM.

7.3.2 Cylindrical cup drawing test

The second example considers the simulation of the cylindrical cup drawing process in order to study the earing profile and damage distribution of a strongly textured sheet. Deep drawing refers to a class of sheet metal forming operation in which a flat metal sheet (the blank) is radially drawn into a die by the action of a punch resulting in a three-dimensional shape. This near-net-shape technology is widely used in industries such as automotive, naval, beverage can, as well as in domestic and decorative applications. Due to its industrial relevance and geometrical simplicity, the cylindrical cup drawing process is one of the most frequently used benchmarks of assess the performance of constitutive models. Material anisotropy often leads to earing phenomena, i.e., the undulation of the top-edge of the fully drawn cup. Depending on the texture degree, four, six or more ears may result from the drawing process. A schematic view of a typical cylindrical cup drawing setup is shown in Figure 7.11.

In this subsection, the cup drawing test of a strongly textured AA5042-H2 aluminium sheet reported in Yoon *et al.* (2010) is considered. The process parameters and the dimensions of the tools are given in Table 7.3. Due to geometric and material symmetry conditions of the cup drawing process, only one quarter of the model is analysed. For computational efficiency, the blank (one-quarter) is divided in two zones: a central zone which contacts with the flat region of the punch (and therefore experiences virtually no plastic deformation); and an outer zone where large deformations occur. Accordingly, the former is discretized with a relatively coarse unstructured mesh, and the latter is discretized with a fine structured mesh as shown in Figure 7.12. The structured zone is discretized with a 30×28 (radial × circumferential) partition in the plane of the sheet. Two layers along the thickness direction (ND) are used. The FE mesh consists of a total of 1896 eight-node hexahedral SRI finite elements and a total of 3012 nodes. The tools are modelled as analytical rigid bodies with their surface modelled by Nagata patches (Neto *et al.*, 2014). The friction between the sheet and the tools is assumed constant, described by the classical Coulomb's law with a friction coefficient $\mu = 0.008$ (after Yoon *et al.*, 2010). The contact problem is regularized through the augmented Lagrangian method (Alart and Curnier, 1991).

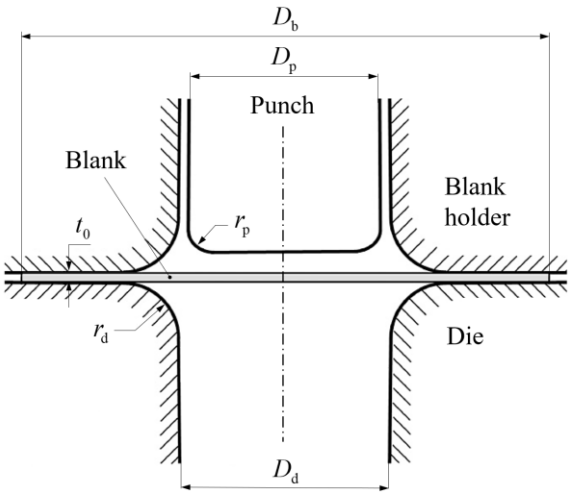

Figure 7.11 Schematic view of the cylindrical cup drawing process (adapted from Yoon *et al.*, 2004).

Table 7.3 Process parameters and the dimensions of the tools (after Yoon *et al.*, 2010).

Parameter		Value	
Blank diameter	D_b	76.07	[mm]
Die opening diameter	D_d	46.74	[mm]
Punch diameter	D_p	45.72	[mm]
Die profile radius	r_d	2.28	[mm]
Punch profile radius	r_p	2.28	[mm]
Initial blank thickness	t_0	0.274	[mm]
Punch stroke	u_p	22.75	[mm]
Blank-holder force (total)	f_{bh}	10.0	[kN]

Both the experimental and constitutive identification of the yielding behaviour of the AA5042-H2 alloy are extracted from Yoon *et al.* (2010). These authors used the non-quadratic form of the Plunkett *et al.* (2008) yield criterion using two transformations (alias CPB06ex2) to characterize the anisotropic behaviour of the sheet for three levels of plastic work. Similarly to the previous example (§7.3.1), only the initial yielding behaviour of the alloy is considered. Figure 7.13 shows the evolution of the normalized uniaxial tensile yield stress and *r*-values in the plane of the sheet as captured by the CPB06ex2 criterion as well as the respective experimental data. Note that while the anisotropy of the yield stresses is mild, the evolution of *r*-value is extremely anisotropy: the *r*-value along the TD is about five times that of along the RD. The elastic behaviour is assumed isotropic and constant, i.e., the degradation of the elastic modulus is neglected (unitary weakening factor, $\omega_\infty = 1$, Eq. (7.59)). The isotropic hardening of the matrix material is described by the Voce-type law (Eq. (7.190)). Strain-controlled nucleation is considered, yet stress-controlled nucleation is neglected. Table 7.4 summarizes the parameters of the material model. The RVE cubature parameters are set to $(N, \bar{n}_r) = (706,14)$ in order to verify a maximum cubature error $e = 10^{-4}$.

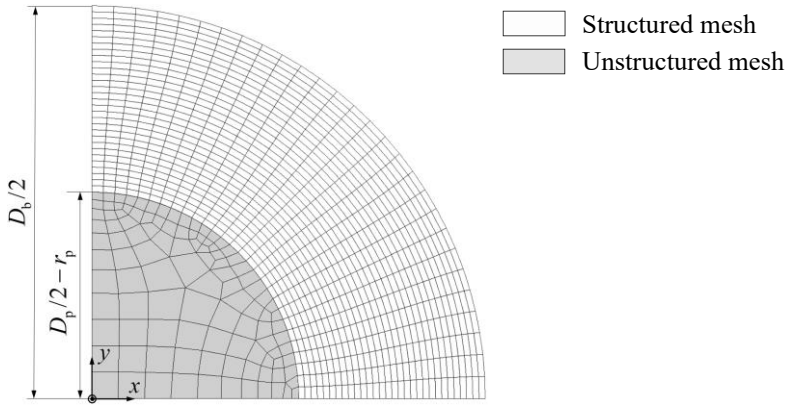

Figure 7.12 FE mesh of the blank in the reference configuration, $\mathcal{B}_0$. Two through-thickness layers are used.

Figure 7.14 represents cross sections of the macroscopic yield surface in the principal stress space with varying hydrostatic level as predicted by the HM and the CHM. The yield surface of the latter model exhibits a remarkable asymmetry with respect to the purely deviatoric plane (it is however symmetric with respect to the origin). Note that this is a result of the matrix anisotropy alone (indeed, tension-compression asymmetry is assumed null for this Al alloy). Moreover, the shape change along the hydrostatic axis of the is very pronounced.

Table 7.4 Material coefficients for the AA5042-H2 alloy (partially after Yoon *et al.*, 2010).

Elasticity (isotropic)

Young moduli [GPa]	Poisson ratio [-]
E	υ
68.9	0.33

Plasticity: *matrix behaviour*

CPB06ex2 parameters ($a = 10$)

$k^{(1)}$	$C_{11}^{(1)}$	$C_{12}^{(1)}$	$C_{13}^{(1)}$	$C_{22}^{(1)}$	$C_{23}^{(1)}$	$C_{33}^{(1)}$	$C_{44}^{(1)}$	$C_{55}^{(1)}$	$C_{66}^{(1)}$
0.0	1.0	-0.0272	-0.6011	1.2870	0.6864	-0.2736	1.0	1.0	1.1514
$k^{(2)}$	$C_{11}^{(2)}$	$C_{12}^{(2)}$	$C_{13}^{(2)}$	$C_{22}^{(2)}$	$C_{23}^{(2)}$	$C_{33}^{(2)}$	$C_{44}^{(2)}$	$C_{55}^{(2)}$	$C_{66}^{(2)}$
0.0	1.0	-0.0897	0.0112	1.1322	-0.1092	-1.2009	1.0	1.0	1.3093

Isotropic hardening

Voce law

Y_0 [MPa]	Y_{sat} [MPa]	C_Y [-]
267.80	375.08	17.859

Porosity

Initial porosity	Critical porosity	Strain-controlled nucleation		
f_0	f_C	f_N	$\bar{\epsilon}_N$	s_N
0.001	0.1	0.01	0.3	0.1

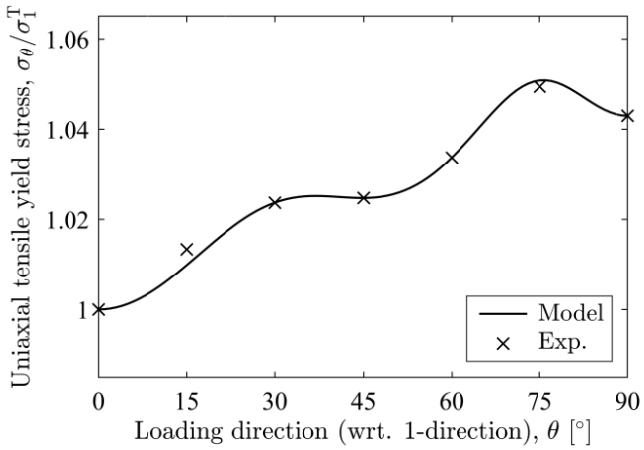

(a)

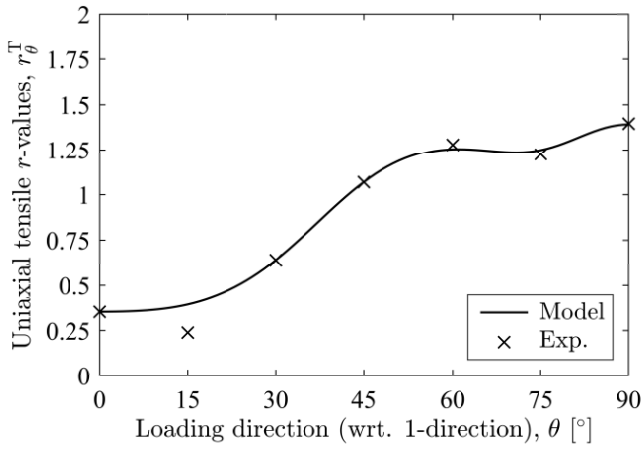

(b)

Figure 7.13 Uniaxial tensile behaviour of the AA5042-H2 matrix (dense phase) in the plane of the sheet as predicted by the CPB06ex2 criterion (and its dual, Eq. (4.22)): (a) normalized yield stresses; (b) *r*-values. Comparison with experimental data (after Yoon *et al.*, 2010). Note the extreme variation of the *r*-values.

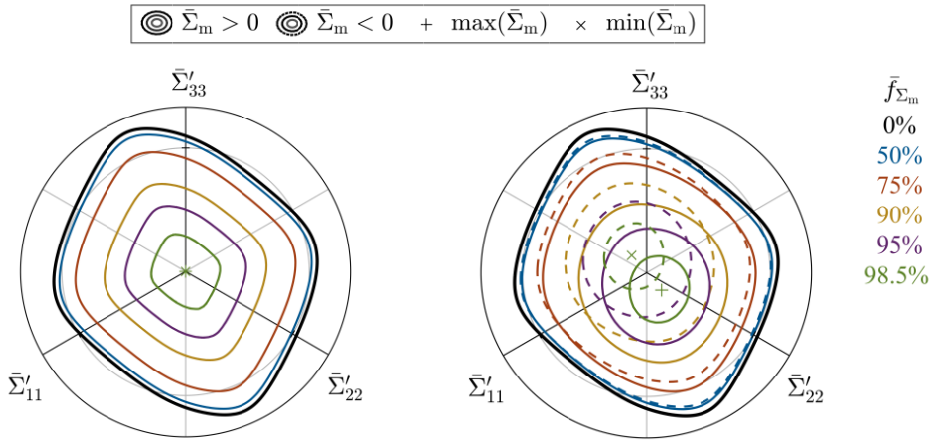

(a) (b)

Figure 7.14 π-plane representation of the macroscopic stress potential (Eq. (5.45)) unitary isovalue surface in the principal stress space for a AA5042 porous alloy with $f_0 = 0.01$ according to: (a) HM; (b) CHM. Cross sections with varying hydrostatic fraction are plotted with a fraction $\bar{f}_{\Sigma_{\mathrm{m}}} = \{0.5, 0.75, 0.9, 0.95, 0.985\}$ with respect to the tensile and compressive hydrostatic extreme values. The location of the latter is represented with markers.

Likewise the previous numerical example, the simulation of the cup drawing test is carried out using four plasticity formulations: (i) the dense model (dual of the CPB06ex2 criterion, Eq. (4.22)); (ii) the Gurson (1977) spherical-void-based model (Eq. (3.9)); (iii) the mixed numerical-analytical heuristic model (HM) (Eq. (7.185)); (iv) the computational homogenization model (CHM) proposed in Chapter 5, using the Predict-Correct strategy described in §7.2.7.

Table 7.5 compares the computational performance of the simulations for each material model. It is concluded that the simulation using the CHM is $\mathcal{O}(30)$ times more costly than that using the numerical-analytical model (HM) for the considered cubature tolerance. This ratio greatly beats that of the previous example. This is explained by: (i) the small number of Correction (C) FE equilibrium iterations in each time increment compared to those of the Predict (P) stage (§7.2.7), since the contact problem is mostly solved in the P-stage; and (ii) the relaxed cubature tolerance. In contrast to the first application example, the computational effort using the (orthotropic) HM is now much larger than that using the (isotropic) Gurson model. The reasons are as follows: (i) the evaluation of the strain-rate potential at the microscale (Box 4.1) is much more challenging for non-quadratic criteria $(a \neq 2)$, since the Jacobian of the system of equations in Box 4.2 needs to be regularly updated in order to achieve convergence; (ii) two transformations entail nearly twice as many operations in Box 4.2 (e.g. eigendecomposition, matrix multiplication), since the computational effort for evaluating the local strain-rate potential increases quasi-linearly with the number of orthotropic transformations.

Figure 7.15 shows the deformed configurations of the FE model at intermediate punch displacements up to the completely drawn cup after elastic recovery (springback) as predicted by the CHM. Note that eight ears of varying height are predicted. This is in agreement with the experimental data as discussed in the following.

Table 7.5 Computational performance measurements of the cup drawing test simulations for the four plasticity models: dense (CPB06) (Eq. (4.22)); Gurson (1977) (Eq. (3.9)); heuristic model (HM) (Eq. (7.185)); and the computational homogenization model (CHM) (Chapter 5).

		Dense	Gurson	HM	CHM
No. of increments		129	121	133	124
Computational time	Absolute [h]	2.73	0.18	2.04	46.97
	Relative	1.34	0.087	1.0	31.85

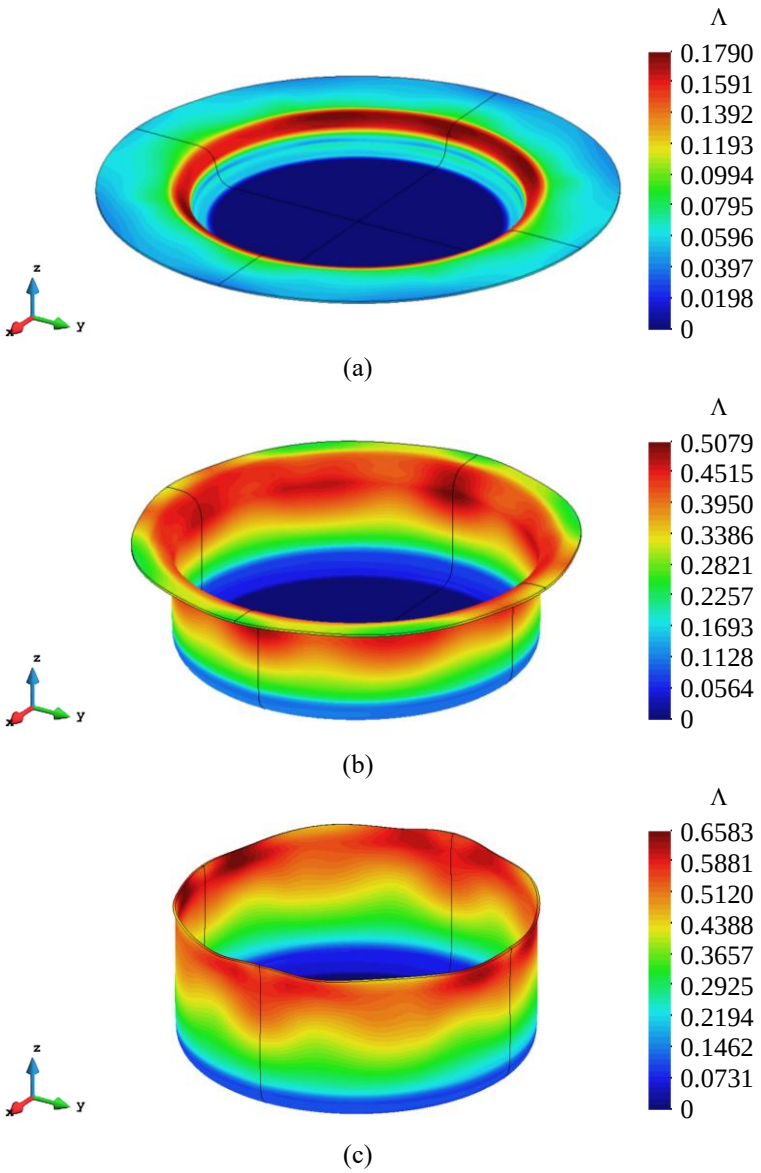

Figure 7.15 Drawing process of the AA5042-H2 cup at a punch displacement: (a) $u_p = 5$ mm; (b) $u_p = 15$ mm; (c) $u_p = 22.75$ mm (completely drawn cup). Isocontours of the accumulated equivalent plastic strain, $\Lambda = \int \dot{\Lambda} dt$.

The punch force-displacement evolutions obtained in each FE simulation are depicted in Figure 7.16. Negligible differences are observed between the criteria accounting for the matrix orthotropy. The curve corresponding to the Gurson model is a lower bound throughout the drawing process. Unfortunately, no experimental data is available to quantitatively assess the force-displacement predictions. Figure 7.17 compares the experimental and the theorical earing profiles according to each model. In agreement with the experimental procedure of Yoon *et al.* (2010), the earing profile was measured from the bottom to the edge of the completely drawn-cup after springback. The experimental earing profile of the cylindrical cup shows eight ears. This behaviour is indeed captured by the formulations accounting for the matrix orthotropy. Conversely, the Gurson model does not predict earing, as expected. While the dense model predicts the correct number of ears, their height is overestimated. The HM and the CHM present remarkably similar predictions of the earing profile and are in overall better agreement with the experimental curve.

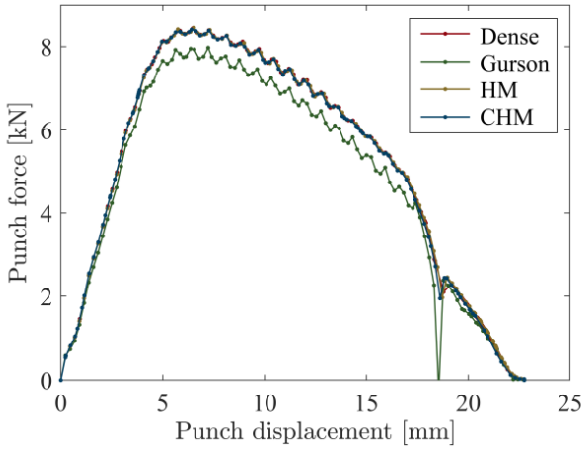

Figure 7.16 FE results of the punch force-displacement curves using: the dense model (CPB06ex2); the Gurson (1977) model; the heuristic model (HM); and the computational homogenization model (CHM).

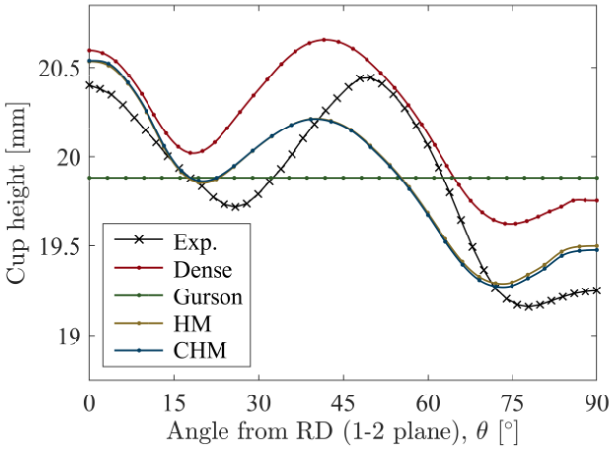

Figure 7.17 FE results of the earing profile of the AA5042-H2 cup using: the dense model (CPB06ex2); the Gurson (1977) model; the heuristic model (HM); and the computational homogenization model (CHM). Comparison with the experimental data (after Yoon *et al.*, 2010).

In the following, the distribution of some fields is analysed in order to further compare the predictions of the considered models. Figure 7.18 and Figure 7.19 represent the distribution of the accumulated equivalent plastic strain, $\Lambda = \int \dot{\Lambda} dt$, (Eq. (7.133)) and the von Mises equivalent stress, $\|\boldsymbol{\sigma}\|_{\mathrm{vM}}$, respectively, as predicted by each orthotropic criterion: the dense model, the HM and the CHM. It is shown that these models predict nearly equal results. This observation is somewhat surprising given the outstandingly different material characterization displayed in Figure 7.14 regarding the HM and CHM. This is thought to be explained by the considered low initial porosity of the AA5042-H2 alloy and the moderate stress (and thus strain-rate) triaxiality states during the drawing process. The predicted porosity distribution of the fully drawn cup is represented in Figure 7.20 for each porous criterion. Again, the HM and the CHM present identical results: porosity concentrates along RD at the about mid-height of the cylindrical wall. The Gurson model predicts a lower porosity in this zone.

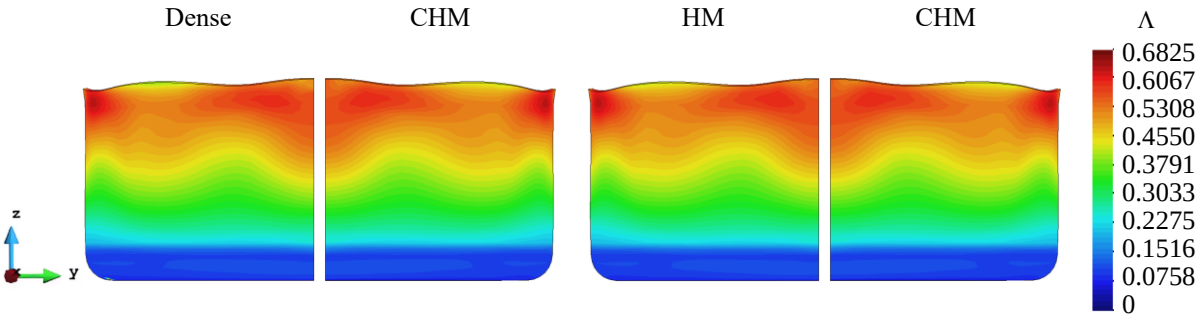

Figure 7.18 Comparison of the accumulated equivalent plastic strain, $\Lambda = \int \dot{\Lambda} dt$, isocontours of the completely drawn cup as predicted by: (a) the dense model (CPB06ex2); and (b) the heuristic model (HM); with the FE results using the computational homogenization model (CHM).

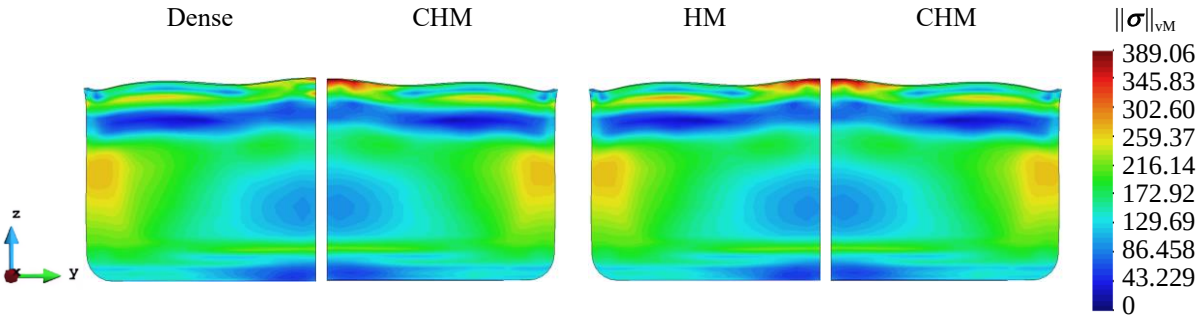

Figure 7.19 Comparison of the von Mises equivalent stress [MPa] isocontours of the completely drawn cup as predicted by: (a) the dense model (CPB06ex2); and (b) the heuristic model (HM); with the FE results using the computational homogenization model (CHM).

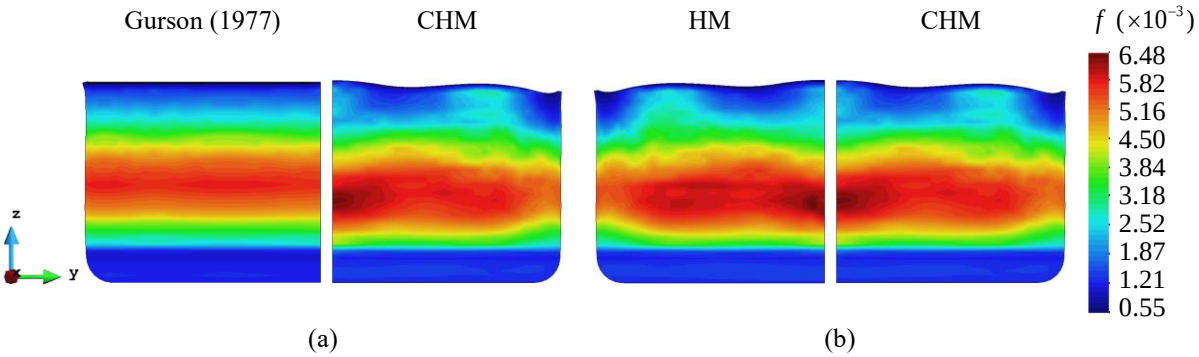

Figure 7.20 Comparison of the porosity isocontours of the completely drawn cup as predicted by: (a) the Gurson (1977) model; and (b) the heuristic model (HM); with the FE results using the computational homogenization model (CHM).

7.4 Concluding remarks

It is important to highlight that the constitutive framework proposed in this chapter (summarized in Box 7.1 and Box 7.2 regarding the rate form and its incremental form, respectively) for describing the elastoplastic behaviour of porous solids is no more than a starting point for the formulation of ductile fracture models. In fact, the goal here was mainly on providing the key mathematical tools upon which ductile failure criteria grounded on the framework of porous media can be built. Actual ductile failure predictions, either damage-controlled and plastic localization-controlled (recall Figure 2.5), must consider three important topics that this chapter has not done justice: (i) void coalescence models and post-coalescence criteria to describe the initiation and propagation of macrocracks; (ii) regularization methods; and (iii) the macrocrack advance in the context of fracture mechanics (see Figure 3.1). These topics are beyond the scope of the present work, nevertheless, a brief discussion on each one of these issues is provided in the following paragraphs.

As discussed in §3.4.4 (p. 54), void coalescence can be described phenomenologically in the context of the f^*-approach of Tvergaard and Needleman (1984) (Eq. (3.30)), or adopting more sound, physically-motivated, approach to formulate coalescence conditions, as in Thomason's (1985) limit-load criterion and extensions thereof (Benzerga and Leblond, 2014; Gallican and Hure, 2017; Hure and Barrioz, 2016; Keralavarma, 2017; Keralavarma and Chockalingam, 2016; Morin, Leblond and Benzerga, 2015; Morin, Leblond, Benzerga, *et al.*, 2016; Scheyvaerts *et al.*, 2010; Torki *et al.*, 2015, 2017).

If the equations describing the boundary value problem (BVP) lose ellipticity at some point in the continuum (interpreted as a discontinuous bifurcation mode[31]), the BVP becomes *ill-posed*. Fundamentally, loss of ellipticity results from the fact that the porous criteria developed in this work are obtained from a homogenization scheme in such way that no length scale is present in the analysis. Being based on the concept of the RVE (in line with the local continuum framework, in which material behaviour is assumed to be independent of neighbouring points), this ultimately weakens the relevance of such models at the smaller scales, over which strain is bound to concentrate (Benzerga *et al.*, 2016). Note that the problem is exactly the same for other 'softening' criteria such as phenomenological CDM models. In turn, in the absence of a characteristic length scale for the continuum, the size of the localization zone is left unspecified, and thus, arbitrary (Nguyen, 1993). The numerical solution of an ill-posed problem in a spatially discretized domain (e.g. using the FEM) is strongly dependent on the discretization[32]. In particular, for damage-induced softening models, strain and damage tends to concentrate within a band of equal width to the size of the finite elements, with the propagation path of the bands being set by the mesh orientation (Besson *et al.*, 2004). This is, obviously, in opposition with the notion of mesh refinement within the FEM. In short, after strain localization takes place, no reliable solution of an ill-posed BVP can be obtained as both the dissipated energy and fracture path become pathologically mesh-

[31] A bifurcation is said to take place when an initially stable, unique, homogeneous, continuous everywhere, strain-rate field undergoes a perturbation, leading to an inhomogeneous alternative one, possibly discontinuous (Bigoni, 2012).

[32] The FEM sorts out a single (non-unique) solution of the BVP. In addition to the discretization, the solution may also depend on other numerical aspects (e.g. integration methods), number precision, residual tolerance, etc.

dependent. In order to retrieve, or ideally, preserve, the well-posedness of the problem, length-scale effects must be included in the continuum theories. Any enhancement of a top-down model (§3.2) able to remove spurious mesh-dependency at the macroscale is known as *regularization method*. Several regularization alternatives have been proposed in the literature. These can classified into three groups: (i) higher order continua (micropolar continuum), where additional degrees of freedom (viz. microrotation) introduce an internal scale, (de Borst, 1991; Enakoutsa and Leblond, 2009); (ii) higher gradient theories, which introduce higher spatial derivatives to the displacement fields other than the usual deformation gradient, $\boldsymbol{F}$, (de Borst and Mühlhaus, 1992; Gologanu *et al.*, 1997); and (iii) nonlocal theories which consist on *ad hoc* methods to mimic length scale effects on existing materially simple continua, based on the substitution of the 'local' state variables (or conjugated forces) by their smoothed counterparts in the governing equations. In turn, the smoothed, non-local, field can be formulated either in a gradient- (Aifantis, 1987) or an integral-fashion (Pijaudier-Cabot and Bažant, 1987). Regularization may also be achieved by deliberately including rate effects into the constitutive formulation (Needleman, 1988), however, this is less pragmatic and uncommon approach. For further in-sights on nonlocal regularization methods, refer, e.g. to Al-Rub and Voyiadjis (2003); Andrade (2011); Andrade *et al.* (2011); Arriaga *et al.* (2015); César de Sá *et al.* (2010); Huespe *et al.* (2009, 2012); Jirásek and Bazant (2002); Al Kotob *et al.* (2019); Leblond, Perrin and Devaux (1994); Mediavilla *et al.* (2006); Peerlings *et al.* (1996); de Sa *et al.* (2010); and Tvergaard and Needleman (1995). In summary, the analysis of the post-localization response of an elastoplastic rate-independent material is only viable if the resulting ill-posed problem is regularized. One cannot emphasise enough the need for such enhancements to the development of accurate and reproducible analyses of the final stages of the ductile fracture.

Regarding the numerical simulation of the final stages of the ductile fracture process using the FEM, macrocrack advance and surface decohesion may be considered by means of several strategies. These include: (i) element deletion methods; (ii) remeshing with nodal splitting and relaxation (Mediavilla, 2005); (iii) embedded discontinuities (Areias *et al.*, 2004; Huespe *et al.*, 2012); (iv) interelement crack methods, viz. cohesive-zone models (Leclerc *et al.*, 2018); (v) enrichment methods, e.g. the XFEM (Zi and Belytschko, 2003); (see also Song *et al.* (2008) on a review of some of these models). One simpler approach is to define the crack by completely damaged elements with no stiffness (zero stress condition at the integration points), which allows one to remain on a continuous medium, in view of the standard continuum mechanics.

Chapter 8

Conclusions and Future Perspectives

This chapter presents an overview of the research issues addressed in this thesis and summarizes its key findings and conclusions. The advantages and limitations of the present contribution are highlighted, and its encouraging prospects are emphasised. Finally, some recommendations for future work are listed.

8.1 Summary and general conclusions

In this work, numerical-based plastic potentials for ductile porous materials whose matrix behaviour is governed by advanced orthotropic criteria have been developed and implemented. The pursued micromechanically-based modelling scheme was inspired by the work of Gurson (1977) (Chapter 3), using the kinematical-type Hill-Mandel homogenization formulation. The novelty of this contribution is that the developed potentials are no longer evaluated analytically, but by numerical integration of the relevant local fields. While numerical integration has been used in the past in the framework of homogenization, its purpose was limited to the assessment of the corresponding close-form (often approximate) analytical criteria and/or in standalone micromechanical studies regarding the dilatational response of porous media. In contrast, the proposed numerical-based plastic potentials can be used in place of their classical analytical counterparts since these are, by their own nature, suitable for numerical implementation in the context of the finite element method.

It is clear that the adoption of a numerical-based approach paves the way the consideration of more complex material behaviours (and, for that matter, trial fields and RVE geometries) since the analytical evaluation of the volume integrals is no longer an issue. The adoption of such approach in this work is, however, not an option but a requirement since, in general, analytical expressions are not available for the considered microscopic strain-rate potential, here taken as the conjugate of the non-quadratic Plunkett *et al.* (2008) orthotropic stress potential.

The exact dual of the stress potential of Plunkett *et al.* (2008) was first derived (Chapter 4). In line with the underlying stress potential, the developed strain-rate potential accounts for an arbitrary number of orthotropic transformations and for tension-compression asymmetry effects. Given the exact duality property, the material parameters are the same for the stress and strain-rate potentials. Unfortunately, It has been shown that, in general, the transformed strain-rate tensors entering the strain-rate potential closed-form expression cannot be determined in explicit fashion. Accordingly, an efficient numerical

algorithm was proposed in order to evaluate the strain-rate potential and its first derivative concurrently. The presented application examples illustrated the (exact) duality of the potentials and demonstrated their exceptional flexibility and overall accuracy to describe the initial yielding behaviour of textured cubic and hexagonal structure metals and alloys.

With the expression of the local strain-rate potential in hand, the corresponding macroscopic plastic potentials for porous solids containing randomly distributed spherical voids were defined based on rigorous upscaling methods (Chapter 5). Two types of trial velocity fields were considered in the kinematic homogenization problem: (i) the standard Rice and Tracey (1969) ones; and (ii) the so-called Eshelby-type fields, based on the exterior point solution of the well-known Eshelby (1957, 1959) inclusion problem for the particular case of a spherical inclusion. As previously mentioned, since the integrand of the governing volume integrals is not readily available in analytical form, the homogenization analysis must be tackled numerically. Hence, an efficient cubature method for the volume averaging operations over the hollow spherical RVE was developed. The proposed method is grounded on the split of the volume (triple) integrals into surface (double) integrals and one-dimensional integrals over the radial direction. The former are evaluated based on the theory of spherical designs and the latter are determined using a tailor-made adaptative integration scheme based on cubic splines. A convergence study was conducted in order to provide reference values for the two RVE discretization parameters in terms of the specified integration tolerance and the complexity of the matrix behaviour, viz. its homogeneity degree parameter. The results showed that the surface integrals of non-quadratic potentials is more challenging than that of quadratic ones, with the typical number of quadrature points increasing with increasing homogeneity parameter. Conversely, the convergence behaviour of the one-dimensional radial integrals turned out to be practically independent of the matrix behaviour. An algorithm for evaluating the macroscopic stress potential, dual of a given numerical-based macroscopic strain-rate potential, was also proposed. Finally, a detailed description of the computational aspects of the implementation of the proposed numerical-based homogenization scheme was presented.

The predictions of the porous criteria obtained from the Rice and Tracey and the Eshelby-type fields were compared (Chapter 6): (i) with each other; (ii) with the results of finite element limit analyses on spherical unit cells; and (iii) with existing analytical criteria inspired on these fields, viz. the criteria of Gurson (1977) and Cazacu and Stewart (2009) concerning the former and the criterion of Monchiet *et al.* (2011) concerning the latter. Regarding the first point, it was confirmed that the presence of a void phase induces dependence on all invariants of the macroscopic stress state and that considerable shape changing behaviour of the yield locus is predicted with increasing hydrostatic contribution. The shape change has been shown to follow similar trends in both formulations. More crucially, the differences between the formulations vanish with decreasing porosity, viz. the predictions using the Eshelby-type formulation reduce to those of Rice and Tracey. Regarding the second point, it was concluded that the Rice and Tracey formulation is in overall good agreement with the FE results for all matrix behaviours and porosity degrees considered. More importantly, the respective yield loci are indeed exterior to those of the FE limit analysis, given the upper-bound nature of the latter formulation. On the other hand, the

Eshelby-type formulation was shown to predict an excessively low dissipation for high porosities under predominantly deviatoric loadings. This behaviour stems from the violation of the uniform strain-rate boundary conditions in the kinematical homogenization problem. It should be noted that both formulations appear to underestimate the dependence on the macroscopic third deviatoric stress invariant, J_3^{Σ}, (alias Lode-angle dependence), however the general trends and couplings with the other stress invariants are in fact captured. This is in contrast to the predictions of the analytical criteria described above since all of these are incapable of representing void-induced J_3^{Σ} effects and the intricate (I_1, J_3^{Σ})- couplings that give rise to the shape change of the yield loci. The key conclusion is that these limitations are not attributable to the quality of the employed velocity fields, but to the simplification hypotheses, whether or not upper-bound preserving, employed in the respective analytical analysis which, ultimately, erased the intrinsic modelling capability of the homogenization problem. Of course, analytical solutions are preferable both from a conceptual and computational point of view, but if these are obtained at the cost of the oversimplification of the underlying problem, then their relevance is questionable. This clearly emphasizes the value of pursuing a numerical-based homogenization approach.

The computational performance of the proposed algorithms was assessed in Chapter 6. It was shown that that the computational cost of evaluating the macroscopic SRP (and its first derivative) associated with the Rice and Tracey trial fields with a tolerance compatible with that usually involved in nonlinear computational continuum mechanics is *not* prohibitively high. Indeed, the developed numerical scheme should be several orders of magnitude faster than multi-scale FE-based computational homogenisation formulations. The evaluation of the SRP associated with the Eshelby-type fields was shown to be $\mathcal{O}(50)$ times more expressive than the Rice and Tracey counterpart. Since these formulations virtually coincide for low porosities, the usage of the Eshelby-type fields within a numerical homogenization analysis is thus not recommended for modelling porous solids with vanishing porosity. The recent trend in microprocessor development has been towards increasing the number of cores. The number of cores of new chips is expected to accelerate in next few years driven by the demand of emerging technologies such as artificial intelligence and virtual reality. High-end professional desktop-grade architectures with *hundreds* of threads are now available and are likely to become the standard in the future, even for the non-professional/mainstream sector. In summary, the increased computational effort associated with the proposed numerical homogenization scheme should be offset by the technologic advances in microprocessor performance and parallelism in a short timeframe.

The numerical-based criteria proposed in this work have been formulated with the intention of being easily integrated in large-scale engineering simulations. In order to demonstrate this procedure, the developed potentials were implemented in a large-strain elastic-plastic constitutive framework grounded on an hyperelastic-based multiplicative split formulation coupled with a strain-rate potential flow rule for describing the plastic dissipation (Chapter 7). It has been shown that the adoption of a numerical-based SRP does not actually add complexity to the constitutive formulation since: (i) the plastic correction problem can be solved using a quasi-Newton method based on finite differences; and (ii) the elastoplastic moduli can be readily estimated based on their small-strain theory counterparts.

The application examples demonstrated that the proposed mixed numerical-analytical criterion, originally developed as an estimate of the full homogenization solution, actually leads to remarkably similar results to those of the latter approach, even when dealing with complex matrix behaviours and loading conditions. As such, the proposed Gurson-type heuristic model is a cost-effective approach that can be employed in early development stages in lieu of the actual homogenization solution. Nevertheless, it should be emphasized that this may not hold for anisotropic porous media with high porosity (e.g. textured sheet metals in the coalescence regime; metal additive manufacturing parts) for which the 'exact' homogenization solution may actually be required, given the limitations of the Gurson-type expression.

8.2 Strengths and limitations of the proposal

The main advantages and limitations of this contribution are summarized as follows:

Strengths

- *Exactness of the analysis*: the plastic potentials are determined based on a sound upscaling theory without the need for adopting any simplification hypothesis (excluding, of course, the adoption the trial local field), viz., restrict the loading type, restricting the type of orthotropy, defining new upper-bounds, *ad hoc* truncation and/or averaging of the integrands, among others. The micro- and macro- plasticity couplings are therefore as accurate as permitted by the scale transition operation;
- *No need for heuristics*: given the rigor of the analysis, there is no need for heuristic modifications in order to improve its global accuracy, (e.g., Tvergaard's (1981) q_i - fitting parameters, Table 3.1) in order to mimic micromechanical FE unit cell studies;
- *Modularity*: the consideration of other trial velocity fields and/or microscale plasticity criteria is trivial. Additionally, the theory of spherical designs, employed in this work to compute the surface integrals, can be effortlessly adapted to integrate over ellipsoidal surface (e.g., An and Chen, 2016). Therefore, the proposed numerical integration scheme can be easily extended to account for non-spherical, viz., spheroidal or ellipsoidal, void shapes;

Limitations

- *The spherical void*: similarly to the work of Gurson (1977), the presented porous framework can only handle the growth of spherical voids remaining spherical throughout the deformation process, consistent with the concept of isotropic damage. However, void shape effects are known to be important under vanishing (including negative) stress triaxialities, for which the voids tend to become elongated and to rotate under shear-dominated loadings (recall §2.2.3). Hence, as it stands, the proposed model is not adequate to predict the microstructural evolution features of porous solids under shear dominated loadings.
- *Hardening and rate-independence*: the criteria developed in this work are restricted to modelling the behaviour of anisotropic porous solids under proportional, quasi-static and monotonic loadings. In order to deal with cyclic and/or nonproportional plastic loadings, porous

criteria should, ideally, account for kinematic hardening effects, in practice, manifest as a specific type of matrix anisotropy at the macroscale. Moreover, for high strain-rate loading conditions, these must also include temperature and strain-rate dependence.

- *Frozen orthotropy*: this work enforced that the principal orthotropic directions do not change during plastic deformation (recall Eq. (7.33)), thus, the orthotropy is considered static during the deformation process. However, texture evolution and/or twinning-detwinning activation are known to lead to an evolving anisotropic behaviour. Therefore, the proposed yield criteria should only be used to describe the initial yielding response of porous media.

8.3 Suggestions for future research

This work has opened up many opportunities, both from a modelling point of view and in terms of numerical implementation. In particular, the proposed numerical homogenization scheme is well positioned to facilitate future developments, not only on the void-growth stage of the ductile failure, which has been the primary focus here, but also on the development of improved void nucleation- and coalescence criteria. Some aspects concerning the continuity of this work and general topics regarding future research are briefly discussed in the following. These are mainly aimed at addressing the current limitations this proposal, listed above.

- Extend the criteria developed here in a similar fashion as the extensions of the model of Gurson (1977) (as in Table 3.1), including, but not limited to: (i) void shape extensions, e.g. by considering an ellipsoidal void embedded in a ellipsoidal RVE; (ii) high strain-rates by including temperature sensitivity and strain-rate dependence; (iii) kinematical hardening; and (iv) evolving plastic anisotropy.
- Apply the proposed numerical-integration scheme to derive improved coalescence criteria, (e.g. accounting for more complex matrix behaviours) within the framework of the Thomason (1985) model, for instance, using the recent "unified" velocity fields approach of Morin *et al.* (2016), based on a seamless transition from the void growth to the void coalescence stage;
- In order to provide a 'complete' model for ductile damage assessments, the proposed finite-strain elastoplastic constitutive framework (Chapter 7) must be supplemented with: (i) a regularization method, e.g., with a non-local (either integral -type or gradient-enhanced) approach; and (ii) a model to predict the onset of void coalesce model, e.g., Thomason-like models.

Appendices

Appendix A. Voigt notation of the product of symmetric second order tensors

Let $\boldsymbol{A}$ and $\boldsymbol{B}$ denote second order symmetric tensors in $\mathbb{R}^3$ whose product $\boldsymbol{C} = \boldsymbol{AB}$ is also symmetric, (thus $\boldsymbol{A}$ and $\boldsymbol{B}$ commute), and $\underline{\mathbf{B}}$ and $\underline{\mathbf{C}}$ Voigt's pseudo-vectorial notation of $\boldsymbol{B}$ and $\boldsymbol{C}$, respectively, i.e.:

$$\begin{aligned} \underline{\mathbf{B}} &= [B_{11} \;\; B_{22} \;\; B_{33} \;\; B_{23} \;\; B_{13} \;\; B_{12}]^{\mathrm{T}}, \\ \underline{\mathbf{C}} &= [C_{11} \;\; C_{22} \;\; C_{33} \;\; C_{23} \;\; C_{13} \;\; C_{12}]^{\mathrm{T}}, \end{aligned} \tag{A.1}$$

It is possible to define an operation $\mathrm{voigt}_{33}^{66}(\cdot)$ which transforms a symmetric second order tensor into a 6x6-Voigt matrix format such that:

$$C_{ij} = C_{ji} = A_{ik} B_{kj} \Rightarrow \mathrm{C}_I = \bar{\mathrm{A}}_{IJ} \mathrm{B}_J, \;\; i, j, k = 1, 2, 3, \text{ and } \; I, J = 1, ..., 6, \tag{A.2}$$

where

$$\bar{\mathbf{A}} = \mathrm{voigt}_{33}^{66}(\boldsymbol{A}) = \begin{bmatrix} A_{11} & 0 & 0 & 0 & A_{13} & A_{12} \\ 0 & A_{22} & 0 & A_{23} & 0 & A_{12} \\ 0 & 0 & A_{33} & A_{23} & A_{13} & 0 \\ 0 & A_{23}/2 & A_{23}/2 & A_{22}/2 + A_{33}/2 & A_{12}/2 & A_{13}/2 \\ A_{13}/2 & 0 & A_{13}/2 & A_{12}/2 & A_{11}/2 + A_{33}/2 & A_{23}/2 \\ A_{12}/2 & A_{12}/2 & 0 & A_{13}/2 & A_{23}/2 & A_{11}/2 + A_{22}/2 \end{bmatrix}. \tag{A.3}$$

The operation $\bar{\mathbf{A}} = \mathrm{voigt}_{6\mathrm{x}6}(\boldsymbol{A})$ can be viewed as the Voigt notation of a fourth-order tensor $\bar{\mathbf{A}} \leftarrow \bar{\mathcal{A}}_{ijkl}$, $i, j, k, l = 1, 2, 3,$ which verifies $C_{ij} = \bar{\mathcal{A}}_{ijkl} B_{kl}$, $i, j, k, l = 1, 2, 3.$ If $\boldsymbol{C}$ describes a flux tensor (e.g. strain-like) and $\boldsymbol{B}$ its thermodynamic conjugated tensor (e.g. stress-like), (as in Eq.(4.36)), then, by convention, it is common to rewrite the Voigt form in Eq. (A.1) as:

$$\begin{aligned} \underline{\mathbf{B}} &= [B_{11} \;\; B_{22} \;\; B_{33} \;\; B_{23} \;\; B_{13} \;\; B_{12}]^{\mathrm{T}}, \\ \underline{\mathbf{C}} &= [C_{11} \;\; C_{22} \;\; C_{33} \;\; 2C_{23} \;\; 2C_{13} \;\; 2C_{12}]^{\mathrm{T}}, \end{aligned} \tag{A.4}$$

such that $B_{ij} C_{ij} = \mathrm{B}_I \mathrm{C}_I, \;\; i, j = 1, 2, 3, \;\; I, J = 1, ..., 6.$ In this case, the operation $\bar{\mathbf{A}} = \mathrm{voigt}_{33}^{66}(\boldsymbol{A})$ must be likewise corrected by a factor of 2, i.e. $\bar{\mathrm{A}}_{IJ} \leftarrow 2\bar{\mathrm{A}}_{IJ}$, $I = 4, 5, 6$ and $J = 1, ..., 6,$ rendering $\bar{\mathbf{A}}$ symmetric.

Appendix B. Pentadimensional deviatoric space

Let $\boldsymbol{A}$ denote a second order tensor in $\mathbb{R}^3$. If $\boldsymbol{A}$ is symmetric and deviatoric, i.e. $\boldsymbol{A} = \boldsymbol{A}^{\mathrm{T}}$ and tr($\boldsymbol{A}$)=0, respectively, then $\boldsymbol{A}$ has only 5 independent components. Accordingly, one can map $\boldsymbol{A}$ into a pentadimensional deviatoric space to obtain a pseudo-vector $\underline{\mathbf{A}}^{(5)}$ containing the information of these components. The mapping $\boldsymbol{A} \to \underline{\mathbf{A}}^{(5)}$, or, equivalently, $A_{ij} \to A_I^{(5)}$, $i, j = 1,2,3$ and $I = 1,...,5$ is defined as:

$$\begin{gathered} A_1^{(5)} = \frac{1}{\sqrt{2}}\left(A_{11} - A_{22}\right), \quad A_2^{(5)} = \frac{1}{\sqrt{6}}\left(A_{11} + A_{22}\right) - \frac{2}{\sqrt{6}} A_{33}, \\ A_3^{(5)} = \sqrt{2} A_{23}, \quad A_4^{(5)} = \sqrt{2} A_{13}, \quad A_5^{(5)} = \sqrt{2} A_{12}. \end{gathered} \tag{B.1}$$

If Voigt notation is adopted, the mapping $\boldsymbol{A} \to \underline{\mathbf{A}}^{(5)}$ can be written in matrix form as:

$$\underline{\mathbf{A}}^{(5)} = \mathbf{P}_6^5 \underline{\mathbf{A}}, \text{ with } \mathbf{P}_6^5 = \begin{bmatrix} 1/\sqrt{2} & -1/\sqrt{2} & 0 & 0 & 0 & 0 \\ 1/\sqrt{6} & 1/\sqrt{6} & -2/\sqrt{6} & 0 & 0 & 0 \\ 0 & 0 & 0 & \sqrt{2} & 0 & 0 \\ 0 & 0 & 0 & 0 & \sqrt{2} & 0 \\ 0 & 0 & 0 & 0 & 0 & \sqrt{2} \end{bmatrix}. \tag{B.2}$$

where $\underline{\mathbf{A}} = [A_{11} \;\; A_{22} \;\; A_{33} \;\; A_{23} \;\; A_{13} \;\; A_{12}]^{\mathrm{T}}$ is the pseudo-vectorial representation of tensor $\boldsymbol{A}$. The inverse mapping, $\underline{\mathbf{A}}^{(5)} \to \boldsymbol{A}$, essentially describing a 'pull-back' operation to the reference orthonormal basis, is defined as:

$$\begin{gathered} A_{11} = \frac{1}{\sqrt{2}} A_1^{(5)} + \frac{1}{\sqrt{6}} A_2^{(5)}, \quad A_{22} = -\frac{1}{\sqrt{2}} A_1^{(5)} + \frac{1}{\sqrt{6}} A_2^{(5)}, \; A_{33} = -\sqrt{\frac{2}{3}} A_2^{(5)}, \\ A_{23} = \frac{1}{\sqrt{2}} A_3^{(5)}, \quad A_{13} = \frac{1}{\sqrt{2}} A_4^{(5)}, \quad A_{12} = \frac{1}{\sqrt{2}} A_5^{(5)}. \end{gathered} \tag{B.3}$$

which can also be written in matrix form as:

$$\underline{\mathbf{A}} = \mathbf{P}_5^6 \underline{\mathbf{A}}^{(5)}, \text{ with } \mathbf{P}_5^6 = \begin{bmatrix} 1/\sqrt{2} & 1/\sqrt{6} & 0 & 0 & 0 \\ -1/\sqrt{2} & 1/\sqrt{6} & 0 & 0 & 0 \\ 0 & -2/\sqrt{6} & 0 & 0 & 0 \\ 0 & 0 & 1/\sqrt{2} & 0 & 0 \\ 0 & 0 & 0 & 1/\sqrt{2} & 0 \\ 0 & 0 & 0 & 0 & 1/\sqrt{2} \end{bmatrix}. \tag{B.4}$$

Let $\mathcal{C}$ denote a fourth order tensor in $\mathbb{R}^3$ containing the major symmetry, $\mathcal{C}_{ijkl} = \mathcal{C}_{klij}$, $i, j, k, l = 1,2,3$, and both minor symmetries, $\mathcal{C}_{ijkl} = \mathcal{C}_{jikl} = \mathcal{C}_{ijlk}$, $i, j, k, l = 1,2,3$. If $\mathcal{C}$ is deviatoric, i.e., $\mathcal{C} : \mathcal{K} = \mathcal{C}$, where $\mathcal{K}_{ijkl} = 1/2(\delta_{ik}\delta_{jl} + \delta_{il}\delta_{jk}) - 1/3(\delta_{ij}\delta_{kl})$, $i, j, k, l = 1,2,3$ is the deviatoric fourth order unit tensor, then the Voigt notation of $\mathcal{C}$, represented by the symmetric 6x6-matrix $\mathbf{C}$, (satisfying $\mathbf{CK} = \mathbf{C}$, where $\mathbf{K}$ is the

Voigt notation of $\mathcal{K}$) can also be mapped into the pentadimensional deviatoric space, $\mathbf{C} \to \mathbf{C}^{(5)}$, by the matrix products:

$$\mathbf{C}^{(5)} = \mathbf{P}_6^5 \mathbf{C} \mathbf{P}_5^6, \tag{B.5}$$

and the inverse mapping, $\mathbf{C}^{(5)} \to \mathbf{C}$, using:

$$\mathbf{C} = \mathbf{P}_5^6 \mathbf{C}^{(5)} \mathbf{P}_6^5, \tag{B.6}$$

where the transformation matrices $\mathbf{P}_6^5$ and $\mathbf{P}_5^6$ are those in Eq. (B.2) and Eq. (B.4), respectively. Note that $\mathbf{P}_6^5 \neq (\mathbf{P}_5^6)^{\mathrm{T}}$ and, in general, $\mathbf{C}^{(5)}$ is not symmetric. Moreover, $\mathbf{P}_6^5 \mathbf{P}_5^6 = \mathbf{I}^{(5)}$ and $\mathbf{P}_5^6 \mathbf{P}_6^5 = \mathbf{K}$.

Appendix C. Rice and Tracey (1969) strain-rate field in Cartesian coordinates

In order to determine the local strain-rate tensor associated with the Rice and Tracey velocity fields in Cartesian coordinates, let us start by defining the spherical-to-Cartesian rotation matrix, $\boldsymbol{R}$, as

$$\boldsymbol{R} = \left[\underline{\boldsymbol{e}}_i^{\mathrm{cart}} \cdot \underline{\boldsymbol{e}}_j^{\mathrm{sph}} \right]_{ij} = \begin{bmatrix} \sin\theta\cos\phi & \cos\theta\cos\phi & -\sin\phi \\ \sin\theta\sin\phi & \cos\theta\sin\phi & \cos\phi \\ \cos\theta & -\sin\theta & 0 \end{bmatrix}, \ \theta \in [0,\pi], \ \phi \in [0,2\pi], \tag{C.1}$$

where $\boldsymbol{R}^T \boldsymbol{R} = \boldsymbol{R}\boldsymbol{R}^T = \boldsymbol{I}$, such that the following transformations on an arbitrary symmetric second order tensor $\boldsymbol{A}$ in $\mathbb{R}^3$ hold:

$$\boldsymbol{A}_{(1,2,3)} = \boldsymbol{R} \hat{\boldsymbol{A}}_{(r,\theta,\phi)} \boldsymbol{R}^{\mathrm{T}}, \text{ and } \hat{\boldsymbol{A}}_{(r,\theta,\phi)} = \boldsymbol{R}^T \boldsymbol{A}_{(1,2,3)} \boldsymbol{R}, \tag{C.2}$$

where the notation is self-explanatory. Let $\hat{\boldsymbol{d}}_{\mathrm{ex}}$ denote the 'direction' of the isotropic expansion field of the Rice and Tracey local strain-rate tensor (the second term of the right-hand side of Eq. (5.20)), given in spherical coordinates as:

$$\hat{\boldsymbol{d}}_{\mathrm{ex}} = \left(-2\underline{\boldsymbol{e}}_r \otimes \underline{\boldsymbol{e}}_r + \underline{\boldsymbol{e}}_\theta \otimes \underline{\boldsymbol{e}}_\theta + \underline{\boldsymbol{e}}_\phi \otimes \underline{\boldsymbol{e}}_\phi \right) = -\begin{bmatrix} 2 & 0 & 0 \\ 0 & -1 & 0 \\ 0 & 0 & -1 \end{bmatrix}_{(r,\theta,\phi)}, \tag{C.3}$$

Application of the transformation in Eq. (C.2) with Eq. (C.1) to the definition in Eq. (C.3) leads to:

$$\boldsymbol{d}_{\mathrm{ex}} = \boldsymbol{R} \hat{\boldsymbol{d}}_{\mathrm{ex}} \boldsymbol{R}^{\mathrm{T}} = \begin{bmatrix} 1-3\sin^2\theta\cos^2\phi & -3\sin^2\theta\sin\varphi\cos\phi & -3\sin\theta\cos\theta\cos\phi \\ & 1-3\sin^2\theta\sin^2\phi & -3\sin\theta\cos\theta\sin\phi \\ \text{sym.} & & 1-3\cos^2\theta \end{bmatrix}_{(1,2,3)}. \tag{C.4}$$

Accordingly, Eq. (5.20) can be written in the Cartesian frame (with respect to the spherical coordinates (r,θ,ϕ)), as:

$$\forall \underline{\boldsymbol{x}} \in \Omega \backslash \omega, \ \boldsymbol{d}^{\mathrm{RT}}\left(\underline{\boldsymbol{x}}\right) = \boldsymbol{D}' + D_{\mathrm{m}} \left(\frac{b}{r} \right)^3 \boldsymbol{d}_{\mathrm{ex}}. \tag{C.5}$$

Box C.1 resumes the above scheme in a pseudo-code format. Voigt pseudo-vectorial notation is adopted (see Appendix A).

Box C.1 Determination of the Rice and Tracey local strain-rate tensor in Cartesian coordinates.

0. Inputs: $\underline{\mathbf{D}}$, b, (r,θ,ϕ)

1. Compute deviatoric and hydrostatic part of macroscopic strain-rate tensor

- $D_{\mathrm{m}} = \mathrm{sum}(\underline{\mathbf{D}}(1:3))/3$
- $\underline{\mathbf{D}}' = \underline{\mathbf{D}} - D_{\mathrm{m}} \left[1\ 1\ 1\ 0\ 0\ 0\right]^{\mathrm{T}}$

2. Compute isotropic expansion term

- Define $\hat{\boldsymbol{d}}_{\mathrm{ex}}$ % (Eq. (C.3))
- Compute rotation matrix: $\boldsymbol{R} \leftarrow \boldsymbol{R}(r,\theta,\phi)$ % (Eq. (C.1))
- Compute $\boldsymbol{d}_{\mathrm{ex}} = \boldsymbol{R}\hat{\boldsymbol{d}}_{\mathrm{ex}}\boldsymbol{R}^{\mathrm{T}}$ % (Eq. (C.4))
- Convert to Voigt pseudo-vector: $\underline{\mathbf{d}}_{\mathrm{ex}} \leftarrow \boldsymbol{d}_{\mathrm{ex}}$ % (Appendix A)

3. Output:

- $\underline{\mathbf{d}}^{\mathrm{RT}} \leftarrow \underline{\mathbf{D}}' + D_{\mathrm{m}} \left(\frac{b}{r}\right)^3 \underline{\mathbf{d}}_{\mathrm{ex}}$

Appendix D. Eshelby-based strain-rate field in Cartesian coordinates

For practical reasons, the expansion field in the Eshelby-based strain-rate tensor, $\boldsymbol{d}^{\mathrm{E},\infty}$, entering Eq. (5.30) is determined in the spherical frame using Eq. (5.28) and then rotated to the Cartesian frame. As such, the eigenstrain-rate tensor, $\boldsymbol{d}^{*}$, must also be transformed into the spherical basis. Since the macroscopic strain-rate potential entails minimization on the deviatoric part of $\boldsymbol{d}^{*\prime}$ (Eq. (5.43)), (which has only five independent components), for computational convenience this tensor is mapped into a pseudo-vector notation in the pentadimensional space, as described in Appendix B. The determination of the Eshelby-based local fields is summarized in Box D.1 in a pseudo-code format.

Box D.1 Determination of the Eshelby-based local strain-rate tensor in Cartesian coordinates.

0. Inputs: $(\underline{\mathbf{D}}, \underline{\mathbf{d}}^{*(5)})$, f, b, (r,θ,ϕ)

1. Compute deviatoric and hydrostatic part of macroscopic strain-rate tensor

- $D_{\mathrm{m}} = \mathrm{sum}(\underline{\mathbf{D}}(1:3))/3$
- $\underline{\mathbf{D}}' = \underline{\mathbf{D}} - D_{\mathrm{m}} \left[1\ 1\ 1\ 0\ 0\ 0\right]^{\mathrm{T}}$

2. Compute the eigenstrain rate tensor in the Cartesian frame

- Pull-back to reference space: $\underline{\mathbf{d}}^{*\prime} \leftarrow \underline{\mathbf{d}}^{*(5)}$ % (Appendix B)
- Compute hydrostatic component of $\boldsymbol{d}^{*}$: $d^{*}_{\mathrm{m}} = D_{\mathrm{m}}/f$
- Compute the total: $\underline{\mathbf{d}}^{*} = \underline{\mathbf{d}}^{*\prime} + d^{*}_{\mathrm{m}} \left[1\ 1\ 1\ 0\ 0\ 0\right]^{\mathrm{T}}$

3. Compute the eigenstrain rate tensor in the spherical frame

- Voigt vector to matrix notation: $\underline{\mathbf{d}}^{*} \rightarrow \boldsymbol{d}^{*}$ % (Appendix A)
- Compute rotation matrix: $\boldsymbol{R} \leftarrow \boldsymbol{R}(r,\theta,\phi)$ % (Eq. (C.1))
- Compute $\hat{\boldsymbol{d}}^{*} = \boldsymbol{R}^{\mathrm{T}} \boldsymbol{d}^{*} \boldsymbol{R}$ % (cf. Eq. (C.4))

4. Compute the uniform deviatoric strain-rate component

- $\underline{\mathbf{A}} = \underline{\mathbf{D}}' - f\left(\frac{2}{5}\underline{\mathbf{d}}^{*\prime}\right)$ % (Eq. (5.34))

5. Compute the Eshelby external-solution field in the spherical frame

- Compute inner radius: $a = bf^{1/3}$
- Compute $\hat{\boldsymbol{d}}^{\mathrm{E},\infty} = \hat{\boldsymbol{d}}^{\mathrm{E},\infty}(a, r, \hat{\boldsymbol{d}}^{*})$ % (Eq. (5.34))

5. Transform the Eshelby external-solution field into the Cartesian frame

- Compute $\boldsymbol{d}^{\mathrm{E},\infty} = \boldsymbol{R}\hat{\boldsymbol{d}}^{\mathrm{E},\infty}\boldsymbol{R}^{\mathrm{T}}$
- Transform to pseudo-vector Voigt notation: $\boldsymbol{d}^{\mathrm{E},\infty} \rightarrow \underline{\mathbf{d}}^{\mathrm{E},\infty}$ % (Appendix A)

6. Output:

- $\underline{\mathbf{d}}^{\mathrm{E}} \leftarrow \underline{\mathbf{A}} + \underline{\mathbf{d}}^{\mathrm{E},\infty}$

Appendix E. Determination of the eigenstrain-rate tensor of the Eshelby-based fields

The infimum in Eq. (5.41) is determined by solving the following equation system:

$$\nabla_{\boldsymbol{d}^{*\prime}} \Upsilon^{\mathrm{E}} = \frac{\partial \Upsilon^{\mathrm{E}}\left(\boldsymbol{D}, \boldsymbol{d}^{*\prime}\right)}{\partial \boldsymbol{d}^{*\prime}} = \boldsymbol{0}, \tag{E.1}$$

where $\nabla(\cdot)$ denotes the gradient operation. Since $\boldsymbol{d}^{*\prime}$ is symmetric and deviatoric, the previous equation can be rewritten in the pentadimensional space (see Appendix B) as:

$$\frac{\partial \Upsilon^{\mathrm{E}}\left(\boldsymbol{D}, \boldsymbol{d}^{*\prime}\right)}{\partial \underline{\mathbf{d}}^{*(5)}} = \underline{\mathbf{0}}^{(5)}, \tag{E.2}$$

where $\underline{\mathbf{d}}^{*(5)} \leftarrow \boldsymbol{d}^{*\prime}$ is the pseudo-vector in the pentadimensional space. Since the analytical expression for $\Upsilon^{\mathrm{E}}(\boldsymbol{D},\boldsymbol{d}^{*\prime})$ is unknown, Eq. (E.2) is replaced by numerical differentiation using a forward difference scheme:

$$\frac{\Delta\Upsilon^{\mathrm{E}}(\boldsymbol{D},\boldsymbol{d}^{*\prime})}{\Delta\underline{\mathbf{d}}^{*(5)}} = \underline{\mathbf{0}}, \tag{E.3}$$

with a sufficiently small relative step increment $\zeta = \|\Delta\underline{\mathbf{d}}^{*(5)}\|_2 / \|\underline{\mathbf{d}}^{*(5)}\|_2$, (e.g., $\zeta = 10^{-6}$). Once Eq. (E.3) is solved the solution is 'pulled-back' to the reference orthonormal basis, i.e. $\underline{\mathbf{d}}^{*(5)} \rightarrow \boldsymbol{d}^{*\prime}$, and the Eshelby-based macroscopic SRP based is determined: $\Psi^{\mathrm{E}}(\boldsymbol{D}) \leftarrow \Upsilon^{\mathrm{E}}(\boldsymbol{D},\boldsymbol{d}^{*\prime})$. Box E.1-Box E.2 resume this algorithm in pseudo-code format. Voigt Notation is adopted. Note that updating the error function, $\underline{\mathbf{F}}$, in Box E.2, implies carrying out $n = 6$ (using a forward or backwards scheme) up to $n = 10$ (using a central scheme) homogenization tasks. Moreover, when using a quasi-Newton method, a Jacobian matrix, of the type $\mathbf{J} = \partial\underline{\mathbf{F}}/\partial\underline{\mathbf{d}}^{*(5)}$ must be defined. Since the analysis is restricted to numerical differentiation, this implies evaluating the error function, $\underline{\mathbf{F}}$, $m = 6$ (using a forward or backwards scheme) up to $m = 10$ (using a central scheme) times. Accordingly, each iteration of the equation system in Box E.1, implies mn homogenizations. From what precedes, minimizing the potential $\Upsilon^{\mathrm{E}}(\boldsymbol{D},\boldsymbol{d}^{*\prime})$ is exceptionally costly from the computational viewpoint. The computation can be reliably speed-up by adopting strategies such as those described in the last paragraph of §5.5, hence, in practice, the computational impart is actually much lower that the theoretical one described above (see e.g. Figure 6.15).

Box E.1 Determination of the eigenstrain-rate tensor concerning the Eshelby-based local fields.

0. Inputs: $\underline{\mathbf{D}}$, $\{f, b\}$, $\{\mathbf{L}^{(n)}, k^{(n)}, a\}$

1. Solve the system of equations

- Set initial guess $\underline{\mathbf{d}}_0^{*(5)}$ and relative convergence tolerances for the optimization: $\{\varepsilon_{\mathrm{tol}}^{\mathrm{fun}}, \varepsilon_{\mathrm{tol}}^{\Delta\mathrm{x}}\}$
- Solve the system in Box E.2 for $\underline{\mathbf{d}}^{*(5)}$ with a quasi-Newton method, such that:

$$\left(\frac{\left\| \mathbf{F}(\underline{\mathbf{d}}_{k+1}^{*(5)}) \right\|_2}{\Upsilon(\underline{\mathbf{D}}, \underline{\mathbf{d}}_{k+1}^{*(5)})} < \varepsilon_{\mathrm{tol}}^{\mathrm{fun}} \right) \quad \text{and} \quad \left(\frac{\left\| \underline{\mathbf{d}}_{k+1}^{*(5)} - \underline{\mathbf{d}}_{k}^{*(5)} \right\|_2}{\left\| \underline{\mathbf{d}}_{k+1}^{*(5)} \right\|_2} < \varepsilon_{\mathrm{tol}}^{\Delta\mathrm{x}} \right),$$

  where k is the number of the iteration.

2. Output: $\underline{\mathbf{d}}^{*(5)} \leftarrow \underline{\mathbf{d}}_{k+1}^{*(5)}$, $\Psi(\underline{\mathbf{D}}) \leftarrow \Upsilon(\underline{\mathbf{D}}, \underline{\mathbf{d}}_{k+1}^{*(5)})$, $\partial\Psi(\underline{\mathbf{D}})/\partial\underline{\mathbf{D}} \leftarrow \partial\Upsilon(\underline{\mathbf{D}}, \underline{\mathbf{d}}^{*(5)})/\partial\underline{\mathbf{D}}$

Box E.2 Determination of the eigenstrain-rate tensor concerning the Eshelby-based local fields.

0. Inputs: $\{\underline{\mathbf{D}}, \underline{\mathbf{d}}^{*(5)}\}$, $\{f, b\}$, $\{\mathbf{L}^{(n)}, k^{(n)}, a\}$

1. Construct the error vector function

- Determine $\Upsilon(\underline{\mathbf{D}}, \underline{\mathbf{d}}^{*(5)})$: CALL Box 5.1 % Eq. (5.41)
- Set relative step size: ζ
- Determine the gradient of $\Upsilon(\underline{\mathbf{D}}, \underline{\mathbf{d}}^{*(5)})$

  % Numerical differentiation with a forward difference scheme:

  $\Delta \underline{d}^{*} = \zeta \|\underline{\mathbf{d}}^{*(5)}\|_2$

  for $i = 1:5$

  $\Delta \underline{\mathbf{d}}^{*(5)} = \underline{\mathbf{0}}$

  $\Delta \underline{\mathbf{d}}^{*(5)}(i) = \Delta \underline{d}^{*}$

  - Determine $\Upsilon(\underline{\mathbf{D}}, \underline{\mathbf{d}}^{*(5)} + \Delta \underline{\mathbf{d}}^{*(5)})$: CALL Box 5.1 % Eq. (5.41)

  $\Delta \Upsilon_i = \Upsilon(\underline{\mathbf{D}}, \underline{\mathbf{d}}^{*(5)} + \Delta \underline{\mathbf{d}}^{*(5)}) - \Upsilon(\underline{\mathbf{D}}, \underline{\mathbf{d}}^{*(5)})$

  end

  - Finite differences scheme: $\dfrac{\partial \Upsilon(\underline{\mathbf{D}}, \underline{\mathbf{d}}^{*(5)})}{\partial \underline{\mathbf{d}}^{*(5)}} \leftarrow \dfrac{\Delta \Upsilon_i}{\Delta \underline{d}^{*}}, \quad i = 1, \ldots, 5$

- Error vector: $\underline{\mathbf{F}} \leftarrow \dfrac{\partial \Upsilon(\underline{\mathbf{D}}, \underline{\mathbf{d}}^{*(5)})}{\partial \underline{\mathbf{d}}^{*(5)}}$

2. Output: $\underline{\mathbf{F}}$

Appendix F. Fortran90 code: computational homogenization

Fortran 90 code for the algorithms described in Box 5.1 to Box 5.4 and their dependencies is freely available for personal use at: https://github.com/joaobrito95/CH.git.

Appendix G. The exponential map

This appendix presents a review on the exponential map operation, alias tensor exponential function, of symmetric and non-symmetric second-order tensors (after de Souza Neto *et al.*, 2011).

G.1 Definition

Consider the initial value problem defined by the tensor-valued ordinary differential equation:

$$\dot{\boldsymbol{Y}}(t) = \boldsymbol{A}\boldsymbol{Y}(t), \tag{G.1}$$

with the initial condition:

$$\boldsymbol{Y}(t_0) = \boldsymbol{Y}_0, \tag{G.2}$$

where the superimposed dot denotes differentiation with respect to time, t, and $\boldsymbol{A}$ and $\boldsymbol{Y}_0$ are known symmetric constant tensors. The tensor exponential function (or exponential map), $\exp(\cdot)$ is the (unique) solution to the problem in Eq. (G.1), i.e.:

$$\boldsymbol{Y}(t) = \exp[(t - t_0)\boldsymbol{A}]\boldsymbol{Y}_0 \,. \tag{G.3}$$

The tensor exponential function of a (generally *non-symmetric*) tensor $\boldsymbol{X}$, can be expressed by means of its series representation, i.e. (Hirsch *et al.*, 2012):

$$\exp[\boldsymbol{X}] = \sum_{n=0}^{\infty} \frac{1}{n!} \boldsymbol{X}^n. \tag{G.4}$$

The above series is absolutely convergent for any argument $\boldsymbol{X}$. For computational applications, the tensor exponential function is evaluated by truncating the above infinite series with $n_{\max}$ terms, such that a given accuracy degree if arrived, i.e., $||\boldsymbol{X}^{n_{\max}}||_2 / n_{\max}! < \varepsilon_{\text{tol}}$, where ε_{tol} is a prescribed tolerance, typically of the order of the machine precision[33]. If the argument tensor is *symmetric*, then the exponential map is more conveniently written in terms of its eigendecomposition in a close-form fashion as:

$$\exp[\boldsymbol{X}] = \sum_{\alpha=1}^{3} \exp(\lambda_\alpha)\, \underline{\boldsymbol{E}}_\alpha \otimes \underline{\boldsymbol{E}}_\alpha, \tag{G.5}$$

where λ_α, and $\underline{\boldsymbol{E}}_\alpha$, $\alpha = 1,2,3$ are the eigenvalues and eigenvectors of $\boldsymbol{X}$. In this work, the previous expression is used in lieu of Eq. (G.4).

G.2 Some mathematical properties

The exponential map enjoys the following proprieties:

(i) Given any invertible tensor $\boldsymbol{D}$,

$$\exp[\boldsymbol{D}\boldsymbol{X}\boldsymbol{D}^{-1}] = \boldsymbol{D}\exp[\boldsymbol{X}]\boldsymbol{D}^{-1}, \tag{G.6}$$

and thus, for the particular case of an orthogonal tensor $\boldsymbol{Q}$:

$$\exp[\boldsymbol{Q}\boldsymbol{X}\boldsymbol{Q}^{\mathrm{T}}] = \boldsymbol{Q}\exp[\boldsymbol{X}]\boldsymbol{Q}^{\mathrm{T}}, \tag{G.7}$$

i.e., the tensor exponential is an isotropic function;

(ii) Given generic tensor $\boldsymbol{X}$,

$$\exp[-\boldsymbol{X}] = (\exp[\boldsymbol{X}])^{-1}, \tag{G.8}$$

and

$$\exp[n\boldsymbol{X}] = (\exp[\boldsymbol{X}])^n; \tag{G.9}$$

(iii) The determinant of the exponential of an arbitrary tensor $\boldsymbol{X}$ satisfies:

$$\det(\exp[\boldsymbol{X}]) = \exp[tr(\boldsymbol{X})], \tag{G.10}$$

therefore, the exponential tensor function maps traceless tensors onto unimodular tensors, i.e.:

[33] In practice, given the typical tolerances involved in nonlinear computational continuum mechanics, only a few terms of the series (about six or seven) must be considered for guarantee a truncation error compatible with the underlying model (de Souza Neto *et al.* 2011).

$$\mathrm{tr}[\boldsymbol{X}] = 0 \Leftrightarrow \det(\exp[\boldsymbol{X}]) = 1, , \tag{G.11}$$

which is a valuable property when dealing with isochoric plasticity.

G.3 Generalized exponential map midpoint rule

Consider the initial value problem defined by the tensor differential equation with a general format:

$$\dot{\boldsymbol{Y}}(t) = \boldsymbol{A}(t)\boldsymbol{Y}(t) , \tag{G.12}$$

with the initial condition:

$$\boldsymbol{Y}(t_0) = \boldsymbol{Y}_0 . \tag{G.13}$$

The problem in Eq. (G.12) differs from that in Eq. (G.1), since tensor $\boldsymbol{A}$ is now also a function of time, i.e., $\boldsymbol{A} = \boldsymbol{A}(t)$. Unfortunately, Eq. (G.3) is no longer the exact solution of Eq. (G.12). However, the latter can be used to generate *approximate* solutions of the problem in Eq. (G.12). Analogously to the generalised midpoint scheme based on the standard Euler approximation, one defines the generalised exponential map midpoint rule as follows. Consider a time interval $[t_n, t_{n+1}]$. Then an approximation of the solution of Eq. (G.12) is given by:

$$\boldsymbol{Y}_{n+1} = \exp[\Delta t \boldsymbol{A}(t_{n+\theta})]\boldsymbol{Y}_n , \tag{G.14}$$

where

$$\Delta t = t_{n+1} - t_n , \text{ and } t_{n+\theta} = t_n + \theta \Delta t, \tag{G.15}$$

with $\theta \in [0,1]$. Essentially, the algorithm in Eq. (G.14) estimates $\boldsymbol{Y}_{n+1}$ as the exact solution that would be obtained at t_{n+1} *if* $\boldsymbol{A}(t)$ was constant over $[t_n, t_{n+1}]$. The choices $\theta = 0$, $\theta = \frac{1}{2}$, and $\theta = 1$ result in the so-called *explicit*, *midpoint*, and *backward* (or fully-implicit) exponential map integrators, respectively. The algorithm is first-order accurate for $\theta = 1$.

References

Abedini, A., Butcher, C., Nemcko, M.J., Kurukuri, S. and Worswick, M.J. (2017), "Constitutive characterization of a rare-earth magnesium alloy sheet (ZEK100-O) in shear loading: Studies of anisotropy and rate sensitivity", *International Journal of Mechanical Sciences*, Elsevier, Vol. 128, pp. 54–69.

Achouri, M., Germain, G., Dal Santo, P. and Saidane, D. (2013), "Experimental characterization and numerical modeling of micromechanical damage under different stress states", *Materials & Design*, Elsevier, Vol. 50, pp. 207–222.

Addessio, F.L. and Johnson, J.N. (1993), "Rate-dependent ductile failure model", *Journal of Applied Physics*, American Institute of Physics, Vol. 74 No. 3, pp. 1640–1648.

Aifantis, E.C. (1987), "The physics of plastic deformation", *International Journal of Plasticity*, Elsevier, Vol. 3 No. 3, pp. 211–247.

Alart, P. and Curnier, A. (1991), "A mixed formulation for frictional contact problems prone to Newton like solution methods", *Computer Methods in Applied Mechanics and Engineering*, Elsevier, Vol. 92 No. 3, pp. 353–375.

Alekseyenko, A.P. and Liu, Y.C. (1966), "The Anisotropy of Youngs Modulus in Cold-Rolled Sheets of Binary Cu-Zn Alloys", *Trans Metall Soc AIME*, Vol. 236, pp. 489–495.

Al-Rub, R.K.A. and Voyiadjis, G.Z. (2003), "On the coupling of anisotropic damage and plasticity models for ductile materials", *International Journal of Solids and Structures*, Elsevier, Vol. 40 No. 11, pp. 2611–2643.

Alves, J.L. and Cazacu, O. (2015), "Micromechanical study of the dilatational response of porous solids with pressure-insensitive matrix displaying tension-compression asymmetry", *European Journal of Mechanics, A/Solids*, Elsevier Masson SAS, Vol. 51, pp. 44–54, doi: 10.1016/j.euromechsol.2014.11.010.

Alves, J.L., Revil-Baudard, B. and Cazacu, O. (2014), "Importance of the coupling between the sign of the mean stress and the third invariant on the rate of void growth and collapse in porous solids with a von Mises matrix", *Modelling and Simulation in Materials Science and Engineering*, Vol. 22 No. 2, doi: 10.1088/0965-0393/22/2/025005.

An, C. and Chen, S. (2016), "Numerical integration over the unit sphere by using spherical t-design", *ArXiv Preprint ArXiv:1611.02785*.

Anand, L. (1979), "On H. Hencky's approximate strain-energy function for moderate deformations", *Journal of Applied Mechanics*, Citeseer, Vol. 46 No. 1, pp. 78–82, doi: 10.1115/1.3424532.

Anand, L. (1985), “Constitutive equations for hot-working of metals”, *International Journal of Plasticity*, Elsevier, Vol. 1 No. 3, pp. 213–231.

Anand, L. and Kalidindi, S.R. (1994), “The process of shear band formation in plane strain compression of fcc metals: effects of crystallographic texture”, *Mechanics of Materials*, Elsevier, Vol. 17 No. 2–3, pp. 223–243.

Anand, L. and Spitzig, W.A. (1980), “Initiation of localized shear bands in plane strain”, *Journal of the Mechanics and Physics of Solids*, Elsevier, Vol. 28 No. 2, pp. 113–128.

Anand, L. and Spitzig, W.A. (1982), “Shear-band orientations in plane strain”, *Acta Metallurgica*, Elsevier, Vol. 30 No. 2, pp. 553–561.

Anderson, T.L. (2017), *Fracture Mechanics: Fundamentals and Applications*, CRC press.

Andrade, F.X.C. (2011), *Non-Local Modelling of Ductile Damage: Formulation and Numerical Issues*, PhD Thesis, Faculdade de Engenharia da Universidade do Porto.

Andrade, F.X.C., César de Sá, J.M.A. and Andrade Pires, F.M. (2011), “A ductile damage nonlocal model of integral-type at finite strains: formulation and numerical issues”, *International Journal of Damage Mechanics*, SAGE Publications Sage UK: London, England, Vol. 20 No. 4, pp. 515–557.

Aravas, N. (1987), “On the numerical integration of a class of pressure-dependent plasticity models”, *International Journal for Numerical Methods in Engineering*, Wiley Online Library, Vol. 24 No. 7, pp. 1395–1416.

Areias, P.M.A., de Sa, J.M.A.C., Antonio, C.A.C., Carneiro, J. and Teixeira, V.M.P. (2004), “Strong displacement discontinuities and Lagrange multipliers in the analysis of finite displacement fracture problems”, *Computational Mechanics*, Springer, Vol. 35 No. 1, pp. 54–71.

Aretz, H. and Barlat, F. (2013), “New convex yield functions for orthotropic metal plasticity”, *International Journal of Non-Linear Mechanics*, Elsevier, Vol. 51, pp. 97–111.

Argon, A.S. (1976), “Formation of Cavities From Nondeformable Second-Phase Particles in Low Temperature Ductile Fracture”, *Journal of Engineering Materials and Technology*, Vol. 98 No. 1, pp. 60–68, doi: 10.1115/1.3443338.

Argon, A.S. and Im, J. (1975), “Separation of second phase particles in spheroidized 1045 steel, Cu-0.6pct Cr alloy, and maraging steel in plastic straining”, *Metallurgical Transactions A*, Vol. 6 No. 4, p. 839, doi: 10.1007/BF02672307.

Argon, A.S., Im, J. and Safoglu, R. (1975), “Cavity formation from inclusions in ductile fracture”, *Metallurgical Transactions A*, Springer, Vol. 6 No. 4, p. 825.

Arminjon, M., Bacroix, B., Imbault, D. and Raphanel, J.L. (1994), “A fourth-order plastic potential for anisotropic metals and its analytical calculation from the texture function”, *Acta Mechanica*, Springer, Vol. 107 No. 1, pp. 33–51.

Arndt, S., Svendsen, B. and Klingbeil, D. (1997), “Modellierung der Eigenspannungen an der Rissspitze mit einem Schädigungsmodell”, *Technische Mechanik. Scientific Journal for Fundamentals and Applications of Engineering Mechanics*, Vol. 17 No. 4, pp. 323–332.

Arriaga, M., McAuliffe, C. and Waisman, H. (2015), "Onset of shear band localization by a local generalized eigenvalue analysis", *Computer Methods in Applied Mechanics and Engineering*, Elsevier, Vol. 289, pp. 179–208.

Asaro, R. and Lubarda, V. (2006), *Mechanics of Solids and Materials*, Cambridge University Press.

Asaro, R.J. (1983), "Micromechanics of crystals and polycrystals", *Advances in Applied Mechanics*, Elsevier, Vol. 23, pp. 1–115.

Ashby, M.F. (1966), "Work hardening of dispersion-hardened crystals", *The Philosophical Magazine: A Journal of Theoretical Experimental and Applied Physics*, Taylor & Francis, Vol. 14 No. 132, pp. 1157–1178, doi: 10.1080/14786436608224282.

Asserin-Lebert, A., Besson, J. and Gourgues, A.-F. (2005), "Fracture of 6056 aluminum sheet materials: effect of specimen thickness and hardening behavior on strain localization and toughness", *Materials Science and Engineering: A*, Elsevier, Vol. 395 No. 1–2, pp. 186–194.

Ayada, M. (1987), "Central bursting in extrusion of inhomogeneous materials", *Proceedings of 2nd International Conference on Technology for Plasticity, Stuttgart, 1987*, Vol. 1, pp. 553–558.

Babout, L., Brechet, Y., Maire, E. and Fougeres, R. (2004), "On the competition between particle fracture and particle decohesion in metal matrix composites", *Acta Materialia*, Elsevier, Vol. 52 No. 15, pp. 4517–4525.

Babout, L., Maire, E., Buffiere, J.-Y. and Fougeres, R. (2001), "Characterization by X-ray computed tomography of decohesion, porosity growth and coalescence in model metal matrix composites", *Acta Materialia*, Elsevier, Vol. 49 No. 11, pp. 2055–2063.

Babout, L., Maire, E. and Fougeres, R. (2004), "Damage initiation in model metallic materials: X-ray tomography and modelling", *Acta Materialia*, Elsevier, Vol. 52 No. 8, pp. 2475–2487.

Bacroix, B. and Gilormini, P. (1995), "Finite-element simulations of earing in polycrystalline materials using a texture-adjusted strain-rate potential", *Modelling and Simulation in Materials Science and Engineering*, IOP Publishing, Vol. 3 No. 1, p. 1.

van Bael, A. and van Houtte, P. (2003), "Convex fourth and sixth-order plastic potentials derived from crystallographic texture", *Journal de Physique IV (Proceedings)*, Vol. 105, EDP sciences, pp. 39–46.

Bai, Y. and Wierzbicki, T. (2008), "A new model of metal plasticity and fracture with pressure and Lode dependence", *International Journal of Plasticity*, Vol. 24 No. 6, pp. 1071–1096, doi: https://doi.org/10.1016/j.ijplas.2007.09.004.

Balan, T. and Cazacu, O. (2013), "Elastic–plastic ductile damage model based on strain-rate plastic potential", *Mechanics Research Communications*, Elsevier, Vol. 54, pp. 21–26.

Bannai, E. and Bannai, E. (2009), "A survey on spherical designs and algebraic combinatorics on spheres", *European Journal of Combinatorics*, Vol. 30 No. 6, pp. 1392–1425, doi: https://doi.org/10.1016/j.ejc.2008.11.007.

Bao, Y. (2003), *Prediction of Ductile Crack Formation in Uncracked Bodies*, PhD Thesis, Massachusetts Institute of Technology.

Bao, Y. and Wierzbicki, T. (2004), "On fracture locus in the equivalent strain and stress triaxiality space", *International Journal of Mechanical Sciences*, Vol. 46 No. 1, pp. 81–98, doi: https://doi.org/10.1016/j.ijmecsci.2004.02.006.

Bao, Y. and Wierzbicki, T. (2005), "On the cut-off value of negative triaxiality for fracture", *Engineering Fracture Mechanics*, Vol. 72 No. 7, pp. 1049–1069, doi: https://doi.org/10.1016/j.engfracmech.2004.07.011.

Baral, M., Hama, T., Knudsen, E. and Korkolis, Y.P. (2018), "Plastic deformation of commercially-pure titanium: experiments and modeling", *International Journal of Plasticity*, Elsevier, Vol. 105, pp. 164–194.

Barlat, F., Aretz, H., Yoon, J.W., Karabin, M., Brem, J.C. and Dick, R. (2005), "Linear transfomation-based anisotropic yield functions", *International Journal of Plasticity*, Elsevier, Vol. 21 No. 5, pp. 1009–1039.

Barlat, F., Brem, J.C., Yoon, J.W., Chung, K., Dick, R.E., Lege, D.J., Pourboghrat, F., *et al.* (2003), "Plane stress yield function for aluminum alloy sheets—part 1: theory", *International Journal of Plasticity*, Elsevier, Vol. 19 No. 9, pp. 1297–1319.

Barlat, F. and Chung, K. (2005), "Anisotropic strain rate potential for aluminum alloy plasticity", *Proc. 8th ESAFORM Conference on Material Forming. Cluj-Napoca April*, pp. 415–418.

Barlat, F., Chung, K. and Richmond, O. (1993), "Strain rate potential for metals and its application to minimum plastic work path calculations", *International Journal of Plasticity*, Elsevier, Vol. 9 No. 1, pp. 51–63.

Barlat, F., Lege, D.J. and Brem, J.C. (1991), "A six-component yield function for anisotropic materials", *International Journal of Plasticity*, Elsevier, Vol. 7 No. 7, pp. 693–712.

Barsoum, I. and Faleskog, J. (2007), "Rupture mechanisms in combined tension and shear—Experiments", *International Journal of Solids and Structures*, Elsevier, Vol. 44 No. 6, pp. 1768–1786.

Bataille, J. and Kestin, J. (1979), "Irreversible processes and physical interpretation of rational thermodynamics", *Journal of Non-Equilibrium Thermodynamics*, Walter de Gruyter, Berlin/New York, Vol. 4 No. 4, pp. 229–258.

Becker, R. and Needleman, A. (1986), "Effect of yield surface curvature on necking and failure in porous plastic solids".

Becker, R., Needleman, A., Richmond, O. and Tvergaard, V. (1988), "Void growth and failure in notched bars", *Journal of the Mechanics and Physics of Solids*, Elsevier, Vol. 36 No. 3, pp. 317–351.

Beentjes, C.H.L. (2015), "Quadrature on a spherical surface", *Working Note Available on the Website Http://People. Maths. Ox. Ac. Uk/Beentjes/Essays*.

Belytschko, T., Liu, W.K., Moran, B. and Elkhodary, K. (2014), *Nonlinear Finite Elements for Continua and Structures*, John Wiley & Sons.

Benallal, A. (2017), "Constitutive equations for porous solids with matrix behaviour dependent on the second and third stress invariants", *International Journal of Impact Engineering*, Elsevier, Vol. 108, pp. 47–62.

Benseddiq, N. and Imad, A. (2008), "A ductile fracture analysis using a local damage model", *International Journal of Pressure Vessels and Piping*, Elsevier, Vol. 85 No. 4, pp. 219–227.

Benzerga, A. and Leblond, J.-B. (2014), "Effective yield criterion accounting for microvoid coalescence", *Journal of Applied Mechanics*, American Society of Mechanical Engineers Digital Collection, Vol. 81 No. 3.

Benzerga, A.A. (2000), *Rupture Ductile Des Tôles Anisotropes. Simulation de La Propagation Longitudinale Dans Un Tube Pressurisé*, PhD Thesis, Paris, ENMP.

Benzerga, A.A. and Besson, J. (2001), "Plastic potentials for anisotropic porous solids", *European Journal of Mechanics - A/Solids*, Elsevier Masson, Vol. 20 No. 3, pp. 397–434, doi: 10.1016/S0997-7538(01)01147-0.

Benzerga, A.A., Besson, J., Batisse, R. and Pineau, A. (2001), "Synergistic effects of plastic anisotropy and void coalescence on fracture mode in plane strain", *Modelling and Simulation in Materials Science and Engineering*, IOP Publishing, Vol. 10 No. 1, p. 73.

Benzerga, A.A., Besson, J. and Pineau, A. (2004a), "Anisotropic ductile fracture: Part I: experiments", *Acta Materialia*, Elsevier, Vol. 52 No. 15, pp. 4623–4638.

Benzerga, A.A., Besson, J. and Pineau, A. (2004b), "Anisotropic ductile fracture: Part II: theory", *Acta Materialia*, Elsevier, Vol. 52 No. 15, pp. 4639–4650.

Benzerga, A.A. and Leblond, J.-B. (2010), "Ductile fracture by void growth to coalescence", *Advances in Applied Mechanics*, Vol. 44, Elsevier, pp. 169–305.

Benzerga, A.A., Leblond, J.-B., Needleman, A. and Tvergaard, V. (2016), "Ductile failure modeling", *International Journal of Fracture*, Springer, Vol. 201 No. 1, pp. 29–80.

Benzerga, A.A., Thomas, N. and Herrington, J.S. (2019), "Plastic flow anisotropy drives shear fracture", *Scientific Reports*, Nature Publishing Group, Vol. 9 No. 1, pp. 1–9.

Berdin, C. (2004), "Damage evolution laws and fracture criteria", *Local Approach to Fracture, Ed. by J. Besson, Paris*, pp. 147–174.

Beremin, F.M. (1981), "Cavity formation from inclusions in ductile fracture of A508 steel", *Metallurgical Transactions A*, Springer, Vol. 12 No. 5, pp. 723–731.

Besson, J. (2010), *Continuum Models of Ductile Fracture: A Review*, *International Journal of Damage Mechanics*, Vol. 19, doi: 10.1177/1056789509103482.

Besson, J., Berdin, C., Bugat, S., Desmorat, R., Feyel, F., Forest, S., Lorentz, E., *et al.* (2004), *Local Approach to Fracture*, École des Mines de Paris.

Besson, J., Cailletaud, G., Chaboche, J.-L. and Forest, S. (2009), *Non-Linear Mechanics of Materials*, Vol. 167, Springer Science & Business Media.

Besson, J. and Guillemer-Neel, C. (2003), "An extension of the Green and Gurson models to kinematic hardening", *Mechanics of Materials*, Elsevier, Vol. 35 No. 1–2, pp. 1–18.

Bieler, T.R., Eisenlohr, P., Roters, F., Kumar, D., Mason, D.E., Crimp, M.A. and Raabe, D. (2009), "The role of heterogeneous deformation on damage nucleation at grain boundaries in single phase metals", *International Journal of Plasticity*, Elsevier, Vol. 25 No. 9, pp. 1655–1683.

Bigoni, D. (2012), *Nonlinear Solid Mechanics: Bifurcation Theory and Material Instability*, Cambridge University Press, Cambridge, doi: DOI: 10.1017/CBO9781139178938.

Bishop, R.F., Hill, R. and Mott, N.F. (1945), "The theory of indentation and hardness tests", *Proceedings of the Physical Society*, IOP Publishing, Vol. 57 No. 3, p. 147.

Blazy, J.-S., Marie-Louise, A., Forest, S., Chastel, Y., Pineau, A., Awade, A., Grolleron, C., *et al.* (2004), "Deformation and fracture of aluminium foams under proportional and non proportional multiaxial loading: statistical analysis and size effect", *International Journal of Mechanical Sciences*, Elsevier, Vol. 46 No. 2, pp. 217–244.

Böhlke, T. and Bertram, A. (2001), "The evolution of Hooke's law due to texture development in FCC polycrystals", *International Journal of Solids and Structures*, Elsevier, Vol. 38 No. 52, pp. 9437–9459.

Bonet, J. and Wood, R.D. (1997), *Nonlinear Continuum Mechanics for Finite Element Analysis*, Cambridge university press.

De Boor, C. (1978), *A Practical Guide to Splines*, Vol. 27, Springer-Verlag , New York, doi: 10.2307/2006241.

Borja, R.I. and Tamagnini, C. (1998), "Cam-Clay plasticity Part III: Extension of the infinitesimal model to include finite strains", *Computer Methods in Applied Mechanics and Engineering*, Elsevier, Vol. 155 No. 1–2, pp. 73–95.

de Borst, R. (1991), "Simulation of strain localization: a reappraisal of the Cosserat continuum", *Engineering Computations*, MCB UP Ltd.

De Borst, R., Crisfield, M.A., Remmers, J.J.C. and Verhoosel, C. V. (2012), *Nonlinear Finite Element Analysis of Solids and Structures*, John Wiley & Sons.

de Borst, R. and Mühlhaus, H. (1992), "Gradient-dependent plasticity: formulation and algorithmic aspects", *International Journal for Numerical Methods in Engineering*, Wiley Online Library, Vol. 35 No. 3, pp. 521–539.

Brauchart, J.S. and Grabner, P.J. (2015), "Distributing many points on spheres: minimal energy and designs", *Journal of Complexity*, Elsevier, Vol. 31 No. 3, pp. 293–326.

Brepols, T., Vladimirov, I.N. and Reese, S. (2014), "Numerical comparison of isotropic hypo-and hyperelastic-based plasticity models with application to industrial forming processes", *International Journal of Plasticity*, Elsevier, Vol. 63, pp. 18–48.

Brito, J.P. (2018), *Ductile Fracture Prediction Using a Coupled Damage Model*, MsC Thesis, Universidade de Coimbra, Coimbra.

Broek, D. (2012), *Elementary Engineering Fracture Mechanics*, Springer Science & Business Media.

Bron, F. and Besson, J. (2006), "Simulation of the ductile tearing for two grades of 2024 aluminum alloy thin sheets", *Engineering Fracture Mechanics*, Elsevier, Vol. 73 No. 11, pp. 1531–1552.

Bron, F., Besson, J. and Pineau, A. (2004), "Ductile rupture in thin sheets of two grades of 2024 aluminum alloy", *Materials Science and Engineering: A*, Elsevier, Vol. 380 No. 1–2, pp. 356–364.

Bronkhorst, C.A., Cerreta, E.K., Xue, Q., Maudlin, P.J., Mason, T.A. and Gray Iii, G.T. (2006), "An experimental and numerical study of the localization behavior of tantalum and stainless steel", *International Journal of Plasticity*, Elsevier, Vol. 22 No. 7, pp. 1304–1335.

Brozzo, P., Deluca, B. and Rendina, R. (1972), "A new method for the prediction of formability limits in metal sheets", *Proc. 7th Biennal Conf. IDDR*.

Brunet, M. and Morestin, F. (2001), "Experimental and analytical necking studies of anisotropic sheet metals", *Journal of Materials Processing Technology*, Elsevier, Vol. 112 No. 2–3, pp. 214–226.

Brunet, M., Morestin, F. and Walter-Leberre, H. (2005), "Failure analysis of anisotropic sheet-metals using a non-local plastic damage model", *Journal of Materials Processing Technology*, Elsevier, Vol. 170 No. 1–2, pp. 457–470.

Budiansky, B., Hutchinson, J.W. and Slutsky, S. (1982), "Void growth and collapse in viscous solids", *Mechanics of Solids*, Elsevier, pp. 13–45.

Bunge, H.-J. (1969), *Texture Analysis in Materials Science*, Butterworth-Heinemann.

Bunge, H.J., Ebert, R. and Günther, F. (1969), "On the Angular Variation and Texture Dependence of Young's Modulus in Cold-Rolled Copper Sheet", *Physica Status Solidi (b)*, John Wiley & Sons, Ltd, Vol. 31 No. 2, pp. 565–569, doi: https://doi.org/10.1002/pssb.19690310216.

Bunge, H.J., Kiewel, R., Reinert, T. and Fritsche, L. (2000), "Elastic properties of polycrystals—influence of texture and stereology", *Journal of the Mechanics and Physics of Solids*, Elsevier, Vol. 48 No. 1, pp. 29–66.

Burshtein, A.I. (2008), *Introduction to Thermodynamics and Kinetic Theory of Matter*, John Wiley & Sons.

Butcher, C., Chen, Z., Bardelcik, A. and Worswick, M. (2009), "Damage-based finite-element modeling of tube hydroforming", *International Journal of Fracture*, Vol. 155 No. 1, pp. 55–65, doi: 10.1007/s10704-009-9323-x.

Caminero, M.Á., Montáns, F.J. and Bathe, K.-J. (2011), "Modeling large strain anisotropic elasto-plasticity with logarithmic strain and stress measures", *Computers & Structures*, Elsevier, Vol. 89 No. 11–12, pp. 826–843.

Carstensen, J.V. (1998), *Structural Evolution and Mechanisms of Fatigue in Polycrystalline Brass*, Risø National Laboratory.

Casey, J. and Naghdi, P.M. (1980), "A Remark on the Use of the Decomposition F = FeFp in Plasticity", *Journal of Applied Mechanics*, Vol. 47 No. 3, pp. 672–675, doi: 10.1115/1.3153756.

Castañeda, P.P. (1991), "The effective mechanical properties of nonlinear isotropic composites", *Journal of the Mechanics and Physics of Solids*, Elsevier, Vol. 39 No. 1, pp. 45–71.

Castañeda, P.P. and Zaidman, M. (1994), "Constitutive models for porous materials with evolving microstructure", *Journal of the Mechanics and Physics of Solids*, Elsevier, Vol. 42 No. 9, pp. 1459–1497.

Cazacu, O. (2018), "New yield criteria for isotropic and textured metallic materials", *International Journal of Solids and Structures*, Elsevier, Vol. 139, pp. 200–210.

Cazacu, O. and Barlat, F. (2001), "Generalization of Drucker's yield criterion to orthotropy", *Mathematics and Mechanics of Solids*, Sage Publications Sage CA: Thousand Oaks, CA, Vol. 6 No. 6, pp. 613–630.

Cazacu, O. and Barlat, F. (2003), "Application of the theory of representation to describe yielding of anisotropic aluminum alloys", *International Journal of Engineering Science*, Elsevier, Vol. 41 No. 12, pp. 1367–1385.

Cazacu, O., Ionescu, I.R. and Yoon, J.W. (2010), "Orthotropic strain rate potential for the description of anisotropy in tension and compression of metals", *International Journal of Plasticity*, Elsevier, Vol. 26 No. 6, pp. 887–904.

Cazacu, O., Plunkett, B. and Barlat, F. (2006), "Orthotropic yield criterion for hexagonal closed packed metals", *International Journal of Plasticity*, Vol. 22 No. 7, pp. 1171–1194, doi: 10.1016/j.ijplas.2005.06.001.

Cazacu, O. and Revil-Baudard, B. (2015), "New three-dimensional plastic potentials for porous solids with a von Mises matrix", *Comptes Rendus Mécanique*, Elsevier, Vol. 343 No. 2, pp. 77–94.

Cazacu, O., Revil-Baudard, B. and Barlat, F. (2013), "New interpretation of monotonic Swift effects: Role of tension–compression asymmetry", *Mechanics of Materials*, Elsevier, Vol. 57, pp. 42–52.

Cazacu, O., Revil-Baudard, B. and Chandola, N. (2019), *Plasticity-Damage Couplings: From Single Crystal to Polycrystalline Materials*, Springer, doi: 10.1007/978-3-319-92922-4.

Cazacu, O., Revil-Baudard, B., Chandola, N. and Kondo, D. (2014), "New analytical criterion for porous solids with Tresca matrix under axisymmetric loadings", *International Journal of Solids and Structures*, Elsevier, Vol. 51 No. 3–4, pp. 861–874.

Cazacu, O., Revil-Baudard, B., Lebensohn, R.A. and Gărăjeu, M. (2013), "On the Combined Effect of Pressure and Third Invariant on Yielding of Porous Solids With von Mises Matrix", *Journal of Applied Mechanics*, Vol. 80 No. 6, doi: 10.1115/1.4024074.

Cazacu, O. and Stewart, J.B. (2009), "Analytic plastic potential for porous aggregates with matrix exhibiting tension-compression asymmetry", *Journal of the Mechanics and Physics of Solids*, Vol. 57 No. 2, pp. 325–341, doi: 10.1016/j.jmps.2008.10.010.

César de Sá, J.M. de A., Pires, F.M.A. and Andrade, F.X.C. (2010), "Local and nonlocal modeling of ductile damage", *Advanced Computational Materials Modeling: From Classical to Multi-Scale Techniques*, Wiley Online Library, pp. 23–72.

Chaboche, J.L. (1977), "Sur l'utilisation des variables d'état interne pour la description du comportement viscoplastique et de la rupture par endommagement", *Problems Non-Lineaires de Mécanique*, PWN, pp. 137–159.

Chaboche, J.L. (1978), "Description Thermodynamique et phénoménologique de la viscoplasticité cyclique avec endommagement Publication", *Office National d'Etudes et Recherches Aérospatiales, Chatillon, France*.

Chaboche, J.-L. (1981), “Continuous damage mechanics—a tool to describe phenomena before crack initiation”, *Nuclear Engineering and Design*, Elsevier, Vol. 64 No. 2, pp. 233–247.

Chaboche, J.-L. (1984), “Anisotropic creep damage in the framework of continuum damage mechanics”, *Nuclear Engineering and Design*, Elsevier, Vol. 79 No. 3, pp. 309–319.

Chaboche, J.L. (1988), “Continuum Damage Mechanics: Part II—Damage Growth, Crack Initiation, and Crack Growth”, *Journal of Applied Mechanics*, Vol. 55 No. 1, pp. 65–72, doi: 10.1115/1.3173662.

Chae, D. and Koss, D.A. (2004), “Damage accumulation and failure of HSLA-100 steel”, *Materials Science and Engineering: A*, Elsevier, Vol. 366 No. 2, pp. 299–309.

Cheng, L., Danas, K., Constantinescu, A. and Kondo, D. (2017), “A homogenization model for porous ductile solids under cyclic loads comprising a matrix with isotropic and linear kinematic hardening”, *International Journal of Solids and Structures*, Elsevier, Vol. 121, pp. 174–190.

Christian, J.W. (1983), “Some surprising features of the plastic deformation of body-centered cubic metals and alloys”, *Metallurgical Transactions A*, Springer, Vol. 14 No. 7, pp. 1237–1256.

Christian, J.W. and Mahajan, S. (1995), “Deformation twinning”, *Progress in Materials Science*, Elsevier, Vol. 39 No. 1–2, pp. 1–157.

Chu, C.C. and Needleman, A. (1980), “Void Nucleation Effects in Biaxially Stretched Sheets”, *Journal of Engineering Materials and Technology*, ASME, Vol. 102 No. 3, pp. 249–256.

Chung, K., Barlat, F., Richmond, O. and Yoon, J.W. (1999), “Blank design for a sheet forming application using the anisotropic strain-rate potential Srp98”, *The Integration of Material, Process and Product Design, Zabaras et al.(Eds.), Balkema, Rotterdam*, pp. 213–219.

Chung, K. and Richmond, O. (1993), “A deformation theory of plasticity based on minimum work paths”, *International Journal of Plasticity*, Elsevier, Vol. 9 No. 8, pp. 907–920.

Clayton, J.D. (2011), “Mechanical twinning in crystal plasticity”, *Nonlinear Mechanics of Crystals*, Springer, pp. 379–421.

Cockcroft, M.G. and Latham, D.J. (1968), “Ductility and the workability of metals”, *J Inst Metals*, Vol. 96 No. 1, pp. 33–39.

Cocks, A.C.F. (1989), “Inelastic deformation of porous materials”, *Journal of the Mechanics and Physics of Solids*, Elsevier, Vol. 37 No. 6, pp. 693–715.

Coleman, B.D. and Hodgdon, M.L. (1987), “On shear bands in ductile materials”, *Analysis and Thermomechanics*, Springer, pp. 227–255.

Cordebois, J.P. and Sidoroff, F. (1979), “Anisotropie élastique induite par endommagement”, *Comportement Mécanique Des Solides Anisotropes*, No. 295, pp. 761–774.

Cottrell, A.H. (1961), *Dislocations and Plastic Flow in Crystals*, Oxford University Press.

Cox, T.B. and Low, J.R. (1974), “An investigation of the plastic fracture of AISI 4340 and 18 Nickel-200 grade maraging steels”, *Metallurgical Transactions*, Springer, Vol. 5 No. 6, pp. 1457–1470.

Cuitino, A.M. and Ortiz, M. (1996), “Ductile fracture by vacancy condensation in fcc single crystals”, *Acta Materialia*, Elsevier, Vol. 44 No. 2, pp. 427–436.

Curran, D.R., Seaman, L. and Shockey, D.A. (1987), "Dynamic failure of solids", *Physics Reports*, Elsevier, Vol. 147 No. 5–6, pp. 253–388.

Dæhli, L.E., Morin, D., Børvik, T. and Hopperstad, O.S. (2018), "A Lode-dependent Gurson model motivated by unit cell analyses", *Engineering Fracture Mechanics*, Elsevier, Vol. 190, pp. 299–318.

Dæhli, L.E.B., Faleskog, J., Børvik, T. and Hopperstad, O.S. (2017), "Unit cell simulations and porous plasticity modelling for strongly anisotropic FCC metals", *European Journal of Mechanics-A/Solids*, Elsevier, Vol. 65, pp. 360–383.

Dæhli, L.E.B., Hopperstad, O.S. and Benallal, A. (2019), "Effective behaviour of porous ductile solids with a non-quadratic isotropic matrix yield surface", *Journal of the Mechanics and Physics of Solids*, Elsevier, Vol. 130, pp. 56–81.

Dafalias, Y.F. (1985), "The Plastic Spin", *Journal of Applied Mechanics*, Vol. 52 No. 4, pp. 865–871, doi: 10.1115/1.3169160.

Dafalias, Y.F. (1998), "Plastic spin: necessity or redundancy?", *International Journal of Plasticity*, Elsevier, Vol. 14 No. 9, pp. 909–931.

Danas, K. and Castañeda, P.P. (2009), "A finite-strain model for anisotropic viscoplastic porous media: I–Theory", *European Journal of Mechanics-A/Solids*, Elsevier, Vol. 28 No. 3, pp. 387–401.

Delsarte, P., Goethals, J.M. and Seidel, J.J. (1977), "Spherical codes and designs", *Geometriae Dedicata*, Vol. 6 No. 3, pp. 363–388, doi: 10.1007/BF03187604.

Deng, N. and Korkolis, Y.P. (2018), "Elastic anisotropy of dual-phase steels with varying martensite content", *International Journal of Solids and Structures*, Vol. 141–142, pp. 264–278, doi: https://doi.org/10.1016/j.ijsolstr.2018.02.028.

d'Escatha, Y. and Devaux, J.C. (1979), "Numerical study of initiation, stable crack growth, and maximum load, with a ductile fracture criterion based on the growth of holes", *Elastic-Plastic Fracture*, ASTM International.

Devaux, J.C., Rousselier, G., Mudry, F. and Pineau, A. (1985), "An experimental program for the validation of local ductile fracture criteria using axisymmetrically cracked bars and compact tension specimens", *Engineering Fracture Mechanics*, Elsevier, Vol. 21 No. 2, pp. 273–283.

Dieter, G.E. and Bacon, D.J. (1986), *Mechanical Metallurgy*, Vol. 3, McGraw-Hill New York.

Doege, E., El-Dsoki, T. and Seibert, D. (1995), "Prediction of necking and wrinkling in sheet-metal forming", *Journal of Materials Processing Technology*, Elsevier, Vol. 50 No. 1–4, pp. 197–206.

Dormieux, L., Kondo, D. and Ulm, F.-J. (2006), *Microporomechanics*, John Wiley & Sons.

Drucker, D.C., Prager, W. and Greenberg, H.J. (1952), "Extended limit design theorems for continuous media", *Quarterly of Applied Mathematics*, Vol. 9 No. 4, pp. 381–389.

Duesbery, M. and-S. and Vitek, V. (1998), "Plastic anisotropy in bcc transition metals", *Acta Materialia*, Elsevier, Vol. 46 No. 5, pp. 1481–1492.

Duesbery, M.S., Vitek, V. and Bowen, D.K. (1973), "The effect of shear stress on the screw dislocation core structure in body-centred cubic lattices", *Proceedings of the Royal Society of London. A. Mathematical and Physical Sciences*, The Royal Society London, Vol. 332 No. 1588, pp. 85–111.

Duva, J.M. (1986), "A constitutive description of nonlinear materials containing voids", *Mechanics of Materials*, Elsevier, Vol. 5 No. 2, pp. 137–144.

Duva, J.M. and Hutchinson, J.W. (1984), "Constitutive potentials for dilutely voided nonlinear materials", *Mechanics of Materials*, Elsevier, Vol. 3 No. 1, pp. 41–54.

Ebrahimi, F., Liscano, A.J., Kong, D., Zhai, Q. and Li, H. (2006), "Fracture of bulk face centered cubic (FCC) metallic nanostructures", *Rev. Adv. Mater. Sci*, Vol. 13 No. 1, pp. 33–40.

Edelson, B.I. (1962), "The Effect of Sencond Phases on the Mechanical Properties of Alloys", *Trans. Asm*, Vol. 55, pp. 230–250.

Enakoutsa, K. and Leblond, J.-B. (2009), "Numerical implementation and assessment of the GLPD micromorphic model of ductile rupture", *European Journal of Mechanics-A/Solids*, Elsevier, Vol. 28 No. 3, pp. 445–460.

Enakoutsa, K., Leblond, J.-B. and Audoly, B. (2005), "Influence of continuous nucleation of secondary voids upon growth and coalescence of cavities in porous ductile metals", *Proceedings of the 11th International Conference on Fracture, March*, pp. 20–25.

Engel, L. and Klingele, H. (1981), *An Atlas of Metal Damage: Surface Examination by Scanning Electron Microscope*, English ed., Wolfe Science.

Eshelby, J.D. (1957), "The determination of the elastic field of an ellipsoidal inclusion, and related problems", *Proceedings of the Royal Society of London. Series A. Mathematical and Physical Sciences*, The Royal Society London, Vol. 241 No. 1226, pp. 376–396.

Eshelby, J.D. (1959), "The elastic field outside an ellipsoidal inclusion", *Proceedings of the Royal Society of London. Series A. Mathematical and Physical Sciences*, The Royal Society London, Vol. 252 No. 1271, pp. 561–569.

Eterovic, A.L. and Bathe, K. (1990), "A hyperelastic-based large strain elasto-plastic constitutive formulation with combined isotropic-kinematic hardening using the logarithmic stress and strain measures", *International Journal for Numerical Methods in Engineering*, Wiley Online Library, Vol. 30 No. 6, pp. 1099–1114.

Faleskog, J., Gao, X. and Shih, C.F. (1998), "Cell model for nonlinear fracture analysis–I. Micromechanics calibration", *International Journal of Fracture*, Springer, Vol. 89 No. 4, pp. 355–373.

Fenchel, W. (2014), "On conjugate convex functions", *Traces and Emergence of Nonlinear Programming*, Springer, pp. 125–129.

Fisher, J.R. and Gurland, J. (1981), "Void nucleation in spheroidized carbon steels part 1: experimental", *Metal Science*, Taylor & Francis, Vol. 15 No. 5, pp. 185–192.

Flandi, L. and Leblond, J.-B. (2005), "A new model for porous nonlinear viscous solids incorporating void shape effects–I: Theory", *European Journal of Mechanics-A/Solids*, Elsevier, Vol. 24 No. 4, pp. 537–551.

Fonseka, G.U. and Krajcinovic, D. (1981), "The Continuous Damage Theory of Brittle Materials, Part 2: Uniaxial and Plane Response Modes", *Journal of Applied Mechanics*, Vol. 48, pp. 816–824.

Fortunier, R. (1989), "Dual potentials and extremum work principles in single crystal plasticity", *Journal of the Mechanics and Physics of Solids*, Elsevier, Vol. 37 No. 6, pp. 779–790.

Freudenthal, A.M. and Geiringer, H. (1958), "The Mathematical Theories of the Inelastic Continuum BT - Elasticity and Plasticity / Elastizität und Plastizität", in Flügge, S. (Ed.), , Springer Berlin Heidelberg, Berlin, Heidelberg, pp. 229–433, doi: 10.1007/978-3-642-45887-3_3.

Fritzen, F., Forest, S., Böhlke, T., Kondo, D. and Kanit, T. (2012), "Computational homogenization of elasto-plastic porous metals", *International Journal of Plasticity*, Elsevier, Vol. 29, pp. 102–119.

Gallican, V. and Hure, J. (2017), "Anisotropic coalescence criterion for nanoporous materials", *Journal of the Mechanics and Physics of Solids*, Vol. 108, pp. 30–48, doi: https://doi.org/10.1016/j.jmps.2017.08.001.

Gao, X., Faleskog, J. and Shih, C.F. (1998), "Cell model for nonlinear fracture analysis–II. Fracture-process calibration and verification", *International Journal of Fracture*, Springer, Vol. 89 No. 4, pp. 375–398.

Gărăjeu, M., Michel, J.C. and Suquet, P. (2000), "A micromechanical approach of damage in visco-plastic materials by evolution in size, shape and distribution of voids", *Computer Methods in Applied Mechanics and Engineering*, Elsevier, Vol. 183 No. 3–4, pp. 223–246.

Gardner, R.N., Pollock, T.C. and Wilsdorf, H.G.F. (1977), "Crack initiation at dislocation cell boundaries in the ductile fracture of metals", *Materials Science and Engineering*, Elsevier, Vol. 29 No. 2, pp. 169–174.

Garrison Jr, W.M. and Moody, N.R. (1987), "Ductile fracture", *Journal of Physics and Chemistry of Solids*, Pergamon, Vol. 48 No. 11, pp. 1035–1074.

Germain, P. (1973), *Cours de Mécanique Des Milieux Continus*, Vol. 1, Masson.

Gologanu, M., Leblond, J.-B. and Devaux, J. (1993), "Approximate models for ductile metals containing non-spherical voids—case of axisymmetric prolate ellipsoidal cavities", *Journal of the Mechanics and Physics of Solids*, Elsevier, Vol. 41 No. 11, pp. 1723–1754.

Gologanu, M., Leblond, J.-B. and Devaux, J. (1994), "Approximate Models for Ductile Metals Containing Nonspherical Voids—Case of Axisymmetric Oblate Ellipsoidal Cavities", *Journal of Engineering Materials and Technology*, ASME, Vol. 116 No. 3, pp. 290–297.

Gologanu, M., Leblond, J.-B., Perrin, G. and Devaux, J. (1997), "Recent extensions of Gurson's model for porous ductile metals", *Continuum Micromechanics*, Springer, pp. 61–130.

Gologanu, M., Leblond, J.-B., Perrin, G. and Devaux, J. (2001), "Theoretical models for void coalescence in porous ductile solids. I. Coalescence 'in layers'", *International Journal of Solids and Structures*, Elsevier, Vol. 38 No. 32–33, pp. 5581–5594.

Goods, S.H. and Brown, L.M. (1979), "Overview No. 1: The nucleation of cavities by plastic deformation", *Acta Metallurgica*, Elsevier, Vol. 27 No. 1, pp. 1–15.

Gräf, M. (2013a), *Efficient Algorithms for the Computation of Optimal Quadrature Points on Riemannian Manifolds*, PhD Thesis, Chemnitz University of Technology.

Gräf, M. (2013b), "Quadrature Rules on Manifolds", available at: https://www-user.tu-chemnitz.de/~potts/workgroup/graef/quadrature/index.php.en (accessed 26 October 2022).

Gräf, M., Potts, D. and Steidl, G. (2012), "Quadrature Errors, Discrepancies, and Their Relations to Halftoning on the Torus and the Sphere", *SIAM Journal on Scientific Computing*, Vol. 34 No. 5, pp. A2760–A2791, doi: 10.1137/100814731.

Grange, M., Besson, J. and Andrieu, E. (2000), "An anisotropic Gurson type model to represent the ductile rupture of hydrided Zircaloy-4 sheets", *International Journal of Fracture*, Springer, Vol. 105 No. 3, pp. 273–293.

Green, A.E. and Naghdi, P.M. (1965), "A general theory of an elastic-plastic continuum", *Archive for Rational Mechanics and Analysis*, Vol. 18 No. 4, pp. 251–281, doi: 10.1007/BF00251666.

Green, R.J. (1972), "A plasticity theory for porous solids", *International Journal of Mechanical Sciences*, Elsevier, Vol. 14 No. 4, pp. 215–224.

Greenfield, M.A. and Margolin, H. (1972), "The mechanism of void formation, void growth, and tensile fracture in an alloy consisting of two ductile phases", *Metallurgical Transactions*, Springer, Vol. 3 No. 10, pp. 2649–2659.

Greer, A.L., Cheng, Y.Q. and Ma, E. (2013), "Shear bands in metallic glasses", *Materials Science and Engineering: R: Reports*, Elsevier, Vol. 74 No. 4, pp. 71–132.

Griffith, A.A. (1921), "VI. The phenomena of rupture and flow in solids", *Philosophical Transactions of the Royal Society of London. Series A, Containing Papers of a Mathematical or Physical Character*, The royal society London, Vol. 221 No. 582–593, pp. 163–198.

Gruben, G., Morin, D., Langseth, M. and Hopperstad, O.S. (2017), "Strain localization and ductile fracture in advanced high-strength steel sheets", *European Journal of Mechanics-A/Solids*, Elsevier, Vol. 61, pp. 315–329.

Gullerud, A.S., Gao, X., Dodds Jr, R.H. and Haj-Ali, R. (2000), "Simulation of ductile crack growth using computational cells: numerical aspects", *Engineering Fracture Mechanics*, Elsevier, Vol. 66 No. 1, pp. 65–92.

Guo, T.F., Faleskog, J. and Shih, C.F. (2008), "Continuum modeling of a porous solid with pressure-sensitive dilatant matrix", *Journal of the Mechanics and Physics of Solids*, Elsevier, Vol. 56 No. 6, pp. 2188–2212.

Guo, X.Q., Wu, W., Wu, P.D., Qiao, H., An, K. and Liaw, P.K. (2013), "On the Swift effect and twinning in a rolled magnesium alloy under free-end torsion", *Scr. Mater*, Vol. 69 No. 4, pp. 319–322.

Gurson, A. (1977), "Continuum Theory of Ductile Rupture by Void Nucleation and Growth: Part I—Yield Criteria and Flow Rules for Porous Ductile Media", *Journal of Engineering Materials and Technology*, ASME, Vol. 99 No. 1, pp. 2–15.

Gurson, A.L. (1975), *Plastic Flow and Fracture Behavior of Ductile Materials Incorporating Void Nucleation, Growth and Interaction*, PhD Thesis, Brown University, Providence.

Haghi, M. and Anand, L. (1992), "A constitutive model for isotropic, porous, elastic-viscoplastic metals", *Mechanics of Materials*, Elsevier, Vol. 13 No. 1, pp. 37–53.

Hahn, G.T. and Rosenfield, A.R. (1965), "Local yielding and extension of a crack under plane stress", *Acta Metallurgica*, Elsevier, Vol. 13 No. 3, pp. 293–306.

Hall, E.O. (1951), "The deformation and ageing of mild steel: III discussion of results", *Proceedings of the Physical Society. Section B*, IOP Publishing, Vol. 64 No. 9, p. 747.

Hama, T., Nagao, H., Kobuki, A., Fujimoto, H. and Takuda, H. (2015), "Work-hardening and twinning behaviors in a commercially pure titanium sheet under various loading paths", *Materials Science and Engineering: A*, Elsevier, Vol. 620, pp. 390–398.

Hama, T., Tanaka, Y., Uratani, M. and Takuda, H. (2016), "Deformation behavior upon two-step loading in a magnesium alloy sheet", *International Journal of Plasticity*, Elsevier, Vol. 82, pp. 283–304.

Han, X., Besson, J., Forest, S., Tanguy, B. and Bugat, S. (2013), "A yield function for single crystals containing voids", *International Journal of Solids and Structures*, Elsevier, Vol. 50 No. 14–15, pp. 2115–2131.

Hancock, J.W. and Mackenzie, A.C. (1976), "On the mechanisms of ductile failure in high-strength steels subjected to multi-axial stress-states", *Journal of the Mechanics and Physics of Solids*, Elsevier, Vol. 24 No. 2–3, pp. 147–160.

Hardin, R.H. and Sloane, N.J.A. (1996), "McLaren's improved snub cube and other new spherical designs in three dimensions", *Discrete & Computational Geometry*, Springer, Vol. 15 No. 4, pp. 429–441.

Hardin, R.H. and Sloane, N.J.A. (2002), " Spherical Designs ", available at: http://neilsloane.com/sphdesigns/ (accessed 26 October 2022).

Harren, S. V, Deve, H.E. and Asaro, R.J. (1988), "Shear band formation in plane strain compression", *Acta Metallurgica*, Elsevier, Vol. 36 No. 9, pp. 2435–2480.

Hencky, H. (1933), "The Elastic Behavior of Vulcanized Rubber", *Journal of Applied Mechanics*, Vol. 1 No. 2, pp. 45–48, doi: 10.1115/1.4012174.

Hering, O. and Tekkaya, A.E. (2020), "Damage-induced performance variations of cold forged parts", *Journal of Materials Processing Technology*, Vol. 279, p. 116556, doi: https://doi.org/10.1016/j.jmatprotec.2019.116556.

Hershey, A. V. (1954), "The plasticity of an isotropic aggregate of anisotropic face-centered cubic crystals", American Society of Mechanical Engineers.

Hill, R. (1948), "A theory of the yielding and plastic flow of anisotropic metals", *Proceedings of the Royal Society of London. Series A. Mathematical and Physical Sciences*, The Royal Society London, Vol. 193 No. 1033, pp. 281–297.

Hill, R. (1950), "The mathematical theory of plasticity, Clarendon", *Oxford*, Vol. 613, p. 614.

Hill, R. (1951), "LXXXVIII. On the state of stress in a plastic-rigid body at the yield point", *The London, Edinburgh, and Dublin Philosophical Magazine and Journal of Science*, Taylor & Francis, Vol. 42 No. 331, pp. 868–875.

Hill, R. (1958), "A general theory of uniqueness and stability in elastic-plastic solids", *Journal of the Mechanics and Physics of Solids*, Elsevier, Vol. 6 No. 3, pp. 236–249.

Hill, R. (1962), "Acceleration waves in solids", *Journal of the Mechanics and Physics of Solids*, Elsevier, Vol. 10 No. 1, pp. 1–16.

Hill, R. (1967), "The essential structure of constitutive laws for metal composites and polycrystals", *Journal of the Mechanics and Physics of Solids*, Elsevier, Vol. 15 No. 2, pp. 79–95.

Hill, R. (1979a), "Theoretical plasticity of textured aggregates", *Mathematical Proceedings of the Cambridge Philosophical Society*, Vol. 85, Cambridge University Press, pp. 179–191.

Hill, R. (1979b), "Aspects of invariance in solid mechanics", *Advances in Applied Mechanics*, Elsevier, Vol. 18, pp. 1–75.

Hill, R. (1987), "Constitutive dual potentials in classical plasticity", *Journal of the Mechanics and Physics of Solids*, Elsevier, Vol. 35 No. 1, pp. 23–33.

Hill, R. (1998), *The Mathematical Theory of Plasticity*, Vol. 11, Oxford university press.

Hirsch, M.W., Smale, S. and Devaney, R.L. (2012), *Differential Equations, Dynamical Systems, and an Introduction to Chaos*, Academic press.

Hiwatashi, S., van Bael, A., van Houtte, P. and Teodosiu, C. (1997), "Modelling of plastic anisotropy based on texture and dislocation structure", *Computational Materials Science*, Elsevier, Vol. 9 No. 1–2, pp. 274–284.

Hoger, A. (1987), "The stress conjugate to logarithmic strain", *International Journal of Solids and Structures*, Elsevier, Vol. 23 No. 12, pp. 1645–1656.

Horstemeyer, M.F. and Gokhale, A.M. (1999), "A void–crack nucleation model for ductile metals", *International Journal of Solids and Structures*, Vol. 36 No. 33, pp. 5029–5055, doi: https://doi.org/10.1016/S0020-7683(98)00239-X.

Hosford, W.F. (1972), "A generalized isotropic yield criterion", *Journal of Applied Mechanics*, ASME International, Vol. 39 No. 2, pp. 607–609.

Hosford, W.F. (2010), *Mechanical Behavior of Materials*, Cambridge university press.

Hosford, W.F. and Allen, T.J. (1973), "Twinning and directional slip as a cause for a strength differential effect", *MT*, Vol. 4 No. 5, pp. 1424–1425.

van Houtte, P. (1994), "Application of plastic potentials to strain rate sensitive and insensitive anisotropic materials", *International Journal of Plasticity*, Elsevier, Vol. 10 No. 7, pp. 719–748.

van Houtte, P. and van Bael, A. (2004), "Convex plastic potentials of fourth and sixth rank for anisotropic materials", *International Journal of Plasticity*, Elsevier, Vol. 20 No. 8–9, pp. 1505–1524.

Hsu, C.Y., Lee, B.J. and Mear, M.E. (2009), "Constitutive models for power-law viscous solids containing spherical voids", *International Journal of Plasticity*, Elsevier, Vol. 25 No. 1, pp. 134–160.

Hu, C. and Ghosh, S. (2008), "Locally enhanced Voronoi cell finite element model (LE-VCFEM) for simulating evolving fracture in ductile microstructures containing inclusions", *International Journal for Numerical Methods in Engineering*, Wiley Online Library, Vol. 76 No. 12, pp. 1955–1992.

Hu, J., Jonas, J.J. and Ishikawa, T. (1998), "FEM simulation of the forming of textured aluminum sheets", *Materials Science and Engineering: A*, Elsevier, Vol. 256 No. 1–2, pp. 51–59.

Huang, M. and Man, C.-S. (2003), "Constitutive Relation of Elastic Polycrystal with Quadratic Texture Dependence", *Journal of Elasticity*, Vol. 72 No. 1, pp. 183–212, doi: 10.1023/B:ELAS.0000018756.58679.43.

Huang, Y. (1991), "Accurate dilatation rates for spherical voids in triaxial stress fields", Citeseer.

Huber, G., Brechet, Y. and Pardoen, T. (2005), "Predictive model for void nucleation and void growth controlled ductility in quasi-eutectic cast aluminium alloys", *Acta Materialia*, Elsevier, Vol. 53 No. 9, pp. 2739–2749.

Huespe, A.E., Needleman, A., Oliver, J. and Sánchez, P.J. (2009), "A finite thickness band method for ductile fracture analysis", *International Journal of Plasticity*, Elsevier, Vol. 25 No. 12, pp. 2349–2365.

Huespe, A.E., Needleman, A., Oliver, J. and Sánchez, P.J. (2012), "A finite strain, finite band method for modeling ductile fracture", *International Journal of Plasticity*, Elsevier, Vol. 28 No. 1, pp. 53–69.

Hughes, T.J.R. (1984), "Numerical Implementation of Constitutive Models: Rate-Independent Deviatoric Plasticity", in Nemat-Nasser, S., Asaro, R.J. and Hegemier, G.A. (Eds.), *Theoretical Foundation for Large-Scale Computations for Nonlinear Material Behavior: Proceedings of the Workshop on the Theoretical Foundation for Large-Scale Computations of Nonlinear Material Behavior Evanston, Illinois, October 24, 25, and 26, 1983*, Springer Netherlands, Dordrecht, pp. 29–63, doi: 10.1007/978-94-009-6213-2_3.

Hull, D. and Bacon, D.J. (2001), *Introduction to Dislocations*, Butterworth-Heinemann.

Hure, J. and Barrioz, P.O. (2016), "Theoretical estimates for flat voids coalescence by internal necking", *European Journal of Mechanics - A/Solids*, Vol. 60, pp. 217–226, doi: https://doi.org/10.1016/j.euromechsol.2016.08.001.

Hutchinson, J.W. and Evans, A.G. (2000), "Mechanics of materials: top-down approaches to fracture", *Acta Materialia*, Vol. 48 No. 1, pp. 125–135, doi: https://doi.org/10.1016/S1359-6454(99)00291-8.

Hutchinson, J.W. and Tvergaard, V. (1981), "Shear band formation in plane strain", *International Journal of Solids and Structures*, Elsevier, Vol. 17 No. 5, pp. 451–470.

Inoue, J., Fujii, Y. and Koseki, T. (2008), "Void formation in nanocrystalline Cu film during uniaxial relaxation test", *Acta Materialia*, Elsevier, Vol. 56 No. 17, pp. 4921–4931.

Janson, J. (1978), "A continuous damage approach to the fatigue process", *Engineering Fracture Mechanics*, Elsevier, Vol. 10 No. 3, pp. 651–657.

Jiang, W., Li, Y. and Su, J. (2016), "Modified GTN model for a broad range of stress states and application to ductile fracture", *European Journal of Mechanics-A/Solids*, Elsevier, Vol. 57, pp. 132–148.

Jirásek, M. and Bazant, Z. (2002), *Inelastic Analysis of Structures*.

Johnson, G.R. and Cook, W.H. (1985), “Fracture characteristics of three metals subjected to various strains, strain rates, temperatures and pressures”, *Engineering Fracture Mechanics*, Pergamon, Vol. 21 No. 1, pp. 31–48.

Jones, R.M. (1998), *Mechanics of Composite Materials*, CRC press.

Ju, J.W. and Sun, L.Z. (1999), “A novel formulation for the exterior-point eshelby’s tensor of an ellipsoidal inclusion”, *Journal of Applied Mechanics*, The American Society of Mechanical Engineers, Vol. 66 No. 2, pp. 570–574.

Kachanov, L.M. (1958), “On creep rupture time”, *Izv. Acad. Nauk SSSR, Otd. Techn. Nauk*, Vol. 8, pp. 26–31.

Kailasam, M. and Castaneda, P.P. (1998), “A general constitutive theory for linear and nonlinear particulate media with microstructure evolution”, *Journal of the Mechanics and Physics of Solids*, Elsevier, Vol. 46 No. 3, pp. 427–465.

Kaiser, T., Lu, J., Menzel, A. and Papadopoulos, P. (2020), “A covariant formulation of finite plasticity with plasticity-induced evolution of anisotropy: Modeling, algorithmics, simulation, and comparison to experiments”, *International Journal of Solids and Structures*, Elsevier, Vol. 185, pp. 116–142.

Keralavarma, S.M. (2017), “A multi-surface plasticity model for ductile fracture simulations”, *Journal of the Mechanics and Physics of Solids*, Vol. 103, pp. 100–120, doi: https://doi.org/10.1016/j.jmps.2017.03.005.

Keralavarma, S.M. and Benzerga, A.A. (2008), “An approximate yield criterion for anisotropic porous media”, *Comptes Rendus Mécanique*, Elsevier, Vol. 336 No. 9, pp. 685–692.

Keralavarma, S.M. and Benzerga, A.A. (2010), “A constitutive model for plastically anisotropic solids with non-spherical voids”, *Journal of the Mechanics and Physics of Solids*, Elsevier, Vol. 58 No. 6, pp. 874–901.

Keralavarma, S.M. and Chockalingam, S. (2016), “A criterion for void coalescence in anisotropic ductile materials”, *International Journal of Plasticity*, Vol. 82, pp. 159–176, doi: https://doi.org/10.1016/j.ijplas.2016.03.003.

Keralavarma, S.M., Reddi, D. and Benzerga, A.A. (2020), “Ductile failure as a constitutive instability in porous plastic solids”, *Journal of the Mechanics and Physics of Solids*, Elsevier, p. 103917.

Kestin, J. and Bataille, J. (1977), “Irreversible thermodynamics of continua and internal variables”, *Continuum Models of Discrete Systems*, University of Waterloo Press, pp. 39–67.

Kim, D., Barlat, F., Bouvier, S., Rabahallah, M., Balan, T. and Chung, K. (2007), “Non-quadratic anisotropic potentials based on linear transformation of plastic strain rate”, *International Journal of Plasticity*, Elsevier, Vol. 23 No. 8, pp. 1380–1399.

Kim, D., Chung, K., Barlat, F., Youn, J.R., Kang, T.J. and Xu, B. (2003), “Non-quadratic plane-stress anisotropic strain-rate potential”, *Sixth International Symposium on Microstructures and Mechanical Properties of New Engineering Materials (IMMM 2003), Wuhan, China*, pp. 46–51.

Kim, J., Gao, X. and Srivatsan, T.S. (2004), "Modeling of void growth in ductile solids: effects of stress triaxiality and initial porosity", *Engineering Fracture Mechanics*, Elsevier, Vol. 71 No. 3, pp. 379–400.

Klöcker, H. and Tvergaard, V. (2003), "Growth and coalescence of non-spherical voids in metals deformed at elevated temperature", *International Journal of Mechanical Sciences*, Elsevier, Vol. 45 No. 8, pp. 1283–1308.

Knezevic, M., Beyerlein, I.J., Lovato, M.L., Tomé, C.N., Richards, A.W. and McCabe, R.J. (2014), "A strain-rate and temperature dependent constitutive model for BCC metals incorporating non-Schmid effects: application to tantalum–tungsten alloys", *International Journal of Plasticity*, Elsevier, Vol. 62, pp. 93–104.

Knott, J.F. (1973), *Fundamentals of Fracture Mechanics*, Gruppo Italiano Frattura.

Kocks, U.F., Tomé, C.N. and Wenk, H.-R. (1998), *Texture and Anisotropy: Preferred Orientations in Polycrystals and Their Effect on Materials Properties*, Cambridge University Press.

Kocks, U.F., Tomé, C.N. and Wenk, H.-R. (2000), *Texture and Anisotropy: Preferred Orientations in Polycrystals and Their Effect on Materials Properties*, Cambridge university press.

Kondori, B. and Benzerga, A.A. (2014), "Effect of stress triaxiality on the flow and fracture of Mg alloy AZ31", *Metallurgical and Materials Transactions A*, Springer, Vol. 45 No. 8, pp. 3292–3307.

Kondori, B. and Benzerga, A.A. (2017), "Modeling damage accumulation to fracture in a magnesium-rare earth alloy", *Acta Materialia*, Elsevier, Vol. 124, pp. 225–236.

Koneti, S.R., Gokhale, S.R. and Wadsworth, T.M. (2011), "Intergranular Cracking of Oil Field Tubular Components Resulting from the Tempering Process", *SPE/IADC Drilling Conference and Exhibition*, Society of Petroleum Engineers, Amsterdam, The Netherlands, doi: 10.2118/139762-MS.

Koplik, J. and Needleman, A. (1988), "Void growth and coalescence in porous plastic solids", *International Journal of Solids and Structures*, Elsevier, Vol. 24 No. 8, pp. 835–853.

Kõrgesaar, M., Remes, H. and Romanoff, J. (2014), "Size dependent response of large shell elements under in-plane tensile loading", *International Journal of Solids and Structures*, Elsevier, Vol. 51 No. 21–22, pp. 3752–3761.

Al Kotob, M., Combescure, C., Mazière, M., Rose, T. and Forest, S. (2019), "A general and efficient multistart algorithm for the detection of loss of ellipticity in elastoplastic structures", *International Journal for Numerical Methods in Engineering*, Wiley Online Library.

Krajcinovic, D. (1983), "Constitutive equations for damaging materials".

Krajcinovic, D. (1985), "Continuous damage mechanics revisited: basic concepts and definitions".

Krajcinovic, D. and Fonseka, G.U. (1981), "The continuous damage theory of brittle materials, part 1: general theory".

Krajcinovic, D. and Selvaraj, S. (1984), "Creep rupture of metals—an analytical model".

Kroner, E. and Teodosiu, C. (1974), "Lattice defect approach to plasticity and viscoplasticity", pp. 45–70, doi: 10.1007/978-94-010-2311-5_3.

Krüger, M., Dittmann, M., Aldakheel, F., Härtel, A., Wriggers, P. and Hesch, C. (2019), "Porous-ductile fracture in thermo-elasto-plastic solids with contact applications", *Computational Mechanics*, Springer, pp. 1–26.

Kuroda, M. and Tvergaard, V. (2007), "Effects of texture on shear band formation in plane strain tension/compression and bending", *International Journal of Plasticity*, Elsevier, Vol. 23 No. 2, pp. 244–272.

Lacroix, R., Leblond, J.-B. and Perrin, G. (2016), "Numerical study and theoretical modelling of void growth in porous ductile materials subjected to cyclic loadings", *European Journal of Mechanics-A/Solids*, Elsevier, Vol. 55, pp. 100–109.

Lassance, D., Scheyvaerts, F. and Pardoen, T. (2006), "Growth and coalescence of penny-shaped voids in metallic alloys", *Engineering Fracture Mechanics*, Elsevier, Vol. 73 No. 8, pp. 1009–1034.

Latorre, M. and Montans, F.J. (2016), "Stress and strain mapping tensors and general work-conjugacy in large strain continuum mechanics", *Applied Mathematical Modelling*, Elsevier, Vol. 40 No. 5–6, pp. 3938–3950.

Lawn, B. (1993), *Fracture of Brittle Solids*, Cambridge university press.

Lebedev, V.I. (1976), "Quadratures on a sphere", *USSR Computational Mathematics and Mathematical Physics*, Elsevier, Vol. 16 No. 2, pp. 10–24.

Lebensohn, R.A. (2001), "N-site modeling of a 3D viscoplastic polycrystal using fast Fourier transform", *Acta Materialia*, Elsevier, Vol. 49 No. 14, pp. 2723–2737.

Lebensohn, R.A. and Cazacu, O. (2012), "Effect of single-crystal plastic deformation mechanisms on the dilatational plastic response of porous polycrystals", *International Journal of Solids and Structures*, Elsevier Ltd, Vol. 49 No. 26, pp. 3838–3852, doi: 10.1016/j.ijsolstr.2012.08.019.

Lebensohn, R.A., Idiart, M.I., Castañeda, P.P. and Vincent, P.-G. (2011), "Dilatational viscoplasticity of polycrystalline solids with intergranular cavities", *Philosophical Magazine*, Taylor & Francis, Vol. 91 No. 22, pp. 3038–3067.

Leblond, J., Perrin, G. and Devaux, J. (1995), "An improved Gurson-type model for hardenable ductile metals", *European Journal of Mechanics. A. Solids*, Vol. 14 No. 4, pp. 499–527.

Leblond, J.-B., Kondo, D., Morin, L. and Remmal, A. (2018), "Classical and sequential limit analysis revisited", *Comptes Rendus Mécanique*, Elsevier, Vol. 346 No. 4, pp. 336–349.

Leblond, J.-B. and Morin, L. (2014), "Gurson's criterion and its derivation revisited", *Journal of Applied Mechanics*, American Society of Mechanical Engineers Digital Collection, Vol. 81 No. 5.

Leblond, J.B., Perrin, G. and Devaux, J. (1994), "Bifurcation Effects in Ductile Metals With Nonlocal Damage", *Journal of Applied Mechanics*, Vol. 61 No. 2, pp. 236–242, doi: 10.1115/1.2901435.

Leblond, J.B., Perrin, G. and Suquet, P. (1994), "Exact results and approximate models for porous viscoplastic solids", *International Journal of Plasticity*, Elsevier, Vol. 10 No. 3, pp. 213–235.

Leckie, F.A. and Hayhurst, D.R. (1974), "Creep rupture of structures", *Proceedings of the Royal Society of London. A. Mathematical and Physical Sciences*, The Royal Society London, Vol. 340 No. 1622, pp. 323–347.

Leclerc, J., Wu, L., Nguyen, V.D. and Noels, L. (2018), "A damage to crack transition model accounting for stress triaxiality formulated in a hybrid nonlocal implicit discontinuous Galerkin-cohesive band model framework", *International Journal for Numerical Methods in Engineering*, Wiley Online Library, Vol. 113 No. 3, pp. 374–410.

Ledbetter, H.M. and Austin, M.W. (1985), "Effects of carbon and nitrogen on the elastic constants of AISI type 304 stainless steel", *Materials Science and Engineering*, Elsevier, Vol. 70, pp. 143–149.

Lee, B.J. and Mear, M.E. (1992), "Axisymmetric deformation of power-law solids containing a dilute concentration of aligned spheroidal voids", *Journal of the Mechanics and Physics of Solids*, Vol. 40 No. 8, pp. 1805–1836, doi: https://doi.org/10.1016/0022-5096(92)90052-4.

Lee, B.J. and Mear, M.E. (1999), "Stress concentration induced by an elastic spheroidal particle in a plastically deforming solid", *Journal of the Mechanics and Physics of Solids*, Elsevier, Vol. 47 No. 6, pp. 1301–1336.

Lee, E.H. (1969), "Elastic-Plastic Deformation at Finite Strains", *Journal of Applied Mechanics*, Vol. 36 No. 1, pp. 1–6, doi: 10.1115/1.3564580.

Lee, E.H. and Liu, D.T. (1967), "Finite stain elastic-plastic theory particularly for plane wave analysis", *J. Appl. Phys*, Vol. 38, p. t9.

Lehmann, T. (1991), "The conjugacy between Cauchy stress and logarithm of the left stretch tensor", *European Journal of Mechanics, A/Solids*, Vol. 10 No. 4, pp. 395–404.

Lemaitre, J. (1984), "A three-dimensional ductile damage model applied to deep-drawing forming limits", *Mechanical Behaviour of Materials*, Elsevier, pp. 1047–1053.

Lemaitre, J. (1985a), "A continuous damage mechanics model for ductile fracture".

Lemaitre, J. (1985b), "Coupled elasto-plasticity and damage constitutive equations", *Computer Methods in Applied Mechanics and Engineering*, Elsevier, Vol. 51 No. 1–3, pp. 31–49.

Lemaitre, J. (1987), "Formulation and identification of damage kinetic constitutive equations", *Continuum Damage Mechanics Theory and Application*, Springer, pp. 37–89.

Lemaitre, J. (2012), *A Course on Damage Mechanics*, Springer Science & Business Media.

Lemaitre, J. and Chaboche, J.-L. (1978), "Aspect phénoménologique de la rupture par endommagement", *J Méc Appl*, Vol. 2 No. 3.

Lemaitre, J. and Chaboche, J.-L. (1994), *Mechanics of Solid Materials*, Cambridge University Press.

Lemaitre, J. and Desmorat, R. (2005), *Engineering Damage Mechanics: Ductile, Creep, Fatigue and Brittle Failures*, Springer Science & Business Media.

Lemaitre, J., Desmorat, R. and Sauzay, M. (2000), "Anisotropic damage law of evolution", *European Journal of Mechanics-A/Solids*, Elsevier, Vol. 19 No. 2, pp. 187–208.

Lemaitre, J. and Dufailly, J. (1987), "Damage measurements", *Engineering Fracture Mechanics*, Elsevier, Vol. 28 No. 5–6, pp. 643–661.

Li, S., van Bael, A., van Houtte, P. and Hoferlin, E. (2001), "Application of a texture-based plastic potential in earing prediction of an IF steel", *Advanced Engineering Materials*, Vol. 3.

Li, S., Sauer, R.A. and Wang, G. (2007), "The Eshelby tensors in a finite spherical domain—part I: theoretical formulations".

Li, Z. and Steinmann, P. (2006), "RVE-based studies on the coupled effects of void size and void shape on yield behavior and void growth at micron scales", *International Journal of Plasticity*, Elsevier, Vol. 22 No. 7, pp. 1195–1216.

Lian, J. and Chen, J. (1991), "Isotropic polycrystal yield surfaces of bcc and fcc metals: crystallographic and continuum mechanics approaches", *Acta Metallurgica et Materialia*, Elsevier, Vol. 39 No. 10, pp. 2285–2294.

Liao, K.C., Pan, J. and Tang, S.C. (1997), "Approximate yield criteria for anisotropic porous ductile sheet metals", *Mechanics of Materials*, Elsevier, Vol. 26 No. 4, pp. 213–226, doi: 10.1016/S0167-6636(97)00033-1.

Licht, C. and Suquet, P. (1988), "Growth of cylindrical voids in nonlinear viscous material at arbitrary void volume fractions: a simple model", *Arch. Mech*, Vol. 40, pp. 741–757.

Lloyd, J.T. and Priddy, M.W. (2017), "Simulating strain localization in rolled magnesium", *Acta Materialia*, Elsevier, Vol. 129, pp. 149–158.

Lou, X.Y., Li, M., Boger, R.K., Agnew, S.R. and Wagoner, R.H. (2007), "Hardening evolution of AZ31B Mg sheet", *International Journal of Plasticity*, Elsevier, Vol. 23 No. 1, pp. 44–86.

Lou, Y., Chen, L., Clausmeyer, T., Tekkaya, A.E. and Yoon, J.W. (2017), "Modeling of ductile fracture from shear to balanced biaxial tension for sheet metals", *International Journal of Solids and Structures*, Vol. 112, pp. 169–184, doi: https://doi.org/10.1016/j.ijsolstr.2016.11.034.

Lou, Y., Huh, H., Lim, S. and Pack, K. (2012), "New ductile fracture criterion for prediction of fracture forming limit diagrams of sheet metals", *International Journal of Solids and Structures*, Vol. 49 No. 25, pp. 3605–3615, doi: https://doi.org/10.1016/j.ijsolstr.2012.02.016.

Lou, Y., Yoon, J.W. and Huh, H. (2014), "Modeling of shear ductile fracture considering a changeable cut-off value for stress triaxiality", *International Journal of Plasticity*, Vol. 54, pp. 56–80, doi: https://doi.org/10.1016/j.ijplas.2013.08.006.

Lubarda, V.A. (2002), *Elastoplasticity Theory*, CRC press.

Lubarda, V.A. and Lee, E.H. (1981), "A Correct Definition of Elastic and Plastic Deformation and Its Computational Significance", *Journal of Applied Mechanics*, Vol. 48 No. 1, pp. 35–40, doi: 10.1115/1.3157589.

Lubarda, V.A., Schneider, M.S., Kalantar, D.H., Remington, B.A. and Meyers, M.A. (2004), "Void growth by dislocation emission", *Acta Materialia*, Elsevier, Vol. 52 No. 6, pp. 1397–1408.

Lubliner, J. (1984), "A maximum-dissipation principle in generalized plasticity", *Acta Mechanica*, Springer, Vol. 52, pp. 225–237.

Lubliner, J. (1986), "Normality rules in large-deformation plasticity", *Mechanics of Materials*, Elsevier, Vol. 5 No. 1, pp. 29–34.

Lubliner, J. (2008), *Plasticity Theory*, Courier Corporation.

Ma, C., Wang, H., Hama, T., Guo, X., Mao, X., Wang, J. and Wu, P. (2019), "Twinning and detwinning behaviors of commercially pure titanium sheets", *International Journal of Plasticity*, Elsevier, Vol. 121, pp. 261–279.

Madou, K. and Leblond, J.-B. (2012a), "A Gurson-type criterion for porous ductile solids containing arbitrary ellipsoidal voids-I: Limit-analysis of some representative cell", *Journal of the Mechanics and Physics of Solids*, Elsevier, Vol. 60 No. 5, pp. 1020–1036.

Madou, K. and Leblond, J.-B. (2012b), "A Gurson-type criterion for porous ductile solids containing arbitrary ellipsoidal voids-II: Determination of yield criterion parameters", *Journal of the Mechanics and Physics of Solids*, Elsevier, Vol. 60 No. 5, pp. 1037–1058.

Madou, K. and Leblond, J.-B. (2013), "Numerical studies of porous ductile materials containing arbitrary ellipsoidal voids-I: Yield surfaces of representative cells", *European Journal of Mechanics-A/Solids*, Elsevier, Vol. 42, pp. 480–489.

Madou, K., Leblond, J.-B. and Morin, L. (2013), "Numerical studies of porous ductile materials containing arbitrary ellipsoidal voids-II: Evolution of the length and orientation of the void axes", *European Journal of Mechanics-A/Solids*, Elsevier, Vol. 42, pp. 490–507.

Maire, E., Bordreuil, C., Babout, L. and Boyer, J.-C. (2005), "Damage initiation and growth in metals. Comparison between modelling and tomography experiments", *Journal of the Mechanics and Physics of Solids*, Elsevier, Vol. 53 No. 11, pp. 2411–2434.

Malcher, L., Pires, F.M.A. and De Sá, J.M.A.C. (2014), "An extended GTN model for ductile fracture under high and low stress triaxiality", *International Journal of Plasticity*, Elsevier, Vol. 54, pp. 193–228.

Malvern, L.E. (1969), *Introduction to the Mechanics of a Continuous Medium*.

Mandel, J. (1966), "Cours de mécanique des milieux continus", Gauthier-Villars.

Mandel, J. (1971), "Plasticite classique et viscoplasticite. course and lectures", *Int. Centre for Mech. Sciences*, Vol. 97.

Mandel, J. (1972), *Plasticite Classique et Viscoplasticite:*, Springer.

Mandel, J. (1973), "Equations constitutives et directeurs dans les milieux plastiques et viscoplastiques", *International Journal of Solids and Structures*, Vol. 9 No. 6, pp. 725–740, doi: https://doi.org/10.1016/0020-7683(73)90120-0.

Marino, B., Mudry, F. and Pineau, A. (1985), "Experimental study of cavity growth in ductile rupture", *Engineering Fracture Mechanics*, Elsevier, Vol. 22 No. 6, pp. 989–996.

Marquis, D. and Lemaitre, J. (1988), "Constitutive equations for the coupling between elasto-plasticity damage and aging", *Revue de Physique Appliquée*, Société française de physique, Vol. 23 No. 4, pp. 615–624.

Maudlin, P.J., Bingert, J.F., House, J.W. and Chen, S.R. (1999), "On the modeling of the Taylor cylinder impact test for orthotropic textured materials: experiments and simulations", *International Journal of Plasticity*, Elsevier, Vol. 15 No. 2, pp. 139–166.

McClintock, F.A. (1968), "A Criterion for Ductile Fracture by the Growth of Holes", *Journal of Applied Mechanics*, Vol. 35 No. 2, pp. 363–371, doi: 10.1115/1.3601204.

McClintock, F.A. (1971), "Plasticity aspects of fracture", *Engineering Fundamentals and Environmental Effects*, Elsevier, pp. 47–225.

McClintock, F.A. and Argon, A.S. (1966), *Mechanical Behavior of Materials*, Addison Wesley.

McClintock, F.A., Kaplan, S.M. and Berg, C.A. (1966), "Ductile fracture by hole growth in shear bands", *International Journal of Fracture Mechanics*, Springer, Vol. 2 No. 4, pp. 614–627.

McLaren, A.D. (1963), "Optimal numerical integration on a sphere", *Mathematics of Computation*, JSTOR, Vol. 17 No. 84, pp. 361–383.

Mear, M.E. and Hutchinson, J.W. (1985), "Influence of yield surface curvature on flow localization in dilatant plasticity", *Mechanics of Materials*, Elsevier, Vol. 4 No. 3–4, pp. 395–407.

Mediavilla, J., Peerlings, R.H.J. and Geers, M.G.D. (2006), "A nonlocal triaxiality-dependent ductile damage model for finite strain plasticity", *Computer Methods in Applied Mechanics and Engineering*, Elsevier, Vol. 195 No. 33–36, pp. 4617–4634.

Mediavilla, V.J. (2005), *Continuous and Discontinuous Modelling of Ductile Fracture*, PhD Thesis, Technische Universiteit Eindhoven.

Menezes, L.F. and Teodosiu, C. (2000), "Three-dimensional numerical simulation of the deep-drawing process using solid finite elements", *Journal of Materials Processing Technology*, Vol. 97 No. 1–3, pp. 100–106, doi: 10.1016/S0924-0136(99)00345-3.

Michel, J.C., Moulinec, H. and Suquet, P. (2001), "A computational scheme for linear and non-linear composites with arbitrary phase contrast", *International Journal for Numerical Methods in Engineering*, Wiley Online Library, Vol. 52 No. 1-2, pp. 139–160.

Michel, J.C. and Suquet, P. (1992), "The constitutive law of nonlinear viscous and porous materials", *Journal of the Mechanics and Physics of Solids*, Elsevier, Vol. 40 No. 4, pp. 783–812.

Miller, B.A. (2002), "Overload Failures", edited by Becker, W.T. and Shipley, R.J.*Failure Analysis and Prevention*, ASM International, 1 January, doi: 10.31399/asm.hb.v11.a0003543.

Miner, M.A. (1945), "Cumulative fatigue damage", *Journal of Applied Mechanics*, Vol. 12 No. 3, pp. A159–A164.

Mises, R. von. (1928), "Mechanik der plastischen Formänderung von Kristallen", *ZAMM-Journal of Applied Mathematics and Mechanics/Zeitschrift Für Angewandte Mathematik Und Mechanik*, Wiley Online Library, Vol. 8 No. 3, pp. 161–185.

Mohr, D. and Marcadet, S.J. (2015), "Micromechanically-motivated phenomenological Hosford–Coulomb model for predicting ductile fracture initiation at low stress triaxialities", *International Journal of Solids and Structures*, Vol. 67–68, pp. 40–55, doi: https://doi.org/10.1016/j.ijsolstr.2015.02.024.

Monchiet, V. and Bonnet, G. (2013), "A Gurson-type model accounting for void size effects", *International Journal of Solids and Structures*, Elsevier, Vol. 50 No. 2, pp. 320–327.

Monchiet, V., Cazacu, O., Charkaluk, E. and Kondo, D. (2008), "Macroscopic yield criteria for plastic anisotropic materials containing spheroidal voids", *International Journal of Plasticity*, Vol. 24 No. 7, pp. 1158–1189, doi: https://doi.org/10.1016/j.ijplas.2007.08.008.

Monchiet, V., Charkaluk, E. and Kondo, D. (2007), "An improvement of Gurson-type models of porous materials by using Eshelby-like trial velocity fields", *Comptes Rendus Mecanique*, Elsevier, Vol. 335 No. 1, pp. 32–41.

Monchiet, V., Charkaluk, E. and Kondo, D. (2011), "A micromechanics-based modification of the Gurson criterion by using Eshelby-like velocity fields", *European Journal of Mechanics-A/Solids*, Elsevier, Vol. 30 No. 6, pp. 940–949.

Monchiet, V., Charkaluk, E. and Kondo, D. (2014), "Macroscopic yield criteria for ductile materials containing spheroidal voids: An Eshelby-like velocity fields approach", *Mechanics of Materials*, Vol. 72, pp. 1–18, doi: https://doi.org/10.1016/j.mechmat.2013.05.006.

Monchiet, V., Gruescu, C., Charkaluk, E. and Kondo, D. (2006), "Approximate yield criteria for anisotropic metals with prolate or oblate voids", *Comptes Rendus Mécanique*, Vol. 334 No. 7, pp. 431–439, doi: https://doi.org/10.1016/j.crme.2006.06.001.

Montáns, F.J. and Bathe, K.J. (2007), "Towards a model for large strain anisotropic elasto-plasticity", *Computational Plasticity*, Springer, pp. 13–36.

Montáns, F.J., Benítez, J.M. and Caminero, M.Á. (2012), "A large strain anisotropic elastoplastic continuum theory for nonlinear kinematic hardening and texture evolution", *Mechanics Research Communications*, Elsevier, Vol. 43, pp. 50–56.

Montheillet, F. and Moussy, F. (2012), *Physique et Mécanique de l'endommagement*, EDP Sciences.

Moran, B., Asaro, R.J. and Shih, C.F. (1991), "Effects of material rate sensitivity and void nucleation on fracture initiation in a circumferentially cracked bar", *Metallurgical Transactions A*, Springer, Vol. 22 No. 1, pp. 161–170.

Moreau, J.-J. (1966), "Fonctionnelles convexes", *Séminaire Jean Leray*, No. 2, pp. 1–108.

Moreau, J.J. (1970), "Sur les lois de frottement, de viscosité et de plasticité", *CR Acad. Sci. Paris Sér. II Méc. Phys. Chim. Sci. Univers Sci. Terre*, Vol. 271, pp. 608–611.

Morgeneyer, T.F., Taillandier-Thomas, T., Helfen, L., Baumbach, T., Sinclair, I., Roux, S. and Hild, F. (2014), "In situ 3-D observation of early strain localization during failure of thin Al alloy (2198) sheet", *Acta Materialia*, Elsevier, Vol. 69, pp. 78–91.

Morin, D., Dæhli, L.E.B., Børvik, T., Benallal, A. and Hopperstad, O.S. (2019), "Numerical study of ductile failure under non-proportional loading", *European Journal of Mechanics-A/Solids*, Elsevier, Vol. 74, pp. 221–241.

Morin, L. (2015), *Influence Des Effets de Forme et de Taille Des Cavités, et de l'anisotropie Plastique Sur La Rupture Ductile*, PhD Thesis, Université Pierre et Marie Curie, Paris VI.

Morin, L., Leblond, J.-B. and Benzerga, A.A. (2015), "Coalescence of voids by internal necking: theoretical estimates and numerical results", *Journal of the Mechanics and Physics of Solids*, Elsevier, Vol. 75, pp. 140–158.

Morin, L., Leblond, J.-B., Benzerga, A.A. and Kondo, D. (2016), "A unified criterion for the growth and coalescence of microvoids", *Journal of the Mechanics and Physics of Solids*, Elsevier, Vol. 97, pp. 19–36.

Morin, L., Leblond, J.-B. and Kondo, D. (2015), "A Gurson-type criterion for plastically anisotropic solids containing arbitrary ellipsoidal voids", *International Journal of Solids and Structures*, Elsevier, Vol. 77, pp. 86–101.

Morin, L., Leblond, J.-B. and Tvergaard, V. (2016), "Application of a model of plastic porous materials including void shape effects to the prediction of ductile failure under shear-dominated loadings", *Journal of the Mechanics and Physics of Solids*, Elsevier, Vol. 94, pp. 148–166.

Morin, L., Madou, K., Leblond, J.-B. and Kondo, D. (2014), "A new technique for finite element limit-analysis of Hill materials, with an application to the assessment of criteria for anisotropic plastic porous solids", *International Journal of Engineering Science*, Elsevier, Vol. 74, pp. 65–79.

Morin, L. and Michel, J.-C. (2018), "Void coalescence in porous ductile solids containing two populations of cavities", *European Journal of Mechanics-A/Solids*, Elsevier, Vol. 72, pp. 341–353.

Morin, L., Michel, J.-C. and Leblond, J.-B. (2017), "A Gurson-type layer model for ductile porous solids with isotropic and kinematic hardening", *International Journal of Solids and Structures*, Elsevier, Vol. 118, pp. 167–178.

Mouritz, A.P. (2012), *Introduction to Aerospace Materials*, Elsevier.

Mühlich, U. and Brocks, W. (2003), "On the numerical integration of a class of pressure-dependent plasticity models including kinematic hardening", *Computational Mechanics*, Springer, Vol. 31 No. 6, pp. 479–488.

Müller, C. (2006), *Spherical Harmonics*, Vol. 17, Springer.

Mura, T. (2013), *Micromechanics of Defects in Solids*, Springer Science & Business Media.

Murakami, S. and Ohno, N. (1981), "A continuum theory of creep and creep damage", *Creep in Structures*, Springer, pp. 422–444.

Nagata, T. (2005), "Simple local interpolation of surfaces using normal vectors", *Computer Aided Geometric Design*, Elsevier, Vol. 22 No. 4, pp. 327–347.

Naghdi, P.M. (1990), "A critical review of the state of finite plasticity", *Zeitschrift Für Angewandte Mathematik Und Physik ZAMP*, Vol. 41 No. 3, pp. 315–394, doi: 10.1007/BF00959986.

Nahshon, K. and Hutchinson, J.W. (2008), "Modification of the Gurson Model for shear failure", *European Journal of Mechanics - A/Solids*, Elsevier Masson, Vol. 27 No. 1, pp. 1–17, doi: 10.1016/J.EUROMECHSOL.2007.08.002.

Needleman, A. (1972a), "A numerical study of necking in circular cylindrical bar", *Journal of the Mechanics and Physics of Solids*, Elsevier, Vol. 20 No. 2, pp. 111–127.

Needleman, A. (1972b), "Void growth in an elastic-plastic medium", *Journal of Applied Mechanics*, Vol. 39 No. 4, pp. 964–970, doi: 10.1115/1.3422899.

Needleman, A. (1987), "A continuum model for void nucleation by inclusion debonding", *Journal of Applied Mechanics*, Vol. 54 No. 3, pp. 525–531, doi: 10.1115/1.3173064.

Needleman, A. (1988), "Material rate dependence and mesh sensitivity in localization problems", *Computer Methods in Applied Mechanics and Engineering*, Vol. 67 No. 1, pp. 69–85, doi: https://doi.org/10.1016/0045-7825(88)90069-2.

Needleman, A. (1989), "Dynamic shear band development in plane strain".

Needleman, A. (1990), "An analysis of tensile decohesion along an interface", *Journal of the Mechanics and Physics of Solids*, Elsevier, Vol. 38 No. 3, pp. 289–324.

Needleman, A. and Rice, J.R. (1978), "Limits to ductility set by plastic flow localization", *Mechanics of Sheet Metal Forming*, Springer, pp. 237–267.

Needleman, A. and Tvergaard, V. (1984), "An analysis of ductile rupture in notched bars", *Journal of the Mechanics and Physics of Solids*, Elsevier, Vol. 32 No. 6, pp. 461–490.

Neff, P., Eidel, B. and Martin, R.J. (2016), "Geometry of logarithmic strain measures in solid mechanics", *Archive for Rational Mechanics and Analysis*, Springer, Vol. 222, pp. 507–572.

Nemat-Nasser, S. and Hori, M. (2013), *Micromechanics: Overall Properties of Heterogeneous Materials*, Elsevier.

Neto, D.M., Oliveira, M.C., Menezes, L.F. and Alves, J.L. (2014), "Applying Nagata patches to smooth discretized surfaces used in 3D frictional contact problems", *Computer Methods in Applied Mechanics and Engineering*, Elsevier, Vol. 271, pp. 296–320.

Nguyen, Q.S. (1993), *Bifurcation and Stability of Dissipative Systems*, Springer-Verlag Wien.

Nielsen, K.L. and Tvergaard, V. (2010), "Ductile shear failure or plug failure of spot welds modelled by modified Gurson model", *Engineering Fracture Mechanics*, Elsevier, Vol. 77 No. 7, pp. 1031–1047.

Nixon, M.E., Cazacu, O. and Lebensohn, R.A. (2010), "Anisotropic response of high-purity α-titanium: Experimental characterization and constitutive modeling", *International Journal of Plasticity*, Elsevier, Vol. 26 No. 4, pp. 516–532.

Noell, P., Carroll, J., Hattar, K., Clark, B. and Boyce, B. (2017), "Do voids nucleate at grain boundaries during ductile rupture?", *Acta Materialia*, Elsevier, Vol. 137, pp. 103–114.

Noell, P., Carroll, J., Hattar, K.M., Clark, B. and Boyce, B.L. (2018), *Ductile Fracture in Pure Metals: From Void Nucleation to Final Fracture.*, Sandia National Lab.(SNL-NM), Albuquerque, NM (United States).

Oliveira, M.C., Alves, J.L. and Menezes, L.F. (2008), "Algorithms and strategies for treatment of large deformation frictional contact in the numerical simulation of deep drawing process", *Archives of Computational Methods in Engineering*, Vol. 15 No. 2, pp. 113–162, doi: 10.1007/s11831-008-9018-x.

Ortiz, M. and Popov, E.P. (1985), "Accuracy and stability of integration algorithms for elastoplastic constitutive relations", *International Journal for Numerical Methods in Engineering*, Wiley Online Library, Vol. 21 No. 9, pp. 1561–1576.

Pan, J., Saje, M. and Needleman, A. (1983), "Localization of deformation in rate sensitive porous plastic solids", *International Journal of Fracture*, Springer, Vol. 21 No. 4, pp. 261–278.

Pardoen, T. and Delannay, F. (1998), "Assessment of void growth models from porosity measurements in cold-drawn copper bars", *Metallurgical and Materials Transactions A*, Springer, Vol. 29 No. 7, pp. 1895–1909.

Pardoen, T. and Hutchinson, J.W. (2000), "An extended model for void growth and coalescence", *Journal of the Mechanics and Physics of Solids*, Elsevier, Vol. 48 No. 12, pp. 2467–2512.

Pastor, F., Kondo, D. and Pastor, J. (2013), "3D-FEM formulations of limit analysis methods for porous pressure-sensitive materials", *International Journal for Numerical Methods in Engineering*, Wiley Online Library, Vol. 95 No. 10, pp. 847–870.

Pastor, F., Loute, E. and Pastor, J. (2009), "Limit analysis and convex programming: A decomposition approach of the kinematic mixed method", *International Journal for Numerical Methods in Engineering*, Wiley Online Library, Vol. 78 No. 3, pp. 254–274.

Pastor, F., Pastor, J. and Kondo, D. (2012), "Limit analysis of hollow spheres or spheroids with Hill orthotropic matrix", *Comptes Rendus Mécanique*, Elsevier, Vol. 340 No. 3, pp. 120–129.

Paux, J., Morin, L., Brenner, R. and Kondo, D. (2015), "An approximate yield criterion for porous single crystals", *European Journal of Mechanics-A/Solids*, Elsevier, Vol. 51, pp. 1–10.

Peerlings, R.H.J., de Borst, R., Brekelmans, W.A.M. and De Vree, J.H.P. (1996), "Gradient enhanced damage for quasi-brittle materials", *International Journal for Numerical Methods in Engineering*, Wiley Online Library, Vol. 39 No. 19, pp. 3391–3403.

Perić, D., Owen, D.R.J. and Honnor, M. (1992), "A model for finite strain elasto-plasticity based on logarithmic strains: Computational issues", *Computer Methods in Applied Mechanics and Engineering*, Elsevier, Vol. 94 No. 1, pp. 35–61.

Perrin, G. and Leblond, J.B. (1990), "Analytical study of a hollow sphere made of plastic porous material and subjected to hydrostatic tension-application to some problems in ductile fracture of metals", *International Journal of Plasticity*, Elsevier, Vol. 6 No. 6, pp. 677–699.

Perrin, G. and Leblond, J.-B. (2000), "Accelerated void growth in porous ductile solids containing two populations of cavities", *International Journal of Plasticity*, Elsevier, Vol. 16 No. 1, pp. 91–120.

Petch, N.J. (1953), "The cleavage strength of polycrystals", *Journal of the Iron and Steel Institute*, Vol. 174, pp. 25–28.

Pijaudier-Cabot, G. and Bažant, Z.P. (1987), "Nonlocal damage theory", *Journal of Engineering Mechanics*, American Society of Civil Engineers, Vol. 113 No. 10, pp. 1512–1533.

Pineau, A., Benzerga, A.A. and Pardoen, T. (2016), "Failure of metals I: Brittle and ductile fracture", *Acta Materialia*, Elsevier, Vol. 107, pp. 424–483.

Pineau, A. and Pardoen, T. (2007), "Failure of Metals", in Milne, I., Ritchie, R.O. and Karihaloo, B.B.T.-C.S.I. (Eds.), , Pergamon, Oxford, pp. 684–797, doi: https://doi.org/10.1016/B0-08-043749-4/02109-1.

Pires, F.M.A. (2005), *Issues on the Finite Element Modelling of Degradation and Prediction of Failure in Finitely Straining Ductile Materials*, PhD Thesis, School of Engineering, University of Wales, Swansea.

Plunkett, B., Cazacu, O. and Barlat, F. (2008), "Orthotropic yield criteria for description of the anisotropy in tension and compression of sheet metals", *International Journal of Plasticity*, Elsevier, Vol. 24 No. 5, pp. 847–866.

Plunkett, B., Lebensohn, R.A., Cazacu, O. and Barlat, F. (2006), "Anisotropic yield function of hexagonal materials taking into account texture development and anisotropic hardening", *Acta Materialia*, Vol. 54 No. 16, pp. 4159–4169, doi: https://doi.org/10.1016/j.actamat.2006.05.009.

Prager, W. and Hodge, P.G. (1968), *Theory of Perfectly Plastic Solids*, Dover Publications.

Puttick, K.E. (1959), "Ductile fracture in metals", *Philosophical Magazine*, Taylor & Francis, Vol. 4 No. 44, pp. 964–969.

Qin, Q. and Bassani, J.L. (1992), "Non-Schmid yield behavior in single crystals", *Journal of the Mechanics and Physics of Solids*, Elsevier, Vol. 40 No. 4, pp. 813–833.

Raabe, D. (1998), "Computational materials science-the simulation of materials microstructures and properties", Wiley-Vch.

Raabe, D. (2014), "Recovery and Recrystallization: Phenomena, Physics, Models, Simulation", in Laughlin, D.E. and Hono, K.B.T.-P.M. (Fifth E. (Eds.), , Elsevier, Oxford, pp. 2291–2397, doi: https://doi.org/10.1016/B978-0-444-53770-6.00023-X.

Rabahallah, M., Balan, T. and Barlat, F. (2009), "Anisotropic strain-rate potential based on multiple linear transformations", *International Journal of Material Forming*, Springer, Vol. 2 No. 1, pp. 479–482.

Rabahallah, M., Balan, T., Bouvier, S. and Teodosiu, C. (2009), "Time integration scheme for elasto-plastic models based on anisotropic strain-rate potentials", *International Journal for Numerical Methods in Engineering*, Wiley Online Library, Vol. 80 No. 3, pp. 381–402.

Rabotnov, Y.N. (1963), "Paper 68: On the equation of state of creep", *Proceedings of the Institution of Mechanical Engineers, Conference Proceedings*, Vol. 178, SAGE Publications Sage UK: London, England, pp. 2–117.

Raemy, C., Manopulo, N. and Hora, P. (2017), "On the modelling of plastic anisotropy, asymmetry and directional hardening of commercially pure titanium: A planar Fourier series based approach", *International Journal of Plasticity*, Elsevier, Vol. 91, pp. 182–204.

Raniecki, B. and Nguyen, H.V. (1984), "Isotropic elastic-plastic solids at finite strain and arbitrary pressure", *Arch. Mech.;(Poland)*, Vol. 36.

Revil-Baudard, B. and Cazacu, O. (2014), "New three-dimensional strain-rate potentials for isotropic porous metals: role of the plastic flow of the matrix", *International Journal of Plasticity*, Elsevier, Vol. 60, pp. 101–117.

Revil-Baudard, B., Cazacu, O., Flater, P., Chandola, N. and Alves, J.L. (2016), "Unusual plastic deformation and damage features in titanium: Experimental tests and constitutive modeling", *Journal of the Mechanics and Physics of Solids*, Elsevier, Vol. 88, pp. 100–122, doi: 10.1016/j.jmps.2016.01.003.

Revil-Baudard, B., Cazacu, O. and Massoni, E. (2021), "Room-temperature plastic behavior and formability of a commercially pure titanium: Mechanical characterization, modeling, and validation", *International Journal of Solids and Structures*, Elsevier, Vol. 228, p. 111121.

Revil-Baudard, B., Chandola, N., Cazacu, O. and Barlat, F. (2014), "Correlation between swift effects and tension–compression asymmetry in various polycrystalline materials", *Journal of the Mechanics and Physics of Solids*, Elsevier, Vol. 70, pp. 104–115.

Revil-Baudard, B., Yoon, J., Stewart, J.B. and Cazacu, O. (2012), "On the influence of damage evolution in an incompressible material with matrix displaying tension-compression asymmetry", *Procedia IUTAM*, Vol. 3, pp. 331–349, doi: 10.1016/j.piutam.2012.03.021.

Rice, J. (1976), "Localization of plastic deformation", *Theoretical and Applied Mechanics*.

Rice, J. and Budiansky, B. (1973), "Conservation laws and energy-release rates", *J Appl Mech*, Vol. 40, pp. 201–203.

Rice, J.R. (1971), "Inelastic constitutive relations for solids: an internal-variable theory and its application to metal plasticity", *Journal of the Mechanics and Physics of Solids*, Elsevier, Vol. 19 No. 6, pp. 433–455.

Rice, J.R. and Tracey, D.M. (1969), "On the ductile enlargement of voids in triaxial stress fields", *Journal of the Mechanics and Physics of Solids*, Pergamon, Vol. 17 No. 3, pp. 201–217.

Richman, R.H. (1964), "The diversity of twinning in body-centered cubic structures", *Deformation Twinning*, Gordon and Breach Science Publisher, pp. 237–271.

Richmond, O. and Smelser, R.E. (1985), "Alcoa technical center memorandum, March 7", *Void Growth in Elastic–Plastic Materials. J Appl Mech*, Vol. 56, pp. 309–317.

Ristinmaa, M. (1997), "Void growth in cyclic loaded porous plastic solid", *Mechanics of Materials*, Elsevier, Vol. 26 No. 4, pp. 227–245.

Rivalin, F., Besson, J., Pineau, A. and Di Fant, M. (2001), "Ductile tearing of pipeline-steel wide plates: II. Modeling of in-plane crack propagation", *Engineering Fracture Mechanics*, Elsevier, Vol. 68 No. 3, pp. 347–364.

Rodriguez, A.K., Ayoub, G.A., Mansoor, B. and Benzerga, A.A. (2016), "Effect of strain rate and temperature on fracture of magnesium alloy AZ31B", *Acta Materialia*, Elsevier, Vol. 112, pp. 194–208.

Roth, C.C., Morgeneyer, T.F., Cheng, Y., Helfen, L. and Mohr, D. (2018), "Ductile damage mechanism under shear-dominated loading: In-situ tomography experiments on dual phase steel and localization analysis", *International Journal of Plasticity*, Elsevier, Vol. 109, pp. 169–192.

Rousselier, G. (1987), "Ductile fracture models and their potential in local approach of fracture", *Nuclear Engineering and Design*, Elsevier, Vol. 105 No. 1, pp. 97–111.

Le Roy, G., Embury, J.D., Edwards, G. and Ashby, M.F. (1981), "A model of ductile fracture based on the nucleation and growth of voids", *Acta Metallurgica*, Elsevier, Vol. 29 No. 8, pp. 1509–1522.

Rudnicki, J.W. and Rice, J.R. (1975), "Conditions for the localization of deformation in pressure-sensitive dilatant materials", *Journal of the Mechanics and Physics of Solids*, Citeseer, Vol. 23 No. 6, pp. 371–394.

Ryu, S., Lee, S., Jung, J., Lee, J. and Kim, Y. (2019), "Micromechanics-based homogenization of the effective physical properties of composites with an anisotropic matrix and interfacial imperfections", *Frontiers in Materials*, Frontiers, p. 21.

de Sa, J.M.A.C., Andrade, F.X.C. and Pires, F.M.A. (2010), "Theoretical and numerical issues on ductile failure prediction-an overview", *Computer Methods in Materials Science*, Vol. 10 No. 4, pp. 279–293.

Saanouni, K. (2013), *Damage Mechanics in Metal Forming: Advanced Modeling and Numerical Simulation*, John Wiley & Sons.

Saanouni, K., Chaboche, J.L. and Lesne, P.M. (1989), "On the creep crack-growth prediction by a non local damage formulation", *European Journal of Mechanics. A. Solids*, Vol. 8 No. 6, pp. 437–459.

Saje, M., Pan, J. and Needleman, A. (1982), "Void nucleation effects on shear localization in porous plastic solids", *International Journal of Fracture*, Springer, Vol. 19 No. 3, pp. 163–182.

Salençon, J. (1983), *Calcul à La Rupture et Analyse Limite*.

Scheyvaerts, F., Onck, P.R., Tekoglu, C. and Pardoen, T. (2011), "The growth and coalescence of ellipsoidal voids in plane strain under combined shear and tension", *Journal of the Mechanics and Physics of Solids*, Elsevier, Vol. 59 No. 2, pp. 373–397.

Scheyvaerts, F., Pardoen, T. and Onck, P.R. (2010), "A new model for void coalescence by internal necking", *International Journal of Damage Mechanics*, Sage Publications Sage UK: London, England, Vol. 19 No. 1, pp. 95–126.

Schmid, E. (1924), "Yield point of crystals, critical shear stress law", *Proceedings of the First International Congress for Applied Mechanics, Delft*.

Schofield, A. and Wroth, P. (1968), *Critical State Soil Mechanics*, McGraw-hill.

Segurado, J. and LLorca, J. (2004), "A new three-dimensional interface finite element to simulate fracture in composites", *International Journal of Solids and Structures*, Elsevier, Vol. 41 No. 11–12, pp. 2977–2993.

Seymour, P.D. and Zaslavsky, T. (1984), "Averaging sets: a generalization of mean values and spherical designs", *Advances in Mathematics*, Academic Press, Vol. 52 No. 3, pp. 213–240.

Shi, B., Peng, Y., Yang, C., Pan, F., Cheng, R. and Peng, Q. (2017), "Loading path dependent distortional hardening of Mg alloys: Experimental investigation and constitutive modeling", *International Journal of Plasticity*, Elsevier, Vol. 90, pp. 76–95.

Shinohara, Y., Madi, Y. and Besson, J. (2016), "Anisotropic ductile failure of a high-strength line pipe steel", *International Journal of Fracture*, Springer, Vol. 197, pp. 127–145.

Simo, J.C. (1985), "On the computational significance of the intermediate configuration and hyperelastic stress relations in finite deformation elastoplasticity", *Mechanics of Materials*, Elsevier, Vol. 4 No. 3–4, pp. 439–451.

Simo, J.C. (1992), “Algorithms for static and dynamic multiplicative plasticity that preserve the classical return mapping schemes of the infinitesimal theory”, *Computer Methods in Applied Mechanics and Engineering*, Vol. 99 No. 1, pp. 61–112, doi: https://doi.org/10.1016/0045-7825(92)90123-2.

Simo, J.C. and Govindjee, S. (1991), “Non-linear B-stability and symmetry preserving return mapping algorithms for plasticity and viscoplasticity”, *International Journal for Numerical Methods in Engineering*, Wiley Online Library, Vol. 31 No. 1, pp. 151–176.

Simo, J.C. and Hughes, T.J.R. (2006), *Computational Inelasticity*, Vol. 7, Springer Science & Business Media.

Simo, J.C. and Ju, J.W. (1987), “Strain-and stress-based continuum damage models—I. Formulation”, *International Journal of Solids and Structures*, Elsevier, Vol. 23 No. 7, pp. 821–840.

Simo, J.C. and Ortiz, M. (1985), “A unified approach to finite deformation elastoplastic analysis based on the use of hyperelastic constitutive equations”, *Computer Methods in Applied Mechanics and Engineering*, Elsevier, Vol. 49 No. 2, pp. 221–245.

Simo, J.C. and Taylor, R.L. (1985), “Consistent tangent operators for rate-independent elastoplasticity”, *Computer Methods in Applied Mechanics and Engineering*, Elsevier, Vol. 48 No. 1, pp. 101–118.

Siruguet, K. and Leblond, J.-B. (2004a), “Effect of void locking by inclusions upon the plastic behavior of porous ductile solids-part II: theoretical modeling and numerical study of void coalescence”, *International Journal of Plasticity*, Elsevier, Vol. 20 No. 2, pp. 255–268.

Siruguet, K. and Leblond, J.-B. (2004b), “Effect of void locking by inclusions upon the plastic behavior of porous ductile solids-I: theoretical modeling and numerical study of void growth”, *International Journal of Plasticity*, Elsevier, Vol. 20 No. 2, pp. 225–254.

Sobolev, S.L. (1962), “Cubature Formulas on the Sphere Invariant under Finite Groups of Rotations”, edited by Demidenko, G. v and Vaskevich, V.L.*Dokl. Akad. Nauk SSSR*, Springer US, Boston, MA, Vol. 146 No. 2, pp. 310–313, doi: 10.1007/978-0-387-34149-1_21.

Song, J.-H., Wang, H. and Belytschko, T. (2008), “A comparative study on finite element methods for dynamic fracture”, *Computational Mechanics*, Springer, Vol. 42 No. 2, pp. 239–250.

de Souza Neto, E.A., Peric, D. and Owen, D.R.J. (2011), *Computational Methods for Plasticity: Theory and Applications*, John Wiley & Sons.

Spitzig, W.A., Smelser, R.E. and Richmond, O. (1988), “The evolution of damage and fracture in iron compacts with various initial porosities”, *Acta Metallurgica*, Elsevier, Vol. 36 No. 5, pp. 1201–1211.

Steglich, D. and Brocks, W. (1997), “Micromechanical modelling of the behaviour of ductile materials including particles”, *Computational Materials Science*, Elsevier, Vol. 9 No. 1–2, pp. 7–17.

Steglich, D., Siegmund, T. and Brocks, W. (1999), “Micromechanical modeling of damage due to particle cracking in reinforced metals”, *Computational Materials Science*, Elsevier, Vol. 16 No. 1–4, pp. 404–413.

Steglich, D., Wafai, H. and Besson, J. (2010), "Interaction between anisotropic plastic deformation and damage evolution in Al 2198 sheet metal", *Engineering Fracture Mechanics*, Elsevier, Vol. 77 No. 17, pp. 3501–3518.

Steinmann, P., Kuhl, E. and Stein, E. (1998), "Aspects of non-associated single crystal plasticity: influence of non-Schmid effects and localization analysis", *International Journal of Solids and Structures*, Elsevier, Vol. 35 No. 33, pp. 4437–4456.

Stewart, J.B. (2009), *Development of Yield Criteria for Describing the Behavior of Porous Metals with Tension-Compression Asymmetry*, PhD Thesis, University of Florida.

Stewart, J.B. and Cazacu, O. (2011), "Analytical yield criterion for an anisotropic material containing spherical voids and exhibiting tension-compression asymmetry", *International Journal of Solids and Structures*, Elsevier Ltd, Vol. 48 No. 2, pp. 357–373, doi: 10.1016/j.ijsolstr.2010.10.009.

Stroh, A.N. (1954), "The formation of cracks as a result of plastic flow", *Proceedings of the Royal Society of London. Series A. Mathematical and Physical Sciences*, The Royal Society London, Vol. 223 No. 1154, pp. 404–414.

Sumikawa, S., Ishiwatari, A., Hiramoto, J. and Urabe, T. (2016), "Improvement of springback prediction accuracy using material model considering elastoplastic anisotropy and Bauschinger effect", *Journal of Materials Processing Technology*, Elsevier, Vol. 230, pp. 1–7.

Suquet, P. (1982), *Plasticité et Homogénéisation*, PhD Thesis, Université Pierre et Marie Curie, Paris VI.

Swift, H.W. (1952), "Plastic instability under plane stress", *Journal of the Mechanics and Physics of Solids*, Pergamon, Vol. 1 No. 1, pp. 1–18, doi: 10.1016/0022-5096(52)90002-1.

Szabó, L. and Jonas, J.J. (1995), "Consistent tangent operator for plasticity models based on the plastic strain rate potential", *Computer Methods in Applied Mechanics and Engineering*, Elsevier, Vol. 128 No. 3–4, pp. 315–323.

Tan, M.J., Zhu, X.J. and Thiruvarudchelvan, S. (2007), "Cavitation phenomenon of commercially pure titanium", *Journal of Materials Processing Technology*, Elsevier, Vol. 191 No. 1–3, pp. 202–205.

Tari, D.G., Worswick, M.J., Ali, U. and Gharghouri, M.A. (2014), "Mechanical response of AZ31B magnesium alloy: Experimental characterization and material modeling considering proportional loading at room temperature", *International Journal of Plasticity*, Elsevier, Vol. 55, pp. 247–267.

Tasan, C.C., Hoefnagels, J.P.M., Ten Horn, C. and Geers, M.G.D. (2009), "Experimental analysis of strain path dependent ductile damage mechanics and forming limits", *Mechanics of Materials*, Elsevier, Vol. 41 No. 11, pp. 1264–1276.

Taylor, G.I. (1938), "Plastic strain in metals", *J. Inst. Metals*, Vol. 62, pp. 307–324.

Tekkaya, A.E., Bouchard, P.-O., Bruschi, S. and Tasan, C.C. (2020), "Damage in metal forming", *CIRP Annals*, Elsevier.

Tekoğlu, C., Hutchinson, J.W. and Pardoen, T. (2015), "On localization and void coalescence as a precursor to ductile fracture", *Philosophical Transactions of the Royal Society A: Mathematical,*

Physical and Engineering Sciences, The Royal Society Publishing, Vol. 373 No. 2038, p. 20140121.

Thomason, P.F. (1985), "A three-dimensional model for ductile fracture by the growth and coalescence of microvoids", *Acta Metallurgica*, Vol. 33 No. 6, pp. 1087–1095, doi: https://doi.org/10.1016/0001-6160(85)90202-0.

Thomason, P.F. (1990), "Ductile fracture of metals", *Pergamon Press Plc, Ductile Fracture of Metals(UK), 1990,* p. 219.

Thompson, A.W. and Williams, J.C. (1978), "Nuclei for ductile fracture in titanium", *Advances in Research on the Strength and Fracture of Materials*, pp. 343–348.

Thoré, P., Pastor, F. and Pastor, J. (2011), "Hollow sphere models, conic programming and third stress invariant", *European Journal of Mechanics-A/Solids*, Elsevier, Vol. 30 No. 2, pp. 63–71.

Tipper, C.F. (1949), "The fracture of metals", *Metallurgia*, Vol. 39 No. 231, pp. 133–137.

Tome, C.N. and Lebensohn, R.A. (2023), *Material Modeling with the Visco-Plastic Self-Consistent (VPSC) Approach: Theory and Practical Applications*, Elsevier.

Torki, M.E., Benzerga, A.A. and Leblond, J.-B. (2015), "On void coalescence under combined tension and shear", *Journal of Applied Mechanics*, American Society of Mechanical Engineers Digital Collection, Vol. 82 No. 7.

Torki, M.E., Tekoğlu, C., Leblond, J.-B. and Benzerga, A.A. (2017), "Theoretical and numerical analysis of void coalescence in porous ductile solids under arbitrary loadings", *International Journal of Plasticity*, Vol. 91, pp. 160–181, doi: https://doi.org/10.1016/j.ijplas.2017.02.011.

Trillat, M. and Pastor, J. (2005), "Limit analysis and Gurson's model", *European Journal of Mechanics-A/Solids*, Elsevier, Vol. 24 No. 5, pp. 800–819.

Tuninetti, V., Gilles, G., Milis, O., Pardoen, T. and Habraken, A.-M. (2015), "Anisotropy and tension–compression asymmetry modeling of the room temperature plastic response of Ti–6Al–4V", *International Journal of Plasticity*, Elsevier, Vol. 67, pp. 53–68.

Tvergaard, V. (1981), "Influence of voids on shear band instabilities under plane strain conditions", *International Journal of Fracture*, Springer, Vol. 17 No. 4, pp. 389–407.

Tvergaard, V. (1982a), "Material failure by void coalescence in localized shear bands", *International Journal of Solids and Structures*, Elsevier, Vol. 18 No. 8, pp. 659–672.

Tvergaard, V. (1982b), "On localization in ductile materials containing spherical voids", *International Journal of Fracture*, Springer, Vol. 18 No. 4, pp. 237–252.

Tvergaard, V. (1987), "Effect of yield surface curvature and void nucleation on plastic flow localization", *Journal of the Mechanics and Physics of Solids*, Elsevier, Vol. 35 No. 1, pp. 43–60.

Tvergaard, V. (1989), "Material failure by void growth to coalescence", *Advances in Applied Mechanics*, Elsevier, Vol. 27, pp. 83–151.

Tvergaard, V. (2012), "Effect of stress-state and spacing on voids in a shear-field", *International Journal of Solids and Structures*, Elsevier, Vol. 49 No. 22, pp. 3047–3054.

Tvergaard, V. and Hutchinson, J.W. (1992), "The relation between crack growth resistance and fracture process parameters in elastic-plastic solids", *Journal of the Mechanics and Physics of Solids*, Vol. 40 No. 6, pp. 1377–1397, doi: https://doi.org/10.1016/0022-5096(92)90020-3.

Tvergaard, V. and Needleman, A. (1984), "Analysis of the cup-cone fracture in a round tensile bar", *Acta Metallurgica*, Pergamon, Vol. 32 No. 1, pp. 157–169, doi: 10.1016/0001-6160(84)90213-X.

Tvergaard, V. and Needleman, A. (1995), "Effects of nonlocal damage in porous plastic solids", *International Journal of Solids and Structures*, Elsevier, Vol. 32 No. 8–9, pp. 1063–1077.

Tvergaard, V., Needleman, A. and Lo, K.K. (1981), "Flow localization in the plane strain tensile test", *Journal of the Mechanics and Physics of Solids*, Elsevier, Vol. 29 No. 2, pp. 115–142.

Vadillo, G., Reboul, J. and Fernández-Sáez, J. (2016), "A modified Gurson model to account for the influence of the Lode parameter at high triaxialities", *European Journal of Mechanics - A/Solids*, Vol. 56, pp. 31–44, doi: https://doi.org/10.1016/j.euromechsol.2015.09.010.

Venables, J.A. (1961), "Deformation twinning in face-centred cubic metals", *Philosophical Magazine*, Taylor & Francis, Vol. 6 No. 63, pp. 379–396.

Vincent, P.-G., Monerie, Y. and Suquet, P. (2009), "Porous materials with two populations of voids under internal pressure: I. Instantaneous constitutive relations", *International Journal of Solids and Structures*, Elsevier, Vol. 46 No. 3–4, pp. 480–506.

Vitek, V., Mrovec, M. and Bassani, J.L. (2004), "Influence of non-glide stresses on plastic flow: from atomistic to continuum modeling", *Materials Science and Engineering: A*, Elsevier, Vol. 365 No. 1–2, pp. 31–37.

Vitek, V., Mrovec, M., Gröger, R., Bassani, J.L., Racherla, V. and Yin, L. (2004), "Effects of non-glide stresses on the plastic flow of single and polycrystals of molybdenum", *Materials Science and Engineering: A*, Elsevier, Vol. 387, pp. 138–142.

Vladimirov, I.N., Pietryga, M.P. and Reese, S. (2008), "On the modelling of non-linear kinematic hardening at finite strains with application to springback—Comparison of time integration algorithms", *International Journal for Numerical Methods in Engineering*, John Wiley & Sons, Ltd, Vol. 75 No. 1, pp. 1–28, doi: https://doi.org/10.1002/nme.2234.

Voce, E. (1948), "The relationship between stress and strain for homogeneous deformation", *Journal of the Institute of Metals*, Vol. 74, pp. 537–562.

Voyiadjis, G.Z. (2015), *Handbook of Damage Mechanics: Nano to Macro Scale for Materials and Structures*, Springer.

Weber, G. and Anand, L. (1990), "Finite deformation constitutive equations and a time integration procedure for isotropic, hyperelastic-viscoplastic solids", *Computer Methods in Applied Mechanics and Engineering*, Elsevier, Vol. 79 No. 2, pp. 173–202.

Weck, A., Wilkinson, D.S., Maire, E. and Toda, H. (2008), "Visualization by X-ray tomography of void growth and coalescence leading to fracture in model materials", *Acta Materialia*, Elsevier, Vol. 56 No. 12, pp. 2919–2928.

Wen, J., Huang, Y., Hwang, K.C., Liu, C. and Li, M. (2005), "The modified Gurson model accounting for the void size effect", *International Journal of Plasticity*, Elsevier, Vol. 21 No. 2, pp. 381–395.

Wierzbicki, T., Bao, Y., Lee, Y.-W. and Bai, Y. (2005), "Calibration and evaluation of seven fracture models", *International Journal of Mechanical Sciences*, Elsevier, Vol. 47 No. 4–5, pp. 719–743.

Wilner, B. (1988), "Stress analysis of particles in metals", *Journal of the Mechanics and Physics of Solids*, Elsevier, Vol. 36 No. 2, pp. 141–165.

Wilsdorf, H.G.F. (1983), "The ductile fracture of metals: a microstructural viewpoint", *Materials Science and Engineering*, Elsevier, Vol. 59 No. 1, pp. 1–39.

Womersley, R.S. (2017), "Efficient spherical designs with good geometric properties", available at: https://web.maths.unsw.edu.au/~rsw/Sphere/EffSphDes/index.html (accessed 26 October 2022).

Womersley, R.S. (2018), "Efficient spherical designs with good geometric properties", *Contemporary Computational Mathematics-A Celebration of the 80th Birthday of Ian Sloan*, Springer, pp. 1243–1285.

Won, J.W., Kim, D., Hong, S.-G. and Lee, C.S. (2016), "Anisotropy in twinning characteristics and texture evolution of rolling textured high purity alpha phase titanium", *Journal of Alloys and Compounds*, Elsevier, Vol. 683, pp. 92–99.

Wu, S.J., Davis, C.L., Shterenlikht, A. and Howard, I.C. (2005), "Modeling the ductile-brittle transition behavior in thermomechanically controlled rolled steels", *Metallurgical and Materials Transactions A*, Vol. 36 No. 4, pp. 989–997, doi: 10.1007/s11661-005-0292-z.

Xia, L. and Shih, C.F. (1995a), "Ductile crack growth-I. A numerical study using computational cells with microstructurally-based length scales", *Journal of the Mechanics and Physics of Solids*, Elsevier, Vol. 43 No. 2, pp. 233–259.

Xia, L. and Shih, C.F. (1995b), "Ductile crack growth-II. Void nucleation and geometry effects on macroscopic fracture behavior", *Journal of the Mechanics and Physics of Solids*, Elsevier, Vol. 43 No. 12, pp. 1953–1981.

Xiao, H., Bruhns, O.T. and Meyers, A. (1997), "Hypo-elasticity model based upon the logarithmic stress rate", *Journal of Elasticity*, Springer, Vol. 47, pp. 51–68.

Xiao, H., Bruhns, O.T. and Meyers, A. (2006), "Elastoplasticity beyond small deformations", *Acta Mechanica*, Springer, Vol. 182 No. 1–2, pp. 31–111.

Xue, L. (2008), "Constitutive modeling of void shearing effect in ductile fracture of porous materials", *Engineering Fracture Mechanics*, Pergamon, Vol. 75 No. 11, pp. 3343–3366, doi: 10.1016/J.ENGFRACMECH.2007.07.022.

Xue, Z., Pontin, M.G., Zok, F.W. and Hutchinson, J.W. (2010), "Calibration procedures for a computational model of ductile fracture", *Engineering Fracture Mechanics*, Elsevier, Vol. 77 No. 3, pp. 492–509.

Yamamoto, H. (1978), "Conditions for shear localization in the ductile fracture of void-containing materials", *International Journal of Fracture*, Springer, Vol. 14 No. 4, pp. 347–365.

Yang, Y.F., He, Z.R., Ma, J., Yang, H., Min, J.Y., Zang, S.L. and Li, H. (2022), "Evolving asymmetric and anisotropic hardening of CP-Ti sheets under monotonic and reverse loading: Characterization and modeling", *International Journal of Plasticity*, Vol. 159, p. 103445, doi: https://doi.org/10.1016/j.ijplas.2022.103445.

Yi, N., Hama, T., Kobuki, A., Fujimoto, H. and Takuda, H. (2016), "Anisotropic deformation behavior under various strain paths in commercially pure titanium grade 1 and grade 2 sheets", *Materials Science and Engineering: A*, Elsevier, Vol. 655, pp. 70–85.

Yoon, J., Cazacu, O. and Mishra, R.K. (2013), "Constitutive modeling of AZ31 sheet alloy with application to axial crushing", *Materials Science and Engineering: A*, Elsevier, Vol. 565, pp. 203–212.

Yoon, J.-H., Cazacu, O. and Yoon, J.W. (2011), "Strain-rate potential based elastic/plastic anisotropic model for metals displaying tension–compression asymmetry", *Computer Methods in Applied Mechanics and Engineering*, Elsevier, Vol. 200 No. 23–24, pp. 1993–2004.

Yoon, J.-H., Cazacu, O., Yoon, J.W. and Dick, R.E. (2010), "Earing predictions for strongly textured aluminum sheets", *International Journal of Mechanical Sciences*, Elsevier, Vol. 52 No. 12, pp. 1563–1578.

Yoon, J.H., Stewart, J.B. and Cazacu, O. (2011), "Coupled elastic-plastic damage model for a porous aggregate with an incompressible matrix displaying tension-compression asymmetry", *Engineering Fracture Mechanics*, Elsevier Ltd, Vol. 78 No. 7, pp. 1407–1423, doi: 10.1016/j.engfracmech.2011.03.003.

Yoon, J.-W., Barlat, F., Dick, R.E., Chung, K. and Kang, T.J. (2004), "Plane stress yield function for aluminum alloy sheets—part II: FE formulation and its implementation", *International Journal of Plasticity*, Elsevier, Vol. 20 No. 3, pp. 495–522.

Yoon, J.W., Song, I.S., Yang, D.-Y., Chung, K. and Barlat, F. (1995), "Finite element method for sheet forming based on an anisotropic strain-rate potential and the convected coordinate system", *International Journal of Mechanical Sciences*, Elsevier, Vol. 37 No. 7, pp. 733–752.

Zeng, X.-H. and Ericsson, T. (1996), "Anisotropy of elastic properties in various aluminium-lithium sheet alloys", *Acta Materialia*, Elsevier, Vol. 44 No. 5, pp. 1801–1812.

Zhai, J., Luo, T., Gao, X., Graham, S.M., Baral, M., Korkolis, Y.P. and Knudsen, E. (2016), "Modeling the ductile damage process in commercially pure titanium", *International Journal of Solids and Structures*, Elsevier, Vol. 91, pp. 26–45.

Zhang, K.S., Bai, J.B. and François, D. (2001), "Numerical analysis of the influence of the Lode parameter on void growth", *International Journal of Solids and Structures*, Vol. 38 No. 32, pp. 5847–5856, doi: https://doi.org/10.1016/S0020-7683(00)00391-7.

Zhang, P., Duan, Q.Q., Li, S.X. and Zhang, Z.F. (2008), "Cyclic deformation and fatigue cracking behaviour of polycrystalline Cu, Cu–10 wt% Zn and Cu–32 wt% Zn", *Philosophical Magazine*, Taylor & Francis, Vol. 88 No. 16, pp. 2487–2503.

Zhou, J., Gao, X., Sobotka, J.C., Webler, B.A. and Cockeram, B. V. (2014), "On the extension of the Gurson-type porous plasticity models for prediction of ductile fracture under shear-dominated

conditions", *International Journal of Solids and Structures*, Vol. 51 No. 18, pp. 3273–3291, doi: https://doi.org/10.1016/j.ijsolstr.2014.05.028.

Zhou, Y., Jonas, J.J., Savoie, J., Makinde, A. and MacEwen, S.R. (1998), "Effect of texture on earing in FCC metals: finite element simulations", *International Journal of Plasticity*, Elsevier, Vol. 14 No. 1–3, pp. 117–138.

Zi, G. and Belytschko, T. (2003), "New crack-tip elements for XFEM and applications to cohesive cracks", *International Journal for Numerical Methods in Engineering*, Wiley Online Library, Vol. 57 No. 15, pp. 2221–2240.

Ziegler, H. (1977), *An Introduction to Thermodynamics*, North-Holland Publishing Company.

Zienkiewicz, O.C. and Taylor, R.L. (2005), *The Finite Element Method for Solid and Structural Mechanics*, Elsevier.